Available online at www.sciencedirect.com

ScienceDirect

Procedia IUTAM 26 (2018) 1–2

Procedia IUTAM

www.elsevier.com/locate/procedia

IUTAM Symposium Wind Waves, 4-8 September 2017, London, UK

Preface

Roger Grimshaw[a], Julian Hunt[a], Edward Johnson[a]

[a]*Department of Mathematics, University College London, London, WC1E 6BT, UK*

1. Background

Wind-driven water waves play an essential role, both on the large scale ocean dynamics, with implications for weather and climate, and on the local scale where they affect transfer processes across the ocean-atmosphere interface, including extreme forces on marine structures, ships and submersibles. After 150 years of research, the dynamics of ideal linear and nonlinear waves, including their interaction and their evolution are broadly understood, although only recently have extremely large waves been identified through observations and in laboratory experiments. There are still conflicting theories, however, about how wind generates waves, and there are only tentative theories about how wind forces affect the dynamics of extreme waves and wave groups. Current research on wind-wave dynamics by the proposers, and by other groups, is focussing on what is still a major question for water waves, namely, how in the presence of wind, do they form into characteristic groups (with or without white caps) and what are their essential properties, depending on the local atmospheric and oceanic conditions. The prediction of extreme events, such as rogue waves in the open ocean, or in shallow water, and waves driven by tropical cyclones, is becoming of increasing concern due to effects induced by climate change. Further, wind-driven waves, especially through their effect on small-scale motions and turbulence near the surface, need to be better understood in order to improve predictions of heat and mass transfer at the atmosphere-ocean interface, essential for the development of climate models. Improved satellite observations and laboratory experiments are now becoming available to guide theoretical and modeling progress. Also, the general theme of transfer processes across a gas-liquid interface is relevant for flows in large pipes.

2. Symposium

The IUTAM Symposium took place at University College London (UCL) from September 4-8 2017 with the theme “Research on wind wave groups, applications to improved ocean wave modelling, and estimation of wave hazards”. This brought together theoreticians, numerical modellers, experimentalists and end-users in a forum where the latest research developments were presented, provided an environment with constructive interchanges, and with the outcome that clear directions were established for future research, and for the implementation of research advances into operational use. All sessions were held in the seminar room in the Mathematics Department at UCL, and all lunches, tea/coffee breaks and the reception were held in an adjacent room on the same floor. This enabled a relaxed environment where as well as the scientific talks there was ample opportunity for informal discussions. A special

E-mail address: r.grimshaw@ucl.ac.uk

Peer-review under responsibility of the scientific committee of the IUTAM Symposium Wind Waves.
10.1016/j.piutam.2018.03.001

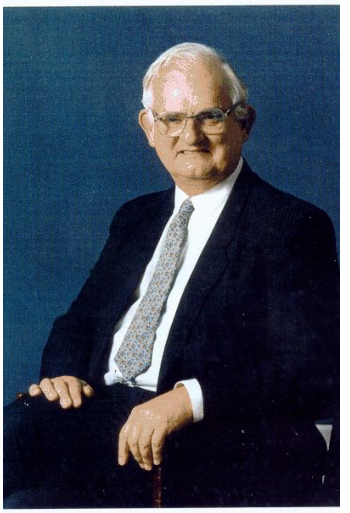

Sir James Lighthill
(1924 - 1998)

feature was the Lighthill lecture honouring the contribution of the eminent applied mathematician and fluid dynamicist Sir James Lighthill, who made profound contributions to wind wave research amongst his many accomplishments and was Provost at UCL 1979-1989.

There were 5 plenary talks and 41 contributed talks. The plenary talks were:

- Peter Janssen: Progress in operational wave forecasting
- Julian Hunt: (Lighthill Lecture) Mechanisms and modeling of wind-driven waves
- Guillemette Caulliez: Wind wave evolution observed in a large wind-wave tank: statistical wave properties, wave groups and wave breaking
- Ken Melville: Wind-wave breaking
- Vladimir Zakharov: Analytic Theory of Wind Driven Sea

Some highlights of the symposium were:

- Robust discussion of generation mechanisms, with some agreement about the importance of wave groups, either directly or by the necessity to consider non-monochromatic waves.
- Demonstration in laboratory experiments of the rapid development of fully two-dimensional (horizontally) wave fields, from uni-directional wind forcing.
- Role of wave-breaking in the formation and maintenance of wave groups, and through observations and numerical simulations the development of universal scaling laws for dissipation due to breaking.
- The increased capacity of DNS and LES simulations to study the air flow over wind waves in great detail, although the analogous capacity for two-phase (air and water) simulations is still in a developmental stage.
- The increased understanding and potential importance of rogue waves, not just for impact on shipping and marine structures, but for a full understanding of the wave spectrum.
- Wide range of applications for wind-wave forecasting, including surf conditions and tropical cyclone forecasts
- Importance and lack of current knowledge of the directionally of the fully-developed wind wave sea.

These proceedings contain articles emanating from four of the plenary talks, in alphabetical order of the first author, and a further sixteen articles, also in alphabetical order, emanating from the contributed talks. Altogether representing the flavour of the meeting.

Available online at www.sciencedirect.com

ScienceDirect

Procedia IUTAM 26 (2018) 3–13

Procedia IUTAM

www.elsevier.com/locate/procedia

IUTAM Symposium Wind Waves, 4-8 September 2017, London, UK

Mechanisms And Modelling of Wind Driven Waves

J.C.R. Hunt[a], S.G. Sajjadi[b]

[a]*University College London, UK.*
[b]*Embry-Riddle Aeronautical University, Florida, USA.*

Abstract

This paper reviews (in qualitative and order of magnitude terms) the main mechanisms determining wind driven waves and their quantitative modelling for the different stages as the wind speed and the Reynolds number both increase, initially through coupling the instability 'waves' in the laminar boundary layers above and below the water surface, secondarily through initiation of eddy structures in turbulent boundary flow over flat water surface ('cats paws') and thirdly as distorted airflow passes over the undulating water surface with different kinds of dynamics, wave shapes (ranging from sinusoidal to pointed forms), amplitude H, wavelength L, travelling at speed c_r and growth rate c_i/U_*, coupled with the flow below the water surface. Significant flow features are the turbulent thin shear layers on the surface and detached 'critical' layers above the surface, which are also affected by the variation of surface roughness near the crests of the waves, by recirculating, separated flows near the surface and by high gradients of turbulence structure in the detached critical layers. Two phase flows in the recirculation zones on the lee side of waves leads to spray in the air above the water surface which also amplifies the boundary layer turbulence. Two phase bubbly flows below the surface generate near surface bubbles and may increases the surface drag downstream of the wave crests. The topology of node and saddle singular points in these mean recirculating flows provides a kinematic description of these flows. Idealised dynamical studies are presented of the variation of the wave amplitude through wind forces on waves moving in groups of waves, and thence physical models are proposed for the transfer of wave energy between large and small frequencies and length scales of wave spectra.

Peer-review under responsibility of the scientific committee of the IUTAM Symposium Wind Waves.

Keywords: Type your keywords here, separated by semicolons ;

1. Introduction

The basic forms of inertial-gravity waves are those that are produced at flat air-water surfaces by unsteady forces below the surface, the basic type being the waves driven by oscillating paddles in laboratory water tanks, that are initially unidirectional and monochromatic. These were first analysed by Stokes (see e.g. Lamb 1932). Different kinds of growing water waves on initially flat water surfaces are produced when air flow with mean velocity Uo passes over

* Corresponding author. Tel.: +0-000-000-0000 ; fax: +0-000-000-0000.
E-mail address: julian.hunt@ucl.ac.uk

2210-9838
Peer-review under responsibility of the scientific committee of the IUTAM Symposium Wind Waves.
10.1016/j.piutam.2018.03.002

the water surface, causing small viscous and larger turbulent shear stresses at the air-water interface which couple the air and water motions above and below this level (Hunt *et al.* 2010). The forms of these wind driven waves depend on the relative speed c_r/U, and the Reynolds number $Re = U_0 L/\nu$.

There are several stages in the non-linear development of these basic types of surface wave, which are associated with growing amplitude of the waves (defined by the ratio of their heights to lengths H/L) and their interactions.

As inertial-gravity waves grow in amplitude, provided viscous stresses are small (i.e. $Re \gg 1$), certain small fluctuations of wave shape develop and persist in the direction of the propagating wave. The most significant of these finite slope and persistent forms are 'fully non-linear Stokes' waves with steep crests and troughs with low slopes, (Longuet-Higgins 1978, Sajjadi 1988). The other kinds of non-linear waves are where there are two or more distinct types of wave with different wave lengths and frequencies, as discovered by Benjamin & Feir (1967). With larger amplitude and greater distances, these types of waves form wave groups with larger and smaller wave lengths travelling at different speeds. Following Hasselman (1962), Longuet-Higgins (1962), Phillips (1977) these interactions can be described by the changes to the energy spectrum of the waves. With further growth the interactions affect the gradients of the wave surface, and typically smaller breaking waves within larger groups (Longuet-Higgins & Turner 1974).

This paper first reviews briefly how small waves grow from small stresses into larger waves, and then for monochromatic and Stokes waves how the wave structure changes as a result of wind-wave interactions. Finally we consider how wave groups affect the wind structure over the waves, which can lead to a significant transfer of energy from the wind to the waves, their related turbulent boundary-layer flows, and thin recirculating shear layers close to and above the wave surfaces. Sharp variations in the distortion of turbulence also occur within and outside these layers. By extension, the study of these fluid-dynamical problems contributes to our fundamental understanding of mechanisms that occur in wave dominated environmental and engineering flows of many kinds. For example improvements to the modelling of wind -driven ocean waves have led to improved forecasts of ocean waves, which typically have global rms errors of 0.6 m (Fuller & Kellett 1997), which is only about 15-20% of the rms wave height. These errors increase systematically when large waves are forecast, when the waves are not forced locally by wind, and when the mean wind conditions are changing.

An important feature of turbulent boundary-layer flow over waves is that the boundary layer is distorted over a horizontal length scale, L, that is comparable to, or shorter than, the depth of the boundary layer, h, so that a large fraction of the depth of the boundary layer does not have time to come into equilibrium during the distortion. This significantly affects the turbulent stresses, as will be explained in section 3. In this paper we explain how various aspects of the changes in the flow over hills and waves vary across different parts of the flow by identifying the largest terms in the equations governing the mean dynamics, as well as the main mechanisms and timescales that govern perturbations to the turbulence. We also review the ways in which various approaches to modeling these aspects are being used for research and for practical problems involving environmental flows. Atmospheric flows are signicantly accelerated over the tops of waves and hills even when the maximum slopes are quite small, because shear in the approaching wind amplies this acceleration (Belcher & Hunt 1998).

The bulk effect of flow over waves is to increase the drag of the surface on the large-scale atmospheric motion. Some of the mean streamlines are determined both by the accelerating/decelerating wind over wave surfaces, and by recirculating flow in the wake regions. Furthermore, turbulence in the flow is greatly changed in the wake. Together these changes to the mean flow and turbulence affect mixing and exchange processes. Research and forecasting models of ocean waves have been guided by the theory of wind-wave generation proposed by Miles (1957) and by Hasselmanns(1962) theory of weakly nonlinear transfer of energy between waves of different wavelength (e.g. Komen *et al.* 1994). We highlight here recent research developments, including those that remain controversial.

Turbulent momentum transfer across a flat gas-liquid interface depends on the interactions between shear-free turbulence in the two regions (denoted as +, −) on either side of the nearly flat horizontal interface. These are controlled by mechanisms, which depend on the magnitudes of the ratios $s = \rho_+/\rho_-, \nu = \nu_+/\nu_-, \gamma = u_{0+}/u_{0-}$ of the densities and viscosities of the fluids and the r.m.s. velocities of the turbulence u_{0+}, u_{0-} above and below the interface (Belcher *et al.* 2005).

This study focuses on situations where γ is very large or very small, and where the interface is nearly flat, so that coupling between turbulence on either side of the interface is determined by viscous stresses. Linearized rapid-distortion theory (RDT) with viscous effects has been developed by extending the previous studies of shear-free

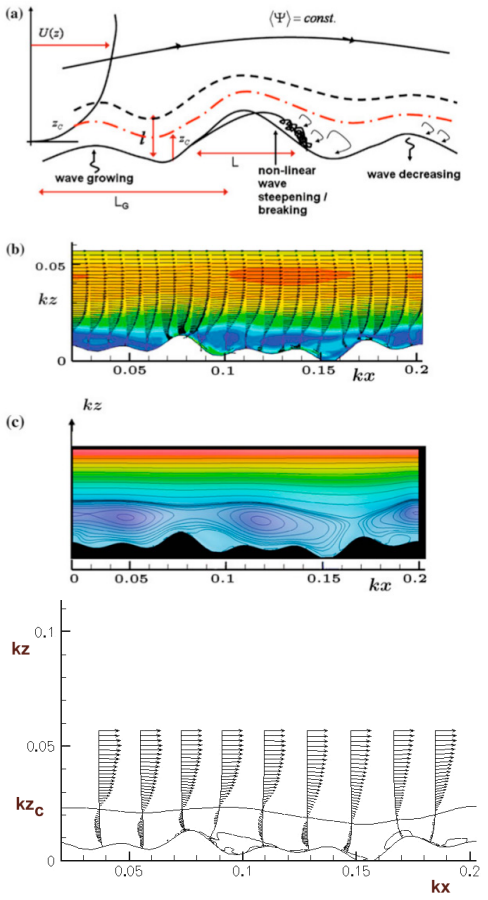

Fig. 1. From top to bottom: Top: (a) schematic of asymmetric wind flow over wave groups showing separation and changing behaviour of critical layer. Note the growing/decreasing wave amplitude in the group. This increases critical height $z_c(\ )$ on the downwind side of a group $\propto H$ where the wave shape changes. Second from the top (b) and second from the bottom (c): computations of turbulent flows over wave groups: (b) mean velocity, (c) mean streamlines relative to average velocity of the waves. Bottom: (d) unsteady critical layer and velocity vectors for (b) and (c).

turbulence near rigid plane boundaries, Hunt & Graham (1978), and over wavy surfaces (Belcher & Hunt 1992, Mastenbroek *et al.* 1996 and Ngata *et al.* 2006). The physical process also includes the blocking effect of the interface on normal components of the turbulence in 'source' layers and the viscous coupling of the horizontal field across thin interfacial viscous boundary layers. The horizontal divergence in the perturbation velocity field in the viscous layer also drives a weak inviscid irrotational velocity fluctuations outside the viscous boundary layers in a mechanism analogous to Ekman pumping.

As with other RDT analyses, the results are formally valid only over distortion times that are small compared with the Lagrangian time scales T_L. They show that

(a) the blocking effects are similar to those near rigid boundaries on each side of the interface, but through the action of the thin viscous layers above and below the horizontal and vertical velocity components differ from those near a rigid surface and are correlated or anti correlated respectively,

(b) the rapid growth of the viscous layers on either side of the interface is also significant so that the ratio of the r.m.s. values of the interfacial velocity fluctuations, u'_+ to that of the homogeneous turbulence far above the interface, u_0, does not vary with time. Note that if the turbulence is driven in the water then ($\gamma \ll 1$).

At the interface the horizontal straining is increased by the blocking, but decreases with time, and also the horizontal component of vorticity decreases with time. Where homogeneous turbulence is generated in the gas, at the shear-free gas-liquid interface ($\gamma \gg 1$), and the interface turbulence is given by $u'_I/u'_0 \sim 1/Re$.

(c) Non-linear interfacial effects are significant for times greater than T_L. When turbulence is generated in the liquid layer, it drives gas motions in the upper viscous layer at a high enough Reynolds number to generate turbulence. In the liquid the eddying motions are mainly determined by the linear blocking mechanism and u_{0+} is of the same order as u_{0-} as shown by Calmet & Magnaudet (2003); but at large times (e.g. in decaying turbulence) the vertical vorticity of the eddies dominates their structure near the interface as it is deformed by the growing viscous layer (Tsai *et al.* 2005).

When shear-free turbulence is generated in the upper layer and if the Reynolds number is less than about $10^6 - 10^7$ the fluctuations in the viscous surface layer do not become turbulent. However if additional fluctuations are stimulated in the lower layer by other mechanisms, such as mean shear, convection, waves, raindrops etc., the non-linear amplification leads to a more intense statistically steady state of turbulence in the liquid below the interface. Either for sheared or shear free turbulence in the gas, there is a large increase of the ratio of u'_I/u_{0+} to $s^{1/2} \sim 1/30$. This agrees with the direct numerical simulation of turbulent flow over a wavy wall reported by De Angelis *et al.* (1997). Even in this case (provided the surface is flat) the linear viscous coupling mechanism is still significant; for example, it ensures that the eddy motions on either side of the interface have a similar horizontal structure, although their vertical structure differs.

A number of mechanisms have been proposed for how air-flow over a horizontal body of liquid produces waves on its surface. Most of those proposed have been linear and therefore can be applied to any spectrum of waves. But the mechanisms and models based on them are regularly applied when the surface disturbances induce gas and liquid flows that are non-linear, and where the waves are not monochromatic. Typically the waves move in groups and the slopes of the water surface may become so large that the waves break and droplets form.

Very small unsteady waves are initiated by turbulence and/or growing Tollmien-Schlichting instabilities in the sheared air flow over the surface and Kelvin-Helmholtz coupled instability of the airflow over the liquid (Tsai *et al.* 2005). However, when steady waves are generated artificially in an airflow, e.g. in a wind-wave tank, the linear mechanisms for the growth of the waves are the pressure drag caused by asymmetric slowing of airflow over the downwind slopes of the waves and turbulence stresses caused by the disturbed flow, and wind-induced variations of surface roughness disturbed surface (Belcher & Hunt,1998). Both mechanisms are affected by the relative speed of the wave c_r to the friction velocity U_* of the airflow, and the disturbed flow changes at the critical height z_c, where the wave speed c_r is equal to the wind speed $U(z_c)$.

When the waves begin to grow at a significant rate kc_i, comparable with U_*k, the critical layer is above the inner shear layer near the surface, and the dynamics across the critical layer are determined by inertial forces as the flow accelerates and decelerates over the wave. If the wave is growing (or decaying), i.e. $|c_i| > 0$, and if the perturbation is finite there is a net force on the wave caused by critical layer dynamics (Belcher *et al.* 1999). But the integral inviscid analysis Miles (1957) for a growing wave, which was explained by Lighthills (1962) inviscid analysis and physical discussion showed that, even when $c_i \to 0$, there is apparently a finite drag force. However the computation of Sajjadi *et al.* (2014) showed that this inviscid limit is associated with an unphysical singular jet on the down-slope face of the wave (which have never been observed by experiments!). But for realistic viscous flows, critical layers of finite strength do form on the slopes and do contribute to the wind driven growth of the wave, typically when $c_i > 0$.

Nevertheless Miles inviscid result about the growth rate of monochromatic waves is still widely assumed to be the dominant mechanism for wind-wave momentum transfer and has been used to correlate data on the growth of wind-generated waves, and became the standard model for ocean wave forecasts (Janssen 2018).

An explanation is outlined below. In section 3 we analyse the combination of how realistic waves develop as a combination the inertial mechanism, and the wind drag mechanism acting together. The latter mechanism is based on the perturbation sheltering theory and computation by Belcher & Hunt (1992) and Mastenbroek *et al.* (1996), which assume c_r is small. But both models under estimate the energy-transfer parameter (being proportional to the wave growth) when c_r is comparable with the mean wind speed, because it does not represent the dynamics of realistic waves which grow and decrease in groups. Analytical models of steadily moving wave-group dynamics have been developed for the laminar/turbulent shear flow (Sajjadi *et al.* 2016), see also by McIntyre (1992).

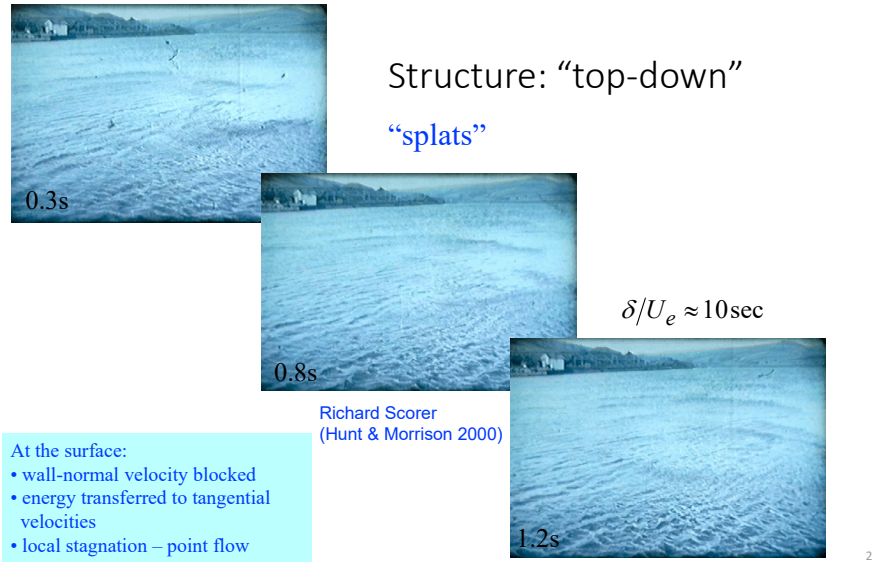

Fig. 2. Turbulent flow in the atmosphere over a flat surface generating ripples and showing gust structure - or ‘cats paws’ (Ref R.S.Scorer in Hunt & Morrison 2000)

Quasi-linear theory shows how individual waves in the group interact with the combined effects of the unsteady critical layer flow, and the viscous /turbulent sheltering on the lee sides of the waves. This wave group analysis can be extended and applied quantitatively or qualitatively to many environmental and industrial problems, and also to estimating heat and mass transfer. Thence by using weakly non-linear theory to analyse the disturbed air flow over the waves in groups, it is shown how the air flow over the downwind part of the group is slower than over the upwind part. This asymmetry causes the critical layer height to be higher where the waves slope downwards. This leads to the critical layer group (CLaG) effect producing a net horizontal force on the waves, in addition to the sheltering effect associated with monochromatic waves. This analysis, which is supported by numerical simulations (Sajjadi *et al.* 2018), shows why the critical layer is present over monochromatic waves but does not produce a net force, despite earlier arguments to the contrary.

Other wave-wind dynamics also affect the wave growth. Whether, as in the photographs by Jeffreys (1925) of wave groups of capillary waves on a Cambridge duck pond or breaking rollers in the Atlantic ocean, the wave shapes as well as their height vary in a group, with their slopes increasing downwind. This is likely to amplify the CLaG mechanism. By considering the dynamics of typical wave groups, it becomes possible to estimate rationally how air flow affects the non-linear interactions between waves, and compare how this relates to the wave-wave hydrodynamic interactions, that are assumed to dominate the distribution of ocean waves. For example variations of wave shapes within a group can also affect the net wave growth (Sajjadi *et al.* 2016) while violent erratic winds can prevent the formation of wave groups, so that wave growth may be reduced. This is observed in the downwind parts of wave groups located near the centre of hurricanes.

Wave group dynamics are particularly affected are also affected by the critical layers when they are located above the surface shear layer (i.e. $c_r > U_*$), where they can act to reduce the sheltering mechanism and reduce the drag

(Sajjadi *et al.* 2018). This contrasts with the upward trend of the drag of slower waves (when $c_r < U_*$) because the critical layer is now located within the shear layer, which increases the sheltering mechanism. Thus the decrease of the growth rate as c_r/U_* increases is partly compensated by the increase in growth rate as waves form into groups at higher wind speeds (which also needs to be modelled). This trend is also limited by the decrease in the sheltering mechanism as z_c increases over the downwind part of a wave group. Moreover, as $c_r = U_*$ increases the cat's-eye becomes larger and become significantly asymmetrical, with a stronger reverse flow below them, see (Sajjadi *et al.* 2014 and 2018).

Mean shear flows above and below gas-liquid interfaces generate turbulence with length scales of the order of that of the shear layer thickness h. Unstable buoyancy fluxes further increases the turbulent energy. But as two dimensional waves, moving parallel to the mean flow, develop on the liquid surface, the turbulence production is increased, through stretching of the vortex lines of the turbulent eddies (Texeira & Belcher 2002). But if elongated eddies are present, their longitudinal component of vorticity is systematically stretched as the flow moves over and under the waves, and steady roll structures are generated in the down wind direction (Belcher & Hunt 1998) These structures are observed in the air flow over rigid wavy surfaces in wind tunnels (Gong *et al.* 1996). Note also that low frequency, low wave number eddy motion can amplify the heat transfer between the gas flow and the surface, e.g. by 20% in the atmosphere Smedman *et al.* (2007). Recirculating and regular Langmuir patterns below liquid wavy surfaces are also driven significant gas shear flow U_* above the surface (Craik & Leibovich 1976) and (Sajjadi & Longuet-Higgins 2017). Their scalar transfer properties are also significant. These organised rolls above or below the surface are non-linearly amplified (i.e. increasing as their strength u/r increases relative to the mean flow) by the presence of the turbulence. As explained by Townsend (1976), extra turbulence is generated where the motions in the rolls impinge on the resistive surface, and less where the motions leave the surface, thus producing stresses parallel to the surface which further drive the roll motions. This explains why extra turbulence ($\sim w_*$) produced by buoyancy below the interface also amplifies the strength of rolls until $w_* > u/r$. Shorter and less coherent roll structures also form on the scale of the waves' lengths if the gas flow amplifies the surface waves sufficiently that they become three-dimensional, (Komori *et al.* 1993, Hunt *et al.* 2003)

2. Various mechanism related to air-sea interactions

We now review some of the mechanisms governing air-sea interface for ideal, non-ideal and group of waves.

2.1. Initial growth of wind driven waves

The growth of fluctuations in low wind speed flows over smooth water surfaces is the mechanism for how waves begin to grow, as shown for by the idealised inviscid flows of Kelvin-Helmholtz model (Lamb 1932). But for realistic, laminar viscous-inertial flows, where the Reynolds number is close to its critical value, the dynamical balance matches smoothly growing, sinusoidal fluctuations grow above and below air water surface Tsai *et al.* (2005) which are similar to the original one sided boundary layer fluctuations on a plane surface.

However when the Reynolds number significantly exceeds the critical value, the atmospheric boundary layer becomes fully turbulent, with characteristic eddy structures (with cats' paws growing as they cause ripples on the surface) and which are associated with well defined, self-similar spectra for large and small length scales. (Hunt & Morrison 2000). In particular the stream-wise wind energy spectrum has the form $kE_{11}(k) \sim U_*^2$, where U_* is the mean friction velocity. These eddy structures are associated with growing wind and pressure fluctuations leading to the growth of wind waves (Phillips 1977). These fluctuations near the water surface disturb the mean profile, as defined by the roughness length z_0.

The dynamics and thermodynamics of the small scale turbulence over wind driven waves are also changed when spray droplets and bubbles are generated above and below the water surface. These changes are especially significant for high intensity Tropical Cyclone winds, (where field measurements were performed by Lixiao *et al.* 2015), and laboratory measurements in a wind-wave tunnel by Iwano *et al.* (2013).

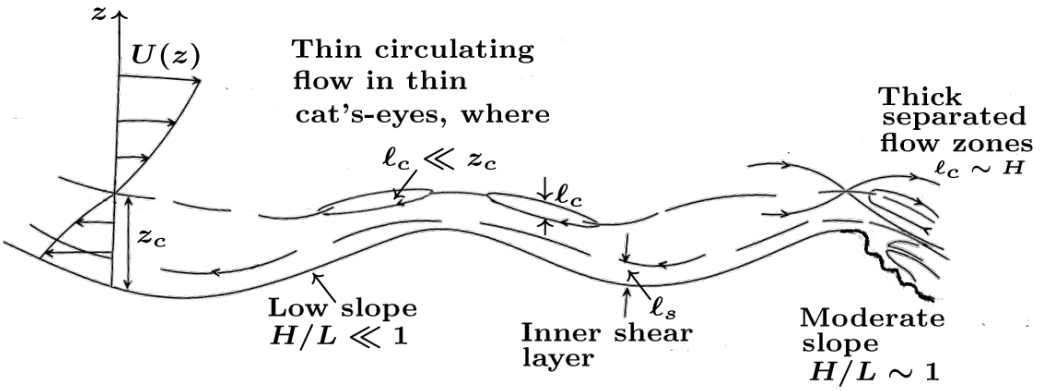

Fig. 3. Schematic diagram showing quasi-steady structure of mean streamlines over wind driven waves, for low and moderate slopes, at high wave speed $c_r \gg U_*$.

2.2. *Turbulent wind over wave trains*

We first consider the turbulent boundary layer above the air-water interface that generates low amplitude,($H \ll L$) travelling waves (with speed c_r) with very low growth rate i.e. $c_i \ll c_r \ll 1$, where

$$\Delta z = H(\exp[ik(x - c_r t) + kc_i t])$$

(see Fig 2). A thin surface shear layer forms with thickness $\ell \sim L/10$, As it passes over the wave surface. Near the surface, the mean profile is disturbed by variations of the surface roughness $z_0(\ll \ell)$ over the wave, typically reaching a maximum near the peak height of the wave surface (Gent & Taylor 1976). This critical cats-eye layer also forms at height z_c where the wind speed is equal to the wave speed, i.e.

$$U(z_c) - c_r = (U_*/\kappa)\ln(z_c/z_0) - c_r = 0.$$

When $z_c < \ell$ (as shown in Fig 2) the thickness ℓ_c of the critical layer is of order z_c, (and much larger than z_0). The phase-averaged turbulent shear stress and inertial dynamics within the surface layer matches the mean distorted flow outside the shear layer, which is determined both by the rapidly distortion eddies and by the inviscid field. Both the inner and outer flow contribute to determine the drag force on the wave surface. Either asymptotic multi-layer turbulence analysis, (Belcher & Hunt 1998), based on the original laminar 'triple deck methods' (Stewartson 1974) or complex Reynolds stress computation methods (Townsend 1972, Sajjadi *et al.* 2001) are used for quantitative results.

Note that at higher wave speeds, when the critical layer is located outside the inner shear layer, i.e. $z_c > \ell$, and the thickness ℓ_c of the layer is less than z_c. The critical layer tends to reduce mean vertical motions below the critical layer – a 'blocking effect'. The analysis by Belcher *et al.* (1999) shows that the drag force on the wave and its growth rate of the waves β tends to decrease as c_r/U_* increases.

3. Growing wave trains and breaking waves

Generally wind forces lead to the growth over time, or distance, of the amplitude H, length L and slope of the waves H/L, resulting from the balance of forces, at, above, and below the surface. The growth also tends to change the shape

of the waves, generally making slopes sharper near the crests and flatter near the troughs. Also, through fundamental instabilities, initially two-dimensional wave trains become three-dimensional. These overall developments also depend on the turbulent shear layer structure of the flow, both above and below the air-water surface, see Fig 3.

Physical understanding of these factors benefits from studies of relations between these general developments, and on improved modelling. For slow wave trains, i.e. $z_c < \ell$, moving with moderate to high slope, i.e. $H/L \gtrsim 1$, separated recirculating flow occurs on the lee slope (Figs 2 and 3). But if $H/L \sim 1$, and the waves are in the form of isolated two or three dimensional structures, then the recirculating wake flows can extend over a significant down wind distance (Jeffreys 1925).

Where waves travel at faster speeds, the elevations of the critical layers increase (i.e. $z_c > \ell$); they also grow in height H and length L, leading to separate and significant recirculating flows developing in the critical layer largely above the lee side, see Fig 3. Conditional sampling (e.g. relative to the maximum height of the wave) shows the distinction between the recirculating flows within the critical layer and separately in the recirculating shear layers that extends above and below the lee-side water surface.

For higher wind speeds, two phase flow physics is needed to model recirculating layers above the water surface which contain droplets and spray.While below the air-water surface there are bubbles produced by air entrained by the breaking wave. These distinct flow patterns were observed in gas-liquid turbulent flow in a pipe by Ayati *et al.* (2016). A new approach for modelling the interface between the highly turbulent shear layer near the water and

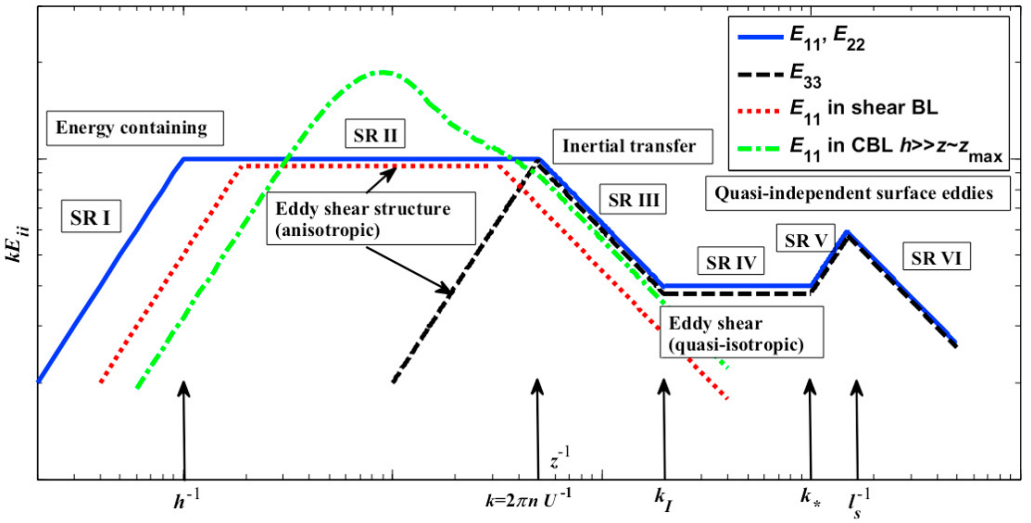

Fig. 4. Spectra of three-dimensional turbulent wind structure in a Tropical Cyclone over coastal area showing small scale energy from spray/wave process (Lixao, *et al.* 2015).

the weaker turbulence in the atmospheric boundary layer could be based on the phase averaged velocity profiles across the high-low intensity turbulent interfaces of separated aerofoil wakes-with application to the eddy wake structure of separated/breaking waves (Szubert *et al.* 2015). Following Lighthill (1963) and Hunt *et al.* (1978), the patterns of these conditionally sampled recirculating mean flows are defined by the points where the local flow is stationary, and defined topologically by saddle point and nodal points, as shown in Fig 3. These 'singular' points can be located in the air and/or water flow (Banner & Melville 1976). Fig 3 also shows how the surface shear stress and the plunging motion of fluid lumps in breaking waves drive the mean recirculation flow below the lee slope (Hunt *et al.* 2003). This process not only amplifies the turbulence and mean shear below the water surface, but also amplifies the streamwise Langmuir circulations, that can reduce the spanwise extent of waves on the surface (Belcher *et al.* 2012).

4. Wind effects on wave groups

Since laboratory driven waves (e.g. Benjamin & Feir 1967), as confirmed by wind driven waves, show that when the amplitude and wave length of monochromatic wave trains exceed a critical level, inertial-buoyancy forces induce wave trains to form into wave groups with amplitude H_G and overall length L_G, while the smaller amplitudes H_C of the component waves rise and fall as they travel through the group. The average speeds of the wave groups C_G are significantly smaller than the average speed C_c of the individual waves within the group (typically about $2C_G$). In such groups the wind flow and surface forces, on the scale of the group L_G, are significantly affected by the amplification and diminution of the wind waves within the group, notably by differing upwind and downwind of the maximum waves. The key point is that because the speed of the component waves within the group $u_{r,C}$ exceeds the wind speed U over the waves in the group, the height of the critical layer z_c exceeds the height of the surface shear layer ℓ.

However unlike the wind over steadily moving monochromatic waves (as analysed in previous sections), the perturbed wind flow above the critical layer (i.e. $z_c > \ell$) increases in amplitude over the component waves on the upwind side of the group over the component waves.They are travelling over the wave at a frequency c_i/L, where typically $c_i \ll U_*$. The amplitudes of the maximum of the wind speed over these unsteady waves in the critical layer at z_c, shown in Fig 1, are larger than for the steady air flow described in section 2.

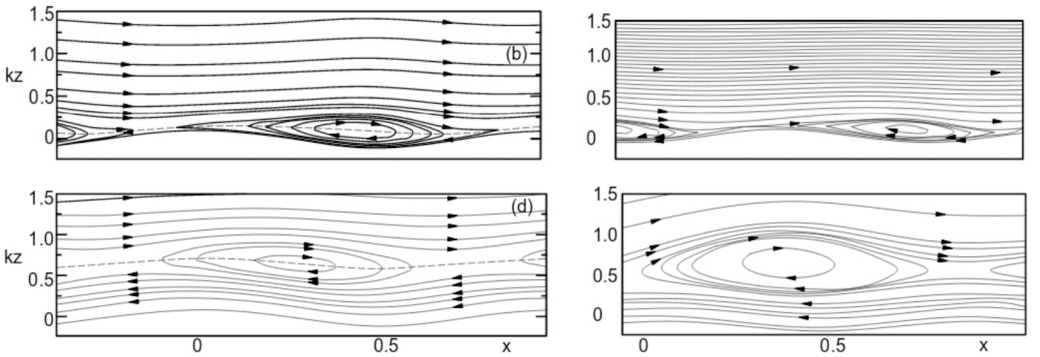

Fig. 5. Phase-averaged streamlines over stationary and moving waves with steepness 0.1. (b) $c/U_* = 3.9$; (d) $c/U_* = 11.5$. The dotted line corresponds to the height of the critical layer where $\langle u \rangle + u_w = 0$. Left diagrams from Sullivan's *et al.* (2000); right diagrams from Sajjadi *et al.* (2017).

But, as shown in Fig 1, on the downwind side of the group in the outer flow (above the critical layer) the mean wind flow is decelerating; also above the critical layer the amplitude of the component waves decrease. This is the reverse of the mechanism that amplifies outer wind speed on the upwind side. But, although there is an overall wind drag produced by the wind over the wave group, the average acceleration of the outer wind flow exceeds the deceleration downwind of the crest of the wave group. This also implies that there is net transfer of large scale wave energy over the scale of the wave group to the energy of the smaller scale 'component' waves within the wave group. This is an idealised analysis for how the different wave lengths and wave amplitudes contribute to the wind-wave process for the transfer between the energy of different spectral components of water waves and the wind field.

Quantitative estimates of the wave group mechanisms can be derived from critical layer dynamics using the eddy viscosity ν_e in the flow at and above the component critical layer $z_{c,C}$. Sajjadi *et al.* (2014) This shows how the component of the perturbed horizontal wind speed $u_{r,C}(x, z)$ is in phase with the deflection of the wave surface and has the profile of a mixed (or tanh) shear layer. This does not affect the net drag (Fig 5). But the wind speed component that is out of phase $u_{i,C}(x, z)$ is in the form of a thin jet on the downwind face of the component wave located at the critical layer height, and leads to the net drag. Alternatively, using the inviscid integral analyses by Miles (1957), Lighthill (1962) the explicit form of the net drag of the 'component' waves in the group can be derived (proportional to the property of the mean profile *viz* $U''(z_c)/(U'(z_c))^3$. Following the explanation in section 3, and Fig 4, the wind wave energy multi-scale transfer process also depends on two phase surface level energy transfer and subsurface turbulence (e.g. Phillips 1977, Hunt *et al.* 2003).

5. Conclusions

This paper has firstly reviewed the characteristic flow of monochromatic wind driven gas-liquid waves in relation to the qualitative and statistical structure of the mean and turbulent air flow above and below the water surface. A key feature of the development of the waves is the changing structure of separate layers with varying inertial and turbulent shear layer dynamics, depending on their Reynolds number and amplitude and length variations. Dissipative processes are an essential part of the dynamics when the wave growth is small. Analytic asymptotic solutions for these layers have been derived which are in the forms of quasi-steady and time dependent perturbations both near the turbulent surface shear layer and in the separate recirculating flows in detached critical layers. Variation of surface roughness also affects shear layers over the waves, which contributes to wave growth. Computation of non-linear turbulent and recirculating flows using new approaches, such as conditional sampling and modal analysis near sharp interfaces, are features of the overlapping flow structures such as recirculating separated flows and turbulent critical layers. We emphasize that the existence of a critical layer over a monochromatic with a significant dynamical role still does not mean that the Miles inviscid mechanism is operative, (Sullivan *et al.* 2000).

The second broad conclusion is that when there is significant growth of wind waves, this is significantly increased when the waves are formed into groups. In this common situation, inviscid theory (built on the Miles and Lighthill concepts) leads to growing individual waves on the upwind part of the wave group and reducing waves downwind of the peak of the wave group (Fig 1). This process leads to a net growth of waves if dissipation processes in the surface shear layers are included approximately in the model. Numerical simulations of wind over wave groups also show positive transfer wind energy to the wave groups. Wave groups are also significant when large and small waves shapes have sharp peaks – as is visible in the wave photograph in Sajjadi *et al.* 2014. This requires further research.

Topological description of critical points are shown to be effective in description and analysis of these different flow regions. These methods can be applied for showing how wind drag forces affect the interactions between larger and smaller waves, and thence can lead to a more physical model for wind effect on wave spectra (Phillips 1977).

Acknowledgements. SGS would like to thank the Trinity College, Cambridge, for their support as a visiting research fellow in the course of this research. We also are grateful for fruitful conversations with P. Janssen, R. Grimshaw and T. Johnson.

References

1. H. Lamb 1932. *Hydrodynamics*. Cambridge University Press. Cambridge.
2. M.S. Longuet-Higgins 1978. On the Dynamics of Steep Gravity Waves in Deep Water. In book: *Turbulent Fluxes Through the Sea Surface, Wave Dynamics, and Prediction*. DOI 10.1007/978 – 1 – 4612 – 9806 – 9 – 14.
3. S.G. Sajjadi SG 1988. Shearing flows over Stokes waves. Department of Mathematics Internal Report, Coventry Polytechnic, UK.
4. T.B Benjamin and J.E. Feir 1967. The disintegration of wave trains on deep water. Part 1. Theory. *J. Fluid Mech.* **27**, 417–430.
5. K. Hasselmann 1962. On the non-linear transfer in a gravity wave spectrum. Part 1. General theory. *J. Fluid Mech.* **12**, 481–500.
6. M.S. Longuet-Higgins 1962. Resonant interactions between two trains of gravity waves. *J. Fluid Mech.* **12**, 321–332.
7. O.M. Phillips 1977. *Dynamics of the upper ocean*. Cambridge University Press.
8. M.S. Longuet-Higgins and J.S. Turner 1974. An "entraining plume" model of spilling breaker. *J. Fluid Mech.* **63**, 1–20.
9. S. Fuller and M.Kellett 1997. *Annual Forecast Verification Statistics 1996*. Bracknell, UK: Meteorological Office.
10. S.E. Belcher and J.C.R. Hunt 1998. Turbulent flow over hills and waves. *Annu. Rev. Fluid Mech.* **30**, 507–538.
11. J.W. Miles 1957. On the generation of surface waves by shear flows. *J. Fluid Mech.* **3**, 185–204.
12. G.J. Komen, L. Cavaleri, M.A. Donelan, K. Hasselmann, S. Hasselmann and P.A.E.M. Janssen 1994. *Dynamics and modelling of ocean waves*. Cambridge University Press, Cambridge.
13. S.E. Belcher, J.N. Hacker and D.S. Powell 2005. Constructing design weather data for future climates. *Building Services Engineering Research And Technology*, **26**, 49-62.
14. J.C.R. Hunt and J.M.R. Graham 1978. Free-stream turbulence near plane boundaries. *J. Fluid Mech.* **84**, 209-235.
15. S.E. Belcher and J.C.R. Hunt 1993. Turbulent shear flow over slowly moving waves. *J. Fluid Mech.* **251**, 109-114.
16. C. Mastenbroek, V.K. Makin, M.H. Garat and J.P. Giovanangeli 1996. Experimental evidence of the rapid distortion of turbulence in air flow over waves. *J. Fluid Mech.*, textbf318, 273-302.
17. K. Nagata, H. Wong, J.C.R. Hunt, S.G. Sajjadi and P.A. Davidson 2006. Weak mean flows induced by anisotropic turbulence impinging onto planar and undulating surfaces. *J. Fluid Mech.*, textbf556, 329-360.
18. I. Calmet and J. Magnaudet 2003. Statistical structure of high-Reynolds-number turbulence close to the free surface of an open-channel flow. *J. Fluid Mech.*, textbf474, 355-378.

19.Y.S. Tsai YS, A.J. Grass and R.R. Simons 2005. On the spatial linear growth of gravity-capillary waves sheared by a laminar flow. *Phys. Fluids*, **17**, 95-101.
20.V. De Angelis, P. Lombardi, and S. Banerjee 1997. Direct numerical simulation of turbulent flow over a wavy wall. *Phys. Fluids*, **9**, 2429. Physics of Fluids 9, 2429 (1997)
21.S.E. Belcher, J.C.R. Hunt and J.E. Cohen 1999. Turbulent flow over growing waves. In *Proceedings of IMA Conference on Wind Over Waves*. Sajjadi, S.G., Thomas, N.H. and Hunt, J.C.R. (eds). Oxford University Press, pp. 19–30.
22.M.J. Lighthill, M.J. 1962. Physical interpretation of the theory of wind generated waves. *J. Fluid Mech.*, **14**, 385–398.
23.S.G. Sajjadi, J.C.R. Hunt and F. Drullion 2014. Asymptotic multi-layer analysis of wind over unsteady monochromatic surface waves. *J. Eng. Math.*, **84**, 73–85.
24.P.A.E.M. Janssen and J-R. Bidlot 2018. Progress in operational wave forecasting. In: *IUTAM Symposium Wind Waves*, 4–8 September 2017, London, UK.
25.S.G. Sajjadi, J.C.R. Hunt and F. Drullion 2016. Growth of unsteady wave groups by shear flows, *Proc. of IMA Conference on Turbulence, Waves and Mixing*, S.G. Sajjadi and H.J.S. Fernando (eds). IMA Press, 79–84.
26.M.E. McIntyre 1992. On the role of wave propagation and wave breaking in atmosphereocean dynamics. In: *Proceedings of the 18th international congress theoretical and applied mechanics*, Haifa. Elsevier, Amsterdam, pp 281–304.
27.S.G. Sajjadi, J.C.R. Hunt and F. Drullion 2018. Computational turbulent shear flows over growing and non-growing wave groups In: *IUTAM Symposium Wind Waves, 4–8 September 2017, London, UK*.
28.H. Jeffreys 1925. On the formation of water waves by wind. *Proc. R. Soc. Lond.* A **107**, 189-206.
29.M.A.C. Teixeira and S.E. Belcher 2002. On the distortion of turbulence by a progressive surface wave. *J. Fluid Mech.*, **458**, 229-267.
30.W.M. Gong, P.A. Taylor and A. Dornbrack 1996. Turbulent boundary-layer flow over fixed aerodynamically rough two-dimensional sinusoidal waves. *J. Fluid Mech.*, **312**, 1-37.
31.A. Smedman, U. Högström, J.C.R. Hunt and E. Sahlée 2007. Heat/mass transfer in the slightly unstable atmospheric surface layer. *Q.J. Roy. Met. Soc.*, **133**, 622.
32.A.D.D. Craik and S. Leibovich 1976. A rational model for Langmuir circulations. *J. Fluid Mech.*, **73**, 401-426.
33.S.G. Sajjadi and M.S. Longuet-Higgins 2017. Instability of Langmuir circulations by wind. *Adv. Appl. Fluid Mech.* **19**, 725–763.
34.A.A. Townsend 1976. *The Structure of Turbulent Shear Flow*, 2nd edn., Cambridge University Press.
35.S. Komori, R. Nagaosa, Y. Murakami 1993. Turbulence structure and mass transfer across a sheared airwater interface in wind-driven turbulence. *J. Fluid Mech.*, **249**, 161-183.
36.J.C.R. Hunt, I. Eames and S.E. Belcher 2003. Vorticity dynamics in the water below steep and breaking waves. Proc. *Wind over waves; IMA conference* September 2001. S.G. Sajjadi and J.C.R. Hunt (eds), Ellis Horwood.
37.J.C.R. Hunt and J.F. Morrison 2000. Eddy structure in turbulent boundary layers. *Eur. J. Mech. B.* **19**, 673–694.
38.L. Lixiao, A. Kareem, Y. Xiao, L. Song and C. Zhou 2015. A comparative study of field measurements of the turbulence characteristics of typhoon and hurricane winds. *J. of Wind Engineering and Industrial Aerodynamics*, 140, DOI10.1016/j.jweia.2014.12.008
39.N. Iwano, N. Takagaki, R. Kurose and S. Komori 2013. Mass transfer velocity across the breaking air-water interface at extremely high wind speeds. *Tellus* B **65**, 21341.
40.P.R. Gent and P.A. Taylor 1976. A numerical model of the air flow above water waves *J. Fluid Mech.*, **77**, 105-128.
41.K. Stewartson 1974. Boundary layers on flat plates and related bodies. *Adv. Appl. Mech.*, **14**, 145-239.
42.A.A. Townsend 1972. Flow in a deep turbulent boundary layer over a surface distorted by water waves. *J. Fluid Mech.*, **55**, 719-735.
43.S.G. Sajjadi, T.J. Craft and Y. Feng 2001. A numerical study of turbulent flow over a two-dimensional hill. *Int. J. Numer. Methods Fluids*, **35**, 1-23.
44.S.G. Sajjadi, J.C.R. Hunt and F. Drullion 2017. Turbulent shear flows over smooth or peaked, and steady or unsteady monochromatic water wave. *J. Fluid Mech.*, to appear.
45.D. Szubert, F. Grossi, A.J. Garcia, Y. Hoarou, J.C.R. Hunt and M. Braza 2015. Shock-vortex shear-layer interaction in the transonic flow around a supercritical airfoil at high Reynolds number in buffet conditions. *J. Fluids Struct.*, **55**, 276-302.
46.J.C.R. Hunt, T. Ishihara, D. Szubert, I. Asproulias, Y. Hoarau and M. Braza 2016. Turbulence Near Interfaces-Modelling and Simulations M. Braza *et al* (eds.) Advances in Fluid-Structure Interaction, Notes on Numerical Fluid Mechanics and Springer Multidisciplinary Design 133, DOI 10.1007/978 – 3 – 319 – 27386 – 0 – 17, Springer.
47.M.J. Lighthill 1963. Attachment and separation in three-dimensional flows. In *Laminar Boundary Layers*, L. Rosenhead (ed). Ch. 2, pp. 72-82. Oxford University Press, Oxford.
48.J.C.R. Hunt, C.J. Abell, J.A. Peterka and H. Woo 1978. Kinematical studies of the flows around free or surface-mounted obstacles; applying topology to flow visualization. *J. Fluid Mech.*, **86**, 179-200.
49.M.L. Banner and W.K. Melville 1976. On separation of air flow over water waves. *J. Fluid Mech.*, **77**, 825-842.
50.S.E. Belcher, A.L.M. Grant, K.E. Hanley, B. Fox-Kemper, L. Van Roekel, P.P. Sullivan, W.G. Large, A. Brown, A. Hines, D. Calvert, A. Rutgersson, H. Pettersson, J.R. Bidlot, P.A.E.M. Janssen and J.A. Polton 2012. A global perspective on Langmuir turbulence in the ocean surface boundary layer. *Geophysical Research Letters*, **39** (L18605).
51.J.C.R. Hunt, S.E. Belcher, D.D. Stretch, S.G. Sajjadi, J.R. Clegg 2010. Turbulence and wave dynamics across gas-liquid interfaces. In: *Proceedings of the symposium on gas transfer at water surfaces*, S. Komori, R. Kurose (eds.) Kyoto, Japan.
52.P.P. Sullivan, J.C. McWilliams and C.H. Moeng 2000. Simulation of turbulent flow over idealized water waves. *J. Fluid Mech.*, **404**, 47–85.

Available online at www.sciencedirect.com

ScienceDirect

Procedia IUTAM 26 (2018) 14–29

Procedia IUTAM

www.elsevier.com/locate/procedia

IUTAM Symposium Wind Waves, 4-8 September 2017, London, UK

Progress in Operational Wave Forecasting

Peter A.E.M. Janssen[a], Jean-Raymond Bidlot[a]

[a]*E.C.M.W.F., Shinfield Park, Reading RG2 9AX, U.K.*

Abstract

Progress in operational sea state forecasting is discussed in the context of the energy balance equation. This fundamental law describes the evolution of the wave spectrum due to adiabatic processes such as advection and refraction and due to physical processes such as generation of waves by wind, nonlinear interactions and wave dissipation. Progress in wave prediction is illustrated by means of a verification of operational wave height forecasts against wave height observations from buoys over the last 25 years of operational practice. Verification of modelled spectra against observed spectra by buoys is shown as well.

At the moment a number of weather forecasting centres spend a considerable amount of effort in the development of a fully comprehensive coupled atmosphere, ocean-wave, ocean circulation, sea-ice model. Central in the coupling of atmosphere and ocean in the ECMWF earth system model (see e.g. [1]) are the ocean waves that determine the momentum and energy transfer across the sea surface. In this paper we therefore concentrate of the sea-state dependence of the momentum (and heat) fluxes by studying in some detail the wind input source function of the energy balance equation. The importance of the strong coupling between wind and waves is illustrated by means of impact studies.

Peer-review under responsibility of the scientific committee of the IUTAM Symposium Wind Waves.

Keywords: Type your keywords here, separated by semicolons ;

1. Introduction.

The fundamental law for wave prediction, namely the energy balance equation, describes the evolution of the wave spectrum due to adiabatic processes such as advection and refraction and due to physical processes such as generation of waves by wind, nonlinear interactions and wave dissipation. In this context, progress in operational wave prediction is discussed using verification results of forecast wave height against wave height observations from buoys. Also, evidence is presented that modelled spectral shape has improved over the past 20 years.

At ECMWF, the development of a first version of a fully comprehensive coupled atmosphere, ocean-wave, ocean circulation, sea-ice model is near completion. Presently, the interactions between the several components are as follows: Momentum loss from the atmosphere depends on the sea state following the approach of Janssen ([2], [3]). The

* Peter Janssen. Tel.: +44-1189499216; fax: +0-000-000-0000.
E-mail address: p.janssen@ecmwf.int

2210-9838
Peer-review under responsibility of the scientific committee of the IUTAM Symposium Wind Waves.
10.1016/j.piutam.2018.03.003

ocean circulation is driven by the sea state dependent stresses and produces surface currents, which are returned to the ocean-wave model and the atmospheric model needed for wave-current interaction and momentum flux. In addition, we have introduced effects of Stokes-Coriolis forcing, while the ocean circulation model is driven by momentum and energy fluxes directly from the wave model [4].

In this paper we concentrate in some detail on the wind input source function and its role in the interaction of atmosphere and ocean. It turns out that the wind input allows for a strong interaction between wind and waves. The reason for this is that while the ocean waves grow because they receive momentum from the sheared airflow, in turn the wind profile changes because the growing waves have removed momentum from the airflow. The momentum transfer from wind to waves may be so large that the associated wave-induced stress becomes a substantial fraction of the turbulent stress. Therefore, the velocity profile over sea waves is controlled by both turbulent and wave-induced momentum flux. Over a flat surface the profile of turbulent wind is usually logarithmic, but in the presence of growing wind waves deviations from the classical wind profile are to be expected. In addition, the momentum transfer from the air to the waves will be affected by the sea state, in other words one expects a strong interaction between the turbulent boundary layer and the surface waves. The importance of this process for wind and wave forecasting is illustrated by means of impact studies. Furthermore, it turns out that not only the momentum transfer, but also the heat transport is affected by the sea state, giving, again using impact studies, quite large changes in the (Tropical) circulation.

Therefore, the programme of the paper is as follows. We briefly introduce the subject of ocean wave forecasting, which is mainly about a statistical description of the sea state using the 2D wave spectrum. Improvement of ocean wave forecasting skill is illustrated by comparing forecast results with buoy observations for different years. Finally, we discuss in some detail the wind input source function which describes the generation of ocean waves by wind, and the consequent slowing down of the airflow. Consequences of the sea state dependence of momentum and heat transfer of weather and wave forecasting are briefly presented.

2. Ocean Waves.

Wave forecasting took off as an important subject when knowledge of the sea state was required for numerous landing operations during the second World War, for D-Day for example. From then onwards there followed a rapid development because of improved weather forecasting (better surface winds), an enormous increase in the number of observations (from buoys and satellites) and faster and bigger computers. From the beginning it was clear, however, that the sea state was so complicated that only a prediction of the average sea state at a location of interest was possible. Example of forecast parameters are the average wave height, the average period of the waves, and the wave spectrum.

In a statistical description of ocean waves the sea state is represented by the wave spectrum $F = F(\mathbf{k}, \mathbf{x}, t)$. Here $\mathbf{k}$ is the wavenumber vector, such that $k = 2\pi/\lambda$ with λ the wave length.

The spectrum is normalized in such a way that the integral over the spectrum gives, apart from a factor $\rho_w g$ (with ρ_w the water density and g acceleration of gravity), the wave energy:

$$\int \mathrm{d}\mathbf{k} F(\mathbf{k}) = \frac{E}{\rho_w g}, \; E = \rho_w g \langle \eta^2 \rangle$$

where η denotes the surface elevation. Thus, the wave spectrum is normalized so that it equals the wave variance $\langle \eta^2 \rangle$.

In order to establish a connection with the common practice to think in terms of wave heights (for a single wave this is the distance between crest and trough), we use the concept of significant wave height. This is a statistical measure, defined as

$$H_S = 4\sqrt{\langle \eta^2 \rangle}.$$

In a similar vein, other variables may be defined using the spectrum, e.g. mean frequency, mean wave direction, wave steepness, etc.

For ocean waves, the fundamental quantity is the action density spectrum $N(\mathbf{k}, \mathbf{x}, t)$, because it is an adiabatic invariant. Given N, the energy spectrum F then follows from

$$F(\mathbf{k}) = \frac{\sigma(\mathbf{k}) N(\mathbf{k})}{g}$$

with σ the intrinsic frequency for a gravity wave in water of depth D, while the dispersion relation for angular frequency ω reads

$$\omega = \sigma(k, D) + \mathbf{k} \cdot \mathbf{U}, \ \sigma = \sqrt{gk \tanh(kD)},$$

where $\mathbf{U}$ is the surface current.

From first principles (see [5]) one finds the following evolution equation for the action density spectrum $N(\mathbf{k}, \mathbf{x}, t)$

$$\frac{\partial}{\partial t} N + \nabla_{\mathbf{x}} \cdot (\dot{\mathbf{x}} N) + \nabla_{\mathbf{k}} \cdot (\dot{\mathbf{k}} N) = S = S_{in} + S_{nl} + S_{ds}, \tag{1}$$

where $\dot{\mathbf{x}} = \partial\omega/\partial\mathbf{k}$ is the group velocity, $\dot{\mathbf{k}} = -\partial\omega/\partial\mathbf{x}$ gives the refraction of ocean waves, and the source functions S represent the physics of wind-wave generation, dissipation by wave breaking and nonlinear four-wave interactions.

It is emphasized that the energy balance equation describes the evolution of the average sea state. Formally, it is obtained by deriving the average evolution of an ensemble of oceans and it assumes that on the short scales of the wave length the wave field is **homogeneous and random**. In this approach it is assumed that the wave components are independent and have random phase. To a good approximation the probability distribution of the ocean surface elevation is Gaussian.

2.1. The source functions

The source functions describe the generation of waves by wind (S_{in}), the dissipation of ocean waves by e.g. wave breaking (S_{diss}) and the energy and momentum conserving resonant four-wave interactions (S_{nl}). A considerable amount of work in the past 50 years has been devoted to the formulation of the source functions.

Nonlinear transfer

The nonlinear interactions, introduced by K. Hasselmann [6], describe the energy transfer between the different wave components in the spectrum. Energy transfer takes place between 4 different waves that satisfy the resonance conditions

$$\omega_1 + \omega_2 = \omega_3 + \omega_4, \ \mathbf{k}_1 + \mathbf{k}_2 = \mathbf{k}_3 + \mathbf{k}_4.$$

Nonlinear interactions play an important role in shaping the spectrum and in freak wave formation. They give rise to an energy cascade through the spectrum. Its representation is known exactly, but is operationally very expensive, therefore an approximation ([7]), called the Direct Interaction Approximation (DIA) is used.

Wind Input

The form of the wind input source function S_{in} was already suggested by Miles [8] in 1957. It depends on the surface stress $\tau = \rho_a u_*^2$ (with ρ_a the air density and u_* the friction velocity) and is proportional to the action density spectrum:

$$S_{in} = \gamma N(\mathbf{k}), \ \frac{\gamma}{\omega} = \epsilon \beta(z_0) \left(\frac{u_* \cos(\theta - \phi)}{c} \right)^2$$

with $c = \omega/k$ the phase speed of the waves, $\epsilon = \rho_a/\rho_w$, and z_0 the roughness length experienced by the airflow.

The wave growth by wind implies a sea-state dependent momentum loss for the airflow [9]. As a consequence, for steep waves the roughness length is larger than for gentle waves. Therefore, in particular for initial growth, there is a strong **mutual interaction** between wind and waves, its strength is determined by the ratio of wave-induced stress τ_w to total kinematic stress τ, with,

$$\tau_w = \rho_w \int \mathrm{d}\mathbf{k} \, \mathbf{k} S_{in}.$$

Dissipation

The dissipation source function describes the reduction of wave momentum and energy caused by processes such as white capping/ wave breaking, the damping by water turbulence, etc. It is modelled in such a way that steep waves experience more dissipation than gentle waves, as steep waves are more likely to break and/or have whitecaps. The breaking waves will give rise to turbulence in the water, resulting in additional mixing of momentum and heat in the upper part of the ocean.

2.2. Energy balance for growing wind waves

The numerical aspects of the action balance equation (1) are presented in WAMDIG [10], [11] and [3]. In this section we discuss the solution of the energy balance equation for the simple case of the generation of ocean waves by wind. To that end we will study the idealized situation of duration-limited wave growth (when a uniform and steady wind has blown over an unlimited ocean for time t after a sudden onset and starting from a flat, calm sea. The case of an unlimited ocean follows when the advection and refraction terms in the action balance equation have been switched off so that one can simulate the duration-limited case by means of a single grid point version of the wave prediction model.

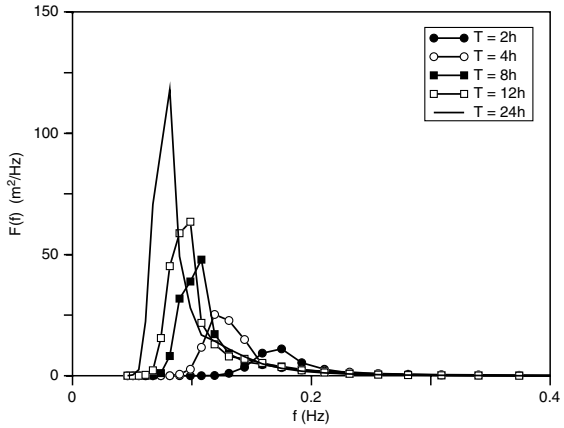

Fig. 1. Evolution of sea state from young windsea (wave age $c_p/u_* \simeq 7$) to older windsea ($c_p/u_* \simeq 25$).

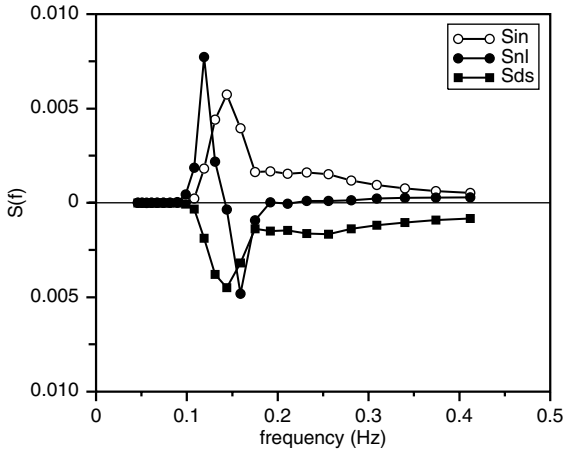

Fig. 2. The energy balance for young wind sea at a duration of 4 h.

In Fig. 1 the evolution in time of the one-dimensional frequency spectrum $F(f)$ over the first 24 hours of the simulation is shown. The stage of development of windsea is usually measured in terms of the wave age parameter

c_p/u_* where c_p is the phase speed of the peak of the spectrum and u_* is the friction velocity which is a measure for the forcing by wind. Typically, for young windsea ($c_p/u_* = 5 - 10$) the waves are strongly forced and steep and the slowing down of wind by the wave-induced stress is large. On the other hand, for old windsea ($c_p/u_* \simeq 25$), the waves are more gentle and weakly forced and the slowing down of the wind by waves is small. This will be discussed in more detail in the section on wind-wave interaction.

The evolution of the simulated frequency spectrum is in accord with the results found during the JONSWAP campaign [12]. In particular, in the course of time a considerable downshift of the peak of the spectrum is seen, corresponding with the generation of longer waves, and, in addition a pronounced overshoot of the peak of the spectrum is noted. Both downshift and overshoot are connected to the action of the nonlinear interactions on the wave spectrum.

In order to better understand the evolution of the gravity wave spectrum we need to study the source functions. To that end, the energy balance equation for young windsea (duration is 4 h corresponding to $c_p/u_* \simeq 12$) is shown in Fig. 2, by plotting the directional averages of S_{in}, S_{nl}, and S_{ds} as function of frequency. Thus, the intermediate frequencies receive energy from the airflow (since S_{in} is positive) which is transported by the nonlinear interactions towards the high and low frequency range. In the high frequency range the nonlinear energy flux maintains an equilibrium spectrum which has an f^{-4} shape, while in the low-frequency range the nonlinear interactions maintain an 'inverse' energy cascade transferring energy towards the region just below the spectral peak, thereby shifting the peak of the spectrum towards lower frequencies. This frequency downshift is to a large extent determined by the shape and the magnitude of the spectral peak itself. For young windsea, having a narrow peak with a considerable peak enhancement, the rate of downshifting is considerable, while for gentle, old windsea this is much less so. In the course of time the peak of the spectrum gradually shifts towards lower frequencies (as may be seen from Fig. 1) until the peak of the spectrum no longer receives input from the wind but instead returns momentum to the airflow because these waves are running faster than the wind. Under these circumstances the waves around the spectral peak are subject to a considerable dissipation so that their steepness reduces. Consequently, because the nonlinear interactions depend on the steepness, the nonlinear transfer is reduced as well, with the result that slowly a quasi-equilibrium spectrum emerges. For old windsea the timescale of downshifting becomes larger than the typical duration of a storm so that for all practical purposes the wind-generated waves evolve towards a steady state.

2.3. Wave forecasting and Validation

A key task in operational wave forecasting is the validation of analysis and forecast against wave observations (see [13]). For reasons of briefness, we concentrate on the verification against buoy data, although there is also very valuable information on the quality of the wave forecasting system by comparison with space borne Altimeter data of significant wave height (see, e.g. [14]. By plotting the verification statistics as function of time, one may monitor the quality of the forecast and analysis system. This shows that there are significant improvements in wave height analysis and forecast over the past 25 years. Spectral shape has improved as well as follows by a comparison with buoy spectra.

It is of course of interest to try to understand the reasons for the improvement in wave height forecast skill over time. Based on extensive experimentation, it turns out that a considerable part ($\approx 75\%$) of the improvement is related to the fact that in the course of time the atmospheric model has improved considerably producing higher quality surface winds. The remainder part of the improvement is caused by wave model improvements such as two-way interaction, better numerics, representation of unresolved bathymetry, a better representation of wave dissipation and increases in spatial and spectral resolution. Also, the use of high quality Altimeter wave height data in the wave analysis has given improvements in wave height forecast skill in particular in the short range forecast.

Let us now present some verification statistics against buoy observations. A wave buoy is basically a float of which the acceleration owing to the surface wave motion is determined. Integrating twice in time then gives the surface elevation signal from which quantities such as the wave energy, frequency spectrum and maximum wave height can be obtained. Note that buoys come in different shapes and sizes and therefore may have a different dynamic range. Thus, there is no garantee that they measure the same wave height. Nevertheless, wave modellers still regard buoys as the ground truth, although there is of course no global coverage.

Fig. 3 shows the results of the verification of analyzed and forecast wave height against buoy data for different forecast ranges over the period of January 1993 until June 2017. The overall trend is that over the years there is a clear reduction in wave height scatter index, defined as the standard deviation of the difference between model and

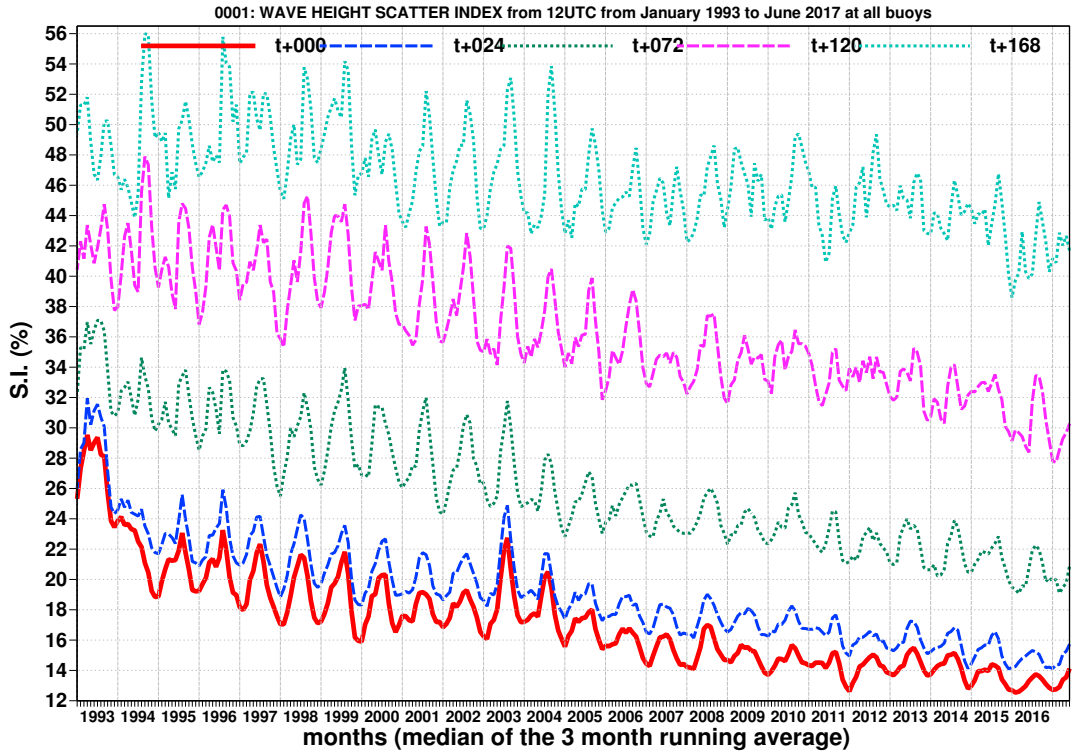

Fig. 3. Evolution of verification statistics for model against buoy data over a 23 year period for analysis and different forecast ranges. In this case the scatter index is shown. Most buoys are located in the Northern hemisphere.

observed wave height, normalized with the mean of observed wave height. In particular, this is the case for the short range forecast up to 5 days ahead, but in the past 5 years there are also definite signs that the medium-range wave forecast is improving as well. As pointed out, an important reason for the improvements in the quality of forecast wave height are better winds. The improvements in wind speed follow from a verification against buoy observations and a more detailed discussion on this topic is given in [15].

The discussion on verification is closed by presenting a relatively new diagnostic tool which enables to study problems in the modelled spectral shape. This is now opportune because a consequence of the large improvements in the forcing wind fields is that it is nowadays more straightforward to identify (systematic) errors in the wave model. This tool was first introduced by [16] in a study to validate SAR and wave model frequency spectra against buoy spectra. One simply determines for each frequency, hence wave period, the wave variance from the modelled and observed frequency spectra in a period bin of, say, two seconds and one obtains the 'equivalent' wave height by the usual definition. The resulting period dependent bias is then plotted as a function of time. In Fig. 4 (see also [17]) an example is given involving all American and Canadian one-dimensional frequency spectra over the period of February 1998 until July 2009. In the range of 10 to 15 seconds there is up to the year 2003 a clear seasonal dependence of the 'equivalent' wave height bias, being large in the summer time and vanishingly small in the winter time.

It turns out that these large positive biases are related to swell events generated by the storms in the Southern Hemisphere winter time. It is tempting to dwell on the causes of the overestimate by the wave model. An obvious candidate would be the dissipation source function, because this source term is the least well-understood. Another candidate is the representation of unresolved islands and atolls. A closer inspection of the verification results revealed that the main problem occurs in the Pacific ocean and not in the Atlantic (not shown). An important difference between the Pacific and the Atlantic ocean is that in the equatorial region of the Pacific there are a vast number of small islands and atolls which are not resolved by the present operational resolution of the wave model. Although these islands are small, they nevertheless block considerable amounts of low-frequency wave energy [18]. Therefore, using a high resolution global topography of 2 minutes, Bidlot (private communication, 2003) determined a wavenumber

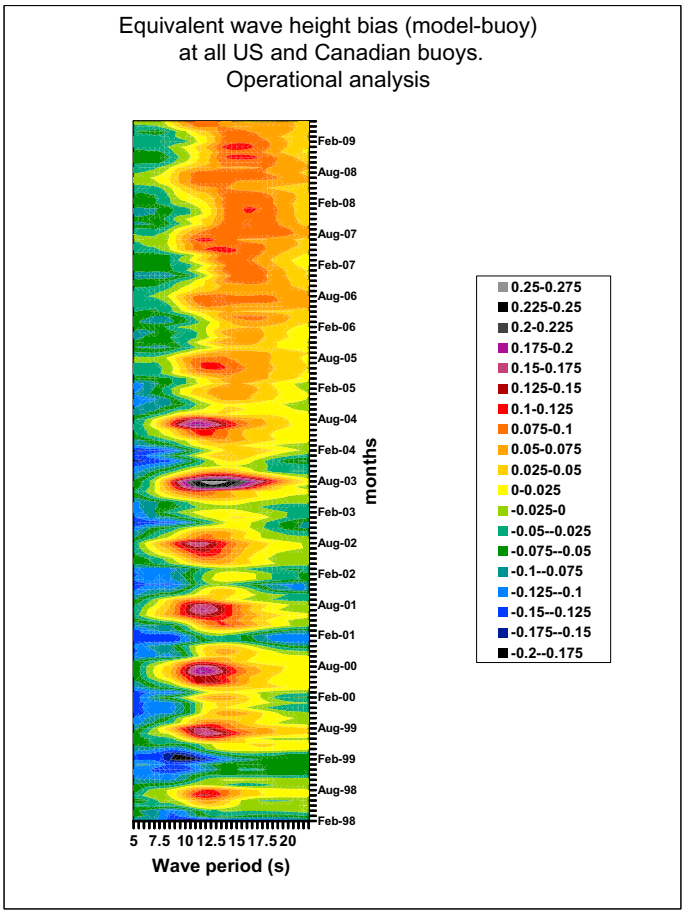

Fig. 4. Spectral bias (model-buoy) at all US and Canadian buos for the period February 1998 until February 2009.

dependent blocking factor. This change was introduced operationally in February 2004 and, as can be seen from Fig. 4, gave a substantial reduction of the bias in the Summer of 2004. Nevertheless, it did not disappear completely.

In March 2005, a new version of the dissipation source function was introduced, which used an alternative definition of the integral parameters, such as mean frequency, in the expression for the dissipation. As can be seen in Fig. 4, this change had a further beneficial impact as in the Summer of 2005 there is virtually no bias anymore in the range of 10 to 15 seconds.

This shows that verification of model forecasts against observations is of vital importance. On the one hand it gives users a good idea of the quality of modelled wave height and spectra, and, on the other hand such an exercise provides modellers important clues to improve the wave prediction system.

3. Wind-Wave Interaction.

In the remainder of this paper we would like to discuss the role of ocean waves in the momentum and heat transfer of a coupled atmosphere-ocean circulation model.

Starting from critical layer theory results are presented on the sea state dependence of the momentum transfer and its impact on the atmospheric circulation and the sea state forecast which is then followed by a discussion of some new results regarding the sea-state dependent heat transfer. Note that in the past (see e.g. [19], [20]) there has been much debate about the use of the critical layer approach in the presence of turbulence. However, field observations of

Hristov *et al.* [21] combined with direct numerical simulations of Sullivan *et al.* [22] have shown that this approach produces realistic results.

3.1. Quasilinear Theory of momentum flux.

According to critical layer theory waves with phase speed c grow when the curvature in the wind profile $U_0(z)$ at the critical height is negative. Introducing the Doppler-shifted velocity $W = U_0(z) - c$, where the critical height z_c follows from the condition $W = 0$, one finds

$$\frac{\partial}{\partial t}F(k)\Big|_{wind} = \gamma F(k),\ \gamma = -\epsilon\pi c\mid\chi_c\mid^2\frac{W_c''}{\mid W_c'\mid},$$

where the growthrate γ of ocean waves by wind is proportional to the curvature W_c'' in the wind profile (Miles [8]). Here, the wave-induced vertical velocity χ satisfies the Rayleigh equation

$$W\nabla^2\chi - W''\chi = 0,\ \chi(0) = 1,\ \chi(\infty) = 0.$$

Wave growth results in a slowing down of the airflow (see Fabrikant [23] and Janssen [24]) according to

$$\frac{\partial}{\partial t}U_0 = (\nu_a + D_W)\frac{\partial^2}{\partial z^2}U_0 + \frac{1}{\rho_a}\frac{\partial}{\partial z}\tau_{turb},\ D_W = \frac{\pi\omega^2\mid\chi\mid^2}{\mid c - v_g\mid}F(k),$$

where the turbulent stress is modelled by means of a mixing length model, i.e.

$$\tau_{turb} = \rho_a l^2\left|\frac{\partial}{\partial z}U_0\right|\frac{\partial}{\partial z}U_0,\ l(z) = \kappa(z + z_b),$$

while κ is the von Kármán constant and z_b a background roughness length.

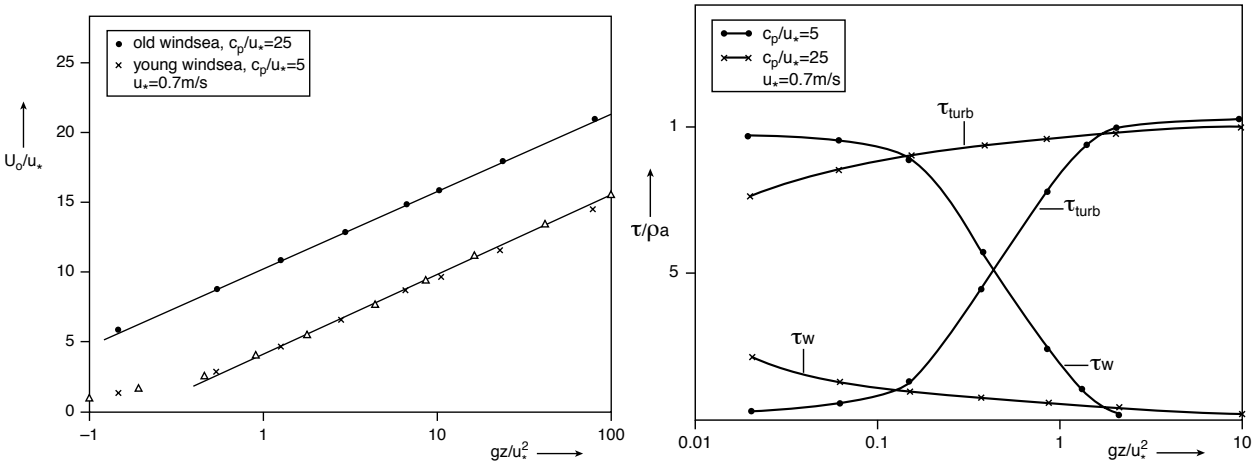

Fig. 5. Left Panel: Effect of waves on wind profile for old and young windsea, shown by plotting dimensionless wind speed U_0/u_* as a function of dimensionless height $z_* = gz/u_*^2$. The wind profile parametrization $1/\kappa\log(1 + z_*/z_0^*)$ is denoted by a $\triangle$. The right Panel shows turbulent stress τ_{turb} and wave stress τ_w as a function of dimensionless height gz/u_*^2 for young and old windsea.

For given spectral shape one may search for steady state solutions of the airflow over wind waves by means of an iteration method. The rate of convergence of this procedure was judged by calculating the total stress $\tau_{tot} = \rho_a u_*^2$

$$\tau_{tot} = \tau_v + \tau_{turb} + \tau_w,$$

where $\tau_v = \rho_a\nu_a\partial U_0/\partial z$ and the wave-induced stress can be shown to be given by

$$\tau_w = -\int_z^\infty \mathrm{d}z D_W\frac{\partial^2}{\partial z^2}U_0 = \int \mathrm{d}\mathbf{k}\ \frac{\partial P}{\partial t}\Big|_{wind}$$

with wave momentum $P = \rho_w g F(\mathbf{k})/c$.

For the actual calculations, reported in [9], the wave spectrum is given by the JONSWAP spectrum with a Phillips parameter α_p which depends in a sensitive manner on the wave age c_p/u_*, i.e.

$$\alpha_p = 0.57(c_p/u_*)^{-3/2},$$

hence young wind waves ($c_p/u_* = 5$) are steep while old wind sea ($c_p/u_* = 25$) is a smooth sea state.

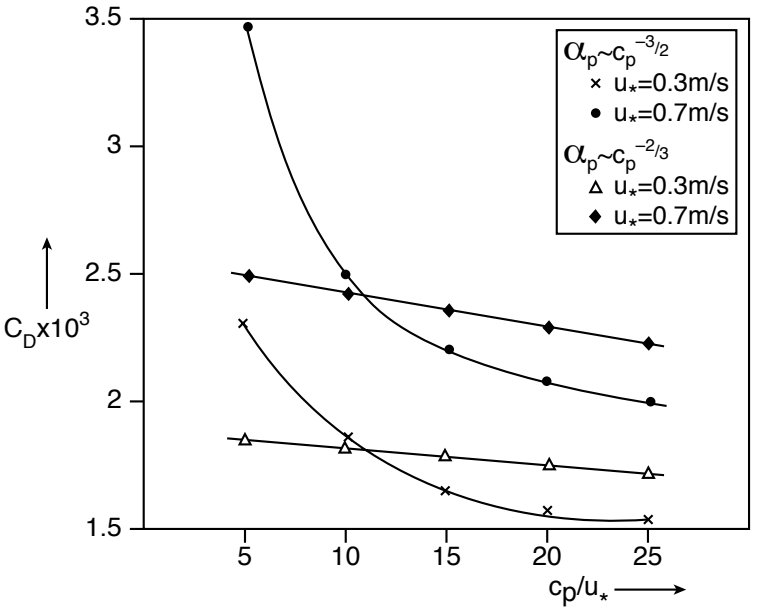

Fig. 6. The wave age dependence of the drag coefficient for two different friction velocities.

The results of the iteration process are given in the Figs. 5 and 6. In the present context the most important result is given in the left panel of Fig. 5. It shows the impact of the sea state on the wind profile. Young waves have a large roughness giving a considerable slowing down of the wind and therefore the equilibrium wind is quite reduced compared to the case of old windsea for which the airflow is much smoother. However, the shape of the wind profile away from the surface still has a logarithmic shape, but close to the surface there are deviations from the logarithmic wind profile, which is a reflection of the impact of growing waves on the wind. This follows immediately from the right panel of Fig. 5 which shows profiles of wave-induced stress and turbulent stress for two different wave ages. For young windsea, the wave-induced stress dominates the total stress near the surface, giving an additional slowing down of the wind, hence a rougher airflow. Finally, Fig. 6 nicely summarizes the effect of growing waves on the wind by showing the dependence of the drag coefficient, defined as $C_D = u_*^2/U_{10}^2$, on the wave age parameter c_p/u_*, which is in good agreement with observations by Donelan [25] and HEXOS [26].

3.2. Parametrization of quasi-linear theory.

The numerical results suggest that air viscosity is not important so for the parametrization we start from the stress relation $\tau_{turb} + \tau_w = \tau$, or explicitely, with $l = \kappa(z + z_b)$[1]

$$l^2 \left| \frac{\partial U_0}{\partial z} \right| \frac{\partial U_0}{\partial z} + \tau_w(z) = \tau.$$

In principle, one could try to solve this differential equation for wind velocity with boundary condition $U_0(z = 0) = 0$ if one knows the wave-induced stress τ_w. However, things turn out to be simpler if one starts from the fit of the

[1] In the original treatment of [2] $l = \kappa z$ and the boundary condition $U_0(z = z_b) = 0$ was specified at $z = z_b$.

wind-profile to the numerical data of [9], which is displayed in the left Panel of Fig. 5,

$$U_0(z) = \frac{u_*}{\kappa} \log\left(1 + \frac{z}{z_0}\right),$$

and determines the τ_w-profile. It is given by

$$\frac{\tau_w(z)}{\tau} = 1 - \frac{(z+z_b)^2}{(z+z_0)^2}$$

Applying the above for $z = 0$, one immediately finds for the roughness length z_0

$$z_0 = \frac{z_b}{\sqrt{1-\tau_w(0)/\tau}} \rightarrow \alpha_{CH} = \frac{g z_0}{u_*^2},$$

with α_{CH} the Charnock parameter. Here, $\tau_w(0)$ at the surface is obtained from the wave model.

Furthermore, from the above one obtains, using the relation $\partial\tau_w/\partial z = D_W \partial^2 U_0/\partial z^2$ an expression for the wave-diffusion coefficient D_W,

$$D_W = 2\kappa u_* \frac{(z+z_b)(z_0-z_b)}{z+z_0}.$$

Another advantage of using the logarithmic wind profile is that it provides a simple parameterization of the wave growth by wind. In order to obtain the growthrate γ one needs to solve the Rayleigh equation which cannot be solved exactly. In stead we use as a starting point an approximate expression for the growth rate that has been obtained by Miles [27] by means of asymptotic matching.

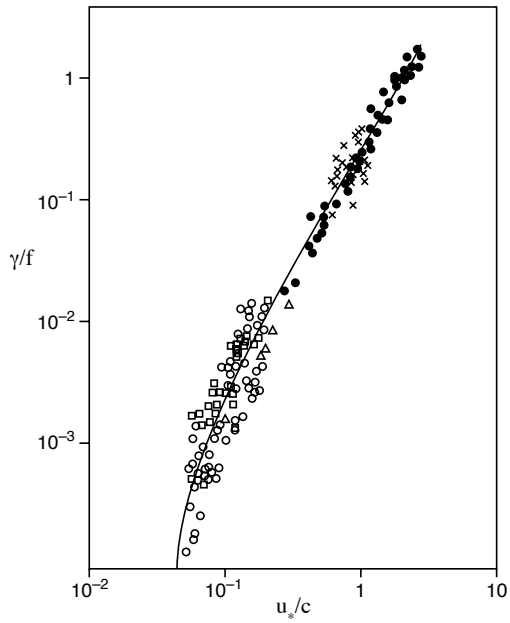

Fig. 7. Comparison of modelled growth rate (with Charnock parameter $\alpha_{CH} = 0.0144$) with observations compiled by Plant [28].

The main result is

$$\gamma/\omega_0 = \epsilon\beta\frac{u_*^2}{c^2},$$

where the Miles' parameter β is given by

$$\beta = \frac{\pi}{\kappa^2} y_c \log^4\left(\frac{y_c}{\lambda}\right), y_c \leq \lambda = \frac{1}{2}e^{-\gamma_E} = 0.281,$$

Here, $y_c = kz_c$ is the dimensionless critical height and ϵ is the air-water density ratio. This expression is valid for slow waves only so in order to have a reasonable approximation also for the long waves, parameters were rescaled by replacing $\lambda = 0.281$ by $\lambda = 1$, and by replacing π by the factor 1.2. In addition, in the formula for the critical height, the parameter u_*/c was shifted by a factor $z_\alpha = 0.08$. As a result the following parametrization for the Miles' parameter β is used:

$$\beta = \frac{1.2}{\kappa^2} y_c \log^4(y_c), y_c \leq 1,$$

where

$$y_c = kz_0\left(e^{\kappa/x} - 1\right), \; x = (u_*/c + z_\alpha)\cos(\theta - \phi), z_\alpha = 0.08.$$

The parametrized wave growth is shown in the Fig. 7 and is compared with observations by Plant [28]. Although there is a big scatter in the observations, the agreement of the parametrization with observations seems fair.

3.3. Validation of the approach.

We have performed an extensive validation of the drag coefficient C_D of the coupled ocean-wave, atmosphere system. Two examples are shown in Fig. 8. In the left panel the modelled sea state dependent drag is compared to a parametrization, based on observations from a number of field campaigns, proposed by Huang [29]), which is of the form

$$C_D(\lambda_p/2) = A(c_p/u_*)^a,$$

where λ_p is the peak wavelength, $A = 1.220 \times 10^{-2}$, and $a = -0.704$. The model relation is obtained from one global forecast by averaging $C_D(\lambda_p/2)$ as function of the wave age parameter c_p/u_*. For large wave ages a good agreement between model and observed drag coefficient is obtained while for young windseas there is a some underestimation and there is more scatter. In the right panel of 8 the drag coefficient at 10 m height as function of windspeed U_{10} is

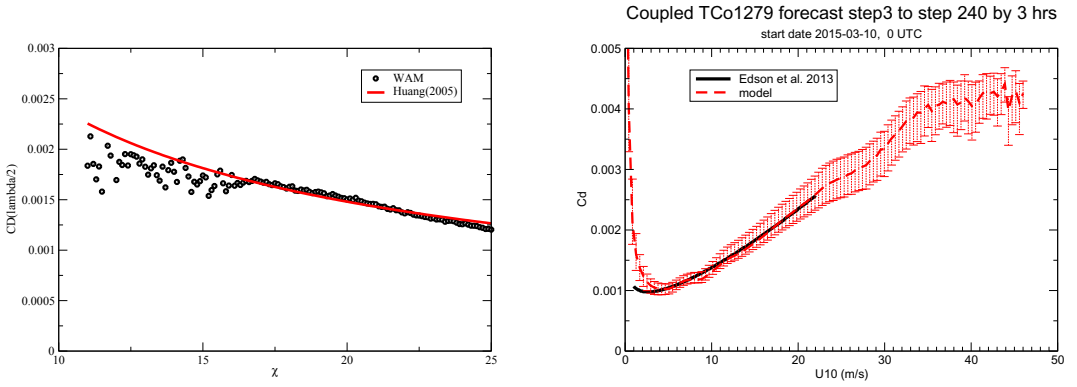

Fig. 8. Left panel compares modelled drag with Huang's [29] emprical relation of sea-state dependent drag coefficient. The right panel compares modelled and observed ([30]) drag coefficient relation with wind speed.

.

validated. The model data are obtained by averaging 80 forecasts of the drag coefficient as function of windspeed. The empirical fit of Edson *et al.* [30] is obtained from eddy correlation data for the COARE 4.0 parametrization of the drag. Noting that this empirical fit is valid up to a wind speed of 23 m/s, it is seen that on average there is a good agreement between modelled drag and observed drag. For extreme, hurricane windspeeds modelled drag shows a tendency to become less sensitive to increases in wind speed, and even shows signs of saturation. This is in qualitative agreement with empirical findings, although it must be emphasized that the scatter in the field observations is large.

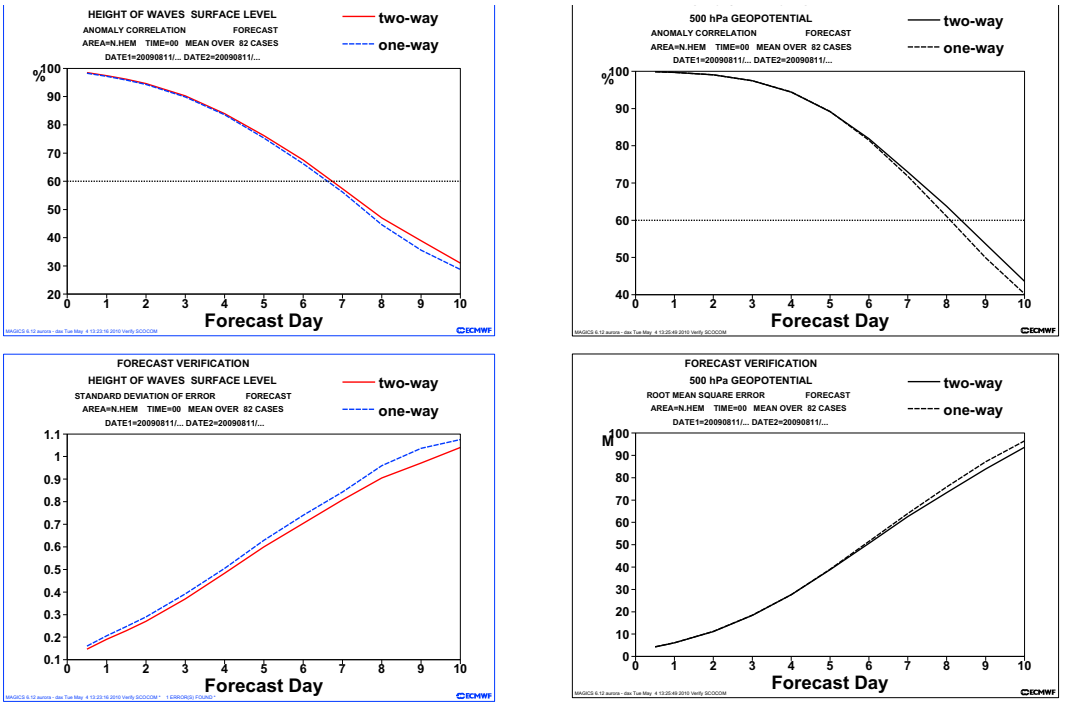

Fig. 9. Left panels show anomaly correlation and standard deviation of error of forecast significant wave height averaged over 82 cases, while the right panel shows the same scores but now for 500 mb geopotential height. Area is the Northern Hemisphere. Coupled forecast is labelled as two-way and no coupling is labelled as one-way.

The next question of interest is whether coupling of wind and waves (two-way interaction for short) has impact on the forecast skill of ocean waves and atmosphere. For medium-range forecasting, evidence that this is indeed the case has been presented by Janssen *et al.* [31] and by Janssen [3], while evidence of impact on the seasonal timescale is given by [32]. Further evidence may be found in Fig. 9. This Figure is based on a comparison of scores of coupled (two-way) and control (one-way) forecasts of significant wave height and 500 mb geopotential height (against the verifying analysis). The number of analyses and 10 day forecasts was 82 and the period was the Summer of 2009. The spatial resolution of the atmospheric component was 40 km while the wave model had a resolution of 28 km. The Figure shows that both near the surface (significant wave height) and in the upper air two-way interaction reduces forecast error and increases the anomaly correlation from 6 days in the forecast.

3.4. Theory and parametrization of heat flux

We have seen that growing ocean waves may have impact on the momentum flux across the air-sea interface. However, it turns out that the sea-state also has a significant impact on the latent and sensible heat flux. In order to see this, the theory of wind-wave generation is extended to include thermal stratification (see for an early account [33]), but the effect of spray as generated by whitecaps and breaking waves is ignored.

In the passive scalar approximation the evolution of mean temperature is found to be

$$\frac{\partial}{\partial t}T_0 = \frac{\partial}{\partial z}\left\{\left(D_w + l^2\left|\frac{\partial U_0}{\partial z}\right| + \delta\nu_z\right)\frac{\partial}{\partial z}T_0\right\}.$$

where it is assumed that close to the surface the heat transport is also determined by molecular conduction, which gives the additional diffusivity $\delta\nu_z$, where δ is a constant of the order of 0.1-0.5.

Assume steady state and introduce the heat flux q_*. Integrating the T-equation one finds

$$\left\{D_w + l^2\left|\frac{\partial U_0}{\partial z}\right| + \delta\nu_z\right\}\frac{\partial}{\partial z}T_0 = q_*,$$

which is a differential equation for the air-temperature profile subject to the boundary condition that $T_0(z=0) = T_S$ with T_S the sea surface temperature.

Using the just found parametrization for the wave diffusion coefficient,

$$D_w = 2\kappa u_* \frac{(z+z_b)(z_0-z_b)}{z+z_0},$$

and solving the differential equation for $\Delta T = T_a - T_s$ with boundary condition that $\Delta T = 0$ at $z = 0$, gives a logarithmic profile with 'thermal' roughness z_T,

$$\Delta T = \frac{q_*}{\kappa u_*}\log\left(\frac{z}{z_T}\right)$$

where for small $z_\nu = \delta\nu_z/\kappa u_*$ the thermal roughness becomes $z_T = (z_\nu z_0)^{1/2}$.

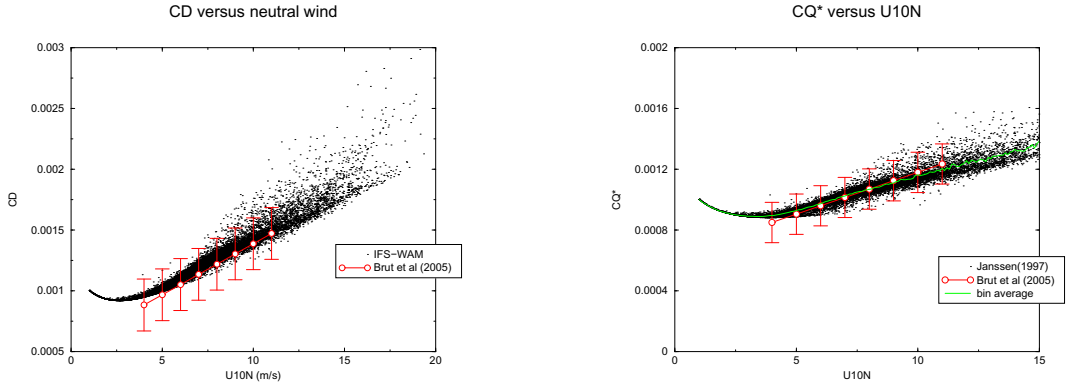

Fig. 10. Comparison of simulated drag coefficient (left panel) and Dalton number (right panel) with empirical fits obtained by Brut *et al.* [34] for the Tropical Atlantic.

Note that by definition $\tau = C_D(10)U_{10}^2$ and $q_* = C_q(10)U_{10}\Delta T_{10}$ so that from the wind and temperature profile one now immediately finds expressions for the drag coefficient C_D and the Dalton number C_q:

$$C_D(10) = \left\{\frac{\kappa}{\log(10/z_0)}\right\}^2$$

while

$$C_q(10) = \frac{\kappa}{\log(10/z_T)}C_D^{1/2}$$

It is straightforward to evaluate these coefficients from ECMWF's IFS. Results, as shown in Fig. 10 show, in agreement with Brut *et al.* [34], an increase of C_D with wind while C_q also increases with wind but to a lesser extent.

However, the result for C_q is in sharp contrast with HEXOS (De Cosmo *et al.* [35] which suggests a constant for the Dalton number. But, subsequent work by Smedman *et al.* [36] (and also Oost *et al.* [37]) do indicate that C_q increases with wind speed.

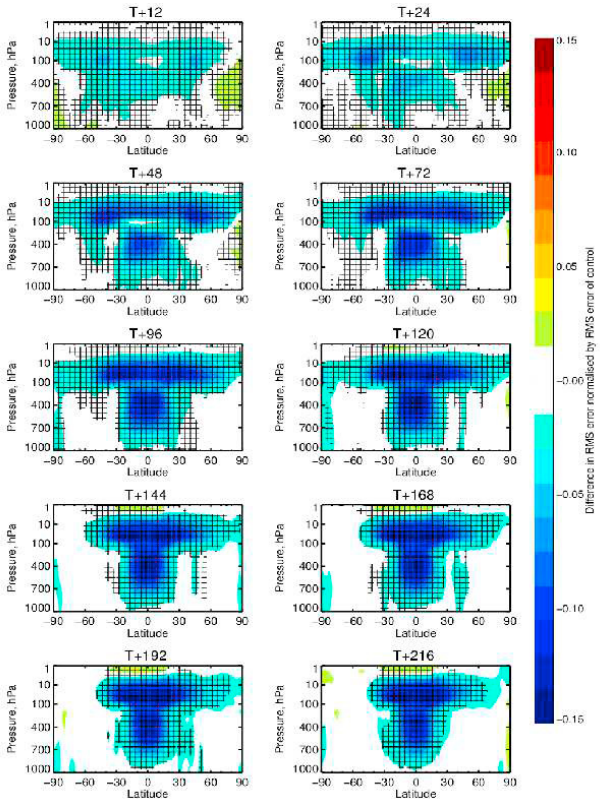

Fig. 11. Zonal mean plots of the impact of the new heat flux parametrization on the relative rms error in geopotential height.

3.5. Impact on Tropical Circulation.

In the past 5-10 years work has been underway to develop a comprehensive coupled forecasting system (atmosphere, ocean-wave, ocean-circulation, and a sea-ice model). It is expected that this system will produce operational deterministic forecasts by the middle of the year 2018.

In the context of this fully coupled system (CY43R1 with resolution TCO 399, corresponding to a spatial resolution of 30 km), we now show impact of the new formulation for the heat flux on the tropical circulation by doing forecasts over a period of one year. The control forecasts were performed with a heat flux formulation that has almost no wind speed dependence. Results of these 10-day forecasts are verified against the operational analysis. As shown in Fig. 11, comparing the verification results for geopotential height shows a significant reduction in forecast error for the experiment with sea-state dependent thermal roughness.

Earlier experiments with a forecast system with fixed SST (so no dynamic ocean) showed much smaller impact, therefore also a dynamic ocean plays an important role in a realistic representation of the Tropical circulation.

4. Conclusions.

Although we have seen that there has been considerable progress in operational wave forecasting over the past 25 years, that does not mean that we are at the end of the journey.

There are still a number of important questions to be solved. For example, the wind-wave interaction approach is extremely simple and might require improvements (essentially it is now one-dimensional theory as vorticity is conserved, effects of vortex stretching need to be included). Furthermore, effects of spray on momentum flux and heat flux need to be incorporated as well.

Also, nonlinear effects such as the generation of second and third harmonics need to be included in a more systematic way, while also the role of ocean waves in upper-ocean mixing (wave breaking and generation of Langmuir turbulence) needs to be better understood. Nevertheless, we are able to give already fairly accurate estimates of the stress (and heatflux) over the oceans.

References

1. Peter A.E.M. Janssen, Øyvind Saetra, Cecilie Wettre, Hans Hersbach and Jean Bidlot, Impact of the sea state on the atmosphere and ocean. *Annales Hydrographiques*, 2004; **3** 3.1-3.23.
2. P.A.E.M. Janssen, Quasi-linear theory of wind wave generation applied to wave forecasting. *J. Phys. Oceanogr.*, 1991; **21** 1631-1642.
3. Peter Janssen, *The Interaction of Ocean Waves and Wind*, 2004, Cambridge University Press, Cambridge, U.K., 300+viiipp.
4. Øyvind Breivik, Kristian Mogensen, Jean-Raymond Bidlot, Magdalena Alonso Balmaseda, Peter A.E.M. Janssen, Surface Wave Effects in the NEMO Ocean Model: Forced and Coupled Experiments. *Journal of Geophysical Research: Oceans* 04/2015; DOI:10.1002/2014JC010565
5. J. Willebrand, Energy transport in a nonlinear and inhomogeneous random gravity wave field, *J. Fluid Mech.*, 1975; **70** 113-126.
6. K. Hasselmann, On the non-linear energy transfer in a gravity-wave spectrum, part 1: general theory, it J. Fluid Mech., 1962; **12** 481.
7. S. Hasselmann, K. Hasselmann, J.H. Allender, T.P. Barnett, Computations and parameterizations of the nonlinear energy transfer in a gravity wave spectrum, part 2: Parameterizations of the nonlinear energy transfer for application in wave models, *J. Phys. Oceanogr.*, 1985; **15** 1378-1391.
8. J.W. Miles, On the generation of surface waves by shear flows. *J. Fluid Mech.*, 1957; **3** 185-204.
9. P.A.E.M. Janssen, Wave-induced stress and the drag of air flow over sea waves, *J. Phys. Oceanogr.*, 1989; **19** 745-754.
10. WAMDI group: S. Hasselmann, K. Hasselmann, E. Bauer, P.A.E.M. Janssen, G.J. Komen, L. Bertotti, P. Lionello, A. Guillaume, V.C. Cardone, J.A. Greenwood, M. Reistad, L. Zambresky and J.A. Ewing, The WAM model - a third generation ocean wave prediction model, *J. Phys. Oceanogr.*, 1988; **18** 1775-1810.
11. G.J. Komen, L. Cavaleri, M. Donelan, K. Hasselmann, S. Hasselmann, and P.A.E.M. Janssen, *Dynamics and Modelling of Ocean waves* 1994, Cambridge University Press, Cambridge, 532 p.
12. K. Hasselmann, T.P. Barnett, E. Bouws, H. Carlson, D.E. Cartwright, K. Enke, J.A. Ewing, H. Gienapp, D.E. Hasselmann, P. Kruseman, A. Meerburg, P. Müller, D.J. Olbers, K. Richter, W. Sell, H. Walden, Measurements of wind-wave growth and swell decay during the Joint North Sea Wave Project (JONSWAP), *Dtsch. Hydrogr. Z.* Suppl. A, 1973; **8**(12), 95p.
13. J.-R. Bidlot, D. J. Holmes, P. A. Wittmann, R. Lalbeharry, H. S. Chen, Intercomparison of the Performance of Operational Ocean Wave Forecasting Systems with Buoy Data, *Weather and Forecasting*, 2002; **17** 287-310.
14. S. Abdalla and P. Janssen, Monitoring Waves and Surface Winds by Satellite Altimetry: Applications, in *Satellite Oceanography over Oceans and Land Surfaces*, 2017; edited by D. Stammer and A. Cazenave, CRC Press, Taylor & Francis group.
15. P.A.E.M. Janssen, Progress in ocean wave forecasting. *Journal of Computational Physics*, 2008; **227** 3572-3594.
16. A.C. Voorrips, C. Mastenbroek, B. Hansen, Validation of two algorithms to retrieve ocean wave spectra from ERS synthetic aperture radar, *J. Geophys. Res.*, 2001; **106** No. C8 16,825-16,840.
17. J.-R. Bidlot, P.A.E.M Janssen, S. Abdalla, On the importance of spectral wave observations in the continued development of global wave models, Proc. Fifth Int. Symposium on Ocean Wave Measurement and Analysis WAVES2005: 3rd-7th July 2005, Madrid, Spain.
18. H.L. Tolman, Treatment of unresolved islands and ice in wind wave models, *Ocean Modelling*,2003; **5** 219-231.
19. D.V. Chalikov and V.K. Makin, Models of the wave boundary layer. *Boundary Layer Meteorol.*,1991; **56** 83-99.
20. S.E. Belcher and J.C.R. Hunt, Turbulent shear flow over slowly moving waves. *J. Fluid Mech.*,1993; **251** 109-148.
21. T.S. Hristov, S.D. Miller, C.A. Friehe, Dynamical coupling of wind and ocean waves through wave-induced air flow, *Nature*, 2003; **442** 55-58.
22. P. Sullivan, J. McWilliams, C.-H. Moeng, Simulation of turbulent flow over idealized water waves, *J. Fluid. Mech.*, 2000; **404** 47-85.
23. A.L. Fabrikant, Quasilinear theory of wind-wave generation. *Izv. Atmos. Ocean. Phys.*,1976; **12** 524-526.
24. P.A.E.M. Janssen, Quasilinear approximation for the spectrum of wind-generated water waves. *J. Fluid Mech.*, 1982; **117** 493-506.
25. M.A. Donelan, The dependence of the aerodynamic drag coefficient on wave parameters, p381-387 in: *Proc. of the first international conference on meteorological and air/sea interaction of the coastal zone*, 1982; Amer. Meteor. Soc., Boston, Mass.
26. S.D. Smith, R.J. Anderson, W.A. Oost, C. Kraan, N. Maat, J. DeCosmo, K.B. Katsaros, K.L. Davidson, K. Bumke, L. Hasse and H.M. Chadwick, Sea surface wind stress and drag coefficients: the HEXOS results. *Boundary Layer Meteorol.*, 1992; **60** 109-142.
27. J.W. Miles, Surface wave generation revisited. *J. Fluid Mech.*, 1993; **256** 427-441.
28. W.J. Plant, A relation between wind stress and wave slope. *J. Geophys. Res.*, 1982; **C87** 1961-1967.
29. P.A. Huang, Temporal and spatial variation of the drag coefficient of a developing sea under steady wind-forcing. *J. Geophys. Res.*, 2005; **110**, C07024. doi:10.1029/2005JC002912
30. J.B. Edson, V. Jampana, R.A. Weller, S.P. Bigorre, A.J. Pluedemann, C.W. Fairall, S.D. Miller, L. Mahrt, D. Vickers and H. Hersbach, On the exchange of Momentum over the Open Ocean, *J. Phys. Oceanogr.*, 2013; **43**, 1378-1391.
31. P.A.E.M. Janssen, J.D. Doyle, J. Bidlot, B. Hansen, L. Isaksen and P. Viterbo, 2002: Impact and feedback of ocean waves on the atmosphere. in *Advances in Fluid Mechanics*, 2002; **33**, Atmosphere-Ocean Interactions ,Vol. I, Ed. W.Perrie.
32. P.A.E.M. Janssen and P. Viterbo, Ocean Waves and the atmospheric Climate. *J. Climate*, 1996; **9** 1269-1287.
33. P.A.E.M. Janssen, Effect of surface gravity waves on the heat flux. ECMWF Technical Memorandum, 1997; no. 239.
34. A. Brut, A. Butet, P. Durand, G. Caniaux and S. Planton, Air-sea exchanges in the equatorial area from the EQUALANT99 dataset: Bulk parametrizations of turbulent fluxes corrected for airflow distortion. *Quarterly Journal of the Royal Meteorological Society*, 2005; **131** 2497-

2538.
35.J. DeCosmo, K. Katsaros, S. Smith, R. Anderson, W. Oost, K. Bumke, and H. Chadwick, Air-sea exchange of water vapor and sensible heat: The Humidity Exchange Over the Sea (HEXOS) results, *J. Geophys. Res.*, 1996; **101(C5)** 12001-12016.
36.Ann-Sofi Smedman, Ulf Sahlée, Erik Högström, and Cecilia Johansson, Critical re-evaluation of the bulk transfer coefficient for sensible heat over the ocean during unstable and neutral conditions. *Quarterly Journal of the Royal Meteorological Society*, 2007; **133** 227-250.
37.W.A. Oost, C.M.J. Jacobs, C. Van Oort, Stability effects on heat and moisture fluxes at sea. *Boundary-Layer Meteorol.*, 2000; **95** 271302.

Available online at www.sciencedirect.com

ScienceDirect

Procedia IUTAM 26 (2018) 30–42

Procedia IUTAM

www.elsevier.com/locate/procedia

IUTAM Symposium Wind Waves, 4–8 September 2017, London, UK

Wind-Wave Breaking

W. Kendall Melville*

Scripps Institution of Oceanography, U.C. San Diego, 9500 Gilman Dr., La Jolla, CA 92093-0213, USA

Abstract

Rational models of wind-wave growth were proposed in the 1950s (Miles 1957, Phillips 1957), theories of wave-wave interactions (Phillips 1960, Hasselmann 1962, Zakharov 1968) and wave-action conservation for waves in fluids (Whitham 1965, Bretherton and Garrett 1969) in the 1960s, but it was not until the 1980s that laboratory experiments (Duncan 1981, Melville and Rapp 1985) and a seminal paper by Owen Phillips in 1985 on a model of the equilibrium range in wind-wave spectra, and a formulation of breaking, began a rational program of research into the role of breaking in surface wave kinematics and dynamics. Two important features of Phillips' 1985 paper were the introduction of $\Lambda(c)dc$, the average total length of breaking fronts per unit area of ocean moving with velocities in the range (c, c + dc) and the statement that the average rate of energy loss per unit area by breakers in the same velocity range was given by

$$\varepsilon_b(c)dc = b(c)\rho g^{-1}c^5\Lambda(c)dc$$

where b is a dimensionless breaking strength and g is gravity. The energy loss per unit length of breaker, $b\rho g^{-1}c^5$, was based on Duncan's work, but anticipated in part by Lighthill (1978). Lower order moments of $\Lambda(c)$ describe kinematical features of breaking up to the third moment, with the fourth moment describing the momentum flux from waves to currents. The structure of the dissipation equation imposes a combination of different approaches to quantifying it. Estimates of b have depended on arguments based on Taylor's (1935) inertial scaling of turbulence dissipation, supported by laboratory experiments and recent DNS and LES numerical experiments, while $\Lambda(c)$ over any significant dynamical range can only be measured in the field. The success of the early attempts to follow this approach has led to recent work on air entrainment for gas transfer, and theoretical uses of fundamental vortex dynamics to develop our knowledge of the role of breaking in air-sea interaction. In this paper I will review the material from the laboratory, through scaling arguments, modeling and field measurements.

Peer-review under responsibility of the scientific committee of the IUTAM Symposium Wind Waves.

* Corresponding author. Tel.: +1-858-534-0478; fax: +1-858-534-7132.
E-mail address: kmelville@ucsd.edu

2210-9838
Peer-review under responsibility of the scientific committee of the IUTAM Symposium Wind Waves.
10.1016/j.piutam.2018.03.004

Keywords: Wind waves; wave spectra; wave breaking; breaking statistics.

1. Introduction

Modern studies of wave breaking in deep water have accelerated significantly since the 1980s. Early modeling of wave breaking was essentially a tuning exercise to maintain consistency with parts of the physics that were thought to be better understood: i.e. the wind input to the wave field and the nonlinear four-wave interactions. Much of the progress on breaking has been due to the influence of Owen Phillips' 1985 paper on the equilibrium spectrum of wind waves and his seminal ideas on the formulation and statistics of the breaking problem. Progress has proceeded through laboratory experiments, scaling arguments, theory, numerical modeling and field work, with the latter depending to a great extent on instrument development in both the laboratory and the field. While there appears to have been significant progress, many problems remain. Furthermore, it is likely that as our understanding of breaking improves it will point to weaknesses in other areas of wind-wave science.

Breaking limits the height of surface waves, mixes the ocean surface, generates currents, and enhances air-sea fluxes of heat, mass and momentum through the generation of turbulence, the entrainment of air and the creation of spray and aerosols. Breaking is a transition process from pure wave dynamics, which may be considered laminar, to two-phase turbulent flow dynamics. In the field these patches of turbulence are intermittent in space and time, and depend, in ways that are yet not completely understood, on the group statistics of the wave field. Figure 1 shows examples of wind-forced breaking wave fields off the coast of California.

In this paper I provide a brief review of work done by my research group on the title problem using laboratory and field experiments, theory and numerical work. A more complete review of the topic is beyond the constraints of these conference proceedings. Despite the complexity of the breaking problem, we find that progress has been made on understanding the kinematics and dynamics. While this progress depends on advances in observational and DNS numerical techniques, it also depends on the use of classical scaling arguments from turbulence theory.

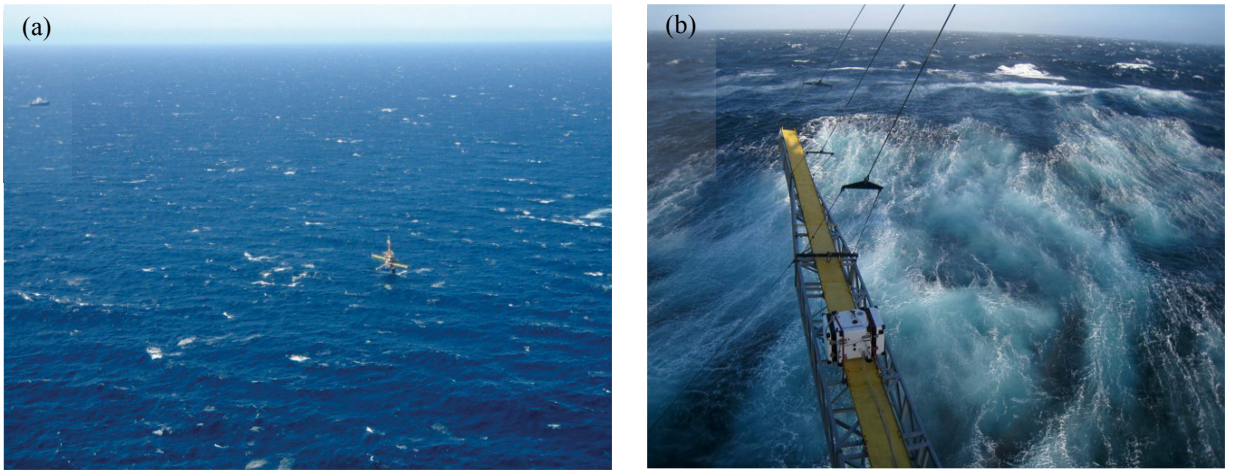

Figure 1. (a) left: Breaking wave field off S. California, March 2017. Note R/P FLIP (centre) and R/V Sally Ride (top left). (b) right: Rear face of a breaking wave taken from FLIP off N. California, June 2010. FLIP's boom is approximately 20 m long. Photo credit: Nick Statom.

2. Phillips (1985) model

2.1 The Wave Field

Before considering breaking it is important to describe the underlying wave field. Phillips (1985) started with the radiative transfer equation

$$\frac{dN}{dt} = \frac{\partial N}{\partial t} + (\mathbf{c}_g + \mathbf{U})\mathbf{g}\nabla N = \frac{S_{in} + S_{nl} + S_{ds}}{\sigma} , \tag{2.1}$$

where N is the wave action, $\mathbf{c}_g$ is the group velocity, $\mathbf{U}$ the current, S_{in} the wind input, S_{nl} the nonlinear wave-wave interaction, S_{ds} the dissipation due to breaking and σ the intrinsic frequency. The energy "source" terms comprise the numerator on the right-hand side of equation (2.1). If dN/dt is slow enough, then to leading order Phillips assumed equilibrium, that is

$$S_{in} + S_{nl} + S_{ds} = 0 , \tag{2.2}$$

and that all three "source" terms were of comparable magnitude and proportional to one another. With these assumptions he found that the directional wave spectrum was given by

$$\Psi(\mathbf{k}) = k^{-4} B(\mathbf{k}) = \beta(\cos\theta)^p u_* g^{-1/2} k^{-7/2}, \quad p \sim 1/2 , \tag{2.3}$$

with an omnidirectional spectrum proportional to $k^{-5/2}$ and a frequency spectrum $\Phi(\sigma) = \alpha g u_* \sigma^{-4}$. Here $\mathbf{k}$ is the vector wavenumber, $k = |\mathbf{k}|$, $B(\mathbf{k})$ is the saturation of the wave spectrum and u_* is the friction velocity in the marine atmospheric boundary layer. Figure 2 shows recent data with the $k^{-5/2}$ equilibrium spectrum followed by a k^{-3} saturation spectrum, measured by airborne lidar, and the corresponding frequency spectrum measured from FLIP (Lenain & Melville, 2017)

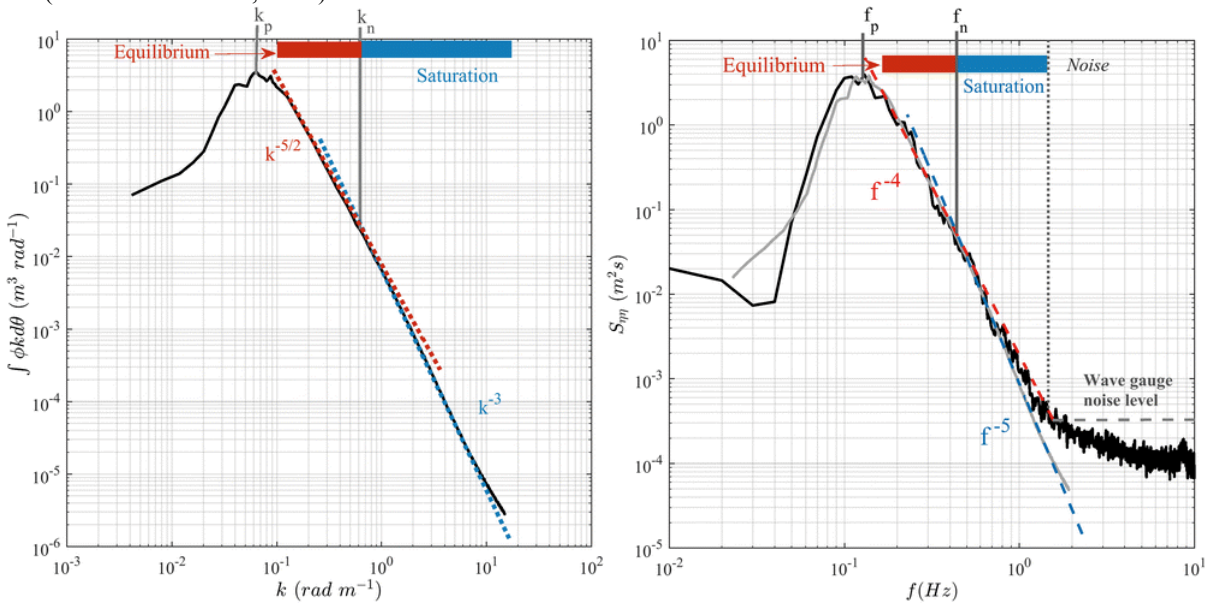

Figure 2. Wind-wave wavenumber (left) and frequency (right) omnidirectional spectra (Lenain & Melville 2017).

2.2 Breaking statistics

Phillips defined the average length of breaking fronts per unit area of ocean surface moving with velocities in the range $(\mathbf{c}, \mathbf{c} + d\mathbf{c})$ by $\Lambda(\mathbf{c})d\mathbf{c}$. The fraction of surface turned over by breaking per unit time is then $R = \int c\Lambda(c)dc$, where $c = |\mathbf{c}|$. Following Duncan (1981) the average rate of wave energy loss by breakers per unit area of ocean surface is given by the fifth moment of Λ:

$$\varepsilon_b(c)dc = b\rho g^{-1} c^5 \Lambda(c)dc \tag{2.4}$$

where $\varepsilon_b dc$ is the dissipation due to breaking in $(c, c + dc)$ and b is a dimensionless strength of breaking (the "breaking parameter").

The related momentum flux from waves to currents is

$$m_b(\mathbf{c})d\mathbf{c} = b\rho g^{-1}c^4\Lambda(\mathbf{c})d\mathbf{c}. \tag{2.5}$$

In the equilibrium model,

$$\Lambda(\mathbf{c}) \propto b^{-1}(\cos\theta)^{3p}u_*^3 gc^{-7} \text{ while } \Lambda(c) \propto c^{-6}. \tag{2.6}$$

2.3 What is c?

Phillips (1985) assumed, but did not explicitly state, that c is the characteristic linear phase speed of the breaking wave. This was based on the quasi-steady experiments of Duncan (1981), in which geometric similarity of the breaking region relative to the underlying wave was found. This requires that c be the phase speed. Early breaking criteria assumed it was associated with Stokes limiting wave form for which the phase speed is approximately 9% more than the linear value; however, as shown below, the speed of the unsteady breaking fronts is typically O(10%) less than a characteristic linear phase speed for the group and can lead to significant differences due to the importance of higher order moments of $\Lambda(c)$. In what follows we will use $c = (gk^{-1})^{1/2}$ to represent the linear phase speed of gravity waves and $c_b = |\mathbf{c}_b|$ to represent the speed of the breaking front.

3. Generating breaking in the laboratory.

Field data (Terrill & Melville 1988) shows that breaking of the dominant waves correlates with the wave groups. Laboratory data (Melville 1982, 1983) shows that Benjamin-Feir instability also leads to breaking by dispersive focusing following the amplitude and frequency modulation of the waves resulting from the B-F instability. The latter breaking is very gentle with no significant air entrainment and may be associated with the generation of dissipative parasitic capillaries. Longuet-Higgins (1974) suggested the use of the focusing of dispersive wave packets as a means of generating breaking in the laboratory and this technique has been exploited by Melville & Rapp (1985), Rapp & Melville (1990) and others to do controlled experiments on breaking. Figure 3 shows an x-t diagram of the focusing of the incident waves, the various phenomena resulting from breaking, and the path of the transmitted waves. Since the incident and transmitted waves become linear far enough upstream and downstream of breaking, x_1 and x_2 respectively, then equipartition applies and, since the radiated waves are found to be negligible, it is a relatively simple matter to measure the energy lost from the wave field due to breaking.

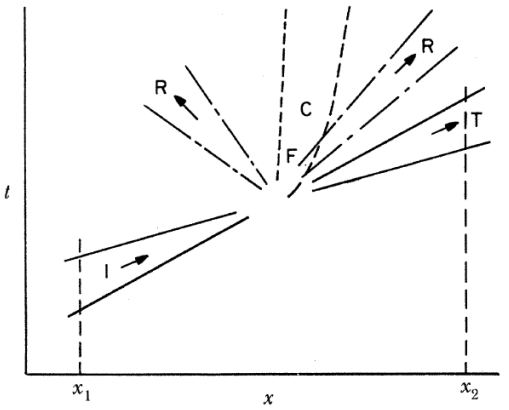

Figure 3. Schematic of focusing waves packet: I=incident waves, T=transmitted waves, R=radiated waves, C=current, F=turbulence (Rapp & Melville 1990).

Rapp & Melville (1990) used the dispersive focusing method to generate breaking of wave groups. By spreading dye over the surface pre-breaking and imaging the evolution of the dye during breaking, both c_b and the mixing down of the surface layer by breaking could be measured. Figure 4 shows examples of such an analysis where the initial value of $c_b = 0.8c$, and c is a characteristic phase speed of the waves in the group.

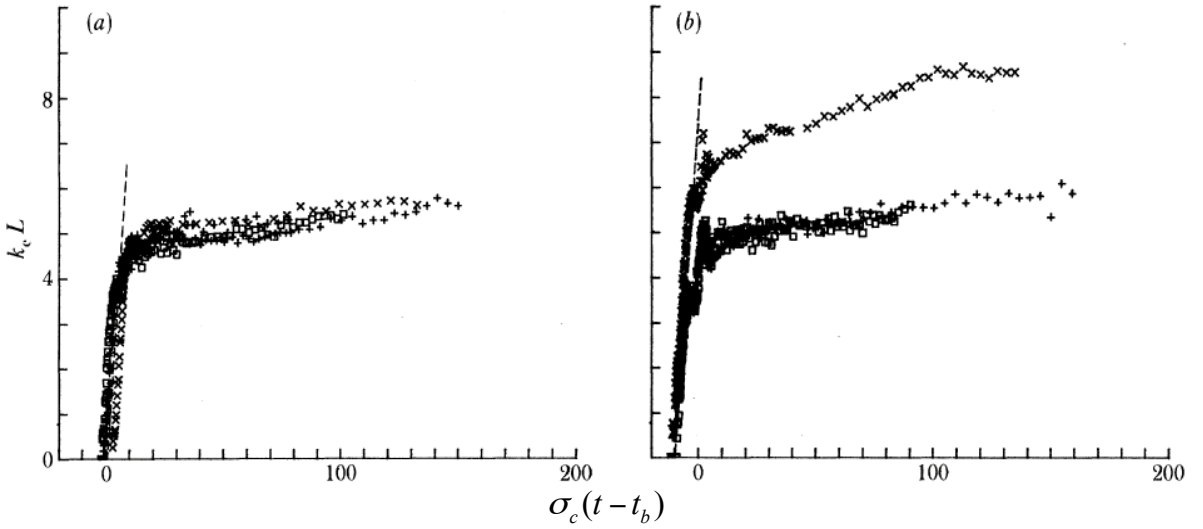

Figure 4. Non-dimensional length of surface mixed by breaking as a function of dimensionless time where (σ_C, k_C) are the center frequency and wavenumber and t_b is the linear prediction of time to focusing for (a) spilling wave and (b) plunging waves. Wave group centre frequency $f_C = 0.88$ Hz (×), 1.08 (+), 1.28 (W) and $\Delta f / f_C = 0.73$; $x_b k_c = 27.4$. The dashed lines correspond to a speed of $0.8c_c$.(Rapp & Melville 1990)

4. Wave energy dissipation

One of the overarching goals of breaking research is to measure or infer the wave energy dissipation in the field and use the results to improve the dissipation component of wind-wave models. We can write this dissipation as

$$S_{ds} = \int b\rho g^{-1} c^5 \Lambda(c) dc \tag{4.1}$$

where the breaking parameter, b, can be measured in the laboratory (Drazen et al. 2008), but $\Lambda(c)$ must be measured in the field since it is generally not possible to reproduce the dynamic directional range of the surface wave field in the laboratory. As mentioned above, breaking is a transition process, from wave motion to turbulence. Now one of the cornerstones of turbulence theory is G.I. Taylor's (1935) inertial model of dissipation: $\varepsilon = \chi u^3 / l$, where χ is a constant of O(1), u is an integral velocity scale and l an integral length scale, and the Reynolds number $\mathrm{Re} = ul/\nu$? 1. If we consider a plunging breaking wave as shown in Figure 5, the toe of the breaker travels at a ballistic velocity. If we assume that Taylor's inertial result applies, now with the initial wave variables rather than the integral turbulence scales, then we have a length scale from the vertical distance the toe of the breaker travels before hitting the surface, h, and the ballistic vertical velocity at impact , $w = (2gh)^{1/2}$. The inertial approach was initially considered by Melville (1994) who erroneously chose the incorrect initial velocity scale. The approach was subsequently followed by Drazen et al. (2008) who showed that the dissipation rate per unit length of breaking front was given by

$$\varepsilon_l = b\frac{\rho c^5}{g}; \tag{4.2}$$

here c *is* a characteristic phase speed, and

$$b = \beta(hk)^{5/2} \tag{4.3}$$

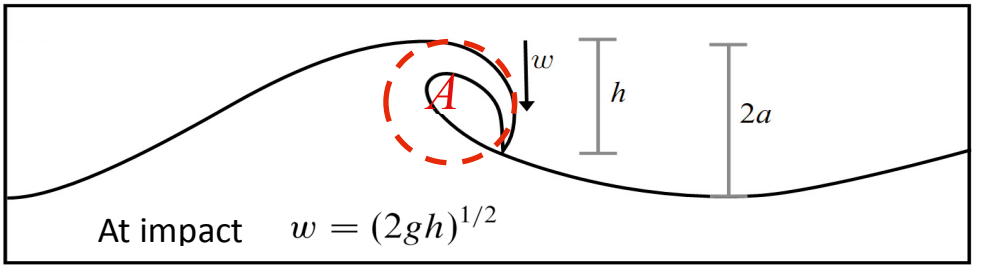

Figure 5. Schematic figure for inertial estimate of wave dissipation due to a plunging breaker. Red circle diameter h corresponds to area A of inertial dissipation. (Drazen et al. 2008)

Note that β is an O(1) constant and hk is a slope parameter with k a characteristic wavenumber. Drazen et al. (2008) found that laboratory experiments for strong breaking waves gave $b \propto (hk)^{5/2}$ within the scatter of the data. The disadvantage of this result, is that it is expressed in terms of hk a measure of the wave slope at breaking, something we do not know a priori. However, it was found that by using the linear prediction of the slope at focusing, S, that the best fit to the data was $b \propto S^{2.77}$, close to the 5/2 result. Subsequently, Romero et al. (2012) showed that by using a threshold slope, or offset, all the known laboratory measurements of b at that time could be accounted for by $b = 0.4(S - 0.08)^{5/2}$. These measurements ranged from incipient breaking to plunging waves over three orders of magnitude of b. This result is shown in Figure 6, where a cubic fit to the data is also shown, but one that is purely empirical with no physical foundation as is the case for $b \propto S^{5/2}$. Since these laboratory results were established, DNS (Deike et al. 2015, 2016, 2017) and LES (Derakhti & Kirby 2016: DK2016) have shown similar results, with the LES (DK2016, Fig. 14) showing that the use of a spectrally weighted slope, S_{so}, rather than S reduced the scatter about the curve $b = 0.3(S_{so} - 0.07)^{5/2}$.

Romero et al. (2012) used lidar measurements of the fetch-limited wave field in the Gulf of Tehuantepec (Romero & Melville (2010a,b) and simultaneous airborne video measurements of the whitecap kinematics to infer $\Lambda(c)$ (Kleiss & Melville 2010, see below) to see whether the laboratory measurements of b could be used to close the radiative balance equation, neglecting the currents and balancing the advective term by the source terms:

$$\begin{aligned} S_{ds}(x,k) &= c_g \cdot \nabla\Psi(x,k,\theta) - S_{in}(x,k) - S_{nl}(x,k) \\ \rho_w g S_{ds}(c)dc &= b\rho_w g^{-1} c^5 \Lambda(c)dc \end{aligned} \tag{4.4}$$

Since the mean square slope $mss = \int B(k)k^{-1}dk$, where $B(k) = \int \Psi(\mathbf{k})k^4 d\theta$ is the saturation, in defining the breaking strength b in the spectral model, Romero et al. (2012) used $b = A(B(k)^{1/2} - B_T(k)^{1/2})^{5/2}$. They found that in order to close the equations that they had to extrapolate $\Lambda(c)$ to values of c lower than those reliably measured by using whitecap kinematics (See dashed line in Figure 7a). The inference of this result was that the dynamics depended on breakers for which there was little or no significant air entrainment, certainly less than could be measured by airborne visible imagery.

5. Field measurements of breaking

5.1 Field measurements of $\Lambda(c)$

The need to measure both air-entraining and non-air-entraining breakers has introduced the need to use both visible and infrared (IR) imagery to measure the kinematics of the breaking. Evaporative cooling of a thin surface layer even by a slight wind means that when a wave gently breaks without significant air entrainment that cool skin is broken and is visible in the IR imagery.

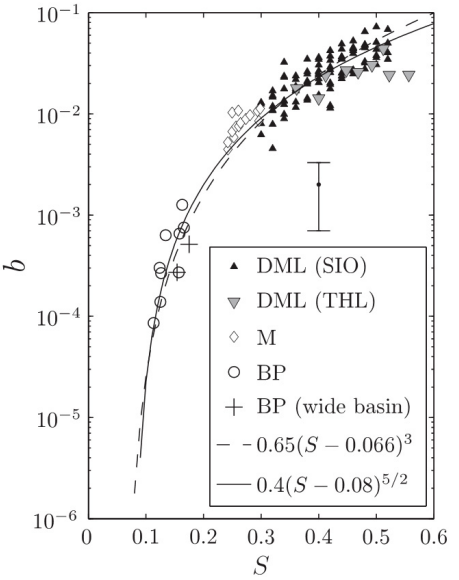

Figure 6. Breaking strength parameter b as a function of the linear prediction of the wave slope at breaking, S (Romero et al. 2012)

In a series of experiments from the research platform FLIP, Sutherland and Melville (2013; SM2013) used visible and IR imagery to measure $\Lambda(c)$ and acoustic Doppler instruments to measure the energy dissipation rate in the surface layers of the ocean. Figure 7 shows their $\Lambda(c)$ data, color coded by wave age, along with field data by others (Melville & Matusov 2002, Gemmrich et al. 2008, Phillips et al. 2001, Kleiss & Melville 2010), and laboratory measurements by Jessup & Phadnis (2005). Also shown are the predictions of Romero et al. (2012) based on the Kleiss & Melville (2010) $\Lambda(c)$ data from airborne visible imagery. The wave-age colour-coded SM2013 data generally show a decrease in $\Lambda(c)$ as the wave age increases. There was good agreement with Zappa et (2012) in measuring $\Lambda(c)$ with visible imagery from FLIP. Using dimensional analysis, and assuming the fetch dependence was included in other variables, Sutherland & Melville (2013) found that

$$\Lambda(c)\frac{c_p^3}{g}\left(\frac{c_p}{u_*}\right)^{0.5} = f\left(\frac{c_b}{\sqrt{gH_s}}\left\{\frac{gH_s}{c_p^2}\right\}^{0.1}\right) \tag{5.1}$$

provided a collapse of their data as shown in going from Figure 7a to Figure 7b. While they included the dependence on (gH_s/c_p^2), it is so weak as to be negligible within the scatter of the data. (Note that in Figures 7-9 from the papers of Sutherland and Melville, c is equivalent to our c_b.)

Sutherland & Melville (2013) also examined the relationship between the measurements of the wave energy dissipated by breaking and modeling of dissipation by Romero & Melville (2010b) where the dissipation term was based on Alves & Banner (2003) but explicitly forced saturation at the higher wavenumbers. The measured breaking- induced momentum flux from waves to currents was compared with the measured wind stress. These results are shown colour-coded by wave age in Figures 8a and 8b, respectively. It is clear from the figure that there is good agreement between the dissipation and momentum flux inferred from the $\Lambda(c)$ measurements and the

modeling (for dissipation) or wind stress (momentum flux) at the lower wave ages up to full development. However, both show differences for the largest wave ages, when the underlying waves are swell. Firstly, the differences at the larger wave ages might be expected since we do not expect much, if any, significant breaking of the swell. Secondly, we expect a significant correlation between the momentum and energy fluxes, **M** and E respectively, since they are related by

$$\mathbf{M} = \frac{\mathrm{E}}{c}\frac{\mathbf{k}}{k}. \tag{5.2}$$

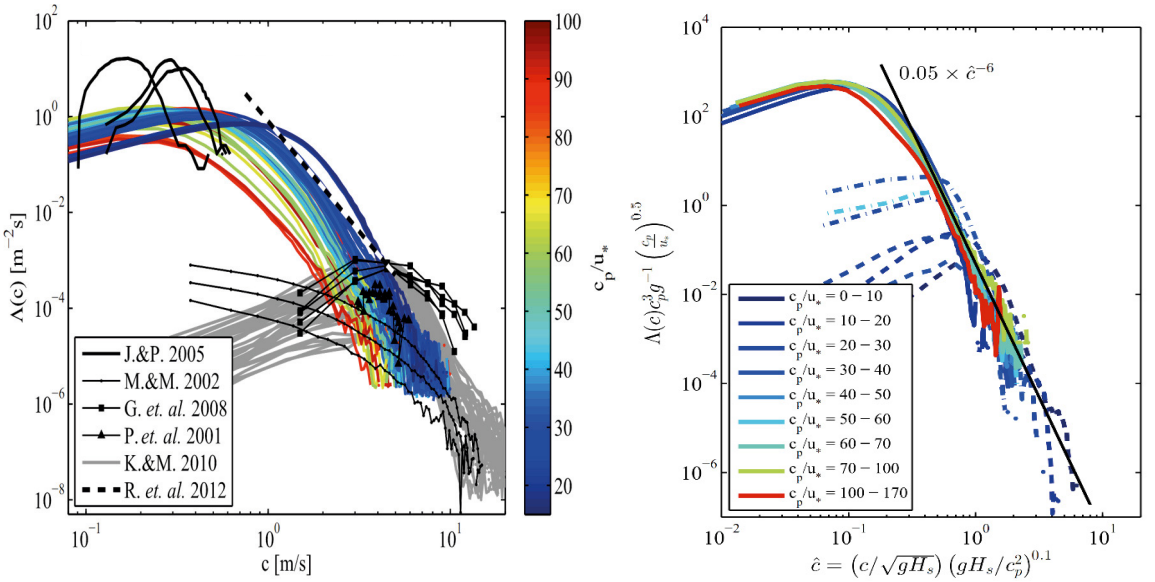

Figure 7. (a) left: Field and laboratory data and prediction described in the text. (b) right: Collapse of the SM2013 data with non-dimensional variables. (Sutherland & Melville 2013)

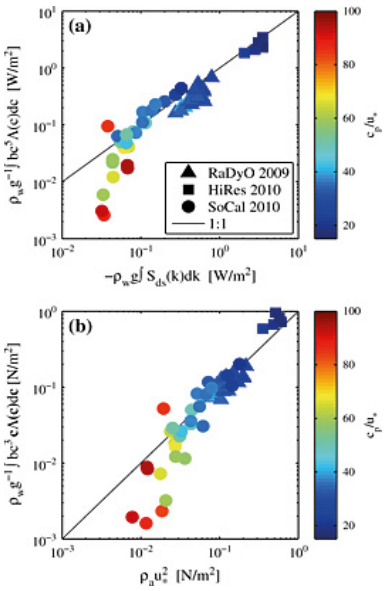

Figure 8. (a) Dissipation by breaking (ordinate) compared with modeled wave field dissipation (abscissa). (b) Momentum flux from waves to currents due to wave breaking (ordinate) plotted against wind stress (abscissa). Color shows wave age and solid line indicates 1:1 correspondence. (Sutherland & Melville 2013)

It is important to remember that the momentum flux from the atmosphere to the ocean, and the flux from the waves to currents are not necessarily locally equal. For example, some swell from Southern Ocean storms ends up providing momentum for wave set-up and along-shore currents on the beaches of the US west coast.

5.2 Field measurements of turbulent dissipation, ε

It has been known for some time that the dissipation rate per unit mass, ε, in the near-surface waters may be

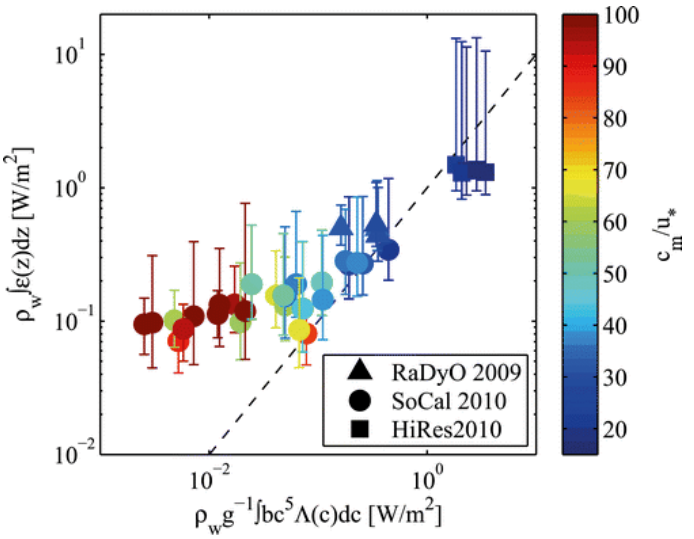

one Figure 9. Comparison between dissipation measured in the water column (ordinate) and by breaking (abscissa).(Sutherland & Melville 2015a)

to two orders of magnitude greater than that in the classical boundary layer over a rigid surface (Kitaigorodski et al.1983, Agrawal et al. 1992). In that classical case $\Phi_\varepsilon \equiv \varepsilon \kappa z / u_{*w}^3 = 1$ applies in the logarithmic law-of-the-wall region where κ is the von Karman constant, z is the distance from the surface and u_{*w} is the friction velocity in the water. The early measurements were not able to sample the data between wave troughs and crests but using acoustic Doppler techniques Gemmrich (2010) was able to reach within O(1) cm of the surface from below and found that the dissipation correlated with the wave spectrum saturation, a measure of breaking investigated by Banner et al. (2002). Sutherland & Melville (2015a) were able to measure dissipation in the water column using acoustic instrumentation and at the surface using stereo IR imagery from above (Sutherland & Melville (2015b). Over short intervals the sea surface temperature may be considered a passive tracer and so the velocity of the surface fluid can be measured using image processing techniques. See Figure 9.

6. Wave-current interaction and breaking

In what we have discussed so far we have just considered breaking in the context of a wind-forced wave field in the absence of inhomogeneous unsteady currents. However, it is well-known that waves propagating into an opposing current steepen, shorten and may break. This is most commonly seen in the nearshore when waves incident on the coast meet a river outflow on the ebb tide; however, the same physics is at play in deep water current systems when wind waves or swell meet opposing currents, extreme and breaking waves may be generated. This is the case in the Agulhas current and other major western boundary currents. There is also growing evidence of wave-current interaction leading to breaking at oceanic fronts as is shown in Figure 10. See Romero et al. (2017)

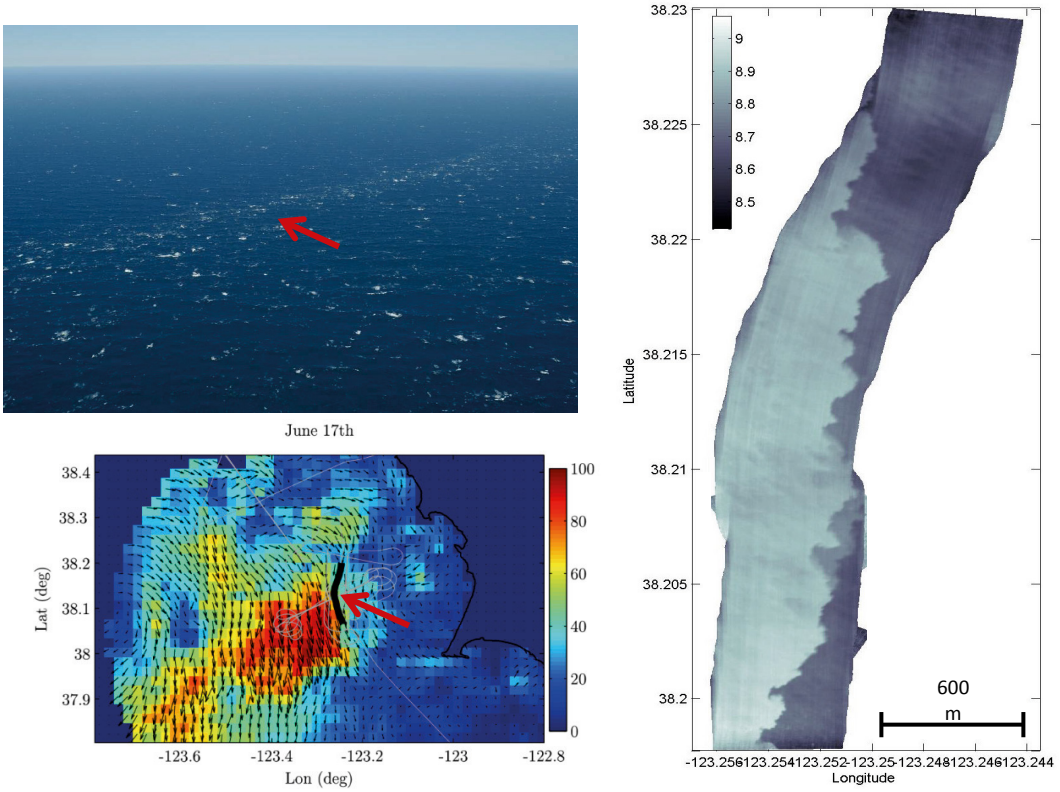

Figure 10. Clockwise from top left. Visible image of sharp gradient in breaking intensity at ocean front off Bodega Bay, CA, June 17, 2010. Infrared image of the sharp front in the sea surface temperature. Surface current vectors and color-coded speed with color bar in cm/s. The black line and red arrow matches with the front and arrow in the visible image (Romero et al. 2017)

The striking feature in Figure 10 is how sharp the spatial gradients are in the visible image (breaking) and IR image (temperature). In each case we estimate that the length scale of these gradients is O(10) m. While the spatial resolution of the coastal radar is only 2 km, it shows changes in surface currents across the front from approximately 20-60 cm/s or 0.4-1.2 kts. If the change in the current is small compared to the group velocity of the waves then we would expect little wave-current interaction over scales that are not large compared to the wavelength. In this case, waves of group velocity 1.2 kts have a wavelength of approximately 3.6 m, so we expect that large gradients and significant breaking over the scale of the current gradient will be limited to the shorter gravity waves, not those near the peak of the spectrum. This is consistent with the data from Romero et al. (2017).

Very recent numerical modeling and satellite remote sensing data across the Gulf Stream and in the Southern Ocean have shown that "…variations in currents at scales of 10-100 km are the main source of variations in wave heights at the same scales". (Ardhuin et al. 2017)

7. Discussion

Considerable progress has been made in better understanding the kinematics and dynamics of wind-wave breaking in the approximately thirty years since Phillips' 1985 paper. He acknowledged that his assumptions in predicting the $k^{-5/2}$ equilibrium wave spectrum are not unique. Furthermore, given the fact that S_{nl} has zero crossings, whereas S_{in} and S_{ds} are positive and negative definite, respectively, over a wide range of frequencies or

wavenumbers, his assumption that $S_{in} \propto S_{nl} \propto S_{ds}$ can only apply over a single lobe of the three in S_{nl}. Lenain & Melville (2017), using spectra like those in Figure 2 and computing S_{nl}, found that the transition wavenumber from equilibrium to saturation spectrum k_n was in the range of $(1,2)k_u$, where k_u is the zero up-crossing wavenumber going from the negative to positive lobes in S_{nl} as k increases.

This review has focused mainly on the impact of breaking on the wave field. However, breaking is the physical process by which there is a momentum flux from waves to currents, and so is very important for upper ocean dynamics and kinematics involving the vortex force due to the Eulerian vorticity and the mean Lagrangian current, which for unbroken waves includes the Stokes drift. But what is the Lagrangian drift in a breaking wave field? This was recently investigated numerically by Deike et al. (2017) who found that in breaking waves the average Lagrangian drift $\overline{u}_L \propto Sc$ significantly larger than $u_L \propto S^2 c$ for unbroken wave groups, which is consistent with Stokes classical result. With this result and the measurements of $\Lambda(c)$ we are currently investigating the contribution of breaking to the mean Lagrangian current at the ocean surface.

It has been known for some time that breaking waves contribute to air entrainment at the ocean surface and therefore to air-sea gas transfer. In a several papers the air entrainment and bubble size distribution have been considered using DNS and theoretical modeling. Deike et al. (2016) used DNS to study the air entrainment and bubble size distributions in single breaking events. Good agreement was found with the laboratory measurements of bubble size distributions (c.f. Deane & Stokes 2002) and a model based on the hypothesis that there is a balance between the buoyancy force due to the bubbles and the wave energy dissipated was successfully tested. Deike et al. (2017) went on to use the field measurements of $\Lambda(c)$ described above and the numerical results from the single breaking events to develop a model of the entrained air in the ocean that was proportional to the third moment of $\Lambda(c)$ and a function of a measure of the wave slope.

Given the inhomogeneity of breaking demonstrated in Figure 10 it is clear that this is a topic that will draw much attention in the future. One of the major trends in physical oceanography research is towards submesoscale and microscale processes at the ocean surface that contribute to vertical transport. This places an emphasis on processes at the boundaries of fronts, eddies and filaments like those visible in Figure 10. It is clear that understanding the dynamics associated with breaking will play a significant role in that research.

Acknowledgements

I wish to thank my students, postdoctoral fellows and others in my research group for making much of this work possible. They include Luc Deike, David Drazen, Laurent Grare, Jessica Kleiss, Luc Lenain, Nick Pizzo, Ron Rapp, Leonel Romero, Nick Statom, Peter Sutherland, Eric Terrill, Fabrice Veron and Chris White. My work on these topics has been supported by the physical oceanography programs at the National Science Foundation and the Office of Naval Research.

References

Agrawal, Y. C., E. A. Terray, M. A. Donelan, P. A. Hwang, A. J. Williams, W. M. Drennan, K. K. Kahma, and S. A. Kitaigorodskii (1992), Enhanced dissipation of kinetic energy beneath surface waves, *Nature*, *359*(6392), 219-220.

Alves, J., and M. L. Banner (2003), Performance of a saturation-based dissipation-rate source term in modeling the fetch-limited evolution of wind waves, *Journal of Physical Oceanography*, *33*(6), 1274-1298.

Ardhuin, F., S. T. Gille, D. Menemenlis, C. B. Rocha, N. Rascle, B. Chapron, J. Gula, and J. Molemaker (2017), Small-scale open ocean currents have large effects on wind wave heights, *Journal of Geophysical Research-Oceans*, *122*(6), 4500-4517, doi:10.1002/2016jc012413.

Banner, M.L., J. R. Gemmrich, and D. M. Farmer, 2002: Multiscale measurement of ocean wave breaking probability. J. Phys. Oceanogr.,32, 3364–3375.

Bretherton, F.P. and C. J. R. Garrett (1968), Wavetrains in inhomogeneous media, *Proceedings of the Royal Society of London Series a-Mathematical and Physical Sciences*, *302*(1471), 529-&, doi:10.1098/rspa.1968.0034.
Deane, G. B., and M. D. Stokes (2002), Scale dependence of bubble creation mechanisms in breaking waves, *Nature*, *418*(6900), 839-844, doi:10.1038/nature00967.
Deike, L., L. Lenain, and W. K. Melville (2017), Air entrainment by breaking waves, *Geophys. Res. Lett.*, *44*(8), 3779-3787, doi:10.1002/2017gl072883.
Deike, L., W. K. Melville, and S. Popinet (2016), Air entrainment and bubble statistics in breaking waves, *Journal of Fluid Mechanics*, *801*, 91-129, doi:10.1017/jfm.2016.372.
Deike, L., S. Popinet, and W. K. Melville (2015), Capillary effects on wave breaking, *Journal of Fluid Mechanics*, *769*, 541-569, doi:10.1017/jfm.2015.103.
Derakhti, M., and J. T. Kirby (2016), Breaking-onset, energy and momentum flux in unsteady focused wave packets, *Journal of Fluid Mechanics*, *790*, 553-581, doi:10.1017/jfm.2016.17.
Drazen, D. A., W. K. Melville, and L. Lenain (2008), Inertial scaling of dissipation in unsteady breaking waves, *Journal of Fluid Mechanics*, *611*, 307-332, doi:10.1017/s0022112008002826.
Duncan, J. H. (1981), An experimental investigation of breaking waves produced by a towed hydrofoil, *Proceedings of the Royal Society of London Series a-Mathematical Physical and Engineering Sciences*, *377*(1770), 331-&, doi:10.1098/rspa.1981.0127.
Gemmrich, J. (2010), Strong Turbulence in the Wave Crest Region, *Journal of Physical Oceanography*, *40*(3), 583-595, doi:10.1175/2009jpo4179.1.
Gemmrich, J. R., M. L. Banner, and C. Garrett (2008), Spectrally resolved energy dissipation rate and momentum flux of breaking waves, *Journal of Physical Oceanography*, *38*(6), 1296-1312, doi:10.1175/2007jpo3762.1.
Hasselmann, K. (1962), On the nonlinear energy transfer in a gravity-wave spectrum. 1. General theory, *Journal of Fluid Mechanics*, *12*(4), 481-500, doi:10.1017/s0022112062000373.
Jessup, A. T., and K. R. Phadnis (2005), Measurement of the geometric and kinematic properties of microscale breaking waves from infrared imagery using a PIV algorithm, *Measurement Science & Technology*, *16*(10), 1961-1969, doi:10.1088/0957-0233-16/10/011.
Kitaigorodskii, S. A., M. A. Donelan, J. L. Lumley, and E. A. Terray (1983), Wave turbulence interactions in the upper ocean. 2. Statistical characteristics of wave and turbulent components of the random velocity field in the marine surface layer, *Journal of Physical Oceanography*, *13*(11), 1988-1999, doi:10.1175/1520-0485(1983)013<1988:wtiitu>2.0.co;2.
Kleiss, J. M., and W. K. Melville (2010), Observations of Wave Breaking Kinematics in Fetch-Limited Seas, *Journal of Physical Oceanography*, *40*(12), 2575-2604, doi:10.1175/2010jpo4383.1.
Lenain, L., and W. K. Melville (2017), Measurements of the Directional Spectrum across the Equilibrium Saturation Ranges of Wind-Generated Surface Waves, *Journal of Physical Oceanography*, *47*(8), 2123-2138, doi:10.1175/jpo-d-17-0017.1.
Lighthill, J. (1978), *Waves in Fluids*, 504 pp., Cambridge University Press, Cambridge.
Longuet-Higgins, M. S. 1974 Breaking waves in deep or shallow water. In Proc. 10th Conf. on Naval Hydrodynamics, , Office of Naval Research, Dept of the Navy, ACR-204, Washington, DC, pp597-605. Melville, W. K. (1982), The instability and breaking of deep-water waves, *Journal of Fluid Mechanics*, *115*(FEB), 165-185.
Melville, W. K. (1983), Wave modulation and breakdown, *Journal of Fluid Mechanics*, *128*(MAR), 489-506.
Melville, W. K. (1994), Energy dissipation by breaking waves, *Journal of Physical Oceanography*, *24*(10), 2041-2049.
Melville, W. K., and P. Matusov (2002), Distribution of breaking waves at the ocean surface, *Nature*, *417*(6884), 58-63.
Melville, W. K., and R. J. Rapp (1985), Momentum flux in breaking waves, *Nature*, *317*(6037), 514-516.
Phillips, O. M. (1960), On the dynamics of unsteady gravity waves of finite amplitude. 1. The elementary interactions, *Journal of Fluid Mechanics*, *9*(2), 193-217.
Phillips, O. M. (1985), Spectral and statistical properties of the equilibrium range in wind-generated gravity waves, *Journal of Fluid Mechanics*, *156*, 505-531, doi:10.1017/s0022112085002221.
Phillips, O. M., F. L. Posner, and J. P. Hansen (2001), High range resolution radar measurements of the speed distribution of breaking events in wind-generated ocean waves: Surface impulse and wave energy dissipation rates, *Journal of Physical Oceanography*, *31*(2), 450-460.
Rapp, R. J., and W. K. Melville (1990), Laboratory measurements of deep-water breaking waves, *Philosophical*

Transactions of the Royal Society of London Series a-Mathematical Physical and Engineering Sciences, *331*(1622), 735-&, doi:10.1098/rsta.1990.0098.
Romero, L., L. Lenain, and W. K. Melville (2017), Observations of Surface Wave-Current Interaction, *Journal of Physical Oceanography*, *47*(3), 615-632, doi:10.1175/jpo-d-16-0108.1.
Romero, L., and W. K. Melville (2010a), Airborne Observations of Fetch-Limited Waves in the Gulf of Tehuantepec, *Journal of Physical Oceanography*, *40*(3), 441-465, doi:10.1175/2009jpo4127.1.
Romero, L., and W. K. Melville (2010b), Numerical Modeling of Fetch-Limited Waves in the Gulf of Tehuantepec, *Journal of Physical Oceanography*, *40*(3), 466-486, doi:10.1175/2009jpo4128.1.
Romero, L., W. K. Melville, and J. M. Kleiss (2012), Spectral Energy Dissipation due to Surface Wave Breaking, *Journal of Physical Oceanography*, *42*(9), 1421-1444, doi:10.1175/jpo-d-11-072.1.
Song, J. B., and M. L. Banner (2002), On determining the onset and strength of breaking for deep water waves. Part I: Unforced irrotational wave groups, *Journal of Physical Oceanography*, *32*(9), 2541-2558.
Sutherland, P., and W. K. Melville (2013), Field measurements and scaling of ocean surface wave-breaking statistics, *Geophys. Res. Lett.*, *40*(12), 3074-3079, doi:10.1002/grl.50584.
Sutherland, P., and W. K. Melville (2015a), Field Measurements of Surface and Near-Surface Turbulence in the Presence of Breaking Waves, *Journal of Physical Oceanography*, *45*(4), 943-965, doi:10.1175/jpo-d-14-0133.1.
Sutherland, P., and W. K. Melville (2015b), Measuring turbulent kinetic energy dissipation at a wavy sea surface, *Journal of Atmospheric and Oceanic Technology*, doi:10.1175/JTECH-D-14-00227.1.
Taylor, G. I. (1935), Statistical theory of turbulence, *Proceedings of the Royal Society of London Series a-Mathematical and Physical Sciences*, *151*(A873), 0421-0444, doi:10.1098/rspa.1935.0158.
Terrill, E., and W. K. Melville (1997), Sound-speed measurements in the surface-wave layer, *Journal of the Acoustical Society of America*, *102*(5), 2607-2625.
Whitham, G. B. (1965), A general approach to linear and nonlinear dispersive waves using a Lagrangian, *Journal of Fluid Mechanics*, *22*, 273-&, doi:10.1017/s0022112065000745.
Zakharov, V. E. (1968), Stability of periodic waves of finite amplitude on the surface of a deep fluid, *Journal of Applied Mechanics and Technical Physics*, *9*(2), 190-194, doi:10.1007/bf00913182.
Zappa, C. J., M. L. Banner, H. Schultz, J. R. Gemmrich, R. P. Morison,D. A. LeBel, and T. Dickey (2012), An overview of sea state conditions and air-sea fluxes during RaDyO, *J. Geophys. Res.*, *117*, C00H19, doi:10.1029/2011JC007336.

Available online at www.sciencedirect.com

ScienceDirect

Procedia IUTAM 26 (2018) 43–58

Procedia IUTAM

www.elsevier.com/locate/procedia

IUTAM Symposium Wind Waves, 4-8 September 2017, London, UK

Analytic theory of a wind-driven sea

Vladimir Zakharov[a]

[a] *University of Arizona, 617 N. Santa Rita Ave., Tucson, AZ 85721-0089 USA*

Abstract

A self-sustained analytic theory of a wind-driven sea is presented. It is shown that the wave field can be separated into two ensembles: the Hasselmann sea that consists of long waves with frequency $\omega < \omega_H$, $\omega_H \sim 4 - 5\omega_p$ (ω_p is the frequency of the spectral peak), and the Phillips sea with shorter waves. In the Hasselmann sea, which contains up to 95 % of wave energy, a resonant nonlinear interaction dominates over generation of wave energy by wind. White-cap dissipation in the Hasselmann sea in negligibly small. The resonant interaction forms a flux of energy into the Phillips sea, which plays a role of a universal sink of energy. This theory is supported by massive numerical experiments and explains the majority of pertinent experimental facts accumulated in physical oceanography.

Peer-review under responsibility of the scientific committee of the IUTAM Symposium Wind Waves.

Keywords: Kinetic (Hasselmann) equation; wave turbulence; Kolmogorov-Zakharov spectra; self-similarity of wave spectra; wind-wave forecasting.

1. Introduction

We will start with the taken-for-granted aphorism that ”there is nothing more practical than a good theory.” Since the time of Galileo, physicists have tried to develop theoretical models of natural phenomena. They have succeeded for phenomena of very different scales: from the scale of elementary particles to the scale of the Universe. Geophysical phenomena - weather forecasting, prediction of earthquakes or origin of hurricanes - are intermediate in scale but not in complexity. As a rule, these phenomena are very difficult for theoretical investigation because there are too many factors involved. Creation of a theoretically justified analytic theory of wind-driven sea looks, at first glance, to be ”mission impossible.” Waves are generated by turbulent winds; these waves break, forming white caps, sprays, bubbles, etc. Nevertheless, the development of an adequate analytic theory of wind-driven sea is possible. The purpose of this paper is to demonstrate this possibility.

It is obvious that a wind-driven sea needs a statistical description. In the system under consideration, such a description can be performed efficiently if we have at least one small parameter. The absence of a small parameter makes

* Corresponding author. Tel.: +1-520-621-6892 ; fax: +1-520-621-8322.
E-mail address: zakharov@math.arizona.edu

2210-9838
Peer-review under responsibility of the scientific committee of the IUTAM Symposium Wind Waves.
10.1016/j.piutam.2018.03.005

development of a good theory that describes turbulence in an incompressible fluid quite problematic. Fortunately, in the case of a wind-driven sea we can find two small parameters. The first one is the ratio of air and water densities, $\rho = \frac{\rho_a}{\rho_w} \sim 1.2 \times 10^{-3}$. Smallness of this parameter is responsible for the fact that generation of waves by wind is a slow process: development of an intense wave takes thousands of its periods. Another small parameter is the steepness, μ, defined as follows: $\mu^2(k_0) = \int_{|k|<k_0} k^2 \epsilon(k) dk$. Here $\epsilon(k)$ is the energy spectrum. Disastrously long and high waves of a strong storm are just gently sloping. A wave with steepness $\mu \simeq 0.1$ is considered by seafarers as dangerously steep. A typical value of steepness is $\mu \simeq 0.04 - 0.07$. Smallness of μ allows us to sort out the nonlinear interaction processes and determine the leading process, which is the four-wave resonant interaction. It was done by O. Phillips in 1960 [1]. A statistical description of weakly nonlinear waves can be accomplished by standard methods of theoretical physics. It was performed by K. Hasselmann in 1962-63 [2], [3]. He derived what we call the "Hasselmann kinetic equation," which became a new member of the big family of kinetic equations widely used in theoretical physics.

In spite of the fact that the mentioned seminal results were obtained long ago, the development of wind-wave theory was slow. Some important advances were achieved in research articles of late 1960's - 1980's [4-9] but they exerted little influence on development of the theory.

For half a century oceanographers have constructed operational models for wave forecasting. In these models, the tuning of parameters made it possible to improve the forecasting, but the use of heuristic models added little to the understanding of the physical processes that take place on the surface of wind-driven sea. During the last decade the analytical theory of wind-driven sea got a new life [10-19]. It became obvious that the majority of data obtained in physical experiments (in ocean and wave tanks) together with numerical experiments can be explained in a framework of a well-justified simple theory. The presented paper is a first brief systematic description of this theory. Its main points were reported at the Lorentz lecture on the AGU Fall meeting, December 2016, San Francisco.

The central point of the proposed analytical wind-driven sea theory is the following. Wind-driven waves can be separated into two ensembles: the Hasselmann sea and the Phillips sea. The Hasselmann sea contains long waves with frequencies $\omega < \omega_H$, $\omega_H \simeq 4 - 5\,\omega_p$. Here ω_p is the frequency of the spectral peak. The Phillips sea consists of shorter waves. In the Hasselmann sea the waves are generated by wind, mostly near the spectral peak, but their spectral distribution is shaped by a resonant nonlinear interaction. This interaction throws the wave energy into the Phillips sea, where it dissipates due to breaking. We don't need to know the details of wave-breaking. The Phillips sea works as a universal sink that absorbs all energy sent there by resonant interactions. The white-cap dissipation inside the Hasselmann sea is negligibly small. This is a crucial point that makes possible to develop a self-sustained theory of the Hasselmann sea, which contains the bulk of the wave energy (up to 95 %).

2. Quasi-Conservative Hasselmann equation

It is accepted by the physical oceanography community (see, for example [20]) that deep water ocean gravity surface wave forecasting models are described by the Hasselmann equation [2, 3] This equation is also known as the kinetic equation for waves [4]. Sometimes it is called the Bolzmann equation [21] or energy balance equation [22].

$$\frac{\partial \epsilon}{\partial t} + \frac{\partial \omega_k}{\partial \mathbf{k}} \frac{\partial \epsilon}{\partial \mathbf{r}} = S_{nl} + S_{in} + S_{diss} \tag{1}$$

Here $\epsilon = \epsilon(\omega_k, \theta, r, t)$ is the wave energy spectrum. This spectrum is a function of wave frequency $\omega_k = \omega(k)$, angle θ, two-dimensional real space coordinate $r = (x, y)$, and time t. The terms S_{nl}, S_{in} and S_{diss} are the nonlinear, wind input and wave-breaking dissipation source terms. We will consider the deep water case only: the dispersion law is $\omega_k = \sqrt{gk}$, where g is the gravitational acceleration and $k = |\mathbf{k}|$ is the absolute value of the vector wavenumber $\mathbf{k} = (k_x, k_y)$. Since Hasselmann's work, Eq.(1) has become the basis of operational wave forecasting models.

While the physical oceanography community agrees on the general applicability of Eq. (1), there is no consensus on universal parameterizations of the source terms S_{nl}, S_{in} and S_{diss}. In this paper we put $S_{diss} = 0$. It is astonishing how many nontrivial facts extracted from field and numerical experiments confirm this statement [10],[12],[13]. Of course, $S_{diss} = 0$ only in the Hasselmann sea.

We start our consideration with the study of the quasi-conservative Hasselmann kinetic equation written for the wave action spectrum $N_{\mathbf{k}}(t)$.

$$\frac{dN}{dt} = S_{\mathrm{nl}} \tag{2}$$

$$S_{\rm nl} = \pi g^2 \int\limits_{\mathbf{k}_1,\mathbf{k}_2,\mathbf{k}_3} (T_{\mathbf{k}\mathbf{k}_1\mathbf{k}_2\mathbf{k}_3})^2 \times (N_{\mathbf{k}}N_{\mathbf{k}_2}N_{\mathbf{k}_3} + N_{\mathbf{k}_1}N_{\mathbf{k}_2}N_{\mathbf{k}_3} - N_{\mathbf{k}}N_{\mathbf{k}_1}N_{\mathbf{k}_2} - N_{\mathbf{k}}N_{\mathbf{k}_1}N_{\mathbf{k}_3}) \times$$
$$\times\, \delta(\mathbf{k} + \mathbf{k}_1 - \mathbf{k}_2 - \mathbf{k}_3)\, \delta(\omega + \omega_1 - \omega_2 - \omega_3) \times\, d\mathbf{k}_1\, d\mathbf{k}_2\, d\mathbf{k}_3 \tag{3}$$

The energy spectrum $\epsilon(k)$ is connected with wave action spectrum by relation $\epsilon(k) = \frac{1}{2}\omega_k(N_k + N_{-k})$. Here $\omega(k) = \sqrt{gk}$ is the dispersion law. The coefficient $T_{kk_1k_2k_3}$ in Eq. (3) is the coupling coefficient introduced in [23], [24]:

$$T_{\mathbf{k}_1\mathbf{k}_2\mathbf{k}_3\mathbf{k}_4} = \frac{1}{2}\left(\hat{T}_{\mathbf{k}_1\mathbf{k}_2\mathbf{k}_3\mathbf{k}_4} + \hat{T}_{\mathbf{k}_3\mathbf{k}_3\mathbf{k}_1\mathbf{k}_2}\right)$$

$$\begin{aligned}\hat{T}_{\mathbf{k}_1\mathbf{k}_2\mathbf{k}_3\mathbf{k}_4} = -\frac{1}{4}\frac{1}{(k_1k_2k_3k_4)^{1/4}}\Bigg\{ & \frac{1}{2}\left(k_{1+2}^2 - (\omega_1+\omega_2)^4\right)\times\left(\mathbf{k}_1\mathbf{k}_2 - k_1k_2 + \mathbf{k}_3\mathbf{k}_4 - k_3k_4\right)\\ & -\frac{1}{2}\left(k_{1-3}^2 - (\omega_1-\omega_3)^4\right)\times\left(\mathbf{k}_1\mathbf{k}_3 + k_1k_3 + \mathbf{k}_2\mathbf{k}_4 + k_2k_4\right)\\ & -\frac{1}{2}\left(k_{1-4}^2 - (\omega_1-\omega_4)^4\right)\times\left(\mathbf{k}_1\mathbf{k}_4 + k_1k_4 + \mathbf{k}_2\mathbf{k}_3 + k_2k_3\right)\\ & +\left(\frac{4(\omega_1+\omega_2)^2}{k_{1+2}-(\omega_1+\omega_2)^2} - 1\right)\times(\mathbf{k}_1\mathbf{k}_2 - k_1k_2)(\mathbf{k}_3\mathbf{k}_4 - k_3k_4)\\ & +\left(\frac{4(\omega_1-\omega_3)^2}{k_{1-3}-(\omega_1-\omega_3)^2} - 1\right)\times(\mathbf{k}_1\mathbf{k}_3 + k_1k_3)(\mathbf{k}_2\mathbf{k}_4 + k_2k_4)\\ & +\left(\frac{4(\omega_1-\omega_4)^2}{k_{1-4}-(\omega_1-\omega_4)^2} - 1\right)\times(\mathbf{k}_1\mathbf{k}_4 + k_1k_4)(\mathbf{k}_2\mathbf{k}_3 + k_2k_3)\Bigg\}\end{aligned} \tag{4}$$

Here k_{1+2}, k_{1-3} and k_{1-4} are the moduli of the $\mathbf{k}_1 + \mathbf{k}_2$, $\mathbf{k}_1 - \mathbf{k}_3$ and $\mathbf{k}_1 - \mathbf{k}_4$ vectors respectively. It should be stressed that we need to know the coupling coefficient at the resonant manifold only:

$$\mathbf{k}_1 + \mathbf{k}_2 = \mathbf{k}_3 + \mathbf{k}_4; \qquad \omega_1 + \omega_2 = \omega_3 + \omega_4 \tag{5}$$

The coupling coefficient satisfies the symmetry conditions $T_{1234} = T_{2134} = T_{1243} = T_{3412}$. Now suppose that the wave vectors $\mathbf{k}_1$ and $\mathbf{k}_3$ are much shorter than the wave vectors $\mathbf{k}_2$ and $\mathbf{k}_4$. Taking Eq. (5) into account we see that $\mathbf{k}_1$ and $\mathbf{k}_3$ have nearly equal length. Vectors $\mathbf{k}_2$ and $\mathbf{k}_4$ are nearly equal, both in length and direction. An example of such configuration is shown on Fig. 1.

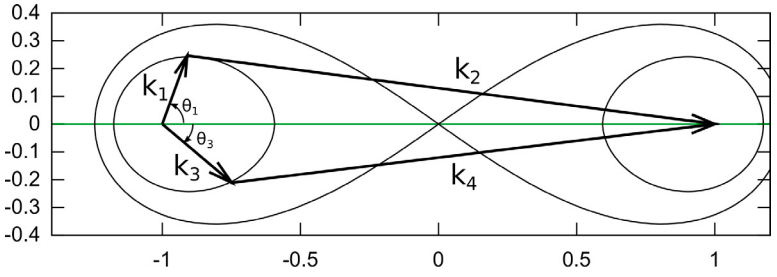

Fig. 1. A wave vector quadruplet of a long-short interaction. A curve $\omega_1 + \omega_2 = \text{const}$ is drawn; any two points of the curve constitute a resonant quadruplet. The θ_1 and θ_3 angles are given with respect to the vector $\mathbf{k}_1 + \mathbf{k}_2 = \mathbf{k}_3 + \mathbf{k}_4$. The eight-shape figure is the Phillips curve.

Let us underline one important property of the resonant manifold (5). Suppose that the three wave vectors, k_1, k_2, k_3 in (5) are bound in length by some number $|k_i| < k_0$, $i = 1, 2, 3$. However, the last term in (5) might have a longer absolute value. In fact, in virtue of (5) we have $|k_1| < 5/4\, k_0$.

Hereafter we define $k_1 = |\mathbf{k}_1|$, $k_2 = |\mathbf{k}_2|$, etc. We have $k_1 \approx k_3 \ll k_2 \approx k_4$. After tedious algebra one may find the following asymptotic behavior for the coupling coefficient:

$$T_{\mathbf{k}_1,\mathbf{k}_2,\mathbf{k}_3,\mathbf{k}_4)} \to \frac{1}{2}k_1^2k_2T_{\theta_1\theta_3}, \qquad T_{\theta_1\theta_3} = (\cos\theta_1 + \cos\theta_3)(1 + \cos(\theta_1 - \theta_3))$$

Here θ_1 is the angle between the small vector $\mathbf{k}_1$ and $\mathbf{k}_1 + \mathbf{k}_2$ (see Fig. 1); the same stands for θ_3.

In the diagonal case $\theta_1 = \theta_3$, $\mathbf{k}_1 = \mathbf{k}_3$, $\mathbf{k}_2 = \mathbf{k}_4$.

$$T(\mathbf{k}_1, \mathbf{k}_2) = 2k_1^2 k_2 \cos(\theta_1) \tag{6}$$

A systematic derivation of the nonlinear term S_{nl} is described in detail in [25]. The expression for the coupling coefficient presented in that paper differs from Eq. (4), however on the resonant manifold Eq. (5) both expressions coincide.

The derivation of the Hasselmann equation is based on the assumption that the total steepness μ is small. In fact, one must demand that $\mu(k_0) < 0.1$. In the real sea, the steepness $\mu(k_0)$ is a function growing with k_0. This means that Hasselmann equation is only valid inside the limited spectral band $0 < \omega < (4-6)\omega_p$, where ω_p is the frequency of the spectral peak. It is fortunate that in a typical case this "allowed" band contains more than 95% of the wave energy.

We should stress one important point. The Hasselmann equation is derived not for the real observable energy spectrum but for the "refined" spectrum cleared of "slave harmonics." This question is studied in detail in [14], [15]. It is shown there that "slave harmonics" can be neglected only in the case of very small steepness, $\mu \ll 1$. This is correct for long enough waves, but in the small-scale spectral area ($k > 20 \sim 30k_p$) the contribution of slave harmonics becomes dramatically more important. This fact is supported by direct phase-resolving numerical experiments [26], [27], [28], [29]. In this spectral area, the sea is a mixture of "leading harmonics" obeying the dispersion law $\omega \simeq \sqrt{gk}$ and slave harmonics that have combined frequencies. Also, in this spectral area we can observe either the formation of parasitic capillary ripples (for small wind velocity, $v < 3 \sim 5m/sec$) or intensive wave breaking (for stronger wind).

For strong enough wind we can separate wind-driven sea into two parts: the "Hasselmann sea" with long waves and the "Phillips sea" with shorter waves. This question was studied theoretically in [30] and numerically in [27]. Can we "improve" the Hasselmann equation to make it applicable to description of the Phillips sea? The answer to this question is still open.

Another important point is the question of conservation laws. The widely accepted opinion is that the quasi-conservative Hasselmann equation Eq. (2) has basic conservation laws, i.e. wave action, energy and momentum:

$$N = \int N_k \, dk, \qquad E = \int \omega_k N_k \, dk, \qquad \mathbf{M} = \int \mathbf{k} N_k \, dk$$

Another widely accepted opinion is the following: A wave field cannot gain or loose energy through resonant interaction; growth or loss of wave action, momentum or energy must therefore take place through other processes such as wind input, whitecapping or bottom interaction (see, for example Chapter II in the well-known book "Dynamics and Modelling of Ocean Waves" [31]. This statement is gravely erroneous. Certainly, the resonant interaction cannot gain energy, but this interaction provides for the loss of energy and momentum into the spectral area of infinitely small scales. This process really occurs and takes a leading role in establishing the energy and momentum balance in the wind-driven sea.

Let us study more carefully the conservation laws. Apparently

$$\frac{dE}{dt} = \int \omega_k S_{nl} \, dk \tag{7}$$

If we boldly perform the permutation of integration order in Eq. (7) we will end up with relation

$$\frac{dE}{dt} = \pi g^2 \int |T_{kk_1k_2k_3}|^2 N_{k_1} N_{k_2} N_{k_3} \times (\omega_k + \omega_{k_1} - \omega_{k_2} - \omega_{k_3}) \delta(\omega_k + \omega_{k_1} - \omega_{k_2} - \omega_{k_3}) \times$$
$$\times \delta(\mathbf{k} + \mathbf{k}_1 - \mathbf{k}_2 - \mathbf{k}_3) \, d\mathbf{k} \, d\mathbf{k}_1 \, d\mathbf{k}_2 \, d\mathbf{k}_3 \tag{8}$$

It seems that Eq. (7) means that $dE/dt = 0$, but this would be correct only if all terms in this relation are finite and represented by convergent integrals. Now assume that N_k has asymptotic behavior $N_k \to 1/k^4$, $k \to \infty$. Then all terms in Eq. (7) will diverge logarithmically and will actually be infinite. Different terms in $d\mathbf{M}/dt$ will diverge even worse. Thus, in the presence of spectral tails, the conservation of energy and momentum fails. The asymptotic behavior $N_k \sim 1/k^4$ means that $I_k \simeq k^{-5/2}$ and $F(\omega) \simeq \omega^{-4}$. These spectra are commonly observed in the wind-driven sea in the spectral range $\omega_p < \omega < 5\omega_p$, where ω_p the is frequency of the spectral peak.

Let us add a little piece of pure mathematics. Strictly speaking, even the simple Eq. (7) is not correct. Permutation of integration order in multi-dimensional integrals is allowed under strict limitations that are dictated by the so-called "Fubini theorem." In our case this theorem demands that action spectra should decay fast enough at $k \to \infty$:

$$N(k) < \frac{c}{k^{25/6+\epsilon}}, \quad \epsilon > 0$$

This means that the energy spectrum $F(\omega)$ must decay faster than $\omega^{-13/3}$. In the short-scale region of a real sea we usually observe the Phillips spectrum $F(\omega) \simeq \alpha g^2/\omega^5$. Because $5 > 13/3$ the integrals are conserved.

Let us notice that this takes place in the Phillips sea, consisting of short waves ($\omega > \omega_H$), outside of the Hasselmann sea, consisting of long waves ($\omega < \omega_H \sim 5\omega_p$). The resonant nonlinear interaction throws energy and momentum from the Hasselmann sea into the Phillips sea. Thus:

$$P = -\int_0^{2\pi} d\theta \int_0^{\omega_H} \frac{d\epsilon(\omega,\theta)}{dt} d\omega, \quad R_x = -\frac{1}{g}\int_0^{2\pi} d\theta \int_0^{\omega_H} \omega \cos\theta \frac{d\epsilon(\omega,\theta)}{dt} d\omega$$

P and R_x are fluxes of energy and momentum from the Hasselmann sea into the Phillips sea. Because they are not zero, one can call Eq. (2) a quasi-conservative equation. Notice, that Eq. (2) is a natural model for study of the ocean swell evolution. We have solved this equation numerically and have observed a permanent loss of energy and momentum [44].

3. Kolmogorov-type spectra

Let us study isotropic solutions of the stationary quasi-conservative Hasselmann equation:

$$S_{\rm nl} = 0 \tag{9}$$

We assume that the solution of Eq. (8) is a powerlike function $N = ak^{-x}$. Then

$$S_{\rm nl} = a^3 g^{\frac{3}{2}} k^{-3x+\frac{19}{2}} F(x)$$

where F is a dimensionless function depending on x only.

It was shown in [6], [32] that $F(x) = 0$ at the two points $x = 4$ and $x \simeq 23/6$ only. This is a strict mathematical theorem, which is supported by careful numerical experiments [33], [12], [13]. Integrals in Eq. (9) converge if $5/2 < x < 19/4$ [19]. Function F is shown on Fig. 2.

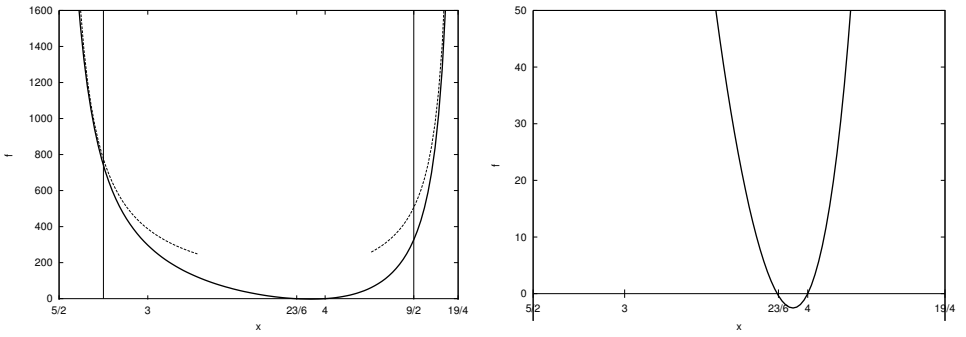

Fig. 2. F function graph and its asymptotes. The second picture is the closeup of the function zeroes.

This means that Eq. (9) has exactly two powerlike solutions:

$$N_k^{(1)} = c_p \frac{P_0^{1/3}}{g^{2/3}} \frac{1}{k^4}, \qquad N_k^{(2)} = c_q \frac{Q_0^{1/3}}{g^{1/2}} \frac{1}{k^{23/6}}. \tag{10}$$

Here P_0 is the energy flux and Q_0 is the wave action flux. The dimensionless constants c_p and c_q are defined from the first derivatives of F

$$c_p = \left(\frac{3}{2\pi F'(4)}\right)^{1/3}, \qquad c_q = \left(-\frac{3}{2\pi F'(23/6)}\right)^{1/3}$$

Our numerical calculation of the derivatives of F at $x = 4$ and $x = 23/6$ gives

$$c_p = 0.203, \quad c_q = 0.194 \tag{11}$$

One can mention that the "unidirectional" (integrated by angle) energy spectra $E(\omega)$ are connected with the isotropic wave action spectra by the relation

$$F(\omega)\, d\omega = 2\pi\omega_k N_k\, k\, dk \tag{12}$$

Hence we find the following exact solutions of Eq. (9):

$$F_1(\omega) = \frac{4\pi\, c_p}{\omega^4}\, g^{4/3}\, P_0^{1/3} \tag{13}$$

This expression is known as the Zakharov-Filonenko spectrum and was found in 1966 [4]. It is a Kolmogorov-type spectrum that presumes the presence of a source of energy $P_0 = d\epsilon/dt$ at $k = 0$. This is the spectrum of "direct inverse cascade" similar to the classical Kolmogorov spectrum in the theory of turbulence in a three-dimensional incompressible fluid. The second spectrum first introduced in [5], [6] is the following:

$$F_2(\omega) = \frac{4\pi\, c_q}{\omega^{11/3}}\, g\, Q_0^{1/3} \tag{14}$$

It describes the "inverse cascade" of wave action, and can be compared with the Kolmogorov spectrum of the energy inverse cascade in the theory of turbulence in a two-dimensional incompressible fluid.

The existence of solutions of Eq. (8) originates from possibility of splitting S_{nl} as follows:

$$S_{nl} = F_k - \Gamma_k N_k, \tag{15}$$

where

$$F_k = \pi g^2 \int |T_{kk_1k_2k_3}|^2\, \delta(k + k_1 - k_2 - k_3)\, \delta(\omega_k + \omega_{k_1} - \omega_{k_2} - \omega_{k_3})\, N_{k_1} N_{k_2} N_{k_3}\, dk_1 dk_2 dk_3 \tag{16}$$

and Γ_k, the dissipation rate due to the presence of four-wave processes, is the following:

$$\Gamma_k = \pi g^2 \int |T_{kk_1,k_2k_3}|^2\, \delta(k + k_1 - k_2 - k_3)\, \delta(\omega_k + \omega_{k_1} - \omega_{k_2} - \omega_{k_3}) \times \\ \times (N_{k_1} N_{k_2} + N_{k_1} N_{k_3} - N_{k_2} N_{k_3})\, dk_1 dk_2 dk_3. \tag{17}$$

One can call F_k the "income term" and $\Gamma_k N_k$ the "outcome term". Solutions of Eq. (8) are the result of competition between the income and outcome terms. In statistical physics the separate study of income and outcome terms is a routine procedure. In stationarity they compensate each other, and this is the "principle of detailed equilibrium". Competition of these terms leads to the establishment of of stationary thermodynamic equilibrium spectra like the Maxwell distribution in the kinetic theory of gases or the Plank distribution in optics and physics of condensed matter. It is important to mention that Eq. (2) is the limiting case of a more general quantum kinetic equation for bosonic quasiparticles derived by Nordheim in 1929 [34]. Kolmogorov-type spectra of the Nordheim equation were studied by Y.V. Lvov et al [35].

There is one more reason why the splitting of S_{nl} is so useful. First of all, it explains why the conservation laws in reality do not conserve. Suppose, in the initial moment of time, $N(k) = 0$. Thus $S_{nl} > 0$ in the spectral area $k_0 < |k| < 5/4\, k_0$. As a result, energy inside the area $|k| < k_0$ decreases in time. This fact is very important in connection with numerical solution of equation (2). Any numerical scheme provides that frequency varies in a bounded interval

$0 < \omega < \omega_{max}$ and automatically provides the leakage of energy outside the area $\omega < \omega_{max}$. A good numerical experiment can be performed in the absence of all S_{diss}.

We can expect that Eq. (8) has thermodynamic equilibrium solutions, the Rayley-Jeans spectra

$$\epsilon(k) = \frac{T}{\omega_k + \mu}$$

Here T is temperature and μ is chemical potential. However these solutions have no physical meaning because a real sea is very far from thermodynamic equilibrium. Moreover, the substitution of thermodynamic spectra into S_{nl} leads to bad divergences of integrals. It is important to stress that the spectra (13) and (14) are the simplest examples of exact solution of Eq. (9). To outline a broader class of its solutions one can introduce the elliptic differential operator [14]:

$$L f(\omega, \phi) = \left(\frac{\partial^2}{\partial \omega^2} + \frac{2}{\omega^2} \frac{\partial^2}{\partial \phi^2} \right) f(\omega, \phi) \tag{18}$$

with following parameters: $0 < \omega < \infty, \;\; 0 < \phi < 2\pi$. The equation

$$L G = \delta(\omega - \omega') \, \delta(\phi - \phi') \tag{19}$$

with boundary conditions $G|_{\omega \to 0} = 0$, $G_{\omega \to \infty} < \infty$, $G(2\pi) = G(0)$ can be resolved as

$$G(\omega, \omega', \phi - \phi') = \frac{1}{4\pi} \sqrt{\omega \omega'} \sum_{n=-\infty}^{\infty} e^{in(\phi - \phi')} \times \left[\left(\frac{\omega}{\omega'} \right)^{\Delta_n} \Theta(\omega' - \omega) + \left(\frac{\omega'}{\omega} \right)^{\Delta_n} \Theta(\omega - \omega') \right], \tag{20}$$

where $\Delta_n = 1/2 \sqrt{1 + 8n^2}$. Now we define:

$$A(\omega, \phi) = \int_0^{\infty} d\omega' \int_0^{2\pi} d\phi' \, G(\omega, \omega', \phi - \phi') \, S_{nl}(\omega', \phi'). \tag{21}$$

Then Eq. (2) takes the following form

$$\frac{\partial N}{\partial t} = L A \tag{22}$$

and the stationary equation is

$$L A = 0 \tag{23}$$

The operator A is a regular integral operator. This fact leads to a bold idea. If we assume that

$$A = \frac{H_0}{g^4} \, \omega^{15} \, N^3, \tag{24}$$

then the nonlinear term S_{nl} turns into the elliptic operator:

$$S_{nl} = \frac{H_0}{g^4} \left(\frac{\partial^2}{\partial \omega^2} + \frac{2}{\omega^2} \frac{\partial^2}{\partial \phi^2} \right) \omega^{15} \, N^3. \tag{25}$$

This is a so-called "diffusion approximation", first introduced in article [23] and later on developed in [36]. In spite of being very simple, this approximation grasps the basic features of the wind-driven sea theory. We will refer mostly to this model, having in mind that the real case Eq. (21) does not differ much from it, at least qualitatively.

H_0 is a dimensionless tuning constant. In Eq. (22), $N = N(\omega, \phi)$, $\epsilon(\omega, \phi) = \omega \, N(\omega, \phi)$. Eq. (25) has the following anisotropic KZ solution

$$A = \frac{1}{2\pi \, g} \left\{ P + \omega \, Q + \frac{R_x}{\omega} \cos \phi \right\}, \tag{26}$$

where P and R_x are fluxes of energy and momentum as $\omega \to \infty$ and Q is the flux of wave action directed to small wave numbers. In a general case, Eq. (21) is a nonlinear integral equation; however in the diffusion approximation the KZ solution can be found in the explicit form:

$$N(\omega,\phi) = \frac{1}{(2\pi H_0)^{1/3}} \frac{g}{\omega^5} \left(P + \omega Q + \frac{R_x}{\omega} \cos\phi\right)^{1/3}. \tag{27}$$

By comparison with (11) we easily find that in this case

$$c_p = c_q = \frac{1}{2(2\pi H_0)^{1/3}} = 0.199, \qquad H_0 = 2.57.$$

This is exactly the arithmetic mean between the values of Kolmogorov constants given by (11).

By multiplication of Eq. (27) by $2\pi\omega$ we get the general KZ spectrum in the diffusion approximation:

$$F(\omega) = 2.78 \frac{g^{4/3}}{\omega^4} \left(P + \omega Q + \frac{R_x}{\omega} \cos\phi\right)^{1/3}. \tag{28}$$

For the real sea, Eq. (23) is a nonlinear integral equation which can be solved numerically only. The "toy" diffusion model allows us to find the explicit equation for the KZ-solution which grasps the main features of real solution. One can assert that the real KZ solution is

$$F(\omega) = \frac{g^{4/3} P^{1/3}}{\omega^4} R\left(\frac{\omega Q}{P}, \frac{R_x}{g\,\omega\,P}, \phi\right) \tag{29}$$

In the limit $P \to 0$, $R_x \to 0$ we have $R \to 4\pi c_p$. In the limit $R_x = 0$, $P \to 0$

$$R \to 4\pi c_q \left(\frac{\omega Q}{P}\right)^{1/3}$$

We have to mention that Q is the flux of wave action coming from the spectral area of very small scales. In the majority of physical situations one can put $Q = 0$. From the physical viewpoint the most interesting case is $Q = 0$, for which

$$F(\omega) = \frac{g^{4/3} P^{1/3}}{\omega^4} R_0\left(\frac{R_x}{g\,\omega\,P}, \phi\right) \tag{30}$$

Here R_0 is an unknown function that we believe describes the angular spreading of wave spectra. It was shown long ago [37] that as $\omega \to 0$

$$R_0 \to 4\pi c_p \left(1 + \frac{\lambda R_x}{g\,\omega\,P} \cos\phi + \cdots\right) \tag{31}$$

where λ is a dimensionless constant. In the "toy" diffusion model $\lambda = 1/3$. We should stress that all KZ spectra are isotropic in the limit $\omega \to \infty$ and are very close to $F(\omega) \sim 1/\omega^4$.

Let us return to the representation of S_{nl} in the "split" form (15). Apparently the solution of the equation $S_{nl} = 0$ is given by the expression

$$N_k = \frac{F_k}{\Gamma_k} \tag{32}$$

For KZ-spectra both F_k, Γ_k diverge as $k \to \infty$. However these divergences are cancelled.

A detailed numerical study of the function $R_0(\frac{R_x}{g\,\omega,P}\,\phi)$ and its comparison with observed in experiments angular spectra is the problem of most importance in our agenda.

4. Energy balance in wind-driven sea

To answer the most painful question - which source terms in Eq. (1) are dominant? - one should present S_{nl} in the split form. This is clear to any physicist (pity, not to oceanographers). After the splitting, Eq. (1) takes the following form:

$$\frac{\partial N}{\partial t} + \frac{\partial \omega_k}{\partial k}\frac{\partial N}{\partial r} = F_k - \Gamma_k N_k + S_{in} + S_{diss}$$

In fact, the forcing terms S_{in} and S_{dis} are not known well enough; thus it is reasonable to accept the simplest models of both terms assuming that they are proportional to the action spectrum:

$$S_{in} = \gamma_{in}(k)\, N(k), \quad S_{dis} = -\gamma_{dis}(k)\, N(k). \tag{33}$$

Hence

$$\gamma(k) = \gamma_{in}(k) - \gamma_{dis}(k). \tag{34}$$

In reality $\gamma_{dis}(k)$ depends dramatically on the overall steepness μ. So far, let us notice that the stationary balance equation can be written in the form

$$F_k - \Gamma_k N_k + \gamma_k N = 0 \tag{35}$$

Definitions of Γ_k and F_k are given by Eq. (16) and Eq. (17).

The stationary solution of Eq. (1) is the following:

$$N_k = \frac{F_k}{\Gamma_k - \gamma_k}. \tag{36}$$

The positive solution exists if $\Gamma_k > \gamma_k$. The term Γ_k can be treated as the nonlinear damping that appears due to four-wave interaction. In the presence of nonlinear damping the dispersion relation must be renormalized

$$\omega_k \to \omega_k + \frac{1}{2}\int T_{kk_1kk_1}\, N_k\, dk + i\Gamma_k$$

The main point of the proposed theory is that the nonlinear dumping has a very powerful effect. In reality, $\Gamma_k \gg \gamma_k$. A "naive" dimensional consideration gives

$$\Gamma_k \simeq \frac{4\pi g^2}{\omega_k}\, k^{10}\, N_k^2, \tag{37}$$

However, this estimate works only if $k \simeq k_p$, where k_p is the wave number of the spectral maximum.

Let $k \gg k_p$. Then for Γ_k we get

$$\Gamma_k = 2\pi g^2 \int |T_{kk_1,kk_3}|^2\, \delta(\omega_{k_1} - \omega_{k_3})\, N_{k_1} N_{k_3}\, dk_1 dk_2. \tag{38}$$

The main source of Γ_k is the interaction of long and short waves. To estimate Γ_k more accurately, we assume that the spectrum of long waves is narrow in angle, $N(k_1, \theta_1) = \tilde{N}(k_1)\, \delta(\theta_1)$. Long waves propagate along the axis x, and $\vec{k}$ is the wave vector of short wave propagating in direction θ. For the coupling coefficient we can use the asymptotic Eq. (6) and obtain

$$\Gamma_k = 8\pi g^{3/2}\, k^2\, \cos^2\theta \int_0^\infty k_1^{13/2}\, \tilde{N}^2(k_1)\, dk_1. \tag{39}$$

Even for the most mildly decaying KZ spectrum, $N_k \simeq k^{-23/6}$, the integrand behaves like $k_1^{-7/6}$ and the integral converges as $k \to \infty$. Thus the main contribution in (39) is given by $k_1 \sim k_p$. For an accurate estimate of Γ_k we need to know the detailed structure of the spectrum near the spectral peak. Let us make the most "mild assumption" and

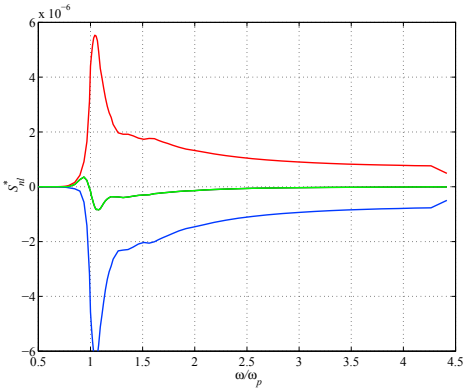

Fig. 3. Split of nonlinear interaction term S_{nl} (central curve) into F_k (upper curve) and $\Gamma_k N_k$ (lower curve)

consider that there is no peakedness and the spectrum looks like the Pierson-Moscowitz spectrum of a "mature sea" [38]:

$$N_k \simeq \frac{3}{2}\frac{E}{\sqrt{g}}\frac{k_p^{3/2}}{k^4}\,\theta(k-k_p). \tag{40}$$

Here E is the total energy. By plugging Eq. (40) into Eq. (39) we get the equation

$$\Gamma_\omega = 36\,\pi\omega\left(\frac{\omega}{\omega_p}\right)^3 \mu_p^4\,\cos^2\theta, \quad \mu_p^2 = \frac{g^2\,E}{\omega\,p^4} \tag{41}$$

that includes a huge enhancing factor: $36\pi \simeq 113.04$. For very modest value of steepness, $\mu_p \simeq 0.05$, we get

$$\Gamma_\omega \simeq 7.06\cdot 10^{-4}\omega\left(\frac{\omega}{\omega_p}\right)^3 \cos^2\theta. \tag{42}$$

In the real sea the spectra usually have "peakedness" which enhances (39) essentially. We must underline that the splitting of S_{nl} can be studied numerically. We have modified the well-known Resio-Tracy code for solving the Hasselmann equation to calculate competing terms F_k and $\Gamma_k N$ separately [15]. A typical splitting is shown in Fig. 3. For a nonlinear interaction term $S_{nl} = F_k - \Gamma_k N_k$, the magnitudes of the constituents F_k and $\Gamma_k N_k$ essentially exceed their difference. They are one order higher than the magnitude of S_{nl}.

The dominance of S_{nl} was not apparent for two reasons. First, it is not correct to compare S_{nl} and S_{in}; instead one should compare Γ_k and γ_k. Second, the widely accepted models for S_{diss} overestimate dissipation due to white capping. As a result, the dominance of S_{nl} is masked.

Concerning interaction with wind, at the moment there are at least a dozen models for $\Gamma(k) = \gamma(\omega, \phi)$. Some of them are derived by the use of conflicting theoretical models; others are taken from experimental data. None of the proposed models are convincing. They are essentially different and the scatter is very large, 300 − 500 %. A critical review of different models is presented in [27].

The dimensionless quantities $\gamma/\omega \times 10^3$ as functions of dimensionless frequency $\omega\,u_{10}/g$ are plotted on Fig. 4 taken from [12].

We pay special attention to two models:

1. The Plant model [39] $\gamma = 0.03\frac{\rho_a}{\rho_\omega}\,\omega\left(\frac{\omega\,U}{g}\right)^2\cos\phi, \qquad \cos\phi > 0$

2. ZRP model [17] $\gamma = 0.05\frac{\rho_a}{\rho_\omega}\,\omega\left(\frac{\omega U}{g}\right)^{4/3}\cos^2\phi, \qquad -\pi/2 < \phi < \pi/2$

In both models $\gamma \simeq \omega^{1+s}$ is a powerlike function on frequency.

Comparison of all known models for S_{in} with the nonlinear dumping term Γ_k calculated according to Eq. (17) is presented on Fig. 5 One can see that Γ_k, at least in order of magnitude, is larger than $\gamma_{in}(k)$. This figure conspicuously demonstrates that the nonlinear wave interaction is the leading term in the energy balance of a wind-driven sea.

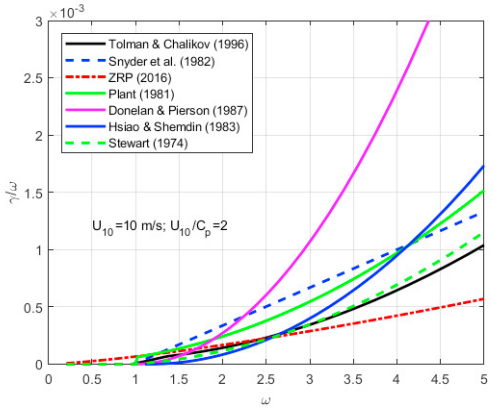

Fig. 4. Dimensionless wind input for $u_{10} = 10m/sec$.

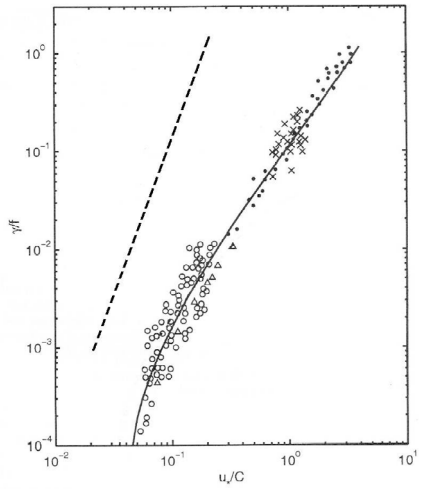

Fig. 5. Comparison of experimental data for the wind-induced growth rate $2\pi\gamma_{in}(\omega)/\omega$ taken from [14], [15] and the damping due to four-wave interactions $2\pi\Gamma(\omega)/\omega$, calculated for narrow in angle spectrum at $\mu \simeq 0.05$ using Eq. (42) (dashed line)

5. Experimental evidence of S_{nl} domination

In the previous chapter we have shown analytically and numerically that the S_{nl} term dominates over the S_{in} term. Because in the Hassenlmann sea the term S_{diss} cannot be stronger than γ_{in} (otherwise waves would not be excited), the term S_{nl} dominates over both. Both the source term and the nonlinear wave interaction are the dominating physical processes that take place in a wind-driven sea.

This fact is supported by convincing experimental data collected in a broad ranges of wind velocities: $3m/sec < U, 30m/sec$. Following Kitaigorodski [40], hereafter we will use the dimensionless duration and fetch, as well as the dimensionless frequency and energy:

$$\tau = \frac{tg}{U}, \quad \chi = \frac{xg}{U^2}, \quad \sigma = \frac{\omega U}{g}, \quad F = \frac{\epsilon g^2}{U^4} \tag{43}$$

Also, we introduce integral dimensionless quantities

$$\tilde{F} = \int_0^\infty F(\sigma)d\sigma, \qquad \tilde{\sigma} = \frac{1}{\tilde{F}}\int_0^\infty \sigma F(\sigma)d\sigma \tag{44}$$

The steepness of the main energy capacity wave can be estimated as follows

$$\mu_p \simeq \tilde{F}\,\tilde{\sigma}^4 \tag{45}$$

During the last seven decades many experiments measuring energy spectra of a wind-driven sea and its integral characteristics were performed in laboratory, on lakes, and in the different parts of the ocean. The most significant experiments were conducted in the "fetch dominating frame," where the sea is stationary in time and the wind has the opposite direction. In these challenging and expensive experiments, $\tilde{F}$ and $\tilde{\sigma}$ were measured as functions of fetch only: $\tilde{F} = \tilde{F}(\chi)$, $\tilde{\sigma} = \tilde{\sigma}(\chi)$. All experimenters unanimously agree that $\tilde{F}$ and $\tilde{\sigma}$ are powerlike functions

$$\tilde{F} = \epsilon_0 \chi^p, \qquad \tilde{\sigma} = \omega_0 \chi^{-q} \tag{46}$$

Exponents p, q are different in different experiments. They vary inside the following ranges

$$0.7 < p < 1.1 \qquad 0.22 < q < 0.33 \tag{47}$$

Suppose that F obeys the stationary Hasselmann equation. After transition to dimensionless variable this equation reads

$$\frac{\cos\theta}{2\sigma}\,\frac{\partial F}{\partial \chi} = S_{nl} + \gamma_{in}(\sigma)\,F \tag{48}$$

We include in Eq. (48) the interaction with wind. Let us make a very crude estimate of the different terms in this equation. Neglecting the wind input term we come to the following balance relation

$$\frac{F}{\tilde{\sigma}\chi} \simeq \tilde{\sigma}\,F\,\mu_p^4$$

or, after cancelling F and using Eq. (45)

$$\chi \tilde{F}^2\,\tilde{\sigma}^{10} \simeq 1 \tag{49}$$

Substituting (46) into Eq. (49) one can see that dependance on χ drops out if the exponents p, q are connected by the relation

$$10q - 2p = 1 \tag{50}$$

We call it the "magic relation." In virtue of this relation

$$q = q_{th} = \frac{2p+1}{10}$$

Moreover, from condition (49) we can conclude that $s = \epsilon_0^{1/5}\,\omega_0$ is a universal constant. Comparison with numerical experiments show that

$$s = \epsilon_0^{1/5}\,\omega_0 \simeq 1 \tag{51}$$

Results of 23 experiments performed in the open sea and Lake Michigan are presented in Table 1, which represents the majority (but not all) of the field experiments collected in physical oceanography for almost half of a century. References can be found in [13]. Experimental data are compared with predictions of the analytic theory presented in the present paper. According to theory, the exponents q_{chi} must coincide with the theoretically predicted value $q_{th} = 2p_\chi + 1/10$. One can see that the relative difference $\delta q \simeq \frac{1}{q_\chi}|q_\chi - q_{th}|$ does not exceed 10%. According to theory, the dimensionless quantity $s = \epsilon_0^{1/5}\,\omega_0$ must be a universal constant of order one. More accurate theoretical value of s (which is actually a slow varying function of p) will be presented shortly. Table 1 shows that experimentally measured values of s are close to unit. The data accumulated in Table 1 support theory very well.

One can add to Table 1 the composite data presented by I.R. Young in monograph [21] on page 105. This is a result obtained by the author by averaging over many field experiments. According to Young:

$$p_x = 0.8 \quad q_x = 0.25 \quad \epsilon_0 = 7.5 \cdot 10^{-7} \quad \omega_0 = 12.56 \quad s = 0.75$$

Table 1. Comparison of experimental data and predictions of theory

	Case	$\varepsilon_0 \times 10^7$	p_χ	ω_0	q_χ	q_{th}	S
1	Wen. et al. (1989)	18.900	0.700	10.40	0.23	0.24	0.75
2	Romero & Melville (2009) stabl	9.230	0.740	8.93	0.22	0.25	0.55
3	Donelan et al. (1985) var. der	8.410	0.760	11.60	0.23	0.25	0.71
4	Dobson et al. (1989) wind. int	12.700	0.750	10.68	0.24	0.25	0.71
5	Kahma & Calkoen (1992) stabl	9.300	0.760	12.00	0.24	0.25	0.75
6	Evans & Kibblewhite (1990) stra	5.900	0.786	16.27	0.28	0.26	0.92
7	Romero & Melville (2009) unstab	5.750	0.810	10.64	0.23	0.26	0.60
8	Hwang & Wang (2004)	6.191	0.811	11.86	0.24	0.26	0.68
9	SMB CERC (1977) by Young	7.820	0.840	10.82	0.25	0.27	0.65
10	Davidan (1996), U_{10} scaling	5.550	0.840	16.34	0.29	0.27	0.92
11	Evans & Kibblewhite (1990) neut	2.600	0.872	18.72	0.30	0.27	0.90
12	Black. Sea	4.410	0.890	15.14	0.28	0.28	0.81
13	Kahma & Calkoen (1992) composit	5.200	0.900	13.70	0.27	0.28	0.76
14	Kahma & Pettersson (1994)	5.300	0.930	12.66	0.28	0.29	0.70
15	Kahma & Calkoen (1992) unstab	5.400	0.940	14.20	0.28	0.29	0.79
16	JONSWAP no lab (Phllips 1977)	2.600	1.000	11.18	0.25	0.30	0.54
17	Davidan (1980)	4.363	1.000	16.02	0.28	0.30	0.86
18	Walsh, US coast (1989)	1.860	1.000	14.45	0.29	0.30	0.65
19	Mitsuyasu (1971)	1.600	1.000	21.99	0.33	0.30	0.96
20	JONSWAP (1973)	2.890	1.008	19.72	0.33	0.30	0.97
21	Donelan et al. (1992)	1.700	1.000	22.62	0.33	0.30	1.00
22	Kahma (1986)average. growth	2.000	1.000	22.00	0.33	0.30	1.01
23	Kahma (1981, 1986)rapid. growth	3.600	1.000	20.00	0.33	0.30	1.03

Table 2. Data of numerical experiments

Experiment	p_x	q_x	$10q - 2p$	ε_0	ω_0	$\varepsilon_0^{1/5}\omega_0$
ZRP	1	0.3	1	$2.9 \cdot 10^{-7}$	21.35	1.05
Snyder	0.7	0.23	1	$1.24 \cdot 10^{-5}$	9.04	0.94
Tolman-Chalikov	0.5	0.2	0.9	$3.2 \cdot 10^{-5}$	7.91	1.00
Hsiao-Shemdin	0.5	0.19	0.9	$2.0 \cdot 10^{-5}$	8.16	0.94
Donelan (with dissipation)	0.6	0.21	0.83	$6.1 \cdot 10^{-6}$	10.17	0.92
Donelan (without dissipation)	0.53	0.19	0.84	$2.05 \cdot 10^{-5}$	7.85	0.91
Plant	0.77	0.254	1	$2.9 \cdot 10^{-6}$	12.89	1.006
Stuart-Plant	0.5	0.21	1.1	$1.15 \cdot 10^{-5}$	9.48	0.975

Theory predicts $q_{th} = 0.26$, $s \simeq 1$. These data also support our statement on dominance of the nonlinear resonant process over income from wind. Other experimental and numerical data supporting our theory are collected in article [16]. In field experiments presented in Table 1 the dimensionless fetch χ varies inside the following range: $10^2 < \chi < 10^5$.

We solved the stationary Hasselmann equation (48) numerically, using various models for $\gamma(\omega, \theta)$ (see [18]). The results are presented in the Table 2. The data for the Plant and Stuart-Plant models will be commented on in the paper [41].

In these experiments fetch, χ, varies typically in the limits $0 < \chi < 10^5$. Numerical modeling shows that asymptotically for $\chi > 10^3$ all models of S_{in} lead to formation of powerlike behavior (46) of functions $\tilde{F}(\chi)$ and $\tilde{\sigma}(\chi)$. The prediction of the analytic theory, $10q - 2p = 1$, $s \sim 1$, is satisfied very well. In cases when $\gamma(\sigma)$ is a powerlike function

(ZRP and Plant models), the establishment of powerlike behavior of $\tilde{F}(\chi)$ and $\tilde{\sigma}(\chi)$ occurs for much lower fetches, $\chi \sim 10^2$.

We must stress that in spite of demonstrated universality, different models of wind input lead to completely different predictions on growth of wave energy with fetch. Models of Snyder and Hsiao-Shemdin differ especially dramatically. For all values of fetch $0 < \chi < 10^5$ we have $\tilde{F}_{Snyder}(\chi) > 5\tilde{F}_{Hsiao-Shemdin}(\chi)$

6. Self-similaruty of wind-driven sea

Now we can answer the most "sharpest" questions: Why do both field and laboratory experiments assert that $\tilde{F} = F(\chi)$ and $\sigma = \sigma(\chi)$ are powerlike functions (46)? Why are the exponents p, q are contained inside intervals (47)? We will discuss the Hasselmann sea only, where the Hasselmann equation is applicable.

Let us consider Eq. (48) and assume that $\gamma_{in}(\sigma)$ is a powerlike function

$$\gamma_{in}(\sigma) = \gamma_0 \, \sigma^{1+l} \cdot f(\phi) \tag{52}$$

One can check that Eq. (48) has the following self-similar solution

$$F = \chi^{p+q} \, G(\sigma, \chi, \phi) \tag{53}$$

which leads to powerlike expressions (46) where

$$\epsilon_0 = \int_0^{2\pi} d\phi \int_0^{\infty} G(\sigma, \phi) \, d\sigma \qquad \omega_0 = \frac{1}{\epsilon_0} \int_0^{2\pi} d\phi \int_0^{\infty} \sigma G(\sigma, \phi) \, d\sigma \tag{54}$$

In Eq. (53)

$$q = \frac{1}{2 + l}, \quad p = \frac{8 - l}{2(2 + l)} \tag{55}$$

The function $G(\xi, \phi)$, $\xi = \sigma\chi^q$, satisfies the following equation:

$$\cos\phi[(p + q)G + q\xi\frac{\partial G}{\partial \xi}] = \tilde{S}_{nl} + \gamma_0 \xi^{1+l} \, f(\phi) \, G \tag{56}$$

Here $\tilde{S}_{nl}$ is a dimensionless S_{nl} and $\gamma_0 \simeq 10^{-5}$ is a dimensionless small parameter. An explicit equation for $\tilde{S}_{nl}$ is presented in [19]. This term can be split into income and outcome terms. Each of them dominates over S_{in}; thus near the spectral peak S_{in} can be neglected and the condition $s = \epsilon^{1/5} \, \omega_0 \sim 1$ still holds.

Now let us notice that in the ZRP model of S_{in} , $l = 4/3$. This gives $q = 0.3$, $p = 1$, in good accordance with experiments 13-23 presented in Table 1. For the Plant model, $l = 2$; this gives $q = 0.25$, $p = 0.75$, in good accordance with experiments 3-7 in Table 1. In all offered models for S_{in}, $\gamma(\sigma)/\sigma$ is a growing function, and $1 < S < 2.3$. This gives, in virtue of Eq. (55) the following frames for the variation of exponents:

$$0.67 < p < 7/6, \quad 0.22 < q < 0.33$$

These frames are very close to experimentally observed frames (47) and results presented in Table 1. The results of numerical experiments collected in Table 2 show that models of S_{nl} different from the ZRP and Plant models lead to exponents outside the frame (47). This is not a weak point of theory; rather it is a weakness of the discussed models. The major prediction of the theory, the magic relation $10q - 2p = 1$, is satisfied pretty well.

In these models, $\gamma(\sigma)$ are not pure powerlike functions. However S_{in} is still a small term in Eq. (48), and we may seek "quasimodular solutions" such that exponents are "slow functions" of fetch $p = p(\chi)$, $q = q(\chi)$.

Critical analysis of data from field, wave tanks and numerical experiments is summarized in [16], [45]. In these articles the data that cover variation of averaged functions $\tilde{F}(\chi)$ and $\tilde{\sigma}(\chi)$ are collected. In a huge range of fetches, $10 < \chi < 10^6$ the magic relation is valid!

But it doesn't mean that all models for S_{in} are equally good. The analytic model predicts the "magic relation" between p and q as well as a relation between ϵ_0 and ω_0, but it says nothing about absolute values of these quantities. Comparing the first line of Table 1 (Wel et al experiments) with the second line in Table 2 (Snyder model prediction)

we see very good qualitative coincidence but large quantitative differences. The Snyder model overestimates the rate of energy growth with fetch by almost an order of magnitude. Because of the limited length of this article we cannot discuss an extremely important question: the shape of spectra in the universal spectral range $1 < \sigma < 5$. Eq. (48) does not preserve energy that leaks from the Hasselmann sea to the Phillips sea, forming an energy flux P. Thus the solution of Eq. (48) must have asymptotic behavior

$$G(\xi) \to \beta \frac{P^{1/3}}{\sigma^4} \tag{57}$$

Because $\gamma_0 \ll 1$, β is a small number. This implies the inevitable formation of Zakharov-Filonenko spectral tails $F(\omega) \sim 1/\omega^4$. Such tails are routinely observed in numerous field and laboratory experiments, see for example [42], [43]. This important subject deserves a special consideration.

7. Conclusions

Let us summarize the results. We claim that the majority of data obtained in field and numerical experiments can be explained in a framework of a simple model

$$\frac{d\epsilon}{dt} = S_{nl} + \gamma_{in}(\omega, \phi)\epsilon$$

Moreover, most of the facts can be explained by the assumption that $\gamma_{in}(\omega, \phi)$ is a powerlike function on frequency, $\gamma_{in}(\omega, \phi) = \gamma_0 \omega^{1+s} f(\phi)$. Here $1 < s < 2.3$ and $f(\phi), \gamma_0$ are tunable. This model pertains only to the description of the Hasselmann sea, $0 < \omega < \omega_H$, $\omega_H \simeq (4-5)\omega_p$.

In fact, this model is a simplification of the widely accepted model in oceanography (1). What is the difference between these models? The main difference is obvious: we excluded from our consideration any mention of wave energy dissipation. This does not mean that we deny a crucial role of wave-breaking in the dynamics of ocean surface. But, from the spectral viewpoint, the wave-breaking takes place outside the Hasselmann sea. It is going into the Phillips sea, in the spectral area of short scales. This very important statement is supported by experimental data and by numerical solutions of dynamical phase-resolving equations for a free surface.

What we offer could be called "poor man's oceanography." A "poor man" refuses attempts to derive the equation for S_{in} from "first principles," but has in his possession powerful analytic and computer models to use as test beds for compatibility of models for $\gamma_{in}(\omega, \phi)$ with experimental data. The Snyder model does not pass this test and should be excluded from operational models.

Acknowledgements

The author expresses gratitude to his permanent collaborators S. Badulin, V. Geogjaev and A. Pushkarev for a fruitful collaboration. This work was supported by RSF project no. 14-22-00174.

References

1. O.M. Phillips, On the dynamics of unsteady gravity waves of finite amplitude, Part 1, *J. Fluid Mech.*, 1960; **9** 193-217.
2. K. Hasselmann, On the nonlinear energy transfer in a gravity-wave spectrum. Part 1. General theory.*J. Fluid Mech.*, 1962; **12** 481-500.
3. K. Hasselmann, On the nonlinear transfer in a gravity-wave spectrum. Part II. Conservation theorems; wave-particle analogy; irreversibility. *J. Fluid Mech.*, 1963; **12** 273-281.
4. V.E. Zakharov, N.N. Filonenko, Energy spectrum for stochastic oscillations of the surface of liquid, *Doclady Akad. Nauk SSSR*, 1966; **170(6)** 1292-1295; English:*Sov. Phys. Dokl.*, 1967; **11** 881-884.
5. M.M. Zaslavskii, V.E. Zakharov, The theory of wind wave forecast (in Russian), *Doklady Akad. Nauk SSSR*, 1982; **265 (3)** 567-571.
6. M.M. Zaslavski, V.E. Zakharov, The kinetic equation and Kolmogorov spectra in the weak turbulence theory of wind waves, *Izvestiya Atmospheric and Oceanic Physics*, 1982; **18** 747-753.
7. M.M. Zaslavski, V.E. Zakharov, The shape of the spectrum of energy containing components of the water surface in the weakly turbulent theory of wind waves, *Izvestiya Atmospheric and Oceanic Physics*, 1983; **19** 207-212.
8. S.A. Kitaigorodskii, On the theory of the equilibrium range in the spectrum of wind-generated gravity waves, *J. Phys. Oceanogr.*, 1983; **13** 816-826.

9. V.E. Zakharov, Direct and inverse cascade in wind-driven sea and wave breaking, *Proc. IUTAM Meeting on Wave Breaking, Sydney, 1991*, Eds. M.L. Banner and R.H.Y. Grimshaw, Springer-Verlag, Berlin; 1992, 69-91.
10. V.E. Zakharov, Theoretical interpretation of fetch limited wind-driven sea observations, *Nonlin. Process. Geophys.*, 2005; **12 (6)** 1011-1020.
11. A. Pushkarev, D. Resio, V. Zakharov, Weak turbulent approach to the wind-generated gravity sea waves, *Physica D*, 2003; **184 (1-4)** 29-63).
12. S.I. Badulin, A.N. Pushkarev, D. Resio, V.E. Zakharov, Self-similarity of wind driven seas, *Nonlin. Process. Geophys.*, 2005; **12(6)** 891-945.
13. S.I. Badulin, A.V. Babanin, D. Resio, V.E. Zakharov, Weakly turbulent laws of wind-wave growth, *J. Fluid Mech.*, 2007; **591** 339-378.
14. V.E. Zakharov, Energy balance in a wind-driven sea, *Physica Scripta*, 2010; **T142** 014052.
15. V.E. Zakharov, S.I. Badulin, On energy balance of wind-driven seas, *Doklady Earth Sciences*, 2011; **440(2)** 1440-1444.
16. V. E. Zakharov, S. I. Badulin, Paul A. Hwang, Guillemette Caulliez, Universality of sea wave growth and its physical roots, *J. Fluid Mech.*, 2015; **780** 503-535.
17. V. Zakharov, A. Pushkarev, D. Resio, New wind input term consistent with experimental, theoretical and numerical considerations, *Nonlin. Processes Geophys.*, 2017; **24** 581-597.
18. A. Pushkarev, V. Zakharov, Limited fetch revisited: Comparison of wind input terms, in surface wave modeling, *Ocean Modelling*, 2016; **103** 18-37.
19. V. Geogjaev, V. Zakharov, Numerical and analytical calculations of the parameters of power-law spectra for deep water gravity waves, *JETP Letters*, 2017; **106(3)** 184-187.
20. Cavaleri, L., Alves, J.-H., Ardhuin, F., Babanin, A., Banner, M., Belibassakis, K., Benoit, M., Donelan, M., Groeneweg, J., Herbers, T., Hwang, P., Janssen, P., Janssen, T., Lavrenov, I., Magne, R., Monbaliu, J., Onorato, M., Polnikov, V., Resio, D., Rogers, W., Sheremet, A., I. Smith, J. M., Tolman, H., van Vledder, G., Wolf, J., and Young, I.: Wave modelling The state of the art, Progress in Oceanography, 75, 603 674.
21. Ian R. Young, Wind Generated Ocean Waves, Elsevier, 1999.
22. P. Janssen, The Interaction of Ocean Waves and Wind. Cambridge University Press, 2004.
23. V. Zakharov and A. Pushkarev, Diffusion model of interacting gravity waves on the surface of deep fluid, *Nonlin. Proc. Geophys.*, 1999; **6 (1)** 1-10.
24. V. Geogjaev, V. Zakharov, Self–Similar Swells, (in preparation)
25. V. Zakharov, Statistical theory of gravity and capillary waves on the surface of a finite-depth fluid, *Eur. J. Mech. B/Fluids*, 1999; **18 (3)** 327-344.
26. V. Zakharov, A.O. Korotkevich, A.N. Pushkarev, D. Resio, Coexistence of weak and strong wave turbulence in a swell Propagation, *Phys. Rev. Lett.*, 2007; **99** 164501.
27. A. O. Korotkevich, V. E. Zakharov, Evaluation of a spectral line width for the Phillips spectrum by means of numerical simulation, *Nonlin. Processes Geophys.*, 2015; **22** 325-335.
28. S.Y. Annenkov, V.I. Shrira, Numerical modelling of water-wave evolution based on the Zakharov equation, *J. Fluid Mech.*, 2001; **449** 341-371.
29. S.Y. Annenkov, V.I. Shrira, Direct numerical simulation of downshift and inverse cascade for water wave turbulence, *Phys. Rev. Lett.*, 2006; **96(20)** 204501.
30. A.C. Newell, V.E. Zakharov, Rough sea foam, *Phys. Rev. Lett.*, 1992; **69 (8)** 1149-1151.
31. G.J. Komen, L. Cavaleri, M. Donelan, K. Hasselmann, S. Hasselmann, P.A.E.M. Janssen. Dynamics and Modelling of Ocean Waves. Cambridge University Press (1994)
32. V.E. Zakharov, V.S. L'vov, G. Falkovich, Kolmogorov spectra of turbulence I. Wave turbulence, Springer Series in Nonlinear Dynamics. Berlin: Springer-Verlag. xiii, 264 p. (1992).
33. I. Lavrenov, D. Resio, V. Zakharov, Numerical simulation of weak-turbulent Kolmogorov spectra in water surface waves, Proc. 7th Int. Workshop on Wave Hindcasting and Forecasting, Banff, Alberta, Canada, October 21-25, 2002.
34. L.W. Nordheim, On the kinetic method in the new statistics and its applications in the electron theory of conductivity, *Proc. Roy. Soc. London A*, 1928; **119** 689-698.
35. Y. Lvov, R. Binder, A. Newell, Quantum weak turbulence with applications to semiconductor lasers, *Physica D*, 1998; **121** 317-343.
36. A. Pushkarev, D. Resio, V. Zakharov, Second generation diffusion model of interacting gravity waves on the surface of deep fluid, *Nonlin. Process Geophys.*, 2004; **11 (3)** 329-342.
37. A. Katz, V. Kantorovich, Anisotropic turbulent distribution for waves with a non-decay dispersion laws, *Soviet Physics JETP*, 1974; **38** 102-107.
38. W. Pierson, L. Moscowitz, A proposed spectral form for fully developed wind seas based on the similarity theory, *J. Geophys. Res.*, 1964; **69** 5181-5190.
39. W.J. Plant, A relationship between wind stress and wave slope, *J. Geophys. Res.*, 1982; **87 (C3)** 1961-1967.
40. S.A. Kitaigorodskii, On the equilibrium ranges in wind-wave dynamics and ratio probing of the ocean surface, Ed. by O.M. Phyllips and K. Hasselmann. Plenum Press Corp. 9-40, 1986.
41. A. Pushkarev, Comparison of different models for wave generation of the Hasselmann equation (to be published).
42. Y. Toba, Local balance in the air-sea boundary processes. III. On the spectrum of wind waves, *J. Oceanogr. Soc. Japan*, 1973; **29** 209-220.
43. O. Phillips, Spectral and statistical properties of the equilibrium range in wind-generated gravity waves, *J. Fluid Mech.*, 1985; **156** 505-561.
44. S. Badulin, V. Zakharov, Ocean swell within the kinetic equation for water waves, *Nonlin. Processes Geophys.*, 2017; **24** 237253.
45. E. Gagnaire-Renou, M. Benoit, S. Badulin, On weakly turbulent scaling of wind sea in simulations of fetch-limited growth, *J. Fluid Mech.*, 2011; **669** 178213.

Available online at www.sciencedirect.com

ScienceDirect

Procedia IUTAM 26 (2018) 59–69

Procedia IUTAM

www.elsevier.com/locate/procedia

IUTAM Symposium Wind Waves, 4-8 September 2017, London, UK

Detailed measurements of interfacial dynamics in air-water pipe flow

A.A. Ayati, P. Vollestad, A. Jensen

Department of Mathematics, University of Oslo, N-0316 Oslo, Norway

Abstract

Stratified air-water flow in a horizontal pipe is investigated experimentally using particle image velocimetry and conductance probes. This flow regime is characterized by a complex interplay between a turbulent airflow and propagating waves at the interface. The waves are generated by interfacial shear and pressure forces exerted by the faster flowing airflow. The goal of this study is to characterize the waves by means of statistical and spectral methods, and to explore the influence of different wave regimes on the airflow.

Two cases in which the air bulk velocity increases from 2.4 m/s (case A) to 3.5 m/s (case B), while the liquid velocity remains constant at 0.26 m/s, are assessed in detail. Case A belongs to a region of flow conditions in which wave amplitudes grow as a consequence of increasing gas flow rates, i.e., wave growth regime. Meanwhile, case B is in a regime of saturated wave amplitudes. In the first case, the interface was populated by small amplitude 2D waves of relatively small steepness ($ak \approx 0.07$). These waves obey Gaussian statistics and are thus considered to be linear. In the second case, the waves are larger, steeper ($ak \approx 0.13$) and considerably more irregular. They display non-linear behaviour (steep crests and long troughs) and their exceedance probability distribution deviates significantly from Gaussian statistics. Bicoherence maps show evidence of both overtone and sub-harmonic interactions.

Airflow velocity fields acquired by PIV were subjected to a conditional phase-averaging method based on a steepness criterion. The phase-averaged vorticity field shows evidence of shear-layer separation above the steeper waves of case B. Hence, in addition to non-linear mode interactions and micro-breaking, shear-layer separation may contribute to the transition from the growth regime to the saturation regime.

Peer-review under responsibility of the scientific committee of the IUTAM Symposium Wind Waves.

Keywords: Gas-liquid pipe flow; Non-linear wave interaction; Airflow separation.

1. Introduction

Gas-liquid flow in pipes is relevant to a variety of industrial applications, ranging from nuclear and petroleum industries to waste water mains [32, 37, 16]. Inside natural gas pipelines, the flow often consists of both a gaseous and a liquid phase, in the form of gas-water or gas-condensate combination. Both phases are usually turbulent and flow in the same direction. Generally, the gaseous phase flows significantly faster than the liquid phase giving rise

* Corresponding author. Tel.: +47-22855988
E-mail address: awalaa@math.uio.no

2210-9838
Peer-review under responsibility of the scientific committee of the IUTAM Symposium Wind Waves.
10.1016/j.piutam.2018.03.006

to waves at the interface which separates the two fluids. It is known that the presence of interfacial waves enhances drag between the phases, and consequently increases the pressure drop [4]. For this reason, there have been intense efforts, within multiphase flow research, to build models that are able to accurately predict the pressure drop, among other important system parameters. The most common modelling approach related to this problem has been based on the use of semi-empirical correlations for the interfacial friction factor. Since this approach is very system dependent, significant discrepancies in proposed correlations are found in the literature, see for instance [38, 3, 43].

Another issue related to this flow takes place at high flow rates. Under such conditions, the interfacial waves may grow to block the pipe cross-section and onset slug flow, i.e., an intermittent flow regime which induces large pressure fluctuations in the system. This flow regime can be detrimental to pipelines as well as their supporting infrastructure. Transition to slug flow, which is a direct consequence of the confined pipe geometry, represents one of the major differences between gas-liquid flow in pipes and open wind-wave systems. Accurate prediction of this flow regime transition is yet another important motivation for two-phase pipe flow research. In the framework of the one-dimensional two-fluid model [40], this transition has traditionally been modelled using a viscous Kelvin Helmholtz approach [10, 42]. More recent approaches consist of solving the two-dimensional Orr-Sommerfeld eigenvalue problem [30, 9], and including weakly non-linear wave interaction [19]. Although some of these approaches are sophisticated, there is still no consensus regarding the solution of this problem as predictions fail to accurately reproduce experimental results, see [33] for a review.

At lower flow rates, beneath the conditions for slug onset, the small-scale dynamics that govern the interfacial region in gas-liquid pipe flow are reminiscent of open wind-wave systems. Interfacial perturbations are excited at the inlet region of the pipe by means of turbulent pressure fluctuations in the airflow [36] and/or shear-instabilities. Once present, these perturbations grow with fetch, most likely as a result of Miles's mechanism [34], and become gravity-capillary waves. Further downstream, the waves interact with each other, both linearly and non-linearly, depending on the flow rates. The non-linear interactions appear first as sub-harmonic bifurcation, i.e., period doubling [27, 14]. Even further downstream, the waves may reach a state of equilibrium between energy input from the airflow and dissipation due to viscous effects, wave breaking and non-linear energy transfer towards stable modes [29]. The flow is then considered as fully developed and the wave amplitudes remain more or less constant even with increasing the airflow forcing.

In their study of interfacial gravity-capillary waves in horizontal gas-liquid flows, Jurman et al. [29] pointed out non-linear modal interactions as the main mechanism for the observed amplitude saturation. However, their study did not include any investigation of the momentum input source, i.e., the airflow. Numerous subsequent studies, both experimental and numerical [45, 23, 44, 17] have reported evidence of intermittent flow separation events above relatively steep non-breaking waves. Such events are believed to reduce the momentum transfer from the airflow to the waves as the contact surface between the phases diminishes. Therefore, this mechanism should probably be considered as yet another contributor to the transition to the saturated regime.

The complexity of the system under investigation lies in the fact that all above mentioned mechanisms take place simultaneously. Furthermore, the circular pipe geometry certainly adds complexity, in ways that have not yet been fully understood. Thus, there is still a need for conducting phenomenological studies such as the present one, in order to identify and quantify the various mechanisms that govern the fully stratified flow regime.

The specific aim of this paper is to address interfacial mode interaction and airflow separation by, firstly, characterizing the interfacial waves through statistical and spectral methods, and secondly, use PIV measurements to explore the effect of different wave regimes on the airflow structure. Two cases are depicted amongst a larger set in which the liquid flow rate is kept constant while the gas superficial velocity increases from approx. 1 m/s to 4 m/s. These cases lie in two observed regimes, i) wave growth and ii) wave saturation regime. Note that all measurements are acquired at a single position approximately 25 m (250D) downstream of the inlet, at which the flow is considered to be fully developed.

This manuscript is organized in the following manner. After this short introduction, the experimental set-up and methodology are described in section 2. The latter consists of a zero-crossing analysis of wave probe signals as well as a phase-averaging procedure applied on airflow PIV velocity fields. The results are then presented in section 3. These consist of i) a characterization of interfacial wave regime through the assessment of exceedance probability distributions, power spectra and bicoherence plots, and ii) a presentation of the phase-averaged airflow velocity and

vorticity fields with emphasis on shear-layer separation above steep waves. Finally, concluding remarks are presented in section 4.

2. Experimental set-up and methodology

Experiments were conducted at the Hydrodynamic Laboratory, University of Oslo. The laboratory has a 31 m long horizontal acrylic pipe with internal diameter D=10 cm. The test fluids were air and water at atmospheric pressure. Both fluids were introduced at the pipe inlet using a frequency-regulated pump and fan, for the water and air, respectively. The water and air mass flow rates were measured with an Endress Hauser Promass and an Emerson MicroMotion Coriolis flow meter, with 0.2 % and 0.05 % of maximum measured values in accuracy, respectively. A schematic view of the pipe-loop is shown in figure 1.

During the experimental campaign, three experimental techniques were employed; i) Simultaneous Two-Phase Particle Image Velocimetry (PIV), ii) Conductance Probes (CP) and iii) Hot-Wire (HW) anemometry. However, in this paper, only data acquired by PIV and conductance probes will be assessed. The PIV set-up was located 26m (260D) downstream of the pipe inlet. It provided velocity fields in the pipe centre plane in both the gaseous and liquid phase simultaneously using two cameras with high spatial resolution and one high-energy Nd:YAG laser. Small water droplets ($\overline{d} \sim 6\mu$m) were introduced at the pipe inlet as tracers in the airflow, whilst the water flow was seeded with commercial spherical polyamide particles ($\overline{d} \sim 50\mu$m). It should be emphasised that only airflow velocity fields will be presented in this paper.

The CP section was located 10D downstream of the PIV section. It consisted of two double-wire conductance probes made of platinum. The wires were 0.3 mm thick and separated by 4 mm. Both probes were placed at the centre of the pipe with a distance 6 cm in the stream wise direction. Interface elevation time series were sampled at 500 Hz for approximately 30 minutes.

For more details about the experimental set-up and data processing routines, the reader is referred to [6, 7, 8].

2.1. Wave signal analysis

Local wave parameters, e.g., elevation (η), amplitude (a), length (λ), speed (c), were extracted for each wave cycle, w_n, by means of the zero-crossing method. First, the mean elevation was subtracted from the raw signal given by each probe $\eta_i'(t) = \eta_i(t) - \overline{\eta_i}$. A zero-down-crossing is then defined as the location at which the signal changes sign from positive to negative. Wave crests and troughs are defined as the global maximum and minimum in between two subsequent zero down-crossings, respectively. Probability distributions of any given wave parameter were obtained by means of kernel density estimation [15]. In this paper, exceedance probability distribution (epd) will be evaluated. For more details about this procedure, see [5].

Power spectral densities (PSD) and bicoherence (Bc) will be assessed in the analysis of modal interaction (sec. 3.2). The Bc, here denoted as $\beta(f_j, f_k)$ is a normalized bispectrum, $\phi_{\hat{\eta}\hat{\eta}\hat{\eta}}(f_j, f_k)$. The latter is a triple correlation function in

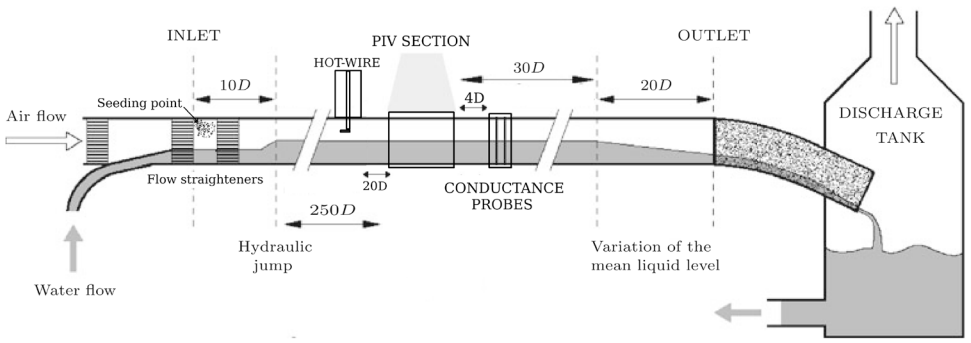

Fig. 1: Schematic view of the experimental setup in use.

the Fourier space which identifies spectral modes that are coherent in phase. The normalization process eliminates any amplitude dependency from the bispectrum. Thus, phase-correlated modes that exactly satisfy the selection criterion $f_1 + f_2 = f_3$ yield $\beta(f_1, f_2) = 1$. The bispectrum and bicoherence are defined as follows (see for instance [29]):

$$\phi_{\hat{\eta}\hat{\eta}\hat{\eta}}(f_j, f_k) = \mathbb{E}\left[\hat{\eta}(f_j)\hat{\eta}(f_k)\hat{\eta}^*(f_j + f_k)\right], \qquad j, k = 0, 1, ..., M/2 \tag{1}$$

$$\beta(f_j, f_k) = \frac{\left|\phi_{\hat{\eta}\hat{\eta}\hat{\eta}}(f_j, f_k)\right|^2}{\mathbb{E}\left[\left|\hat{\eta}(f_j)\hat{\eta}(f_k)\right|^2\right]\mathbb{E}\left[\left|\hat{\eta}^*(f_j + f_k)\right|^2\right]} \tag{2}$$

where $\hat{\eta}^*$ is the complex conjugate of $\hat{\eta}$ and M is the sample size of the signal.

Here, the bicoherence was calculated using 250 overlapping widows of 264 points. This choice proved to provide adequate resolution for the bicoherence maps shown in Fig. 5. According to numerical simulations conducted by [25], the minimum significant value of bicoherence required for 95% significance level is given by $\beta^2_{95\%} \geq 6/N_{im}$, where N_{im} is the number of windows used in the calculation of β. Thus, this threshold was set in our calculations.

2.2. Conditional averaging of PIV velocity fields

From a given PIV image, the interfacial profile was extracted using an intensity-gradient based method. The PIV field of view (FOV) was 90mm wide. This was not enough to fully resolve the spectral peak component, which wave length varied between 1.8 and 2.5 times the FOV, in case A and B, respectively. Nevertheless, by dividing the interface into quadrant and averaging fields over quadrants of similar shape, it was possible to perform meaningful phase-averaging of the velocity fields above the waves. A similar approach was employed by [39] and [12]. However, these studies focused on the water velocity field, i.e., under the interface.

Wave quadrants were identified by means of a zero-crossing procedure. Between two consecutive zero-crossings, global maxima/minima were identified as crests/troughs. The region in between a zero-crossing and a crest/trough was then classified as a wave quadrant according to the definition in figure 2. A minimum wave amplitude of 1 mm was used as a threshold in order to limit the influence of measurement uncertainties close to the interface.

As the interfacial elevation consists of a spectrum of wave components with varying heights, lengths and steepnesses, a criteria is employed prior to averaging. The wave steepness is known to have a significant impact on the airflow above waves, affecting the critical layer height and the streamline pattern above the waves [22]. For this reason, wave steepness was chosen as the averaging criterion in this study. Conditional averaging based on wave steepness was also performed by [2], in investigating the velocity field in the liquid phase below 2D millimetre-scale waves.

The airflow domain was subjected to a coordinate transformation from Cartesian coordinates (x, y) to wave-following coordinates (θ, ζ). The crest, trough and zero crossings were assigned phases of 0°, 180° and +/- 90°, respectively (see figure 2), whilst phases in between were linearly distributed. The vertical coordinate $\zeta = (y - \eta(x))/\eta_c$ is the dimensionless distance from the interface, normalized by the crest amplitude. The resulting coordinate system is illustrated in figure 2 for a single Q2 observation. The velocity fields above the identified wave quadrants are sampled from $\zeta = 0$ to 5. For each quadrant observed, all variables of the flow field (u, v, vorticity etc.) were sampled at the equally distributed (θ, ζ) coordinates, with 180 points in the θ direction and 100 points ζ direction. More details about this phase-averaging procedure may be found in [44].

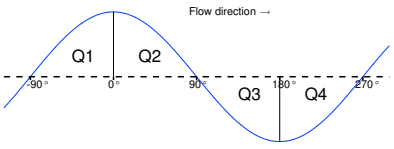

a) Wave quadrants.

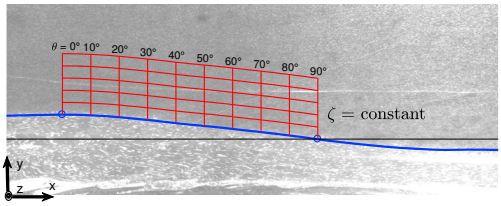

b) Coordinate system.

Fig. 2: Left: Definition of quadrants. Dotted line represents mean water level. x-axis represents the wave phase. Right: Example of an identified quadrant (Q2 event), and wave following coordinate system above the wave quadrant. Note that in the laboratory frame of reference, the x-axis is in the flow direction, y points upwards, while z goes out of the $x-y$ plane.

3. Results

The cases under investigation in this study are depicted amongst a larger data bank. Some important parameters concerning these cases are listed in Table 1. Figure 3 shows the evolution of RMS amplitude normalized by the pipe diameter σ_η/D, as well as the steepness (ak) of the most probable wave as a function of increasing gas superficial velocity U_{sg}. Both cases under investigation are shown as red squares. Note that in all cases shown in the figure, the liquid superficial velocity was kept constant at 0.1m/s. The corresponding bulk velocity varied between 0.24 and 0.32 m/s. This variation is dictated by conservation of mass in a confined space, i.e., as the gas flow rate increases, the liquid level decreases (from 0.45D to 0.37D) and thus the liquid bulk velocity increases.

The first measurable waves appeared at air velocity $U_{sg} \approx 1$ m/s. At velocities up to $U_{sg} \approx 1.7$ m/s, the waves grow, both in height and length. The relative growth in height is greater than the corresponding growth in length. Thus, the average wave steepness also with increasing gas velocity. Above $U_{sg} \approx 1.7$, the RMS amplitude stabilizes around 2.3 mm, while the steepness oscillates around 0.13. Note that these values stem from the conductance probe measurement and differ slightly from PIV measurements taken slightly upstream [44]. Based on available data, one may claim that the evolution wave amplitudes can be categorized into two regimes; i) wave growth regime in which case A features, and ii) wave saturation regime which includes case B. Note that in both cases under investigation, the effective wave speed $(c - U_{bl})$ is well described by the dispersion relation for finite depth gravity waves, see [7].

Exp. case	U_{sl} [m/s]	U_{sg} [m/s]	U_{bl} [m/s]	U_{bg} [m/s]	Re_{Dg} [-]	Re_{Dl} [-]	σ_η/D [-]	c [m/s]	λ_p/D [-]	$\bar{h}_w/D$ [-]	c/u_* [-]
A	0.1	1.5	0.26	2.44	11 238	25 167	0.7%	0.71	0.25	0.41	2.1
B	0.1	2.1	0.26	3.49	15 793	24 921	2.2%	0.81	2.1	0.42	2.7

Table 1: Characteristics of experimental cases under investigation.

3.1. Statistical characterization of interfacial waves

In both cases A and B, the interfacial waves display rather random behaviour to the naked eye. Although it is possible to visually identify a dominant mode, figure 5 reveals that the spectral content is relatively broad-banded and multimodal. Thus in order to categorize the wavy regimes, we evaluate the statistical properties of each elevation time series and use the Gaussian wave model as a reference, see for instance [35] for a review on Gaussian wave statistics. To this end, exceedance probability distributions of the elevation time series $\eta(t)$ and the Hilbert upper envelope $A_{up}(t)$ are compared to their associated Gaussian and Rayleigh distributions, respectively, in figure 4.

With small discrepancies at the tails, the exceedance distribution of case A is well described by Gaussian statistics. This means that the wave field consists of a linear superposition of statistically independent Fourier modes. It is thus reasonable to categorize the waves in case A within a "linear regime" in which non-linear contributions are negligible. Case B, however, deviates significantly from linear Gaussian theory. In contrary to rogue ocean surface waves for which Gaussian statistics is expected to underestimate the most extreme waves, both the normal and Rayleigh dis-

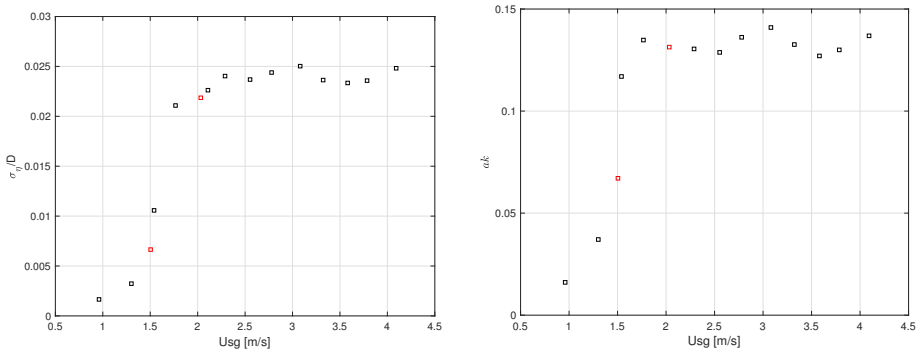

a) Evolution of RMS amplitude. b) Evolution of steepness.

Fig. 3: Evolution of RMS amplitude σ/D and steepness ak with increasing gas velocity. Note that the two cases under detailed investigation are depicted by red squares.

tributions strongly overestimate the exceedance distributions of measured elevation and upper envelope, respectively. This is especially the case in the tail region of the exceedance distributions, i.e., at $y/\sigma > 2$. This means that the wave field does not contain large amplitude waves which are expected to be present on a Gaussian surface. However, by closer investigation, it appears that the exceedance distribution of A_{up} first overshoots above the Rayleigh distribution for y-values up to 1.8σ, before undershooting.

This behaviour is attributed to non-linear effects. Most likely, the dominant (and most common) wave grows by means of energy transfer through non-linear wave interaction and wind input, becomes too steep and subsequently breaks. It is worthwhile emphasizing that wave breaking with air entrainment was not observed during the experimental campaign. However, weaker forms of breaking such as spilling or micro-breaking is very likely to have taken place, although this cannot be affirmed by means available experimental data. This is in fact the subject of an ongoing study.

In order to assess modal interaction, power spectral densities and bicoherence maps are analysed in the following section.

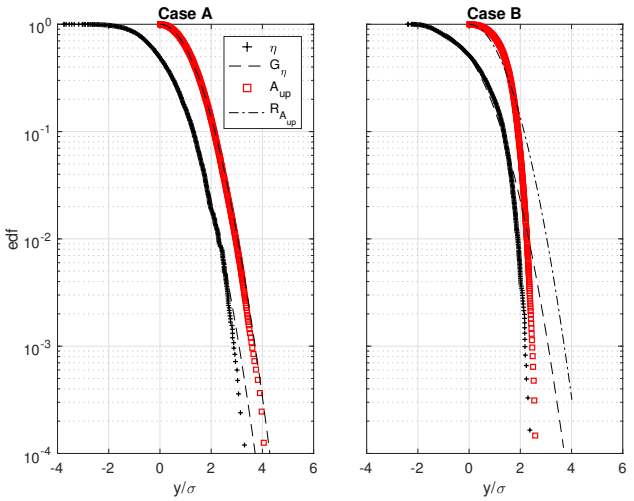

Fig. 4: Exceedence distribution of the wave elevation η and Hilbert upper envelope A_{up}, here normalized by the elevation standard deviation. The associated Gaussian (black dashed line) and Rayleigh (red dashed line) distributions are plotted for comparison.

3.2. Spectral analysis and modal interaction

Power spectral densities shown in figure 5 reveal that both cases have spectral peaks at $f \approx 4$ and 8 Hz. In addition, case B has a third peak at 10 Hz. The 8 Hz mode is likely to be the fundamental mode of this system. It is associated with the first measurable waves that appear at $U_{sg} \approx 1$ m/s (not shown here), see [7]. Their wavelength is approximately half the water depth and their measured celerity is $c \approx 20$ cm/s, which corresponds to the phase speed of gravity-capillary waves. The sub-harmonic mode at ∼4 Hz appears once the gas velocity exceeds 1.30 m/s. This mode has a dominant wavelength $\lambda \approx 2D$ and lies on the gravity side of the dispersion relation [13]. It seems likely that this mode results from sub-harmonic bifurcation (2→ 1), also called period doubling [27]. As the gas velocity increases, the sub-harmonic mode grows and experiences a slight frequency downshift [41, 31, 21], as can be seen in figure 5.

Period doubling is characterized by fast energy transfer from the fundamental to the sub-harmonic mode [27]. Campbell and Liu [18] considered the role of non-linear sub-harmonic resonant wave interaction in the development of interfacial waves. They found that the sub-harmonic mode receives energy from its linearly unstable fundamental mode at a faster than exponential rate. Meanwhile, in his reassessment of Chen and Saffman's experiments [20], Janssen [27] argued that in real wind-wave systems, one should expect a quasi-resonant sub-harmonic interaction since wind induces relatively broad-banded disturbances. Thus, one should expect that the rate of energy transfer is relatively lower than reported by [18]. Our observations are in agreement with Janssen's argument. Some 5 m upstream of the measurement set-up, it was possible to observe the period-doubling process taking place over a distance of approximately 1 m. By increasing the gas velocity, the location at which the period doubling takes place was shifted further upstream, i.e., higher gas velocity accelerates the process of bifurcation. To this end, at even higher gas velocities than case B, the 4 Hz mode has had both more time and space to develop before reaching the test section.

The bicoherence plots in figure 5 reveal that in case A, there is only sign of overtone coupling emerging from interaction of the fundamental 8 Hz mode with itself giving rise to a noticeable small peak at 16 Hz in the power spectrum. Note that the bicoherence peak is at slightly higher frequency (∼ 9 Hz) that the spectral peak. The 16 Hz disturbances are most likely to remain stable as these are capillary waves governed by surface tension. However, this part of the spectrum contributes to the surface roughness. It is interesting to note that the bicoherence map shows no sign of interaction related to sub-harmonic mode at 4 Hz. It is as if this mode behaves as a free wave. Further investigation is needed to draw any conclusion regarding this observation.

In case B, the bicoherence plot indicates the presence of both overtone interaction, $\beta(4\text{Hz}, 4\text{Hz})$ and $\beta(8\text{Hz}, 8\text{Hz})$, as well as sub-harmonic interaction $\beta(8\text{Hz}, 4\text{Hz})$, in addition to contributions from lower frequency modes (2Hz). These large scale fluctuations are believed to increase the irregularity of the wave field. In both cases, the peak bicoherence is related to the overtone interaction of the peak mode with itself, i.e., $\beta(8\text{Hz}, 8\text{Hz})$ in case A and $\beta(4\text{Hz}, 4\text{Hz})$ in case B.

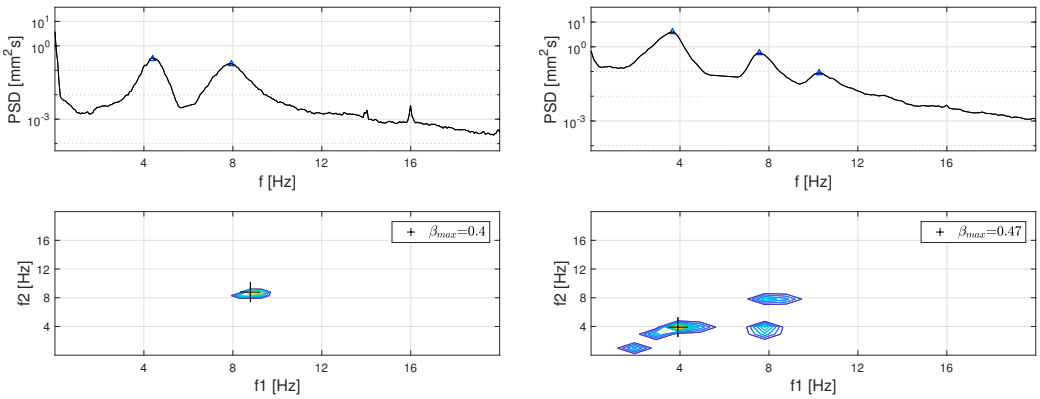

a) Case A. b) Case B.

Fig. 5: PSD and bicoherence map for cases A and B. The '+' sign indicates the peak bicoherence.

In their study of interfacial gravity-capillary waves in horizontal gas-liquid flows, Jurman et al. [29] attributed the observed saturation of wave amplitudes to non-linear energy transfer from unstable to stable modes. Nevertheless, their study did not include any assessment of the flow field above the waves. Recent experimental and numerical studies on turbulent airflow above propagating waves [17, 45] have reported evidence of intermittent airflow separation events above steep non-breaking waves. Airflow separation introduces a velocity discontinuity above the wave trough region, which reduces the momentum transfer between the phases. This phenomenon is therefore expected to play a role in the saturation of wave amplitudes discussed above. In the next section, the structure of airflow is assessed by means of the conditional-averaging procedure outlined in section 2.2.

3.3. Structure of the airflow

Streamlines of the phase-averaged airflow field, seen in a frame of reference moving with the mean wave speed, are plotted for cases A and B in figure 6. The critical height $y_c(\theta)$, i.e., the height at which $U_g(y) = \overline{c}$, is represented by a dashed black line. The viscous sublayer thickness ($y_{vs} = 5\nu_g/u_*$), is shown by a red dashed line. It is normalized by the average crest height η_c in each case. In case A, $y_{vs} = 0.24$ mm $= 0.12\eta_c$, whilst in case B $y_{vs} = 0.25$ mm $= 0.05\eta_c$.

In case A, the critical layer follows the shape of the average wave profile. For the most part, the critical layer lies within the viscous sublayer. However, $y_c(\theta)$ is slightly larger on the lee side of the crest ($0^\circ < \theta < 150^\circ$) compared to its windward side. This is because the airflow velocity is marginally lower in the trough region. Nevertheless, compared to case B, $y_c(\theta)$ is rather symmetric about the crest. The phase-averaged streamlines also follow the shape of the wave surface except near the critical height at $\theta = 100^\circ$ and 180°, where two small region of enclosed streamlines can be depicted.

In case B, the critical layer is adjacent to the surface at $-50^\circ < \theta < 0^\circ$, whilst in the trough region, its height is comparable to the average crest amplitude, i.e., $y_c(\theta > 0^\circ) \sim \eta_c$. Overall, the critical layer height lies substantially far above the viscous sublayer, indicating that the former plays an important role in the development of the waves. The asymmetry in $y_c(\theta)$ is a result of sheltered airflow in this region. Whether this sheltering process implies airflow separation [28] or not (non-separated sheltering [11]), depends on the temporal frame of reference applied to view the flow. In some instantaneous flow fields, there were clear signs of separated streamlines (not shown), with detachment and reattachment points. These features are not seen in the phase-averaged streamlines shown in fig. 6. Nevertheless, a large region of enclosed streamlines "cat's eye" can be seen slightly downstream of the crest ($\theta = 50^\circ$). The position of this "eye" implies that, on average, a wave experiences a co-moving pocket of air located slightly downwind of its crest, thus altering the pressure distribution around the crest.

Hara and Sullivan [24] performed large eddy simulation of strongly forced young waves ($c/u_* = 1.6$) with wave steepness $ak = 0.226$, i.e., a regime which is qualitatively comparable to case B. Their results showed that an asymmetric critical height implies asymmetry in pressure distribution above the wave. The peak pressure moves downstream from the wave towards to the windward side of the next wave. This results in a flux of horizontal momentum locally, pushing the wave in the flow direction. Although we do not have measurements of the pressure field, it is reasonable to assume that similar scenario takes place in case B.

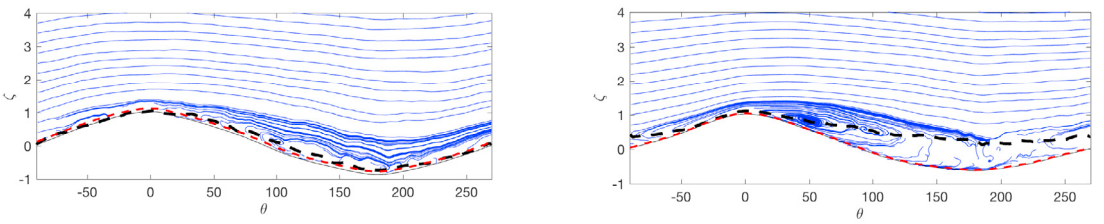

a) Streamlines (case A) b) Streamlines (case B)

Fig. 6: Streamlines of $\boldsymbol{u} - \overline{c}$ for averaged flow field. The critical layer height $y_c(\theta)$ is shown by the dashed black line, whereas the red dashed line indicates the viscous sublayer thickness $y_{vs} = 5\nu_g/u_*$.

Isolated swirling structures in any given instantaneous velocity field were identified by means of the swirling strength criterion (λ_{ci}), see [1] for a review of this method. Figure 7 shows selected instantaneous fields from case A

and B. Both were chosen because they contained a crest of the left side of the PIV-image, thus showing the swirling field downstream of a crest. The figures reveal that as the air flows past a crest, there is a remarkable shedding of negative swirling motion. Note that negative rotation axis points inwards in the (x, y)-plane. The shed vortices in case B are visibly more intense than in case A. This is a consequence of the air velocity being larger and the wave steeper than in case A. Such zones of recirculating airflow have been described by Hunt and Sajjadi [26] for flow above growing wave trains.

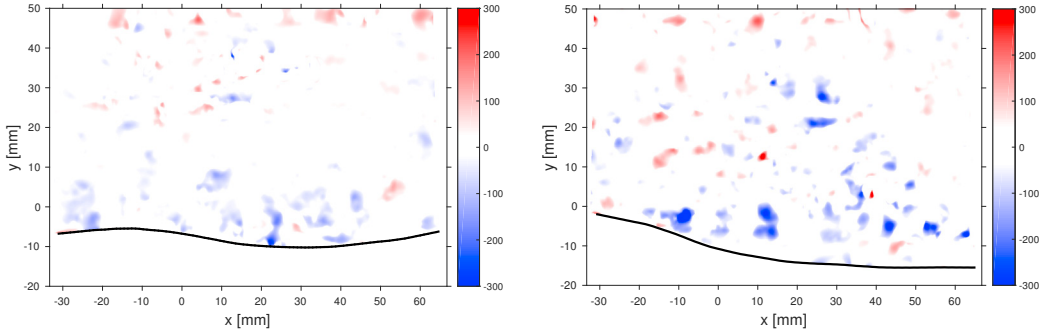

c) Swirling strength (case A) d) Swirling strength (case B)

Fig. 7: Instantaneous swirling strength fields (λ_{ci}-criterion [1]) past wave crests. Blue colour indicates negative swirling (rotation axis inward in the plane), while red indicates positive swirling.

The phase-averaging routine described earlier was applied on instantaneous swirling strength fields. The result is shown in figure 8. This figure is closely related to a phase-averaged vorticity field. It can be seen from the figure that a layer of negative vorticity remains adjacent to average wave surface in case A. In case B, the equivalent layer separates from the interface at $\theta \approx 25°$. This separation takes place at the same location at which the critical layer detaches from the surface. In this case, the criterion for shear-layer separation as defined by Buckley and Veron [17] is fulfilled. It can be noted that below the critical height there is a region dominated by positive vorticity, i.e., opposite direction of the vorticity present in the separated shear layer. This particular phenomenon is expected to lower the rate of vertical momentum transfer contributing to wave growth and thus be a partial cause for the observed amplitude saturation seen in figure 3. Nevertheless, at this stage, we do not attempt to quantify the effect of this process, as this is the subject of an ongoing study in which phase-locked PIV is conducted in order to obtain considerably larger sets of relevant data.

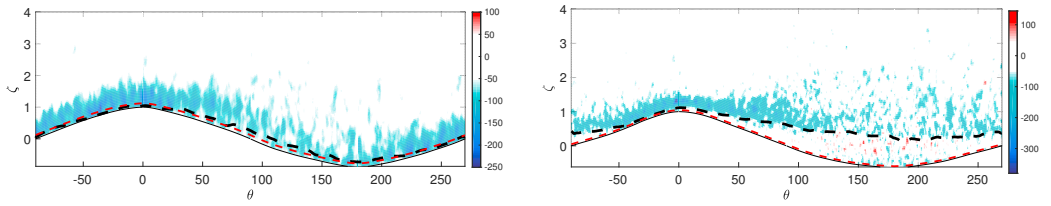

c) Swirling strength (case A) d) Swirling strength (case B)

Fig. 8: Phase-averaged swirling strength fields $\langle \lambda_{ci} \rangle$. Black dashed line represents the critical height, while the viscous sublayer is depicted by the red dashed line.

4. Concluding remarks

We have studied stratified gas-liquid flow experimentally using PIV and conductance probes. Two cases, in which the air bulk velocity increased from 2.4 m/s to 3.5 m/s while the liquid velocity was kept constant at 0.26 m/s, were studied in detail. Case A belongs to a region of flow conditions in which wave amplitudes grow as a consequence of increasing gas flow rates, i.e. growth regime. Meanwhile, case B is in a regime of saturated wave amplitudes.

One of the main goals of this phenomenological study was to categorize the interfacial waves using statistical and spectral methods. We observed that the small amplitude waves present in case A behaved according to Gaussian statistics. This was portrayed by good agreement between the exceedance probability distributions of the wave elevation η and the upper envelope A_{up} with their associated Gaussian and Rayleigh distributions. However, case B showed significant deviation from Gaussian statistics, as both the normal and Rayleigh distributions over-predicted measured exceedance in the tail region. This signifies that large amplitude waves which are expected to be present on a Gaussian surface are suppressed. This behaviour is attributed to non-linear modal interactions that left their mark on bicoherence maps shown in section 3.2. In addition, micro-breaking or spilling was mentioned as an other potential explanation for these deviations.

In the second part of the paper, the structure of airflow above waves in cases A and B was investigated by means of a conditional averaging method applied to the PIV velocity fields. The reason for performing this analysis was to study the influence of two different wave regimes on the airflow, and also to determine whether any form of flow separation takes place. Phase-averaged streamlines showed that a noticeable region of enclosed streamlines (cats eye) was present in case B. Here, the critical layer was distributed asymmetrically about the wave crest, implying asymmetric pressure distribution as described by [24]. An analysis of coherent vortices present in instantaneous airflow snapshots revealed that wave-shed (negative) vortices were more intense in case B as a result of higher air velocity and wave steepness.

The phase-averaged vorticity field in case B showed clear signs of shear-layer separation immediately downstream of the crest. The separated shear layer was found to follow the critical layer. The critical layer itself was dominated dominated by counter-rotating (positive) vortices. Above the average wave of case A, which is less steep than in case B, no signs of separation was found. Here, the negative vorticity layer stayed adjacent to the surface, as too did the critical layer. Thus, one may conclude that as shear-layer separation occurs in the saturation regime. This phenomenon should probably be taken into consideration in attempts to explain the observed transition to the saturated wave amplitude regime.

It was not within the scope of this study to quantify the effect of the above mentioned processes, as this was merely a qualitative study. However, this study has functioned as a foundation for an ongoing experimental campaign in which the aim is to quantify the effect of, amongst other processes, flow separation and micro-breaking.

Acknowledgements

The authors wish thank Prof. Karsten Trulsen for valuable discussions related to statistical and spectral analysis of waves. We also wish to acknowledge the SIU/CAPES joint program UTFORSK2016 (grant UTF.2016-CAPES-SIU/10012) as well as the Akademia program at the Faculty of Mathematics and Natural Sciences, University of Oslo.

References

1. Adrian, R., 2007. Hairpin vortex organization in wall turbulence. Phys. Fluids 19.
2. André, M.A., Bardet, P.M., 2017. Viscous stress distribution over a wavy gas–liquid interface. International Journal of Multiphase Flow 88, 1–10.
3. Andreussi, P., Persen, L., 1986. Stratified gas-liquid flow in downwardly inclined pipes. I. J. Multiphase flow 13, 565–575.
4. Andritsos, N., Hanratty, T., 1987. Influence of interfacial waves in stratified gas-liquid flows. AIChE Journal 33, 444–454.
5. Ayati, A., Carneiro, J., 2018. Statistical characterization of interfacial waves in turbulent stratified gas-liquid pipe flows. Int. Journal of Multiphase Flow (in press) .
6. Ayati, A., Kolaas, J., Jensen, A., Johnson, G., 2014. A PIV investigation of stratified gasliquid flow in a horizontal pipe. International Journal of Multiphase Flow 61, 129 – 143.
7. Ayati, A., Kolaas, J., Jensen, A., Johnson, G., 2015. Combined simultaneous two-phase PIV and interface elevation measurements in stratified gas/liquid pipe flow. International Journal of Multiphase Flow 74, 45 – 58.
8. Ayati, A., Kolaas, J., Jensen, A., Johnson, G., 2016. The effect of interfacial waves on the turbulence structure of stratified air/water pipe flow. International Journal of Multiphase Flow 78, 104 – 116.
9. Barmak, I., Gelfgat, A., Vitoshkin, H., Ullmann, A., Brauner, N., 2016. Stability of stratified two-phase flows in horizontal channels. Physics of Fluids 28, 044101.
10. Barnea, D., Taitel, Y., 1993. Kelvin-Helmholtz stability criteria for stratified flow: viscous versus non-viscous (inviscid) approaches. I. J. Multiphase Flow 19, 639–649.
11. Belcher, S., Hunt, J., 1993. Turbulent shear flow over slowly moving waves. Journal of Fluid Mechanics 251, 109–148.

12.Birvalski, M., Tummers, M., Delfos, R., Henkes, R., 2014. PIV measurements of waves and turbulence in stratified horizontal two-phase pipe flow. I.J. of Multiphase Flow 62, 161–173.
13.Birvalski, M., Tummers, M.J., Delfos, R., Henkes, R., 2015. Laminar-turbulent transition and wave-turbulence interaction in stratified horizontal two–phase pipe flow. Journal of Fluid Mechanics 780, 439–456.
14.Bontozoglou, V., Hanratty, T., 1990. Capillary-gravity Kelvin-Helmholtz waves close to resonance. Journal of Fluid Mechanics 217, 71–91.
15.Bowman, A.W., Azzalini, A., 1997. Applied smoothing techniques for data analysis: the kernel approach with S-Plus illustrations. volume 18. OUP Oxford.
16.Bratland, O., 2010. Pipe flow 2 multi-phase flow assurance. Chapt 18, 274–284.
17.Buckley, M.P., Veron, F., 2016. Structure of the airflow above surface waves. Journal of Physical Oceanography 46, 1377–1397.
18.Campbell, B.K., Liu, Y., 2014. Sub-harmonic resonant wave interactions in the presence of a linear interfacial instability. Physics of Fluids 26, 082107.
19.Campbell, B.K., Liu, Y., 2016. A nonlinear flow-transition criterion for the onset of slugging in horizontal channels and pipes. Physics of Fluids 28, 082103.
20.Chen, B., Saffman, P., 1979. Steady gravity–capillary waves on deep water–1. Weakly nonlinear waves. Studies in Applied Mathematics 60, 183–210.
21.Eeltink, D., Lemoine, A., Branger, H., Kimmoun, O., Kharif, C., Carter, J., Chabchoub, A., Brunetti, M., Kasparian, J., 2017. Spectral up-and downshifting of akhmediev breathers under wind forcing. Physics of Fluids 29, 107–103.
22.Gent, P., Taylor, P., 1977. A note on separationover short wind waves. Boundary-Layer Meteorology 11, 65–87.
23.Grare, L., Peirson, W.L., Branger, H., Walker, J.W., Giovanangeli, J.P., Makin, V., 2013. Growth and dissipation of wind-forced, deep-water waves. Journal of Fluid Mechanics 722, 5–50.
24.Hara, T., Sullivan, P.P., 2015. Wave boundary layer turbulence over surface waves in a strongly forced condition. Journal of Physical Oceanography 45, 868–883.
25.Haubrich, R.A., 1965. Earth noise, 5 to 500 millicycles per second: 1. spectral stationarity, normality, and nonlinearity. Journal of Geophysical Research 70, 1415–1427. Significant bicoherence threshold.
26.Hunt, J., Sajjadi, S., 2018. Mechanisms and modelling of wind driven waves. Procedia IUTAM .
27.Janssen, P.A.E.M., 1986. The period–doubling of gravity–capillary waves. Journal of Fluid Mechanics 172, 531–546.
28.Jeffreys, H., 1925. On the formation of water waves by wind, in: Proc. R. Soc. Lond. A, The Royal Society. pp. 189–206.
29.Jurman, L., Deutsch, S., McCready, M., 1992. Interfacial mode interactions in horizontal gasliquid flows. Journal of Fluid Mechanics 238, 187–219.
30.Kaffel, A., Riaz, A., 2015. Eigenspectra and mode coalescence of temporal instability in two-phase channel flow. Physics of Fluids 27, 042101.
31.Kharif, C., Giovanangeli, J.P., Touboul, J., Grare, L., Pelinovsky, E., 2008. Influence of wind on extreme wave events: experimental and numerical approaches. Journal of Fluid Mechanics 594, 209–247.
32.Lakehal, D., Fulgosi, M., Banerjee, S., Angelis., D., 2003. Direct nnumerical simulation of turbulence in a sheared air water flow with a deformable interface. J. Fluid Mech 482, 319–345.
33.Mata, C., Pereyra, E., Trallero, J., Joseph, D., 2002. Stability of stratified gas–liquid flows. International journal of multiphase flow 28, 1249–1268.
34.Miles, J., 1957. On the generation of surface waves by shear flows. I. J. of Multiphase flow 3, 185–204.
35.Onorato, M., Residori, S., Bortolozzo, U., Montina, A., Arecchi, F., 2013. Rogue waves and their generating mechanisms in different physical contexts. Physics Reports 528, 47 – 89.
36.Phillips, O., 1957. On the generation of waves by turbulent wind. J. Fluid Mech. 2, 417–445.
37.Pothof, I., Clemens, F., 2011. Experimental study of air–water flow in downward sloping pipes. International Journal of Multiphase Flow 37, 278 – 292.
38.Shoham, O., Taitel, Y., 1984. Stratified turbulent-turbulent gas-liquid flow in horizontal and inclined pipes. AIChE journal 30, 377–385.
39.Siddiqui, K., Loewen, M.R., 2010. Phase-averaged flow properties beneath microscale breaking waves. Boundary-Layer Meteorology 134, 499–523.
40.Taitel, Y., Dukler, A., 1976. A theoretical approach to the Lockhart–Martinelli correlation for stratified flow. I.J. Multiphase Flow 2, 591–595.
41.Trulsen, K., Dysthe, K.B., 1992. Action of wind stress and breaking on the evolution of a wave train, in: Breaking Waves. Springer, pp. 243–249.
42.Tzotzi, C., Andritsos, N., 2013. Interfacial shear stress in wavy stratified gas–liquid flow in horizontal pipes. I. J. Multiphase Flow 54, 43 – 54.
43.Ullmann, A., Brauner, N., 2006. Closure relations for two-fluid models for two-phase stratified smooth and stratified wavy flows. International journal of multiphase flow 32, 82–105.
44.Vollestad, P., Ayati, A.A., Angheluta, L., LaCasce, J.H., Jensen, A., 2018. Analysis of airflow above waves in pipes using conditionally averaged piv. Under review at Journal of Fluid. Mech. .
45.Yang, D., Shen, L., 2010. Direct-simulation-based study of turbulent flow over various waving boundaries. Journal of Fluid Mechanics 650, 131–180.

Available online at www.sciencedirect.com

ScienceDirect

Procedia IUTAM 26 (2018) 70–80

Procedia IUTAM

www.elsevier.com/locate/procedia

IUTAM Symposium Wind Waves, 4–8 September 2017, London, UK

What a Sudden Downpour Reveals About Wind Wave Generation

Luigi Cavaleri[a]*, Tom Baldock[b], Luciana Bertotti[a], Sabique Langodan[c], Mohammad Olfateh[b], Paolo Pezzutto[a]

a Institute of Marine Sciences-CNR, Venice, 30122, Italy
b School of Civil Engineering, University of Queensland, Brisbane, 4072, Australia
c King Abdullah University of Sciences and Technology, Thuwal, 23965-6900, Saudi Arabia

Abstract

We use our previous numerical and measuring experience and the evidence from a rather unique episode at sea to summarise our doubts on the present physical approach in wave modelling. The evidence strongly suggests that generation by wind and dissipation by white-capping have a different physics than presently considered. Most of all they should be viewed as part of a single physical process.

Peer-review under responsibility of the scientific committee of the IUTAM Symposium Wind Waves.

Keywords: air-sea interactions; wind wave generation; white-capping; surface processes; wave modelling

* Corresponding author. Tel.: +39-041-2407-955; fax: +39-041-2407-940.
E-mail address: luigi.cavaleri@ismar.cnr.it

2210-9838
Peer-review under responsibility of the scientific committee of the IUTAM Symposium Wind Waves.
10.1016/j.piutam.2018.03.007

1 – The present situation and the first puzzling questions

It is widely accepted that the present situation of wind wave modelling, especially for what practical results are concerned, is very good. It is enough to explore the statistics (of model results versus measured data) of the National Center for Environmental Prediction (NCEP, at http://polar.ncep.noaa.gov/waves/validation) and of the European Centre for Medium-Range Weather Forecasts (ECMWF, at http://www.ecmwf.int/en/forecasts/charts/obstat/?facets=Parameter,Wave%20Height) to be convinced that, at least in terms of overall statistics, it is difficult to expect further significant improvements. Little touches, sometime concerning physics, sometime numerical, are done here and there, but the related improvements are now of the order of a fraction of a percent. To be honest, accuracy drops in the case of the most extreme storms, especially typhoons and hurricanes, but still with very useful results.

Of course the high quality of the present situation is not due only to "perfect" wave modelling. A key factor, that was also the main reason of the past errors, is a drastic improvement of the driving wind fields. The present 9 km resolution of the global fully coupled (meteo-wave-ocean) ECMWF model provides accurate wind fields till a few days in advance, at least in the open oceans. In the inner seas, where coastline and orography play a relevant rôle, the accuracy drops (the wind speeds are often underestimated, see e.g. Cavaleri and Bertotti [1]), but this is a purely meteorological aspect independent of our present interest. In this paper, using some recent findings, we make a keen discussion on the present physics of the so-called advanced third generation wave models. The widely known and used, open source ones are the classical WAM, WaveWatch3 and SWAN. The respective master references are (WAM) Komen et al. [2] and Janssen [3], (WaveWatch3) Tolman [4] and http://polar.ncep.noaa.gov/waves/wavewatch.shtml, (SWAN) Booij et al. [5] and Ris et al. [6], plus various later refinements.

The backbone of these models is the spectral approach suggested by Pierson and Marks [7] that Miles [8] soon exploited providing a theory and the practical formula for the growth of the single spectral components under the action of wind. His theory was later improved by Janssen [9] to take into account the feed-back of waves on the surface wind field. A dissipation term for white-capping (henceforth w-c) was provided by Hasselmann [10], later modified to take into account the different breaking conditions for swell and wind sea (see the work of Bidlot et al. [11]). This overall approach was completed with the definition of the non-linear interactions, a conservative energy exchange among the various spectral components. See in this respect [12], [13] and [2]. Various other tweakings took place or were proposed, but, by and large and certainly so for the following discussion, this is a fair picture of the situation. A key point to remember is that, while wind input (henceforth w-i) and non-linear interactions are in principle theoretically well defined, w-c has more approximate and empirical expressions. Indeed w-c has always been, and still is, the tuning knob of the system.

So far so good. However, if we try to detach from our enthusiasm for the present results and consider the truth of a storm, we may be a bit puzzled. For whoever has been at sea during a raging storm, the idea that a furious, irregularly breaking surface can be decomposed into simple and neat one-dimensional sinusoidal waves over which the wind flows with a regularly oscillating pattern (Miles' process) sounds far fetched. Especially one of us (L.C.) has spent many months measuring stormy waves from an open sea oceanographic tower (see the description by Cavaleri [14]) witnessing the dynamical behaviour of the sea, the vortex shedding of wind behind a sharp or breaking crest, the non-linear mixing of crossing waves. Banner and Melville [15] showed more than forty years ago that most of the momentum from wind to waves happens behind (ahead of) a breaking crest.

Another direct experience at sea, especially from the comfortable position of an oceanographic tower, is to witness how w-c depends on wind. In a gusty wind field, where the local speed can change up to ±30 % within one minute or so, the white-caps adapt instantaneously to the situation, while the general spectrum has hardly any time for a substantial change.

The first theory for wave growth under the action of wind was due to Jeffreys ([16], [17]). He estimated the actual push by wind on the backside of a wave conceived as an obstacle. Jeffreys' consequent estimate fell short of the existing evidence, and it was then forgotten. However, recently Donelan et al. [18] started from this theory to frame a different wave model that, once tuned to reproduce an extended series of measured data in the North Sea and on the Norwegian coast, is reported to work pretty well.

To summarize the situation, we acknowledge we are presently quite successful in terms of results (we do run daily wave forecasts), but at the same time we feel a little uneasy in the general applauding community. We recall a sentence by George Bernard Shaw : "Science becomes dangerous when it imagines that it has reached its goal". In these conditions and wondering where to start from, one needs a good hint of the way to go. This substantial evidence was given by a particular episode on the cited oceanographic tower, episode that we describe in the next section.

Figure 1 – The ISMAR oceanographic tower, 15 km offshore the coast of the Venice lagoon, in the northern Adriatic Sea, East of Italy (see Figure 2). The upper structure has now been replaced by a new, two metre higher, one.

2 – The experience on the tower

In November 2014 a rather complete wind and wave measuring system (whose purpose is irrelevant for the present discussion) had been set up on the cited ISMAR oceanographic tower (see Figure 1). For atmosphere the considered parameters were wind speed and direction, temperature and rain. For the sea the system included a resistance wave gauge, two two-dimensional current metres, three pressure transducers at cross-angle, temperature. The experiment

and the instrumental setting required people on board. To our later dismay (and we will soon see why) the wave gauge did not work.

In November 12 we were measuring a classical mild bora storm. The general situation is shown in Figure 2. Wind from East was blowing at about 10 ms^{-1}, associated to an active generative sea of about 1.4 m significant wave height H_s. Weather was cloudy but dry. Perfect visibility till the horizon. As expected from the situation, frequent white-caps were distributed throughout the surface.

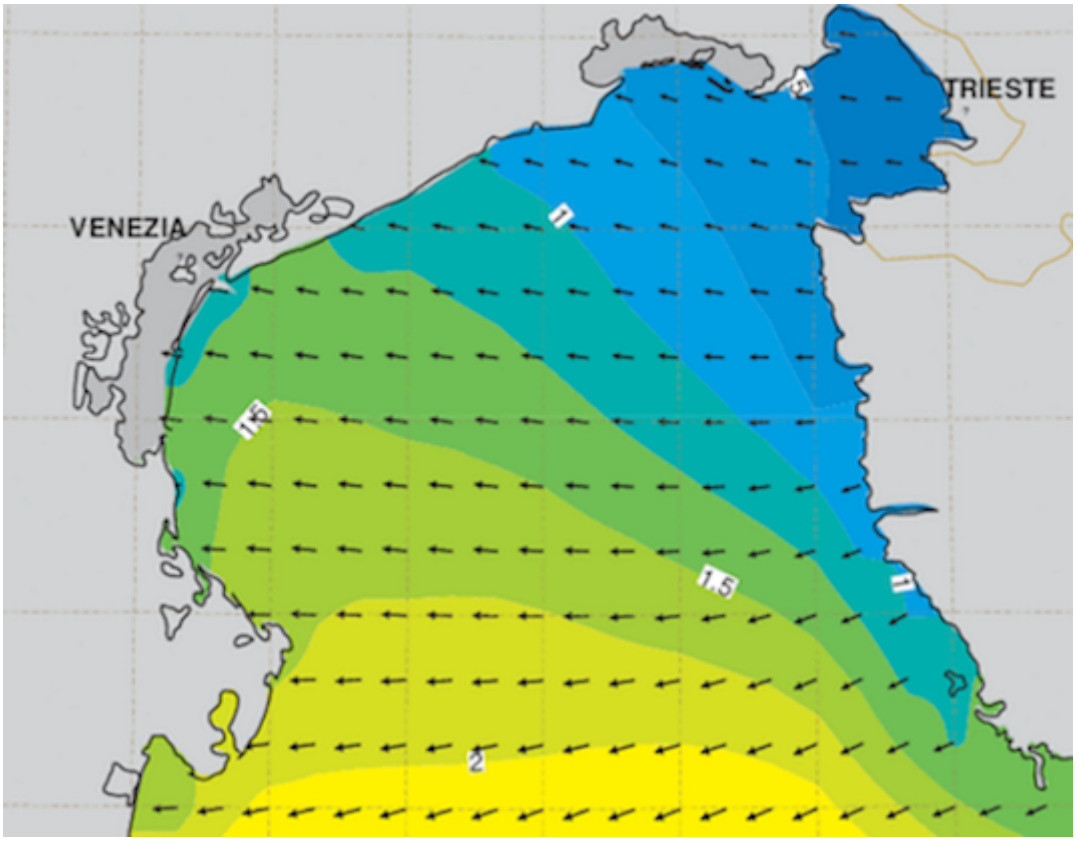

Figure 2 – Wave conditions in the northern Adriatic Sea, east of Italy. The dot shows the position of the ISMAR oceanographic tower (see Figure 1). Arrows, proportional to the local significant wave height, show the local mean wave direction.

All of a sudden there was a tremendous downpour that later we checked (rain gauge) close to 80 mmh^{-1}. For our present interests the relevant point is that at once the appearance of the surface changed completely. White-caps almost disappeared, the sea surface, granted the large drops splashing, was much smoother, waves appeared more relaxed as when during a gusty storm wind speed suddenly decreases. We have photo (see Cavaleri et al., 2015) and video documentation of the two situations (with and without rain). For the videos see

http://www.ismar.cnr.it/divulgazione/Video/video/waves_and_rain. Figure 3 shows the situation before (panel a) and during (panel b) the downpour (images extracted from the videos). In the two 20 second videos a quick counting indicates ~140 (before downpour) and ~20 (during it) white-caps. Figure 4 shows the wind speed (panel a) and pressure (panel b) records, the latter at 3.20 m depth. Wind was recorded at 10 Hz, waves at 25 Hz. The latter, unnecessarily high for a pressure transducer, was dictated by the resistance wave gauge out of which we meant to measure also the high frequency tail of the spectrum. This information would have been extremely important to quantify the surface differences between the two conditions (rain and no rain), but the wave gauge did not work properly.

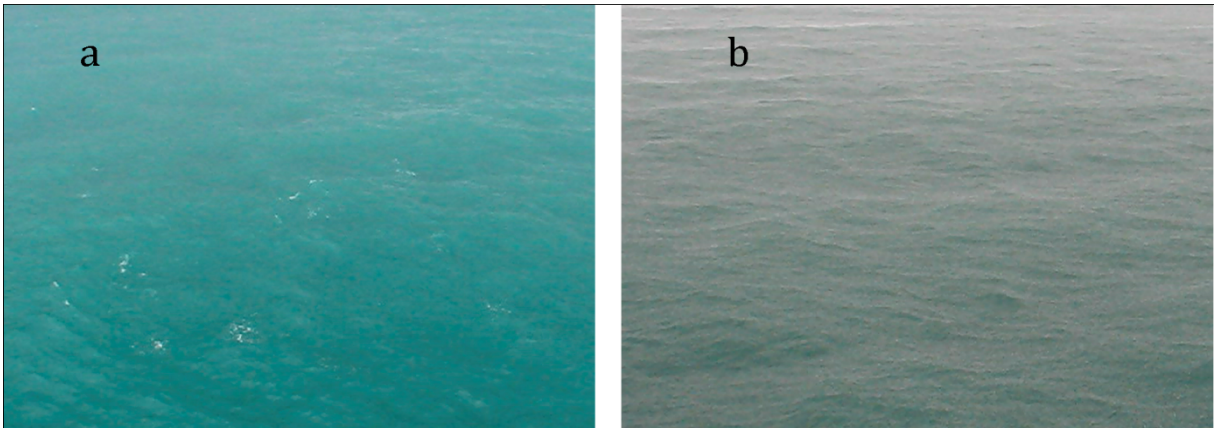

Figure 3 – The sea surface situation before (a) and during (b) the downpour. Note the smoother surface during the rain and the much reduced number of white-caps, strongly indicative of a reduced input by wind. See the videos at http://www.ismar.cnr.it/divulgazione/Video/video/waves_and_rain

One last detail concerning the rain. During the recording periods we were going in and out of the tower cabin. Until two minutes before the downpour there was no rain in the horizon. Soon after it stopped we checked again and there was no visible trace of any rain till the far horizon (as in Figure 3a). So the phenomenon was sudden and local, although we have no way to estimate its actual spatial extent.

This is the detailed account of the event, of the meteorological and wave conditions, and of the measured data we have. What to deduce from this is the subject of the next section.

3 – The implications

We start from the visual evidence about w-c. As soon as rain (very intense) started falling, white-caps virtually disappeared. Our documented estimate for them is close to about 10 % of their original number, but this order of approximation is irrelevant for our considerations.

A wind sea is a dynamical equilibrium expressed with the energy balance equation (see [2] and [19]). In practice an active wind keeps inputting energy (and momentum) into the wave field, most of which (energy and momentum) are counterbalanced by an intense w-c that characterizes an active generation (the lost energy and momentum go into turbulence and current). By and large (and again the exact figure is not relevant) only a net 10 % of the input goes into wave growth, w-c corresponding to about 90 % of the input by wind (see [2]). Should the input be active during the rain, this would have resulted in a rapid growth of wave height. A first hand estimate has been done considering the exchange of energy involved in a time limited growth (see again [2] and the very good book by Holthuijsen [19]).

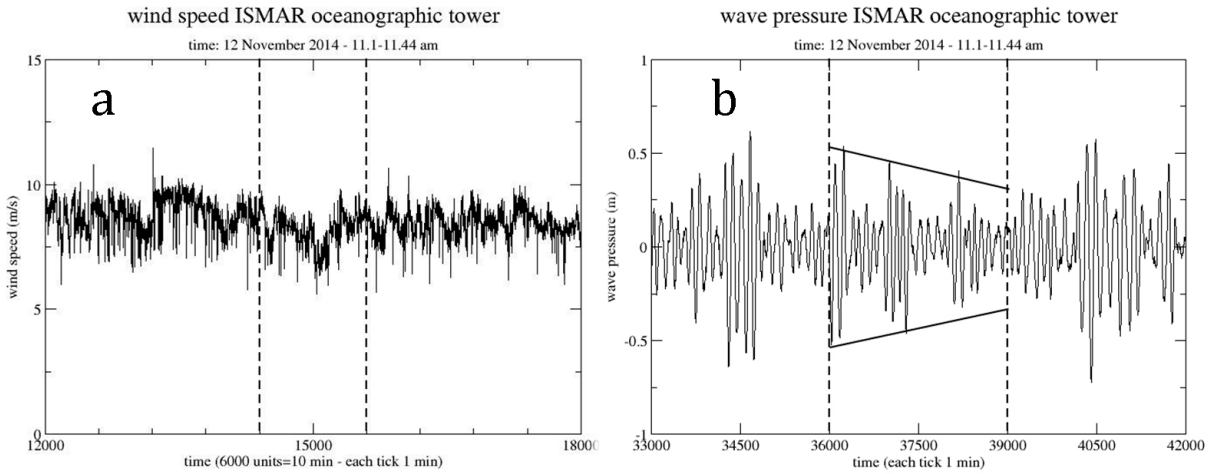

Figure 4 – a) Wind speed history before, during and after the downpour. Sampling at 10 Hz. b) Pressure record at 3.2. m depth. Sampling at 25 Hz. In both the panels the downpour is (approximately) limited by the two dashed vertical lines. Horizontal scales in sampling units. Note the decrease of the maximum wave height in each group during the rain period.

In both the panels the period of the downpour is limited (with some approximation) by the two dashed vertical lines. In panel 4b we have also traced two lines showing how during the downpour the maximum wave height in each group is decreasing, with both decreasing crests and rising troughs. Taking into account the cited approximation, the two lines could also be extended to the groups just before and after the marked interval. This decrease is confirmed by the progressive values of the significant wave height. In the original plan each record would last for more than half an hour. However, the rapidly changing conditions with and during the downpour forced us to estimate five minute spectra. Three sequential pressure spectra around the rain period are shown in Figure 5, the 11.36 being the one across the rain period. The spectra are substantially different, due to the changing conditions and to the large confidence limits (that we have purposely not drawn not to confound the essential information). The overall significant wave height history is in Figure 6. Note the drastic decrease during the downpour and the tendency to grow again when the rain is over. The records stop at minute 32 in the figure as planned in the original purpose of the experiment.

Starting from the conditions before the downpour (Hs~1.5 m, see Figure 6), using U_{10}~10 ms^{-1}, and excluding w-c, in the two minutes of the downpour energy would have grown of about 30 %, with H_s growing to more than 1.7 m. Tests with 8 ms^{-1} wind provide slightly smaller, but similar, figures. Because this did not happen, on the contrary H_s dropped substantially, we conclude that wind input was not active during the rain. Indeed (see Figure 3 and the cited videos) when rain started, the sea immediately "relaxed", crests were no longer sharp and so higher than troughs, as when in a storm wind suddenly ceases or drops to low values. However, in our case wind was actively blowing, but without apparent effect on the waves. The question is which are the possible explanations. Before proceeding further, we point out that this evidence is not supported by present modelling that, also ignoring the disappearance of the white-caps, would indicate a further growth of the wave field. See in this respect Figure 4 of Cavaleri et al. [20].

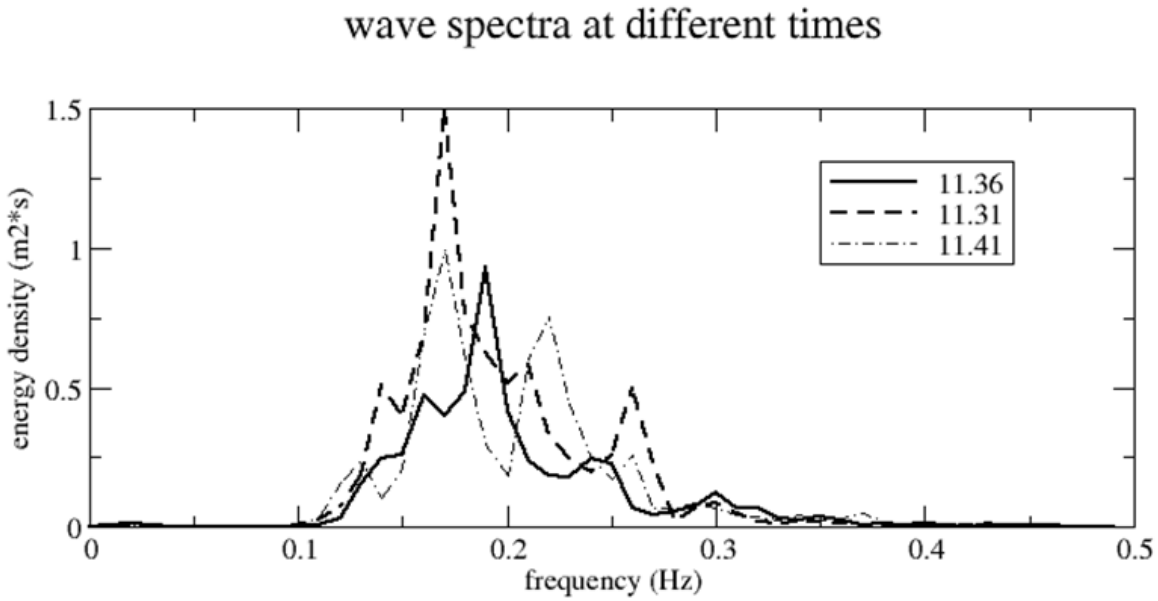

Figure 5 – Three five minute spectra taken across the downpour period. 11.36 marks the time of the shower. We have purposely not drawn the large confidence limits not to confound the essential information.

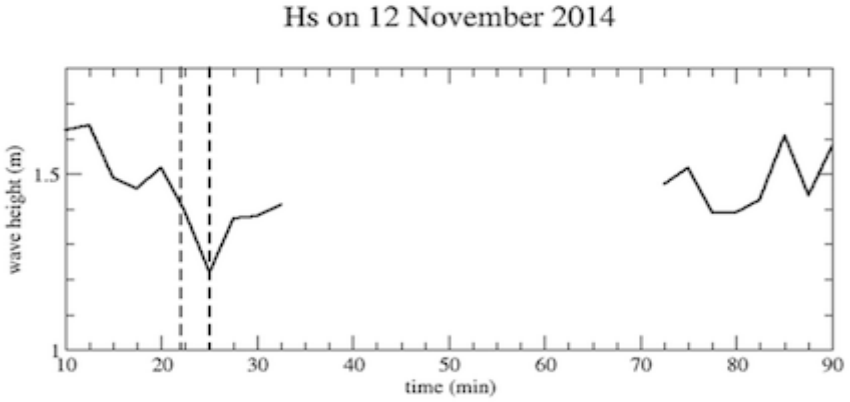

Figure 6 – Variation of the significant wave height across the downpour period, marked by the two dashed vertical lines. Note the substantial decrease during the rain.

Let us consider first the theoretical background of input by wind. Almost all the operational wave models (the exception is Donelan that we discuss later on) are based on the theory by Miles [8] complemented by Janssen [9] with the wave feed-back to the atmosphere. We argue on this basis. Within the wind speed logarithmic vertical profile of the surface boundary layer Miles focused his attention on the so-called "critical layer", i.e. the height at which the wind speed equals the phase one of the specific spectral wave component we are considering. The relevant information is the curvature of the profile at this height. The profile itself depends on, and is due to, the surface roughness. This depends mostly on the shortest waves (till the capillary level), i.e. on the tail of the spectrum. These are the ones cancelled by rain, so in these conditions the vertical profile changes substantially. In practice higher wind speeds are present till much closer to the surface. This changes completely the efficiency of the Miles-Janssen process so that in the downpour conditions hardly any energy was transferred from wind to sea. This is a possible interpretation according to this theory.

W-c is in itself an interesting story. For a long while the number of breakers on the sea was considered a function of only the wind speed. See in this respect the proceedings of the Galway conference edited by Monahan and Macv Niocaill [21]. At the same time the wave modeller community was looking for an expression of the energy lost by w-c, suitable for use in wave modelling. A first solution was provided by Hasselmann [10] as a function of only the wave spectrum, hence, explicitly at least, independent of wind. Improvements were then introduced, see in this respect [3], [22] and [23], and the extensive review by Babanin [24]. The present situation can be summarized saying that modelled energy loss by w-c is still fundamentally a function of the energy in the spectrum. Considered as the least known element of the energy balance equation, it is conveniently used as the tuning knob of the model system to get, on average, very good results. However, direct experience on the sea teaches otherwise. One of the classical storms in the Adriatic Sea (see Figures 1 and 2|) is "clear bora", i.e. clear sky, cold dry strong gusty wind from the East (mutatis mutandis as in Figure 2). The gustiness (see the approach by Abdalla and Cavaleri [25]) can be up to 30 %. Witnessing from the tower, it is immediate to see how, within the order of one minute or so, hence (following present theories) with little time for the wave spectrum to change, the amount of w-c increases drastically with increasing wind speed (and vice versa). In the episode under discussion the wind was more or less the same, and we had a mild reduction of the significant wave height. Direct inspection of the source functions suggest that, still according to present modelling, the spectral changes were not enough to justify the practical disappearance of w-c during the rain.

All this pushes towards a more integrated, although not yet clear, view of the w-i and w-c processes. Different possibilities exist. On one hand we could argue that w-c disappeared because w-i was strongly reduced. At the same time we could follow Banner and Melville [15] and derive that w-i disappeared because w-c was strongly reduced. In our opinion the most likely solution is that, contrarily to the present approach, the two processes are strongly connected and should be viewed as a single one, dependent both on the wave spectrum and the local wind.

If this is the case, which is the role of rain or, in other words, the spectral tail? A first obvious result seems to be that reduced energy in the tail, i.e. a smoother sea surface, implies less input by wind, hence less w-c. However, other opinions exist on the role of short waves destabilizing the single crests. The wind drag on a crest is likely to increase when short waves are present, possibly making the crest breaking more likely.

Where did the wave height decrease during the downpour come from? Direct inspection of mechanical attenuation of waves by rain (see the recent approach by Cavaleri and Bertotti [26]) excludes this as the main culprit. There was the obvious visual relaxation of the wave field that could suggest that certain aspects of the spectrum might change more rapidly than presently supposed. Longuet-Higgins [27] and more recently Cox et al. [28] pointed out the rôle of the non-linear interactions. What Cox [29] and Cox et al defined as a spectral hole, in practice no energy in the tail of the spectrum, could enhance the transfer towards this area, hence the continuous indirect dissipation, of energy from the bulk of the spectrum, leading also to a relatively rapid decrease of the most energetic part.

Obviously the situation is very confused and different possibilities for the right path and solution exist. A general framing of the situation and what to do next is the subject of the final section.

4 – The road ahead

As we pointed out at the beginning, the present results of the operational, or purposely run, wave models are generally good. Granted the necessary good quality of the driving wind fields, by and large the wave results are mostly satisfactory. This is possibly less the case when we go into the details of the results, e.g. of the two-dimensional wave spectrum, or we model extreme situations as typhoons and hurricanes. In all this apparently pleased environment, a keen analysis in specific situations, as when wind and waves are associated to a strong rain, casts some doubts on the present theoretical background. We should not forget a principle of logical deduction: to get correct results is a necessary, but not sufficient, condition to state our model is correct. On the contrary one single wrong result (granted all the other boundary conditions) may suggest that "something" is wrong. This is the case with rain, this was the case at the tower, and this is where we are. The results by Cavaleri et al. [20] and the evidence from the downpour at the tower strongly suggest something needs to be changed. The question is what, how and how much. We do not have the reply now. Definitely more and new research is required involving laboratory, numerical and field experiments.

As a general idea, our opinion is that a more comprehensive and realistic view of the processes at work is required. The almost idealistic view of decomposing a rough raging sea surface into linear one-dimensional sinusoids on which wind is smoothly acting is at odd with the evidence at sea. There must be truth in this approach; the results are too good to be ignored. At the same time the Jeffreys ([16], [17]) approach of wind pushing on the back of the waves, notwithstanding its underestimate of the resulting wave growth, appears too intuitive to be ignored. A possibility is that both the processes, Jeffreys and Miles, are at work, and that their effect should be estimated when acting on the single waves rather than on the sinusoidal spectral components. Indeed, concerning Jeffreys, starting from this theory for the input by wind and using alternative expressions for the other source functions, Donelan et al. [18] obtained good results, including hurricane Ike (2008). The fact that fully different approaches provide good results should make us wonder, especially when the key source function, the wind input, is based on completely different theories.

How do we proceed from here ? There are different levels of approach. The simplest one (but not really simple) is to adapt a theory, e.g. Miles-Janssen, to the new evidence. Here we refer to the smooth sea (when under rain), and the consequent reduction of the surface roughness and drastic change of the wind vertical profile. In the present operational set-ups, as the fully coupled system at ECMWF (see https://www.ecmwf.int/en/forecasts/documentation-and-support/changes-ecmwf-model/ifs-documentation), the apparent roughness felt by the atmosphere, i.e. the momentum transfer to the ocean, involves also the growth of the wave field. However, granted a change of the Charnock parameter and of the driving wind, this does not imply a drastic change of its vertical profile. This is why, contrarily to the measured evidence, in our 2015 numerical experiment waves kept growing also under the rain. Should this be the correct approach, the solution would involve the meteorologists for the need to model with high vertical resolution the wind profile according to wave conditions, something on the contrary done as a relatively simple post-processing starting from the lowest σ-level of the meteorological model, typically at 10 or 20 m height.

We have mentioned the possibility of estimating the w-i not on the single sinusoidal components, but the single real waves, i.e. the ones we see looking at a stormy sea. Without entering into the numerical implications for combining this with a spectral approach, we point out here a permanent substantial difference between a real sea and its spectral representation. A real sea is highly skewed, with higher and peaked crests and lower (closer to mean sea level) and rounded troughs. This is quite different from the up-down symmetrical representation we derive from the straightforward Fourier anti-transform of a spectrum. More sophisticated methods can be used to highlight the non-linearities. However, the basic point is that, while the recorded spectrum of a skewed wind sea shows the so-called ‘locked hyper-frequencies’ (the clearest evidence of skewness), these do not exist in the spectra of the third generation spectral models. Remaining in the real world of the affordable numerical approaches to wave modelling, it is our feeling that we will not succeed in representing the real generation, and also w-c, processes till when we will not devise a way to act on the sharp crests, also modelling w-i and w-c as a single process. How to do this must

be part of the research in the future. However, our first step should be how to verify and improve our recently accepted theories (and approaches) also for the cases where we know they do not work properly. Of course in the while we have to carry on with our present models and generally good results, better if aware of the possible approximations in certain conditions. At the same time and on a parallel course, we need to venture into these (partly) new ideas to build our future on a more solid ground.

Acknowledgements

The rain experience fell on a fertile, although doubtful, ground derived from our previous experience. While we take full responsibility of what we state and suggest, we acknowledge the long discussions with many of our colleagues of the wave and atmosphere modelling community. Luigi Cavaleri, Luciana Bertotti and Paolo Pezzutto have been partly supported by the EU contract 730030 call H2020-EO-2016 'CEASELESS'.

References

1 L. Cavaleri, L., L. Bertotti, 2004. Accuracy of modelled wind and wave fields in enclosed seas, Tellus, 56, 2, 167-175, DOI : 10.1111/j.1600-0870.2004.00042.x.

2 *G.J. Komen,* L. Cavaleri, M. Donelan, K. Hasselmann, S. *Hasselmann,* P.A.E.M. Janssen, 1994. Dynamics and modelling of ocean waves, Cambridge Universoty Press, 532pp,

3 P.A.E.M. Janssen, 2008. Progress in ocean wave forecasting, J. of Comp. Physics, 227, 3572-3594.

4 *H.* Tolm*an*, 2009. User manual and system documentation of WAVEWATCH III^{TM} version 3.14, NOAA-NCEP Technical Note, Contribution No. 276, 220pp.

5 N. Booij, R.C. Ris, L.H. Holthuijsen, 1999. A third-generation wave model for coastal regions : 1. Model description and validation, J. Geoph. Res., 104, C4, 7649-7666, DOI : 10.1029/98JC02622.

6 *R.C. Ris,* L.H. *Holthuijsen,* N. Booij, 1999. A third-generation wave model for coastal regions : 2. Verification, J. Geoph. Res., 104, C4, 7667-7681, DOI : 10.1029/1998JC900123.

7 *W.J. Pierson,* W. Marks, 1952. The power spectrum analysis of ocean-wave records, EOS, 33, 6, 834-844, DOI : 10.1029/TR033i006p00834.

8 *J.W. Miles,* 1957. On the generation of surface waves by shear flows, J. Fluid Mech., 4, 185-204.

9 P.A.E.M. Janssen, 1991. Quasi-linear theort of wind wave generation applied to wave forecasting, J. Phys. Oceanogr., 21, 1631-1642.

10 K. Hasselmann, 1974. On the spectral dissipation of ocean waves due to white capping, Bound.-Layer Meteor., 6, 1-2, 107-127, DOI : 10.1007/BF00232479.

11 J.-R. Bidlot, P. Janssen, S. Abdalla, 2007. A revised formulation of ocean wave dissipation and iys model impact, ECMWF Tech. Mem. 509, 29pp.

12 K. Hasselmann, 1962. On the non-linear energy transfer in a gravity wave spectrum, part 1 : general theory, J. Fluid Mech., 12, 481-500, https://doi.org/10.1017/S0022112062000373.

13 S. Hasselmann, K. Hasselmann, J.H. Allender, T.P. Barnett, 1985. Computations and parameterizations of the nonlinear energy transfer in a gravity wave spectrum, part 2 : Parameterizations of the nonlinear energy transfer for application in wave models, J. Phys. Oceanogr., 15, 1378-1391.

14 L. Cavaleri, 2000. The oceanographic tower Acqua Alta – Activity and prediction of sea states at Venice, Coastal Eng., 39, 1, 29-70, DOI: 10.1016/S0378-3839(99)00053-8

15 M.L. Banner, W.K. Melville, 1976. On the separation of air flow over water waves, J. Fluif Mech., 77, 4, 825-842, DOI : 10.1017/S0022112076002905.

16 H. Jeffreys, 1924. On the formation of water waves by wind, Proc. Royal Soc. of London, 107, No.742,189-206.

17 H. Jeffreys, 1925. On the formation of water waves by wind (Second paper), Proc. Royal Soc. of London, 110, No.754, 241-247.

18 M.A. Donelan, M. Curcic, S.S. Chen, A.K. Magnusson, 2012. Modeling waves and wind stress, J. Geoph. Res., 117, C11, C00J23, 26pp, DOI: 10.1029/2011JC007787.

19 L.H. Holthuijsen, 2007. Waves in oceanic and coastal waters, Cambridge University Press, 347pp.

20 L. Cavaleri, L. Bertotti, J.-R. Bidlot, 2015. Waving in the rain, J. Geoph. Res., 120, 5, 3248-3260, DOI: 10.1002/2014JC010348.

21 E.C. Monahan, G. Mac Niocaill (eds.), 1986. Oceanic whitecaps and their role in air-sea exchange processes, Proceedings of the 1983 Galway "Whitecap workshop", 234pp.

22 F. Ardhuin, E. Rogers, A. Babanin, J.-F. Filipot, R. Magne, A. Roland, A. van der Wtsyhuysen, P. Queffeulou, J.-M. Lefevre, F. Collard, 2010. Semiempirical dissipation source functions for ocean waves. Part I: Definition, calibration and validation, J. Phys. Oceanogr., 40, 1917-1941.

23 L. Romero, W.K. *Melville,* J.M. Kleiss, 2012. Spectral energy dissipation due to surface wave breaking, J. Phys. Oceanogr., 42, 1421-1444, DOI: 10.1175/JPO-D-11-072.1.

24 A. Babanin, 2011. Breaking and dissipation of ocean surface waves, Cambridge University Press, 480pp.

25 S.Abdalla, L. Cavaleri, 2002. Effect of wind variability and variable air density on wave modeling, J. Geoph. Res., 107, C7, 17.1-17.17, DOI : 10.1029/2000JC00639.

26 L. Cavaleri, L. Bertotti, 2017. The attenuation of swell waves by rain, Geoph. Res. Let., 44, 7pp, https:/doi.org/10.1002/2017GL075458.*27 M. Longuet-Higgins,* 1969. On wave breaking and the equilibrium spectrum of wind-generated waves, Proc. R. Soc. London, 310A, 151–159.

28 C.S. Cox, X. Zhang, T.F. Duda, 2017. Suppressing breakers with polar oil films : Using an epic rescue to model wave energy budgets, Geoph. Res., Lett., 44, 3, 1414-1421, DOI: 10.1002/2016GL071505

29 C.S. Cox, 2015. Suppression of breakers in stormy seas by an oil film, Int. J. Marit. Hist., 27, 528–536.

Available online at www.sciencedirect.com

ScienceDirect

Procedia IUTAM 26 (2018) 81–91

Procedia IUTAM

www.elsevier.com/locate/procedia

IUTAM Symposium Wind Waves, 4–8 September 2017, London, UK

Estimation of directional spectra from wave buoys for model validation

Richard M. Gorman

National Institute of Water and Atmospheric Research, Hamilton, 3216, New Zealand

Abstract

In this paper, we consider the problem of estimating a directional wave spectrum from 3-dimensional displacement data recorded by a wave buoy. We look at some of the limitations of existing methods to extend the "first five" directional moments directly obtainable from such data. With a view to providing the most detailed possible comparisons with directional spectra obtained from numerical models, we propose the use of a "diagnostic" directional spectrum, defined to be the closest possible spectrum to a given model spectrum that satisfies all measured directional moments. This method allows us to quantify the *minimum* error in a modelled directional spectrum consistent with a buoy record.

The new method is tested on a range of artificial test cases, and applied to data obtained from a wave buoy deployment off the New Zealand coast, in conjunction with outputs from a numerical spectral wave model simulation. It is shown that the method can provide satisfactory results in a wide range of conditions. Unlike existing approaches, the proposed method can accommodate sea states with more than two directional peaks, and can assist in removing spurious spectral energy arising from existing methods for estimating directional spectra from buoy data.

Peer-review under responsibility of the scientific committee of the IUTAM Symposium Wind Waves.

Keywords: wave buoy; directional wave spectrum; forecast verification

Email address: Richard.Gorman@niwa.co.nz

1. Introduction

Wave conditions in the ocean can be most thoroughly characterised by combining numerical modelling with measurements. *In situ* measurements from wave buoys are most commonly applied to model evaluation through comparison of derived wave statistics (e.g. significant wave height, mean wave direction, peak wave period). But a more thorough comparison of measurements with full directional spectra predicted by modern wave models could

2210-9838
Peer-review under responsibility of the scientific committee of the IUTAM Symposium Wind Waves.
10.1016/j.piutam.2018.03.008

offer greater diagnostic insight, allowing us, for example, to separately compare each component of a complex sea state.

Directional wave buoys work by making simultaneous measurements of a small number of signals, e.g. displacements in each of the 3 spatial dimensions. Fourier co- and cross-spectra between pairs of these signals can then be used to provide a limited estimate of the directional spectrum. That is, only the "first five" parameters moments of the directional distribution are obtained, which is insufficient for a full comparison with model spectra that typically have tens of directional degrees of freedom.

In the following section of this paper we review some existing approaches to the problem of extending beyond the measured "first five" moments to estimate a more complete directional wave spectrum from data. We then, in Section 3, propose a new method, which defines a "diagnostic" directional spectrum $S^{(d)}(f,\theta)$ for comparison with a given model directional spectrum $S^{(m)}(f,\theta)$, such that $S^{(d)}$ is the closest possible spectrum to $S^{(m)}$ that satisfies all measured directional moments. This method allows us to quantify the *minimum* error in a modelled directional spectrum consistent with a buoy record. The method is then applied firstly to some artificial test cases, then to directional data obtained from a wave buoy, in conjunction with outputs from a spectral wave forecast. A brief discussion of these results is then given in Section 4.

2. Fourier representation of sea state

Wave motions can be measured by a floating buoy, such as a Waverider™, that records accelerations in up to three dimensions, from which displacements can be computed by double integration of the signal.

First we consider a non-directional instrument that records only vertical motions. The vertical displacement Δz of the sea surface at a fixed position and time t can be represented as a sum of sinusoidal signals:

$$\Delta z(t) = \sum_{m=1}^{M} A_m \cos[-2\pi f_m t + \phi_m] \tag{1}$$

Here A_m is the amplitude, f_m the frequency, and φ_m the phase, of the m^{th} individual component.

Assuming random phases and summing the square of all amplitudes in a small range df of frequencies gives the wave frequency spectrum $S(f)$ of the wave signal:

$$\frac{1}{df}\sum_{f}^{f+df} \tfrac{1}{2}A_m^2 = S(f) \tag{2}$$

This can be computed as

$$S(f) = Z^* Z = |Z|^2 \tag{3}$$

from the Fourier transform

$$Z(f) = \int \Delta z(t) e^{-i2\pi f t} \mathrm{dt} \tag{4}$$

of the displacement signal.

Directional buoys can also measure horizontal displacements. Using the same sum of sinusoidal signals, these would be given as

$$\Delta x(t) = \sum_{m=1}^{M} A_m \cos\theta_m \sin[-2\pi f_m t + \phi_m] \tag{5}$$

and

$$\Delta y(t) = \sum_{m=1}^{M} A_m \sin\theta_m \sin[-2\pi f_m t + \phi_m] \tag{6}$$

which now include the propagation direction θ_m of each wave component.

Now we can sum the squares of all components within small ranges of both frequency and direction to obtain a directional spectrum

$$\frac{1}{df}\sum_{f}^{f+df}\frac{1}{d\theta}\sum_{\theta}^{\theta+d\theta}\frac{1}{2}A_m^2 = S(f,\theta) \tag{7}$$

We can attempt to estimate the directional spectrum using the Fourier transforms

$$X(f) = \int \Delta x(t) e^{-i2\pi f t}\mathrm{dt} \tag{8}$$

$$Y(f) = \int \Delta y(t) e^{-i2\pi f t}\mathrm{dt} \tag{9}$$

of the horizontal displacement as well as *Z(f)* defined above, but this is restricted to the six possible co- and cross-spectra, which define specific directional moments of $S(f,\theta)$, i.e. (in the deep water case):

$$G_{zz} = Z^*Z = C_{zz} = \int_0^{2\pi} S(f,\theta)\, d\theta = S(f) \tag{10}$$

$$G_{zx} = Z^*Y = iQ_{zx} = i\int_0^{2\pi} S(f,\theta)\cos\theta\, d\theta \tag{11}$$

$$G_{zy} = Z^*Y = iQ_{zy} = i\int_0^{2\pi} S(f,\theta)\sin\theta\, d\theta \tag{12}$$

$$G_{xx} = X^*X = C_{xx} = \int_0^{2\pi} S(f,\theta)\cos^2\theta d\theta \tag{13}$$

$$G_{yy} = Y^*Y = C_{yy} = \int_0^{2\pi} S(f,\theta)\sin^2\theta\, d\theta \tag{14}$$

$$G_{xy} = X^*Y = C_{xy} = \int_0^{2\pi} S(f,\theta)\cos\theta\sin\theta\, d\theta \tag{15}$$

We note that only five of these terms are independent, with $C_{xx} + C_{yy} = C_{zz}$.

Another way of looking at the limited directional information available is to consider the normalised directional distribution $D(f,\theta)$, defined by

$$S(f,\theta) \tag{16}$$

Any function of direction can be represented as a Fourier sum

$$D(f,\theta) = \frac{1}{2\pi}+\frac{1}{\pi}\sum_{n=1}^{\infty}[a_n(f)\cos n\theta + b_n(f)\sin n\theta] \tag{17}$$

Of these terms, the co- and cross-spectra above that are obtainable from three-component buoy data can provide only $S(f)$, $a_1(f)$, $b_1(f)$, $a_2(f)$ and $b_2(f)$ (the so-called "first five" moments) using relationships described by Longuet-

Higgins et al [1]:

$$a_1 = \frac{-Q_{zy}}{\sqrt{(C_{xx} + C_{yy})C_{zz}}} \tag{18}$$

$$b_1 = \frac{-Q_{zx}}{\sqrt{(C_{xx} + C_{yy})C_{zz}}} \tag{19}$$

$$a_2 = \frac{(C_{yy} - C_{xx})}{(C_{xx} + C_{yy})} \tag{20}$$

$$b_2 = \frac{-2C_{xy}}{(C_{xx} + C_{yy})} \tag{21}$$

No measure of the higher terms is, however, available. This means that any attempt to represent the full directional distribution from buoy data must, in effect, introduce some additional criteria to supply estimates of the value of the higher components.

2.1 Approaches to the "first five" problem

The simplest approach to this problem is to assume that all the higher terms are zero [1]. By only including the most slowly varying terms, this approach can only represent broad directional distributions, with one or two peaks. We can illustrate this by some test cases in which we assume a "true" directional distribution with multiple peaks built by a weighted sum of simple parametric forms [1, 2]:

$$D(\theta) = \sum_{m=1}^{M} w_m \left[cos(\theta - \theta_{0,m})/2\right]^{p_m} \tag{22}$$

In which the mth component, with mean direction $\theta_{0,m}$ and directional spreading parameter p_m, contributes to the sum with weight w_m. Then we compute the directional moments and the first five parameters using Equations 10-15 and 18-21 above, to give the estimated directional distribution that the "first five" approximation would give.

Figure 1 shows an example with a single peak with a directional spread of 30° (p = 30), typical of moderately-developed swell. We see that the "first five" approximation ("LH unweighted") overestimates the spread of this peak. It also produces an artificial peak at 180° from the true peak, and unphysical negative values in between.

Longuet-Higgins et al [1] addressed the problem of negative spectral densities by applying weights to the terms in the sum (Eqn 17). While this makes negative values impossible, it does not improve the ability to represent narrow spectra. Indeed, in the example shown in Figure 1, this method ("weighted LH") produces an even broader peak.

A second example (Figure 2) shows a case with three peaks in the input directional distribution, centred on 60°, 150° and 220°, with directional spreads of 15°, 30° and 10°, respectively. The unweighted "first five" approximation results in overly broad representations of two of these peaks, but the third being missed, while the weighted version shows very little ability to resolve any of the peaks.

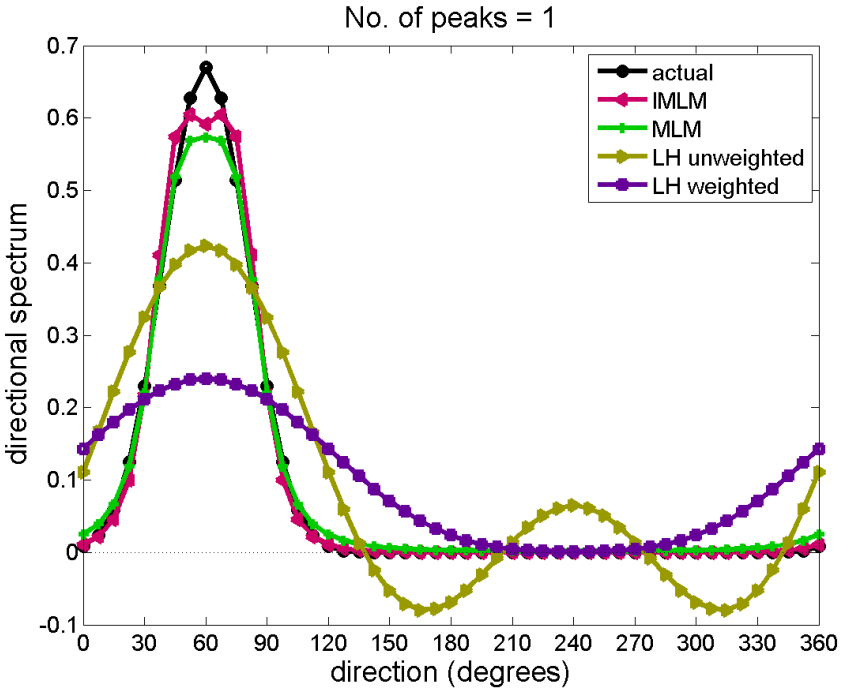

Figure 1 Comparison of a directional distribution of the form $D(\theta) = [\cos(\theta - \theta_0)/2]^p$, with peak direction $\theta_0 = 60°$ and spreading parameter $p = 30$ (black) with the distributions obtained by fitting these data by four methods: MLM [3, 4], IMLM [5], and the unweighted and weighted methods of Longuet-Higgins et al [1].

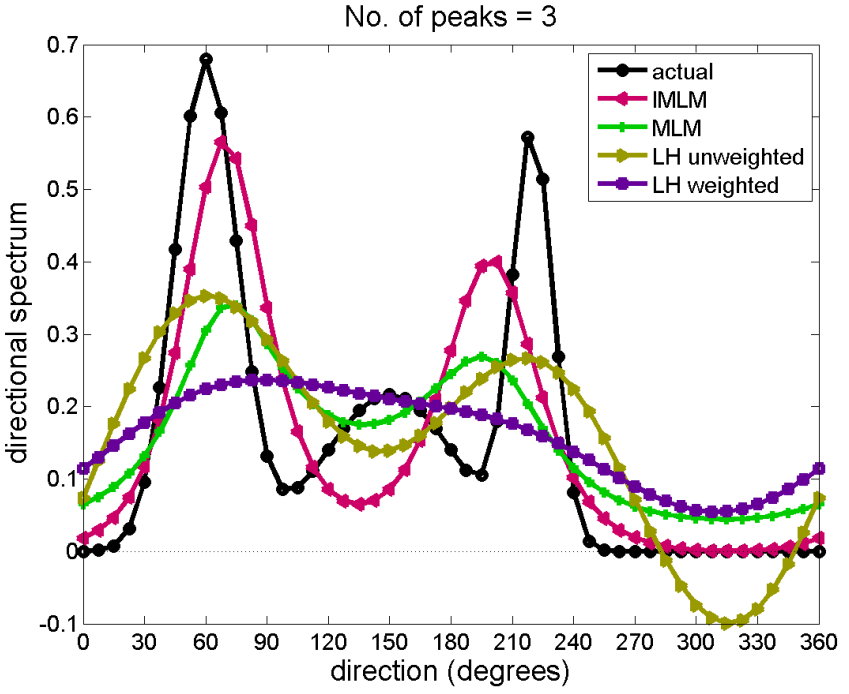

Figure 2 Comparison of a directional distribution combining a weighted sum of three distributions of the form $D(\theta) = [\cos(\theta - \theta_0)/2]^p$ (black) with the distributions obtained by fitting these data by four methods: MLM [3, 4], IMLM [5], and the unweighted and weighted methods of Longuet-Higgins et al [1].

For unimodal spectra, it is possible to provide a better representation by fitting a parametric form, as done by Mitsuyasu et al [2] with the form we used in Eqn (22) above. But clearly this is not suitable for mixed sea states.

Other approaches are based on some metric of statistical "quality" to determine a best fit. Such methods include the Maximum Likelihood Method (MLM) in original and extended versions [3, 4], the Iterated Maximum Likelihood Method (IMLM) [5], the Maximum Entropy Method (MEM) [6], and the Bayesian Method (BM) [7]. We do not present the details of all of those methods here, but note that many of these methods have been incorporated in software and tested, e.g. the DIWASP Matlab package [8], and described in reviews, e.g. by Benoit et al [9].

It is noted that some of these methods can be applied more generally, i.e. to data from other combinations of sensors (e.g. arrays of multiple wire sensors, pitch-roll buoys), supplying more than the three signals available from a Directional Waverider. In such cases, the number of terms fitted in Eqn 17 can be extended beyond the first five. While other methods may be more suited to other data sources, it is observed that the Iterated Maximum Likelihood Method is generally a good choice for directional wave buoy data, which is our main focus. Hence we will concentrate on the IMLM as a benchmark for currently-available methods, and not include any results from the MEM or BD methods in this paper. In particular, the IMLM is capable of reproducing narrower directional spreads than the unweighted and weighted methods of Longuet-Higgins et al [1]. We see this in the single-peak example shown in Figure 1, where both the MLM and IMLM show much better agreement than the LH methods.

Moving to the three-peak example of Figure 2, the (non-iterated) Maximum Likelihood Method shows an ability to resolve the main peaks that is similar to that of the unweighted LH method, while using the Iterated version brings about a closer match to the location and width of the two main peaks. But none of the methods have any ability to resolve the third peak.

3. Comparison of measured and modelled directional spectra

Numerical spectral wave models, such as WAM [10], Wavewatch III [11, 12] and SWAN [13, 14] are now widely used to forecast wave conditions, and in hindcast studies to characterise wave climate. These models all describe the evolution of the directional wave spectrum $S(f,\theta)$. There are limitations in the representation of physical processes and their numerical implementation within these models, and in the inputs forcing them. This makes it essential that simulations are calibrated and verified against available measurements, and records from wave buoys play an important role in this process.

As a first (and most commonly used) level of comparison, integrated statistics such as significant wave height, mean wave period and direction, and directional spread can be used, being quantities that can be readily derived in a consistent way from both model outputs and buoy records. At the next level, more detailed diagnostic information can be obtained by comparing spectra. This is also a robust procedure (in principle) when using the 1-dimensional spectrum $S(f)$, as well as the other "first five" terms which can be directly derived from buoy records, as detailed above.

Ideally, we would like to go to the next level of detail by directly comparing full directional spectra $S(f,\theta)$. from the model with the corresponding quantities from measurements. In, for example, a mixed sea state of multiple swell systems plus local wind sea, such a comparison might highlight that one particular swell component is being poorly represented, leading on to an investigation of errors in the wind fields at the place and time of its initial development.

If, however, we were make such a comparison using a directional spectrum derived from buoy records by one of the methods described above, we need to remember that these derived 2-d spectral estimates are not as robust as the 1-d spectra, otherwise we run the risk of confusing an inaccuracy in the estimated buoy spectrum with an error in the model spectrum.

Hence we seek a method of comparing directional spectra that will use the maximum amount of directional

information obtainable from a buoy record, but no more.

3.1 Method for constructing a diagnostic directional distribution from buoy records using model guidance

Suppose we have a model, using discrete directions $\theta_q,\ q = 1, \ldots Q$ which computes spectral density $S^{(m)}(\theta_q)$. We have dropped the frequency dependence from our notation for convenience, but it should be borne in mind that the following analysis applies at each frequency.

The buoy record gives us a set of five independent cross-spectral estimates $G_p^{(b)}$, for p = 1,...,5. These are just the same terms defined in equations 10-15, re-indexed for convenience.

The "true" spectrum at the same discrete directions that we would like to obtain for comparison with the model is constrained by these cross-spectral estimates, but is otherwise not fully determined by buoy data. Rather, the information available reduces the Q dimensional space of possible values of the discretised directional distribution to a Q-5 dimensional subspace. The buoy record cannot tell us where within this subspace the true directional distribution lies, but we can allow the model estimate to guide us.

We do this by seeking the "diagnostic" directional distribution $S^{(d)}(\theta_q)$ closest to the model's estimate that still satisfies those constraints provided by the buoy cross-spectra

Before we do that, we note that any model involves a degree of error and uncertainty, so we assume that we can attach estimates of the model error $\sigma^{(m)}(\theta_q)$ at some confidence level (say 95%). We can also take into account error estimates $\sigma_p^{(b)}$ for each cross-spectral estimate from the buoy records, at the corresponding confidence level. These are readily estimated alongside the spectral estimates using Welch's averaged periodogram method [15].

Now we can proceed to derive our best fit distribution. We do this by finding the "diagnostic" function $\hat{S}(\theta_q)$ that minimises a quality of fit parameter

$$\chi^2 = \sum_{q=1}^{Q} \Delta\theta \left[\left(\hat{S}(\theta_q) - S^{(m)}(\theta_q)\right)/\sigma^{(m)}(\theta_q)\right]^2 + \sum_{p=1}^{5}\left[(G_p(\hat{S}) - G_p^{(b)})/\sigma^{(b)}(\theta_q)\right]^2 \quad (23)$$

We also have a constraint $\hat{S}(\theta_q) \geq 0$, which makes this a bounded value least squares problem, which can be solved using the algorithm (and Fortran implementation) of Parker and Stark [16].

3.2 Application to parametric test cases

To test this method, we return to the test cases described above, where we assumed the "true" spectrum is a sum of simple parametric distributions (Eqn 22). We also suppose that our "model" produces a similar spectrum, of the same form, with the same number of peaks, but with different central directions, spreading parameters and weightings, to represent the actual errors in the "model". These parameters are listed in Table 1.

For the directional discretisation, Q = 48 bins have been used. We have assumed that all the measured moments have an error $\sigma^{(b)}$ of 2% of their value, while the model errors $\sigma^{(m)}$ are assumed to be of 30%. Note that only the relative value of measurement and model errors plays a role in this method. Here we have deliberately given much higher weighting to the buoy records than to the model.

Table 1. Parameters for the assumed input and "model" directional distributions, as defined in Eqn 22, used in the test cases.

	peak direction	directional spread	weight
	θ_0	$\Delta\theta$ (°)	w
M = 1 test			
input peak 1	60°	20°	0.6
model peak 1	70°	25°	0.55
M = 3 test			
input peak 1	60°	15°	0.45
model peak 1	70°	20°	0.40
input peak 2	150°	30°	0.30
model peak 2	140°	35°	0.35
input peak 3	220°	10°	0.25
model peak 3	230°	15°	0.25

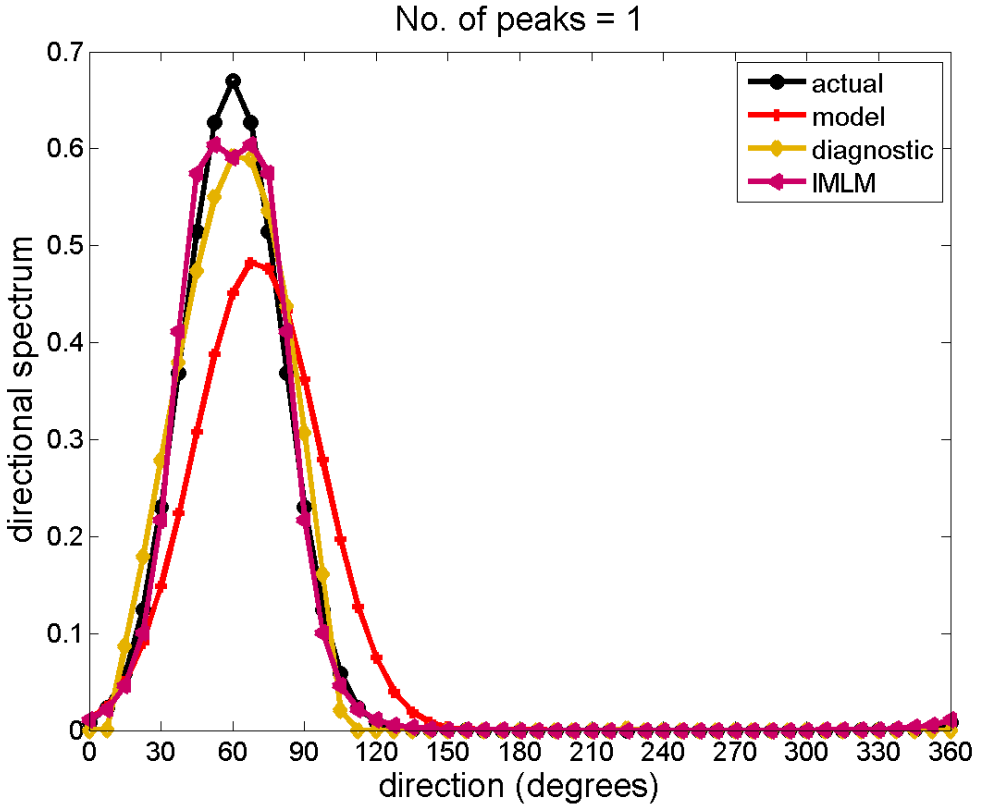

Figure 3 Comparison of a directional distribution of the form $D(\theta) = [\cos(\theta - \theta_0)/2]^p$, with peak direction $\theta_0 = 60°$ and spreading parameter $p = 30$ (black) with the IMLM [5] fit to these data (magenta), a second, independent single-peak "model" distribution (red), and the "diagnostic" distribution obtained by the method described in the present paper (yellow).

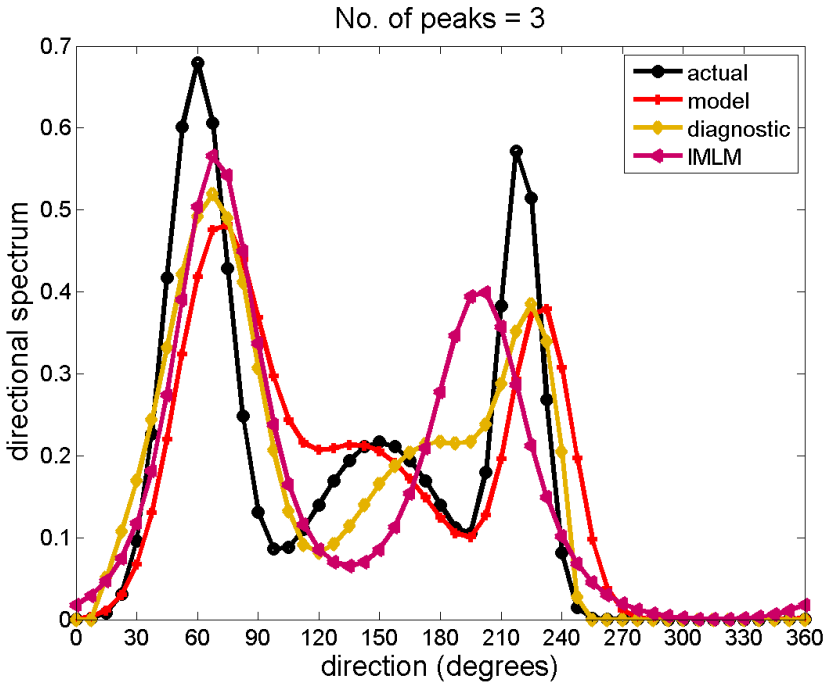

Figure 4 Comparison of a directional distribution combining a weighted sum of three distributions of the form $D(\theta) = [\cos(\theta - \theta_0)/2]^p$ (black) with the IMLM [5] fit to these data (magenta), a second, independent three-peaked "model" distribution (red), and the "diagnostic" distribution obtained by the method described in the present paper (yellow).

The results for the single peak case are shown in Figure 3. This shows a case where we have presupposed that the "model" (red line) has a 10° error in locating the single peak direction, has slightly overestimated the directional spread, and underestimated the total energy.

The "diagnostic" distribution (yellow line) arising from this method gives a very similar result to the IMLM (magenta), relative to which it is only pulled slightly towards the assume "model" distribution.

In the case of the three-peak example (Figure 4), the "diagnostic" distribution is again quite similar to the IMLM result in the vicinity of the largest peak. For the secondary peak, for which we have assumed the model to have captured the width reasonably well, with a moderate offset in peak direction, the "diagnostic" result is more strongly influenced by the "model" distribution. We have also assumed that our "model" does not resolve the third peak very clearly. Consequently, the "diagnostic" solution also struggles to resolve it, but it is encouraging that it shows evidence of its presence at all, something that existing methods are incapable of doing. Further tests not included here indicate that similar results also extend to 4 and 5 peaked distributions.

3.3 Application to Directional Waverider records

We turn now to an application to field measurements, supported by model simulations. The data we consider comes from a Directional Waverider buoy deployed in approximately 76 m water depth off Banks Peninsula, on the east coast of New Zealand's South Island. Figure 5(a) shows the directional wave spectrum computed for 129 discrete frequencies at 0.005 Hz increments from a 30 minute burst sample ending at 21:00 UT on 25/11/2016. The directional distribution over 72 equally spaced directions was estimated using the Iterated Maximum Likelihood Method.

The most prominent feature of the spectrum is a peak at around 0.13 Hz from the NNE (Cartesian direction ~240°), developed from shore parallel winds over much of the previous 24 hours. The local wind at the measurement time had swung to the NW: with a shorter fetch this results in the secondary peak (or possibly a double peak) at higher

frequency. In addition, a SSE swell (0.1 Hz, ~120°) can also be detected, which is typical for this site which has a SE-SW exposure to Southern Ocean sources. We also note small amounts of energy displaced by ~180° in direction from each of the peaks described above.

For comparison, model outputs are available from a wave forecast operated by the National Institute of Water and Atmospheric Research (NIWA). This employed Wavewatch version 3.14 [17] on a New Zealand grid spanning longitudes from 163.21°E to 181.67°E at 15°/512 resolution, and latitudes from 48.54°S to 30.84°S at 10°/512 resolution. This was successively nested in global and regional domains at 15°/64×10°/64 and 15°/128×10°/128 resolutions, respectively. In the spectral domain, 25 frequency bins and 24 directional bins. Atmospheric forcing was provided by the New Zealand Convective Scale Model implementation of the UK MetOffice Unified Model [18].

Figure 5(c) shows the directional spectrum from the model forecast at the nearest grid cell and output time. The forecast spectrum reproduces the general location of the 3 principal sea state components identified in the IMLM estimate from the buoy record (Figure 5(a)). There are differences in the relative contribution of these components, with the forecast giving relatively more weight to the higher-frequency NW wind sea than to the NE component, and being less able to resolve details in the frequency structure. On the other hand, the forecast predicts negligible energy levels where the IMLM estimate gave contributions displaced by 180° from the main peaks.

Figure 5(b) shows the result of applying the procedure described in Section 3.1 above, to produce a merged directional spectrum. The resulting “merged” spectrum retains the directionally-integrated frequency structure from the measured spectrum, hence the relative weighting of the main spectral peaks is not influenced by the model output, only the directional distribution at each frequency. As for the forecast spectrum, the merged spectrum does not show energy at 180° displacement from the main peaks. This illustrates that such components are not a necessary consequence of the “first-5” moments, which are preserved by the merging procedure, but may be a spurious result of the IMLM estimate.

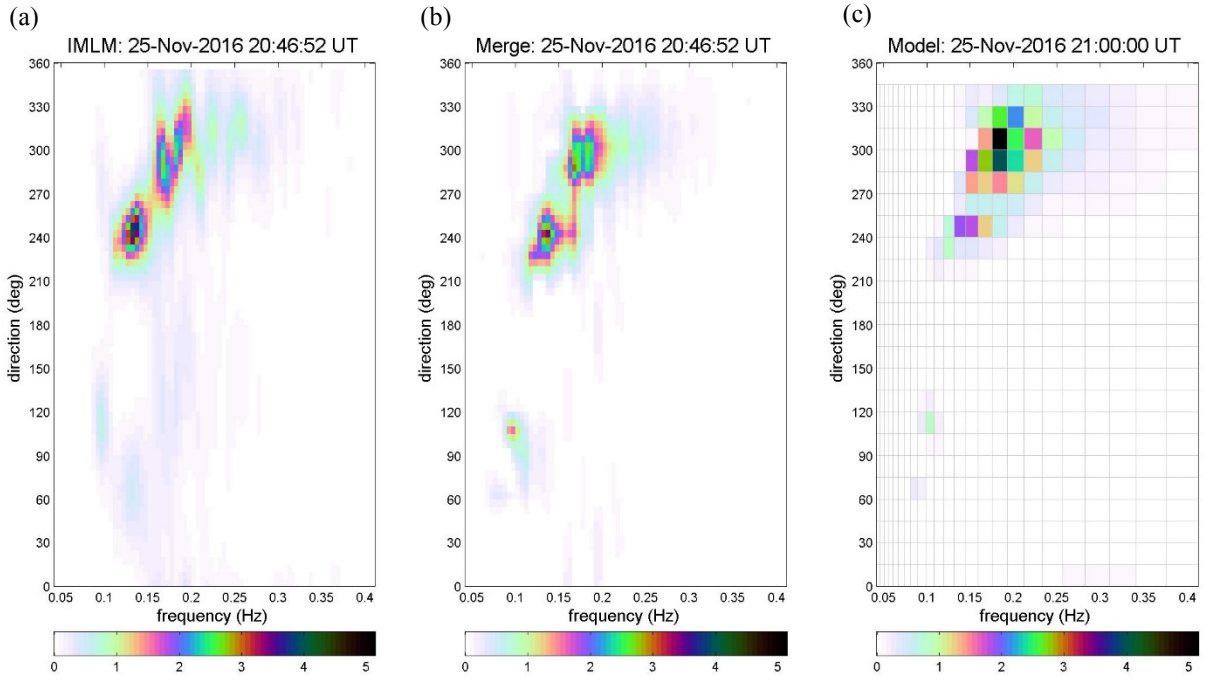

Figure 5 Estimates of the directional wave spectrum from Waverider measurements and a Wavewatch simulation at (42°25´S, 173°20´E), off the east coast of New Zealand’s South Island, at approximately 21:00 UT on 25 November 2016. (a) from

Waverider measurements, using the Iterated Maximum Likelihood Method; (b) derived from a combination of Waverider measurements and model outputs, using the method outlined in this paper; (c) from the Wavewatch simulation. The horizontal axes show wave frequency, while the vertical axes show Cartesian wave direction (i.e. direction towards which waves propagate, in degrees anticlockwise from True East). Colour scales show the estimated spectral density.

4. Discussion

We have presented some initial tests of a method for analysing directional data from wave buoys in a way that can maximise the information that such data can provide for comparisons with directional wave spectra predicted by numerical models. In doing so, we present the concept of a "diagnostic" spectrum, defined as the smallest perturbation of the model spectrum that is fully consistent with the buoy observations.

The point of doing so is not to say that this "diagnostic" spectrum is necessarily a close approximation to the true spectrum, but to use it to identify robust *minimum* values for the errors in the modelled spectrum. This offers potential advantages over comparisons with directional spectra estimated by existing methods, all of which may introduce their own artefacts, especially in mixed sea states of more than two components, for which they inevitably fail.

References

1. Longuet-Higgins, M.S., D.E. Cartwright, and N.D. Smith, *Observations of the directional spectrum of sea waves using the motions of a floating buoy*, in *Ocean wave spectra*. 1963, Englewood Cliffs: New York. p. 111-136.
2. Mitsuyasu, H., et al., *Observations of the directional spectrum of ocean waves using a cloverleaf buoy.* Journal of Physical Oceanography, 1975. **5**: p. 750-760.
3. Isobe, M., K. Kondo, and K. Horikawa. *Extension of MLM for estimating directional wave spectrum*. in *Proc. Symp. on Description and Modeling of Directional Seas*. 1984.
4. Krogstad, H.E., R.L. Gordon, and M.C. Miller, *High-resolution directional wave spectra from horizontally mounted acoustic Doppler current meters.* Journal of Atmospheric and Oceanic Technology, 1988. **5**(2): p. 340-352.
5. Oltman-Shay, J. and R.T. Guza, *A data-adaptive ocean wave directional-spectrum estimator for pitch and roll type measurements.* Journal of Physical Oceanography, 1984. **14**(11): p. 1800-1810.
6. Lygre, A. and H.E. Krogstad, *Maximum entropy estimation of the directional distribution in ocean wave spectra.* Journal of Physical Oceanography, 1986. **16**(12): p. 2052-2060.
7. Hashimoto, N. and K. Kobune. *Estimation of directional spectrum from a Bayesian approach*. in *21st ICCE* 1988. ASCE.
8. Johnson, D., *DIWASP, a directional wave spectra toolbox for MATLAB: User Manual*. 2001, Centre for Water Research, University of Western Australia.
9. Benoît, M., P. Frigaard, and H.A. Schäffer. *Analysing multidirectional wave spectra: a tentative classification of available methods*. in *Proc. IAHR-Seminar: Multidirectional Waves and their Interaction with Structures*. 1997. San Francisco: Canadian Government Publishing.
10. Hasselmann, S., et al., *The WAM Model - a third generation ocean wave prediction model.* Journal of Physical Oceanography, 1988. **18**(12): p. 1775-1810.
11. Tolman, H.L., *A third-generation model for wind waves on slowly varying, unsteady, and inhomogeneous depths and currents.* Journal of Physical Oceanography, 1991. **21**: p. 782-797.
12. Tolman, H.L., *User manual and system documentation of WAVEWATCH-III version 4.18*. 2014, NOAA / NWS / NCEP / OMB. p. 282.
13. Booij, N., R.C. Ris, and L.H. Holthuijsen, *A third-generation wave model for coastal regions 1. Model description and validation.* Journal of Geophysical Research, 1999. **104**(C4): p. 7649-7666.
14. Ris, R.C., L.H. Holthuijsen, and N. Booij, *A third-generation wave model for coastal regions 2. Verification.* Journal of Geophysical Research, 1999. **104**(C4): p. 7667-7681.
15. Oppenheim, A.V. and R.W. Schafer, *Digital Signal Processing*. 1975: Prentice-Hall.
16. Stark, P.B. and R.L. Parker, *Bounded Variable Least Squares: An Algorithm and Applications.* Computational Statistics, 1995. **10**(2).
17. Tolman, H.L., *User manual and system documentation of WAVEWATCH-III version 3.14*. 2009, NOAA / NWS / NCEP / OMB. p. 194.
18. Yang, Y., et al., *Model moist bias in the middle and upper troposphere during DEEPWAVE.* Atmospheric Science Letters, 2017. **18**(4): p. 161-167.

Available online at www.sciencedirect.com

ScienceDirect

Procedia IUTAM 26 (2018) 92–101

Procedia IUTAM

www.elsevier.com/locate/procedia

IUTAM Symposium Wind Waves, 4-8 September 2017, London, UK

Generation of Wave Groups

Roger Grimshaw[a]

[a]*Department of Mathematics, University College London, London, WC1E 6BT, UK*

Abstract

The well-known linear stability theory of wind-wave generation is revisited with a focus on the generation of wave groups. As well as recovering the usual temporal instability, the analysis has the outcome that the wave group must move with a real-valued group velocity. This has the consequence that both the wave frequency and the wavenumber should be complex-valued. In the frame of reference moving with the group velocity, the growth rate is enhanced above that for just a temporally growing monochromatic sinusoidal wave. The analysis is extended to the weakly nonlinear regime where a nonlinear Schrödinger equation with a linear growth term is discussed.

Peer-review under responsibility of the scientific committee of the IUTAM Symposium Wind Waves.

Keywords: Wave group, group velocity, wind wave generation;

1. Introduction

Various mechanisms have been proposed to describe the generation of waves by wind. But despite decades of theoretical research, observations and more recently, detailed numerical simulations, the nature of these mechanisms and their practical applicability remains controversial, see the recent assessments by [12], [16] and [14], and the comprehensive reviews by [1] and [7].

Two main mechanisms have been developed. One is a classical shear flow instability mechanism developed by [10] and subsequently adapted for routine use in wave forecasting models, see the review by [7]. In this theory, turbulence in the wind is used only to determine a logarithmic profile for the mean wind shear $u_0(z)$. Then, a sinusoidal wave field is assumed, with a real-valued wavenumber k and a complex-valued phase speed, $c = c_r + ic_i$ so that the waves may have a growth rate kc_i. In the limit $c_i/u_* \to 0$ where u_* is the wind friction velocity, there is significant transfer of energy from the wind to the waves at the critical level z_c where $u_0(z_c) = c_r$. Pertinent to the context of this paper, we note that that this was extended to allow for spatial growth instead of temporal growth by [18].

* Corresponding author.
E-mail address: r.grimshaw@ucl.ac.uk

2210-9838
Peer-review under responsibility of the scientific committee of the IUTAM Symposium Wind Waves.
10.1016/j.piutam.2018.03.009

The other is a steady-state theory, developed originally by [8] for separated flow over large amplitude waves, and later adapted for non-separated flow over low-amplitude waves, see the reviews by [1] and most recently by [16]. Here the wind turbulence is taken into account through an eddy viscosity term in an inner region near the wave surface. Asymmetry in this inner region then allows for an energy flux to the waves.

Neither theory alone has been found completely satisfactory, and in particular, both fail to take account of wave transience and the tendency of waves to develop into wave groups. This is the issue we propose to address in this article. The strategy we employ is again based on linear shear flow instability theory, but to incorporate at the outset that the waves will have a wave group structure with both temporal and spatial dependence. In fluid flows this was initiated by [4, 5], see the summary by [3] and the reviews by [6, 15]. The essential feature that we exploit is that the wave group moves with a real-valued group velocity $c_g = d\omega/dk$ even when for unstable flows the frequency $\omega = kc$ and the wavenumber k may be complex-valued.

2. Formulation

It is useful to begin with a linear stability theory for a general stratified shear flow, and then develop the theory for the air-water system as a special case. The basic state is the density profile $\rho_0(z)$ and the horizontal shear flow $u_0(z)$. Then the linearized equations are

$$\rho_0(Du + wu_{0z}) + p_x = 0\,, \tag{1}$$

$$\rho_0 Dw + p_z + g\rho = 0\,, \tag{2}$$

$$D\rho + \rho_{0z} w = 0\,, \tag{3}$$

$$u_x + w_z = 0\,. \tag{4}$$

$$\text{where} \quad D = \frac{\partial}{\partial t} + u_0 \frac{\partial}{\partial x}\,. \tag{5}$$

Here, the terms (u, w) are the perturbation velocity components in the (x, z) directions, ρ is the perturbation density, and p is the perturbation pressure. Equations (1 -4) represent conservation of horizontal and vertical momentum, conservation of mass, and incompressibility respectively in this linearised setting. It is useful to introduce the vertical particle displacement ζ defined in this linearised formulation by

$$D\zeta = w\,. \tag{6}$$

Then the density field is given by integrating equation (3) to get

$$\rho = -\rho_{0z}\zeta\,. \tag{7}$$

Substituting (6, 7) into the remaining equations (1, 2, 4) yields

$$\rho_0 D\tilde{u} + p_x = 0\,, \tag{8}$$

$$\rho_0 D^2\zeta + p_z - g\rho_{0z}\zeta = 0\,, \tag{9}$$

$$\tilde{u}_x + D\zeta_z = 0\,,\,, \tag{10}$$

$$\text{where} \quad \tilde{u} = u + u_{0z}\zeta\,.$$

Finally eliminating $\tilde{u}$, p yields a single equation for ζ,

$$\{\rho_0 D^2\zeta_z\}_z + \{\rho_0 D^2\zeta\}_{xx} - g\rho_{0z}\zeta_{xx} = 0\,. \tag{11}$$

This equation, together with the boundary conditions that $\zeta = 0$ at $z = -H$ (the bottom of the ocean) and as $z \to \infty$ (the top of the atmosphere) is the basic equation to be studied here.

Next we seek a solution describing a wave group,

$$\zeta = \{A(X,T)\phi(z) + \phi^{(2)}(X,T,z) + \cdots\} \exp(-ik(x - ct)) + \text{c.c.}\,, \quad \text{where} \quad X = \epsilon x\,,\ T = \epsilon t\,. \tag{12}$$

Here c.c. denotes the complex conjugate, and $\epsilon \ll 1$ is a small parameter describing the slow variation of the amplitude $A(X,T)$ relative to the carrier wave. The frequency $\omega = kc$, the phase speed c and the wavenumber k may be complex-valued, and then the imaginary part of the frequency Im[kc] is the temporal growth rate of an unstable wave. At leading order we obtain the modal equation, well-known as the Taylor-Goldstein equation,

$$(\rho_0 W^2 \phi_z)_z - (g\rho_{0z} + k^2 W^2)\phi = 0\,, \quad W = c - u_0\,. \tag{13}$$

This defines the modal functions and the dispersion relation specifying $\omega = \omega(k)$ where $\omega = kc$ is the frequency. At the next order in ϵ we obtain the equations determining the wave envelope, and these will be presented later. It is useful to note the integral identity

$$P(c,k) \equiv \int_{-H}^{\infty} \rho_0 W^2(|\phi_z|^2 + k^2|\phi|^2) + g\rho_{0z}|\phi^2|\, dz = 0\,. \tag{14}$$

This can be regarded as defining the dispersion relation, expressed here as $c = c(k)$ instead of the more usual $\omega = \omega(k) = kc(k)$. The group velocity can now be defined as

$$c_g = \frac{d\omega}{dk} = c + k\frac{dc}{dk}\,. \tag{15}$$

Differentiation of (14) with respect to k yields

$$k\frac{dc}{dk} = \frac{J}{I}\,, \quad J = -\int_{-H}^{\infty} \rho_0 k^2 W^2 |\phi|^2\, dz\,, \quad I = \int_{-H}^{\infty} \rho_0 W(|\phi_z|^2 + k^2|\phi|^2)\, dz\,. \tag{16}$$

This enables us to obtain a useful expression for the group velocity.

2.1. Air-water system

For an air-water system, we first write

$$\rho_0(z) = \rho_a H(z) + \rho_w H(-z)\,, \quad \rho_{0z} = (\rho_a - \rho_w)\delta(z)\,. \tag{17}$$

Here ρ_a, ρ_w are the constant air and water density respectively, the undisturbed air-water interface is at $z = 0$, $H(z)$ is the Heaviside function and $\delta(z)$ is the Dirac delta function. Further we suppose that $u_0(z)$ is continuous for all z. The water is bounded below at $z = -H$, and the air is unbounded above. Continuity of ζ at the interface $z = 0$ implies that ϕ is continuous across $z = 0$. Since the modal equation (13) is homogeneous, without loss of generality we can set $\phi(z = 0) = 1$. Then in the air ($z > 0$ and water ($z < 0$) the modal equation (13) collapses to the Rayleigh equation

$$(W^2\phi_z)_z - k^2 W^2 \phi = 0\,. \tag{18}$$

The dynamical boundary condition at $z = 0$ is found by integrating (13) across $z = 0$, with the outcome

$$[\rho_0 W^2 \phi_z]_-^+ = g(\rho_a - \rho_w)\phi(0)\,. \tag{19}$$

The system (18, 19) is supplemented by the boundary conditions that $\phi = 0$ at $z = -H$ and that $\phi \to 0$ as $z \to \infty$, where we assume that in $z > 0$ the background shear flow (wind) is such that $u_{0z}/W \to 0, z \to \infty$. This completes the formulation of the eigenvalue problem for the determination of $c(k)$.

Next suppose that in the water, there is no background current, so that $u_0(z) = 0$, $-H \le z \le 0$, and in particular $u_0(0) = 0$. Then in the water

$$\phi = \frac{\sinh\,(k(z+H))}{\sinh\,(kH)}\,, \tag{20}$$

noting that $\phi(0) = 1$. The boundary condition (19) then reduces to

$$s\phi_z(+0) = \{k\coth\,(kH) - (1-s)\frac{g}{c^2}\}\,, \quad s = \frac{\rho_a}{\rho_w}\,. \tag{21}$$

If there is no air ($s = 0$), then this reduces to the usual water wave dispersion relation Note that $s \ll 1$ which we will exploit as the analysis develops.

$$c^2 = c_0^2 = \frac{g}{k}\tanh(kH)\,. \tag{22}$$

It is then convenient to rewrite (21) in the form

$$s\phi_z(0+) = g\{\frac{1}{c_0^2} - (1-s)\frac{1}{c^2}\}\,. \tag{23}$$

Without loss of generality, we assume that $\mathrm{Re}[c_0] > 0$. In deep water $kH \to \infty$, $c_0^2 \to g/|k|$. In general, this finite depth formulation has the same form as the deep water limit, and only c_0 is changed.

2.2. Growth rate

Noting that the growth rate is zero when $s = 0$, we put $\mathrm{Im}[kc] = s\gamma$. It is then useful to write

$$\phi_z(0+) = \frac{g\sigma}{c_0^2}\,, \quad (1-s)\frac{1}{c^2} = \frac{1}{c_0^2}(1 - s\sigma)\,, \tag{24}$$

In the limit $s \to 0$, $c_0 > 0$ is real-valued and then

$$\mathrm{Im}[\phi_z(0+)] \approx \frac{g\mathrm{Im}(\sigma)}{c_0^2}\,, \quad \mathrm{Im}[\sigma] \approx \frac{2\gamma}{|k|c_0}\,, \tag{25}$$

The task now is to solve the modal equation (18) in $z > 0$ with the boundary conditions (24) at $z = 0$ and $\phi \to 0$ as $z \to \infty$. When $c_i \neq 0$, the modal equation is regular and has just one solution. However, in the limit $s \to 0$, $W = u_0 - c \to u_0 - c_0$ is real-valued, and the modal equation (18) is singular at a critical level z_c where $u_0(z_c) = c_0$. We assume henceforth that the wind shear profile is monotonically increasing from a zero value at $z = 0$, so that $u_{0z} > 0$ for $z \geq 0$. We further assume that u_{0z} decreases with height. Then there can be only one critical level. In this limit, the modal equation has real-valued coefficients. But (25) shows that we are seeking complex-valued solutions, so that then there are two linearly independent solutions ϕ, ϕ^* (* indicates the complex conjugate), whose Wronskian

$$\mathcal{W} = -iW^2(\phi_z\phi^* - \phi\phi_z^*)\,, \tag{26}$$

is a constant in any region where the solutions are regular. Evaluating the Wronskian at $z = 0$ yields

$$\mathcal{W} = 2c_0^2\mathrm{Im}[\phi_z(0+)] = 2g\mathrm{Im}[\sigma] = \frac{4g\gamma}{|k|c_0}\,, \quad \text{as} \quad s \to 0\,. \tag{27}$$

Essentially, in this limit the instability arises from a coalescence of two modes. If there is no critical level where $u_0(z_c) = c_0$, then evaluating the solutions as $z \to \infty$ yields $\mathcal{W} = 0$ and there is no instability. Hence, there must be a critical level, and we assume as above that there is only one. Using Frobenius expansions near the critical level, it can be shown that the Wronskian has a jump discontinuity there, and that

$$\mathcal{W}(z = z_c-) = -2\pi|K|^2 u_{0zz}(z_c)|u_{0z}(z_c)|\,, \tag{28}$$

$$\text{where as} \quad z \to z_c\,, \quad \phi \sim K\{\frac{1}{z - z_c} + \frac{u_{0zz}(z_c)}{u_{0z}(z_c)}\log(z - z_c) + \cdots\}\,. \tag{29}$$

Here the branch of the logarithm when $z - z_c < 0$ must be chosen corresponding to the requirement that the growth rate $\gamma > 0$, that is

$$\log(z - z_c) = \log|z - z_c| - i\pi\mathrm{sign}[u_{0z}(z_c)]\,, \quad \text{when} \quad z < z_c\,.$$

Hence, combining (24, 27, 28) yields

$$\gamma = -\frac{kc_0\pi|K|^2 u_{0zz}(z_c)|u_{0z}(z_c)|}{2g}\,. \tag{30}$$

$$\text{so that} \quad \Gamma = \frac{\gamma}{kc_0} = -\frac{\pi|K|^2 u_{0zz}(z_c)|u_{0z}(z_c)|}{2g}\,, \tag{31}$$

is the non-dimensional growth rate. The expression (30) can also be obtained directly from the dispersion relation (14) taking the limit $s \to 0$ and using the Frobenius expansion (29). In the deep water limit $kH \to \infty$ these agree with the corresponding expressions of [10] and many other authors. Instability occurs only when $u_{0zz}(z_c) < 0$.

The remaining task is to determine the constant K, which has the dimensions of a length. It is obtained by solving the modal equation (18) with the boundary condition (24) and matching this with the Frobenius expansion (29). This either requires a specification of the wind profile $u_0(z)$ which allows for an exact solution to be obtained, see [13] for instance, or an asymptotic analysis as performed by [10, 11] and [7] amongst several others using the well-known logarithmic profile, see [10, 11] and [7],

$$u_0(z) = \frac{u_*}{\kappa}\log(1+\frac{z}{z_*})\,, \quad z_* = \frac{\alpha_C u_*^2}{g}\,. \tag{32}$$

Here u_* is the friction velocity, z_* is a roughness length scale, $\kappa = 0.4$ is von Karman's constant, and $\alpha_C \approx 0.01$ is the Charnock parameter. However, the specific value of K is not our main concern here, and we proceed on the basis that it has been determined. A slight variation of the well-known asymptotic determinations of K are described in the Appendix.

3. Wave groups

To find the equation determining the evolution of the amplitude A we return to the expression (12). After substitution into (11) we find that the $O(\epsilon)$ term yields the equation

$$(\rho_0 W^2\phi_z^{(2)})_z - (g\rho_{0z} + k^2W^2)\phi^{(2)} = -\frac{2iF^{(1)}}{k}\,, \tag{33}$$

$$F^{(1)} = \{\rho_0 W\phi_z \mathcal{D}A\}_z + \rho_0 k^2\phi(-W\mathcal{D}A + W^2A_X) - g\rho_{0z}\phi A_X\,, \tag{34}$$

$$\text{and} \quad \mathcal{D}A = A_T + u_0 A_X\,. \tag{35}$$

The left-hand side is just the modal equation operator, and it is readily shown that the forced modal equation (18) has a solution if and only if a certain compatibility condition is satisfied. This is the requirement that $F^{(1)}$ be orthogonal to the complex conjugate of the modal function ϕ,

$$\int_{-H}^{\infty} F^{(1)}\phi^*\,dz = 0\,. \tag{36}$$

Substituting the expression (34) into (36) leads to the desired equation for the amplitude A,

$$A_T + c_g A_X = 0\,, \quad \text{where} \quad c_g = c + k\frac{dc}{dk}\,, \tag{37}$$

where we have used the dispersion relation (14) and the expressions (15, 16).

For stable waves when ω, k are real-valued, c_g is also real-valued and this is the well-known result that the wave group moves with the group velocity. The result obtained here that it also holds for unstable waves when ω, k may be complex-valued is not so well-known. Importantly, causality considerations now demand that nevertheless the group velocity must be real-valued, see the reviews by [6] and [15] for instance. For unstable waves when the frequency ω is complex-valued this leads to the necessity that the wavenumber k also be complex-valued. In the limit as $kc_i \to 0$, we can let $k = k_r + ik_i, |k_i| \ll |k_r|$, and then determine k_i so that c_g is real-valued, that is $\mathrm{Re}[c_{gk}(k_r)]k_i \approx -\mathrm{Im}[c_g(k_r)]$.

The outcome is that, to leading order, the wave group amplitude A propagates with a real-valued group velocity, c_{g0} evaluated at $k = k_r$, with a localised shape determined by the initial conditions.

It is natural here to assume that c_i, k_i are $O(\epsilon)$, and we can write $k_i = \epsilon\delta, kc_i = \epsilon\gamma$. Then we see from the phase expression in (12) that the amplitude is multiplied by the exponential factor

$$E = \exp\left(-\delta(X - c_0T) + \gamma T\right) = \exp\left(-\delta(X - c_{g0}T) + \Sigma T\right), \tag{38}$$

$$\text{where} \quad \Sigma = \gamma + \delta(c_0 - c_{g0}). \tag{39}$$

Thus Σ is the growth rate in the frame of reference moving with the group velocity. We then put

$$\xi = X - c_{g0}T, \quad B(\xi, T) = EA, \quad \text{so that} \quad B_T - \Sigma B = 0. \tag{40}$$

Note then the expression (12) for a wave packet becomes, at leading order,

$$\zeta = \{B(X,T)\phi(z) + \cdots\}\exp(i\Theta) + \text{c.c.}, \qquad \text{where} \quad \Theta = k_r(x - c_r t), \tag{41}$$

for the real-valued phase Θ. Although $\gamma > 0$, Σ could be positive or negative, and correspondingly the instability is absolute or convective in the wave packet reference frame. Note that since $c_0 > c_{g0}$ for water waves, the instability is always absolute if $\delta > 0$ and then the exponential factor E spatially enhances the waves in the rear of the packet.

For the present air-water system, the expressions (16) can be reduced using the density profile (17) and the solution (20) for the modal functions in the water. The small parameter ϵ is now chosen so that $\epsilon = s$ for an optimal balance. Then we get that

$$c = c_0 + sc_1 + \cdots, \quad c_g = c_{g0} + sc_{g1} + \cdots, \tag{42}$$

$$c_{g1} = c_1 - k\frac{dc_0}{dk}\frac{I_1}{I_0} + \frac{J_1}{I_0} + \cdots, \quad I_0 = \frac{g}{c_0}, \tag{43}$$

$$J_1 = -\int_0^\infty k^2 W_0^2 |\phi|^2\, dz, \quad I_1 = \int_0^\infty W_0(|\phi_z|^2 + k^2|\phi|^2)\, dz, \tag{44}$$

Here c_{g0}, is the group velocity for water waves alone, that is $c_{g0} = c_0 + kc_0/dk$, and is real-valued for all real-valued wavenumbers k. In the limit $s \to 0$, at leading order the amplitude propagates with the real-valued group velocity c_{g0} without change of form. At the next order c_{g1} is complex-valued when the wavenumber k is real-valued, with contributions coming from both c_1 where $k_r\text{Im}[c_1] = \gamma$, and I_1, while J_1 is real-valued. We can estimate the imaginary part of I_1 from (43) and the Frobenius expansion (29), expanded here to

$$\phi_z = K\{-\frac{u_{0z}^2(z_c)}{W_0^2} + \frac{k^2}{2} + \cdots\}, \tag{45}$$

Then, using (30) we find that

$$\text{Im}[c_{g1}] = \frac{\gamma}{k} - \frac{\pi|K|^2 c_0}{2g}\{\frac{3u_{0zz}^2(z_c)}{|u_{0z}(z_c)|} - \text{sign}[u_{0z}(z_c)]u_{0zzz}(z_c)\}kc_{0k}, \tag{46}$$

and recalling that then $\text{Re}[c_{gk}(k_r)]\delta \approx -\text{Im}[c_{g1}(k_r)]$, from (39) we get that

$$\Sigma = \gamma\{1 + \frac{c_{0k}}{c_{g0k}} + [\frac{3u_{0zz}(z_c)}{u_{0z}(z_c)^2} - \frac{u_{0zzz}(z_c)}{u_{0zz}(z_c)u_{0z}(z_c)}]\frac{kc_{0k}^2}{c_{g0k}}\}. \tag{47}$$

For water waves, $c_{0k} < 0, c_{g0k} < 0$, and $u_{0zz}(z_c) < 0$ for an instability. Hence, if also $u_{0z}(z_c)u_{0zzz}(z_c) < 3u_{0zz}^2(z_c)^2$, then $\Sigma > 0$ and there is an absolute instability. This is only a necessary condition, but as the first three terms in Σ are positive, it seems very likely that $\Sigma > 0$ for all typical wind profiles. For the well-known logarithmic profile (32),

$$u_0(z) = \frac{u_*}{\kappa}\log(1 + \frac{z}{z_*}), \quad [\frac{3u_{0zz}(z_c)}{u_{0z}(z_c)^2} - \frac{u_{0zzz}(z_c)}{u_{0zz}(z_c)u_{0z}(z_c)}] = -\frac{\kappa}{u_*} < 0, \tag{48}$$

and so $\Sigma > 0$. In the deep water limit, the growth rate Σ is enhanced over the temporal growth rate γ by a factor $3 + (\kappa c_0/u^*)$. The latter term indicates that the amplification enhancement is larger for old wave groups than for young wave groups.

4. Nonlinear Schrödinger equation

This analysis is within the framework of the linearized equations, but we conjecture that a weakly nonlinear asymptotic analysis would lead to a nonlinear Schrödinger equation of the form

$$i(B_T - \Sigma B) - \lambda B_{\xi\xi} - \nu|B|^2 B = 0\,. \tag{49}$$

Here $\lambda = -c_{g0k}/2$ and ν is the well-known Stokes amplitude-dependent frequency correction for water waves. In deep water water $\lambda = c_0/8k$ and $\nu = c_0k^3/2$. Formally, the derivation of (49) requires a re-scaling in which $T = \epsilon^2 t, \xi = \epsilon(x - c_{g0}t)$, the amplitude B is scaled with ϵ and we now put $s = \epsilon^2$. Since $s \approx 1.275 \times 10^{-3}$ this scaling implies that this model is restricted to waves with amplitudes of non-dimensional order 0.035. A nonlinear Schrödinger equation similar to (49) has been discussed by [9], [19], [12], [2] and [17] amongst others, but with the essential difference that they use the temporal growth rate γ instead of the spatial growth rate Σ expressed as here in the frame moving with the group velocity.

However, the nonlinear and dispersive terms in (49) are not sufficient to control the exponential growth of a localised wave packet, since

$$\frac{d}{dT}\int_{-\infty}^{\infty} |B|^2\, d\xi = 2\Sigma \int_{-\infty}^{\infty} |B|^2\, d\xi\,. \tag{50}$$

Further the modulational instability, present when $\nu\lambda > 0$ (as for deep water waves) in the absence of wind, is enhanced in the presence of wind, see [9]. To see this, first transform (49) into

$$B = \tilde{B}\exp(\Sigma T)\,, \quad \tau = \frac{\exp(2\Sigma T) - 1}{2\Sigma}\,, \quad i\tilde{B}_\tau - \lambda F \tilde{B}_{\xi\xi} - \nu|\tilde{B}|^2\tilde{B} = 0\,, \quad \text{where} \quad F = \frac{1}{1 + 2\Sigma\tau}\,. \tag{51}$$

This has the "plane wave" solution $\tilde{B} = B_0 \exp(-i\nu|B_0|^2\tau)$. Modulation instability is then found by putting $\tilde{B} = B_0(1 + b)\exp(-i\nu|B_0|^2\tau)$ into (51) and linearizing in b, so that

$$ib_\tau - \lambda F b_{\xi\xi} - \nu|B_0|^2(b + b^*) = 0\,. \tag{52}$$

Then we seek solutions of the form $b = (p(\tau) + iq(\tau))\cos(K\xi)$ where p, q are real-valued, and find that,

$$\{\frac{p_\tau}{F}\}_\tau + K^2\lambda(K^2\lambda F - 2\nu|B_0|^2)p = 0\,, \quad q = -\frac{p_\tau}{\lambda K^2 F}\,. \tag{53}$$

When $\Sigma = 0, F = 1$, and this yields the usual criterion for modulation instability, namely that $\lambda K^2(\lambda K^2 - \nu|B_0|^2) < 0$. When $\Sigma > 0$, F varies from 1 to 0 as τ increases from 0 to ∞. Then, as $T \to \infty, \tau \to \infty$ there is modulational instability provided only that $\lambda\nu > 0$, and so independent of $K, |B_0|$. The general solution of (53) can be expressed in terms of modified Bessel functions of imaginary order, $I_{in}(LF^{-1/2})$, where $n = \pm\lambda K^2/\Sigma$ and $L = |B_0|K(2\nu\lambda)^{1/2}/\Sigma$, see [9]. Note that as $\tau \to \infty$, $p \sim \tau^{-1/2}\exp(L(2\Sigma\tau)^{1/2})$. Even taking account of the cancellation of the factor $\tau^{-1/2}$ with the pre-factor $\exp(\Sigma T)$ in (51), we see that the growth rate is now super-exponential.

5. Summary and discussion

We have revisited the linear stability theory of wind-wave generation, initiated by [10] and subsequently developed by Miles and many others, see for instance [11, 7]. These theories were for a sinusoidal monochromatic wave, both in an inviscid context for laminar flow and in a context where wind turbulence is represented by an eddy viscosity term. In the former case the well-known logarithmic profile (32) is often invoked as a suitable model for the wind profile, although the theory can be developed for any wind profile for which the wind speed increases monotonically with height so that there is a single critical level.

In this work we have extended this approach to wave groups, using a well-known multi-scale asymptotic expansion to represent the group structure, where the amplitude $A(X, T)$ in the representation of the solution of the linearised stability problem depends on the slow variables $X = \epsilon x, T = \epsilon t$, see (12). At the leading order, discussed in section 2, we recover the familiar theory for the temporal growth of the amplitude of a sinusoidal monochromatic wave, and the main outcome is the temporal growth rate γ, expressed by (30, 31), in agreement with the expressions obtained

by [10] and many others. Crucially in obtaining these expressions, we exploit the approximation $s = \rho_a/\rho_w \ll 1$ by formally taking the limit $s \to 0$.

The main new material is in section 3 where we show that at the next order in the asymptotic expansion the equation (37) determining the evolution of the amplitude is determined. It is no surprise that the amplitude evolves with the group velocity $c_g = \omega_k = c + kc_k$, well-known for stable waves but is also the case, as here, for unstable waves, see the reviews by [6] and [15]. It is an important consequence that the solution of (37) is that A is constant on the characteristics $dX/dT = c_g$ and consequently c_g must be real-valued. In turn, this implies that for unstable waves with a small, but non-zero, imaginary component to the frequency, there must also be a small, but non-zero, imaginary component to the wavenumber. This has the consequence, see (40, 41), that in the reference frame moving with the group velocity the wave group has a growth rate Σ, which differs from the temporal growth rate γ, see (39) for the general expression, and (47) for the present case of wind waves. We find further that for typical wind profiles such as the logarithmic profile (32), Σ is considerably larger than γ, indicating that wave group dynamics, even in this linearised formulation, acts to enhance the generation of wind waves. The implications of this finding for operational wind-wave models remain to be determined, and among the issues that will need to be addressed is how to move from this present deterministic model of a single wave packet, to a statistical ensemble of such wave packets, and in particular to extend this present analysis to two horizontal spatial dimensions. However, it would seem clear that the considerable difference in magnitude between Σ and γ, $\Sigma > \gamma$, will lead to a substantial modification of the growth term in current wind wave operational models.

Although the emphasis here has been on the linear stability problem for a wave group, in section 4 we indicate how an extension to the weakly nonlinear narrow band regime will lead to a nonlinear Schrödinger equation (49) with a forcing term. Because this forcing term is linear, the balance between weak nonlinearity and weak dispersion in this equation in not sufficient to control the instability, and the energy equation (51) shows, all solutions still grow. In particular we examine the effect of this forcing term on modulational instability, and find in agreement with others, such as [9, 17], that the modulational instability is enhanced with super-exponential growth.

Acknowledgement

RG was supported by the Leverhulme Trust through the award of a Leverhulme Emeritus Fellowship, EM-2015-37.

Appendix

The constant K in the Frobenius expansion (29) is formally obtained by solving the modal equation (18) with the boundary condition (24) and matching this with the Frobenius expansion (29). For most wind profiles, this cannot be done exactly, and a variety of asymptotic and approximate analyses have been performed, see [10, 11] and [7] amongst several others.

Here we make a further assumption that $u_0(z) \to U_0$ as $z \to \infty$, where $U_0 > c_0$, and use an approach similar to that of [7], which matches the solutions in two regimes. These are an inner layer including both $z = 0$ and $z \sim z_c$ and an outer layer where $z \gg z_c$. In the inner layer, the right-hand side of (18) is neglected, and then an approximate solution is,

$$\phi \approx \phi_{inner} = 1 + b \int_0^z \frac{dy}{W^2(y)}\,, \tag{54}$$

where the constant b is determined by matching with an outer solution. Formally, this is valid when $kz \ll 1$, and in particular, $kz_c \ll 1$. The second term in (54) is singular at $z = z_c$ and is evaluated by assuming as above that $c_i > 0$ and then taking the limit $c_i \to 0+$ This yields the Frobenius expansion (29,45)), and so

$$b = -Ku_{0z}^2(z_c)\,. \tag{55}$$

Matching with the outer solution will require that the inner solution (54) be expanded for $z > z_c$, yielding

$$\phi_{inner} = 1 + \{\mathcal{P}\int_0^z \frac{dy}{W^2(y)} - \frac{i\pi u_{0zz}(z_c)}{|u_{0z}(z_c)|^3}\}\,, \tag{56}$$

where $\mathcal{P}\int$ denotes the principal value integral.

For the outer solution, we recall that as $z \to \infty$, $u_0 \to U_0, u_{0z} \to 0, z \to \infty$. In this limit an approximate solution of the modal equation (18) is found by setting

$$W\phi = \exp(-kz)\psi\,, \quad \text{so that} \quad \psi_{zz} - 2k\psi_z - \frac{u_{0zz}}{W}\psi = 0\,. \tag{57}$$

For our present purpose it is sufficient it assume that $\psi \sim \psi_{outer} = A$ as $z \to \infty$, where A is a constant. This outer solution is then matched to the inner solution. To this end, we expand the inner solution (56) as $z \to \infty$ so that

$$\phi_{inner} \sim 1 + b\{\frac{(z+z_0)}{W_0^2} - \frac{i\pi u_{0zz}(z_c)}{|u_{0z}(z_c)|^3}\}\,, \quad z_0 = \int_0^\infty \frac{W_0^2 - W^2}{W^2}\,dz\,, \quad W_0 = c_0 - U_0\,. \tag{58}$$

This is then matched to the inner limit of the outer expansion

$$\phi_{outer} \sim A\frac{(1-kz)}{W_0}\,. \tag{59}$$

The outcome, after eliminating the constant A, is

$$b = -\frac{kW_0^2}{\mu}\,, \quad \mu = 1 + kz_0 - \frac{i\pi k W_0^2 u_{0zz}(z_c)}{|u_{0z}(z_c)|^3}\,. \tag{60}$$

Then, using the expression (55) we finally obtain that

$$K = \frac{kW_0^2}{|u_{0z}(z_c)|^2\mu}\,. \tag{61}$$

Then the dimensionless growth rate, given by (31) becomes

$$\Gamma = -\frac{\pi k u_{0zz}(z_c) W_0^4 \tanh(kH)}{2c_0^2|u_{0z}(z_c)|^3|\mu|^2} = -\frac{\pi k^2 u_{0zz}(z_c) W_0^4}{2g|u_{0z}(z_c)|^3|\mu|^2}\,, \quad \text{where} \quad |\mu|^2 = (1+kz_0)^2 + B^2\,, \quad B = \frac{\pi k W_0^2 u_{0zz}(z_c)}{|u_{0z}(z_c)|^3}\,. \tag{62}$$

This depends on the parameters c_0, H and the parameters $u_{0z}(z_c), u_{0zz}(z_c), U_0, z_0$ contained in the shear flow profile $u_0(z)$. Note that the wavenumber k is subsumed into c_0. Note that $z_0 > 0$ when $U_0 > 2c_0$ and then $|\mu|^2 > 1$ for all parameter values. Typically B scales with kz_c, and then if $kz_0, kz_c \ll 1$, $|\mu|^2 \approx 1$.

As an illustration, consider the logarithmic wind profile (32) in the domain $0 < z < z_1$, with $u_0 = U_0, z > z_1$,

$$c_0 = \frac{u_*}{\kappa}\log(1+\frac{z_c}{z_*})\,, \quad U_0 = \frac{u_*}{\kappa}\log(1+\frac{z_1}{z_*})\,, \quad -\frac{u_{0zz}(z_c)}{|u_{0z}(z_c)|} = \frac{1}{z_*+z_c}\,, \tag{63}$$

$$B = \frac{\pi\kappa^2 k(z_c+z_*)W_0^2}{u_*^2} = \pi k(z_*+z_c)\log^2\{\frac{z_*+z_1}{z_*+z_c}\}\,, \tag{64}$$

$$z_0 = \int_0^{z_1}\frac{W_0^2-W^2}{W^2}\,dz = \frac{\kappa z_*}{u_*}\int_{W_0}^{c_0}\frac{W_0^2-W^2}{W^2}\exp(\kappa(c_0-W)/u_*)\,dW\,, \tag{65}$$

$$\text{and} \quad \Gamma = \frac{\pi k(z_*+z_c)}{2\kappa^2|\mu|^2}\frac{ku_*^2}{g}\log^4\{\frac{z_*+z_1}{z_*+z_c}\}\,. \tag{66}$$

The Miles parameter β is defined by

$$\Gamma = \beta\frac{u_*^2}{c_0^2}\,, \quad \text{so that} \quad \beta = \frac{\pi k(z_*+z_c)}{2\kappa^2|\mu|^2}\frac{kc_0^2}{g}\log^4\{\frac{z_*+z_0}{z_*+z_c}\}\,. \tag{67}$$

In the deep water limit, this expression is similar to that obtained by [11], but differs in how the parameter μ is determined. For each fixed wavenumber k, Γ decreases as H decreases, albeit rather slowly, since z_c decreases as c_0 decreases with H for fixed k. Further, for each fixed c_0, and hence fixed z_c, Γ decreases as H decreases, since then k decreases. The expression (66) also contains a dependence on U_0 through z_0, and Γ increases as U_0 increases.

References

1. Belcher, S.E., Hunt, J.C.R., 1998. Turbulent flow over hills and waves. Ann. Rev. Fluid Mech. 30, 507–538.
2. Brunetti, M., Marchiando, N., Berti, N., Kasparian, J., 2104. Nonlinear fast growth of water waves under wind forcing. Phys. Lett. A 378, 1025–1030.
3. Craik, A.D.D., 1985. Wave interactions and fluid flows. Cambridge University Press, UK.
4. Gaster, M., 1967. The development of three-dimensional wave packets in a boundary layer. J. Fluid Mech. 32, 173–184.
5. Gaster, M., Davey, A., 1968. The development of three-dimensional wave-packets in unbounded parallel flows. J. Fluid Mech. 32, 801–808.
6. Huerre, P., Monkewitz, P.A., 1990. Local and global instabilities in spatially developing flows. Ann. Rev. Fluid Mech. 22, 473–537.
7. Janssen, P., 2004. The interaction of ocean waves and wind. Cambridge University Press, UK.
8. Jeffreys, H., 1925. On the formation of water waves by wind. Proc. R. Soc. A 107, 189–206.
9. Leblanc, S., 2007. Amplification of nonlinear surface waves by wind. Phys. Fluids 19, 101705.
10. Miles, J.W., 1957. On the generation of surface waves by shear flows. J. Fluid Mech. 3, 185–204.
11. Miles, J.W., 1993. Surface wave generation revisited. J. Fluid Mech. 256, 427–441.
12. Montalvo, P., Kraenkel, R., Manna, M.A., Kharif, C., 2013. Wind-wave amplification mechanisms: possible models for steep wave events in finite depth. Natural Hazards and Earth System Sciences 13, 2805–2813.
13. Morland, L.C., Saffman, P.G., 1993. Effect of wind profile on the instability of wind blowing over water. J. Fluid Mech. 252, 383–398.
14. Pushkarev, A., Zakharov, V., . Limited fetch revisited: Comparison of wind input terms, in surface wind wave modeling. Ocean Modelling 103, 18–37.
15. Redekopp, L.G., 2001. Elements of instability theory for environmental flows, in: Grimshaw, R. (Ed.), Environmental Stratified Flows. Kluwer, Boston, pp. 223–281.
16. Sajjadi, S.G., Hunt, J.C.R., Drullion, F., . Asymptotic multi-layer analysis of wind over unsteady monochromatic surface waves. J. Eng. Maths 84, 73–85.
17. Slunyaev, A., Sergeeva, A., Pelinovsky, E., . Wave amplification in the framework of forced nonlinear schrödinger equation: The rogue wave context. Physica D 301, 18–27.
18. Stiassnie, M., Agnon, Y., Janssen, P.A.E.M., . Temporal and spatial growth of wind waves. J. Phys. Ocean. 37, 106–114.
19. Touboul, J., Kharif, C., Pelinovsky, E., Giovanangeli, J.P., 2008. On the interaction of wind and steep gravity wave groups using Miles' and Jeffreys' mechanisms. Nonlinear Proc. Geophys. 15, 1023–1031.

Available online at www.sciencedirect.com

ScienceDirect

Procedia IUTAM 26 (2018) 102–111

Procedia IUTAM

www.elsevier.com/locate/procedia

IUTAM Symposium Wind Waves, 4-8 September 2017, London, UK

Mechanistic, empirical and numerical perspectives on wind-waves interaction

Tihomir Hristov

[a]*Department of Mechanical Engineering, Johns Hopkins University, 3400 N. Charles Str., Baltimore, MD 21218, USA*

Abstract

A mechanistic theory of wind-wave interaction must rely on verifiable assumptions and offer reproducible observable predictions. For decades, the limited mechanistic grasp on the problem has motivated RANS and LES modeling and has driven a vast empirical effort to describe the interaction in terms of wave-induced modifications of standard statistical characteristics of the wind, such as wind profile, kinetic energy balance or exchange coefficients. Because the mechanistic, empirical and numerical approaches are all concerned with the same phenomenon occurring in the same media, consistency here requires that the assumptions on which the approaches rest and the predictions they generate are compatible with each other and supported by measurements. Recent findings from theoretical analysis and field experiments advanced the understanding of the statistical and dynamic patterns of the wave-coherent flow, which is at the core of the mechanistic description of the wind-wave exchange. The progress prompts reexamining of earlier concepts, efforts and findings to evaluate their suitability, validity and usefulness. For the purpose, this survey traces the development of ideas, methods and results in the study of the wind wave generation.

Peer-review under responsibility of the scientific committee of the IUTAM Symposium Wind Waves.

Keywords: Wind waves generation; wave-coherent flow; critical layer; equilibrium wave spectra.

1. Introduction

'What causes the waves in the ocean?' is a question that seeks to elucidate an ubiquitous phenomenon and in that sense it stands next to questions such as 'What makes the stars shine?' or 'What causes the lightning?'. In his thesis advised by Richard Feynman, "The growth of water waves due to the action of the wind", Hibbs [22] wondered about *"Why should such a problem still exist, with all the abilities of modern physics and the accomplishments of modern aerodynamics?"*. Indeed, initiated by Kelvin [30], the efforts to reveal the physics behind the wind-generated ocean waves are still ongoing, as evidenced by this meeting. In his influential review on the subject Ursell [63, p. 217] pointed out the key obstacle to understanding the process that is the disconnect between theory and experiment, a disconnect that began to close only recently. Since the times of Ursell [63], however, the lines of inquiry on wind-

* Tihomir Hristov
E-mail address: Tihomir.Hristov@jhu.edu, Hristov.Tihomir@gmail.com

2210-9838
Peer-review under responsibility of the scientific committee of the IUTAM Symposium Wind Waves.
10.1016/j.piutam.2018.03.010

wave interaction have been broadened beyond theory and experiment to include empirical and numerical approaches which, like theory and experiment, have also developed separately and any possible connection between them has stayed unexplored. As all these approaches are concerned with the same phenomenon in the same environment, the results and predictions from different approaches should be consistent with each other. Whether a theory should be about a mechanism or unity, as Poincare [47, p. 177] pondered, this survey pursues both. Because a mechanistic theory on wind-wave interaction should be capable to provide details and physical insight, a summary of a theory is used below to gain an unified mechanistic frame of reference for empirical and numerical approaches and results. For the purpose, here we discuss the corollaries of some recent findings on the problem of waves generation by wind, the analytic and experimental details of which are available in [26], [27] and [24]. To put these findings in perspective and to answer the question raised by Hibbs' [22], we outline the milestones in the early evolution of ideas as they may, justifiably or not, still guide the thinking on the subject.

2. Milestones in the early wind-wave interaction studies

Like Kelvin [30], Jeffreys [29] studied the process of wind waves generation assuming an air flow velocity constant with the distance from the interface. At the time the specific functional form of the wind velocity profile was still unknown and its role in the generation had not been studied and understood. Starting from such unrealistic air flow Jeffreys [29] arrived to unrealistic predictions and incorrectly traced them back to the assumption of irrotational waves. Abandoning that assumption while keeping the unrealistic wind profile, Jeffreys [29] proceeded to hypothesize and prescribe, rather than to derive or otherwise deduce, the physical nature of the interaction. Forty years later Stewart [60, p. S48] found Jeffreys [29] solution of the wind wave generation problem lacking.

The review of Ursell [63] summarized the ideas available at the time, stated the unsatisfactory understanding of the problem, and inspired the works of Phillips [45] and Miles [37]. Phillips [45] built on the work by Eckart [12] and considered a wave generation due to the turbulent air pressure fluctuations as in an oscillator under the action of a random force. Paradoxically, Phillips [45, p. 417] both neglected the wave-coherent motion in the air and found it to be most effective for the generation process: *"Correlations between air and water motions are neglected ... It is found that waves develop most rapidly by means of a resonance mechanism which occurs when a component of the surface pressure distribution moves at the same speed as the free surface wave with the same wavenumber."* For the resonant wave growth to occur, Phillips [45, p. 422] required that *"the pressure distribution contains components whose wave-numbers and frequencies coincide with possible modes of free surface waves"*. Yet, the dispersion of the turbulent motion in a wind with advection velocity U is $U = \omega/k$, also known as Taylor's hypothesis, and the dispersion of surface waves with a phase speed c is $c = g/\omega$, g being the acceleration of gravity. Because for aligned wind and waves same frequency and wave number correspond to different advection velocity U and phase speed c, these dispersions are incompatible for resonance. For a wave mode $\omega(k)$ a resonance may still occur if it propagates obliquely at some angle $\pm\theta$ with respect to the wind, thus predicting a wave field with a bimodal spectral distribution. The observations of Simpson [55, p. 93] detected no bimodal spectrum in the range of the locally generated waves. Longuet-Higgins [34] reported the turbulent air pressure fluctuations to be too small to ensure wave growth rates near the observed, but offered no interpretation. The turbulent pressure fluctuations decay with scale as $k^{-7/3}$ [43, 3], that is faster than the decay rate with scale $k^{-5/3}$ in velocity. As turbulent motion undergoes the energy cascade from integral scales down to the scales of the initiating sea surface ripples, only small magnitude pressure fluctuations are retained. Consequently, the turbulent pressure component on which the random force mechanism relies, is virtually absent, explaining the findings of Longuet-Higgins [34] and causing the reported lack of experimental support for the random forcing mechanism of wave generation [55].

The idea that the generation of wind-driven waves may be viewed as a shear flow instability has its roots in the work of Tollmien [62], published as an obscure technical memorandum for NACA and thus rarely referenced. Its results became available to a broader audience through Lin [33]. Tollmien [62] analyzed the perturbations in laminar shear flows as solutions of the Rayleigh equation and established the dynamic significance of the location where the averaged flow velocity profile matches the phase speed of the perturbation, known as critical layer. In the 1940s and 1950s novel results on flow stability were spreading and igniting interest among fluid dynamicists [41]. Surveying the ideas lying around, Miles [37] postulated that the laminar flow analysis and results of Tollmien [62] apply to the generation of surface waves by a wind that is turbulent. However, Miles [37] offered no physical justification of

the proposition and no testable predictions from it, which greatly influenced the perception, including Miles' own, of that proposition. Sir James Lighthill, at the time already an authority in fluid mechanics and whose life and work are celebrated at this meeting, wrote favorably of Miles [37] and referred to it as 'the Miles theory.' Still, he viewed [37] as a mathematical construct with somewhat tenuous relation to the physical world and hence in [32] he sought an interpretation for it. Like Ursell [63, p. 217], Lighthill [32, p. 385] recognized the agreement between theory and experiment as essential to gaining insight into the wind waves generation. With the observational support still absent, however, Miles [36, p. 1] viewed *'Lighthill's opinion [as] too optimistic'* and cautioned [39, p. 166] that Lighthill's [32] endorsement of the mathematical theory in [37] has been *'interpreted with less reservation than either he or the writer might have wished.'* Miles [40] considered the concept of critical layer in wind-wave interaction only as a *'convenient mathematical notion'*. Uncertain about the suitability of the ideas in the 1957 paper, Miles' later work proceeded with modifications of that paper's concept rather than with its experimental verification, interpretation, potential physical impacts or operational use. Besides Miles, others have explored such modifications, e.g. in specific corners of the parameter space, the work of Sajjadi et al. [52] among the latest.

Miles [37] postulation that the surface waves occur as growing perturbations of the wind profile and are thus described by Rayleigh equation, is now superseded by a derivation that renders moot the gaps and deficiencies in wind input knowledge as perceived by Pushkarev and Zakharov [50, p. 21]. Resting solely on the well-confirmed premise of small slope waves, [27] demonstrated that the Taylor-Goldstein equation describes the wave-coherent component, and thus the wind-wave interaction, in a stratified turbulent wind. Both the Rayleigh and the Taylor-Goldstein equations predict critical layers for a wide variety of wind profiles $U(z)$. The wave-coherent motion there is associated with a kinetic energy production $\langle\tilde{u}\tilde{w}\rangle(\partial U/\partial z)$ that is delivered from the mean flow to the waves and is leading to a wave generation for any of these profiles. Because the logarithmic wind profile $U(z) = (u_*/\kappa)\log(z/z_0)$ is sufficiently representative of the marine atmospheric boundary layer [6, 51, 42, 59], Miles [37] offered numerical estimates for the wave growth rate for the case of that profile. While the key concept in [37] has been only illustrated with a logarithmic profile, that still invites the misinterpretation, e.g. in Pushkarev and Zakharov [50, p. 21], that the concept in [37] requires such profile. It does not. Stratification as well as inhomogeneity and non-stationarity of the marine atmospheric boundary layer may cause departures of the wind profile from its logarithmic shape [27]. While in such cases the wind-wave interaction still occurs through the same physical mechanism of wave-coherent flow with critical layers, the wind-to-wave energy transfer rates may vary substantially from their values obtained for a logarithmic profile. Yet, experimental estimates of the wave growth rates have been compared with theoretical predictions calculated for the case of a logarithmic wind profile. Discrepancies in such comparisons, although not in whole, are related to the unphysical narrowing, as in [50, p. 21], of the theory's scope to a logarithmic wind profile.

Over the decades that followed, review papers have repeatedly described [37] as difficult to understand, interpret, validate or apply [5, 60, 2], and as *"...least well understood because of the less-than-intuitive nature of the theory"* [14]. With such sentiment widely shared, the proposition in [37] has been misconstrued, doubted and dismissed. Regarding the Hibbs' [22] question, that sentiment may have dissuaded close interest in and may have delayed the progress on the wind waves generation problem.

3. Empirical studies of wind-wave interaction

With the mechanistic theory of wind-wave interaction deemed inaccessible, the attention has turned to empirical studies. There, the ocean is treated as a rough aerodynamic surface where the waves of all scales are responsible for the surface roughness and the variability of the surface's drag. Motivated by the need for computational efficiency in large scale models of atmospheric dynamics and ocean circulation, this vast effort has included dozens of experiments in laboratory, over lakes and over the coastal and the open ocean and since the 1960s has produced hundreds of papers. It has been primarily concerned with applied issues, such as establishing empirical relationships between easy-to-measure environmental variables, e.g. wind speed, vertical scalar gradients, etc., and variables of ocean-atmosphere exchange, e.g. fluxes of momentum, heat, species, etc. Among the constraints of this empirical approach is the inability to distinguish between momentum or energy transferred to the waves and those transferred to the currents, leaving a significant blind spot for numerical modeling and forecasting. Among the main interests pursued within this effort have been the empirical estimates of the air-sea exchange coefficients. The scatter of these estimates, however, has not been reduced over time, despite the improved instrumentation and the accumulation of more statistics [8]. The latter

suggests that at the core of the uncertainty is the complex dynamics of the air flow laying outside of the empirical framework, rather than experimental imperfections or isolated statistical aberrations.

A related line of inquiry within the empirical approach on wind-wave interaction and characterization of the marine atmospheric boundary layer has been to seek violations of the Monin-Obukhov similarity theory over the ocean, e.g. in the shape of the wind profiles or in the budgets of momentum flux and kinetic energy, ascribe them to the influence of the surface waves [15, 13, 56, 28, 23], and use these violations to understand and quantify the dynamic wind-waves exchange. The underlying assumption of such studies is that no violations of the Monin-Obukhov similarity theory occur over land, so that any violations of that theory can be interpreted with certainty as a dynamic signature of the surface waves. Once found and their patterns discerned, these violations were to be incorporated in an updated theory, where the universal gradient functions $\{\phi_m(z/L), \phi_h(z/L), \ldots\}$ of the Richardson number (z/L), where L is the Obukhov mixing length, are modified to account for the waves' presence [13]. Such logic, however, ignores multiple reports of discrepancies between the said theory and observations over land [44, 66, 17]. Furthermore, the assumption that the wave influence would depend solely on the Richardson number and be independent of any variables characterizing the sea state, appears unjustified. The research strategy just outlined, has detected no wave signature in the study of Edson and Fairall [15]. Consistent with the report of Charnock [6] and the studies of Ruggles [51], Mitsuyasu and Honda [42], Soloviev and Kudryavtsev [59] and of Bergström and Smedman [4], the Edson and Fairall [15] experiment determined that the kinetic energy balance is virtually unaffected by the presence of waves. Their proposed explanation was that the instruments have been positioned above the layer affected by the wave influence, commonly referred to as the wavy boundary layer (WBL). Sjöblom and Smedman [56] point out that the research strategy produces *"seemingly contrasting results"*, that are circumstantial and inconclusive.

In its broadest formulation the empirical approach would select a statistical characteristic of the atmospheric boundary layer, be that dissipation rate, velocity structure function, velocity spectra, etc., search for differences in that characteristic in measurements over land and over waves and from these differences seek insights into the wind-wave interaction. Schacher et al. [54] have found no detectable wave signature in the rate of kinetic energy dissipation, Van Atta and Chen [64] have failed to identify such signature in the wind velocity structure function. Pond et al. [49, 48], Weiler and Burling [65], Stewart [60], Soloviev and Kudryavtsev [59] have reported no peak at the wave frequency in the wind velocity spectra. All these negative, yet informative results indicate that the mechanical air-sea interaction is both intense and subtle. The size and energy of the waves generated by a storm indicates the interaction's intensity. Yet the interaction does not manifest itself in quantities commonly used to characterize the atmospheric boundary layer (wind profiles, spectra, structure functions, kinetic energy budget, etc.), hence the subtlety. That subtlety may partially hold the answer to the question posed by Hibbs [22]. The negative results listed above suggest that the selected characteristics of the atmospheric boundary layer are insensitive to wave influence and that choosing a different set of informative variables and analysis techniques is essential for gaining a physical insight into the wind-wave coupling.

4. Mechanistic perspective and its observational validation

The generation of ocean waves results from the interaction between two random fields, the air flow and the compliant water surface. Given the surface elevation η, the vertical velocity $\dot{\eta}$, and the atmospheric pressure p_0 at a point of the water surface, the averaged energy exchange rate there is $\langle p_0 \dot{\eta} \rangle$. The latter suggests that the wave-coherent pressure, and generally the wave-coherent motion in the air, carries the interaction. Therefore, the dynamic equations of that motion would be the key to formulating the mechanistic theory, while discerning that motion's dynamic and statistical patterns from field measurements would be key to verifying the theory.

The wave-coherent motion, however, has been perceived as elusive to both define and detect. Phillips [46, p. 108] thought of it: *"In physical space, the induced pressure at any point on the surface of a random wave field is a rather ill-defined functional of both the wind and the wave fields, and it is not easy to separate this from the turbulent contribution."* Hasse and Dobson [20, p. 101] saw experimental challenges: *"This means that in the air above the sea, where there is usually a mean wind many times stronger than the wave-induced flows, the wave-induced motions are hard to detect."*, as did Komen et al. [31, p. 72]: *"The measurement of the energy transfer from wind to waves is, however, a very difficult task, as it involves the determination of the phase difference between the wave-induced pressure fluctuation and the surface elevation signal..."*

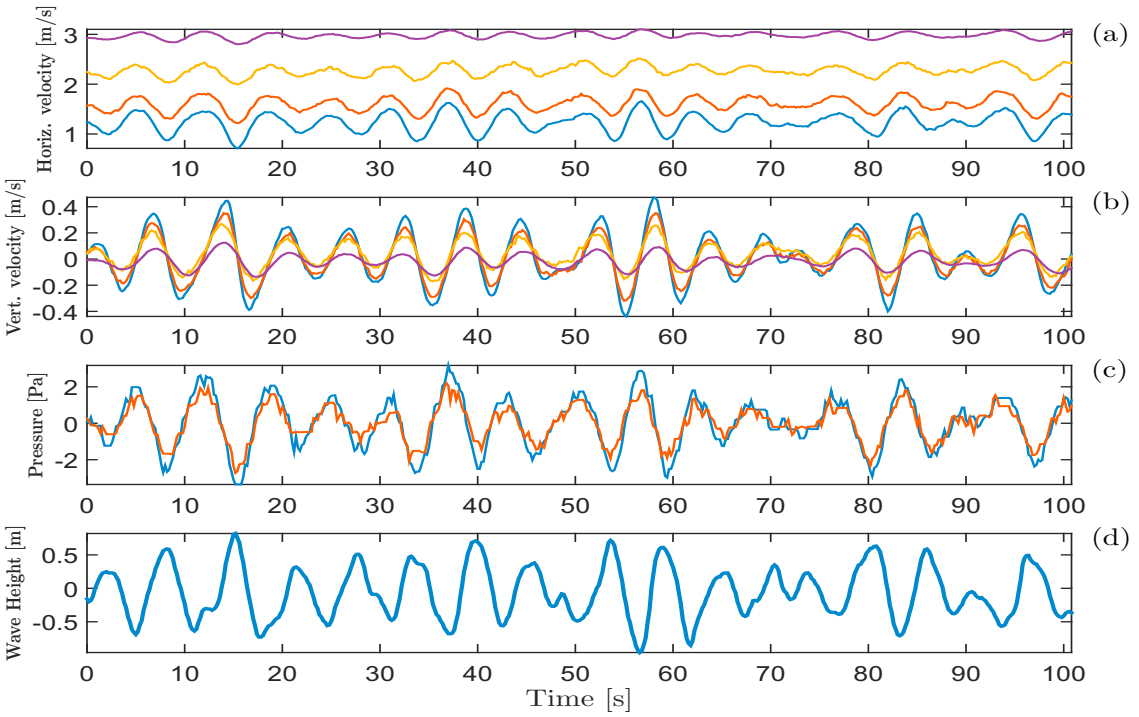

Fig. 1. Wave modulation of the wind during Coupled Boundary Layers Air-Sea Transfer (CBLAST) experiment. (a) Horizontal wind velocity measured by 4 ultrasonic anemometers positioned between 5m and 18m from the surface in the order blue (the lowest), red, yellow, magenta (the highest). (b) Vertical wind velocity, with colors matching the same order of the instruments. (c) Pressure, blue (lower) and red (higher). (d) Surface wave elevation.

When the wind speed and the turbulence intensity in the air are relatively low, the wave-coherent modulation of the wind is directly observable in unprocessed signals of air velocity and pressure (Figure 1). With the increase of wind speed, turbulence begins to dominate and the identification of wave-coherent modulation requires statistical tools [25, 26, 18, 27].

Consider a signal of an air flow variable $u(t)$ that consists of a wave-correlated component $\tilde{u}(t)$ and a uncorrelated component $u'(t)$, so that $u = \overline{u} + \tilde{u}(t) + u'(t)$. Consider a wave signal $\eta(t)$ as consisting of a finite-number narrow-band components $\{\eta_n(t)\}$, i.e. $\eta(t) = \sum_n \eta_n(t)$, for which $\langle \eta_k \eta_l \rangle \sim \delta_{kl}$. Then, the wave-coherent component $\tilde{u}(t)$ can be obtained as a projection of the measured signal $u(t)$ onto the vector space of all wave-coherent signals $W = \text{span}\{\eta_n, \hat{\eta}_n\}$, where $\hat{\eta}_n$ is the in-quadrature counterpart of η_n obtained via the Hilbert transform, i.e.

$$\tilde{u}(t) = \sum_n \left(\frac{\langle u(t)\eta_n(t) \rangle}{\|\eta_n\|^2} \eta_n(t) + \frac{\langle u(t)\hat{\eta}_n(t) \rangle}{\|\hat{\eta}_n\|^2} \hat{\eta}_n(t) \right). \tag{1}$$

The filter $\widetilde{(\cdot)}$ defined this way has the properties $\widetilde{(\overline{u})} = \tilde{u}$, $\widetilde{(\tilde{u})} = \tilde{u}$, $\widetilde{(u')} = 0$, and $\langle u'\tilde{u} \rangle = 0$. Such filter both defines and detects wave-coherent fields in the air flow. It is suitable for deriving the dynamic equations for the wave-coherent flow and for retrieving the time series of the wave-coherent variables in measured signals [25, 26, 27].

Referring to [26], [27] and [24] for analytic and experimental details, below we outline the foundations of the theory there, its experimental verification, its predictions, and their implications. Invoking only the assumption of small slope waves, [27] employs the filter (1) to arrive to the dynamic equations for the wave-coherent flow, thus extending the shear flow instability analysis to the interaction of waves with a turbulent wind. As the transfer functions of the wave-coherent fields in the air are invariant with respect to the wave spectrum and can be produced both theoretically and experimentally, they are well suited for validating theory from measurements. Therefore, the wave-coherent flow structure and dynamics can be described through the transfer functions between the waves and the air velocity. Matching analytical and experimental transfer functions would support the theory that predicted them or,

conversely, would explain the experiment that produced them. The theory predicts that at low wind speeds the wave-coherent flow may form a regime with Stokes drift (e.g. as in Figure 1), causing momentum flux from waves to wind, and a regime with critical layers at moderate and high wind speeds [26, 18, 27], causing momentum and energy fluxes from wind to waves. A distinct flow feature is the discontinuity of the velocity's phase at the critical height [26, 24].

Since coastal ocean and laboratory are much more accessible than the open ocean for wind-wave interaction studies, it is pertinent to recognize the constraints of such environments for observing the critical layer signature. The dispersion of waves in finite-depth water $\omega^2 = gk\tanh(kd)$, where g is the acceleration of gravity and d is the water depth, establishes a maximum for the waves' phase speed $c_{max} = (gd)^{1/2}$. When waves transition from deep to shallow water, the refraction may misalign the wind and the waves, requiring that the relative direction is included in estimating the wave age. Furthermore, for the range of wave frequencies $[0, \infty]$, the range of possible phase speeds contracts from $[0, \infty]$ to $[0, \sqrt{gd}]$. For a frequency range $\Delta\omega$ the corresponding phase speed range in deep water Δc_{deep} contracts to a phase speed range in shallow water $\Delta c_{\text{shallow}}$, so that $\Delta c_{\text{shallow}} < \Delta c_{\text{deep}}$. In turn, the range of critical heights $\Delta z_{c,\text{deep}}$ corresponding to the same frequency range $\Delta\omega$, contracts as well to $\Delta z_{c,\text{shallow}}$, i.e. $\Delta z_{c,\text{shallow}} < \Delta z_{c,\text{deep}}$, as does the range of wave ages $\Delta(c/u_*)$. Compressing the critical layer features of a range of wave modes $\Delta\omega$ into a thinner critical heights range and narrower wave age intervals may cause these features to become poorly resolvable, while the increased wave steepness in shallow water may enhance nonlinearities and distort any critical layer signature.

Measurements over deep water waves, conducted during the Marine Boundary Layer Experiment [26, 24] and the High Resolution Air-Sea Interaction Experiment [18, 27], along with the analytic results in [27, 24] established that:

(i) The wind-wave interaction does occur through a wave-coherent flow in the air and the critical layer pattern of phase discontinuity in that flow is sustained, thus identifying the mechanism responsible for wind wave generation, [26, 18, 24].
(ii) A Stokes drift regime is observed at low wind conditions, associated with weak, yet pronounced wave-to-wind momentum flux [27].
(iii) Relying only on the assumption of small slope waves, that is, $k_p\sigma_\eta \ll 1$, where k_p is the wave number of the spectral peak and $\sigma_\eta = \langle\eta^2\rangle^{1/2}$ is the variance of the sea surface, the analysis in [27] shows that the budgets of second order moments, e.g. kinetic energy and momentum, apply separately to the wave-correlated and wave-uncorrelated motions in the wind. As the phenomenology of the atmospheric boundary layer's kinetic energy budget is the essence of the popular Monin-Obukhov similarity theory (MOST), the separated budgets show how the waves modify the predictions from MOST.
(iv) The key measure of the waves' dynamic influence on the air flow is the ratio of the production terms in the kinetic energy budgets for the correlated $\langle\tilde{u}\tilde{w}\rangle(\partial U/\partial z)$ and uncorrelated $\langle u'w'\rangle(\partial U/\partial z)$ motions, which in turn is expressed as a ratio of the wave-supported $-\langle\tilde{u}\tilde{w}\rangle$ and total $-\langle uw\rangle = u_*^2$ momentum fluxes, i.e. $-\langle\tilde{u}\tilde{w}\rangle/u_*^2$, [27].
(v) At heights available for atmospheric measurements $z \geq 10^4 z_0$, where z_0 is the aerodynamic roughness length of the sea surface, typically between 2×10^{-4}m and 5×10^{-4}m, both theory and experiment find that the ratio $-\langle\tilde{u}\tilde{w}\rangle/u_*^2$ is small, of the order of 5%, [27].
(vi) Consequently, the wave contribution to the sea surface drag coefficient C_D, the wave-induced modification of the kinetic energy budget, the apparent wave-enhanced imbalance between production and dissipation, the wave contribution to the departures from the predictions of the Monin-Obukhov similarity theory and the wave-induced bending of the wind profile are also small and thus virtually undetectable next to other physical influences modifying these characteristics, in agreement with empirical studies, [27].
(vii) The explicit forms of the wave-supported momentum and kinetic energy fluxes indicate that a wave frequency spectrum $\omega^{-\beta}$, through relaxation, converges to a spectral slope $4 \leq \beta \leq 5$, [27].

These findings explain the negative results in the vast body of empirical studies that sought a wave signature in standard characteristics of the flow over waves, such as a wind profile, a dissipation rate, a kinetic energy balance, a momentum flux, or a variation of the drag coefficient with sea state. They show that the predictions of the Monin-Obukhov similarity theory are virtually insensitive to the waves, letting the conclusion that the theory adequately describes the marine atmospheric boundary layer, yet it is a poor instrument for detecting and studying wind-wave coupling. The demonstrated agreement between theory and experiment unifies the mechanistic and empirical perspectives on wind-wave interaction.

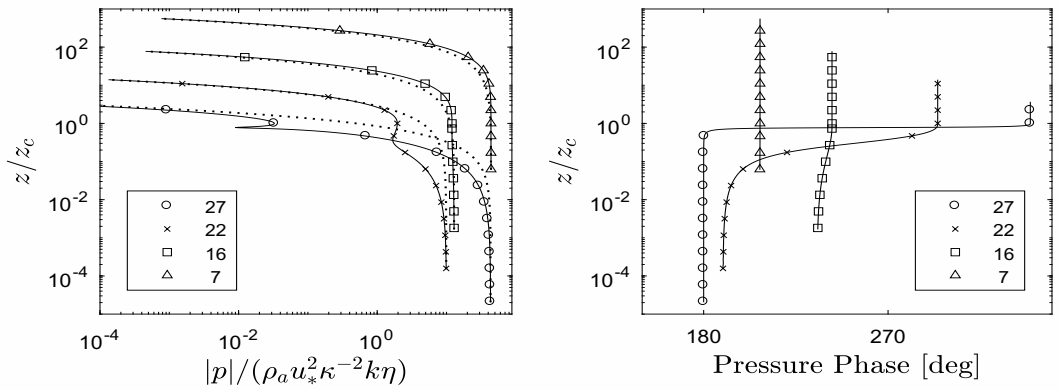

Fig. 2. The normalized magnitude $|p|/(\rho_a u_*^2 \kappa^{-2} k\eta)$ (left), and phase (right) of the wave-coherent pressure vs. the distance from the surface normalized by the critical height z/z_c, obtained from a solution of the Rayleigh equation [26, 27, 24]. The symbols $\circ, \times, \square, \triangle$ distinguish different values of the wave age c/u_*. The dotted lines show exponents that match the pressure magnitude at the endpoints and exhibit a notable departure in the middle.

5. Experimental and numerical studies of wave growth rate and wave energy evolution

Wave growth rate and wave energy evolution under wind forcing are of primary interest for wave modeling and forecasting [50]. The wave growth rate, rather than the air flow pattern, has been central to the thinking and studies of wind waves to the extent that a discrepancy with observed growth rates sufficed for Donelan and Hui [10, p. 228] to dismiss the available theory: *"Thus, our knowledge of the wind input to a spectrum of waves is still rather primitive. The theoretical ideas of the fifties have not been capable of explaining the observed growth rates and no essentially new ideas have followed."* Yet, experimental and numerical estimates of growth rates and of energy evolution depend on the constraints and the uncertainties in the methods used to obtain them. Below, these constraints and uncertainties are outlined for proper interpretation of wave growth rate estimates' relation to a particular theory.

As a wave generation through random force [45] or through shear flow instability [62, 37], would lead to a different growth rate and a different evolution of the wave field's energy, experiments have sought to identify wind-wave generation scenarios through growth rate or energy evolution measurements. Davis [7] noted, however, that the growth rate is a function of the pressure distribution on the surface, yet since the pressure distribution does not uniquely specify the flow structure in the air, it does not determine the mechanism of wind-wave interaction. As for the evolution of the wave field energy observed in an experiment, it depends not only on the wind-wave interaction mechanism, but also on the history and spatial distribution of the variable wind forcing as well as on the action of non-linearity that redistributes the wave energy across the spectrum. Because different wave modes draw momentum and energy from the wind at different rates, a wave field developing with non-linearity may have evolution of its energy significantly different from a wave field developing under the wind forcing alone, i.e. when each mode retains exactly the energy received directly from the wind. Consequently, like the wave growth rate, the observable wave field energy evolution lacks the certainty necessary for identifying the physics of wind-wave interaction.

Multiple experiments [16, 58, 57, 21, 19, 9, 11, 53] have been carried out to measure the wind-to wave energy transfer rate as a correlation between pressure and surface velocity, i.e. $\langle p_0 \dot{\eta} \rangle$ and compare them with predictions from theory. Pressure measurements on the surface risk wetting the sensor or distorting the readings with protective film, etc. Commonly, pressure measurements are conducted at some finite height and later extrapolated to the surface, assuming exponential decay of the pressure's magnitude scaled by the wave number k, i.e. $\propto e^{-kz}$, and no change in phase with height, as in [16, p. 443], [58, p. 508], [57, p. 24], [21, p. 397, p. 405, p. 407-409], [19, p. 1020], [9, p. 190], [11, p. 1174], [53, p. 1334]. However, a theory of wind-wave interaction through wave-coherent flow predicts the wave-coherent pressure from solutions of the Taylor-Goldstein equation [26, 27, 24], which depends on the dimensionless aerodynamic surface roughness $\Omega = y_0 g\kappa^2/u_*^2$ and the wave age parameter c/u_* rather than on the wave number k, and exhibits a dependence on height that is distinctly different from exponential (Figure 2). The dotted lines in Figure 2 show exponents that match the pressure predicted from the Rayleigh equation at the end points

and notably depart, by up to a factor of 10, from it in the middle. Furthermore, the assumption of phase independent of height does not hold for a range of wave ages. Consequently, an assumption of wavenumber-scaled exponential pressure decay with constant phase is inconsistent with the theory that it is employed to test and distorts the pressure extrapolation to the surface. Along with the random variability of the surface roughness Ω, the distortive pressure extrapolation contributes to observed discrepancies between theoretical and experimental estimates of the wind-to-wave energy transfer rates. Furthermore, the wind-to-wave energy transfer depends on the wind profile shape $U(z)$ through the factor U''/U' [62, 38, 27]. The wind's non-stationarity and spatial inhomogeneity along with atmospheric stratification deform the wind profile [27, p. 3192] and through the factor U''/U' add to the variability of the wave-supported energy flux. Although the available theory explains such variability, that variability has been unaccounted in any of the field experiments listed above.

Since the 1970s, RANS and LES models for the flow over waves have been used evaluate wind-to-wave energy transfer. Such models rely on concepts (eddy viscosity, diffusivity) and tools (closures and sub-grid parametrization schemes) developed for describing turbulent flows. The strong sensitivity of modeling results to the choice of closure [1] and the fact that no second-order closure model has detected any critical layer flow features [35, 61], has led some to question the adequacy of these closures. Phillips [46, p. 117] observed that *"Closure schemes in turbulent shear flow are still rather ad hoc and different methods, which may be reasonably satisfactory in other flows, give very different results when applied to this problem. The situation is not one in which firmly established methods lead to results that one might seek, with some confidence, to verify experimentally. On the contrary, because of sensitivity of results to the assumptions made, the air flow over waves appears to provide an ideal context to test the theories of turbulent stress generation themselves."* As outlined below, the inadequacies in such models extend beyond the deficiencies in closures and sub-grid parametrizations.

Starting from Al-Zanaidi and Hui [1], a number of studies have modeled the flow over a Stokes wave, that is

$$\eta(x) = -a\cos(kx) - (ka^2/2)\sin^2(kx), \tag{2}$$

instead of over a monochromatic wave $\eta = ae^{-\mathrm{i}(kx-\omega t)}$. Such studies ascribe to a single mode k the energy flux to two wave modes, k and $2k$, thus producing a spurious enhancement of the wave growth rate.

Contrasting with the widely held views about turbulence, the wave-induced flow is anisotropic at both large and small scales. Its directions of distinct significance are the direction of wave propagation, and the vertical direction, along which the wave signature decays. The critical layers, which both the theory and experiment show to be dynamically essential in wind-wave interaction, create a fine structure in the wind. The wave-induced flow may experience a large variation over a short distance near the distinctly anisotropic critical layer [26, Figure 1e]. The critical layers of different wave modes are densely stacked on top of each other along the vertical coordinate. Closures and sub-grid parameterizations have been proposed with regard to the assumed properties of turbulence and none with regard to the properties of the wave-induced flow, which differs from turbulence in its scales and symmetries. Resolving the wave-induced flow with multiple critical layers [26, Figure 1e] requires a fine spatial grid. The 40 cells along the vertical coordinate used by Al-Zanaidi and Hui [1, p. 234] or LES grids with $\Delta z \geq 1m$ near the surface, [27], define a domain discretization too coarse to capture the wave-induced flow structure just described. Although such coarse grids may resolve the large scale motion of the atmospheric Stokes drift and the associated wave-to-atmosphere momentum transfer, they suppress the critical layers and the concomitant wind-to-wave transfer. This way the grid size selects the elements of wind-wave dynamics that are retained and that are ignored in a LES model.

6. Conclusion

Hibbs [22] contemplated the causes that kept the wind waves generation mechanism as a longstanding open physical problem. Within the century between the pioneering work of Kelvin [30] and Donelan and Hui [10, p. 228] dismissal of the contemporary theory for its inability to explain the experimental growth rates, theoretical, empirical and numerical approaches have been employed inconclusively. Over the last one and a half decade, analytic, numerical and open ocean experimental results [26, 18, 27, 24] have confirmed that the mechanism of wind-wave interaction through wave-coherent flow is indeed active and the critical layer pattern in that flow is persistent and pronounced. Such findings offer a new mechanistic perspective on the constraints and challenges through the evolution of ideas and methods relied on to study the problem. Among these have been:

(i) The lack of physical justification and testable predictions, as well as the *'less-than-intuitive'* [14] analytic details, have made the theoretical ideas to be misconstrued, doubted and dismissed, [5, 60, 39, 2, 10, 40, 36].
(ii) Instead of seeking air flow patterns that uniquely do identify the wind-wave interaction mechanism, the experimental studies [16, 58, 57, 21, 19, 9, 11, 53] have been focused on wave growth rates, that do not [7].
(iii) Improper choice of the wave number k instead of the wave age c/u_* as a governing parameter, distortive exponential extrapolation to the surface, variation of the wind-to-wave energy flux through the factor U''/U' due to deviation of the wind profile from its logarithmic shape, and possibly other experimental imperfections and uncertainties, are contributors to the discrepancy [10] between theoretical and measured wave growth rates.
(iv) Empirical studies have been concerned with air flow characteristics weakly affected by the surface waves, e.g. wind profiles, kinetic energy balance, structure functions and spectra, etc., thus pursuing a wave signature that is virtually undetectable in experiments [15, 27].
(v) The wave-coherent flow (Figure 1), a key to the mechanistic description of wind-wave coupling, has been perceived as elusive to both define and detect in a field experiment [46, p. 108], [20, p. 101], [31, p. 72].
(vi) Numerical studies have relied on concepts, tools and computational grids suitable for turbulent flows. As turbulence differs from the wave-coherent flow in its scales and symmetries, resolving the wave-coherent flow, and by extension the wind-wave interaction, requires computational grids much finer than those used so far in LES [27].

These constraints and challenges may offer at least a partial answer to the question posed by Hibbs' [22], that is, why for more than a century understanding the dynamics of wind-wave interaction has been a tenacious physical problem.

References

1. Al-Zanaidi, M.A., Hui, W.H., 1984. Turbulent airflow over water waves-a numerical study. J. Fluid Mech. 148, 225–246.
2. Barnett, T.P., Kenyon, K.E., 1975. Recent advances in the study of wind waves. Rep. Prog. Phys. 38, 667–729.
3. Batchelor, G.K., 1951. Pressure fluctuations in isotropic turbulence. Proc. Camb. Phil. Soc. 47, 359–374.
4. Bergström, H., Smedman, A.S., 1995. Stably stratified flow in a marine atmospheric surface layer. Boundary-Layer Meteorology 72, 239–265.
5. Bryant, P.J., 1965. The generation of water waves by wind. Fluid Dynamics Transactions 2, 573–576.
6. Charnock, H., 1956. Statistics and aerodynamics of the sea surface. Nature 177, 62–63.
7. Davis, R.E., 1970. On the turbulent flow over a wavy boundary. J. Fluid Mech. 42, 721–731.
8. Donelan, M., 1990. The Sea. John Wiley & Sons, Inc., New York. volume 9 of *Ocean Engineering Science*. chapter Air-Sea Interaction. pp. 239–292.
9. Donelan, M.A., 1999. Wind Induced Growth and Attenuation of Laboratory Waves. Clarendon Press, Oxford. pp. 183–194.
10. Donelan, M.A., Hui, W.H., 1990. Mechanics of Ocean Surface Waves. Springer Netherlands, Dordrecht. pp. 209–246.
11. Donelan, M.A., Madsen, N., Kahma, K., Tsanis, I., Drennan, W., 1999. Aparatus for atmospheric surface layer measurements over waves. J Atmos Oceanic Tech 16, 1172–1182.
12. Eckart, C., 1953. The generation of wind waves on a water surface. Journal of Applied Physics 24, 1485–1494.
13. Edson, J., Fairall, C., Sullivan, P., 2006. Evaluation and continued improvements to the TOGA COARE 3.0 algorithm using CBLAST data, in: 27th Conference on Hurricanes and Tropical Meteorology, American Meteorological Society Committee on Tropical Meteorology and Tropical Cyclones. p. 7C.1.
14. Edson, J., Paluszkiewicz, T., Sandgathe, S., Vincent, L., Goodman, L., Curtin, T., Hollister, J., Colton, M., Anderson, S., Andreas, E., Burk, S., Chen, S., Crescenti, G., D'Asaro, E., Davidson, K., Donelan, M., Doyle, J., Farmer, D., Gargett, A., Graber, H., Haidvogel, D., Kepert, J., Mahrt, L., Martin, M., McClean, J., McGillis, W., McKenna, S., McWilliams, J., Niiler, P., Rogers, D., Skyllingstad, E., Sullivan, P., Weller, R., Wilczak, J., 1999. Coupled marine boundary layers and air-sea interaction initiative: Combining process studies, simulations, and numerical models. `http://www.whoi.edu/science/AOPE/dept/r5.pdf`.
15. Edson, J.B., Fairall, C.W., 1998. Similarity relationships in the marine atmospheric surface layer for terms in the TKE and scalar variance budgets. J. Atmos. Sci. 55, 2311–2328.
16. Elliott, J., 1972. Microscale pressure fluctuations near waves being generated by wind. J. Fluid Mech. 54, 427–448.
17. Foken, T., 2006. 50 years of the Monin-Obukhov similarity theory. Boundary-Layer Meteorology 119, 431–447.
18. Grare, L., Lenain, L., Melville, W.K., 2013. Wave-coherent airflow and critical layers over ocean waves. J. Phys. Oceanography 43, 2156–2172.
19. Hare, J., Hara, T., Edson, J., Wilczak, J., 1997. A similarity analysis of the structure of airflow over surface waves. J. Phys. Oceanography 27, 1018–1037.
20. Hasse, L., Dobson, F., 1986. Introductory Physics of the Atmosphere and Ocean. D. Reidel Publ. Comp., Boston.
21. Hasselmann, D., Bösenberg, J., 1991. Field measurements of wave-induced pressure over wind sea and swell. J. Fluid Mech. 230, 391–428.
22. Hibbs, A.R., 1955. The Growth of Water Waves Due to the Action of the Wind. Ph.D. thesis. California Institute of Technology. Pasadena, California. Advisor Richard P. Feynman.
23. Högström, U., Rutgersson, A., Sahlée, E., Smedman, A.S., Hristov, T.S., Drennan, W.M., Kahma, K.K., 2013. Air-sea interaction features in the Baltic sea and at a Pacific trade-wind site: An inter-comparison study. Boundary-Layer Meteorology 147, 139–163. doi:10.1007/s10546-012-

9776-8.
24.Hristov, T., 2017. Generation of Waves by Wind. John Wiley & Sons, Ltd. URL: http://dx.doi.org/10.1002/9781118476406.emoe081, doi:10.1002/9781118476406.emoe081.
25.Hristov, T., Friehe, C., Miller, S., 1998. Wave-coherent fields in air flow over ocean waves: Identification of cooperative behavior buried in turbulence. Phys Rev Lett 81, 5245–5248.
26.Hristov, T., Miller, S., Friehe, C., 2003. Dynamical coupling of wind and ocean waves through wave-induced air flow. Nature 422, 55–58. URL: https://www.nature.com/articles/nature01382.
27.Hristov, T., Ruiz-Plancarte, J., 2014. Dynamic balances in a wavy boundary layer. J. Phys. Oceanography 44, 3185–3194.
28.Janssen, P., 1999. On the effect of ocean waves on the kinetic energy balance and consequences for the inertial dissipation technique. J. Phys. Oceanog. 29, 530–534.
29.Jeffreys, H., 1924. On formation of waves by wind. Proc. Roy. Soc. A107, 189–206.
30.Kelvin, 1871. Hydrokinetic solutions and observations. Phil. Mag. 42, 362–377. Math and Physical Papers **4** 80.
31.Komen, G., Cavaleri, L., Donelan, M., Hasselmann, K., Hasselmann, S., Janssen, P., 1994. Dynamics and Modelling of Ocean Waves. Cambridge University Press, Cambridge.
32.Lighthill, M.J., 1962. Physical interpretation of the mathematical theory of wave generation by wind. J. Fluid Mech. 14, 385–398.
33.Lin, C., 1955. The theory of hydrodynamic stability. Cambridge University Press, Cambridge.
34.Longuet-Higgins, M.S., 1962. The directional spectrum of ocean waves, and processes of wave generation. Proceedings of the Royal Society of London. Series A, Mathematical and Physical Sciences 265, 286–315. URL: http://www.jstor.org/stable/2414167.
35.Mastenbroek, C., 1996. Wind-wave interaction. Ph.D. thesis. Delft Tech. Univ.
36.Miles, J., 1999. The Quasi-Laminar Model for Wind-to-Wave Energy Transfer. Clarendon Press, Oxford. pp. 1–7.
37.Miles, J.W., 1957. On the generation of surface waves by shear flows. J. Fluid Mech. 3, 185–204.
38.Miles, J.W., 1959. On the generation of surface waves by shear flows. part 2. J. Fluid Mech. 6, 568–582.
39.Miles, J.W., 1967. On the generation of surface waves by shear flows. part 5. J. Fluid Mech. 30, 163–175.
40.Miles, J.W., 1998. Johns Hopkins Conference in Environmental Fluid Mechanics. Answering a question from J.C.R. Hunt after oral presentation.
41.Miles, J.W., 2004. Foreword to P. G. Drazin and W. H. Reid, Hydrodynamic Stability. 2nd ed.. Cambridge University Press, New York. pp. xiii–xvii.
42.Mitsuyasu, H., Honda, T., 1982. Wind-induced growth of water waves. J. Fluid Mech. 123, 425–442.
43.Obukhov, A.M., 1949. Pressure fluctuations in a turbulent flow. Dokl. Acad. Nauk SSSR 66, 17–20.
44.Panofsky, H.A., 1974. The atmospheric boundary layer below 150 meters. Ann. Rev. Fluid Mech. 6, 147–177.
45.Phillips, O.M., 1957. On the generation of waves by turbulent wind. J. Fluid Mech. 2, 417–445.
46.Phillips, O.M., 1977. The Dynamics of the Upper Ocean. Cambridge Univ. Press, Cambridge.
47.Poincare, H., 1905. Science and hypothesis. The Walter Scott Publishing Co., Ltd., New York.
48.Pond, S., Smith, S., Hamblin, P., Burling, R., 1966. Spectra of velocity and temperature fluctuations in the atmospheric boundary layer over the sea. Journal of the Atmospheric Sciences 23, 376–386.
49.Pond, S., Stewart, R., Burling, R.W., 1963. Turbulence spectra in the wind over waves. Journal of the Atmospheric Sciences 20, 319–324.
50.Pushkarev, A., Zakharov, V., 2016. Limited fetch revisited: Comparison of wind input terms, in surface wave modeling. Ocean Modelling 103, 18–37.
51.Ruggles, K.W., 1970. The vertical mean wind profile over the ocean for light to moderate winds. J. Appl. Meteorology 9, 389–395.
52.Sajjadi, S.G., Hunt, J.C.R., Drullion, F., 2014. Asymptotic multi-layer analysis of wind over unsteady monochromatic surface waves. Journal of Engineering Mathematics 84, 73–85. URL: https://doi.org/10.1007/s10665-013-9663-4, doi:10.1007/s10665-013-9663-4.
53.Savelyev, I., Haus, B., Donelan, M., 2011. Experimental study on wind-wave momentum flux in strongly forced conditions. J. Phys. Oceanography 41, 1328–1344.
54.Schacher, G., Davidson, K., Houlihan, T., 1981. Measurements of the rate of dissipation of turbulent kinetic energy, ε, over the ocean. Boundary-Layer Meteorology 20, 321–330.
55.Simpson, J.H., 1969. Observations of the directional characteristics of sea waves. Geophysical Journal of the Royal Astronomical Society 17, 93–120. URL: http://dx.doi.org/10.1111/j.1365-246X.1969.tb06380.x, doi:10.1111/j.1365-246X.1969.tb06380.x.
56.Sjöblom, A., Smedman, A.S., 2002. The turbulent kinetic energy budget in the marine atmospheric surface layer. J. Geophys. Res. 107, 6–1–6–18.
57.Snyder, R., Dobson, F., J.A.Elliott, Long, R., 1981. Array measurements of atmospheric pressure fluctuations above surface gravity waves. J. Fluid Mech. 102, 1–59.
58.Snyder, R.L., 1974. A field study of wave-induced pressure fluctuations above surface gravity waves. J. Marine Research 32, 497–531.
59.Soloviev, Y.P., Kudryavtsev, V.N., 2010. Wind-speed undulations over swell: Field experiment and interpretation. Boundary-Layer Meteorology 136, 341 – 363.
60.Stewart, R.W., 1967. Mechanics of the air-sea interface. Phys. Fluids 10, S47–S55. URL: https://doi.org/10.1063/1.1762504.
61.Sullivan, P., McWilliams, J., Moeng, C.H., 2000. Simulation of turbulent flow over idealized water waves. J. Fluid Mech. 404, 47–85.
62.Tollmien, W., 1931. The Production of Turbulence. Technical Memorandum 609. National Advisory Committee for Aeronautics. Washington.
63.Ursell, F., 1956. Wave generation by wind, in: Batchelor, G.K., Davies, R.M. (Eds.), Surveys in Mechanics. Cambridge University Press, pp. 216–249.
64.Van Atta, C., Chen, W., 1970. Structure functions of turbulence in the atmospheric boundary layer over the ocean. J. Fluid Mech. 44, 145–159.
65.Weiler, H.S., Burling, R.W., 1967. Direct measurements of stress and spectra of turbulence in the boundary layer over the sea. J. Atmospheric Sci. 24, 653–664.
66.Wyngaard, J., 1992. Atmospheric turbulence. Ann. Rev. Fluid Mech. 24, 205–233.

Available online at www.sciencedirect.com

ScienceDirect

Procedia IUTAM 26 (2018) 112–123

Procedia IUTAM

www.elsevier.com/locate/procedia

IUTAM Symposium Wind Waves, 4–8 September 2017, London, UK

Nonlinear Fourier Methods for Ocean Waves

Alfred R. Osborne*

Nonlinear Waves Research Corporation, Alexandria, VA 22314, U. S. A.

Abstract

Multiperiodic Fourier series solutions of *integrable nonlinear wave equations* are applied to the study of ocean waves for scientific and engineering purposes. These series can be used to compute analytical formulae for the *stochastic properties* of nonlinear equations, in analogy to the standard approach for linear equations. Here I emphasize analytically computable results for the *correlation functions*, *power spectra* and *coherence functions* of a *nonlinear random process* associated with an integrable nonlinear wave equation. The multiperiodic Fourier series have the advantage that the *coherent structures* of soliton physics are encoded in the formulation, so that *solitons*, *breathers*, *vortices*, etc. are contained in the *temporal evolution* of the nonlinear power spectrum and phases. I illustrate the method for the Korteweg-deVries and nonlinear Schrödinger equations. Applications of the method to the analysis of data are discussed.

Peer-review under responsibility of the scientific committee of the IUTAM Symposium Wind Waves.

Keywords: nonlinear integrable wave equations; finite gap theory; periodic inverse scattering transform; nonlinear Fourier analysis; nonlinear ocean waves; nonlinear numerical methods; nonlinear time series analysis.

1. Multiperiodic Fourier Series as Solutions of Nonlinear Integrable Wave Equations

I give an overview of *multiperiodic Fourier series solutions of integrable, nonlinear wave equations*. I discuss how these series can be used as practical tools for the study of nonlinear ocean waves in one and two dimensions. This perspective has arisen from the pure mathematical algebraic-geometric construction of *single valued, multiperiodic, meromorphic Fourier series* from *Riemann theta functions* [1-3, 23-24, 29, 32]. Modern interest in this area of research has occurred because recent developments have shown how theta functions can be used to solve *nonlinear integrable wave equations* [4, 24], a field known as *finite gap theory* (FGT) or the *periodic inverse scattering transform*. Many of these developments have been used for oceanographic

* Corresponding author. Tel.: +1-703-351-5063
E-mail address: alosborne@protonmail.com

2210-9838
Peer-review under responsibility of the scientific committee of the IUTAM Symposium Wind Waves.
10.1016/j.piutam.2018.03.011

applications [8, 28]. Here I address how multiperiodic, meromorphic Fourier series constructed from theta functions can themselves also be generically useful as mathematical and data analysis tools. The resultant formulation I refer to as *nonlinear Fourier analysis*, where the *Stokes wave* is a single degree of freedom component of the nonlinear Fourier theory, as opposed to the sine wave of linear Fourier series. *Coherent structures* such as solitons, breathers and vortices are all constructed naturally from the Stokes waves by increasing the nonlinearity and/or by phase locking two Stokes components. Nonlinear interactions amongst the Stokes waves are also formulated. The nonlinear Fourier methods are applicable to many aspects of the study of ocean waves from scientific, engineering, numerical, and data analysis perspectives. Sections 1 and 2 give some historical perspective, while Sections 3-6 discuss applications of physically relevant nonlinear wave equations.

Why do I take the path of periodicity/quasiperiodicity offered by FGT for solving the *spectral structure* of *nonlinear wave equations* describing ocean waves? Why would this approach lead to *multiperiodic Fourier series* for their description rather than ordinary *trigonometric Fourier series*? Here are a few of the reasons:

(1) To analyze *time series data* one most often assumes the data to be *periodic* and *discrete*. The fast Fourier transform (FFT), mathematically a discrete Fourier transform, is used for numerical computations.
(2) To develop a natural theory for the *nonlinear Fourier analysis of wave motion* founded on *Stokes wave basis functions* that *interact nonlinearly* with each other.
(3) To have *data analysis* and *analytical approaches* that include *coherent structures in the nonlinear Fourier analysis*. These include *Stokes waves, solitons, breathers and vortices*.
(4) To develop a full theory of *nonlinear random wave trains* for describing *stochastic ocean waves for nonlinear integrable systems*.
(5) To develop a method which naturally extends to *nonintegrability of perturbed (or higher order) nonlinear systems by finding ordinary differential equations that vary adiabatically in the Riemann spectrum of the solitons, breathers, etc*. This is because nearly integrable systems can often be treated with the slow time evolution of their FGT spectra.

An introduction to some of this material is already presented in Osborne (2010), but much of the work presented here is a new approach for *nonlinear*, *stochastic ocean waves*, in which the *correlation function* and *power spectrum*, together with other stochastic properties, can be computed analytically from the multiperiodic series.

Anticipating later results below, we consider the possibility that there exist *spectral solutions* of *integrable, nonlinear wave equations* that have the form of *multidimensional, quasiperiodic Fourier series*

$$u(x,t)=\sum_{\mathbf{n}\in\mathbb{Z}^N} u_{\mathbf{n}} e^{i\mathbf{n}\cdot\mathbf{k}x-i\mathbf{n}\cdot\boldsymbol{\omega}t+i\mathbf{n}\cdot\boldsymbol{\phi}} \tag{1}$$

We will see that these are regarded, from the point of view of algebraic geometry, as the *most general, single valued, multiply periodic meromorphic functions of N variables with 2N periods (Baker-Mumford Theorem)*. Here the wavenumbers $\mathbf{k}$, the frequencies $\boldsymbol{\omega}$ and the phases $\boldsymbol{\phi}$ are vectors of dimension N (the genus). The summation index $\mathbf{n}$ is over the integer lattice $\mathbb{Z}^N$. Eq. (1) can be written as a nested summation:

$$u(x,t)=\sum_{n_1=-\infty}^{\infty}\sum_{n_2=-\infty}^{\infty}\cdots\sum_{n_N=-\infty}^{\infty} u_{n_1,n_2\ldots n_N} e^{i\sum_{i=1}^{N} n_i k_i x-i\sum_{i=1}^{N} n_i\omega_i t+i\sum_{i=1}^{N} n_i\phi_i} \tag{2}$$

I discuss below how series of this type can be constructed with the aid of the *Baker-Mumford Theorem* and from *finite gap theory using theta functions*. But first I consider a number of properties of these series.

1.1. Reduction of Multiperiodic Fourier Series to Ordinary Trigonometric Series

Assume the solution of an integrable, nonlinear partial differential equation is given by (1). For *spatially periodic boundary conditions* $u(x,t)=u(x+L,t)$ the multidimensional, quasiperiodic Fourier series (1) can be written as a trigonometric series with time varying coefficients [28]:

$$u(x,t)=\sum_{n=-\infty}^{\infty} u_n(t)e^{ik_n x}, \qquad k_n=\frac{2\pi n}{L} \tag{3}$$

$$u_n(t)=\sum_{\left\{\mathbf{n}\in\mathbb{Z}^N:\ k_n=\mathbf{n}\cdot\mathbf{k}\right\}} u_{\mathbf{n}} e^{-i\mathbf{n}\cdot\boldsymbol{\omega}t+i\mathbf{n}\cdot\boldsymbol{\phi}}, \qquad \mathbf{n}\cdot\mathbf{k}=\sum_{i=1}^{N} n_i k_i \tag{4}$$

Thus the solution to a nonlinear integrable partial differential equation (1) is reduced to a *Fourier (trigonometric) series* (3) with *time varying coefficients* $u_n(t)$ represented by *quasiperiodic Fourier series* (4). The coefficients $u_n(t)$ are of course quasiperiodic in time due to the incommensurable frequencies. Traditionally $u_n(t)$ are computed by a set of ordinary differential equations obtained by inserting (3) into a particular *integrable* nonlinear wave equation. Eq. (4) solves these ordinary differential equations.

Herein I seek to show utility for the series of type (1) that might help in better understanding some aspects of the nonlinear behavior of ocean waves. Computer codes for the computation of (1) are often assumed to have spatially periodic boundary conditions so that (3, 4) hold [28]: In this case (3) can be computed by the fast Fourier transform (FFT) and (4) contains the coherent structures such as solitons in the specific form for the $u_{\mathbf{n}}$ in terms of the Riemann spectrum, see the developments for the Korteweg-deVries (KdV) equation below. Extension of (1) and (3, 4) to two dimensions (2D*)* is conceptually simple [28]:

$$u(x,y,t)=\sum_{\mathbf{n}\in\mathbb{Z}^N} u_{\mathbf{n}} e^{i\mathbf{n}\bullet\boldsymbol{\kappa}x+i\mathbf{n}\bullet\boldsymbol{\lambda}y-i\mathbf{n}\bullet\boldsymbol{\omega}t+i\mathbf{n}\bullet\boldsymbol{\phi}} \tag{1a}$$

and

$$u(x,y,t)=\sum_{m=-\infty}^{\infty}\sum_{n=-\infty}^{\infty} u_{mn}(t)e^{i\kappa_m x+i\lambda_n y} \tag{3a}$$

where

$$u_{mn}(t)=\sum_{\left\{\mathbf{n}\in\mathbb{Z}^N:\ \kappa_m=\mathbf{n}\bullet\boldsymbol{\kappa},\ \lambda_n=\mathbf{n}\bullet\boldsymbol{\lambda}\right\}} u_{\mathbf{n}} e^{-i\mathbf{n}\bullet\boldsymbol{\omega}t+i\mathbf{n}\bullet\boldsymbol{\phi}}, \qquad \mathbf{n}\bullet\boldsymbol{\kappa}=\sum_{i=1}^{N} n_i\kappa_i, \quad \mathbf{n}\bullet\boldsymbol{\lambda}=\sum_{i=1}^{N} n_i\lambda_i \tag{4a}$$

This is appropriate for integrable equations in 2D such as the Kadomtsev-Petviashvili (KP) and 2+1 Gardner equations.

In the field of oceanography we traditionally use (3, 3a) for Fourier analysis applications and a set of temporal ordinary differential equations are determined for the $u_{mn}(t)$ rather than the series (4, 4a) [9, 35]. For an integrable system (4, 4a) solves the requisite ordinary differential equations, but for a nonintegrable system one might, at the suggestion of Poincaré [29], provide time dependence for the $u_{\mathbf{n}} \rightarrow u_{\mathbf{n}}(t)$ in (4, 4a) (see further discussion below).

1.2. Perspective in Terms of Stokes Waves and Their Interactions

The above multidimensional, quasiperiodic Fourier series can be expressed as:

$$u(x,t)=\sum_{\mathbf{n}\in\mathbb{Z}^N} u_{\mathbf{n}} e^{i\mathbf{n}\bullet\mathbf{k}x-i\mathbf{n}\bullet\boldsymbol{\omega}t+i\mathbf{n}\bullet\boldsymbol{\phi}}=\sum_{n=1}^{N} S_n(x,t)+\text{pairwise nonlinear interactions} \tag{5}$$

By construction the above solution of some nonlinear, integrable wave equation is a *spectral theory of Stokes waves*, $S_n(x,t)$. To see this we note that a single Stokes wave has the form:

$$S_n(x,t)=\sum_{m=-\infty}^{\infty} u_m^n e^{ik_m^n x-i[\omega_m^n(k_m)+\Delta\omega_m^n]t+i\phi_m^n} \tag{6}$$

The *nth* Stokes wave $S_n(x,t)$ has a set of amplitudes u_m^n, wavenumbers k_m^n, frequencies ω_m^n and phases ϕ_m^n. The dispersion relation is represented by $\omega_m^n(k_m)$. Here $\Delta\omega_m^n(k_m^n)$ is the *frequency shift* first identified by Stokes [34]. From the above multidimensional Fourier series represented by *N* nested sums (2), we see that each of these sums, in the absence of the others, is a single Stokes wave, together with the usual Stokes "amplitude dependent frequency correction," but here computed for a particular nonlinear integrable wave equation. The interactions are accounted for by pairwise cross terms among the individual Stokes waves in (2) [28].

We see that the multiperiodic Fourier series have all of the Stokes wave harmonics, together with all the "cross harmonics" among the Stokes waves. The Stokes wave components u_m^n form the "bound modes" in terms of the index *m* (phase locked together) and the Stokes waves $S_n(x,t)$ themselves are the "free modes" that can move relative to one another and undergo pairwise scattering from the others in the nonlinear dynamics.

2. Construction of Meromorphic Fourier Series from Theta Functions

2.1. The Baker-Mumford Theorem

The formal construction of multiperiodic, meromorphic Fourier series is a problem from 19th century mathematics, see Baker [1-3]. A more modern approach is due to Mumford [23]. I summarize the

Baker-Mumford Theorem – The most general, single-valued, multiply periodic, meromorphic functions of N variables with $2N$ sets of periods (obeying the necessary relations, see Baker [3], p. 224), can be expressed by means of *theta functions*. The construction is obtained in *only three ways*:

$$\text{(i)} \qquad \partial_{xx} \ln \theta(\mathbf{z}) \tag{7}$$

$$\text{(ii)} \qquad \partial_x \ln\left(\frac{\theta(\mathbf{z}+\mathbf{a})}{\theta(\mathbf{z})}\right) \tag{8}$$

$$\text{(iii)} \qquad \frac{\prod_{n=1}^{N}\theta(\mathbf{z}-\mathbf{a}_n)}{\prod_{n=1}^{N}\theta(\mathbf{z}-\mathbf{b}_n)}, \qquad \sum_{n=1}^{N}\mathbf{a}_n = \sum_{n=1}^{N}\mathbf{b}_n \tag{9}$$

where the *theta functions* have the form

$$\theta(\mathbf{z}) = \sum_{\mathbf{n}\in\mathbb{Z}^N} \theta_{\mathbf{n}} e^{i\mathbf{n}\bullet\mathbf{z}}, \qquad \theta_{\mathbf{n}} = e^{-\frac{1}{2}\mathbf{n}\bullet\tilde{\mathbf{B}}\mathbf{n}} \tag{10}$$

and $\tilde{\mathbf{B}}$ is the *period matrix*. Note that, according to this theorem, one describes the most *general* meromorphic functions from theta functions in only three ways, although a construction method is not provided in the theorem. As will be seen below $\mathbf{z} = \mathbf{k}x - \boldsymbol{\omega}t + \boldsymbol{\phi}$ for solutions of nonlinear, integrable wave equations. The utility of this theorem is therefore quite striking and has a number of *practical* uses as seen below.

Furthermore, the implication is that each of the three forms (7)-(9) for constructing *multiply periodic, meromorphic functions* using theta functions can be written explicitly in terms *of multidimensional, quasiperiodic Fourier series*. This means explicitly that for practical applications one must compute:

$$\partial_{xx} \ln \theta(x,t) = \sum_{\mathbf{n}\in\mathbb{Z}^N} u_{\mathbf{n}} e^{i\mathbf{n}\bullet\mathbf{k}x - i\mathbf{n}\bullet\boldsymbol{\omega}t + i\mathbf{n}\bullet\boldsymbol{\phi}} \tag{11}$$

$$\frac{\theta(x,t\,|\,\mathbf{B},\boldsymbol{\phi}^-)}{\theta(x,t\,|\,\mathbf{B},\boldsymbol{\phi}^+)} = \sum_{\mathbf{n}\in\mathbb{Z}^N} u_{\mathbf{n}} e^{i\mathbf{n}\bullet\mathbf{k}x - i\mathbf{n}\bullet\boldsymbol{\omega}t + i\mathbf{n}\bullet\boldsymbol{\phi}} \tag{12}$$

$$\frac{\prod_{n=1}^{N}\theta(\mathbf{z}-\mathbf{a}_n\,|\,\mathbf{B})}{\prod_{n=1}^{N}\theta(\mathbf{z}-\mathbf{b}_n\,|\,\mathbf{B})} = \sum_{\mathbf{n}\in\mathbb{Z}^N} u_{\mathbf{n}} e^{i\mathbf{n}\bullet\mathbf{k}x - i\mathbf{n}\bullet\boldsymbol{\omega}t + i\mathbf{n}\bullet\boldsymbol{\phi}} \tag{13}$$

where the parameters in the series on the right anticipate the physics of the solutions of a particular wave equation: the wavenumber $\mathbf{k}$, frequency $\boldsymbol{\omega}$, and phase $\boldsymbol{\phi}$ vectors and the coefficients $u_{\mathbf{n}}$ that are determined from the *theta function parameters* (specifically the period matrix $\tilde{\mathbf{B}}$) of a *particular nonlinear wave equation*. The Baker-Mumford theorem does not tell us how to make this construction, but I adapt a method of [40] for this purpose. Specific examples are given below for the KdV and nonlinear Schrödinger (NLS) equations.

In a further *tour de force* Baker [2] essentially derived the KdV hierarchy and KP equation by using the bilinear differential operator D (today we attribute this to Hirota [17]), identities of Pfaffians, symmetric functions, hyperelliptic σ-functions and $\wp$-functions. The identification between Baker's differential equations and the soliton equations means that Baker essentially discovered the KdV hierarchy and the KP equation over one hundred years ago. Baker used bilinear forms in his work, although he did not address soliton solutions.

Reevaluation of Baker's work from the perspective of modern soliton theory can be found in a very interesting paper by Matsutani [21].

2.2. Relationship of Theta Functions to Nonlinear Partial Differential Equations

Mumford [20] discusses the relationship of theta functions to the solution of several important nonlinear wave equations. He uses Fay's trisecant identity [12], which takes the form:

$$\sum_{n=1}^{3} c_i \theta(\mathbf{z}+\mathbf{a}_n)\theta(\mathbf{z}+\mathbf{b}_n) = 0 \tag{14}$$

Details of the coefficient values c_i are given in the above papers. Fay's identity is a fundamental identity of theta functions that holds for *period matrices of algebraic curves*, but *not* for *period matrices on general Abelian varieties*. While the limitation to algebraic curves restricts the class of wave equations one can study, Mumford was nevertheless able to construct theta function solutions to a number of equations of mathematical physics using theta functions. These include the KdV, the KP, the sine-Gordon, the nonlinear Schrödinger, the massive Thirring model and presumably many other equations. The important idea here is that the three ways to construct single valued, multiperiodic, meromorphic functions from theta functions, as specified in the above Baker-Mumford theorem, reappear directly in the construction of multiperiodic Fourier series solutions of the integrable wave equations. Table 1 gives a number of results.

Table 1. Integrable equations and solutions in terms of theta functions as derived from the Fay trisecant identity [24].

Name of equation	The equation	Solution in terms of theta functions
Korteweg-deVries	$u_t + 6uu_x + u_{xxx} = 0$	$u(x,t) = 2\partial_{xx} \ln \theta(x,t)$
Kadomtsev-Petviashvili	$(u_t + 6uu_x + u_{xxx})_x + u_{yy} = 0$	$u(x,y,t) = 2\partial_{xx} \ln \theta(x,y,t)$
Nonlinear Schrödinger	$iu_t + u_{xx} + 2\lvert u\rvert^2 u = 0$	$u(x,t) = \theta(x,t \mid \mathbf{B},\boldsymbol{\phi}^-) / \theta(x,t \mid \mathbf{B},\boldsymbol{\phi}^+)$
Sine-Gordon	$u_{xx} - u_{tt} = \sin u$	$u(x,t) = 2i \ln[\theta^*(x,t)/\theta(x,t)]$
Gardner	$u_t + 6uu_x + u_{xxx} + u^2 u_x = 0$	$u(x,t) = 2\partial_x \ln[\theta(x,t \mid \mathbf{B},\boldsymbol{\phi}^-) / \theta(x,t \mid \mathbf{B},\boldsymbol{\phi}^+)]$

It is clear from the Baker-Mumford theorem that it is quite natural to find the solutions in Table 1 are single valued, quasiperiodic, meromorphic Fourier series. Construction of these series from the right hand column of Table 1 and the Riemann spectrum of FGT is a goal of this paper.

2.3. Finite Gap Theory of Nonlinear Wave Equations

The *periodic inverse scattering transform*, or *finite gap theory*, solves nonlinear wave equations starting with knowledge of the Lax pair [4, 22]. The spatial part of the Lax pair is an eigenvalue problem that provides a set of eigenvalues from which particular algebro-geometric loop integrals determine the parameters of the Riemann theta functions. The phase information provides a solution to the Cauchy problem. Random phases allow for the study of nonlinear stochastic systems. The full FGT solution of an integrable equation is contained in the eigenvalue problem, loop integrals and theta functions, together with the time dependant part of the *Lax pair*. The beauty of finite gap theory is that all the information about the solution can be computed *explicitly*.

It is worthwhile noting that the *Its-Matveev formula* for the KdV equation

$$u(x,t) = 2\partial_{xx} \ln \theta(x,t) \tag{15}$$

is a *tour de force* in soliton theory. The original periodic solutions found were related to the hyperelliptic functions, but Its and Matveev brought the power of Riemann theta functions to the forefront of the field. The Its-Matveev formula was hinted at in the work of Baker and Hirota (see also Mumford [24], Table 1), but the real breakthrough came with the derivation of the theta function solutions of the KdV equation using FGT. For those interested in finite gap theory and a historical review by one of the main practitioners, see Matveev [22]. The formula (15) is not very useful for computing the correlation function for random function solutions of KdV. To compute the correlation function of such solutions we use (11) from the Baker-Mumford theorem: To

do this we require a method to compute the coefficients $u_{\mathbf{n}}$ from the Its-Matveev formula. This provides us with the multiperiodic Fourier series solution of KdV. The approach is given in Section 4.1 below.

3. Random Phase Approximation for the Solutions of Nonlinear, Integrable Wave Equations

3.1. The Nonlinear Random Phase Approximation

Osborne [26] has suggested that a kind of *nonlinear random phase approximation* be applied to nonlinear evolution equations. Thus, when the phase vector $\boldsymbol{\phi}$ appears in a theta function or in a multiperiodic series such as (1), (2) or (4), we will often find it is convenient to assume that *the components of the vector* $\boldsymbol{\phi}$ *are uniformly distributed random numbers*. This idea parallels the use of random phases in the Fourier transform, which is often assumed in many applications of wind waves. For example, when we analyse a time series, we typically find that the Fourier analysis gives us random phases as a function of frequency. Thus it seems natural to take the vector phases $\boldsymbol{\phi}$ as random numbers in multiperiodic Fourier series for *nonlinear* systems. However, see eq. (21) below for further perspective.

3.2. Explicit Forms for the Power Spectrum and Other Properties of Random Function Solutions

The power spectrum is usually obtained from a time series by taking the Fourier transform and then graphing the squared-amplitudes as a function of frequency. Let us see how this plays out for a system that uses multiperiodic, meromorphic functions, for which we also assume *spatially periodic boundary conditions*. We use (3) to compute the correlation function

$$C(\mathcal{L}) = \langle u(x,t)u(x+\mathcal{L},t)\rangle\,, \qquad \langle . \rangle = \frac{1}{L}\int_0^L . \, dx \tag{16}$$

where the *spatial average* has the symbol $\langle . \rangle$. We find

$$C(\mathcal{L},t) = \langle u(x,t)u(x+\mathcal{L},t)\rangle = \sum_{n=-\infty}^{\infty} u_n(t)u_n^*(t)e^{ik_n\mathcal{L}} = |u_o(t)|^2 + \frac{1}{2}\sum_{n=1}^{\infty}|u_n(t)|^2\cos(k_n\mathcal{L}) \tag{17}$$

Now address the Fourier coefficients in terms of their modulus $A_n(t)$ and phases $\Phi_n(t)$ from (4)

$$u_n(t) = x_n(t) + iy_n(t) = A_n(t)e^{i\Phi_n(t)} \tag{18}$$

where

$$x_n(t) = \sum_{\{\mathbf{n}\in\mathbb{Z}^N:\ I(\mathbf{n}\bullet\mathbf{k})=n\}} u_{\mathbf{n}}\cos(\mathbf{n}\bullet\boldsymbol{\omega}t - \mathbf{n}\bullet\boldsymbol{\phi}), \qquad y_n(t) = -i\sum_{\{\mathbf{n}\in\mathbb{Z}^N:\ I(\mathbf{n}\bullet\mathbf{k})=n\}} u_{\mathbf{n}}\sin(\mathbf{n}\bullet\boldsymbol{\omega}t - \mathbf{n}\bullet\boldsymbol{\phi}) \tag{19}$$

The *spectral moduli* are given by:

$$A_n(t) = |u_n(t)| = \sqrt{x_n^2(t) + y_n^2(t)} = \tag{20}$$

$$= \left\{\left[\sum_{\{\mathbf{n}\in\mathbb{Z}^N:\ I(\mathbf{n}\bullet\mathbf{k})=n\}} u_{\mathbf{n}}\cos(\mathbf{n}\bullet\boldsymbol{\omega}t - \mathbf{n}\bullet\boldsymbol{\phi})\right]^2 + \left[\sum_{\{\mathbf{n}\in\mathbb{Z}^N:\ I(\mathbf{n}\bullet\mathbf{k})=n\}} u_{\mathbf{n}}\sin(\mathbf{n}\bullet\boldsymbol{\omega}t - \mathbf{n}\bullet\boldsymbol{\phi})\right]^2\right\}^{1/2}$$

and the time evolution of the *linear Fourier phases* $\Phi_n(t)$ in terms of the *FGT phases* $\phi = [\phi_1,\phi_2..\phi_N]$:

$$\tan\Phi_n(t) = \frac{y_n(t)}{x_n(t)} = -\frac{\sum_{\{\mathbf{n}\in\mathbb{Z}^N:\ I(\mathbf{n}\bullet\mathbf{k})=n\}} u_{\mathbf{n}}\sin(\mathbf{n}\bullet\boldsymbol{\omega}t - \mathbf{n}\bullet\boldsymbol{\phi})}{\sum_{\{\mathbf{n}\in\mathbb{Z}^N:\ I(\mathbf{n}\bullet\mathbf{k})=n\}} u_{\mathbf{n}}\cos(\mathbf{n}\bullet\boldsymbol{\omega}t - \mathbf{n}\bullet\boldsymbol{\phi})} \tag{21}$$

Hence the time evolution of the *power spectrum* is given by:

$$P(k_n,t) = |u_n(t)|^2 = \left[\sum_{\{\mathbf{n}\in\mathbb{Z}^N:\ I(\mathbf{n}\bullet\mathbf{k})=n\}} u_{\mathbf{n}}\cos(\mathbf{n}\bullet\boldsymbol{\omega}t - \mathbf{n}\bullet\boldsymbol{\phi})\right]^2 + \left[\sum_{\{\mathbf{n}\in\mathbb{Z}^N:\ I(\mathbf{n}\bullet\mathbf{k})=n\}} u_{\mathbf{n}}\sin(\mathbf{n}\bullet\boldsymbol{\omega}t - \mathbf{n}\bullet\boldsymbol{\phi})\right]^2 \tag{22}$$

One can compute triple correlation functions in a similar way for integrable soliton equations. This is the analytical form of the time varying power spectrum for a multiperiodic, meromorphic Fourier series solution to an integrable, nonlinear partial differential equation for spatially periodic boundary conditions. We have *collapsed* the FGT spectrum $u_{\mathbf{n}}$ (see (32) below) onto the time varying linear Fourier spectrum $u_n(t)$ (see (3, 4) above).

4. The Korteweg-deVries Equation

4.1. Construction of Multiperiodic Meromorphic Fourier Series Solutions of the KdV and exKdV Equations

The above results are possible because theta functions have remarkable properties and these allow one to discuss *an algebra of theta functions,* their derivatives, integrals. Furthermore theta functions can be *added, subtracted, multiplied and divided* as exploited below. As an example for the construction of a multiperiodic Fourier series, I now discuss the KdV and extended KdV (exKdV) equations.

The next equation above KdV in the Whitham hierarchy (exKdV) [15, 36] is:

$$u_t + 6uu_x + u_{xxx} = \lambda_1 u_{xxxxx} + \lambda_2 u_x u_{xx} + \lambda_3 uu_{xxx} + \lambda_4 u^2 u_x \tag{23}$$

Here the coefficients are given by $\lambda_1 = 1$, $\lambda_2 = 100/19$, $\lambda_3 = 230/19$ and $\lambda_4 = -60/19$. The *asymptotic solution* to (23) is given by the *near identity transformation* (Lie-Kodama transform [15, 18, 19, 27]):

$$u = 2Z_x + \varepsilon\left[4\lambda_1 Z_x^2 + 2\lambda_2 Z_{xxx} + 4\lambda_3 Z Z_{xx}\right] \tag{24}$$

where $Z(x,t) = \partial_x \ln\theta(x,t)$.

What follows will be based upon the multidimensional Fourier series for Z:

$$Z(x,t) = \partial_x \ln\theta(x,t) = \frac{\theta_x(x,t)}{\theta(x,t)} = \theta_x(x,t)\theta^{-1}(x,t) = \sum_{\mathbf{n}\in\mathbb{Z}^N} Z_{\mathbf{n}} e^{i\mathbf{n}\bullet\mathbf{k}x - i\mathbf{n}\bullet\boldsymbol{\omega}t + i\mathbf{n}\bullet\boldsymbol{\phi}} \tag{25}$$

Here $\theta^{-1}(x,t)$ means the series

$$Q(x,t) = \frac{1}{\theta(x,t)} = \sum_{\mathbf{n}\in\mathbb{Z}^N} Q_{\mathbf{n}} e^{i\mathbf{n}\bullet\mathbf{k}x - i\mathbf{n}\bullet\boldsymbol{\omega}t + i\mathbf{n}\bullet\boldsymbol{\phi}}, \qquad Q_{\mathbf{n}} = \theta_{\mathbf{n}}^{-1} = \sum_{\mathbf{m}\in\mathbb{Z}^N} \left\{ e^{-(\mathbf{n}-\mathbf{m})\bullet\tilde{\mathbf{B}}(\mathbf{n}-\mathbf{m})/2} \right\}^{-1} \delta_{\mathbf{m}} \tag{26}$$

where $\theta_{\mathbf{n}}^{-1}$ are the coefficients of the series (26). The "-1" serves to remind us that they are coefficients of the series for $\theta^{-1}(x,t)$; $Q_{\mathbf{n}} = \theta_{\mathbf{n}}^{-1}$ does *not* mean $1/\theta_{\mathbf{n}}$, but is given by the right equation of (26), a result that I have determined by a method of Zygmund [40] for ordinary Fourier series, but which is here applied to multiperiodic Fourier series. To get the result (26) set $Q(x,t) = 1/\theta(x,t)$ so that $\theta(x,t)Q(x,t) = 1$, implying a *convolution* for the coefficients of the product $\theta(x,t)Q(x,t)$:

$$\sum_{\mathbf{m}\in\mathbb{Z}^N} \theta_{\mathbf{n}-\mathbf{m}} Q_{\mathbf{m}} = \boldsymbol{\delta}_{\mathbf{n}}, \qquad \boldsymbol{\delta} = \{\delta_{\mathbf{n}}\} = \begin{bmatrix} \vdots \\ 0 \\ 1 \\ 0 \\ \vdots \end{bmatrix}$$

and in matrix-vector notation we have $\tilde{\boldsymbol{\theta}}\mathbf{Q} = \boldsymbol{\delta}$ where $\tilde{\boldsymbol{\theta}} = \{\theta_{\mathbf{n}-\mathbf{m}}\}$ is an infinite dimensional matrix formed from the coefficients $\theta_{\mathbf{n}} = \exp(-\mathbf{n}\bullet\mathbf{B}\mathbf{n}/2)$ of the theta function and $\mathbf{Q} = \{Q_{\mathbf{n}}\}$ is a vector we seek. This leads to the coefficients $\mathbf{Q} = \tilde{\boldsymbol{\theta}}^{-1}\boldsymbol{\delta}$ (or $\{Q_{\mathbf{n}}\} = \{\theta_{\mathbf{n}-\mathbf{m}}\}^{-1}\{\boldsymbol{\delta}_{\mathbf{m}}\}$) of the inverse series (26). Here $\boldsymbol{\delta}$ is an infinite length column vector whose elements are all zero except for that at the central position which is 1, i.e. for which $\mathbf{n} = 0$. The convergence of the series (25, 26) occurs because of the extraordinary properties of theta functions [1-4, 22, 23]. In this way one is led to the conclusion that the matrix $\tilde{\boldsymbol{\theta}} = \{\theta_{\mathbf{n}-\mathbf{m}}\}$ is invertible (see Zygmund [40] for arguments relating to the inversion of ordinary trigonometric series in this way). Furthermore:

$$\theta_x(x,t) = i\sum_{\mathbf{n}\in\mathbb{Z}^N} (\mathbf{n}\bullet\mathbf{k})\theta_{\mathbf{n}} e^{i\mathbf{n}\bullet\mathbf{k}x - i\mathbf{n}\bullet\boldsymbol{\omega}t + i\mathbf{n}\bullet\boldsymbol{\phi}} \tag{27}$$

To compute the multiperiodic Fourier series (25) we compute the product of the two series $\theta_x(x,t)$ and $\theta^{-1}(x,t)$, so that the coefficients of the product $\theta_x(x,t)\theta^{-1}(x,t)$ are a convolution of the coefficients

$$Z_{\mathbf{n}} = i \sum_{\mathbf{m}\in\mathbb{Z}^N} (\mathbf{m}\bullet\mathbf{k})\theta_{\mathbf{m}}\theta^{-1}_{\mathbf{n}-\mathbf{m}} = i \sum_{\mathbf{m}\in\mathbb{Z}^N} (\mathbf{n}-\mathbf{m})\mathbf{m}\bullet\mathbf{k}\,\theta_{\mathbf{n}-\mathbf{m}}\theta^{-1}_{\mathbf{m}} \tag{28a}$$

$$\theta_{\mathbf{n}-\mathbf{m}} = \exp(-(\mathbf{n}-\mathbf{m})\bullet\mathbf{B}(\mathbf{n}-\mathbf{m})/2), \quad Q_{\mathbf{m}} = \theta^{-1}_{\mathbf{m}} = \sum_{\mathbf{n}\in\mathbb{Z}^N} \left\{ e^{-(\mathbf{m}-\mathbf{n})\bullet\tilde{\mathbf{B}}(\mathbf{m}-\mathbf{n})/2} \right\}^{-1} \delta_{\mathbf{n}} \tag{28b}$$

We see that the $Z_{\mathbf{n}}$ are derived entirely from the coefficients $\theta_{\mathbf{n}}$ of the theta function (10).

It is now easy to see that the coefficients of the KdV equation solution (1) are given by

$$u(x,t) = 2Z_x = 2i \sum_{\mathbf{n}\in\mathbb{Z}^N} (\mathbf{n}\bullet\mathbf{k}) Z_{\mathbf{n}} e^{i\mathbf{n}\bullet\mathbf{k}x - i\mathbf{n}\bullet\boldsymbol{\omega}t + i\mathbf{n}\bullet\boldsymbol{\phi}} = \sum_{\mathbf{n}\in\mathbb{Z}^N} u_{\mathbf{n}} e^{i\mathbf{n}\bullet\mathbf{k}x - i\mathbf{n}\bullet\boldsymbol{\omega}t + i\mathbf{n}\bullet\boldsymbol{\phi}} \tag{29}$$

which means that (see (28a) for other forms for $Z_{\mathbf{n}}$):

$$u_{\mathbf{n}} = 2i(\mathbf{n}\bullet\mathbf{k})Z_{\mathbf{n}} = -2(\mathbf{n}\bullet\mathbf{k}) \sum_{\mathbf{m}\in\mathbb{Z}^N} (\mathbf{m}\bullet\mathbf{k})\theta_{\mathbf{m}}\theta^{-1}{}_{\mathbf{n}-\mathbf{m}} \tag{30}$$

It is interesting to consider the *physical meaning* for (29, 30). To do this, write the convolution (30) in the following way

$$c_{\mathbf{n}} = \sum_{\mathbf{m}\in\mathbb{Z}^N} a_{\mathbf{m}} b_{\mathbf{n}-\mathbf{m}} = \sum_{\mathbf{m}+\mathbf{l}=\mathbf{n}\in\mathbb{Z}^N} a_{\mathbf{m}} b_{\mathbf{l}} \tag{31}$$

Hence, the *convolution* between the coefficients $a_{\mathbf{n}}, b_{\mathbf{n}}$ of the product of two multidimensional Fourier series can also be written as a *three-wave interaction coefficient*. Therefore (30), the *coefficients of the multidimensional Fourier series solutions of the KdV equation,* are given by two expressions:

$$u_{\mathbf{n}} = 2i(\mathbf{n}\bullet\mathbf{k}) \sum_{\mathbf{m}\in\mathbb{Z}^N} (\mathbf{m}\bullet\mathbf{k})\theta_{\mathbf{m}}\theta^{-1}_{\mathbf{n}-\mathbf{m}} = 2i(\mathbf{n}\bullet\mathbf{k}) \sum_{\mathbf{m}+\mathbf{l}=\mathbf{n}\in\mathbb{Z}^N} (\mathbf{m}\bullet\mathbf{k})\theta_{\mathbf{m}}\theta^{-1}_{\mathbf{l}} \tag{32}$$

We have an exact equivalency between the *convolution operation* and the *three-wave interaction coefficients* for the solution of the KdV equation. Since the coefficients of the theta function Fourier series (10), $\theta_{\mathbf{n}} = \exp[-\mathbf{n}\bullet\tilde{\mathbf{B}}\mathbf{n}/2]$, contain the *solitons* as *diagonal elements of the period matrix* $\tilde{\mathbf{B}}$, we now have an *exact connection* between the *solitons* (characterized by the *Riemann spectrum*) and *three wave interactions* in the solutions of the KdV equation. Since we have $Z(x,t)$ in (25, 28) we can compute the asymptotic solution of the extended KdV equation via (24). This illustrates the advantage of combining multiperiodic, meromorphic Fourier series from FGT with Lie-Kodama transforms for computing perturbed solutions of nonlinear wave equations.

4.2. Computation of the Nonlinear Dispersion Relation for the KdV Equation

Consider the KdV equation in the usual dimensional form:

$$u_t + c_o u_x + \alpha u u_x + \beta u_{xxx} = 0 \tag{33}$$

The meromorphic series ansatz is

$$u(x,t) = \sum_{\mathbf{n}\in\mathbb{Z}^N} u_{\mathbf{n}} e^{i\mathbf{n}\bullet\mathbf{k}x - i\mathbf{n}\bullet\boldsymbol{\omega}t + i\mathbf{n}\bullet\boldsymbol{\phi}} \tag{34}$$

Remember that $u_{\mathbf{n}}$ can be expressed in terms of the theta functions (10). Then

$$u(x,t)u_x(x,t) = i \left(\sum_{\mathbf{m}\in\mathbb{Z}^N} u_{\mathbf{m}} e^{i\mathbf{m}\bullet\mathbf{k}x - i\mathbf{m}\bullet\boldsymbol{\omega}t + i\mathbf{m}\bullet\boldsymbol{\phi}} \right) \left(\sum_{\mathbf{n}\in\mathbb{Z}^N} (\mathbf{n}\bullet\mathbf{k}) u_{\mathbf{n}} e^{i\mathbf{n}\bullet\mathbf{k}x - i\mathbf{n}\bullet\boldsymbol{\omega}t + i\mathbf{n}\bullet\boldsymbol{\phi}} \right) \tag{35}$$

This results in a new series whose coefficients are a convolution of the coefficients of the series for $u(x,t)$ and $u_x(x,t)$:

$$u(x,t)u_x(x,t) = i\sum_{\mathbf{n}\in\mathbb{Z}^N} U_{\mathbf{n}} e^{i\mathbf{n}\bullet\mathbf{k}\,x - i\mathbf{n}\bullet\omega\, t + i\mathbf{n}\bullet\phi}, \quad U_{\mathbf{n}} = \sum_{\mathbf{m}\in\mathbb{Z}^N} (\mathbf{m}\bullet\mathbf{k}) u_{\mathbf{m}} u_{\mathbf{n}-\mathbf{m}} = \sum_{\mathbf{m}+\mathbf{l}=\mathbf{n}\in\mathbb{Z}^N} (\mathbf{m}\bullet\mathbf{k}) u_{\mathbf{m}} u_{\mathbf{l}} \quad (36)$$

Note that $U_{\mathbf{n}}$ is simultaneously a convolution and three-wave interaction in (36). KdV then becomes:

$$\begin{aligned} &-i\sum_{\mathbf{n}\in\mathbb{Z}^N} (\mathbf{n}\bullet\boldsymbol{\omega}) u_{\mathbf{n}} e^{i\mathbf{n}\bullet\mathbf{k}\,x - i\mathbf{n}\bullet\boldsymbol{\omega}\,t + i\mathbf{n}\bullet\boldsymbol{\phi}} + ic_o \sum_{\mathbf{n}\in\mathbb{Z}^N} (\mathbf{n}\bullet\mathbf{k}) u_{\mathbf{n}} e^{i\mathbf{n}\bullet\mathbf{k}\,x - i\mathbf{n}\bullet\boldsymbol{\omega}\,t + i\mathbf{n}\bullet\boldsymbol{\phi}} + \\ &+ i\alpha \sum_{\mathbf{n}\in\mathbb{Z}^N} U_{\mathbf{n}} e^{i\mathbf{n}\bullet\mathbf{k}\,x - i\mathbf{n}\bullet\boldsymbol{\omega}\,t + i\mathbf{n}\bullet\boldsymbol{\phi}} - i\beta \sum_{\mathbf{n}\in\mathbb{Z}^N} (\mathbf{n}\bullet\mathbf{k})^3 u_{\mathbf{n}} e^{i\mathbf{n}\bullet\mathbf{k}\,x - i\mathbf{n}\bullet\boldsymbol{\omega}\,t + i\mathbf{n}\bullet\boldsymbol{\phi}} = 0 \end{aligned} \quad (37)$$

which means that

$$\mathbf{n}\bullet\boldsymbol{\omega} = c_o \mathbf{n}\bullet\mathbf{k} - \beta(\mathbf{n}\bullet\mathbf{k})^3 + \alpha U_{\mathbf{n}} / u_{\mathbf{n}} \quad (38)$$

This latter is the *N-dimensional nonlinear dispersion relation*. Note that the last term, which includes a convolution, is the *N*-dimensional nonlinear Stokes wave frequency correction. We could also write the above result in the following way:

$$\Omega_{\mathbf{n}} = c_o \mathbf{K}_{\mathbf{n}} - \beta \mathbf{K}_{\mathbf{n}}^3 + \alpha U_{\mathbf{n}} / u_{\mathbf{n}} \quad (39)$$

for $\Omega_{\mathbf{n}} = \mathbf{n}\bullet\boldsymbol{\omega}$ and $\mathbf{K}_{\mathbf{n}} = \mathbf{n}\bullet\mathbf{k}$. So all the frequencies of the discretuum are computed in this way. The Stokes wave for one degree of freedom agrees with that in Whitham for KdV [36].

4.3. Integrable Turbulence

Zakharov has studied integrable turbulence for the KdV equation [39] for a rarified soliton gas. He derived a soliton-gas kinetic equation for the KdV equation using the inverse scattering method. More recently, the kinetic equation for a *dense* soliton gas for KdV has been found by El and Kamchatnov [11] by taking the thermodynamic limit of the Whitham equations to obtain a nonlinear integrodifferential equation for the spectral measure. This result generalizes Zakharov's result for a rarified soliton gas. Experimentally Costa et al [8] have studied soliton turbulence in the surface wave field in Currituck Sound on the coast of North Carolina. Future work will emphasize the study of soliton gases using both the El-Kamchatnov method and finite gap theory, in theoretical, numerical and experimental contexts.

4.4. Fermi-Pasta-Ulam Recurrence

Fermi-Pasta-Ulam recurrence was discovered in the early 1950s and published in a Los Alamos report [14]. The problem was shown to be equivalent to using the Fourier transform to reduce the KdV equation to a set of ordinary differential equations (for spatially periodic boundary conditions) and then to study the time evolution of these equations [20]. Surprisingly, for a sine wave initial condition, the wave dynamics almost returned to the initial conditions after a *recurrence time* [25, 28]. From the perspective given herein the solution to KdV is given by (1) and the Fourier reduction of the equation to ordinary differential equations (for spatially periodic boundary conditions) is given by (2) and (3). The ordinary differential equations are solved by (3), a meromorphic Fourier series with incommensurable frequencies. This means that the dynamics of the ordinary differential equations (3) is quasiperiodic. Therefore FPU recurrence is approximate, not exact, due to the quasiperiodic nature of the ordinary differential equations. The study of the problem in the soliton limit is enlightening and is the topic of a future paper.

4.5. Wind Waves

The study of wind waves is normally based on the Hasselmann equation [16], a kinetic equation that is driven by wind forcing, by damping due to wave breaking and by four-wave nonlinear interactions. This is the basis of models such as WaveWatch III and WAM. The last important term is the full Boltzmann, nonlinear

four-wave interactions represented by the Webb-Resio-Tracy (WRT) algorithm in WaveWatch III. A faster algorithm, but less representative of the physics, is the discrete interaction approximation (DIA). The documentation of the programs, and a full explanation of the physics and the requisite scientific papers, are easily found on the web. It is well known that the Hasselmann formulation equation does *not* reduce to a unidirectional spectrum because the nonlinear interactions reduce to zero for unidirectional wave motion. This of course suggests that the study of the modulational instability for unidirectional waves is "filtered out" in wind/wave models and that breather trains cannot therefore exist in the kinetic equation formulation. However, deterministic, nonlinear wave equations do not have this characteristic, so that unidirectional motion can be studied in a wave equation such as the one dimensional (1D) nonlinear Schrödinger equation, particularly with regard to the modulational instability, while the Hasselmann equation cannot be so studied. In order to fill this "hole" in the kinetic theory and in wind/wave models one might instead consider use of various deterministic equations such as the nonlinear Schrödinger equation and it's higher order versions such as the Dysthe [10] and the Zakharov [37] equations. By applying the methods given herein one could actually write the analytical form of the time varying power spectrum in order to include the coherent structures such as breathers in the wind wave formulation [30, 31]. This would allow the study of rogue waves in the context of wind waves. Using these deterministic wave equations one can formulate their multiperiodic, meromorphic Fourier series solutions, also for the driving terms, leads one to a "transfer function" that drives waves by wind, reduces them by dissipation and carries out the nonlinear four-wave interactions: This occurs because one connects the power spectrum of the waves to the wind, four-wave interactions and dissipation by a time-dependent, nonlinear, frequency domain transfer function. This approach may provide useful information about the behavior of the growth of rogue waves in wind/wave models. I will not discuss further details here.

5. The Nonlinear Schrödinger Equation

Traditionally, ocean waves are viewed as a *random process*: In terms of the Fourier transform this means that for a chosen spectrum, one selects a set of random phases to give a particular *realization* of the random process. For the extension of Fourier analysis to include the class of multiperiodic Fourier series, we once again take the phases to be random, i.e. the vector of phases $\boldsymbol{\phi}$. The procedure is based on (2, 3) where the *correlation function* is computed by $C(\mathcal{L}) = \langle u(x,t)u(x+\mathcal{L},t)\rangle$ and the spatial average has the form given above. In this Section I do *not* assume *spatially periodic boundary conditions*, but assume that the *wavenumbers are incommensurable*. We have the modulational dispersion relation $\Omega_n = \Omega_n(K_n)$ [28]. The nonlinear Schrödinger (NLS) equation has the form $iu_t + \mu u_{xx} + \nu|u|^2 u = 0$, where the solution is a ratio of Riemann theta functions $u(x,t) \sim \theta(x,t \mid \boldsymbol{\tau}, \boldsymbol{\phi}^-)/\theta(x,t \mid \boldsymbol{\tau}, \boldsymbol{\phi}^+) = \sum u_{\mathbf{n}} \exp[i\mathbf{n}\bullet\mathbf{K}x - i\mathbf{n}\bullet\boldsymbol{\Omega} + i\mathbf{n}\bullet\boldsymbol{\phi}]$. Assume that the $u_{\mathbf{n}}$ are already computed for the NLS equation as for KdV above and so we can compute the correlation function.

$$u(x,t)u(x+\mathcal{L},t) = \sum_{\mathbf{m}\in\mathbb{Z}^N} \sum_{\mathbf{n}\in\mathbb{Z}^N} u_{\mathbf{m}}(t)u_{\mathbf{n}}(t) e^{i(\mathbf{m}+\mathbf{n})\bullet\mathbf{K}x} e^{i\mathbf{n}\bullet\mathbf{K}\mathcal{L}}$$

Now take the spatial average:

$$\langle u(x,t)u(x+\mathcal{L},t)\rangle = \lim_{L\to\infty} \frac{1}{L} \sum_{\mathbf{m}\in\mathbb{Z}^N} \sum_{\mathbf{n}\in\mathbb{Z}^N} u_{\mathbf{m}}(t)u_{\mathbf{n}}(t) e^{i\mathbf{n}\bullet\mathbf{K}\mathcal{L}} \int_{-\infty}^{\infty} e^{i(\mathbf{m}+\mathbf{n})\bullet\mathbf{K}x} dx$$

Then write the integral, a Kronecker delta function, in the form:

$$\delta_{\mathbf{m},-\mathbf{n}} = \lim_{L\to\infty} \frac{1}{L} \int_{-L}^{L} e^{i(\mathbf{m}+\mathbf{n})\bullet\mathbf{K}x}\, dx = \lim_{L\to\infty} f(K_{\mathbf{mn}}L) = \begin{cases} 1, & \text{if } \mathbf{m} = -\mathbf{n} \\ 0, & \text{Otherwise} \end{cases}$$

For

$$K_{\mathbf{mn}} = \tfrac{1}{2}(\mathbf{m}+\mathbf{n})\bullet\mathbf{K}, \qquad f\left(K_{\mathbf{mn}}L\right) = \frac{\sin(K_{\mathbf{mn}}L)}{K_{\mathbf{mn}}L}$$

The convergence to a Kronecker delta as $L\to\infty$ is seen in Fig. 1. The *correlation function for a multiperiodic Fourier series* (where we used $u_{-\mathbf{n}}(t) = u_{\mathbf{n}}^*(t)$) becomes:

$$C(\mathcal{L},t) = \langle u(x,t)u(x+\mathcal{L},t)\rangle = \sum_{\mathbf{n}\in\mathbb{Z}^N} u_{\mathbf{n}}^*(t)u_{\mathbf{n}}(t) e^{i\mathbf{n}\bullet\mathbf{K}\mathcal{L}} = \sum_{\mathbf{n}\bullet\mathbf{K}=0} |u_{\mathbf{n}}(t)|^2 + \frac{1}{2} \sum_{\mathbf{n}\in\mathbb{Z}^N:\, \mathbf{n}\neq 0} |u_{\mathbf{n}}(t)|^2 \cos(\mathbf{n}\bullet\mathbf{K}\mathcal{L})$$

Finally, the *power spectrum* is then given by $P(\mathbf{n}\bullet\mathbf{K})=|u_{\mathbf{n}}(t)|^2$. Note that for the multiperiodic Fourier series used here the wavenumbers $\mathbf{n}\bullet\mathbf{K}$ lie on a point set known as a *discretuum* in string theory [6]. There are hundreds of millions of these wavenumbers in a typical numerical simulation for ocean waves, in contrast to the thousands that occur in an ordinary Fourier series.

6. Possible Extensions to Nonintegrable Wave Equations

Just as it is natural to take the Fourier series coefficients to be a function of time in eq. (3) [9, 35, 37, 38], it is also natural to do similarly in (4) to take into account of nonintegrability:

$$u_n(t)=\sum_{\{\mathbf{n}\in\mathbb{Z}^N:\ k_n=\mathbf{n}\bullet\mathbf{k}\}} u_{\mathbf{n}}(t)e^{-i\mathbf{n}\bullet\boldsymbol{\omega}(t)t+i\mathbf{n}\bullet\boldsymbol{\phi}(t)}$$

Poincaré has suggested a similar idea [29]. Perturbations of integrable equations have been studied using FGT [13]. In this case one obtains nonlinear ordinary differential equations for $u_{\mathbf{n}}(t)$, $\boldsymbol{\omega}(t)$ and $\boldsymbol{\phi}(t)$. For example one might think of solving the higher order equations (beyond integrability) using the above series, but with additional adiabatically varying ordinary differential equations for $u_{\mathbf{n}}(t)$, $\boldsymbol{\omega}(t)$ and $\boldsymbol{\phi}(t)$. Poincaré [29] indicates that it may be possible to expand each of these ordinary differential equations in a multiperiodic Fourier series. Such approaches might make it possible to describe the nonintegrable adiabatic motions of time varying solitons or breather states. Calogero [7] has mentioned the technique of imbedding a chaotic (nonintegrable) system into a periodic/multiperiodic series.

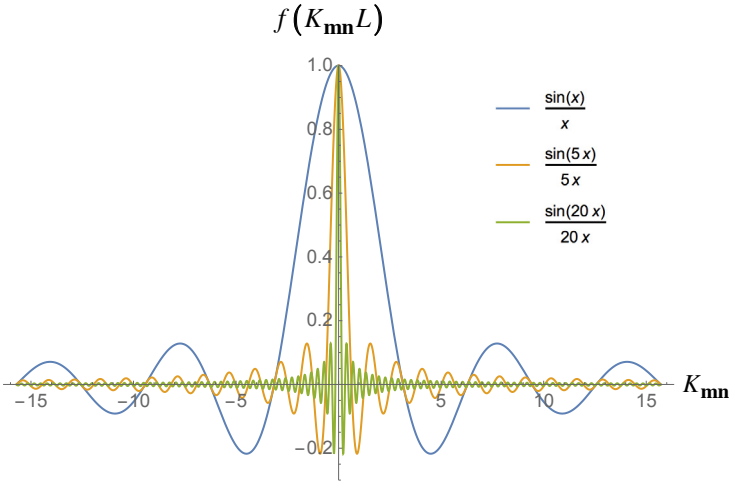

Fig. 1 Convergence of the function $f(K_{\mathbf{mn}}L)$ to a Kronecker delta function $\delta_{\mathbf{m},-\mathbf{n}}$ is shown for increasing values of L = 1, 5 and 20.

7. Conclusions and Projections

The developments here show that multiperiodic Fourier series solutions can be used to analytically compute the important physical properties of nonlinear wave equations with coherent structures such as Stokes waves, solitons, breathers and vortices. Additionally, nonlinear stochastic properties such as the correlation function, power spectrum, coherence functions, x etc. can also be computed. These nonlinear mathematical tools allow us to follow a path parallel to the linear Fourier method for stochastic systems that we have used since the 1930s [5]. The fact that the Baker-Mumford theorem constructs the most general multiperiodic meromorphic functions means that *singularities* can be included in a study of solutions for a number of equations for which "blow-ups" or "collapses" occur. It would seem that equations with blow-ups might be solved (or approximately solved) with multiperiodic Fourier series, thus providing a mathematical and physical description of this interesting phenomena and the types of coherent structures that may occur.

References

1. Baker, H. F., *Abelian Functions: Abel's Theorem and the Allied Theory of Theta Functions* (Cambridge University Press, Cambridge, 1897).
2. Baker, H. F., On a system of equations leading to periodic functions, *Acta Math*. **27**, 135-156, 1903.
3. Baker, H. F., *An Introduction to the Theory of Multiply Periodic Functions* (Cambridge University Press, Cambridge, 1907).
4. Belokolos, E. D., Bobenko, A. I., Enol'skii, V. Z., Its, A. R., and Matveev, V. B., *Algebro-Geometric Approach to Nonlinear Integrable Equations* (Springer-Verlag, Berlin, 1994).
5. Bendat, J. S., and Piersol, A. G., *Random Data: Analysis and Measurement Procedures* (Wiley-Interscience, New York, 1986).
6. Bousso, R. and J. Polchinski, Quantization of Four-form Fluxes and Dynamical Neutralization of the Cosmological Constant, *J. High Energy Phys.* **00006**(6), April, 2000.
7. Calogero, F. and F. Leyvraz, How to embed an arbitrary Hamiltonian dynamics in an integrable Hamiltonian dynamics, *J. Phys. A: Math. Theor.* **42**, 145202, 2009.
8. Costa, A., A. R. Osborne, D. T. Resio, S. Alessio, E. Chrivì, E. Saggese, K. Bellomo and C. E. Long, Soliton turbulence in shallow water ocean surface waves, *Phys. Rev. Lett.* **113**, 108501, 2014.
9. Dommermuth, D. G., and Yue, D. K. P., A higher-order spectral method for the study of nonlinear gravity waves, *J. Fluid Mech.* **184**, 267–288, 1987.
10. Dysthe, K. B., Note on a modification to the nonlinear Schrödinger equation for application to deep water waves *Proc. R. Soc. Lond. A **369***, 105–114, 1979.
11. El, G. A. and A. M. Kamchatnov, *Phys. Rev. Lett.* **95**, 204101, 2005.
12. Fay, J. D., *Theta Functions on Riemann Surfaces*, Lect. Notes Math., Vol. 352 (Springer, Berlin, Heidelberg, 1973).
13. Ferguson, W. E., Flaschka, H., and McLaughlin, D. W., Nonlinear normal modes for the Toda chain, *J. Comp. Physics* **45**, 157, 1982.
14. Fermi, E., Pasta, J., and Ulam, S., *Studies of Nonlinear Problems*, I, Los Alamos Rep. LA1940, 1955; reprod, In Nonlinear Wave Motion, A. C. Newell, ed., (American Mathematical Society, Providence, 1974).
15. Fokas, A. S., and Liu, Q. M., Asymptotic integrability of water waves, *Phys. Rev. Lett.* **77** (12), 2347–2351, 1996.
16. K. Hasselmann, On the non-linear energy transfer in a gravity wave spectrum, Part 1. General theory. *J. Fluid Mech*. ***12***, 481500 (1962).
17. Hirota, R., *The Direct Method in Soliton Theory* (Cambridge University Press, Cambridge, 1992).
18. Kodama, Y., Normal forms for weakly dispersive wave equations, *Phys. Lett.* **112A** (5), 193–196, 1985a.
19. Kodama, Y., On integrable systems with higher order corrections, *Phys. Lett.* **112A** (6), 245–249, 1985b.
20. Kruskal, M. D. and N. J. Zabusky (1963), *Princeton Plasma Physics Laboratory annual report* MATT-Q-21, pp. 301ff, unpublished.
21. Matsutani, S., Hyperelliptic Solutions of KdV and KP equations: Reevaluation of Baker's Study on Hyperelliptic Sigma Functions, *J. Phys. A General Physics*, **34** (22), July 2000.
22. Matveev, V. B., 30 years of finite-gap integration theory, *Phil. Trans. R Soc. A* **366**, 837-875, 2008.
23. Mumford, D., *Tata Lectures on Theta I* (Birkhäuser, Boston, 1982).
24. Mumford, D., *Tata Lectures on Theta II* (Birkhäuser, Boston, 1984).
25. Osborne, A. R., and Bergamasco, L., The solitons of Zabusky and Kruskal revisited: Perspective in terms of the periodic spectral transform, *Physica D* **18**, 26–46, 1986.
26. Osborne, A. R., The behavior of solitons in random-function solutions of the periodic Korteweg-deVries equation, *Phys. Rev. Lett.* **71**(19), 3115–3118, 1993.
27. Osborne, A. R., Approximate asymptotic integration of a higher order water-wave equation using the inverse scattering transform, *Nonlinear Proc. Geophys*. **4(1)**, 29-53, 1997.
28. Osborne, A. R., *Nonlinear Ocean Waves and the Inverse Scattering Transform* (Academic Press, Boston, 2010).
29. Poincaré, H., *New Methods of Celestial Mechanics 1. Periodic and Asymptotic Solutions*, American Institute of Physics, 1993.
30. Ponce de León, S., A. R. Osborne, Properties of rogue waves and the shape of the ocean wave power spectrum, ASME 2017 36th International Conference on Ocean, Offshore and Arctic Engineering, OMA2017-62217, June 25-30 2017, Trondheim, Norway.
31. Ponce de León, S., A. R. Osborne and D. T. Resio, Rogue Waves, Nonlinear Wave Interactions and the Shape of the Ocean Wave Power Spectrum, in preparation (2018).
32. Riemann, B., *Collected Papers*, Kendrick Press, 2004.
33. Schottky, F., Uber eine spezielle Funktion, welche bei einer bestimmten linearen Transformation ihres Arguments unverandert bleibt, J. Reine Angew. Math. **101**, 227–272, 1887.
34. Stokes, G. G., On the theory of oscillatory waves, *Trans. Camb. Philos. Soc*. **8**, 441–455, 1847.
35. West, B. J., Brueckner, K. A., Janda, R. S., Milder, D. M., and Milton, R. L., A New Numerical method for Surface Hydrodynamics, *J. Geophys. Res.* **92**, 11,803–11,824, 1987.
36. Whitham, G. B., *Linear and Nonlinear waves* (John Wiley, New York, 1974).
37. Zakharov, V. E., Stability of periodic waves of finite amplitude on the surface of a deep fluid, *J. Appl. Mech. Tech. Phys. USSR*, **2**, 190, 1968.
38. Zakharov, V. E., JETP 24(2), 455 (1967).
39. Zakharov, V. E., Sov. Phys. JETP 33, 538, 1971; *Stud. Appl. Math*. 122, 219, 2009.
40. Zygmund, A., *Trigonometric Series* (Cambridge University Press, Cambridge, 1959).

Available online at www.sciencedirect.com

ScienceDirect

Procedia IUTAM 26 (2018) 124–131

Procedia IUTAM

www.elsevier.com/locate/procedia

IUTAM Symposium Wind Waves, 4–8 September 2017, London, UK

Wind modulation by variable roughness of ocean surface

Lev Ostrovsky[a,b]

[a]University of Colorado, Boulder, USA
[b]Institute of Applied Physics, Russian Acad. Sci., Nizhny Novgorod, Russia

Abstract

Recent results concerning transient effects of variation of short sea-surface wave roughness on near-surface turbulent wind are briefly outlined. This variation can be caused by oil, surfactants, inhomogeneous currents, internal waves, ship wakes, etc. To describe the wind parameters including surface stress and turbulent energy density, we use a direct solution of the Reynolds-type equations in the boundary-layer approximation. The solutions include a sharp and smooth roughness variation, 2-D surface variation, and a moving slick. The applicability of the theory was verified by comparison with laboratory data. Further on, the theory was applied to a problem related to the devastating tsunami near Fukushima Daichi in 2011.

Peer-review under responsibility of the scientific committee of the IUTAM Symposium Wind Waves.

Keywords: Wind modulation; Sea surface roughness; Reynolds equations;

1. Introduction

The interaction between wind and sea surface is a classic problem of ocean/atmosphere dynamics. The parameters of the wind flow, such as momentum flux and wind drag, are being thoroughly studied, mainly in terms of values averaged over the considered area. Wind variations over curved surfaces (hills, long waves) were also studied in detail, see, e.g., [1]. Transient problems considered in meteorology are generally focused on sharp changes in the underlying terrain; for example, a transition from water surface to shore or from field to forested land (e.g., [2]). Less studied are near-surface wind variations over horizontally varying sea roughness which are of importance in many practical cases, e.g., for evaluation of wind drift of oil spills and tsunami-caused debris, remote sensing of marine slicks, and others.

Methodically, most of the studies of horizontal wind variations were based on the two-layer approach (see [1–3] and references therein). Here we briefly outline the results based on direct solutions of the Reynolds-type equations for wind velocity and turbulent kinetic energy (TKE) simplified for the low boundary layer conditions. This theory, partially described in [3], allows to significantly extend the applications of the model, for example, to consider a smooth variation of roughness, moving inhomogeneities, two-dimensional “spots”, etc. In some cases the theoretical

2210-9838
Peer-review under responsibility of the scientific committee of the IUTAM Symposium Wind Waves.
10.1016/j.piutam.2018.03.012

results are applied to the data of a laboratory experiment and to modeling of wind over the debris floating from the Fukushima tsunami.

2. Basic equations

The general configuration of the considered process is shown in figure 1.

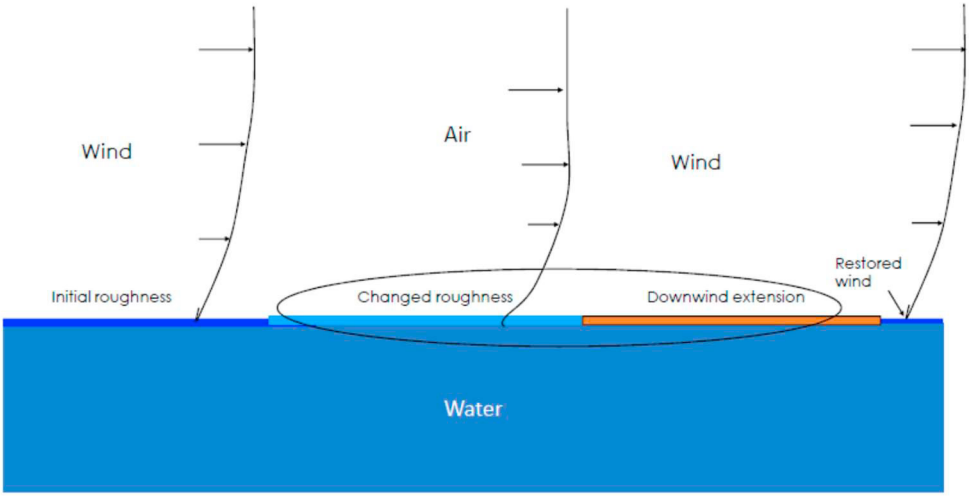

Fig. 1. Schematic of the wind variation over a finite area (spot) of changed roughness. The near-surface air flow changes over the spot and this variation can extend beyond the spot.

The starting point is Reynolds equations for an incompressible turbulent flow with neutral stratification [4, 5]:

$$\frac{\partial u_i}{\partial t}+(\mathbf{u}\cdot\nabla)u_i=-\frac{\partial p}{\partial x_i}-\frac{\partial \tau_{ij}}{\partial x_j},\ \tau_{ij}=-K\left(\frac{\partial u_i}{\partial x_k}+\frac{\partial u_k}{\partial x_i}\right),$$
$$\frac{\partial b}{\partial t}+(\mathbf{u}\cdot\nabla)b=\frac{\partial}{\partial x_i}\left[\kappa_b K\frac{\partial b}{\partial x_i}\right]+K\left(\frac{\partial u_i}{\partial x_k}+\frac{\partial u_k}{\partial x_i}\right)\frac{\partial u_i}{\partial x_k}-K\frac{\gamma b}{l_z^2},\qquad(1)$$
$$\nabla\cdot\mathbf{u}=0.$$

Here **u** is the average air velocity vector, p is pressure, b is the turbulent energy density (TKE), and τ_{ij} is the turbulent stress tensor. The parameters are: K is the turbulent exchange (viscosity) coefficient. In the framework of the Kolmogorov's eddy-viscosity closure hypothesis, $K=l_z\sqrt{b}$, l_z being the vertical turbulence scale, and the empirical coefficients are taken as $\kappa_b=0.7$ and $\gamma=0.05$ to 0.09 in different realizations. In what follows we use the boundary-layer approximation, letting $\partial/\partial x<<\partial/\partial z$ and $w<<u$, where u and w are the horizontal and vertical velocity components, respectively. Thus, the equations to be studied here are reduced to

$$\frac{\partial u}{\partial t}+u\frac{\partial u}{\partial x}+w\frac{\partial u}{\partial z}=\frac{\partial}{\partial z}\left(K\frac{\partial u}{\partial z}\right),$$
$$\frac{\partial u}{\partial x}+\frac{\partial w}{\partial z}=0, \tag{2}$$
$$\frac{\partial b}{\partial t}+u\frac{\partial b}{\partial x}=\kappa_b\frac{\partial}{\partial z}\left(K\frac{\partial b}{\partial z}\right)+K\left(\frac{\partial u}{\partial z}\right)^2-\frac{\gamma b}{l_z^2}.$$

For the stationary, horizontally homogeneous boundary layer above the surface, the solution of Eqs. (2) is the classic "law of the wall" logarithmic profile, which in standard notations is given by

$$u(z)=\frac{u_*}{\kappa}\ln\left(\frac{z}{z_0}\right), \tag{3}$$

with

$$b=b_0=\frac{u_*^2}{\gamma^{1/2}},\ l_z=\gamma^{1/4}\kappa z,\ \tau_{xz}=\tau_0=u_*^2. \tag{4}$$

Here $u(z)$ is the horizontal wind speed at the height z above the surface, u_* is the friction velocity, z_0 is the surface roughness scale, and $\kappa\approx 0.4$ is the dimensionless von Karman constant.

Another important parameter, stress, that is the vertical flux of horizontal momentum per unit mass, is

$$\tau_{xz}=S=l_z\sqrt{b}\frac{\partial u}{\partial z}, \tag{5}$$

and in the non-perturbed flow (3), $S=S_0=u_*^2$.

Evidently, Eqs. (2) and (3) cannot be directly used for modeling the horizontally inhomogeneous air flow considered here. In this case a non-trivial problem is to formulate boundary conditions for Eqs. (2) for a given roughness height $z_0(x)$. Since the general solution is not necessarily logarithmic, the parameters u_* and z_0 in the undisturbed solution, Eqs. (3) and (4), do not describe the transient processes. Thus, we assume that close to the surface at small heights $0 < z < z_1$ the new local logarithmic boundary layer has been quickly established. If $z_0(x, t)$ and $u_{*1}(x,t)$ for this new air flow profile are given, we define boundary conditions at $z = z_1$ as

$$u(z_1,x,t)=\frac{u_{*1}(x,t)}{\kappa}\ln\left(\frac{z_1}{z_0(x,t)}\right),\ b(z_1,x,t)=\frac{u_{*1}^2(x,t)}{\gamma^{1/2}},\ z_0<z_1. \tag{6}$$

These two expressions relate the values at $z = z_1$ with the surface roughness $z_0(x, t)$. In addition, this approach allows to avoid the description of a possible complex structure of turbulence near the surface. [1, 6] At a sufficiently large height, $z = h$, the wind flow is assumed to remain unchanged at the considered distances and time intervals, so that it retains the initial values, described by Eqs. (3) and (4). For control purposes, we performed calculations for different values of h while keeping other parameters fixed. In our case, $z_0 << z_1 << h$. We also suppose that the turbulence scale l_z remains linearly increasing with z, which is justified by the slowness of horizontal variations of all parameters as compared with vertical changes of the boundary layer profile. In what follows we consider different roughness spot geometries.

3. A slick

Consider a "slick spot" decreasing the roughness z_0 from 0.2 mm to 0.11 mm at a finite interval of x of 400 m length, possibly due to the surfactants. According to the above, a new logarithmic velocity profile is supposed to be formed below $z_1 = 4$ mm so that the velocity profile is given for $z = 4$ mm as shown in Fig. 2. The corresponding unperturbed wind velocity extrapolated to z = 10 m is 10.9 m/s.

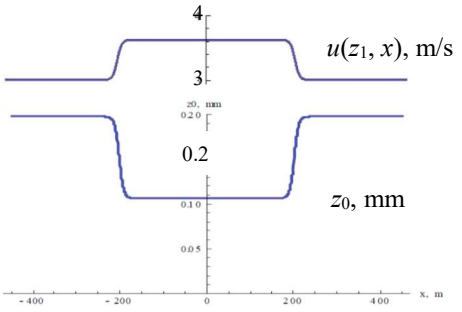

Fig. 2. Variation of surface roughness scale z_0 over a slick and the corresponding variation of wind speed at $z_1 = 4$ mm. The values of u are assumed unchanged from the initial logarithmic profile at at $x < -800$ m and at $z > 4$ m.

The results of calculation of variation of stress and turbulent energy using equations (2) are shown in figure 3.

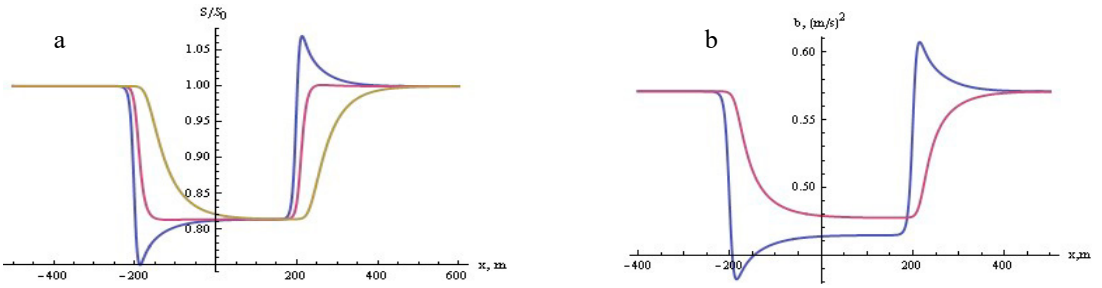

Fig. 3. (a) Relative variation of stress along the x axis at the heights of $z = 4$ mm (blue), 0.5 m (purple), and 2.95 m (olive). $S_0 = 0.16$ m^2/s^2 is an unperturbed value of S. (b) Variation of turbulent energy at the heights of $z = 2$ cm (blue) and 1 m (purple).

It is seen that the air flow characteristics are significantly changed over the slick. It is noteworthy that perturbations are shifted downwind so that a "precursor" perturbation is generated in front of the spot.

As mentioned, equations (2) allow to describe wind flow over a smoothly varying roughness, such as the one created by a surfactant of varying thickness or by a strong internal wave acting on the short surface waves. As an example consider the case when the initial wind's parameters are the same as in the previous example and the variation of velocity near the surface has the form

$$u(z_1 = 4 \text{ mm}) = 3.01 + 0.62\exp(-x^2/150^2) \text{ m/s}. \quad (7)$$

This distribution and the corresponding roughness variation are shown in figures 4a,b. Figure 4c shows the resulting variation of stress at different levels.

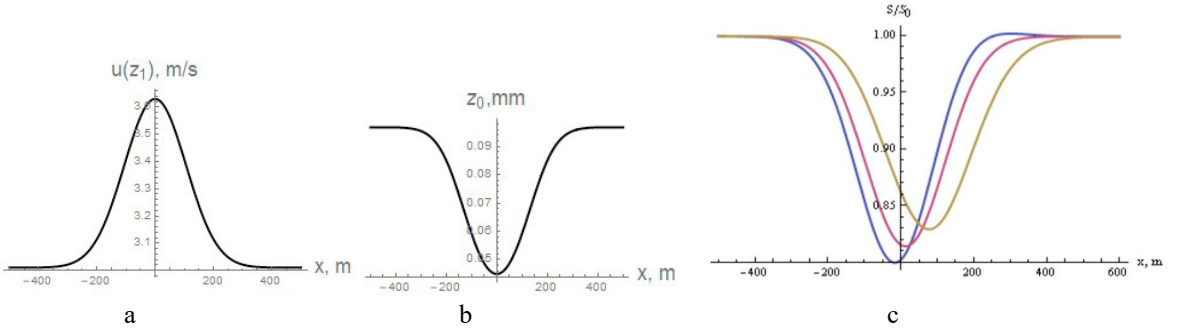

a b c

Fig.4. (a) Distribution of air velocity at z = 4 mm. (b) Variation of surface roughness, $z_0(x)$. (c) Variation of stress at z = 4 mm (blue), 0.5 m (purple) and 2.95 m (olive). Wind velocity at z = 10 m is 10 m/s.

Here again the perturbation is shifted ahead of the spot, especially at larger heights where the stronger wind carries the perturbation forward.

4. Moving spot

In general, system (2) can describe non-steady processes when the roughness varies in time. Fig. 5 gives an example of a perturbation moving with the velocity V as a result of, for example, action of a long wave or a ship changing surface roughness. In this case the left-hand parts of (2) have the form of $(u-V)\partial/\partial x$.

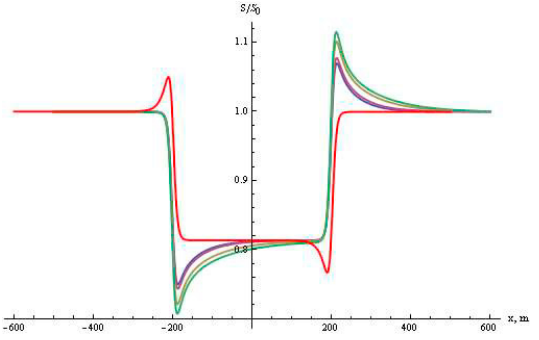

Fig. 5. Relative stress variation along the x axis at z = 4 mm at the upwind motions of the slick with velocities from V = 0 (green line), -1 m/s (olive), -5 m/s (purple), and -8 m/s (blue); and at the downwind motion with the velocity of 10 m/s (red). Other parameters are the same as in Fig. 3.

Here, for a steady upwind motion, stress profiles do not radically differ for a moving slick. However, the downwind curve is "inverted" to produce a “precursor” behind the spot. This indicates one important factor existing for the downwind motion: there can be a *synchronism* between the velocities of air and body at some height $z = z_s$. Thus, to satisfy causality, the wind should be given on the right of the spot at $z < z_s$ and on the left at $z > z_s$, and the solutions in these two areas should be matched. In figure 5 the case V = 10 m/s is shown for which $V > u(z)$ throughout the considered layer, z < 4 m, (indeed, at z = 4 m, wind velocity is 8.92 m/s) so that no singularities exist. For smaller V or for a thicker air layer, the point $u = V$ would be included. This "synchronous" case deserves a special consideration.

5. Finite-area spot

Consider now the case when the roughness area is bounded in all directions. In this case the wind perturbations are three-dimensional. The incident wind flow is still directed along the x-axis. One example is a smooth, two-dimensional variation of the velocity at $z = z_1$:

$$u(z_1 = 4\text{ mm}) = 3.01 + 0.66\exp\left(-x^2/150^2 - y^2/40^2\right)\text{ m/s}. \quad (8)$$

The solution of equations (1) for stress and turbulent energy are shown in figure 6.

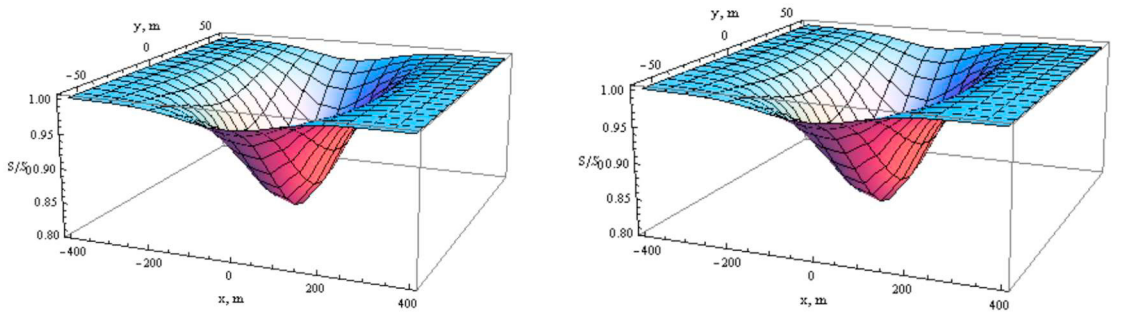

Fig. 6. 3D plots of (a) Variation of stress at z = 4 mm, (b) Variation of TKE at z = 2 cm. Incident wind parameters are the same as in Fig. 4.

Comparison with Fig. 4 shows that the order of variation of wind parameters is the same as in the 2D case. Note, however, that in the 3D case there appears a shear in wind over the spot which can result in instabilities and generation of vortex motions.

6. Comparison with laboratory experiment

In [3] a relevant laboratory experiment (carried out by S. Ermakov and O. Shomina at the Institute of Applied Physics of Russian Acad. Sci.) in a wind-wave tank is described. The tank is a closed channel with a rectangular water cross-section 30 x 30 cm^2 and a 30 x 30 cm^2 air channel above it. The wind over water was produced by a frequency-controlled fan. The water surface roughness was changed by dropping a surfactant (oleic oil) on the water surface. When the dropper worked for a finite time period, a slick was formed, and the wind parameters over the slick were measured. Figure 7 shows the data for one realization. It is seen that the theory yields correct ranges of wind velocity variation over the film at different heights; it also predicts the observed transient areas both in the beginning and at the end of the process, as well as the extension of wind perturbation beyond the roughness variation shown in Fig. 7a.

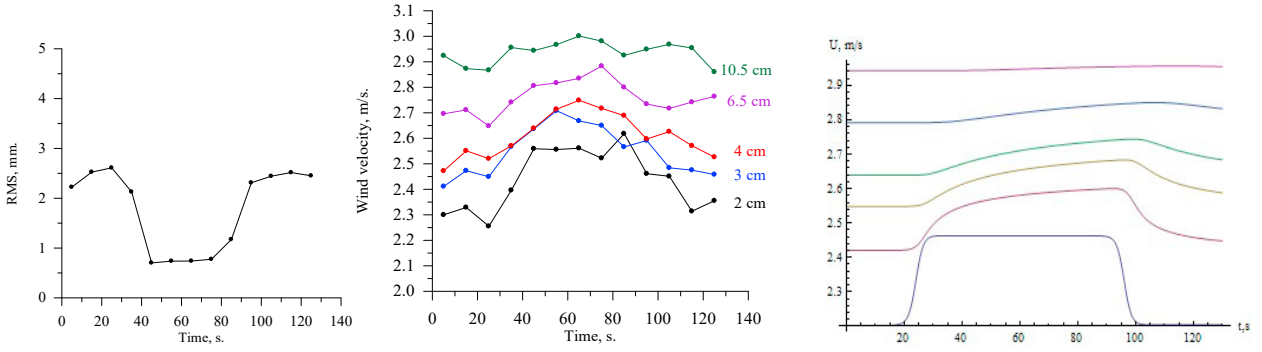

Fig. 7. Wind speed variation over a slick in laboratory tank (a) R.m.s of wind wave height over a film drifting past the wire gauge during about 80 s. (b) Wind velocities at different heights over the water surface, measured by a hot wire anemometer. (c) Theoretical modelling according to the above theory. Theoretical curves are plotted for the same heights (2, 3, 4, 6.5, and 10.5 cm). as the experimental ones, except for the lower one showing the boundary condition at z_1 = 1 cm; the latter was taken from the measured wind profile.

7. Wind variation over floating debris

The approach described above was recently used in [7] for evaluation of early interaction between wind and debris floating after the devastating tsunami having destroyed the Fukushima Daiichi nuclear power station in Japan. On retreating, the tsunami carried oil, loose debris, and wreckage seaward (estimated 5 million tons) which suppresses the surface waves as was confirmed by radar measurements from a SAR satellite. This, according to our estimates, the wind speed increases over the surface and, as a result, provides an additional (of the order of 5 cm/s) acceleration of floating debris against the velocities expected from a current-related drift and an unchanged wind. Figure 8 illustrates some of these results.

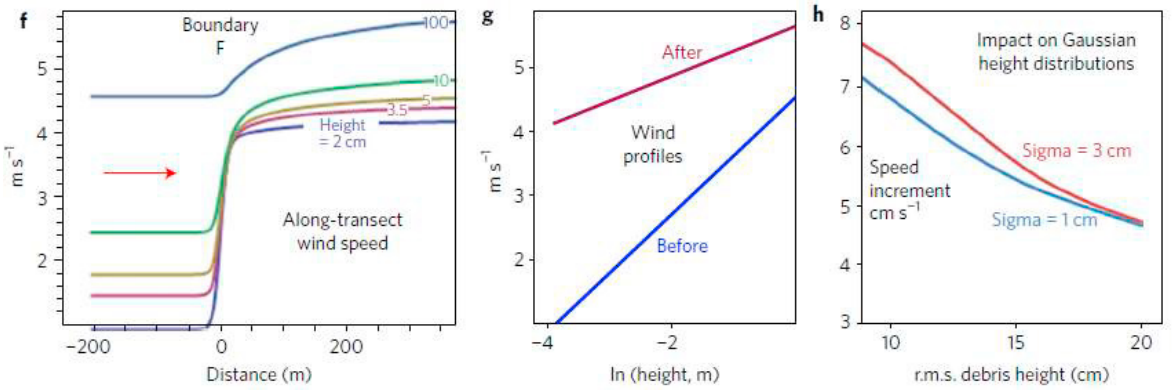

Fig. 8. (f) Wind velocity variation on the path through the slick at heights of 2–100 cm calculated based on Eqs. 2. (g) Calculated logarithmic wind profile before and after crossing the slick edge. (h) Estimated drift speed increments due to wind restructuring for idealized floating debris (6.2m/s local wind at z = 10 m). From [7].

As in the above examples, the wind speed increases over the slick, and after crossing the slick edge a new logarithmic wind profile is eventually formed (Fig. 8g). The enhanced wind, in its turn, accelerates the floating products as follows from independent calculations, see Fig. 8h. These results are in agreement with the measured data.

8. Conclusions

Here the theory of turbulent air flow over a variable sea roughness with using the semi-empirical Reynolds-type equations and simple closure hypotheses has been developed. This theory which does not involve dividing the atmospheric boundary layer to two or more areas looks quite adequate for low heights where the wind most intensively interacts with the waves. It should be noted that for stationary surface inhomogeneities this approach gives the results close to those following from the two-layer consideration [3]. However, the present approach is applicable for more general configurations, such as smooth inhomogeneities, moving slicks, and two-dimensional inhomogeneities. The theory is confirmed by laboratory experiment and it was successfully applied to description of a real tsunami event. Note that effect of the areas of intensified roughness ("suloys") can also be described by the used equations. Note also that although in general equations (2) include the effect of vertical air motion, in many cases it can be neglected which further simplifies the solution; however, it has to be verified in each specific case.

Even in the framework of the simplified approach considered above, there remain interesting unsolved problems. One is, as mentioned, the synchronism between the moving spot velocity V and wind velocity $u(z)$ at some height if the latter is located at some $z = z_c$ within the considered air layer. In this case the boundary condition for x should be prescribed on the right at $z < z_c$ and on the left at $z > z_c$ and the solutions should be matched at $z = z_c$. Another interesting problem is a reciprocal effect: reaction of the surface on the changes of the surface stress due to

wind modification. Our preliminary evaluations of this effect based on the Charnock's formula [8] indicate a possibility of positive feedback when the effect cumulates.

Acknowledgements

Selected results of the recent publications [3] and [7] have been used here, and the author is grateful to the co-authors of these works. Special thanks are to M. Charnotskii for the longtime and fruitful collaboration,

References

1.S. E. Belcher, J. C. R. Hunt, Turbulent flow over hills and waves, *Ann. Rev. Fluid Mech.*, 1998; **30:** 507-5380.
2. S. A. Savelyev, P. A. Taylor, Internal boundary layers: I. Height formulae for neutral and diabatic flows, *Boundary-Layer Meteorology*, 2005; **115**:1-25.
3. M. Charnotskii, S. Ermakov, L. Ostrovsky, O. Shomina, Effect of film slicks on near-surface wind, *Dyn. Atm. Oceans*, 2016; **75**:118-128.
4.A. S. Monin, A. M. Yaglom, (1973) *Statistical Fluid Mechanics - Vol. 1: Mechanics of Turbulence*, 1973; MIT Press, Boston, 782 pp.
5.C. G. Speziale, Analytical methods for the development of Reynolds-stress closures in turbulence, *Ann. Rev Fluid Mech*.,1991; **23**:107-157.
6. O. A. Druzhinin, L. A. Ostrovsky, Dynamics of turbulence under the effect of stratification and internal waves, *Nonlin. Proc. Geophys*., 2015; **22:** 337–348.
7. J. Matthews, L. Ostrovsky, Y. Yoshikawa, S. Komori, H. Tamura, Dynamics and early post-tsunami evolution of floating marine debris near Fukushima Daichi, *Nature Geoscience*, 2017; DOI:10.1038/NGEO2975.
8. H. Charnock, Wind stress on a water surface, *Quart. J. R. Met. Soc*., 1955; **81:** 639-640.

Available online at www.sciencedirect.com

ScienceDirect

Procedia IUTAM 26 (2018) 132–144

Procedia IUTAM

www.elsevier.com/locate/procedia

IUTAM Symposium Wind Waves, 4-8 September 2017, London, UK

Comparison of Different Models for Wave Generation of The Hasselmann Equation

Andrei Pushkarev[a,b,c,*]

[a]Lebedev Physical Institute RAS, Leninsky 53, Moscow 119991, Russia
[b]Novosibirsk State University, Pirogova 1, Novosibirsk 630090, Russia
[c]Waves and Solitons LLC, 1719 W. Marlette Ave., Phoenix, AZ 85015, USA

Abstract

We compare two recently developed sets of source terms, based on different assumptions of wave energy input and dissipation, for Hasselmann equation. The numerical simulation, performed for limited fetch conditions with the constant wind speed shows the difference in total energy and mean frequency distributions along the fetch as well as in wave energy spectra. Possible reasons of such deviations are offered.

Peer-review under responsibility of the scientific committee of the IUTAM Symposium Wind Waves.

Keywords:
Hasselmann equation; wind and dissipation source terms; self-similar solutions; Kolmogorov-Zakharov spectra; wave-breaking dissipation; magic relation

1. Introduction

The physical oceanography community consents on the fact [5] that deep water ocean gravity surface wave forecasting models are described by Hasselmann equation (hearafter HE) [10, 11], also known as kinetic equation for waves, or energy balance equation:

$$\frac{\partial \varepsilon}{\partial t} + \frac{\partial \omega_k}{\partial \vec{k}} \frac{\partial \varepsilon}{\partial \vec{r}} = S_{nl} + S_{in} + S_{diss} \tag{1}$$

where $\varepsilon = \varepsilon(\omega_k, \theta, \vec{r}, t)$ is the wave energy spectral density, as the function of wave frequency $\omega_k = \omega(k)$, angle θ, two-dimensional real space coordinate $\vec{r} = (x, y)$ and time t. S_{nl}, S_{in} and S_{diss} are the nonlinear, wind input and wave-breaking dissipation source terms, respectively. Hereafter, only the deep water case, $\omega = \sqrt{gk}$ is considered, where g is the gravity acceleration and $k = |\vec{k}|$ is the absolute value of the vector wavenumber $\vec{k} = (k_x, k_y)$.

* Corresponding author.
E-mail address: dr.push@gmail.com

2210-9838
Peer-review under responsibility of the scientific committee of the IUTAM Symposium Wind Waves.
10.1016/j.piutam.2018.03.013

Since Hasselmann work, Eq.(1) has become the basis of operational wave forecasting models such as WAM, SWAN and Wavewatch III [24, 22]. While the physical oceanography community consents on the general applicability of Eq.(1), there is no consensus agreement on universal parameterizations of the source terms S_{nl}, S_{in} and S_{diss}.

Two different forms of S_{nl} term have been derived independently from the Euler equations for free surface incompressible potential flow of a liquid by [10, 11] and [30]. Their identity on the resonant surface

$$\omega_{\vec{k_1}} + \omega_{\vec{k_2}} = \omega_{\vec{k_3}} + \omega_{\vec{k_4}} \tag{2}$$

$$\vec{k_1} + \vec{k_2} = \vec{k_3} + \vec{k_4} \tag{3}$$

has been shown in [21].

S_{nl} term is the complex nonlinear operator acting on ε_k, concealing hidden symmetries [31, 33]. The most robust, first approximation of HE

$$S_{nl} = 0 \tag{4}$$

plays the crucial role in the weak turbulent theory [33] due to leading role of the S_{nl} source term in HE [28, 29]. Its simplest solution

$$\varepsilon \simeq \frac{P^{1/3}}{\omega^4} \simeq \beta g \frac{P^{1/3}}{\omega^4} \simeq \frac{\beta g U_*}{\omega^4} \simeq \frac{2\pi\alpha g U_{\lambda/2}}{\omega^4} \tag{5}$$

where P is the energy flux toward high wave numbers, β is small dimensionless parameter (the "Toba constant" [23]), g is the gravity acceleration, U_* is the wind friction velocity, $U_{\lambda/2}$ is the wind velocity at the height of half wavelength of the wave-number, corresponding to the spectral peak, and $\alpha = 0.00553$ [19]. Eq.(5) is known as Zakharov-Filonenko solution of HE [30], which is the subset of Kolmogorov-Zakharov (hearafter KZ) solutions .

The accuracy advantage of knowing the analytical expression for the S_{nl} term, also known in physical oceanography as XNL, is overshadowed by its computational complexity. Today, none of the operational wave forecasting models can afford to perform XNL computations in real time. Instead, their low computational capacity operational approximations, known as DIA and its derivatives, are used as its surrogates. The implication of such simplification is the inclusion of a tuning coefficient in front of nonlinear term; however, several publications have shown that DIA does not provide a good approximation of the actual XNL form. The paradigm of replacement of the XNL by the DIA and its variations leads to even more grave consequences: other source terms must be adjusted to allow the model Eq.(1) to produce desirable results. In other words, deformations suffered by XNL model due to the replacement of S_{nl} by its surrogates, need to be compensated by non-physical modification of other source terms to achieve reasonable model behavior in any specific case, leading to a loss of physical universality in HE model.

In contrast to S_{nl}, the knowledge of S_{in} and S_{diss} source terms is poor; furthermore, both include many heuristic factors and coefficients. The creation of a reliable, well justified theory of S_{in} has been hindered by strong turbulent fluctuations, uncorrelated with the wave motions, in boundary layer over the sea surface. Even one of the most crucial elements of this theory, the vertical distribution of horizontal wind velocity in the region closest to the ocean surface, where wave motions strongly interact with atmospheric motions, is still the subject of debates. The history of the development of different wind input forms is full of heuristic assumptions, which fundamentally restrict the magnitude and directional distribution of this term. As a result, the values of different wind input terms scatter by a factor of $300 - 500\%$ [2, 17]. For example, experimental determination of S_{in}, as provided by direct measurements of the momentum flux from the air to the water, cannot be rigorously performed in a laboratory due to gravity waves dispersion dependence on the water depth, as well as the problems with scale effects for laboratory winds. The good demonstration of the fact has been presented by [9]. Additional information on the detailed analysis of current state of the art of wind input terms can be found in [17].

Similar to the wind input term, there is little consent on the parameterization of the dissipation source term S_{diss}. The physical dissipation mechanism, which most physical oceanographers agree on, is the effect of wave energy loss due to wave breaking, while there are also other dubious ad-hoc "long wave" dissipation source terms, having heuristically justified physical explanations. Currently, there is no even an agreement on the location of wave breaking events in Fourier space. The approach currently utilized in operational wave forecasting models mostly relies on the dissipation, localized in the vicinity of the spectral energy peak. Recent numerical experiments [17, 8, 32] show,

however, that such approach does not pass most of the tests associated with the essentially nonlinear nature of the HE Eq.(1).

As the result of the above mentioned problems, WAVEWATCH operational model [24] has more than two dozens of tuning parameters. There is growing feeling in oceanographic community that new type of physically justified models needs to be developed.

The step in that direction has been done through the development of the alternative ZRP [34, 27] approach to the formulation of balanced source terms for wave generation in HE. Contrary to the previous attempts of building the detailed-balance source terms, it is neither based on the development of a rigorous analytic theory of turbulent atmospheric boundary layer, nor on reliable and repeatable air to ocean momentum measurements. It is constructed in the artificial way, realizing, in a sense, "the poor man approach", based on the finding of two-parameter family of HE self-similar solutions and its restriction to the single-parameter one via comparison with the data of multiple field experimental observations. This ZRP self-similarity analysis is summarized in the following dependencies:

$$\epsilon = \chi^{p+q} F(\omega \chi^q) \tag{6}$$

$$10q - 2p = 1, \quad q = \frac{1}{2+s} \tag{7}$$

$$p = 1, \quad q = 3/10, \quad s = 4/3 \tag{8}$$

$$E(\chi) = E_0 \chi^p \tag{9}$$

$$< \omega(\chi) >= \omega_0 \chi^{-q} \tag{10}$$

where $E(\chi)$ and $< \omega(\chi) >$ are the total wave energy and the mean frequency as the functions of the dimensionless fetch coordinate $\chi = xg/U^2$, where x is the dimensional fetch coordinate in meters, g is the gravity acceleration and U is the wind speed; $s = 4/3$ is the index of power-like wind forcing dependency on frequency $\sim \omega^s$ of ZRP wind source term (see Eq.(13) for details); E_0 and ω_0 are the constants.

In the following chapters we numerically compare ZRP model [34, 27] with the MD1 and MD2 models. MD1 model is based on the set of the forcing and dissipation source functions, described in [7]. MD2 model is the "synthetic" model, carrying the details of ZRP as wells as MD1 model.

One should emphasize that ZRP and MD1 source terms sets assume different underlying physics: ZRP model assumes the leading role of the nonlinear interaction term and wave energy cascade from spectral peak energy input area to the energy dissipation region of high wave numbers, while MD1, as show our numerical experiments, dissipates most of the wave energy at the intermediate wave numbers closer to the spectral peak. That results in significant differences in total wave energy and mean frequency behavior along the fetch as well as the details of wave energy spectral distributions.

The numerical experiments performed with the "synthetic" MD2 model showed the improvement of MD1 model self-similar properties and wave energy spectral characteristics, arguing in favor of high-frequency wave energy dissipation mechanism in HE.

The following chapters describe the details of studied models and present the supporting facts to the explained point of view.

2. The models formulation and numerical approach

The numerical simulation was based on the solution of stationary version of the Eq.(1) in limited fetch approximation $\frac{\partial \varepsilon}{\partial t} = 0$:

$$\frac{1}{2} \frac{g \cos\theta}{\omega} \frac{\partial \epsilon}{\partial x} = S_{nl} + S_{wind} + S_{diss} \tag{11}$$

where $\vec{x}$ is the coordinate axis orthogonal to the shore and θ is the angle between individual wavenumber $\vec{k}$ and the direction of $\vec{x}$.

The stationarity in Eq.(11) is somewhat difficult for numerical simulation, since it contains the singularity in the form of $\cos\theta$ in front of $\frac{\partial \epsilon}{\partial x}$. This problem was overcome by zeroing out of one half of the Fourier space of the system for the waves propagating backward to the shore. Since the energy of the waves against the wind is small with respect to waves propagating in the offshore direction, such an approximation is quite reasonable for our purposes.

All simulations used WRT (Webb-Resio-Tracy) method [25], which calculates the nonlinear interaction term in the exact form. The presented numerical simulation utilized the version of WRT method, previously used in [26, 18, 14, 16, 20, 13, 12, 3, 17, 27, 4], on the grid of 71 logarithmically spaced points in the frequency range from 0.1 Hz to 2.0 Hz and 36 equidistant points in the angle domain from 0 to 2π. The constant space step in the range from 1 m to 2 m has been used for explicit first order accuracy integration in fetch coordinate.

All numerical simulations discussed in the current paper have been started from uniform noise energy distribution in Fourier space $\varepsilon(\omega,\theta) = 10^{-6}\ \ m^4$, corresponding to small initial wave height with effectively negligible nonlinearity level. The constant wind speed 10 m/sec was assumed blowing away from the shore line, along the fetch. The assumption of the constant wind speed is a necessary simplification, due to the fact that ZRP numerical simulation was compared to various field experiments, and the considered set-up is the simplest physical situation, which can be modeled and realized in nature.

2.1. ZRP model

ZRP wind input term has been used in the form [34, 17, 27]

$$S_{in}^{ZRP}(\omega,\theta) = \gamma(\omega,\theta)\cdot\varepsilon(\omega,\theta) \tag{12}$$

$$\gamma(\omega,\theta) = \begin{cases} 0.05\frac{\rho_a}{\rho_w}\omega\left(\frac{\omega}{\omega_0}\right)^{4/3} q(\theta) \ \text{ for } f_{min}\le f\le f_d, \ \ \omega = 2\pi f \\ 0 \ \text{ otherwise} \end{cases} \tag{13}$$

$$q(\theta) = \begin{cases} \cos 2\theta \ \text{ for } -\pi/4\le\theta\le\pi/4 \\ 0 \ \text{ otherwise} \end{cases} \tag{14}$$

$$\omega_0 = \frac{g}{U}, \ \ \frac{\rho_a}{\rho_w} = 1.3\cdot 10^{-3} \tag{15}$$

where $U = 10$ m/sec is the wind speed at the reference level of 10 meters, ρ_a and ρ_w are the air and water density correspondingly. Frequencies $f_{min} = 0.1$ Hz and $f_d = 1.1$ Hz have been used.

The ZRP model source functions set is accomplished with the "implicit dissipation" term S_{diss} playing dual role of direct energy cascade flux sink due to wave breaking as well as numerical scheme stabilization factor at high wave-numbers. It is made via continuation of the spectrum from ω_d by Phillips law $A(\omega_d)\cdot\omega^{-5}$ [15], decaying faster than equilibrium spectrum ω^{-4}, and providing high-frequency wave energy dissipation. The corresponding analytic parameterization of this dissipation term is not determined, while is not in principle impossible to figure out in some way.

The coefficient $A(\omega_d)$ in front of ω^{-5} is unknown, but is not required to be defined in an explicit form. Instead, it is dynamically determined from the continuity condition of the spectrum, at frequency ω_d, on every time step. In other words, the starting point of the Phillips spectrum coincides with the last frequency point of the dynamically changing spectrum, at $\omega_d = 2\pi f_d$, where $f_d \simeq 1.1\ Hz$, as per [13]. This is the way the high frequency "implicit" damping is incorporated into ZRP model.

2.2. MD1 model

The MD1 model [7] is briefly formulated below in relation to the studied deep water case in the absence of average current.

For reader convenience, we briefly reformulate it in here. The wind source function is

$$S_{in}^{MD} = A_1(U_{\lambda/2}\cos\theta - c)|U_{\lambda/2}\cos\theta - c|\frac{k\omega}{g}\frac{\rho_a}{\rho_w}\varepsilon(k,\theta) \tag{16}$$

where θ is the angle between wind direction and waves with the wavenumber k, $A_1 = 0.11$ is the sheltering coefficient, $U_{\lambda/2}$ is the wind speed at one half wavelength above the surface for logarithmic profile

$$U_{\lambda/2} = \frac{U_*}{\kappa}\ln\frac{z}{z_0} \tag{17}$$

where U_* is the friction velocity, $\kappa = 0.41$ - Von Karman constant, $z = \frac{1}{2}\lambda$ is the elevation equal to a fixed fraction $\frac{1}{2}$ of the spectral peak wavelength $\lambda = 2\pi/k_p$ (k_p is the wavenumber of the spectral peak) and $z_0 = \alpha_C u_*^2/g$ is the surface roughness subject to Charnock constant $\alpha_C = 0.015$ ([6]).

The dissipation source function is the "spilling breakers" dissipation function [7]

$$S_{sb}^{MD1} = -A_2 \left[1 + A_3 MS M^2(k,\theta)\right]^2 [B(k,\theta)]^{2.53}\, \omega(k)\varepsilon(k,\theta) \tag{18}$$

where

$$MS M^2(k,\theta) = \int_0^k p^2 \varepsilon(p,\theta) dp \tag{19}$$

is the Mean Square Slope (MSS) in the direction θ of all waves longer than $\frac{2\pi}{k}$, $B(k,\theta) = k^4\varepsilon(k,\theta)$ is the degree of saturation, $A_2 = 46.665$, $A_3 = 240$.

Due to fast growing factor $\omega^{21.24}$ in the Eq.(18), the numerical solution of MD1 model is prone to numerical instabilities, if the dissipation source function is used in a straightforward way as the part of "overall" right-hand side source function, especially due to inability of significantly splitting the characteristic space integration step ~ 1 m for acceptable simulation times. In this case, the different treatment of the nonlinear dissipation Eq.(18) is useful – one can analytically solve the dissipation part of HE

$$\frac{1}{2}\frac{g\cos\theta}{\omega}\frac{\partial\varepsilon}{\partial x} = S_{sb}^{MD} \tag{20}$$

on every space integration step h in the adiabatic approximation, assuming that MMS change is slower than wave energy density ε for every space step h.

$$\varepsilon_{n+1} = \varepsilon_n \Big/ \left[1 + 2.52 A_2 \left[1 + MS M^2\right]^2 \frac{2\omega}{g\cos\theta} h \varepsilon_n^{2.53}\right]^{1/2.53} \tag{21}$$

where n is the numerical integration step number and h is the numerical discretisation step along the fetch. Such treatment of the dissipation function provides relatively instability-free integration technique.

2.3. MD2 model

The MD2 model was created to check the influence of the nonlinear dissipation Eq.(18), through MD1 model modification via keeping the wind source function Eq.(16) with angle and frequency restrictions of Eqs.(13)-(14), but replacing the nonlinear dissipation by the "implicit" dissipation function, described in the subsection 2.1

In other words, the MD2 model is similar to ZRP model up to the substitution of Eq.(12) by Eq.(16).

3. Numerical results

Figure 1 presents the total wave energy as the function of the fetch coordinate for ZRP, MD1 and MD2 models. One should keep in a mind that ZRP curve is consistent with self-similar solution Eq.(6) with the index $p = 1$, reproduces the data of more than a dozen of field observations, analyzed in [1], and can be used, therefore, as the benchmark function.

The corresponding values of indices p for ZRP, MD1 and MD2 models along the fetch are presented on Figure 2. While ZRP model exhibits asymptotic convergence to the self-similar index target value $p = 1$, MD1 model does not. MD2 model does it as well, but to the different index value $p \simeq 0.5$ with somewhat slower convergence. That observation demonstrates self-similar behavior in ZRP and MD2 models. One should note fairly good correspondence between ZRP and MD1 models for wave energy growth on Figure 1 for "practical" dimensional fetches up to ~ 20 km, which justifies MD1 tuning quality against the total energy growth.

The Figure 3 shows the consistency between all three models for the average frequency behavior in the range of 25% scatter for far enough dimensional fetches exceeding 20 km.

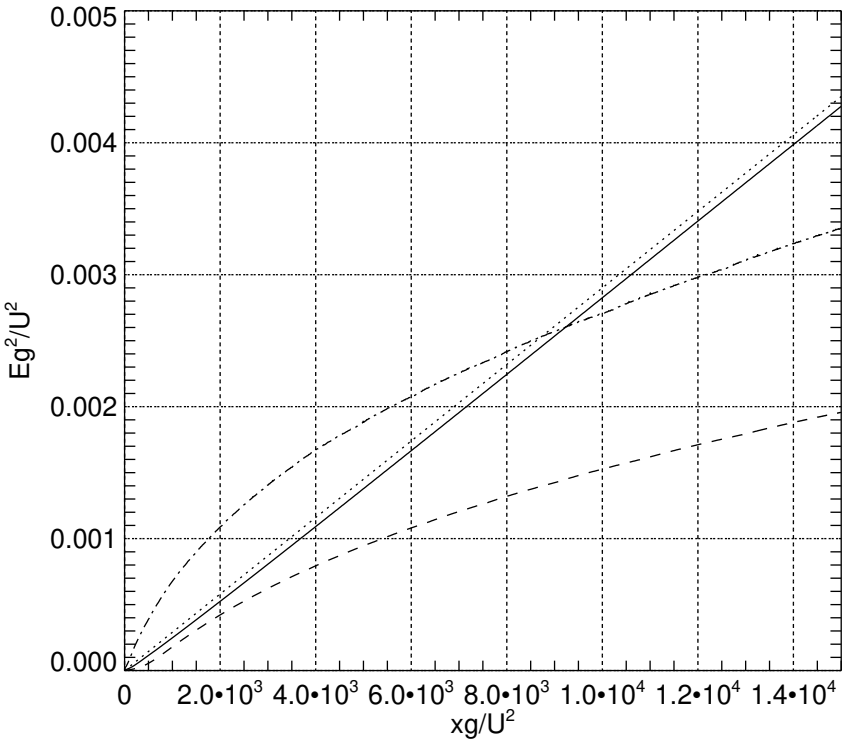

Fig. 1. Dimensionless energy Eg^2/U^4 versus dimensionless fetch xg/U^2 for wind speed $U = 10$ m/sec limited fetch case. Solid line - ZRP case, dotted line - self-similar solution with the empirical coefficient in front of it: $2.9 \cdot 10^{-7} xg/U^2$; dashed line - MD1 case; dash-dotted line - MD2 case.

ZRP model, as seen from Figure 4, demonstrates the behavior consistent with the self-similar dependence Eq.(10) with asymptotic convergence to the target self-similar index value $q = 0.3$, while MD1 and MD2 models show somewhat slower convergence to the different value of self-similar index $q \simeq 0.2$.

The oscillations observed in the behavior of index q could be attributed to the finite grid resolution used in the simulation, since the narrow spectral peak moves continuously between discrete frequencies in a manner that cannot be matched in these discretized simulations.

The check of calculated magic number $(10q - 2p)$ (see Eq.(7)) is presented on Figure 5. It exhibits asymptotic convergence of ZRP model to the target value of 1, while MD1 and MD2 models converge to the slightly lower values $0.8 \div 0.9$ somewhat slower along the fetch.

The nature of oscillation, especially obvious in MD1 and MD2 cases is attributed to the grid discreteness effects, described above.

Fig.6 presents angle-integrated wave energy spectrum for ZRP case, as the function of frequency, in logarithmic coordinates, for the dimensional fetch coordinate $x \simeq 20$ km. One can see that it consists of the segments of:

- the spectral peak region
- the inertial (equilibrium) range ω^{-4} spanning from the spectral peak to the beginning of the "implicit dissipation" $f_d = 1.1$ Hz
- Phillips high frequency tail ω^{-5} starting approximately from $f_d = 1.1$ Hz

Figure 7 presents decimal logarithm of angle-integrated energy spectrum for MD1 case, as the function of decimal logarithm of frequency for the dimensional fetch coordinate $x \simeq 20$ km. One can note that neither portion of the spectral tail to the right of the spectral peak can be approximated by $\sim \omega^{-4}$, or $\sim \omega^{-5}$ spectra. The only portion of the wave energy spectrum, which could be approximated by power-like function, is the region of high frequencies

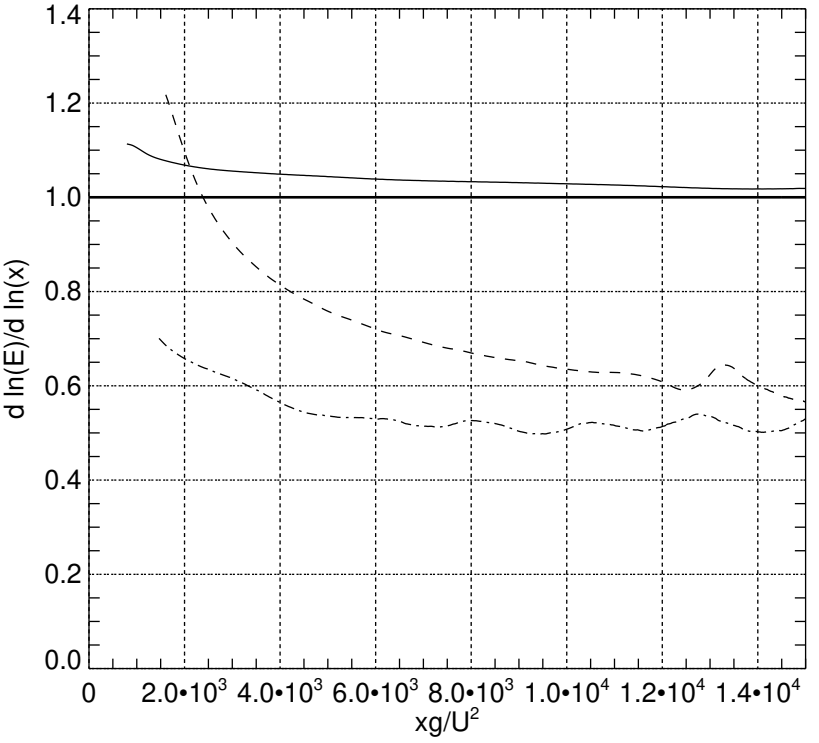

Fig. 2. Energy local power function index $p = \frac{d \ln E}{d \ln x}$ as the function of dimensionless fetch xg/U^2 for wind speed $U = 10$ m/sec fetch limited case. Theoretical value of self-similar index $p = 1$ - thick horizontal solid line. Solid line - ZRP case; dashed line - MD1 case; dash-dotted line - MD2 case.

$f > 1.1$ Hz with $\sim \omega^{-8.4}$ spectral shape. That sort of fast decaying spectra, however, was never observed in the field experiments, to the best of the author knowledge.

Figure 8 presents decimal logarithm of angle-integrated energy spectrum for MD1 case, as the function of frequency, for dimensional fetch coordinate $x \simeq 20$ km. One can see that the portion of the spectrum, for the frequencies range from 0.5 Hz to 1.2 Hz, can be approximated by the function $\sim 10^{-3.3f}$, which is unknown for experimental field observations either.

Appearance of both exponential and power-like spectra for intermediate and high frequency ranges correspondingly, finds its explanation from Figure 9. It shows that significant part of the wave breaking dissipation is localized in the area of intermediate frequencies, right adjacent to the spectral peak area. Such localization of the wave-breaking dissipation causes exponential decay at the intermediate frequencies of the spectral tail.

Fig.10 presents angle-integrated energy spectrum for MD2 case, as the function of the frequency, in logarithmic coordinates, for the dimensional fetch coordinate $x \simeq 20$ km. One can see that, just like in ZRP case, it consists of the segments of:

- the spectral peak region
- the inertial (equilibrium) range ω^{-4} spanning from the spectral peak to the beginning of the "implicit dissipation" $f_d = 1.1$ Hz
- Phillips high frequency tail ω^{-5} starting approximately from $f_d = 1.1$ Hz

That observation is the evidence of domination of nonlinear quadruplet interaction term, exhibiting KZ solution in the inertial range of frequencies from the spectral peak area to $f_d = 1.1$ Hz.

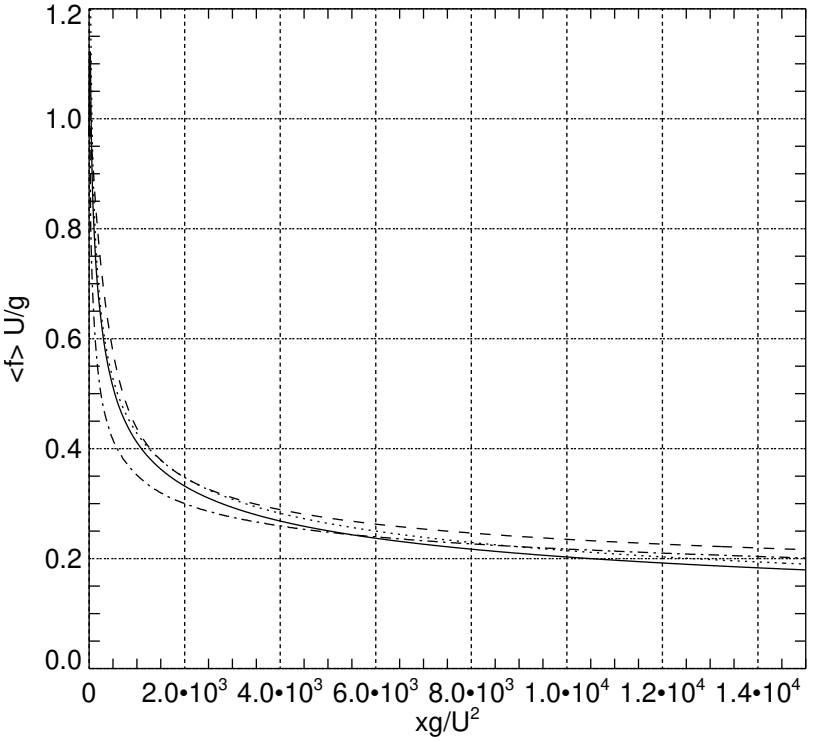

Fig. 3. Dimensionless mean frequency, as the function of the dimensionless fetch, calculated as $< f >= \frac{1}{2\pi}\frac{\int \omega n d\omega d\theta}{\int n d\omega d\theta}$, where $n(\omega,\theta) = \frac{\varepsilon(\omega,\theta)}{\omega}$ is the wave action spectrum, for wind speed 10 m/sec (solid line). The dash-dotted line is the self-similar dependence $3.4 \cdot \left(\frac{xg}{U^2}\right)^{-0.3}$ with the empirical coefficient in front of it; dashed line - MD1 case; dash-dotted line - MD2 case.

4. Conclusions

We analyzed numerically recently developed models for balanced source terms in HE for fetch-limited wind wave growth. These models utilize different techniques: ZRP model studies the family of analytical solutions of HE, restricting them through the experimental observations, while MD1 model utilizes mostly experimental techniques for their formulation. We also studied the "synthetic" approach - MD2 model - incorporating the features from ZRP as well as MD1 models.

The results of numerical simulation show that there is the significant difference between ZRP and MD1 models. While ZRP model exhibits self-similar properties, MD1 model shows only some of them with slower asymptotic convergence. As far as concerns Fourier space of the wave energy spectra, ZRP and MD2 models exhibit KZ spectrum, while MD1 model exhibit exponentially decaying spectral tail in the intermediate wave numbers. It is caused by different localization of the wave energy absorption: while ZRP approach relies of high-frequency dissipation, MD1 model utilizes intermediate wave numbers wave energy absorption. Besides that facts, ZRP model reproduces the wave energy and mean frequency behavior of more than a dozen of field experimental observation.

It is quite fascinating that MD2 "synthetic" model improves the self-similar properties of MD1, such as wave energy, average frequency indices, "magic numbers" as well as spectral characteristics of the angle-averaged spectra, such as $\sim \omega^{-4}$ spectral tails. This observation, in our view, emphasizes the fact that replacement of fairly complex nonlinear wave-breaking dissipation term by simple "implicit" dissipation in the form of Phillips tail could improve the quality of MD1 model under condition of re-tuning of wind wave energy input sheltering coefficient.

The presented research shows that relatively wide class of source terms, used in conjunction with exact nonlinear term S_{nl} and "implicit" high-frequency dissipation, can exhibit consistency with predicted self-similar properties of HE, KZ wave energy spectral shapes and data of the experimental observations.

The authors hope that this research will offer additional guidance for creation of tuning-free operational models .

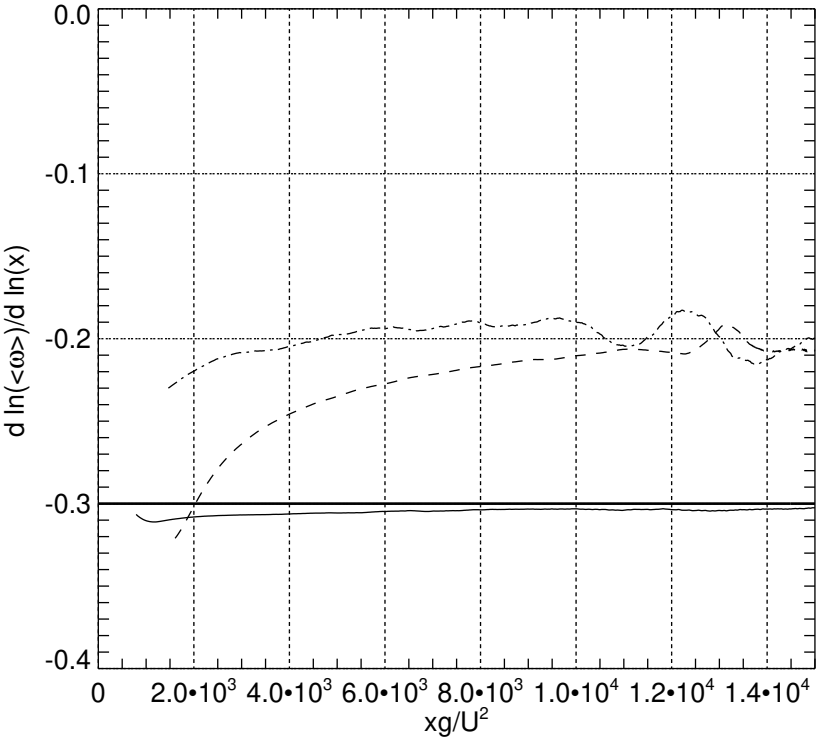

Fig. 4. Local mean frequency exponent $-q = \frac{d\ln<\omega>}{d\ln x}$ as the function of dimensionless fetch xg/U^2 for $U = 10$ m/sec limited fetch case. ZRP case - solid line; dashed line - MD1 case; dash-dotted line - MD2 case. Thick horizontal solid line - target value of the self-similar exponent $q = 0.3$.

5. Acknowledgments

The research presented in the section 3 has been accomplished due to the support of the grant Wave turbulence: the theory, mathematical modeling and experiment of the Russian Scientific Foundation No 14-22-00174. The research set forth in the section 1, was funded by the program of the presidium of RAS "Nonlinear dynamics: fundamental problems and applications".

The authors gratefully acknowledge the support of these foundations.

References

1. Badulin, S., Babanin, A.V., Resio, D.T., Zakharov, V., 2007. Weakly turbulent laws of wind-wave growth. J.Fluid Mech. 591, 339 – 378.
2. Badulin, S.I., Pushkarev, A.N., D.Resio, Zakharov, V.E., 2005. Self-similarity of wind-driven sea. Nonlinear Proc. in Geophysics 12, 891 – 945.
3. Badulin, S.I., Zakharov, V.E., 2012. The generalized Phillips' spectra and new dissipation function for wind-driven seas. arXiv:1212.0963 [physics.ao-ph] , 1 – 16.
4. Badulin, S.I., Zakharov, V.E., 2017. Ocean swell within the kinetic equation for water waves. Nonlinear Processes in Geophysics 24, 237–253. URL: https://www.nonlin-processes-geophys.net/24/237/2017/, doi:10.5194/npg-24-237-2017.
5. Cavaleri, L., Alves, J.H., Ardhuin, F., Babanin, A., Banner, M., Belibassakis, K., Benoit, M., Donelan, M., Groeneweg, J., Herbers, T., Hwang, P., Janssen, P., Janssen, T., Lavrenov, I., Magne, R., Monbaliu, J., Onorato, M., Polnikov, V., Resio, D., Rogers, W., Sheremet, A., Smith, J.M., Tolman, H., van Vledder, G., Wolf, J., Young, I., 2007. Wave modelling the state of the art. Progress in Oceanography 75, 603 – 674. doi:https://doi.org/10.1016/j.pocean.2007.05.005.
6. Charnock, H., 1955. Wind stress on a water surface. Q.J.R. Meteorol. Soc. 81, 639 – 640.
7. Donelan, M.A., Curcic, M., Chen, S.S., Magnusson, A.K., 2012. Modeling waves and wind stress. Journal of Geophysical Research: Oceans 117, n/a–n/a. URL: http://dx.doi.org/10.1029/2011JC007787, doi:10.1029/2011JC007787. c00J23.
8. Dyachenko, A.I., Kachulin, D.I., Zakharov, V.E., 2015. Evolution of one-dimensional wind-driven sea spectra. JETP Letters 102, 577 – 581.
9. Gagnaire-Renou, E., Benoit, M., Badulin, S., 2011. On weakly turbulent scaling of wind sea in simulations of fetch-limited growth. Journal of Fluid Mechanics 669, 178–213. doi:10.1017/S0022112010004921.

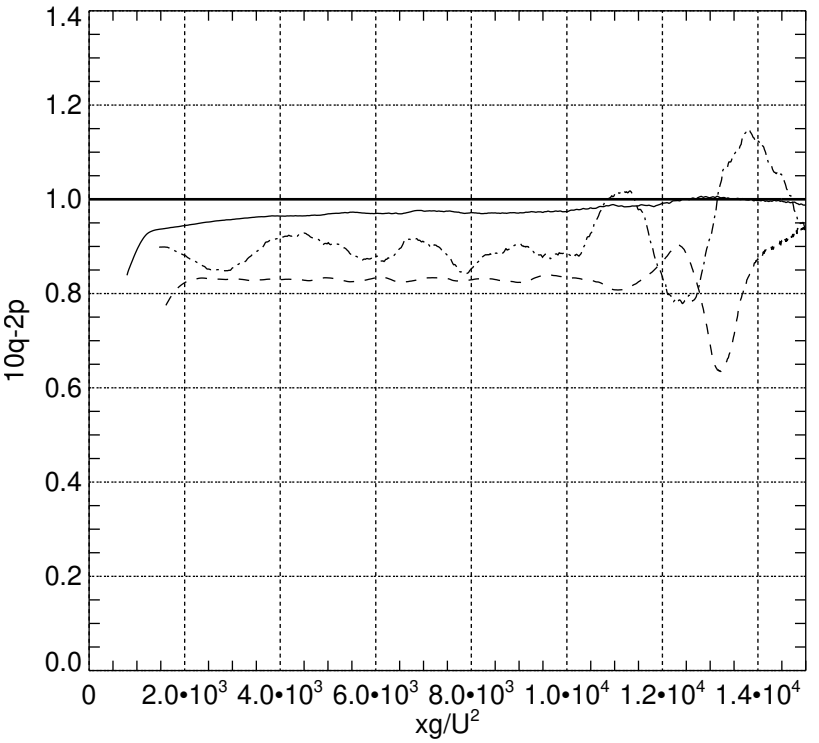

Fig. 5. "Magic number" $10q - 2p$ as a function of dimensionless fetch xg/U^2 for wind speed $U = 10$ m/sec limited fetch case. ZRP case - solid line; dashed line - MD1 case; dash-dotted line - MD2 case. Thick horizontal solid line - self-similar target value $10q - 2p = 1$.

10.Hasselmann, K., 1962. On the non-linear energy transfer in a gravity-wave spectrum. Part 1. General theory. Journal of Fluid Mechanics 12, 481 – 500.
11.Hasselmann, K., 1963. On the non-linear energy transfer in a gravity wave spectrum. Part 2. Conservation theorems; wave-particle analogy; irrevesibility. Journal of Fluid Mechanics 15, 273 – 281.
12.Korotkevich, A.O., Pushkarev, A.N., Resio, D., Zakharov, V.E., 2008. Numerical verification of the weak turbulent model for swell evolution. Eur. J. Mech. B - Fluids 27, 361 – 387.
13.Long, C., Resio, D., 2007. Wind wave spectral observations in Currituck Sound, North Carolina. JGR 112, C05001.
14.Perrie, W., Zakharov, V.E., 1999. The equilibrium range cascades of wind-generated waves. Eur. J. Mech. B/Fluids 18, 365 – 371.
15.Phillips, O.M., 1966. The dynamics of the upper ocean. Cambridge monographs on mechanics and applied mathematics, Cambridge U.P.
16.Pushkarev, A., Resio, D., Zakharov, V., 2003. Weak turbulent approach to the wind-generated gravity sea waves. Physica D 184, 29 – 63.
17.Pushkarev, A., Zakharov, V., 2016. Limited fetch revisited: comparison of wind input terms, in surface wave modeling. Ocean Modeling 103, 18 – 37. doi:10.1016/j.ocemod.2016.03.005.
18.Resio, D., Perrie, W., 1989. Implications of an f^{-4} equilibrium range for wind-generated waves. JPO 19, 193 – 204.
19.Resio, D.T., Long, C.E., 2007. Wind wave spectral observations in Currituck Sound, North Carolina. J. Geophys. Res. 112, C05001.
20.Resio, D.T., Long, C.E., Vincent, C.L., 2004. Equilibrium-range constant in wind-generated wave spectra. J. Geophys. Res. 109, CO1018.
21.Resio, D.T., Perrie, W., 1991. A numerical study of nonlinear energy fluxes due to wave-wave interactions in a wave spectrum. Part I: Methodology and basic results. J. Fluid Mech. 223, 603 – 629.
22.SWAN, 2015. `http://swanmodel.sourceforge.net/`.
23.Toba, Y., 1972. Local balance in the air-sea boundary processes. pt. 1: On the growth process of wind waves. J. Oceanogr. Soc. Japan. 28, 109 – 121.
24.Tolman, H.L., 2013. User manual and system documentation of WAVEWATCH III. Environmental Modeling Center, Marine Modeling and Analysis Branch .
25.Tracy, B., Resio, D., 1982. Theory and calculation of the nonlinear energy transfer between sea waves in deep water. WES report 11, U.S. Army Engineer Waterways Experiment Station, Vicksburg, MS.
26.Webb, D.J., 1978. Non-linear transfers between sea waves. Deep-Sea Res. 25, 279 – 298.
27.Zakharov, V., Resio, D., Pushkarev, A., 2017. Balanced source terms for wave generation within the hasselmann equation. Nonlin. Processes Geophys. 24, 581 – 597. doi:https://doi.org/10.5194/npg-24-581-2017.
28.Zakharov, V.E., 2010. Energy balances in a wind-driven sea. Physica Scripta T142, 014052.
29.Zakharov, V.E., Badulin, S.I., 2011. On energy balance in wind-driven sea. Doklady Akademii Nauk 440, 691 – 695.

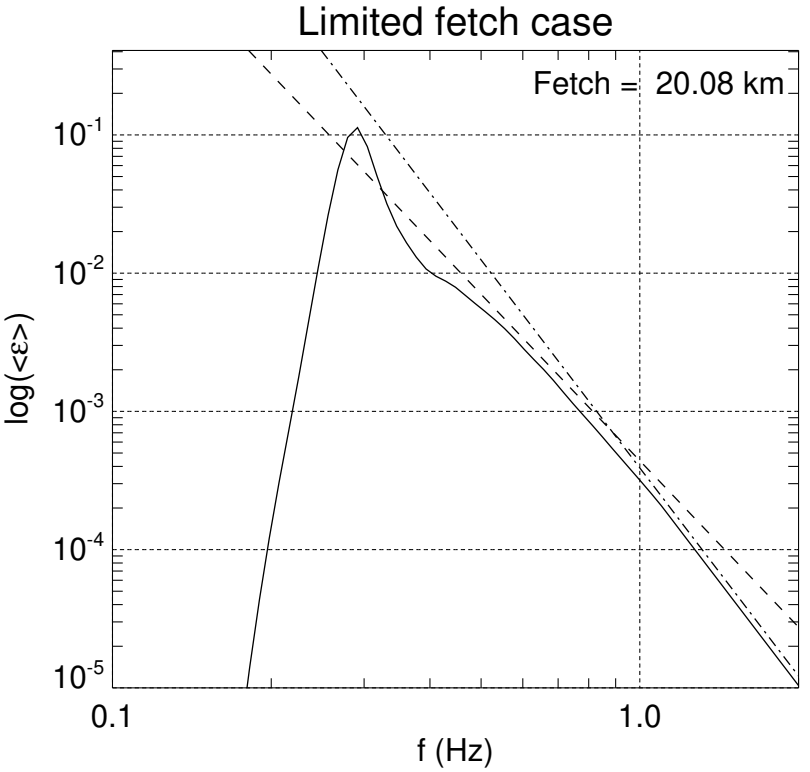

Fig. 6. Decimal logarithm of the angle averaged spectrum as the function of the decimal logarithm of the frequency for wind speed $U = 10$ m/sec fetch limited ZRP case - solid line. Spectrum $\sim f^{-4}$ - dashed line, spectrum $\sim f^{-5}$ - dash-dotted line.

30.Zakharov, V.E., Filonenko, N.N., 1966. The energy spectrum for stochastic oscillation of a fluid's surface. Dokl.Akad.Nauk. 170, 1992 – 1995.
31.Zakharov, V.E., Filonenko, N.N., 1967. The energy spectrum for stochastic oscillations of a fluid surface. Sov. Phys. Docl. 11, 881 – 884.
32.Zakharov, V.E., Korotkevich, A.O., Prokofiev, A.O., 2009. On dissipation function of ocean waves due to whitecapping, in: Simos, T.E., G.Psihoyios, Tsitouras, C. (Eds.), American Institute of Physics Conference Series, pp. 1229 – 1237.
33.Zakharov, V.E., L'vov, V.S., Falkovich, G., 1992. Kolmogorov Spectra of Turbulence I: Wave Turbulence. Springer-Verlag.
34.Zakharov, V.E., Resio, D., Pushkarev, A., 2012. New wind input term consistent with experimental, theoretical and numerical considerations. http://arxiv.org/abs/1212.1069/.

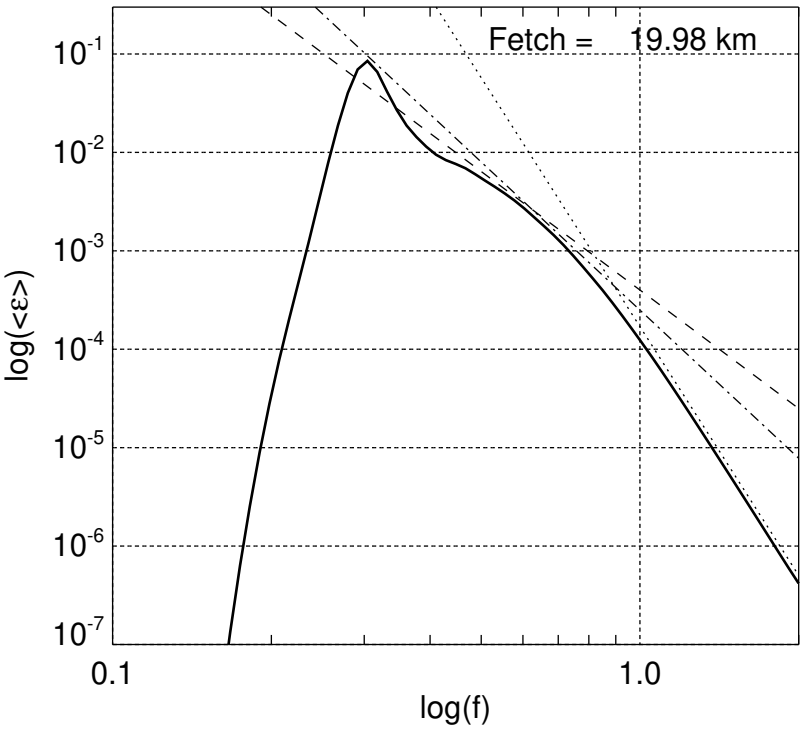

Fig. 7. Decimal logarithm of the angle averaged spectrum as the function of the decimal logarithm of the frequency for wind speed $U = 10$ m/sec limited fetch MD1 case - solid line. Spectrum $\sim f^{-4}$ - dashed line, spectrum $\sim f^{-5}$ - dash-dotted line.

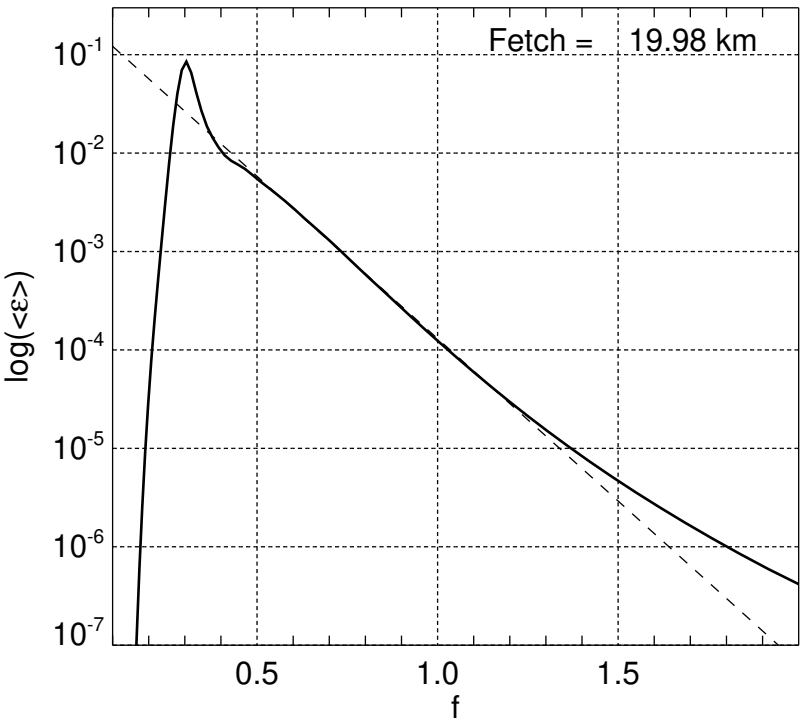

Fig. 8. Decimal logarithm of the angle averaged spectrum as the function of the frequency for wind speed $U = 10$ m/sec limited fetch MD1 case - solid line. Spectrum $\sim 10^{-3.3f}$ - dashed line.

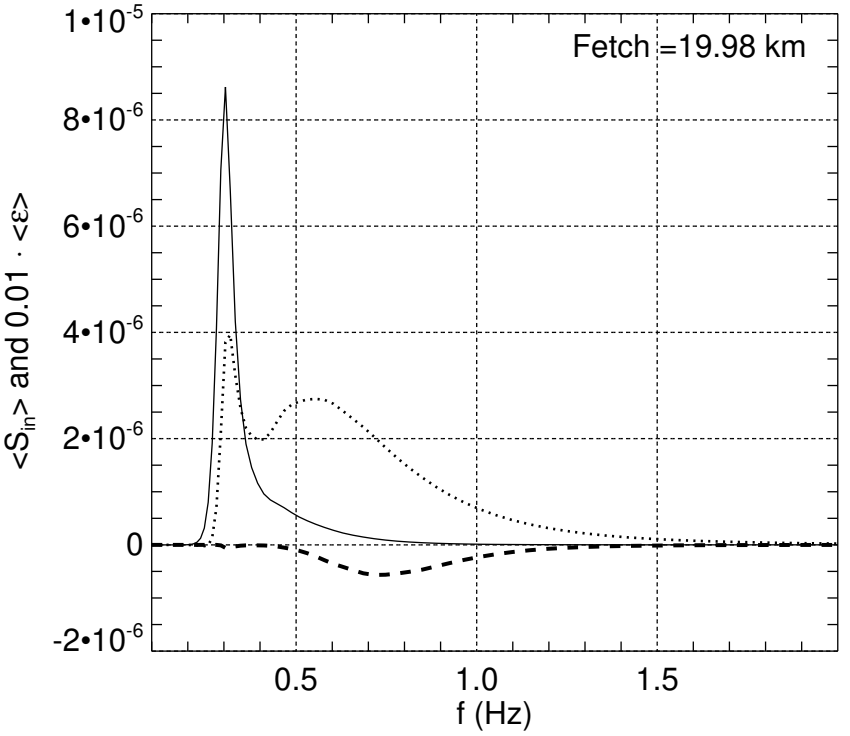

Fig. 9. Angle averaged wave energy wind input $< S_{in} >= \frac{1}{2\pi}\int \gamma_{in}(\omega,\theta)\varepsilon(\omega,\theta)d\theta$ (dotted line), wave braking dissipation $< S_{diss} >= \frac{1}{2\pi}\int \gamma_{diss}(\omega,\theta)\varepsilon(\omega,\theta)d\theta$ (dashed line) and angle averaged spectrum $< \varepsilon >= \frac{1}{2\pi}\int \varepsilon(\omega,\theta)d\theta$ (solid line) as the functions of the frequency f (solid line).

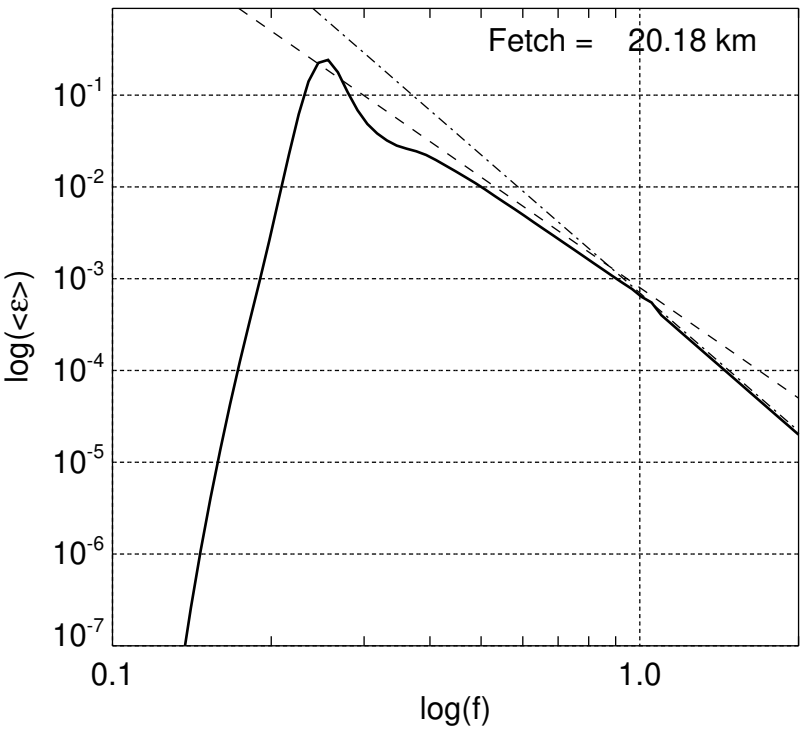

Fig. 10. Decimal logarithm of the angle averaged spectrum as the function of the decimal logarithm of the frequency for wind speed U = 10 m/sec limited fetch MD2 case - solid line. Spectrum $\sim f^{-4}$ - dashed line, spectrum $\sim f^{-5}$ - dash-dotted line.

Available online at www.sciencedirect.com

ScienceDirect

Procedia IUTAM 26 (2018) 145–152

Procedia IUTAM

www.elsevier.com/locate/procedia

IUTAM Symposium Wind Waves, 4-8 September 2017, London, UK

Computational Turbulent Shear Flows Over Growing And Non-Growing Wave Groups

S.G. Sajjadi[a], F. Drullion[a], J.C.R. Hunt[b]

[a]*Embry-Riddle Aeronautical University, Florida, USA.*
[b]*University College London, UK.*

Abstract

A high-Reynolds-number second-order stress closure model is used to perform numerical simulations of the wind flow above different groups of waves. It is shown that the group profiles can change as the individual waves grow within its envelop due to the energy transfer between the wind and the group. The focus of this study is the behaviour of the critical-layer and the associated with "cat's-eye" structures which are centred around the critical height, where the real part of the complex wave speed is equal to the mean flow velocity. It is also shown that the position and size of these structures depend on the wave age and the wave steepness. It is demonstrated that the larger these structures become, the greater disturbance of the wind flow above the wave groups appear. Also, the results obtained here demonstrate how the critical layer structures are asymmetrical over the waves within a group because of the shear driven sheltering effect on the downwind side of the group. The results here complement the general review of wind-wave dynamics by Hunt & Sajjadi [1].

Peer-review under responsibility of the scientific committee of the IUTAM Symposium Wind Waves.

Keywords: Type your keywords here, separated by semicolons ;

1. Introduction

Following the review of Hunt and Sajjadi [1], and the points discussed in our earlier paper [13], we perform a numerical simulations of turbulent shear flows over growing and non-growing wave groups, adopting a second-order Reynolds-stress turbulence closure model.

Although the growth and decay of wind generated waves of monochromatic, idealized wave profiles have been extensively studied and are well understood, the interactions and energy transfer between groups of water waves and the ambient wind above them are still not well understood. Experimental, numerical and analytical studies of ocean waves have shown how ocean waves actually travel in groups in which the profiles change as their envelop are

* Corresponding author. Tel.: +0-000-000-0000 ; fax: +0-000-000-0000.
E-mail address: author@institute.xxx

2210-9838
Peer-review under responsibility of the scientific committee of the IUTAM Symposium Wind Waves.
10.1016/j.piutam.2018.03.014

travelling. In this study we consider how consider in particular how ocean wave groups grow through their dynamical interaction with turbulent wind shear over the waves.

We focus our attention on the region around the height where the real part of the complex wave speed is equal to the mean flow velocity, i.e. when $U(z_c) = c_r$, where c_r is the real part of the wave speed. This region, namely the "critical layer", whose thickness is z_c, where closed streamlines (namely cat's-eye) develop, is the central point in Miles' theory [2] and Lighthill's interpretation of growth of waves [3]. Miles considered the limit as the complex wave speed, c_i, tends to zero, and in his subsequent analysis he assumed the complex part of the waves is identically zero. He argued that in this limit there is a finite positive drag over the waves and the energy-transfer rate is only dependent on the curvature of the velocity profile $U(z_c)$ at the critical height $z = z_c$. Furthermore, he only considered steady monochromatic waves of small steepness which were of the order 0.01. But, if the waves do grow or decay, the amplitude of waves must vary in time [13], i.e. $a(t) = a_0 e^{kc_i t}$, where a_0 is the initial amplitude and k is the wavenumber.

It has been shown by [12], that as the cat's-eye become larger the flow over the waves become more disturbed. Also as the wave age (i.e. U/U_*) increases, the elevation of the cat's-eyes exceed the thickness ℓ of the inner surface layer i.e. $z_c > \ell$, then there is a strong reverse flow below the critical layer which affects the surface drag, and thus the energy-transfer rate, β. This is consistent with recent findings [12, 15] who showed that as waves steepen then β increases. But for monochromatic waves, z_c is symmetrically placed over the waves [12, 5]. However, for wave groups the critical layer becomes more asymmetrical particularly as waves grow [14].

2. Governing equations

The air flow with density ρ_a and kinematic viscosity ν_a over the group of waves is governed by the incompressible Reynolds averaged Navier-Stokes equations:

$$\frac{\partial U_i}{\partial x_i} = 0 \tag{1}$$

$$\frac{DU_i}{Dt} = -\frac{1}{\rho_a}\frac{\partial P}{\partial x_i} + \frac{\partial}{\partial x_j}\left[\nu_a\left(\frac{\partial U_i}{\partial x_j} + \frac{\partial U_j}{\partial x_i}\right) - \overline{u_i' u_j'}\right] \tag{2}$$

where U_i is the mean velocity component in the x_i-direction, P is the mean pressure, $\overline{u_i' u_j'}$ is the Reynolds-averaged stress correlation and t is time.

A model for the Reynolds-averaged stress correlations is needed to close equation (2). A rational approach for providing a model for $\overline{u_i' u_j'}$ in equation (2) relies on its transport equation, which may be written in the following form

$$\frac{D\overline{u_i' u_j'}}{Dt} = P_{ij} + \Pi_{ij} - \varepsilon_{ij} + d_{ij} \tag{3}$$

where $P_{ij} = -(\overline{u_i' u_k'}\partial U_j/\partial x_k + \overline{u_j' u_k'}\partial U_i/\partial x_k)$ is the production term, Π_{ij} represents the velocity-pressure gradient correlation, ε_{ij} the viscous dissipation, and d_{ij} represents diffusion by both molecular viscosity and the triple velocity moments. On the left-hand side of (3), the stress convection, and the production term are both exact and require no further modelling. However, all other terms contain further unknowns which must be modelled. For this we adopt a high-Reynolds-number turbulence model [6]. In this model, the pressure correlation Π_{ij} is decomposed into a redistributive part, ϕ_{ij}^*, and a non-redistributive part by

$$\Pi_{ij} \equiv -\frac{1}{\rho_a}\left(\overline{u_i'\frac{\partial p'}{\partial x_j} + u_j'\frac{\partial p'}{\partial x_i}}\right) = \phi_{ij}^* + \frac{\overline{u_i' u_j'}}{2K} d_{kk}^p \tag{4}$$

where $d_{kk}^p = -(1/\rho_a)\partial\overline{u_k' p'}/\partial x_k$ represents the pressure diffusion of the turbulent kinetic energy $K = \frac{1}{2}\overline{u_i' u_i'}$. The model employed for the redistributive part of the pressure correlation, ϕ_{ij}^*, is based on the cubic realizable form derived by Fu [7]. The dissipation ε_{ij} is modelled as

$$\varepsilon_{ij} = \left(1 - A^{1/2}\right)\frac{\varepsilon}{K}\overline{u_i' u_j'} + \tfrac{2}{3}\varepsilon\delta_{ij} \tag{5}$$

where $A = 1 - 9/8(A_2 - A_3)$, $A_2 = a_{ij}a_{ij}$, $A_3 = a_{ij}a_{jk}a_{ki}$ and $a_{ij} = \overline{u_i'u_j'}/K - \frac{2}{3}\delta_{ij}$. This model is very similar to the form adopted in other high-Reynolds-number flows, see for example Gibson & Launder [8]. In (5) The dissipation rate ε is derived through the solution of its own transport equation:

$$\frac{D\varepsilon}{Dt} = c_{\varepsilon 1}\frac{\varepsilon P_{kk}}{2K} - c_{\varepsilon 2}\frac{\varepsilon^2}{K} + \frac{\partial}{\partial x_l}\left[\left(\nu_a\delta_{lk} + c_\varepsilon\overline{u_l'u_k'}\frac{K}{\varepsilon}\right)\frac{\partial\varepsilon}{\partial x_k}\right] + c_{\varepsilon 3}A^{1/2}(1-A)\frac{\varepsilon}{\sqrt{K}}\overline{u_i'u_j'}\frac{\partial A}{\partial x_i}\frac{\partial}{\partial x_j}\left(\frac{K^{3/2}A^{1/2}}{\varepsilon}\right) \tag{6}$$

with coefficients

$$c_{\varepsilon 1} = 1.0, \quad c_{\varepsilon 2} = 1.92/(1 + 0.7A_dA_2^{1/2}), \quad A_d = \max(0.2, A), \quad c_{\varepsilon 3} = 1.0, \quad c_\varepsilon = 0.18$$

The only remaining term in the stress transport equations is the diffusion term

$$d_{ij} = \frac{\partial}{\partial x_k}\left(\nu_a\frac{\partial\overline{u_i'u_j'}}{\partial x_k} - \overline{u_i'u_j'u_k'}\right) \tag{7}$$

The viscous diffusion is, of course exact, and the triple correlations are modelled via the proposal of Hanjalic & Launder [9] proposal

$$\overline{u_i'u_j'u_k'} = -c_s\frac{K}{\varepsilon}\left[\overline{u_i'u_l'}\frac{\partial\overline{u_j'u_k'}}{\partial x_l} + \overline{u_j'u_l'}\frac{\partial\overline{u_i'u_k'}}{\partial x_l} + \overline{u_k'u_l'}\frac{\partial\overline{u_j'u_i'}}{\partial x_l}\right] \tag{8}$$

where $c_s = 0.11$.

3. Numerical scheme

The finite volume method is used to solve the governing equations. The volumes are non-orthogonal and collocated such that all flow variables are stored at the centered of the cells. The numerical scheme uses a pressure based solver [10]. A first order forward discretization in time is used, and the convective fluxes are approximated with the higher-order upstream-weighted scheme, QUICK of Leonard [11]. The pressure and diffusive fluxes are discretized using a central difference operator. The finite volume method and the chosen discretizations lead to penta-diagonal system solved using a tri-diagonal, matrix algorithm (TDMA). The discretization is proceeded by a transformation of the Cartesian coordinates of the governing equations to the non-orthogonal coordinates ξ and ζ using the Jacobian transformation matrix. The transport equation for any scalar property Φ many be expressed in non-orthogonal direction as

$$\underbrace{\frac{\partial}{\partial t}(J\rho_a\Phi)}_{\text{transient term}} + \underbrace{\frac{\partial}{\partial\xi}\left(\rho_aU^{(\xi,\zeta)}\Phi\right) + \frac{\partial}{\partial\zeta}\left(\rho_aW^{(\xi,\zeta)}\Phi\right)}_{\text{convection}} + \underbrace{\frac{\partial}{\partial\xi}\left(\alpha_\Phi J\frac{\partial\Phi}{\partial\xi}\right) + \frac{\partial}{\partial\zeta}\left(\beta_\Phi J\frac{\partial\Phi}{\partial\zeta}\right)}_{\text{diffusion}} = \underbrace{JS_\Phi}_{\text{source}} \tag{9}$$

where $U^{(\xi,\zeta)} = Uz_\zeta - Wx_\zeta$ and $W^{(\xi,\zeta)} = Wx_\xi - Uz_\xi$ are contravarient velocity components, J is the Jacobian of the transformation, S_Φ is the source term including diffusive terms, pressure terms in the momentum equation, $\alpha_\Phi = \Gamma_\Phi(x_\zeta^2 + z_\zeta^2)$, $\beta_\Phi = \Gamma_\Phi(x_\xi^2 + z_\xi^2)$, where Γ_Φ is isotropic diffusivity, and the subscripts ξ, ζ denote partial differentiations. The mesh covering the computational domain contains 200×100 nodes and extends over six wavelengths in horizontal direction and two wavelength in the vertical direction. As can be seen from figure 1, it is refined near the water surface in order to capture the steep gradients which are inherently present there.

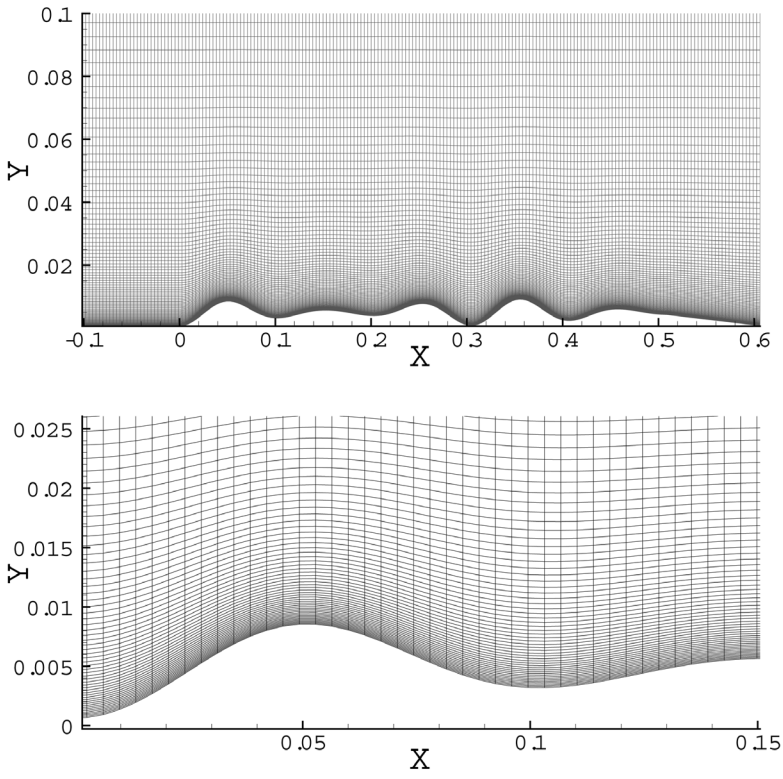

Fig. 1. Computational mesh adopted. Top is the entire region, bottom zoom of a region showing the compression of grids near the surface.

4. Problem set up and wave group construction

We consider groups of waves composed by superposition of three cosine waves (see equation 11 below). The groups are traveling in deep water at the speed $c_r = \frac{1}{2}\sqrt{\frac{g}{k}}$ and a wind whose mean velocity is assumed to be logarithmic is blowing above them. At the height of one wavelength above the surface of the wave, the wind velocity is imposed to be U_λ. The turbulent flow has a mean velocity profile $U(\zeta) = U_1 \ln(\zeta/\zeta_0)$, $U_1 \equiv U_*/\kappa$, U_* being the friction velocity, κ being the von Kármán's constant, and ζ_0 is the surface roughness. Note that, ξ and ζ are the wave-following coordinates, given by the following transformation

$$x = \xi, \qquad z = \zeta + h(\xi, \zeta) \tag{10}$$

where $h = h(\xi, \zeta)$ maps $z = h_0$ onto $\zeta = 0$ and is evanescent for $k\zeta \uparrow \infty$ but is otherwise arbitrary. The computational domain is taken to six wavelengths horizontally and two wavelengths vertically. The groups only extend over four wavelengths (from $x = 0$ to $x = 4\lambda$) and are surrounded by a flat surface. The latter ensures the periodicity in boundary conditions in the x-direction. In our simulations, the frame of reference is traveling with the group. The initial wave group profile is given by:

$$h_0 = a[\cos(k\mathscr{X}) + \epsilon_1 \cos(k_1\mathscr{X}) + \epsilon_2 \cos(k_2\mathscr{X})] \tag{11}$$

where a is the initial wave amplitude k is the wave number, $k_1 = 1 + \sqrt{2}ak$ and $k_2 = 1 - \sqrt{2}ak$ and where $\mathscr{X} = \xi - c_r t$.

5. Boundary conditions

A strictly horizontal velocity $U = U_\lambda - \frac{c_r}{2}$ is imposed at the top of the computational domain, taking into account the fact that the frame of reference is moving with the waves at the speed $\frac{c_r}{2}$.

At the bottom of the domain, the mean velocity components match the wave orbital velocities. The orbital velocities for $0 \le x \le 4\lambda$, are given by

$$u = -c_g ak[\cos(kx) + \epsilon_1 k_1 \cos(k_1 x) + \epsilon_2 k_2 \cos(k_2 x)] - c_g$$
$$v = -c_g ak[\sin(kx) + \epsilon_1 k_1 \sin(k_1 x) + \epsilon_2 k_2 \sin(k_2 x)]$$

Note that, for the flat surfaces surrounding the group portion on the south boundary, namely when $x < 0$ and $x > 4\lambda$, we impose the conditions $u = -c_g$ and $v = 0$. In the streamwise direction, periodic boundary conditions are imposed on all the mean variables and the turbulent stresses together with the turbulent dissipation rate. At the top and the bottom of the computational domain the boundary conditions imposed on the stresses and the dissipation rate are the same as the one used in [12]. The boundary conditions for stresses and dissipation rate is taken from our earlier paper [12].

6. Results

In this paper we report computations of turbulent flow over two groups both in a frame of reference moving with the wave, namely *group1* and *group2*. For both groups, the initial amplitude of the main cosine wave is $a(0) = 0.0025$ m and its wavelength is $\lambda = 0.1016$ m. Here, $(\epsilon_i)_{1,2}$ for *group1* and *group2* are respectively: ($\epsilon_1 = 0.2$, $\epsilon_2 = 0.1$) and ($\epsilon_1 = 0.25$, $\epsilon_2 = 0.5$).

Note that, for all the diagrams, the vertical axis has been normalized using the fundamental wave number k.

6.1. Non-growing groups

We first consider the influence of the wave age on the cat's-eye structures over non-growing groups for the following three wave ages: $c_r/U_* = 1$, $c_r/U_* = 3.5$, and $c_r/U_* = 7$. Figures 2 and 3 show the contour plots of the stream function for respectively *group1* and *group2* as a function for three wave ages $c_r/U_* = 1, 3.5$ and 7. As it can be seen from these figures, at lowest value of c_r/U_* cat's-eye structures are formed downstream of the steepest waves in the group. As the wave age increases to 3.5, we note that new weaker cat's-eye structures appear in the lee of the waves where they were not previously present, the pre-existing structures increase in size and their center slightly shift toward the peak of the wave behind of them, the cat's-eye structures also slightly lift up from the surface of the wave. At $c_r/U_* = 7$ the cat's-eye become stronger and move further over the peak of the waves in the group. At the largest value of the wave age we can observe a maximum disturbance of the mean flow above the waves, the critical height, passing through the center of the cat's-eye structures is lifted above the crests of the waves.

6.2. Growing groups

We next consider the case where group of waves for which the initial profile as well as the lower boundary condition can evolve under the influence of the turbulent wind flow above the wave. For the growing groups, the computational mesh is regenerated every 50 time steps, where each time step consists of 500 iterations and is increased as the waves become steeper. All the variables are then interpolated/extrapolated onto the new mesh. The growth factor for each wave within the group is $e^{\mathsf{K}c_i t}$, where K can be taken to be k, k_1 or k_2 and

$$c_i = 8c_g a/\lambda.$$

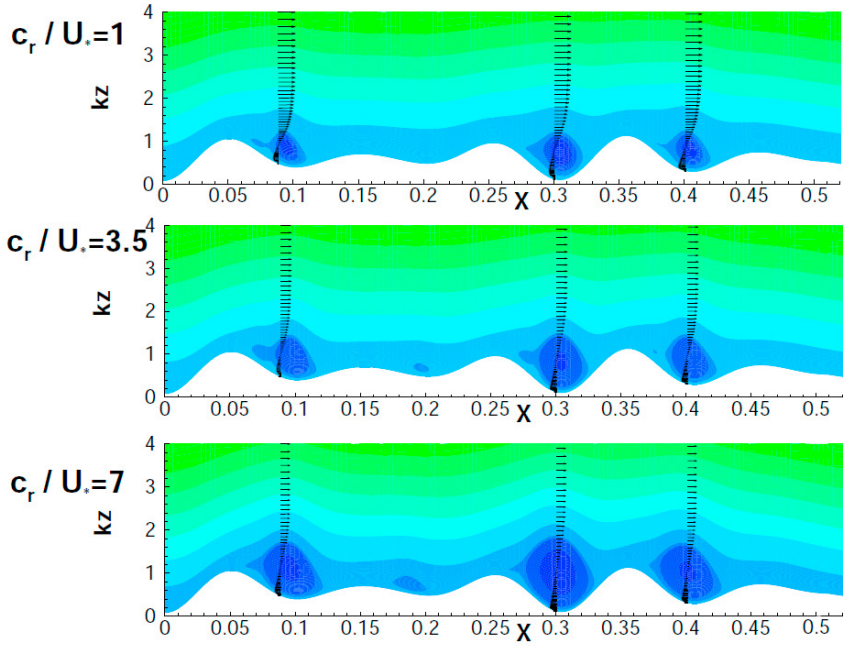

Fig. 2. Contour plots and velocity vector field of the stream function over *group1* wave for three values of the wave age c_r/U_*=1 (top); 3.5 (middle), and 7 (bottom).

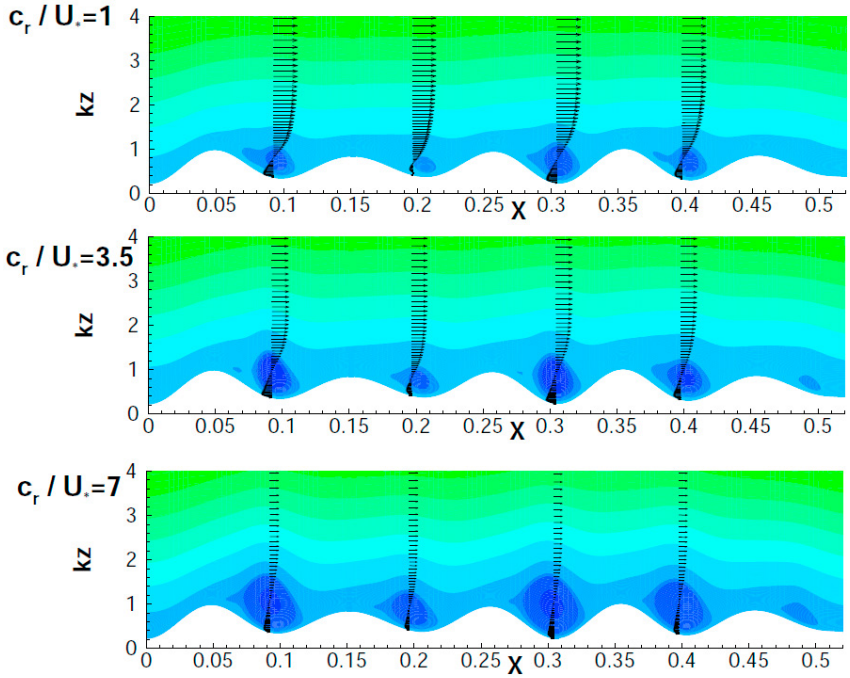

Fig. 3. Contour plots of stream function and velocity vector field over *group2* wave for three values of the wave age c_r/U_*= 1 (top); 3.5 (middle), and 7 (bottom).

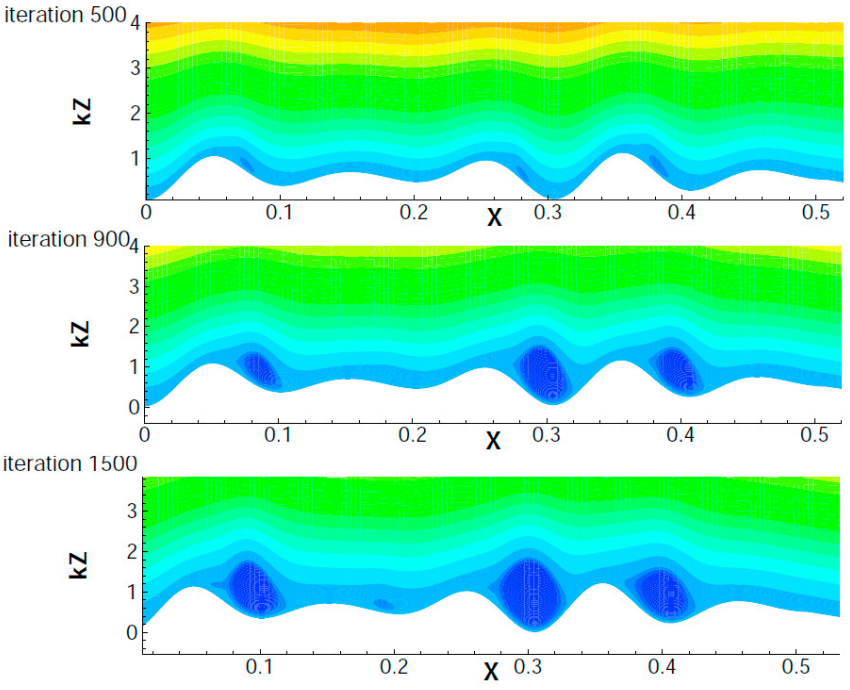

Fig. 4. Contour plots of stream function over growing *group1* wave for a single value of the wave age $c_r/U_* = 5.75$. Steepest wave is depicted at the bottom.

This choice of the complex wave celerity is chosen such that it yields a similar magnitude as that used in our earlier contribution [13]. A more physical expression may be deduced from parameterization expression for the energy-transfer rate from wind to waves, see [15].

In figure 4, we display the result of simulations for *group2* growing under the influence of the surrounding wind, for one fixed value of the wave age $c_r/U_* = 5.75$. As it can be seen, when the wave steepens, the cat's-eye structures are formed in the lee of the waves in the group. As the waves grow so do the cat's-eyes, similarly to our other computations for monochromatic waves and bimodal Stokes waves [12] (see also Sullivan *et al.* [5]). Note also how the critical height rises higher above the surface of the waves. It is also evident that the flow become more asymmetrical. In the air flow over the upwind part of the group where $c_i > 0$, the net drag increases. This increases the general flow over the whole group even though $c_i < 0$ on the downwind side of the group.

7. Conclusion

In this study a high-Reynolds-number stress model is used to simulate the turbulent wind flow above growing and non-growing groups of waves for different ratios of wind speed to turbulence intensity, i.e. 'wave age'. Our simulations show that both the height of the critical layer, as well as the shape and positions of the cat's-eye structures, form over groups of waves dependent on the wave age as previously demonstrated for monochromatic and Stokes waves with the same computational model [12]. As the wave age (c_r/U_*) increases the cat's-eye becomes larger. Consequently the critical layers are elevated higher over the waves and also become significantly asymmetrical, with a stronger reverse flow below them. This asymmetry causes the critical layer height to be lower over the downwind part of the group in accordance with the conclusion drawn from earlier results [13, 14]. Thus, the positive growth of the individual waves on the upwind part of the wave group exceeds the negative growth on the downwind part. Hence, the effect of grouping on the critical layer produces a net horizontal force on the waves, in addition to the sheltering effect. This explains

why the heuristic combinations of inviscid modelling of cat's-eye dynamics (as in Janssen [16]) and inertial-shear stress modelling provide practical methods for wind generated waves.

References

1. J.C.R. Hunt and S.G. Sajjadi, Mechanisms and modelling of wind driven waves, *Proc. Symposium Wind Waves*, 4-8 September 2017, London, UK.
2. J.W. Miles, On the generation of surface waves by shear flows, *J. Fluid Mech.*, **3**, 185, 1957.
3. M.J. Lighthill, Physical interpretation of the theory of wind generated waves, *J. Fluid Mech.* **14**, 385–398, 1962.
4. F. Drullion, & S.G. Sajjadi, Interaction of wind with surface water waves, *Neural, Parallel, and Sci. Comp.* **22**, 303–314, 2014.
5. P.P. Sullivan, J.C. McWilliams & C.H. Moeng, Simulation of turbulent flow over idealized water waves, *J. Fluid Mech.*, **404**, 47–85, 2000.
6. S.G. Sajjadi, T.J. Craft, Y. Feng, A numerical study of turbulent flow over a two-dimensional hill, *Int. J. Numer. Meth. Fl.*, **35**, 1,2001.
7. S. Fu, B.E. Launder and D.P. Tselepidakis, Accommodating the effects of high strain rates in modelling the pressure-strain correlation,*Rep. No. TFD/87/5*, Mechanical Engineering Department, UMIST, 1987.
8. M.M. Gibson and B.E. Launder, Ground effects on pressure fluctuations in the atmospheric boundary layer, *J. Fluid Mech.*, **86**, 491, 1978.
9. K. Hanjalic and B.E. Launder, A Reynolds stress model of turbulence and its application to thin shear flows, *J. Fluid Mech.*, **52**, 609, 1972.
10. S.V. Patankar, *N*umerical Heat Transfer and Fluid Flow, Taylor & Francis, 1980.
11. B.P. Leonard, A stable and accurate convective modelling procedure based on quadratic upstream interpolation, *Comp. Maths. Appl. Mech. Eng.*, **19**, 59, 1979.
12. S.G. Sajjadi and F. Drullion, Numerical study of Turbulent flow over Growing Monochromatic and Stokes waves, *Adv. Appl. Fluid Mech.*, **19**, 47, 2016.
13. S.G. Sajjadi, J.C.R. Hunt, F. Drullion, Asymptotic Multi-Layer Analysis of Wind Over Unsteady Monochromatic Surface Waves, *Journal of Engineering Mathematics*, **84**, 73, 2014.
14. S.G. Sajjadi, J.C.R. Hunt, F. Drullion, Growth of unsteady wave groups by shear flows, *Proc. of IMA Conference on Turbulence, Waves and Mixing, Kings College Cambridge, U.K., July 2016*, 79–84, 2016.
15. S.G. Sajjadi, J.C.R. Hunt, and F. Drullion. Turbulent shear flows over unsteady ideal and non-ideal water waves. To appear in *J. Fluid Mech.*, 2017.
16. P. A.E.M. Janssen and J-R Bidlot. Progress in operational wave forecasting. *Proc. IUTAM Symposium Wind Waves*, 4-8 September 2017, London, UK.

Available online at www.sciencedirect.com

ScienceDirect

Procedia IUTAM 26 (2018) 153–161

Procedia IUTAM

www.elsevier.com/locate/procedia

IUTAM Symposium Wind Waves, 4–8 September 2017, London, UK

Laboratory study of temporal and spatial evolution of waves excited on water surface initially at rest by impulsive wind forcing

Lev Shemer

School of Mechanical Engineering, Tel-Aviv University, Ramat Aviv, Tel-Aviv 69978, Israel

Abstract

Evolution of waves excited by wind that varies in time is not yet understood sufficiently well. In the present study, waves generated from rest by an effectively impulsive wind forcing are studied in a small laboratory wind-wave tank. Multiple parameters characterizing evolution of the wave field in time as well as in space are presented. Measurements of the variation with time of the instantaneous surface elevation were performed simultaneously with determination of two components of the instantaneous surface slope at a number of fetches along the test section. For each wind forcing conditions, numerous independent realizations were recorded. Thus, sufficient data were collected for computation of statistically reliable ensemble-averaged values of parameters characterizing the evolving random wind-wave field as a function of time elapsed since the initiation of wind. In each realization, data acquisition started when the water surface was calm, and lasted until statistically steady random wave field conditions were attained. The analysis of the ensemble-averaged wind-wave characteristics indicated that distinct stages in the wind-waves evolution could be identified. These stages were compared with the predictions based on the viscous instability theory and on the random resonant wind-waves generation model.

Peer-review under responsibility of the scientific committee of the IUTAM Symposium Wind Waves.

Keywords: Generation of waves by wind; unsteady wind forcing; waves under wind gusts; Phillips wind-wave generation model; Kawai model

1. Introduction

The process of generation of sea waves by wind remains at the center of scientific interest for more than 150 years [1]-[3]. About 60 years ago, two different possible mechanisms of water-wave generation by wind were suggested: the resonant pressure fluctuations model by Phillips [4] and the shear-flow model by Miles [5]. Only very limited and not very successful attempts have been made so far to validate the Phillips model. The compilation by Plant [6] of experimental results on wind-waves growth rate from numerous studies exhibits significant scatter around the predictions by Miles theory. Miles [7] stressed that his model is inapplicable to the initial stages of wind-wave generation. Spatial growth rates at the steady wind forcing for fixed Fourier frequency harmonics were measured directly in the experimental facility used in the present study [8]; the results show behavior that is qualitatively inconsistent with the Miles predictions however fall into the domain of data scatter in the Plant [6] plot. Numerous studies [9]-[11] demonstrated that coupled viscous shear flow at the gas-liquid interface has a significant effect on the wave growth rates.

It should be stressed that while most of those theories assume unidirectional waves, the essentially three-dimensional structure of wind-wave field was emphasized in numerous experimental studies [12]-[14]. Moreover, the wind-wave generation theories mentioned above usually consider evolution of the wind-wave field in time (the duration-limited case), often assuming spatial homogeneity, whereas in the experiments the spatial (fetch-limited) evolution of waves due to effects of dispersion, wind input,

Peer-review under responsibility of the scientific committee of the IUTAM Symposium Wind Waves.
10.1016/j.piutam.2018.03.015

nonlinearity, and dissipation is measured. The wave field in this case may be statistically steady for steady wind forcing, but is spatially inhomogeneous.

Additional complexity of the problem of water waves' excitation by wind arises when wind forcing is unsteady, thus the statistical characteristics of waves that always depend on space now vary with time as well. Field experiments on wind waves under unsteady forcing are rare. Therefore, well-designed laboratory studies are needed that may provide detailed experimental data on wave evolution under controlled conditions needed for understanding the relative contribution of different mechanisms that govern the variation of the wind-wave field. However, even at laboratory scale only limited experimental data on waves under time-dependent wind under controlled conditions are currently available. Radars were used mostly in early studies of waves excited by impulsively started wind [15-16]. These data are restricted to waves with fixed lengths only defined by the Bragg resonance conditions.

First experimental and theoretical study of ripple excitation by abruptly started wind was carried out by Kawai [10] and provided evidence that viscous instability mechanism causes exponential growth of waves in time. Time-dependent results were often obtained by selecting short records and assuming quasi-steady conditions within each record. Veron & Melville [17] studied waves under slowly accelerating wind. The spectral information was obtained in this study assuming quasi-steadiness. Different techniques were applied in [18-19] to study wind stress under time-dependent wind, also effectively invoking the quasi-steady assumption.

The present paper is based on the experiments carried out by Zavadsky & Shemer [20] in a small wind-wave facility and presents time-resolved statistically reliable results on waves excited from rest by a (nearly) impulsive wind forcing. These experimental results are further discussed here. Different stages of wind-wave field evolution are delineated. Measurements were performed using multiple sensors and a fully automated experimental procedure. Running experiments without human intervention made it possible to carry out numerous independent realizations of temporally and spatially varying wave field under identical wind forcing conditions. The statistical wave parameters were computed at each fetch and wind forcing by averaging the data recorded for the accumulated ensemble of realizations as a function of time elapsed since the initiation of wind. The validity of different theoretical models is examined. Particular emphasis is given to the implications of nonexistence of spatial homogeneity on the evolution of the duration-limited wind-wave field.

2. Experimental facility and procedure

Experiments were carried out in a wind-wave facility that has a test section, which is 5 m long, 0.4 m wide and 0.5 m high. The test section is covered by removable transparent plates with a partially sealed slot along the centerline that facilitates positing of sensors. The test section is filled to water depth of about 0.2 m, thus deep-water conditions are satisfied for wind-waves with lengths pertinent to this study. Computer-controlled blower provides air flow rate with wind speed in the test section up to about 15 m/s. Instantaneous surface elevation was measured by a capacitance-type wave gauge made of 0.3 mm anodized tantalum wires and mounted on a computer-controlled vertical stage to enable its static calibration. The wind velocity in the test section, $U(t)$ was measured by a Pitot tube. Simultaneously with the surface elevation measurements, two components of the instantaneous surface slope, in the wind direction, $\partial\eta/\partial x$, and in the crosswind direction, $\partial\eta/\partial y$, were determined by a laser slope gauge (LSG). More details about the experimental facility and the instrumentation are given in [8] and [20]; for detailed description of the LSG set up and calibration procedure see [14].

Prior to activation of the blower in each experimental run, the water surface was calm. The blower output voltage represents the airflow rate; this voltage varies linearly at the rate of 1 V/s until the prescribed steady state is attained. The following set of the target wind velocities in the test section was used: U = 6.5 m/s, 7.5 m/s, 8.5 m/s, 9.5 m/s, and 10.5 m/s. Results of simultaneous measurements of the blower output voltage and of the wind velocity $U(t)$ as a function of time elapsed since the activation of the blower by the computer are presented in Fig. 1 for different target wind velocities. The duration of the ramp in the blower-driving signal varies from 3 s to 5 s. At each instant, the wind velocity lags slightly behind the blower output, the delay, however, does not exceed 1 s. Velocities below about 1.5 m/s are not measured adequately by the Pitot tube. Once the target velocity is attained, the blower maintains constant airflow rate in the test section for 120 s and is then shut down.

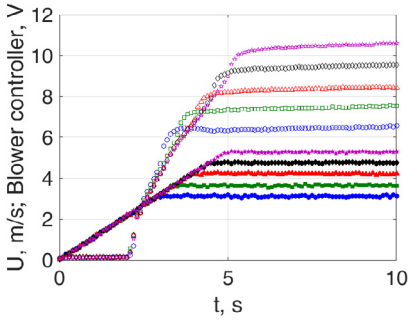

Fig. 1. Mean wind velocity (empty symbols) and the blower output voltage (filled symbols).

For all target wind velocities, turbulent airflow exists in the test section. The friction velocities at the air-water interface measured in our facility under steady forcing for a wide range of steady wind velocities were presented in [22]. Measurements were carried out at three distances from the inlet, at fetches x = 120 cm, 220 cm and 340 cm. The temporal variations of the instantaneous surface elevation η, of the surface slopes components $\partial\eta/\partial x$ and $\partial\eta/\partial y$, of the mean wind velocity $U(t)$, and of the voltage output were recorded at sampling frequency f_s = 300 Hz; data sampling started prior to activation of the blower.

Time interval between successive runs was set at about 6 min, sufficient for decay of all disturbances in the test section, so that at the initiation of the next run the water surface was calm again. The total duration of a single run, including the waiting period, thus exceeds 8 min. Usually at least 100 independent realizations for each set of operational parameters (the target wind velocity and the fetch) were recorded. The total duration of the experiments at a single fetch and wind target velocity thus exceeds 13 hrs. Measurements for all wind velocities at a single fetch, including wave gauge calibration for each wind velocity, last more than two days. Such long continuous experimental sessions and synchronization between the blower operation and data sampling are possible since the whole procedure, including operation of the blower, wave gauge calibration and data acquisition, is fully automated and controlled by a computer using a single LabView program, virtually without human intervention.

The accumulated set of data allows calculation of characteristic wave parameters ensemble-averaged for each fetch x and target wind velocity U over all realizations as a function of time elapsed relative to common reference taken as the instant of the blower initiation in each realization. The characteristic amplitudes of the surface elevation η and of the slope components $\partial\eta/\partial x$ and $\partial\eta/\partial y$ at each instant can be represented by their corresponding ensemble-averaged root-mean-square (r.m.s.) values calculated over the whole set of realizations relative to the reference. A different procedure was applied to determine the dominant wave frequency as a function of time elapsed since the blower activation. To this end, continuous real Morlet wavelet transform that decomposes a time-varying function into wavelets and offers good time and frequency localization was used. The wavelet 'spectrum', or map, was calculated for each realization; the resulting maps were then averaged over the whole set of realizations. The scale corresponding to the maximum intensity of the ensemble-averaged map defines the dominant pseudo-frequency at each instant.

3. Results and discussion

Under steady wind forcing, the wave field in the present experimental facility is essentially three-dimensional, as can be seen in the reconstruction of stereo video images as described in detail in [14]. Typical snapshot of the wave field is presented in Fig. 2.

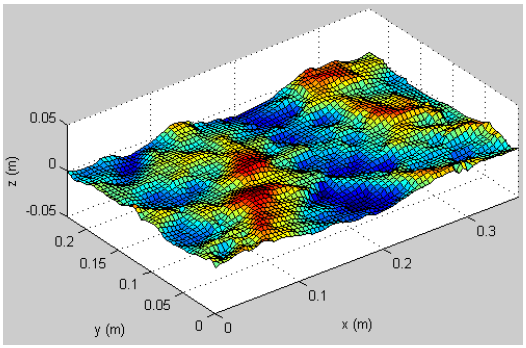

Fig. 2. Three-dimensional reconstruction of the instantaneous wind-wave field.
Steady wind velocity U =8.5 m/s; the centre of the image at x = 220 cm

An insight into the three-dimensional structure of the evolving in time wind-wave field can be obtained by examining the time variation of the simultaneously acquired surface elevation $\eta(t)$ and of both components of surface slope, $\partial\eta/\partial x(t)$ and $\partial\eta/\partial y(t)$, see Fig. 3. The records in this figure are scaled and shifted vertically for convenience.

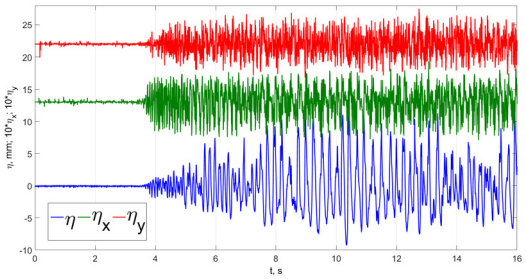

Fig. 3 Records of variation of the instantaneous surface elevation $\eta(t)$ and surface slope components, $\partial\eta/\partial x(t)$ and $\partial\eta/\partial y(t)$ under wind accelerated from rest to the target value U=8.5 m/s at fetch x=220 cm.

During the initial 3.5 s after the activation of the blower, there are no visible fluctuations of the surface elevation, η, as well as of the surface slope components. Comparison of figs. 2 and 3 demonstrates that it can be assumed that the wave field starts to develop only after the constant wind velocity in the test section has been attained, thus for target wind velocities $U \leq 8.5$ m/s, the wind forcing can effectively be presented by a step function. It takes about 9 s since the activation of the blower for the fluctuations of the surface elevation to attain the quasi steady-state; that is more than 5 s after the appearance of the initial visible disturbances at the water surface. The quasi-steady level of fluctuations of the surface slope component, $\partial\eta/\partial x$, however, is attained much faster, already at $t \approx 4$ s, just about 1 s after the inception of the first visible disturbances. The fluctuations of $\partial\eta/\partial y$ lag somewhat after the development of slopes in the wind direction, so that for a very short duration, less than 1 s, the wave field remains approximately unidirectional. Nevertheless, quasi-steady levels of slope fluctuations in both directions are attained at comparable times and notably earlier than that of η.

The main ensemble-averaged parameters are plotted for three fetches and three wind velocities as a function of the time elapsed from the activation of the blower in Fig. 4. The instantaneous r.m.s. values of the surface elevation, $<\eta^2>^{1/2}$, characterize the wave amplitude, while the values of $<(\partial\eta/\partial x)^2>^{1/2}$ serve as an indicator of the instantaneous wave steepness. Note that the behavior of $<(\partial\eta/\partial y)^2>^{1/2}$ is similar to that of $<(\partial\eta/\partial x)^2>^{1/2}$ and therefore not plotted

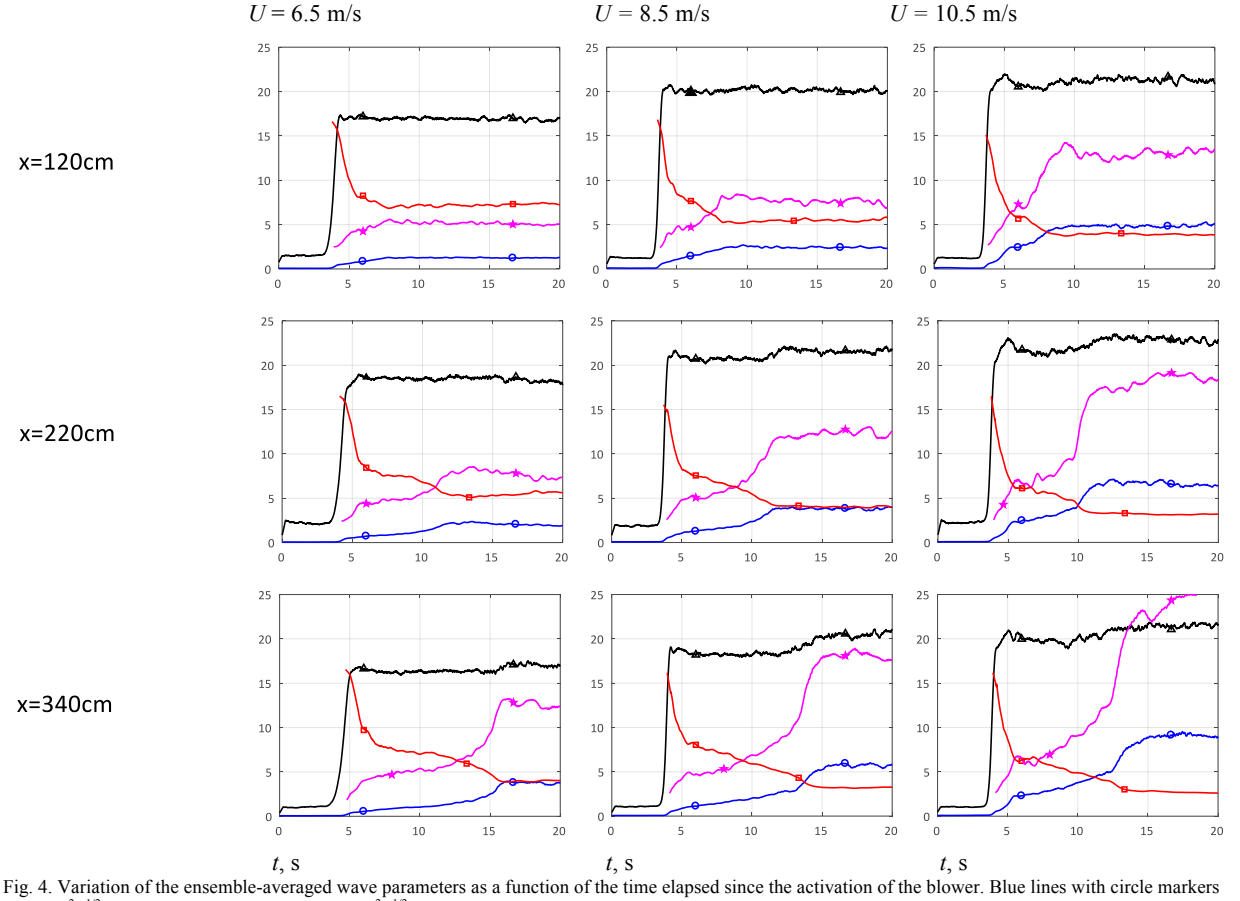

Fig. 4. Variation of the ensemble-averaged wave parameters as a function of the time elapsed since the activation of the blower. Blue lines with circle markers denote $<\eta^2>^{1/2}$, black lines with triangles - $<\partial\eta/\partial x^2>^{1/2}$, red lines with squares - dominant frequency f_d, magenta lines with pentagrams – dominant wavelength, λ_d.

In each panel of Fig. 4 the dominant frequency f_d and the corresponding wavelength, λ_d, are plotted as well. The dominant frequency f_d at each instant corresponds to the maximum scale of the ensemble-averaged wavelet map. The dominant wavelength is calculated for each f_d using the empirical dispersion relation obtained in the present experimental facility that accounts for the Doppler shift due to the induced current, see [8], [20].

All curves in Fig. 4 represent ensemble-averaged results with the temporal resolution of 3.3 ms. High temporal resolution enables distinguishing between stages in the wave field evolution. There are no essential disturbances at the water surface during the initial 4 s following the initiation of the blower at all fetches and wind velocities. During this period with no visible waves, the air velocity in the test section is accelerated to its final value, except for the highest flow rates employed in this study, see Fig. 1. Then, a rapid growth of very short waves with the r.m.s. values of surface elevation not exceeding approximately 1 mm is

observed along the whole length of the test section. This fast initial wave growth is accompanied by a nearly impulsive increase in the r.m.s. values of the characteristic surface slope $<(\partial\eta/\partial x)^2>^{1/2}$ up to the steady-state values that at a given wind velocity are nearly independent of fetch, x, and increase somewhat with U, varying in the range of 0.17 to about 0.22.

The initial ripples have characteristic frequency of f_d=15 Hz at least at all fetches and wind velocities. During the fast growth of the ripples, the values of f_d decrease. Also, for longer fetches and for higher target wind velocities, the characteristic frequencies are lower. Apparently, variation of the dominant wavelength, λ_d, is associated with that of f_d. Contrary to the fast variation of the surface slope components up to their steady-state value, the evolution of $<\eta^2>^{1/2}$, f_d and λ_d is much slower and at all fetches and wind velocities occurs at time scales that characterize the temporal variation of $<\eta^2>^{1/2}$. The time scales of the evolution increase with fetch and wind velocity.

Evolution in time of the characteristic wave amplitude, $<\eta^2>^{1/2}$, and of the characteristic instantaneous dominant frequency, f_d, are compared in Fig. 5 at two fetches x and for two values of the target wind velocity U. The comparison reveals that for each wind velocity U, at the instant when the instantaneous values of $<\eta^2>^{1/2}$ attain the value corresponding to the steady state at the shorter fetch, the corresponding dominant frequencies f_d also attain the steady state value at the shorter fetch. Similar results were obtained for other pairs of fetches and wind velocities considered in this study.

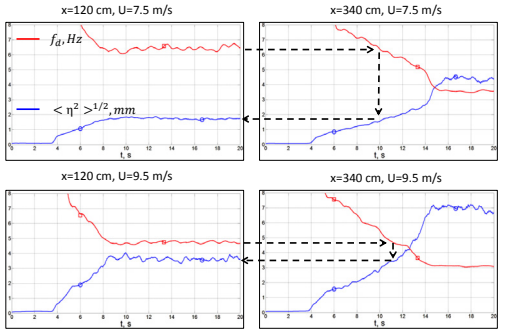

Fig. 5. Comparison of the variation with the elapsed time t of the ensemble-averaged wave amplitudes and the characteristic dominant frequencies at two fetches and two target wind velocities. The broken lines indicate the steady state values at the shorter fetch.

These observations fit within a conjecture that with the initiation of the blower over water at rest, a spatially homogeneous wave field is initially excited that contains a wide spectrum of harmonics. Under the action of wind, different frequency harmonics propagate with their respective group velocities c_g, grow in time and in space, until they attain equilibrium values of amplitude and steepness for the given steady wind forcing. Once a harmonic with the frequency f attains its equilibrium amplitude at a certain fetch $x(f)$, its amplitude remains constant and does not vary fast at longer fetches, $x > x(f)$. The duration of the growth stage at each fetch and wind velocity, $t_{gr}(x)$, can thus be estimated as the required propagation time

$$t_{gr} = x/c_g(f_d(x)) \tag{1}$$

This scenario implies that while short wind-waves are strongly nonlinear, their initial growth can be seen as an essentially linear process.

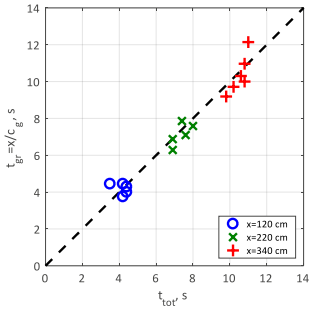

Fig. 6. The calculated according to the model duration of the initial wave growth process, t_{gr}, compared to the measured growth duration t_{tot}.

The values of the total durations of the growth stage, t_{gr}, calculated using the suggested relation, and the empirical values of group velocity for each dominant wavenumber, are compared in Fig. 6 with the actual duration of the growth stage t_{tot} estimated from the experimental data presented in Fig. 4. Note that the initial reference point is taken at the instant when blower capacity attains maximum, *i.e.* 3.5–5.5 s after the activation of the blower, depending on the target value of U, see Fig. 1. Fig. 6 demonstrates that good agreement between these values is obtained for all fetches and wind velocities.

It can clearly be seen in Fig. 4 that there are notable changes of the slopes of the curves representing the temporal variation of the measured parameters that occur essentially simultaneously for all those parameters and suggest division of the temporal

evolution of the wave field into distinct stages. To define those stages, the variation with the elapsed time of the characteristic instantaneous wave amplitude, $<\eta^2>^{1/2}$, is plotted in Fig. 7 for x=340 cm and the target wind velocity U=7.5 m/s.

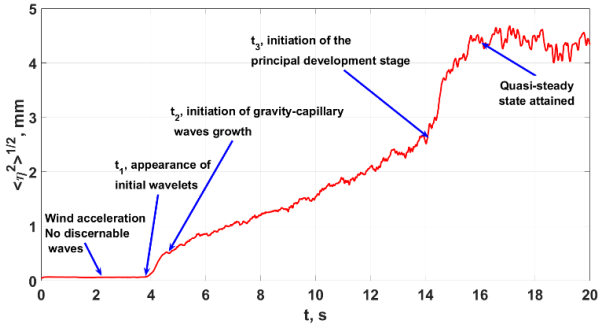

Fig. 7. Definition of characteristic times in temporal variation of the representative wave amplitude (x = 340 cm, U = 7.5 m/s)

When the first wavelets become detectable at the elapsed time t_1, the wind velocity has already attained its target value, see Fig. 1. The fast initial growth of these short ripples decreases abruptly at t=t_2. Note that at t_2, the characteristic wave amplitudes are still less than 0.5 mm, however, the representative wave steepnesses already attain their limit values (*cf.* Fig. 4). The significantly slower wave growth continues for t_2<t<t_3; then at t_3 the rate of wave amplitude growth accelerates, until the temporal wave evolution process ceases at t_4 that in fact corresponds to the total duration of the wave growth at the prescribed location and wind velocity denoted in Fig. 6 as t_{tot}.

The distinct stages in the wind-wave evolution with the elapsed time t identified in Fig. 7 suggest that at each stage, a different mechanism governs the wave growth. Therefore, the temporal evolution of wind-waves is now analyzed separately for at each stage. An attempt is made to relate the experimental results to the existing theoretical models.

In view of delay in the initial response of the water surface to the activation of the blower, for lower target wind velocities, the forcing is effectively impulsive, see Fig. 1. The initial growth of ripples excited by such an impulsive wind forcing is plotted in Fig. 8. Plot in semi-logarithmic coordinates demonstrates that the growth with time of the energy $<\eta^2>$ of the initial ripples is exponential and thus can be approximated as

$$\langle \eta^2(t) \rangle = \langle \eta_0^2 \rangle e^{\beta t} \tag{2}$$

where $\langle \eta_0^2 \rangle$ is the initial disturbance energy and β the growth parameter. The values of β for different target velocities (including those not presented in Fig. 8 are summarized in Table 1.

Table 1. Initial ripples growth parameter β (s^{-1}).

Fetch (cm)	U=6.5 m/s	U=7.5 m/s	U=9.5 m/s	U=10.5 m/s
120	7.6	12.0	11.7	12.2
220	7.1	9.4	12.0	13.9
340	5.9	7.8	10.0	10.7

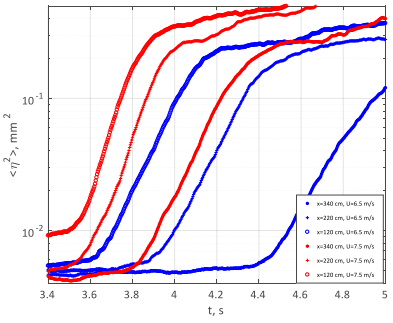

Fig. 8. Exponential growth of the energy of initial ripples for lower target wind velocities U.

As can be seen in Fig. 8, the duration of the exponential growth is only about 200-300 ms. Sufficiently high sampling rates are therefore needed for unambiguous determination of the growth parameter β (3oo Hz were used in this study). The exponential growth of wavelets in Fig. 8 may be attributed to linear instability mechanism that becomes essential at instant t_1, see Fig. 7. Note that for a given target wind velocity U, the growth rate parameter β decreases with fetch. The growth rate parameters β given in Table 1 compare favorably with the computations and the experimental results reported by Kawai [10]. Due to different forcing

conditions in the present study as compared to those in [10], extrapolation of the results of [10] to stronger wind forcing was carried out in this comparison.

Termination of the exponential growth stage of the initial ripples can plausibly be attributed to significant wave nonlinearity characterized in Fig. 4 by the instantaneous representative steepness $<(\partial\eta/\partial x)^2>^{1/2}$ that attain their maximum quasi-steady values at times close to the ending of the exponential growth stage. However, an additional factor may be considered that renders the application of the linear viscous instability theory of unidirectional waves inapplicable at $t>t_2$. Single realization records presented in Fig. 3 suggest that the growth of $\eta_x = <(\partial\eta/\partial x)^2>^{1/2}$ precedes that of $\eta_y = <(\partial\eta/\partial y)^2>^{1/2}$. In Fig. 9, the variation with the elapsed time of these two parameters is plotted during the initial evolution stages for the conditions corresponding to Fig. 7. The slopes in the crosswind direction, y, grow notably slower than those in the wind direction, x, and attain their quasi-steady-state values later. The initial wavelets that grow exponentially are therefore largely unidirectional, in accordance with the assumptions adopted in [10].

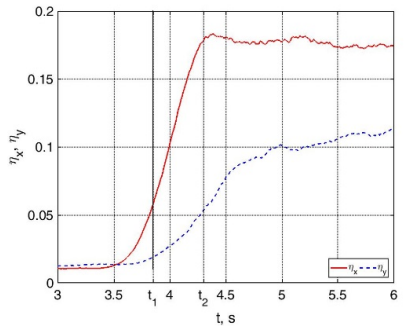

Fig. 9. The initial growth of the r.m.s. values of the ensemble averaged instantaneous slope components $\eta_{x \text{ and }} \eta_y$. Vertical lines denote characteristic times t_1 and t_2 defined in Fig. 7.

The Phillips [4] theory can be applied to describe wave evolution following the appearance of the initial ripples, $t>t_2$. The theory suggests two-stage temporal evolution of wind-waves due random pressure fluctuations. In our experiments, the 'initial growth stage' according to Phillips may be attributed to elapsed times $t_2<t<t_3$. There is no closed expression predicting the wind–wave growth at this stage in [4]; rather, the theory states that the mean values of $<\eta^2>$ initially grow linearly with time. The measured dependence of the mean wave energy $<\eta^2>$ on the elapsed time is therefore plotted in Fig. 10 as a function of $(t - t_2)$. In spite of a considerable scatter in the data, particularly at higher target wind velocities U, the wave energy indeed seems to increases notably on the fetch x. The initial growth stage becomes shorter as the target wind velocity U increases.

At $t = t_3$, the wave energy growth becomes notably faster. The wind–wave field evolution at $t>t_3$ may be associated with 'the principal stage' in the Phillips [4] theory, this stage terminates when the quasi-steady is attained at each fetch and wind velocity at $t \approx t_4$. It can be seen in Fig. 4 that waves observed in our facility at fetches x = 220 cm and x = 340 cm have lengths exceeding 7 cm and thus can be considered as purely gravity waves practically unaffected by capillarity.

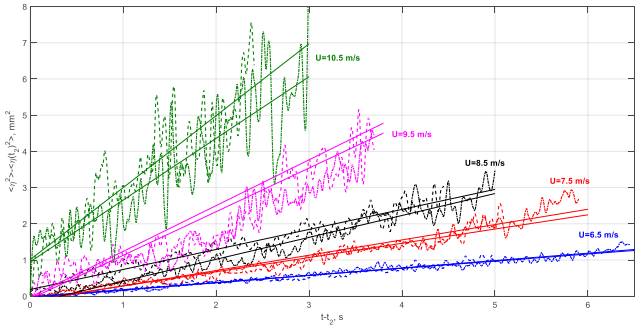

Fig. 10. The temporal growth of wind waves associated with Phillips 'initial growth stage'. Dashed lines correspond to the fetch x=220 cm, dash-dot lines to fetch x=340 cm; solid lines – linear fits.

For temporal growth of gravity waves at the principal stage of development, Phillips obtained the following relation:

$$\overline{\eta^2} \sim \frac{\overline{p^2}t}{2\sqrt{2}\rho_w^2 U_c g} \tag{3}$$

In (3), $\overline{p^2}$ represents mean square pressure fluctuations at the surface, U_c is the convection velocity of those fluctuations that are assumed in [4] to correspond to the phase velocity of water waves, while ρ_w is the water density. It is further assumed that the turbulent pressure fluctuations are related to interfacial shear stress, $\tau = \rho_a u_*^2$, where u_* is the friction velocity at air–water interface, so that $\overline{p^2} \sim u_*^4$. It is also assumed in [4] that the convection velocity of the pressure fluctuations is related to the friction velocity: $U_c = 18u_*$. The relation (3) is thus rewritten as

$$\overline{\eta^2} \sim 0.035 \left(\frac{\rho_a}{\rho_w}\right)^2 \frac{U^3 t}{g} \tag{4}$$

Thus, according to the theory of Phillips the wave energy of short gravity waves grows linearly with time, while the growth rate is proportional to the cube of wind velocity. However, the characteristic wave velocity for short gravity waves (10 cm < λ < 30 cm) measured in the present experimental facility [20] is in fact nearly constant and remains substantially lower than the wind velocity, being essentially independent of U. These observations prompted us to approximate the convection velocity U_c by a constant value for the conditions of the present experiments. By incorporating this assumption into (3), the relation (4) is replaced by

$$\langle \eta^2 \rangle = C U^4 t. \tag{5}$$

In (5), the dimensional coefficient C is supposed to be constant in the framework of Phillips approach.

To examine the validity of (5), the measured variation of $\langle \eta^2 \rangle / U^4$ is plotted in Fig. 11 as a function of time elapsed since the initiation of the principal stage of wind–wave development, $t = t_3$. The results are given for two fetches (x = 220 cm and x=340 cm) and three wind velocities U = 8:5 m/s, U= 9.5 m/s and U=10.5 m/s. All dependencies are well approximated by straight lines thus confirming linear growth of the wave energy with time during this stage as well. The nearly identical slopes are obtained for different wind velocities for the longer fetch, x=340 cm. For the shorter fetch, x=220 cm, the slopes are similar but differ somewhat, with no identifiable trend of the slope dependence on the wind velocity U. All slopes in Fig. 11 are of the same order, in general agreement with the relation $\langle \eta^2 \rangle \sim U^4$.

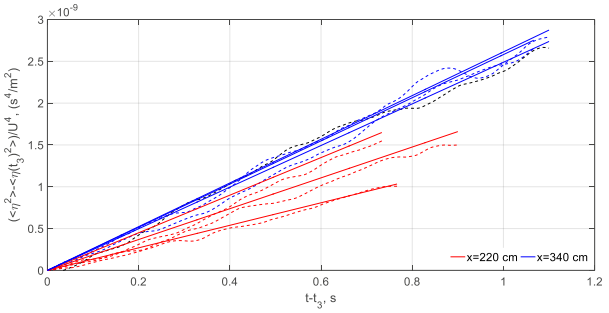

Fig. 11. Variation with time of $\langle \eta^2 \rangle / U^4$ during the 'principal development stage' of Phillips.

Evolution of waves under impulsive wind forcing can thus be characterized by distinct stages. First, initial wavelets appear nearly simultaneously in the whole test section. These wavelets are effectively two-dimensional and their energy grows exponentially with time, thus providing experimental validation of applicability of deterministic 2D viscous instability mechanism [9, 10]. The duration of the exponential growth stage, however, is very short and does not exceed 1 s. The waves at the end of the exponential growth stage are quite steep; however, their height does not exceed about 1 mm. These results on the initial temporal growth are in agreement with the spatial evolution pattern of ripples under steady wind forcing [13]. Following the termination of the exponential growth stage, the wave field becomes essentially random and three-dimensional, see Figs. 3, 9, additional evidence to this effect is presented in [20]. Transition of the wave field from quasi-deterministic and two-dimensional to random and three-dimensional at $t \approx t_2$ results in growth of wind waves at later stages that is qualitatively different. With termination of the exponential growth stage, the wave energy at all fetches and for all target wind-velocities increases essentially linearly with time, see Fig. 10, while the dominant wave frequency continues to decrease, albeit more slowly.

It should be noted that linear with time growth of disturbances under random forcing is quite common in diverse physical systems. For water waves, the linear growth in time was suggested first by Phillips [4] as his 'initial development stage'. More recently, Milewski et al. [23] demonstrated theoretically that the energy of nonlinear wave systems under random forcing with negligible dissipation grows linearly with time. At longer times, $t > t_3$, the wave energy continues to grow linearly with time until the quasi-steady state is attained, but the growth rate increases notably. The wave energy variation at this later evolution stage may be loosely attributed to the Phillips [4] resonant mechanism that becomes dominant, causing linear in time, but notably faster growth; this wave energy growth may be related to the 'principal stage of development' in his theory.

4. Conclusions

Large ensembles of independent experimental runs starting from rest were recorded at sufficiently high sampling frequency for several fetches and target wind velocities. These data enabled computation of variation of wave parameters averaged over the accumulated ensembles of data as a function of time elapsed since the initiation of the blower. The results allow identifying distinct stages of wave field evolution in time under effectively impulsive wind forcing.

Although waves in the present experiments becomes steep very fast and thus essentially nonlinear, variation of the dominant wave frequency and of the characteristic wave amplitude with fetch for a given target wind velocity can be described fairly well by a scenario based on an essentially linear approach.

The initial growth of short ripples measured in the present study is exponential in time. The growth rate is consistent with the prediction based on viscous instability theory [10]. However, the exponential stage of the wave growth lasts for a fraction of a second, and terminates once the wave field becomes strongly nonlinear and essentially three-dimensional, while the characteristic wave heights remain small. It should be stressed that generalizations of the Miles [5, 7] model that take into account viscosity [9, 10] retain the linear, deterministic and two-dimensional approach adopted by Miles.

All those assumptions cease to be valid at the end of the exponential evolution stage. The nonlinearity of the wind wave field in the present experiments cannot be neglected anymore; moreover, waves lose their coherence and become random and three-dimensional. Linear deterministic approach thus fails to explain later evolution stages. An attempt is made here to describe the behavior of wind-waves during the subsequent growth invoking the theory suggested by Phillips for random wind forcing that is free of assumptions of linearity and two-dimensionality.

The present results clearly demonstrate that the temporal evolution of waves on an initially smooth water surface under impulsive wind forcing is inhomogeneous and strongly dependent on fetch. Thus, an approach in which spatially uniform wave field evolves in time only, is physically unrealistic. Temporal evolution of a wave field due to wind input, dissipation and/or nonlinearity is necessarily accompanied by spatial variations. The validity of theoretical and numerical results based on application of spatially periodic boundary conditions thus has to be carefully verified in experiments.

Acknowledgements

Support of this research by the Israel Science Foundation (grant no. 306/15) is gratefully acknowledged.

References

1 H. von Helmholtz, Über discontinuirliche Flüssigkeits-Bewegungen, *Akademie der Wissenschaften zu Berlin*, 1868.
2 Lord Kelvin, Hydrokinetic solutions and observations, *Philosophical Magazine*, 1871, 42: 362–377.
3 H. Jeffreys, On the formation of water waves by wind, *Proceeding of the Royal Society London, Ser. A*, 1925, 107: 189–206.
4 O. M. Phillips, On the generation of waves by turbulent wind, *Journal of Fluid Mechanics*, 1957, 2, 417–445.
5 J. W. Miles, J. W. On the generation of surface waves by shear flows, *Journal of Fluid Mechanics*, 1957, 3: 185–204.
6 W. J. Plant, A relationship between wind stress and wave slope, *Journal of Geophysical Research*, 1982, 87: 1961–1967.
7 J. W. Miles, Surface-wave generation revisited, *Journal of Fluid Mechanics*, 1993, 256: 427–441.
8 D. Liberzon, L. Shemer, Experimental study of the initial stages of wind waves' spatial evolution, *Journal of Fluid Mechanics*, 2011, 681: 462–498.
9 G. R. Valenzuela, 1976 The growth of gravity-capillary waves in a coupled shear flow, *Journal of Fluid Mechanics* 1976, 76: 229-250.
10 S. Kawai, Generation of initial wavelets by instability of a coupled shear flow and their evolution to wind waves, *Journal of Fluid Mechanics,* 1979, 93: 661-703.
11 K. van Gastel, K., P. A. E. M. Janssen, G. J. Komen, 1985 On phase velocity and growth rate of wind-induced gravity-capillary waves, *Journal of Fluid Mechanics,* 1985, 161: 199-216.
12 G. Caulliez, G. F. Collard, Three-dimensional evolution of wind waves from gravity-capillary to short gravity range, *European Journal of Mechanics, B/Fluids*, 1999, 18: 389–402.
13 G. Caulliez, N. Ricci, R. Dupon, The generation of the first visible wind waves, *Physics of Fluids,* 1998, 4: 757-759.
14 A. Zavadsky, A. Benetazzo, L. Shemer, L., On the two-dimensional structure of short gravity waves in a wind wave tank, *Physics of Fluids*, 2017, 29, 016601.
15 T. R. Larson, J. W. Wright, Wind-generated gravity-capillary waves: laboratory measurements of temporal growth rates using microwave backscatter. *Journal of Fluid Mechanics*, 70, 1975: 417–436.
16 W. J. Plant, J. W. Wright, Growth and equilibrium of short gravity waves in a wind–wave tank, *Journal of Fluid Mechanics*, 1977, 82: 767–793
17 F. Veron, W. K. Melville, Experiments on the stability and transition of wind-driven water surfaces, *Journal of Fluid Mechanics,* 2001, 446: 25–65.
18 B. M. Uz, M. A. Donelan, T. Hara, E. J. Bock, Laboratory studies of wind stress over surface waves. *Boundary-Layer Meteorology*, 2002, 102: 301–331.
19 B. M. Uz, T. Hara, E. J. Bock, M. A. Donelan, Laboratory observations of gravity capillary waves under transient wind forcing, *Journal of Geophysical Research,* 2003*,* 108: 3050.
20 A. Zavadsky, L. Shemer, Water waves excited by near-impulsive wind forcing, *Journal of Fluid Mechanics, 2017,* 828: 459-495.
21 A. Zavadsky, D. Liberzon, L. Shemer, Statistical analysis of the spatial evolution of the stationary wind wave field, *Journal of Physical Oceanography,* 2013, 43: 65-79.
22 A. Zavadsky, L. Shemer, Characterization of turbulent air flow over evolving water-waves in a wind wave tank, *Journal of Geophysical Research,* 2012, 117: C00J19.
23 P. A. Milewski, E. G. Tabak, E. Vanden-Eijnden, Resonant wave interaction with random forcing and dissipation. *Studies in Applied Mathematics*, 2002, 108: 123–144.

Available online at www.sciencedirect.com

ScienceDirect

Procedia IUTAM 26 (2018) 162–173

Procedia IUTAM

www.elsevier.com/locate/procedia

IUTAM Symposium Wind Waves, 4-8 September 2017, London, UK

Simulation-based study of wind-wave interaction

Xuanting Hao[a], Tao Cao[a], Zixuan Yang[a], Tianyi Li[a], Lian Shen[a,*]

[a]*Department of Mechanical Engineering and St. Anthony Falls Laboratory, University of Minnesota, Minneapolis, 55455, United States*

Abstract

We use a suite of advanced numerical tools developed in house to investigate the physical processes in three canonical wind–wave interaction problems. First, we use DNS to investigate the sheltering effect of a long wave on a short wave. It is found that in the presence of the long wave the form drag of the short wave decreases, with the magnitude of the reduction depending on the wave age of the long wave. We also observe that the surface friction is highly correlated to the streamwise vorticity upstream. Next, we study the effect of wave breaking on the wind turbulence. We focus on analyzing small-scale flow physics near the wave surface and the influence of wave breaking on turbulence statistics. It is found that plunging breakers induce acceleration of the air flow near the wave surface. During wave plunging, a large spanwise vortex is generated, which enhances the turbulence mixing around it, and induces large magnitude of turbulent kinetic energy. In the final part, results are presented for wind over broad-band waves in realistic ocean settings. By examining the full wavenumber–frequency spectrum of the turbulent wind, we have identified distinct wave signatures in the space–time correlation of wind turbulence. In the evolution of the wave field, its inner physical process known as the four-wave interaction dominates over wind input, as shown in the frequency downshift phenomenon of the wave field throughout the numerical experiments.

Peer-review under responsibility of the scientific committee of the IUTAM Symposium Wind Waves.

Keywords: wind-wave interactions; air-sea interactions; atmospheric boundary layer; geophysical turbulence; free surface flow; wave breaking; nonlinear resonant interactions

1. Introduction

Wind–wave interactions play an important role in the energy and momentum transfer between the marine atmospheric boundary layer and upper oceans. Understanding the wind–wave interaction process is crucial for a number of fundamental scientific studies and engineering applications. However, the complexity of the wind–wave system, particularly that caused by the irregular wave surface and wave breaking, brings significant challenges to the numerical study of wind–wave interactions. With the growth in computing power and the advancements in numerical algorithms, computer simulation has been playing an increasingly important role in the study of wind–wave interactions. Using methods including a high-order spectral (HOS) method for nonlinear waves, direct numerical simulation (DNS) and large-eddy simulation (LES) of wind turbulence on wave-surface-fitted grid, and the coupled level-set and

* Corresponding author.
E-mail address: shen@umn.edu

2210-9838
Peer-review under responsibility of the scientific committee of the IUTAM Symposium Wind Waves.
10.1016/j.piutam.2018.03.016

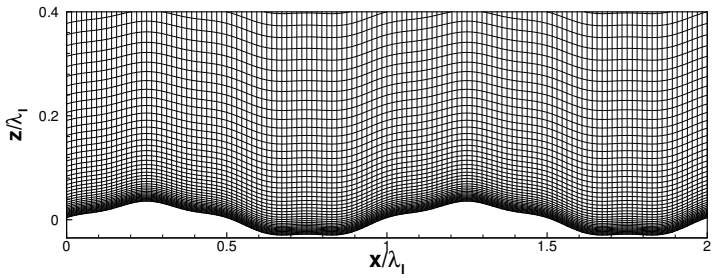

Fig. 1. The grid structure of DNS over two waves.

volume-of-fluid method for breaking waves, we have developed an advanced computational framework for wind–wave interaction called the WOW (Wave–Ocean–Wave). Using the tool of WOW, we have studied different aspects of wind–wave interaction, including wind over two progressive waves, wind over breaking waves, and wind over broad-band waves.

2. Wind over Two Progressive Waves

2.1. Cases description

Table 1. List of case parameters in the DNS of wind turbulence over a long wave and a short wave.

Case	c_l/u_*	c_s/u_*	λ_l/λ_s	$(ak)_l$	$(ak)_s$	$Re = u_*\lambda_l/\nu$
W02	2	1	4	0.2	0.1	283
W14	14	7	4	0.2	0.1	283
W25	25	12.5	4	0.2	0.1	283

In this session, we perform a DNS study of wind over two progressive water waves. The bottom of the simulation domain is the superposition of two linear water waves, including a long wave with wavelength λ_l and a short wave with wavelength λ_s, with a wavelength ratio $\lambda_l/\lambda_s = 4$. The ratio of the phase speed and amplitude between the long wave and short wave can be determined from the wavelength ratio based on the power law of broad-band wave field:

$$c_l/c_s = (\lambda_l/\lambda_s)^{\frac{1}{2}} = 2 \qquad a_l/a_s = (\lambda_l/\lambda_s)^{\frac{3}{2}} = 8 \tag{1}$$

where c_l, c_s are the phase speeds of the long wave and short wave, respectively; a_l, a_s are respectively the amplitudes of the long wave and short wave. In the problem setup, the wave steepness of long wave $(ak)_l$ is set to 0.2. We have studied three wave ages of the long wave, $c_l/u_* = 2$, 14, and 25, corresponding to slow wave case W02, intermediate wave case W14, and fast wave case W25, respectively. The wave age and wave steepness of the short waves are obtained based on equation 1. The surface elevation η is prescribed at each time step in the simulation as

$$\eta = a_l \sin k_l(x - c_l t) + a_s \sin k_s(x - c_s t) \tag{2}$$

We use x, y, and z to denote the streamwise, spanwise, and vertical coordinates, respectively, and u, v, and w to represent the velocity component in each direction. The size of the computational domain is $4\lambda_l$, $3\lambda_l$, and $2\lambda_l$ in x, y, and z directions, respectively, discretized with $256 \times 128 \times 129$ grid points which are evenly spaced in the horizontal plane and stretched in the vertical direction as shown in figure 1. The parameters are summarized in Table 1 and the numerical details and validations can be found in [1] and [2].

2.2. Sheltering effect

The suppress of the growth rate of short waves by the presence of long waves has been reported in literature [3, 4, 5]. However, more research is needed to reveal the underlying mechanism. In the present study, we aim to investigate the

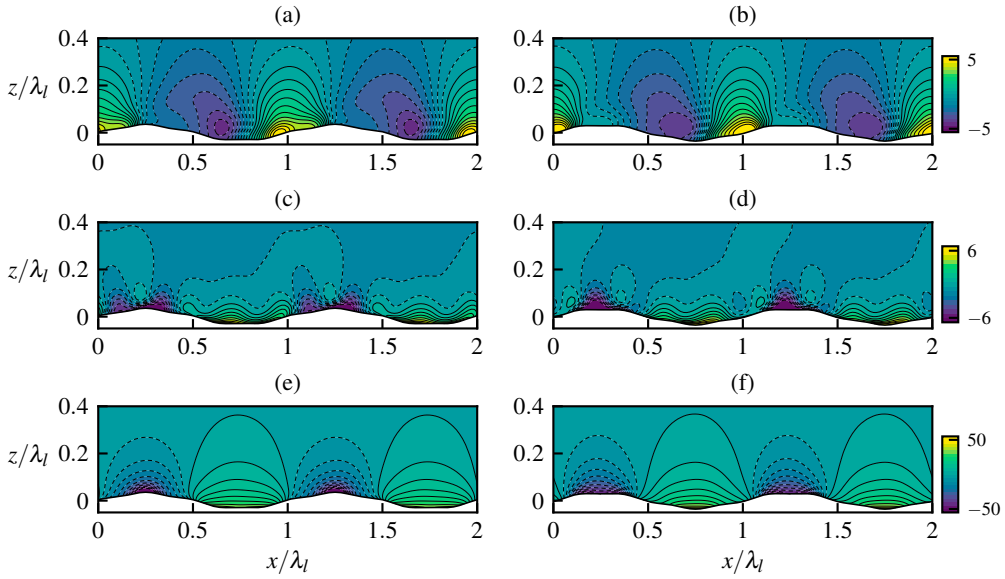

Fig. 2. Contours of phase-averaged pressure with conditional averaging under the crest condition and trough condition at different wave ages. (a) W02C; (b) W02T; (c) W14C; (d) W14T; (e) W25C; (f) W25T.

sheltering effect of long waves with various wave ages on the short waves. To obtain statistics of the turbulence field over two surface waves, we perform conditional averaging, including: (a) a crest condition where the crest of the long wave and that of the short wave coincide, which is indicated by the suffix "C", and (b) a trough condition where the crest of the long wave and the trough of the short wave coincide, which is indicated by the suffix "T". We use W02C, W14C, and W25C to denote the conditional averages of case W02, W14, and W25 respectively, based on the crest condition; and W02T, W14T, and W25T to represent conditional averages based on the trough condition.

Fig. 2 (a, b) shows the phase-averaged pressure field for $c_l/u_* = 2$, (c, d) for $c_l/u_* = 14$, and (d, f) for $c_l/u_* = 25$, corresponding to the slow, intermediate, and fast wave cases, respectively. The signature of short waves on the flow field can be seen from the variation of the spatial distribution of the maxima and minima of the pressure between the two types of conditionally averaged cases for each wave age. For the slow wave case W02, the positive pressure peak is where the windward side of the long wave coincides with that of the short wave, at $x/\lambda_l < 1$ for the conditionally averaged case W02C and at $x/\lambda_l > 1$ for case W02T; for the intermediate wave case W14, there are two peaks of pressure near the crest of the long wave in the conditionally averaged case W14C, while only one negative peak for case W14T; for the fast wave case W25, the difference is less obvious because the pressure distribution is more symmetric.

Table 2. Values of form drag in different cases.

Case	Form drag	Two-wave	Long-wave-only	Short-wave-only
$c_l/u_* = 2$	F_{p_l}+F_{p_s}	0.3646	0.3277	0.0398
	F_{p_l}	0.3488	0.3277	–
	F_{p_s}	0.0158	–	0.0398
$c_l/u_* = 14$	F_{p_l}+F_{p_s}	0.0360	0.0022	0.0714
	F_{p_l}	−0.0189	0.0022	–
	F_{p_s}	0.0550	–	0.0714
$c_l/u_* = 25$	F_{p_l}+F_{p_s}	−0.1423	−0.1275	−0.0206
	F_{p_l}	−0.1292	−0.1275	–
	F_{p_s}	−0.0140	–	−0.0206

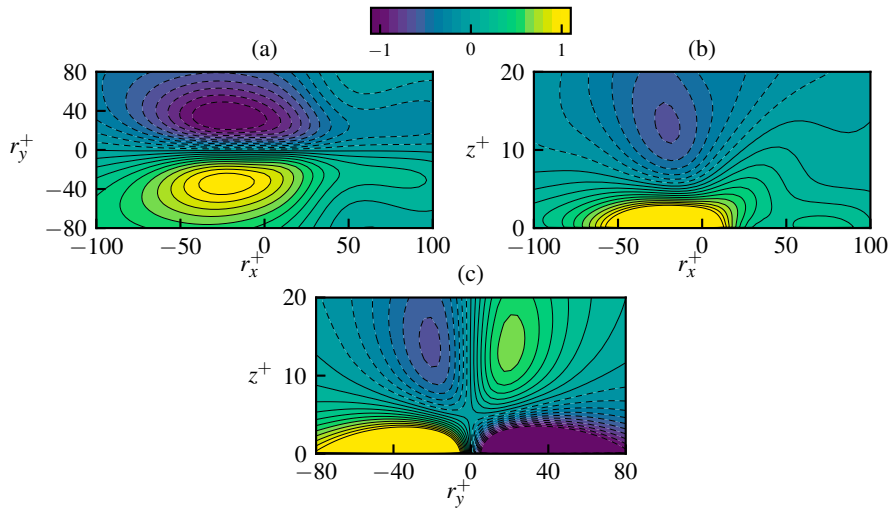

Fig. 3. Contours of the correlation function of the surface friction and streamwise vorticity at different planes: (a) $(z-\eta)^+ = 3.3$; (b) $r_y^+ = -17$; (c) $r_x^+ = -22$.

Next, we analyze the form drag on the surface waves. We decompose the total form drag on the wave surface in the two-wave cases into two parts, namely F_{p_l}, which is the form drag acting on the long wave, and F_{p_s}, which is the form drag on the short wave. The results are shown in Table 2. For comparison, we also include the form drag on the long waves and short waves, respectively in the long-wave-only cases and short-wave-only cases listed in Table 2. As shown, compared with the short-wave-only cases, the form drag on the short waves is reduced significantly in the presence of the long waves. On the other hand, the form drag on the long waves does not vary much between the two-wave cases and long-wave-only cases.

In Table 3, we calculate the reduction of the form drag on the short waves in the two-wave cases compared with the short-wave-only cases. As shown, the reduction is significant, with the relative magnitude depending on the wave age of the long waves, which is associated with the form drag on the long waves. In the slow wave case, in which the magnitude of F_{p_l} is the largest, the reduction in F_{p_s} is the most; in the fast wave case, both F_{p_l} and F_{p_s} are negative, and the magnitude of F_{p_s} is also reduced by the presence of the long wave; in the intermediate wave case, the reduction of F_{p_s} is the smallest, while the magnitude of the form drag on the long wave is also the lowest.

Table 3. Reduction of form drag on the short wave due to the presence of the long wave, and values of form drag on the long waves.

c_l/u_*	2	14	25
$\lvert\Delta F_{p_s}/F_{p_s}\rvert$	60%	22%	32%
F_{p_l}	0.3488	−0.0189	−0.1292

2.3. Correlation between surface friction and streamwise vorticity

In the slow wave case with $c_l/u_* = 2$, we observe that the total form drag in the two-wave case is larger than that in the long-wave-only case. Because the summation of the form drag and viscous drag on the surface is constant in the problem setup, i.e. u_* is kept the same, an increase in the form drag corresponds to a decrease in the friction drag. Our DNS data show that the viscous drag is mainly concentrated on the windward of the long wave both in the two-wave case and the long-wave-only case.

It is found that the reduction of surface friction is related to the vortical structures in wind turbulence. This can be demonstrated using the correlation function of the streamwise vorticity and surface friction defined as

$$R(r_x, r_y, z) = \overline{\tau_S(x, y, 0)\omega_x(x + r_x, y + r_y, z)}/(u_*^4/\nu) \tag{3}$$

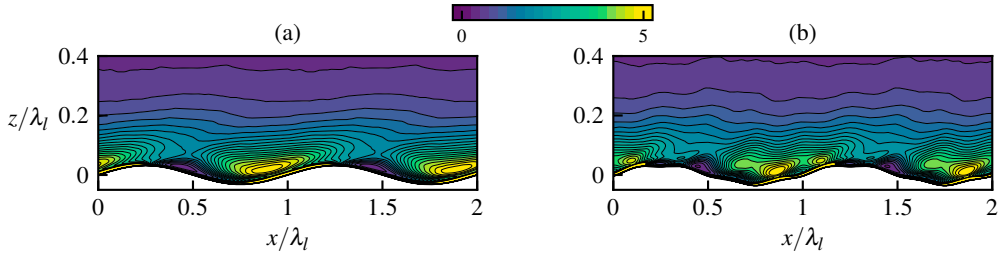

Fig. 4. Contours of phase-averaged enstrophy $\langle\omega_x\omega_x\rangle$ for $c_l/u_* = 2$. (a) long-wave-only case; (b) two-wave case W02T.

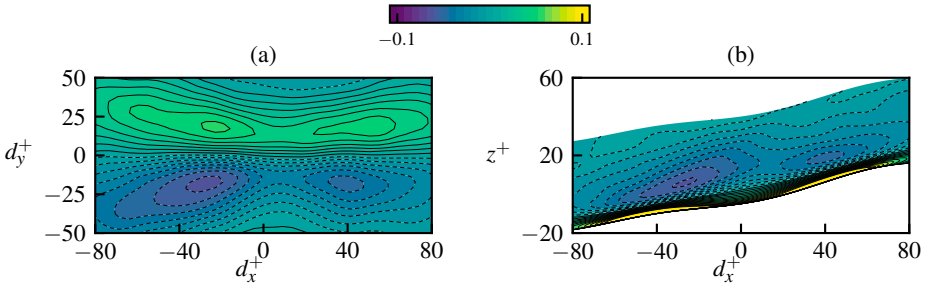

Fig. 5. Contours of conditionally averaged streamwise vorticity. (a) $(z-\eta)^+ = 15$; (b) $d_y^+ = -18$.

where $\omega_x = \partial w/\partial y - \partial v/\partial z$ is the streamwise vorticity, τ_s is surface friction, and r_x and r_y are spatial separations in x and y directions, respectively. The $R(r_x, r_y, z)$ was used in [6] to study the correlation between the friction and streamwise vorticity in channel flows. It was found that in channel flows, the friction is mainly induced by the streamwise vortices. For the present problem of wind turbulence over waves, Fig. 3 illustrates R in case W02T, which is averaged on the windward face of the long wave. As shown in Fig. 3(a) and (c), R has an anti-symmetric distribution with respect to r_y. Fig. 3(a) and (b) shows that R reaches its peak at $r_x^+ \approx -22$, indicating that the surface friction at the wave surface is mainly correlated to the upstream near-wall vorticity, in contrast to the channel flow where the surface friction is mostly correlated to downstream vorticity [6].

Fig. 4 shows the spatial distribution of phase-averaged enstrophy $\langle\omega_x\omega_x\rangle$ for $c_l/u_* = 2$ in the long-wave-only case and two-wave case. A comparison between these two cases indicates that the high concentration of enstropy at the windward side of the long wave in case W02T is broken at the position $x/\lambda_l = 1$ by the presence of the short wave. Also, at this position, it is found that the surface friction is significantly reduced compared with the long-wave-only case (result not plotted here due to space limitation).

The correlation between the streamwise vortical structure and surface friction can also be shown through conditional average, which extracts the coherent structure related to the surface friction by the following criterion [6]

$$\tau_S(x_0, y) > \alpha\langle\tau_S\rangle(x_0) \tag{4}$$

where τ_S represents the surface friction, $\langle\rangle$ denotes the phase average, α is a threshold and equals 2 in the present study, and x_0 is the position of the conditional average. We perform the conditional average at the position $x_0/\lambda_l = 1$ based on equation 4, the result of which is plotted in Fig. 5. As shown, the conditionally averaged ω_x field recovers the "broken" structure of the streamwise vorticity shown in Fig. 4, in which there are peaks of streamwise vorticity both at the upstream and downstream of the detection point.

3. Wind over Breaking Waves

Wave breaking plays an important role in air–sea interactions, which influence the sea states and marine atmospheric boundary layer. It has been summarized in many review papers [7, 8, 9, 10, 11, 12] that due to wave breaking, turbulence, vorticity, and ocean currents are generated, and the mass, momentum, and energy transfer between the

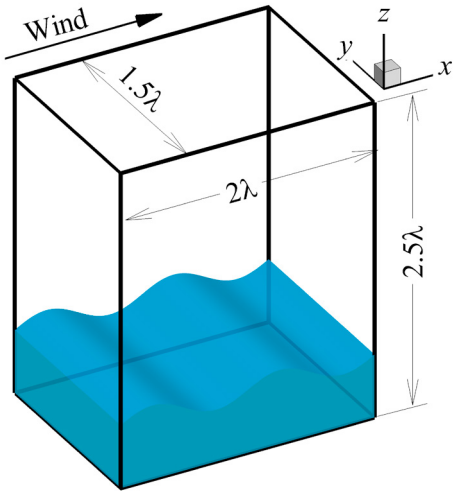

Fig. 6. Computational domain and coordinate system for DNS of wind over breaking waves.

atmosphere and oceans is enhanced. It would be helpful to investigate wind turbulence over breaking waves for improving ocean–atmosphere interaction models.

Wind over breaking waves has been studied in laboratory experiments and field measurements. Although numerical simulations have been performed to study wave breaking [13, 14, 15, 16], much less attention was paid to the wind turbulence over breaking waves. The numerical methods for simulating flows with a wave surface can be categorized into one-fluid and two-fluids simulations. The one-fluid simulation has been successfully used to study airflow over prescribed non-breaking waves [17, 18, 19]. In these one-fluid simulations, the waves act as a bottom boundary with prescribed motions. In two-fluids simulations, the air and water are treated as a coherent system, with an interface-capturing technique, which includes but is not limited to the level-set (LS) method [20], volume-of-fluid (VOF) method [21], and coupled LS and VOF (CLSVOF) method [22].

In the present study, we perform DNS of turbulent wind over breaking waves with the breaking process resolved explicitly. The objective is to study the effect of wave breaking on the momentum and energy transfer in the airflow. We simulate air and water as a coherent system on Eulerian grid. The air–water interface is captured using the CLSVOF method. Because wave breaking is an unsteady process, time averaging is impropriate to define turbulence statistics. Instead, we conduct 100 ensemble runs to calculate turbulence statistics based on ensemble averaging over these runs. Different runs have the same initial wind profile and wave geometry, but different instantaneous turbulence fluctuations.

Fig. 6 shows the computational domain and coordinates used in the present simulations. The streamwise, spanwise, and vertical directions are denoted by x, y, and z, respectively, and the corresponding velocity components are represented by u, v, and w, respectively. The wave propagates in the $+x$-direction. The computational domain size is set to $L_x \times L_y \times L_z = 2\lambda \times 1.5\lambda \times 2.5\lambda$, where λ is the wave length of the primary wave studied (Fig. 6). The mean water depth d and air height h are 0.5λ and 2λ, respectively. The number of grid points used in the simulations is $N_x \times N_y \times N_z = 320 \times 192 \times 360$. In the x- and y-directions, the grid is evenly-spaced. In the z-direction, the grid is clustered between $z = -0.1\lambda$ and $z = 0.15\lambda$ with a fine and constant resolution of $\Delta_z = 0.002\lambda$, and the grid is stretched to the top of air and bottom of water. The initial wave steepness is $ka_0 = 0.55$, where $k = 2\pi/\lambda$ is the wave number, and a_0 is the initial wave amplitude. The wave age c/u_* is 3.7, where c is the wave phase speed, and u_* is the frictional velocity in the air. The Reynolds number is set to $\mathrm{Re} = u_*\lambda/\nu = 180$ to perform DNS, where ν is the kinematic viscosity.

Fig. 7 shows the vertical profiles of the plane-averaged mean streamwise velocity $\langle u \rangle$, Reynolds shear stress $-\langle u'w' \rangle$, turbulent kinetic energy (TKE) $k_{pl} = (\langle u'u' \rangle + \langle v'v' \rangle + \langle w'w' \rangle)/2$, and TKE production $P_k = -\langle u'w' \rangle d\langle u \rangle/dz$ before ($t = 0.0T$), during ($t = 0.8T$), and after ($t = 3.0T$) wave plunging. Here, the angular bracket defines the averag-

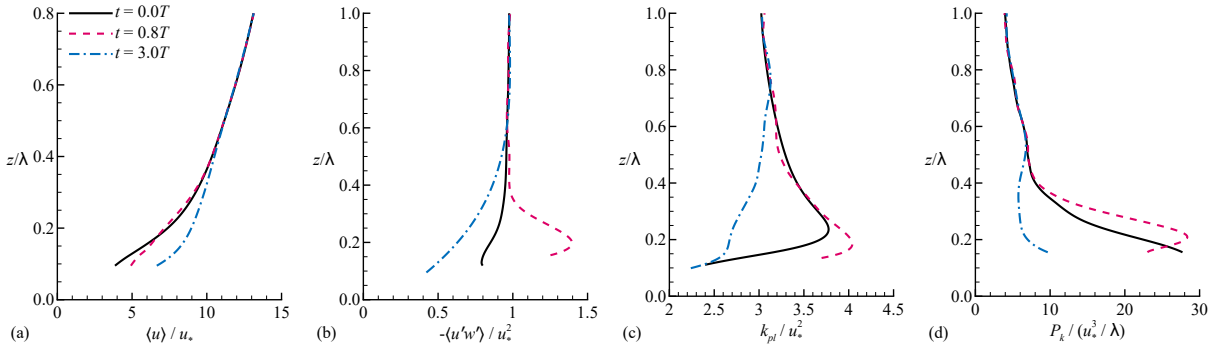

Fig. 7. Vertical profiles of (a) plane-averaged mean streamwise velocity $\langle u\rangle/u_*$, (b) Reynolds shear stress $-\langle u'w'\rangle/u_*^2$, (c) TKE k/u_*^2 , and (d) TKE production $P_k/(u_*^3/h)$ at different stages of wave plunging.

ing in horizontal plane and ensembles, and the prime denotes the corresponding turbulence fluctuations. All profiles in the figure are nondimensionalized using u_* and h as the characteristic velocity and length scales, respectively.

It can be observed from Fig. 7(a) that the magnitude of $\langle u\rangle$ near the wave surface is larger at $t = 3.0T$ than at $t = 0.0T$, indicating the overall transport of momentum from water to air during the wave plunging. However, $\langle u\rangle$ experiences a transient decrease above $z/\lambda = 0.18$ before $t = 0.8T$. The plane-averaged Reynolds shear stress $-\langle u'w'\rangle$ plays an important role in the evolution of the plane-averaged mean streamwise velocity $\langle u\rangle$, of which the governing equation reads

$$\frac{\partial\langle u\rangle}{\partial t} = \nu\frac{\partial^2\langle u\rangle}{\partial z^2} - \frac{\partial\langle u'w'\rangle}{\partial z} \quad . \tag{5}$$

Fig. 7(b) shows that the first plunging event disturbs the air near the wave surface. As a result, there exists a peak in the profile of $-\langle u'w'\rangle$ near $z/\lambda = 0.2$ at $t = 0.8T$. Below and above this peak, the value of $-\partial\langle u'w'\rangle/\partial z$ is positive and negative, respectively. Because the viscous shear stress is less important than the Reynolds shear stress in this region, it is understood from equation (5) that during wave breaking, the wind speed $\langle u\rangle$ is accelerated and decelerated below and above the peak of $-\langle u'w'\rangle$, respectively. The peak of $-\langle u'w'\rangle$ moves upward with its magnitude decreasing after $t = 0.8T$, leading to an expansion of the acceleration region. As a result, the mean velocity increases after $t = 0.8T$ (Fig. 7a).

The wave plunging also influences the TKE k_{pl} near the wave surface significantly. As shown in Fig. 7(c), the value of k_{pl} below $z/\lambda = 0.35$ is higher at $t = 0.8T$ than at $t = 0.0T$, indicating that the turbulence is transiently enhanced due to the wave breaking. The magnitude of k_{pk} is smaller at $t = 3.0T$ than at $t = 0.0T$, indicating that the turbulence is eventually reduced after wave plunging ceases.

To further study why the transient growth of TKE takes place, we compare the production of TKE, P_k. It is evident from Fig. 7(d) that the magnitude of P_k is larger at $t = 0.8T$ than at $t = 0.0T$. From the expression of P_k, it is known that the value of P_k is determined by the vertical gradient of mean velocity $\partial\langle u\rangle/\partial z$ and the Reynolds shear stress $-\langle u'w'\rangle$. Fig. 7(a) shows that $\partial\langle u\rangle/\partial z$ decreases during the first plunging event, which tends to reduce the value of P_k. In contrast, as shown in Fig. 7(b), the magnitude of $-\langle u'w'\rangle$ increases and a peak occurs in its profile due to the disturbance effect of the wave breaking on the turbulent flow, which tends to cause an increase of P_k. Fig. 7(d) indicates that the latter effect is stronger, and as a result k_{pl} experiences a transient growth during the first plunging event (Fig. 7c).

Next, we study the wave-phase-averaged airflow statistics. Fig. 8 shows the phase-averaged mean streamwise velocity $\bar{u}$, mean vertical velocity $\bar{w}$, and mean spanwise vorticity $\bar{\omega}_y$ near the wave surface during the wave plunging at $t = 0.8T$. Here, the bar denotes the averaging in spanwise direction, wave phase, and ensembles. The instantaneous wave surface varies with the spanwise coordinate y. Moreover, it differs among different ensemble runs. Therefore, the air–water interfaces should not be represented deterministically by a single line in a 2D plot of phase-averaged statistics. We use a thick dash-dotted line to denote the upper bound of all interfaces.

As shown in Fig. 8(a), when the overturning jet impinges onto the wave surface, it pushes the air to move forward. This process accelerates the airflow in the streamwise direction, and as a result, a high-speed region is formed ahead

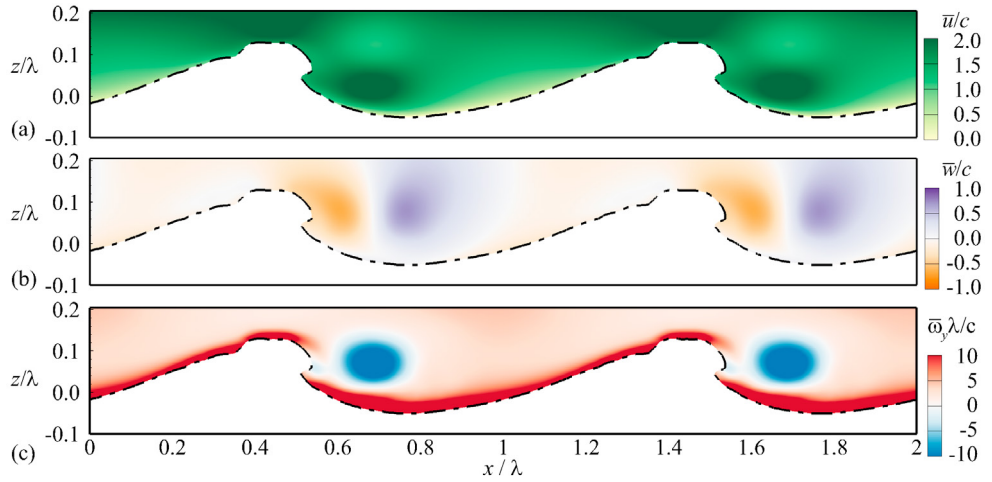

Fig. 8. Phase-averaged flow field at $t = 0.8T$. (a) Mean streamwise velocity $\bar{u}$, (b) mean vertical velocity $\bar{w}$, and (c) mean spanwise vorticity ω_y. The dash-dotted line represents the upper bound of all wave surfaces, defined as the isopleth of $\bar{\psi} = 0.05$, where ψ is the volume fraction of water. Note that the upper bound of wave surface is different from the instantaneous wave surface, which can be represents by the isopleth of $\psi = 0.5$. The wave propagates in the $+x$-direction.

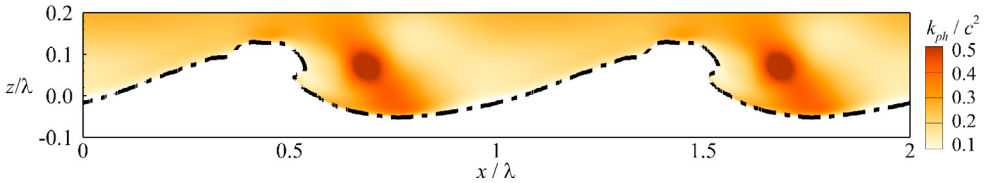

Fig. 9. Contours of phase-averaged TKE k_{ph}/c^2 at $t = 0.8T$. The thick dashed-dotted line represents the top bound of wave surfaces. The waves propagate in the $+x$-direction.

of the wave front. Meanwhile, the jet brings the air particles around it to impinge onto the wave surface. Therefore, the vertical velocity of airflow is negative on the leeward of the wave crest (Fig. 8b). The airflow above the vortex is decelerated to compensate the air moving downward with the jet, such that a low-speed region appears above the vortex (Fig. 8a). A counterclockwise-rotating vortex is generated during wave plunging. This vortex corresponds to the negative vorticity in Fig. 8(c).

Fig. 9 displays the contours of the phase-averaged TKE $k_{ph} = (\overline{u''u''} + \overline{v''v''} + \overline{w''w''})/2$ near the wave surface at $t = 0.8T$. Here, the double prime denotes the fluctuations with respect to the phase averaging. As shown, the magnitude of k_{ph} is large near the spanwise vortex shown in Fig. 8(c), indicating that the turbulence is enhanced by the vortex. This is consistent with the result of the plane-averaged TKE shown in Fig. 7(c).

4. Wind over Broad-Band Waves

In this section, we study wind turbulence over broad-band waves following [35, 36], where the wind field is simulated using LES and the wave evolution is computed using a high-order spectral method [23]. The physical and numerical parameters of the simulation are listed in Table 4. An instantaneous wind field, as denoted by the streamwise velocity in an $x - z$ plane, and a wave field, as denoted by the surface elevation, are plotted in Fig. 10.

We first examine the wind turbulence above the water from the perspective of space–time correlation. The full wavenumber–frequency spectrum of the streamwise velocity [28] is calculated and plotted in Fig. 11. For the purpose of clarity and to simplify the analysis, the spectrum $F_{11}(k_1, k_2, \omega)$ is projected onto the spectral plane (k_1, ω). Fig. 11 shows that the shape of the spectrum is a combined result of different effects caused by the mean flow, large turbulence eddies, and waves. Consider the turbulence motion on a horizontal plane, the convection due to the mean flow $U(z)$

Table 4. Parameters of the wind and wave simulations. Here, L_x, L_y, and L_z are the computational domain size in three directions, N_x, N_y, and N_z are the grid number correspondingly, u_* is the friction velocity, U_{10} is the initial wind speed at 10m above the mean water surface, α_p is the Phillips parameter of the initial JONSWAP spectrum, and $f_{p,0}$ is the initial peak wave frequency.

Simulation	(L_x, L_y, L_z) (m)	$(N_x \times N_y \times N_z)$ (wind) / $(N_x \times N_y)$ (wave)	u_* (m/s)	U_{10} (m/s)	α_p	$f_{p,0}$ (Hz)
Wind field (LES)	200, 100, 100	$256 \times 128 \times 256$	0.22	6	–	–
Wave field (HOS)	200, 100	512×256	–	–	0.0144	0.40

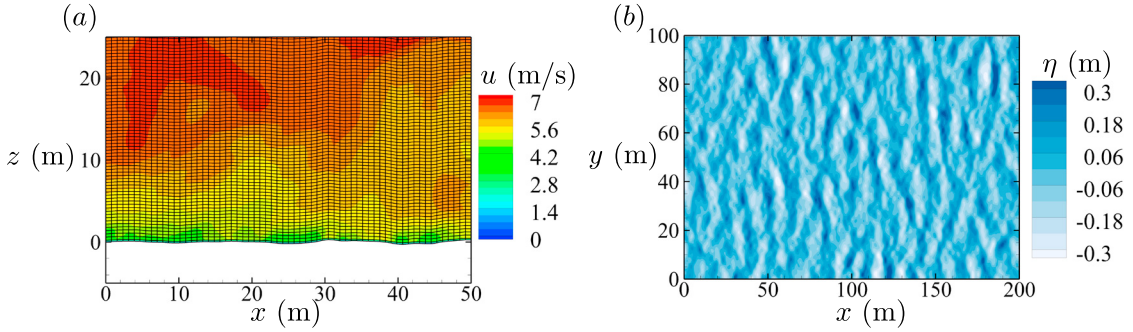

Fig. 10. A snapshot of the contours of the instantaneous (a) wind streamwise velocity u in an $x - z$ plane, and (b) wave surface elevation η. Also plotted in (a) is the wave-boundary-fitted grid in the wind simulation. Only part of the wind field is plotted for clarity.

causes a change in the frequency of turbulence motions, and turns a spatial oscillation into a temporal one, which can be seen from the "frozen turbulence hypothesis" [30]. Large energy-containing eddies lead to a broadening of the spectrum, which can be theoretically explained by the random-sweeping model of the spectrum [33, 34]. Besides these two features related to the Doppler effect, a unique wave signature is found in the spectrum, which is identified by another branch along the dispersion relation of gravity waves $\omega = \sqrt{gk_1}$. It is evident that the wave-induced energy is significant for a wide range of motions of different scales, especially in the high wavenumber region. This discovery can be used as a measure of the wave effect on the wind turbulence.

We next investigate nonlinear wave interactions, a key process in wave field evolution. Here, the nonlinear wave interactions refer to the energy transfer among four wave components, which is quantified by the Hasselmann equation [24, 25, 26]:

$$S_{nl}(\mathbf{k_1}) = \omega_4 \int Q(\mathbf{k_1}, \mathbf{k_2}, \mathbf{k_3}, \mathbf{k_4}) \delta(\mathbf{k_1} + \mathbf{k_2} - \mathbf{k_3} - \mathbf{k_4}) \delta(\omega_1 + \omega_2 - \omega_3 - \omega_4) \\ [n_1 n_2 (n_3 + n_4) - n_3 n_4 (n_1 + n_2)] \mathrm{d}\mathbf{k_1} \mathrm{d}\mathbf{k_2} \mathrm{d}\mathbf{k_3}, \tag{6}$$

where S_{nl} is the rate of change of the wave energy caused by four-wave interaction, ω_i is the angular frequency of a wave component, $n_i(\mathbf{k_i}) = E(\mathbf{k_i})/\omega_i$ is the ratio of wave energy density function $E(\mathbf{k_i})$ to wave frequency, i.e., the wave action density function, and $Q(\mathbf{k_1}, \mathbf{k_2}, \mathbf{k_3}, \mathbf{k_4})$ is a complex function of wavenumber vectors.

We calculate the exact four-wave interaction of the initial spectrum by integrating the Hasselmann equation using two different methods: the quadrature method [27] and the Webb-Resio-Tracy (WRT) method [32, 31]. The results are shown in Fig. 12. While there are some discrepancies because of the different numerical approaches used in the two methods, the main features of the nonlinear interactions are captured as expected [37]. Most notably, there is a change of sign in the value of S_{nl} near the peak $f/f_{p,0}$, suggesting the energy transfer from higher wavenumber components to lower wavenumber ones, resulting in the frequency downshift. This phenomenon is observed in the coupled wind–wave simulation as shown in Fig. 13(a), where the wave peak moves to the lower frequency region near $f = 0.8 f_{p,0}$ after an evolution period of $t \approx 3600 T_{p,0}$. To further investigate the role four-wave interaction plays in this process, we calculate the rate of change of the omnidirectional frequency spectrum $\Delta E/\Delta t$ using the simulation data of the wind-forced wave field, and compare it with S_{nl}. The results are presented in Fig. 13(b). Here, the exact solutions of omnidirectional S_{nl} are directly calculated from the directional result by integration over the coordinate θ (see Fig. 12), while the numerical solution of S_{nl} is calculated from an independent HOS simulation following [29]. We find that

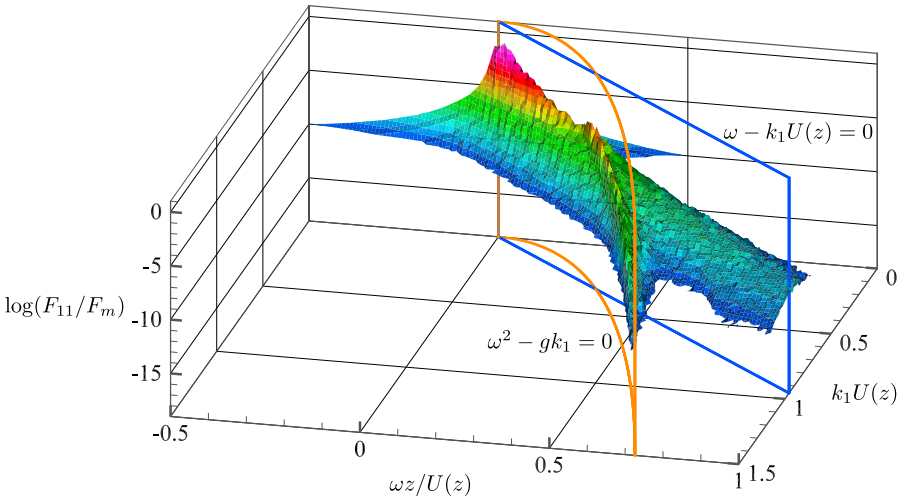

Fig. 11. Wavenumber–frequency spectrum of the streamwise velocity of the wind field. The spectrum is normalized by its maximum value F_m. The raw data used for analysis is from the horizontal plane $z = 1.2$m above the mean water surface. Also plotted are two surfaces denoting the Doppler shift $\omega = k_1 U(z)$ and the dispersion relation of deep water wave $\omega = \sqrt{gk_1}$.

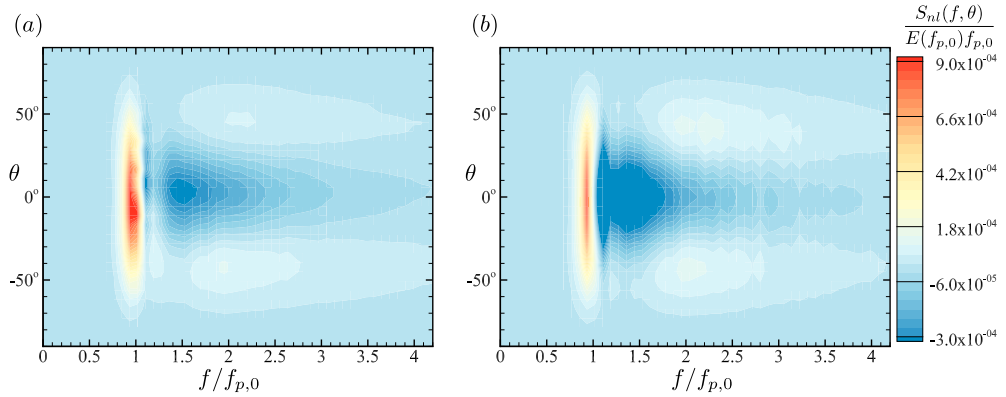

Fig. 12. Four-wave interaction-induced energy transfer $S_{nl}(f,\theta)$ calculated using (a) the quadrature method and (b) the WRT method, normalized by the peak frequency $f_{p,0}$ and the energy density function $E(f_{p,0})$ of the initial wave field.

the shape of the total energy transfer is similar to that of the four-wave interaction term, exhibiting a change of sign. Compared with wind input, four-wave interaction has no net energy contribution to the wave field since it is an internal energy redistribution mechanism among wave components. However, our numerical result shows that the strength of four-wave interaction dominates over wind input locally in the spectral space. Therefore, the four-wave interaction may serve as the dominant mechanism that determines the wave spectrum shape and thus plays an important role in the long-term evolution of wave fields.

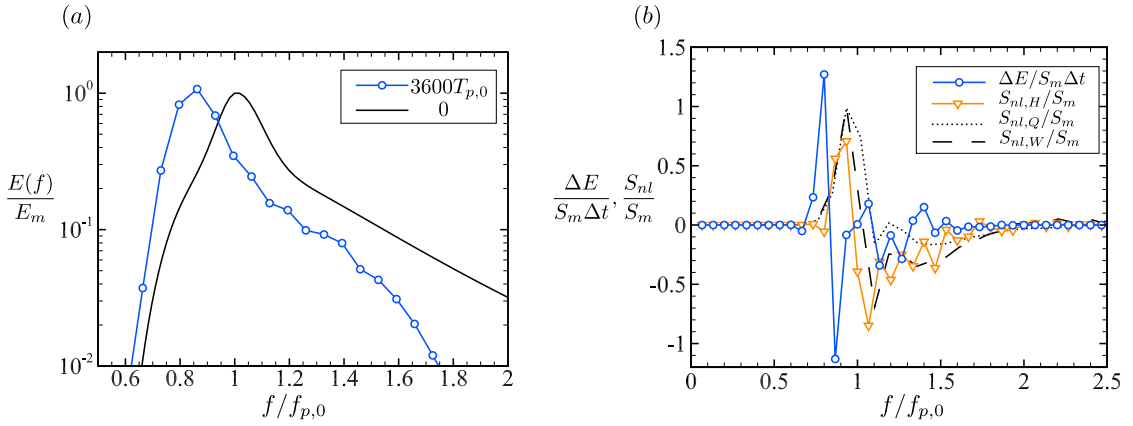

Fig. 13. Normalized omnidirectional wave spectrum (a), and rate of change of the spectrum (b), at $t \approx 3600T_{p,0}$. In (a), the black solid line denotes the initial JONSWAP spectrum, where E_m is its maximum value. Also plotted in (b) are the nonlinear interaction terms based on the initial spectrum calculated using the quadrature method $S_{nl,Q}$, the WRT method $S_{nl,W}$, and the HOS simulation data $S_{nl,H}$. Here, S_m denotes the maximum value of the WRT result.

5. Conclusions

In this paper, we have presented numerical results of wind over different wave fields. In the first part, we use DNS to study wind over two progressive waves and investigate the sheltering effect of a long wave on a short wave. We find that in the presence of the long wave the form drag of the short wave decreases, with the magnitude of the reduction depending on the wave age, or equivalently the magnitude of the form drag on the long wave. The larger the magnitude of the form drag on the long wave, the stronger the sheltering effect, and thus the larger relative reduction of the form drag on the short wave. By calculating the correlation between the spatial distribution of streamwise vorticity and the surface friction on the surface waves, we have shown that the local reduction of the surface friction on the windward face of the long wave by the presence of the short wave is correlated to the breaking of streamwise vortical structures. In the second part, we use DNS to study wind turbulence over breaking waves. It is found that wave plunging significantly influences the turbulence statistics near the wave surface. During the plunging, the air is accelerated in the streamwise direction due to the push of the overturning jet. The wave plunging also induces a large spanwise vortex. Near this vortex, the air is highly disturbed, and the magnitude of TKE increases significantly. Above the wave crest, the magnitude of TKE grows transiently during wave plunging. The investigation of TKE production shows that the transient growth of TKE results from a peak occurring in the profile of the Reynolds shear stress. Finally, we show the result of wind over broad-band waves, simulated using the coupled LES–HOS model. The wave signature on the wind turbulence is elucidated in the wavenumber–frequency spectrum of the streamwise wind velocity, indicating the significance of wave effect on the wave boundary layer. We also observe the frequency downshift phenomenon in the long-term evolution of the wave field. By comparing the total wave energy change and that caused by four-wave interaction, we show that four-wave interaction dominates the evolution of the wind-wave field.

Acknowledgements

The support to this research by ONR and NSF is gratefully acknowledged.

References

1. D. Yang, L. Shen, Simulation of viscous flows with undulatory boundaries. Part I: Basic solver, *Journal of Computational Physics*, 2011; **230** 5488-5509.
2. D. Yang, L.Shen, Direct-simulation-based study of turbulent flow over various waving boundaries, *Journal of Fluid Mechanics*, 2010; **650** 131-80.

3. O. M. Phillips, M. L. Banner, Wave breaking in the presence of wind drift and swell, *Journal of Fluid Mechanics*, 1974; **66** 625-640.
4. M. A. Donelan, The effect of swell on the growth of wind waves, *Johns Hopkins APL Technical Digest*, 1987; **8** 18-23.
5. G. Chen, S.E. Belcher, Effects of long waves on wind-generated waves, *Journal of Physical Oceanography*, 2000; **30** 2246-2256.
6. A. G. Kravchenko, H. Choi, P. Moin, On the relation of near-wall streamwise vortices to wall skin friction in turbulent boundary layers, *Physics of Fluids A: Fluid Dynamics*, 1993; **5** 3307-3309.
7. M. L. Banner, D. H. Peregrine, Wave breaking in deep water, *Annual Review of Fluid Mechanics*, 1993; **25** 373-97.
8. W. K. Melville, The role of surface-wave breaking in air–sea interaction, *Annual Review of Fluid Mechanics*, 1996; **28** 279-321.
9. M. Perlin, W. W. Schultz, Capillary effects on surface waves, *Annual Review of Fluid Mechanics*, 2000; **32** 241-74.
10. J. H. Duncan, Spilling breakers, *Annual Review of Fluid Mechanics*, 2000; **33** 519-47.
11. K. T. Kiger, J. H. Duncan, Air-entrainment mechanisms in plunging jets and breaking waves, *Annual Review of Fluid Mechanics*, 2012; **44** 563-96.
12. M. Perlin, W. Choi, Z. Tian, Breaking waves in deep and intermediate waters, *Annual Review of Fluid Mechanics*, 2013; **45** 115-45.
13. A. Iafrati, Numerical study of the effects of the breaking intensity on wave breaking flows, *Journal of Fluid Mechanics*, 2009; **622** 371-411.
14. M. Derakhti, J. T. Kirby, Bubble entrainment and liquid–bubble interaction under unsteady breaking waves, *Journal of Fluid Mechanics*, 2014; **761** 464-506.
15. L. Deike, S. Popinet, W. K. Melville, Capillary effects on wave breaking, *Journal of Fluid Mechanics*, 2015; **769** 541-69.
16. P. Lubin, S. Glockner, Numerical simulations of three-dimensional plunging breaking waves: generation and evolution of aerated vortex filaments, *Journal of Fluid Mechanics*, 2015; **767** 364-93.
17. P. P Sullivan, J. C. McWilliams, C.-H. Moeng, Simulation of turbulent flow over idealized water waves, *Journal of Fluid Mechanics*, 2000; **404** 47-85.
18. D. Yang, L. Shen, Direct-simulation-based study of turbulent flow over various waving boundaries, *Journal of Fluid Mechanics*, 2010; **650** 131-80.
19. T. Hara, P. P. Sullivan, Wave boundary layer turbulence over surface waves in a strongly forced condition, *Journal of Physics Oceanography*, 2015; **45** 868-83.
20. S. Osher, J. A. Sethian, Fronts propagating with curvature-dependent speed: algorithms based on Hamilton–Jacobi formulations, *Journal of Computational Physics*, 1988; **79** 12-49.
21. R. Scardovelli, S. Zaleski, Direct numerical simulation of free-surface and interfacial flow, *Annual Review of Fluid Mechanics*, 1999; **31** 567-603.
22. M. Sussman, E. G. Puckett, A coupled level set and volume-of-fluid method for computing 3D and axisymmetric incompressible two-phase flows, *Journal of Computational Physics*, 2000; **162** 301-37.
23. D. G. Dommermuth, D. K. P. Yue, A high-order spectral method for the study of nonlinear gravity waves, *Journal of Fluid Mechanics*, 1987; **184** 267-288.
24. K. Hasselmann, On the non-linear energy transfer in a gravity-wave spectrum. Part 1. General theory, *Journal of Fluid Mechanics*, 1962; **12** 481-500.
25. K. Hasselmann, On the non-linear energy transfer in a gravity-wave spectrum. Part 2. Conservation theorems; wave-particle analogy; irreversibility, *Journal of Fluid Mechanics*, 1963; **15** 273-281.
26. K. Hasselmann, On the non-linear energy transfer in a gravity-wave spectrum. Part 3. Evaluation of the energy flux and swell-sea interaction for a Neumann spectrum, *Journal of Fluid Mechanics*, 1963; **15** 385-398.
27. I. V. Lavrenov, Effect of wind wave parameter fluctuation on the nonlinear spectrum evolution, *Journal of Physical Oceanography*, 2001; **31** 861-873.
28. S. B. Pope, *Turbulent Flows*, 2000. Cambridge University Press, Cambridge; New York.
29. M. Tanaka, Verification of Hasselmann's energy transfer among surface gravity waves by direct numerical simulations of primitive equations, *Journal of Fluid Mechanics*, 2001; **444**, 199-221.
30. G. I. Taylor, The spectrum of turbulence, *Proceedings of the Royal Society A: Mathematical, Physical and Engineering Sciences*, 1938;**164**, 476-490.
31. B. A. Tracy, D. T. Resio, Theory and calculation of the nonlinear energy transfer between sea waves in deep water, *Technical Report*, 1982. Hydraulics Laboratory, U.S. Army Engineer Waterways Experiment Station. Vicksburg, Miss.
32. D. J. Webb, Non-linear transfers between sea waves, *Deep Sea Research0*, 1978; **25**, 279-298.
33. M. Wilczek, Y. Narita, Wave-number-frequency spectrum for turbulence from a random sweeping hypothesis with mean flow, *Physical Review E - Statistical, Nonlinear, and Soft Matter Physics*, 2012; **86**, 1-8.
34. M. Wilczek, R. J. A. M. Stevens, Y. Narita, C. Meneveau, A wavenumber-frequency spectral model for atmospheric boundary layers, *Journal of Physics: Conference Series*, 2014; **524**, 012104.
35. D. Yang, C. Meneveau, L. Shen, Effect of downwind swells on offshore wind energy harvesting - A large-eddy simulation study, *Renewable Energy*, 2014; **70**, 11-23.
36. D. Yang, C. Meneveau, L. Shen, Large-eddy simulation of offshore wind farm, *Physics of Fluids*, 2014; **26**, 025101.
37. I. R. Young, *Wind Generated Ocean Waves*, 1999. Elsevier. Amsterdam; New York.

Available online at www.sciencedirect.com

ScienceDirect

Procedia IUTAM 26 (2018) 174–183

Procedia IUTAM

www.elsevier.com/locate/procedia

IUTAM Symposium Wind Waves, 4-8 September 2017, London, UK

Impacts of wave age on turbulent flow and drag of steep waves

Peter P. Sullivan[a,*], Michael L. Banner[b], Russel P. Morison[b], William L. Peirson[c]

[a]National Center for Atmospheric Research, Boulder, Colorado, USA
[b]School of Mathematics and Statistics, The University of New South Wales, Australia
[c]New College, The University of New South Wales, Australia

Abstract

Turbulent flow over steep steady and unsteady wave trains with varying height $h(x,t)$ and propagation speed c is simulated using large-eddy simulation (LES) in a wind-wave channel [17]. The imposed waveshape with steady wave trains is based on measurements of incipient and active breaking waves collected in a wind-wave tank, while a numerical wave code is used to generate an unsteady evolving wave train (or group) [3]. For the adopted waveshapes, process studies are carried out varying the wave age c/u_* from ~ 1 to 10: the airflow friction velocity is u_*. Under strong wind forcing or low wave age $c/u_* \sim 1$, highly intermittent airflow separation is found in all simulations and the results suggest separation near a wave crest occurs prior to the onset of wave breaking. As wave age increases flow separation is delayed or erased for both steady and unsteady wave trains. Flow visualization shows that near the wave surface vertical velocity w and waveslope $\partial h/\partial x$ are positively correlated at $c/u_* \sim 1$ but are negatively correlated at $c/u_* = 10$. The vertical speed of the underlying wave oscillations depends on the local waveslope, increases with phase speed, and is a maximum on the leeward side of the wave. Vigorous boundary movement [8] appears to alter the unsteady flow separation patterns which leads to a reduction in form (pressure) drag as wave age increases. For example, the pressure contribution to the total drag of the active breaker wave train decreases from 74% at $c/u_* = 1.23$ to less than 20% at $c/u_* = 10$. Critical layer dynamics appears to play a secondary role in the air-wave coupling over steep waves, but requires further investigation. For all simulations, the form drag is found to be strongly dependent on both waveslope $\partial h/\partial x$ and wave age c/u_*. The simulations are in good agreement with experimental results for turbulent flow over steep waves under strong wind forcing.

Peer-review under responsibility of the scientific committee of the IUTAM Symposium Wind Waves.

Keywords: turbulence ; water waves ; unsteady separation ; drag ; wave age

1. Introduction

Air-sea interaction fluxes of fundamental scalar and dynamical variables couple the atmosphere and the ocean, and are crucial for short and long term environmental forecasting. Yet, despite decades of intensive research, there remain significant knowledge gaps in the underlying physical processes that need to be resolved in order to improve forecast accuracy for applications ranging from mesoscale to climatic time scales. Wind waves underpin key air-sea interfacial

* Corresponding author. Tel.: +1-303-497-8953 ; fax: +1-303-497-8171.
E-mail address: pps@ucar.edu

2210-9838
Peer-review under responsibility of the scientific committee of the IUTAM Symposium Wind Waves.
10.1016/j.piutam.2018.03.017

exchange processes across the wind-driven sea surface, especially under strong wind forcing. Which wind-wave scales and transfer mechanisms are operative, and under what circumstances are they significant, or even dominant? These questions motivate our simulation study, which focuses on very strongly-forced wave scales and the impact of the wave steepness, wave age and modulational variability of the surface geometry on the interfacial dynamics and scalar fluxes. The role of strongly forced (steep) waves in coupling turbulent winds to the ocean surface and currents is not well understood at a fundamental level because of the inherent nonlinear and dissipative fluid dynamics.

In order to shed light on air-water coupling mechanics for steep waves we recently carried out an investigation of turbulent flow above steady and unsteady wave trains using large eddy simulation (LES) [17]. To carry out the process studies a highly idealized simulation design was adopted: The steep waves imposed at the lower boundary of the LES are synthesized shapes measured in a wind-wave tank [2]. The observed waves are not monochromatic, but feature sharp crests with shallow troughs and local waveslopes $\partial h/\partial x$ that are asymmetrical about the wave crest; $-\partial h/\partial x$ is noticeably larger forward of a wave crest. The waves are near or slightly past the onset of full breaking with spilling fluid down the face of the wave. Also, we examine the impact of modulational variability of the surface by imposing a time and space varying wave packet (group) [3] at the LES lower boundary. In all the simulations, the wave age $c/u_* \sim 1$, where c is the characteristic phase speed of the wave and u_* is the air friction velocity.

The major findings from [17] are: 1) highly intermittent airflow separation is observed and occurs before the onset of full breaking; 2) the form (pressure) drag increases markedly as the waves cross the boundary from incipient to active breaking; 3) the LES results are in good agreement with experimental observations; and 4) intermittent separation is found in flow over the wave packet, and its form drag is well correlated with the evolving waveslope. The goal of the present work is to expand our process studies and examine the impact of increasing wave age on winds and surface drag for steep steady and unsteady wave trains. The simulation design is identical to that described in [17], but now with varying c/u_*.

Nomenclature

ak	root-mean-square (rms) waveslope
c	wave phase speed
c/u_*	wave age
e	subgrid scale energy
$h(x,t)$	wave height
$\partial h/\partial x$	local waveslope
h_{cr}	height of critical layer
J	Jacobian of the grid transformation
(L_x, L_y, H)	dimensions of computational box
(N_x, N_y, N_z)	gridpoints used to discretize (L_x, L_y, L_z)
$\partial \mathcal{P}/\partial x$	imposed pressure gradient
k	wavenumber $= 2\pi/\lambda$
p	static pressure
t	time
$\mathbf{u}$	Cartesian velocity vector $u_i = (u, v, w)$
u_*	surface friction velocity
w_o	vertical velocity of the wave surface
$\mathbf{x}$	Cartesian coordinates $x_i = (x, y, z)$
z_o	surface roughness
z_t	translation speed of vertical gridlines (grid speed)
λ	wavelength
ν_t	subgrid scale eddy viscosity
$\boldsymbol{\xi}$	computational coordinates $\xi_i = (\xi, \eta, \zeta)$
ϖ	stretching factor in grid generation
ρ	air density

τ_{ij}	subgrid scale stress tensor
$\langle f \rangle$	space-time average of f at constant ζ and over t
$[f]$	spanwise y average of f at constant x
$(f)'$	turbulent fluctuation
	(velocity, length, time) are dimensionless by $(u_*, \lambda, \lambda/u_*)$

2. Large-eddy simulation

2.1. Large-eddy simulation

An overview of the LES model is presented here in order to introduce the coordinate system, variables, and the basics of the solution algorithm [21, 10, 17]. The following nomenclature is used: $\mathbf{u} \equiv u_i = (u, v, w)$ denote the Cartesian velocity components and p is the pressure variable normalized by density ρ. The three Cartesian coordinates are $\mathbf{x} \equiv x_i = (x, y, z)$ which are also referred to as (streamwise, spanwise, vertical) directions, respectively, and t is time.

We simulate incompressible turbulent boundary-layer flow in a channel with a flat upper boundary and a wavy moving lower boundary. Then the set of spatially filtered LES equations that describe the flow are:

$$\frac{\partial u_i}{\partial x_i} = 0\,, \tag{1}$$

$$\frac{\partial u_i}{\partial t} = -\frac{\partial u_j u_i}{\partial x_j} - \frac{\partial p}{\partial x_i} - \frac{\partial \tau_{ij}}{\partial x_j} - \frac{\partial \mathcal{P}}{\partial x_i}\delta_{i1} \tag{2}$$

The boundary-layer winds are driven by a large-scale imposed external streamwise pressure gradient $\partial\mathcal{P}/\partial x$ that is constant in space and time. To enforce mass conservation the pressure variable p is determined from an elliptic Poisson pressure equation $\nabla^2 p = \mathcal{R}$ formed by applying the discrete divergence operator to the velocity time tendencies, $\nabla \cdot (\partial_t \mathbf{u})$. To close the system of equations the subgrid-scale (SGS) momentum flux τ_{ij} requires modeling in the interior of the flow and at the lower boundary. We use an eddy viscosity prescription $\nu_t \sim \sqrt{e}$ where e is the subgrid-scale kinetic energy. An additional transport equation for SGS energy e is added to the LES equation set (1, 2). The molecular Reynolds number is assumed to be high and molecular diffusion terms are neglected in (2).

2.2. Coordinate transformation

The LES code integrates the governing equations (1, 2) in a time varying non-orthogonal surface following coordinate system. The computational coordinates are $\xi_i = (\xi, \eta, \zeta)$, and the wave-following grid transformation and metrics that map physical space to computational space $(x, y, z, t) \Longleftrightarrow (\xi, \eta, \zeta, t)$ are

$$x = \xi, \quad y = \eta, \quad z = \zeta + h(x,t)\left(1 - \frac{\zeta}{H}\right)^{\varpi}, \tag{3}$$
$$\xi_x = 1, \quad \zeta_x = -z_\xi J, \quad \zeta_z = 1/z_\zeta = J, \quad z_t = -\zeta_t/J\,.$$

The imposed time varying surface wave height is $h(x, t)$ and the top of the computational domain is H. The Jacobian of the mapping transformation $J = \partial\zeta/\partial z$, and the vertical coordinate lines move up and down with grid speed $z_t \equiv \partial z/\partial t = -(\partial\zeta/\partial t)/J$. The slope of a wave following streamwise gridline is $z_\xi \equiv \partial z/\partial\xi = -(\partial\zeta/\partial x)/J$. Parameter $\varpi = 3$ controls how rapidly the streamwise gridlines become level surfaces with increasing distance from the surface in physical space. The transformation (3) is a smooth single valued function and produces continuous spatial derivatives $\partial\xi_i/\partial x_j$ and time derivatives $\partial\xi_i/\partial t$. The mapping allows an arbitrary waveform to be imposed at the lower boundary with the gridlines translating vertically so as to follow the moving wave.

The governing equations, in transformed coordinates, are discretized in strong conservation flux form using the volume flux or "contravariant flux" velocities positioned at the cell faces of a computational stencil. The Cartesian velocity components, pressure, SGS energy are then conveniently co-located at the center of the stencil. The spatial

differencing is pseudospectral in the (ξ, η) directions and second-order finite difference in the ζ direction. A dynamic time step is used in combination with the third-order Runge-Kutta time integration.

2.3. Simulations

All simulations are performed in non-dimensional units with (length, velocity, time) scales made dimensionless by (wavelength λ, friction velocity u_*, time scale λ/u_*). At the wavy surface, the LES applies wall functions at every (ξ, η) gridpoint assuming a non-dimensional surface roughness $z_{o,s} = 4.3 \cdot 10^{-4}$.

For the simulations of airflow over steady wave trains, the computational domain is $(L_x, L_y, H) = (5, 5, 1)$ and the discretization employs $(N_x, N_y, N_z) = (512, 512, 128)$ gridpoints. Equally spaced grids are used in the horizontal directions while a smoothly stretched mesh is used in the vertical direction with spacing $\zeta_1 = 0.0065$ at the first grid level off the water surface. The wave height $h(x, t)$ imposed at the lower boundary of the LES is a synthesized waveshape observed in a wind-wave tank by Banner [2]. Two types of steep steady waves are considered, *viz.,* waves near the onset of breaking and waves with spilling flow down the forward face of the wave: in the following discussion they are referred to as "incipient" and "active" breaking, respectively. The steady wave trains are assumed to propagate in time with the dominant phase speed c observed in the experiments. The simulations are initiated with turbulent fields archived from a slightly heated surface.

Under steady conditions, the LES equations obey an integral momentum flux balance given by

$$-\frac{\partial \mathcal{P}}{\partial x} H \equiv u_*^2 = -\left\langle \frac{p}{J}\frac{\partial \zeta}{\partial x} + \frac{\tau_{1k}}{J}\frac{\partial \zeta}{\partial x_k} \right\rangle \Bigg|_{\zeta=0}. \tag{4}$$

In the above, angle brackets $\langle\ \rangle$ denote an ensemble space-time average, the spatial averaging is along wave-following (ξ, η) surfaces at constant ζ. As expected (4) shows that the large scale pressure gradient is balanced by a surface drag which is a combination of form and viscous drag. The simulations of steady wave trains are carried out for more than 200,000 timesteps until the time and space varying drag of the underlying wave surface, given by (4), reaches a statistically steady state.

Also, we simulate turbulent flow over an unsteady evolving wave group or chirp packet in the domain $(L_x, L_y, H) = (9.40, 4.695, 1)$ discretized using $(N_x, N_y, N_z) = (1024, 512, 128)$ mesh points. The space-time evolving height $h(x, t)$ of the wave packet is generated by a fully nonlinear wave tank code. A special recipe utilizing fully developed turbulent boundary-layer flow over a flat boundary, described in [17], is used to compute flow over the unsteady wave packet.

Previously, we carried out simulations of both steady and unsteady wave trains under strongly forced conditions with wave age $c/u_* \sim 1$. The focus of the present work is to expand the simulation parameter space and examine the impact of wave age on the airflow and surface drag for steep more rapidly propagating surface waves. Thus, as a first approximation, we simply adopt the same wave height distributions as in [17] but increase the wave age to larger values $c/u_* = (5, 10)$. The LES solutions are obtained using non-dimensional variables and thus increases in wave age can be interpreted as a change in wind speed or wave scale (or a combination of the two) in physical units. For example, for the incipient breaker $c/u_* = 10$ approximately corresponds to either a factor 6 reduction in the surface wind speed or a factor 40 increment in the wavelength λ compared to $c/u_* = 1.58$. Note that values of $c/u_* = (5, 10)$ still represent young (growing) seas compared to wind-wave equilibrium $c/u_* \sim 25 - 30$ [1].

3. Interpretation of results

Inspection of the instantaneous flow fields and low-order statistical moments shows wave age significantly impacts turbulent flow over steep steady and unsteady wave trains. Broadly, we find that wave age and waveslope both significantly impact the velocity and pressure fields, and hence surface drag.

3.1. Flow visualization

A particularly sensitive metric that highlights the wave age dependence is vertical velocity w, furthermore w has the favorable property that it is invariant when viewed in a stationary or horizontally translating frame of reference. Figure 1 shows contours of y (or phase) averaged vertical velocity $[w]$ in a zoom over a limited $x - z$ area for the

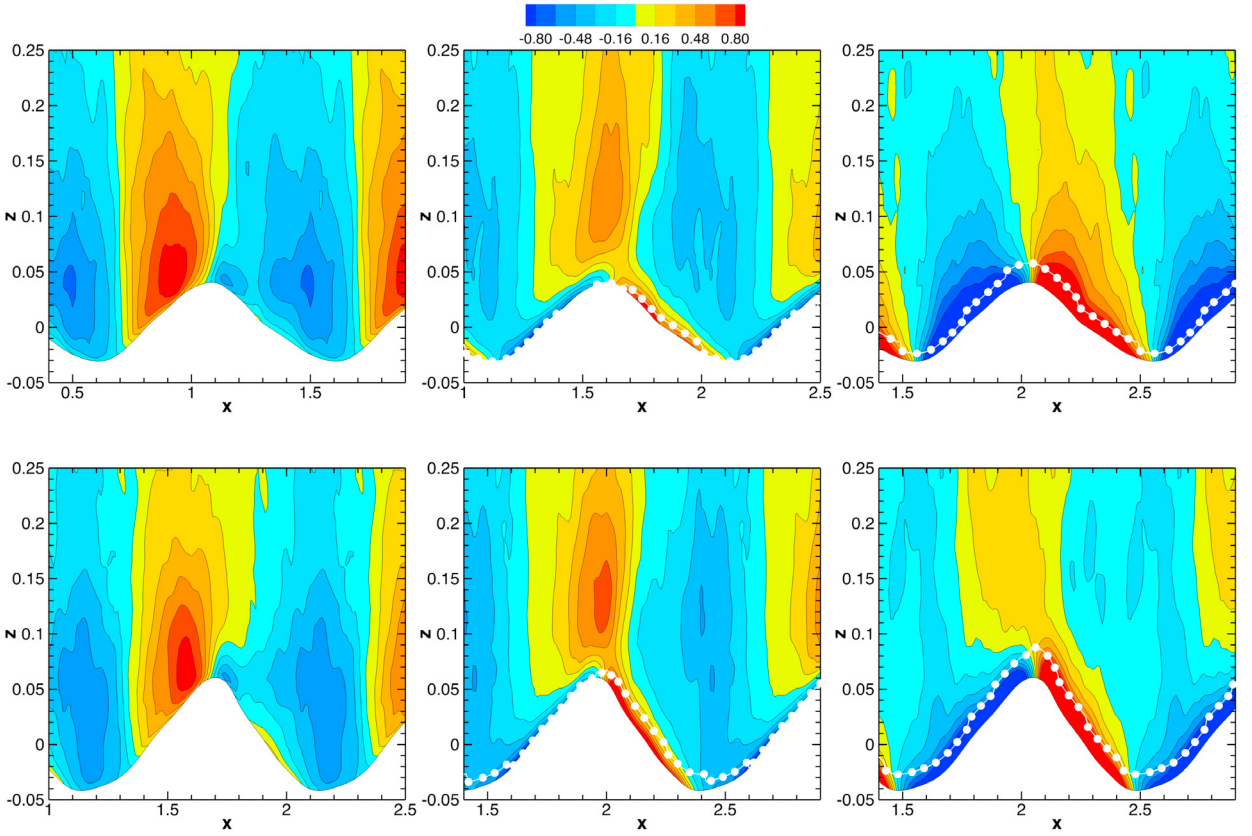

Fig. 1. Contours of y averaged vertical velocity $[w]$ normalized by u_*. Top row, train of incipient breakers with varying wave age, $c/u_* = (1.58, 5, 10)$ (left, middle, right) panels, respectively. Bottom row, train of active breakers with varying wave age, $c/u_* = (1.23, 5, 10)$ (left, middle, right) panels, respectively. The height of the critical layer h_{cr} for simulations with wave age $c/u_* = (5, 10)$ is indicated by the white bullets. Note, for smaller wave age h_{cr} is collapsed down to the wave surface and is not shown. The color bar is held constant between the images. The wind and wave propagation direction is left to right in all cases.

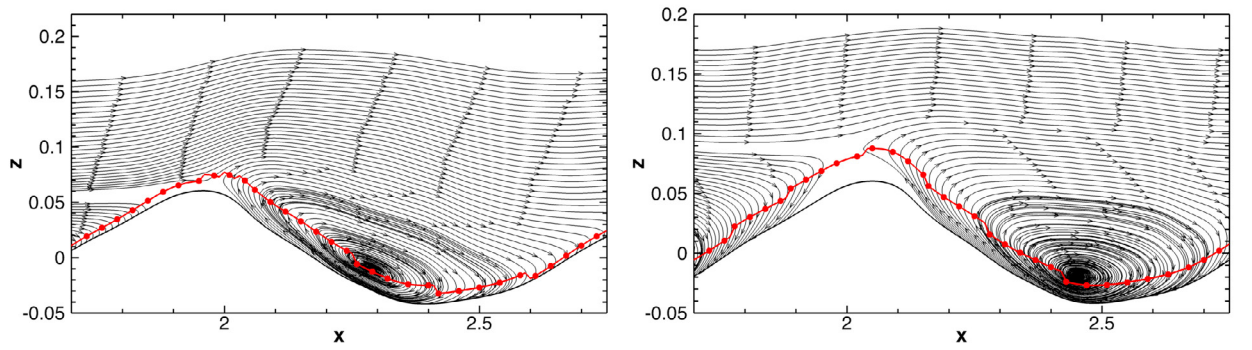

Fig. 2. Phase average streamlines for a train of active breakers in a frame of reference moving with the wave phase speed c. (Left, right) panels $c/u_* = (5, 10)$, respectively. The red line denotes the critical layer height h_{cr}, as shown and computed in Fig. 1.

incipient and active breakers for three values of wave age. Each image displays small random fluctuations because of limited sampling, only a single 3-D volume is used to construct the y average. Systematic pattern shifts with varying c/u_* are however clearly discernible. At small wave age $c/u_* = O(1)$, (positive, negative) vertical velocity is correlated

with (positive, negative) waveslope as expected for slow moving strongly forced waves. In the wave trough, the phase averaged vertical velocity is negative and weak in magnitude, a consequence of the slow rotational motions in the intermittent flow separation zones that develop on the leeward side of steep waves [22, 15, 5, 17]. Notice as wave age increases $c/u_* = (5, 10)$, waveslope and vertical velocity become negatively correlated. At $c/u_* = 10$, for both incipient and active breakers, near surface $[w] > 0$ is correlated with $\partial h/\partial x < 0$, while $[w] < 0$ is correlated with $\partial h/\partial x > 0$. Most importantly these pattern shifts in $[w]$ are also found to coincide with an overall change in the flow separation dynamics for steep waves. Visualization indicates the flow separation observed at low wave age (left panels of Fig. 1) is delayed or erased with increasing wave age – the reduction in flow separation produces a significant impact on the surface pressure and drag of the underlying wavy surface as discussed in section 3.2. At wave age $c/u_* = 5$ an elevated maximum in $[w]$ is also observed well above the wave crest with a thin pocket of positive $[w]$ developing on the leeward face of the wave. The near discontinuous phase jump in w with increasing distance from the wave surface resembles the flow pattern induced by critical layers in direct numerical simulations of turbulent flow over low slope monochromatic waves, see Figs. 18 and 19 in [20], and in observations [11, 9].

Our initial speculation is that the shifting w patterns are a result of critical layer dynamics [12] which emerge with increasing c/u_*. To explore this possibility, the vertical velocity contours in Fig. 1 are overlaid with the local critical layer height h_{cr} computed from the phase average relation $[u(x, z)] = c$. Examination of the curves in all cases shows $h_{cr}(x, z)$ remains tightly confined to the wave surface $h(x, t)$ irrespective of wave age. For example, in Fig. 1 for the highest wave age considered $c/u_* = 10$ at location $x = 2.05$, the vertical separation between the wave and critical layer heights is narrow $(h, h_{cr}) = (0.058, 0.087)$ for the active breaker. The small surface roughness imposed in the LES $z_{o,s} = 4.3 \cdot 10^{-4}$ further collapses the height of the critical layer towards the water surface (see p. 128 of [14] and [4]). A characteristic signature of a critical layer is a closed pattern of streamlines or cat's-eye when viewed in a frame of reference moving with the wave phase speed c [4]. Figure 2 depicts streamlines computed from the phase average vector $([u] - c, [w])$ for the active breaker at two values of wave age. The streamlines are closed but vertically very distorted. The tightly wound center of the cat's-eye is compacted very near the wave surface and its position is slightly upstream of the wave trough. Overall, the shape of the cat's-eye pattern with nonlinear steep waves and turbulence is noticeably different than its theoretical counterpart with low-turbulence stresses and small wave amplitude [4, 16].

Although the critical layer in Fig. 2 potentially plays a role in the air-wave coupling for steep waves, the observed changes in the near surface vertical velocity and separation flow patterns, and surface drag appear to be more closely associated with a wave driving (or boundary pumping) effect that increases with phase speed c. To diagnose the magnitude of the boundary pumping consider the locally varying waveslope of the steep 2-D wave trains in Fig. 1. The lower boundary condition in the simulations imposes no net flow across the wave surface, but the wave boundary temporally and spatially oscillates. Its vertical velocity w_o is approximately given by (see, equation 8 in [17])

$$w_o \sim \frac{\partial h}{\partial t} = -c\frac{\partial h}{\partial x} \tag{5}$$

Thus, boundary movement can generate large (positive, negative) near surface vertical velocities in regions with large (negative, positive) waveslope depending on the phase speed. Since the maximum waveslope $-\partial h/\partial x = (0.25, 0.4)$ for (incipient, active) breakers, respectively, large w and $[w] > 0$ are generated on the leeward side of a wave as shown in the right panels of Fig. 1. In other words, for large wave age near surface $[w]$ and $\partial h/\partial x$ are negatively correlated. The surface boundary pumping velocity $w_o \sim c$ and increases by more than a factor of 6 for $c/u_* = 10$ compared to the strongly forced waves with $c/u_* \sim O(1)$. Because the spatially varying boundary pumping is maximum forward of a wave crest it has the potential to alter flow separation. Analysis of the vertical velocity flowfields for an unsteady chirp packet exhibit similar patterns when the wave age is increased by a factor of 10.

3.2. Pressure, form drag, and velocity profiles

Wave age also leaves a clear imprint on the instantaneous surface pressure and its correlation with waveslope (see Fig. 3), the form drag (see Fig. 4), and the mean velocity profiles (see Fig. 5). For example, the incipient case with $c/u_* = 1.58$, left panel of Fig. 3, features intermittent flow separation zones when viewed in an $x - y$ plane with spatially episodic values of $(p\partial h/\partial x)/u_*^2 > 5$. As c/u_* increases from 1.58 to 5 the fluctuations in the pressure-waveslope correlation decrease considerably, and $|p\partial h/\partial x|/u_*^2 < 2$ over the entire horizontal domain at $c/u_* = 10$ (not shown). The waveshape is held constant in the simulations as c/u_* varies, and then the reduced pressure-waveslope

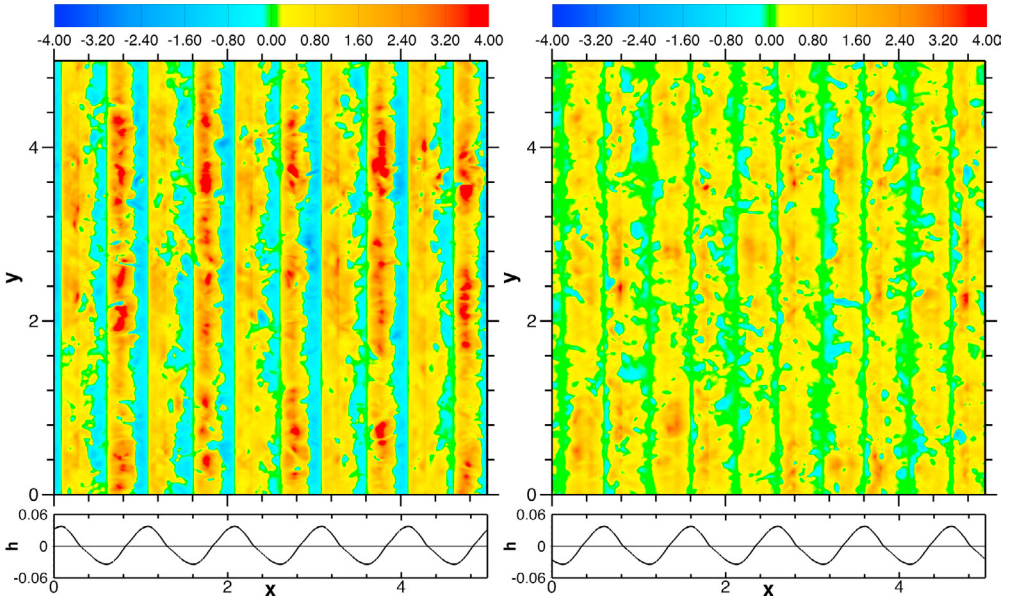

Fig. 3. Pressure waveslope correlation $p\partial h/\partial x$ normalized by u_*^2 for varying wave age, $c/u_* = (1.58, 5)$ (left, right) panels, respectively. The color bar is held constant between the two images. The instantaneous wave height $h(x,t)$ corresponding to each case is shown in the bottom panels. The wind and wave propagation direction is left to right.

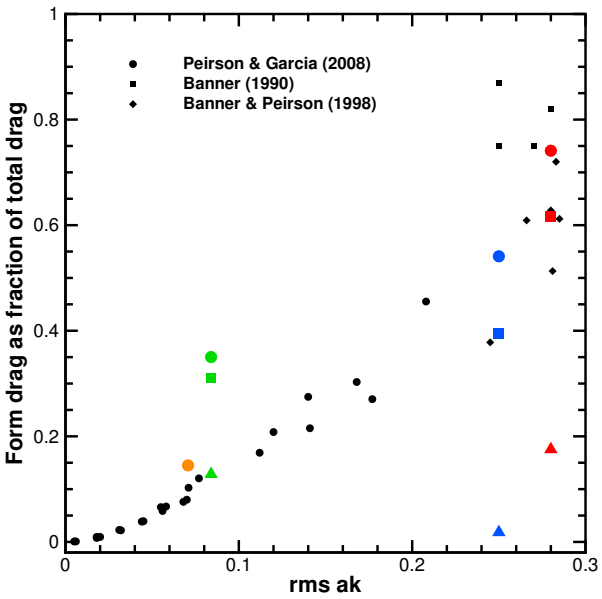

Fig. 4. Form (pressure) drag for LES cases with steady and unsteady waves for varying rms waveslope and wave age. Incipient case with rms ak = 0.25, c/u_* = (1.58 ●, 5 ■, 10 ▲); Active case with rms ak = 0.28, c/u_* = (1.23 ●, 5 ■, 10 ▲); No breaking case with rms ak = 0.071, c/u_* = (1 ●); Unsteady wave packet with rms ak = 0.084, c/u_* = (1 ●, 5 ■, 10 ▲). Black symbols are laboratory measurements with wave age $c/u_* = O(1)$.

correlations in the right panel of Fig. 3 primarily result from a lower magnitude of fluctuating surface pressure p; small phase shifts in the surface pressure relative to the waveshape play a secondary role. Similar changes are also found in the simulations with active breakers and unsteady chirp packets.

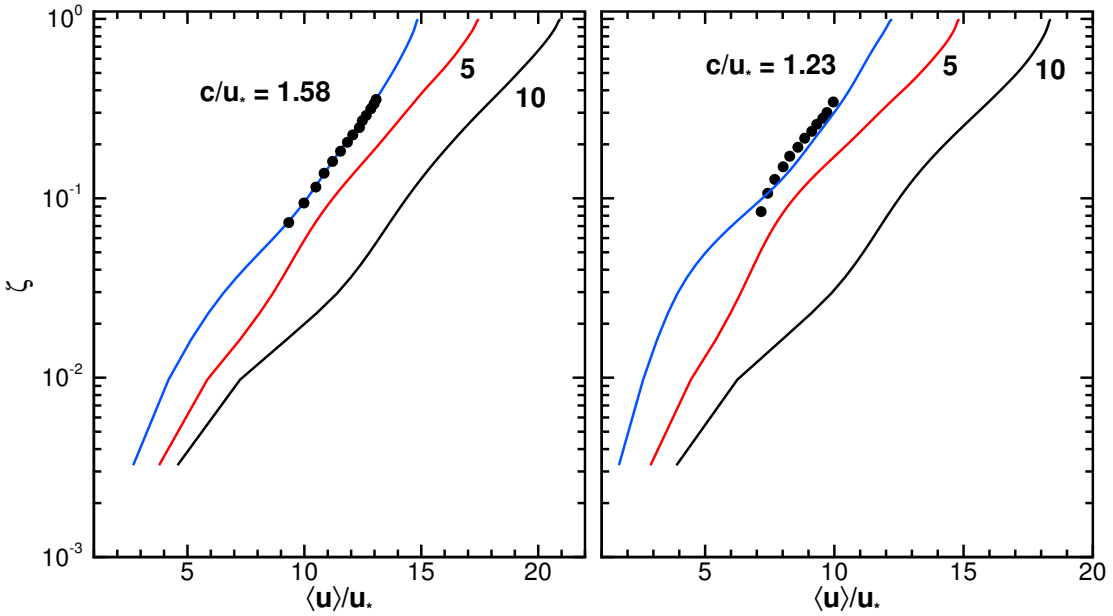

Fig. 5. Vertical wind profiles $\langle u \rangle / u_*$ over (incipient, active) breaking waves (left, right) panels. Measurements from Banner (1990) [2] are indicated by •.

Figure 4 summarizes the form drag variation (or more precisely the ratio of form drag to the total drag, *i.e.,* the form drag fraction) for different combinations of rms waveslope and wave age. Results are obtained by space-time averaging the pressure-waveslope correlations. As anticipated based on the findings in Fig. 3, for a given waveform of fixed steepness the form drag noticeably decreases with increasing wave age. For the active breaker, the form drag fraction decreases from 74% to 17.5% for an increase in wave age from 1.23 to 10. The variability of the wave surface geometry, in terms of amplitude and tilt modulation, is also found to have a substantial effect on the flow separation and hence on the form drag, for very young wave age conditions. This is seen in Fig. 4 when comparing the green and orange symbols for an rms steepness of ~ 0.08 and $c/u_* \sim 1$. The modulational effects are seen to result in a near-doubling of the form drag, see [17].

Thus, form drag is a strong function of at least two-parameters, *viz.,* waveslope and wave age. Simulations of steep waves with increasing wave age produce a surface drag reduction somewhat analogous to swell in the open ocean. In swell-wave driven wind scenarios the form drag can be negative, *i.e.,* upward from the ocean to the atmosphere under light wind conditions. However, remotely generated swell is typically characterized by wave age $c/u_* > 30$, low waveslope $ak < 0.1$ [7, 18, 19], and no flow separation in contrast to the steep waves considered here. The underlying dynamics that lead to a form drag reduction with rapidly moving steep waves appears to be fundamentally different than wind-swell coupling.

Figure 5 adds confidence to our interpretations as it demonstrates good agreement between the simulated and measured wind profiles for the strongly forced conditions observed in the laboratory experiment [2]. As wave age increases, the overlying wind profiles for the incipient and active breakers "feel" the reduction in surface form stress. Notice the wind profiles systematically shift to the right at all values of ζ for increasing c/u_*. This wind speed up is indicative of an overall decrease in total surface drag resulting from a decrease in form drag. For the same steep geometrical waveshape, the underlying wave surface appears effectively smoother when the wave train propagates rapidly with $c/u_* = 10$ compared to when it propagates slowly with $c/u_* \sim 1$.

4. Discussion and summary

Unsteady flow separation impacts numerous applications and continues to be an active area of boundary-layer research, *e.g.,* [8, 6, 13]. While the onset of laminar flow separation over a stationary 2-D wall is accurately defined by the surface shear stress = 0 criterion, no similarly simple rule exists for unsteady turbulent flow over moving walls. For unsteady regimes, theoretical models often adopt the so-called Moore-Rott-Sears criterion, *i.e.,* flow separation over a moving wall requires that the velocity profile has simultaneously zero velocity and shear in a frame of reference moving with the separation point, for example see Fig. 1 in [8] and discussion in [4, 6, 13]. Also, with moving boundaries the location of flow separation occurs in the outer flow away from the surface. Results from physical modeling find wall movement progressing in the freestream direction delays flow separation while wall movement opposite to the freestream advances flow separation. Wall movement is then a technique for active flow separation control in engineering flows, *e.g.,* flow past an airfoil with a rotating leading edge [8].

The large-eddy simulations of turbulent flow over steep steady and unsteady wave trains described here display features similar to their counterparts in engineering flows with moving walls. At low wave age the overlying winds are moving rapidly compared to the slow vertical oscillations of the wave boundary, and analysis of LES solutions finds flow separation on the leeward side of the wave which results in large pressure drag. In this low wave age regime, simulation results [17] for incipient and active breakers are in good agreement with measured wind profiles and form (pressure) drag reported in the literature. The simulations further emphasize the importance of waveslope under strongly forced conditions. Increases in wave age produce an order unity change in the flow dynamics over steep waves. For the same geometrical waveshape, as c/u_* increases the speed of the vertical oscillations of the wave boundary intensify, they are proportional to the wave speed and local waveslope. Because the waveslope is asymmetrical about the wave crest, the forward boundary movement is a maximum on the leeward side of a propagating wave. The boundary movement can then delay or erase flow separation leading to a sharp decrease in form drag. For example, with the active breaker case the pressure drag is nearly 75% of the total drag when $c/u_* = 1.23$ but falls to less than 20% when $c/u_* = 10$. The impact of wave age on flow separation described here appears to be generic for steep steady and unsteady wave trains. Over the range of wave age considered the critical layer height h_{cr} above the waves is confined to a very thin region near the wave surface and its role in turbulent flow over steep waves is not fully understood [12, 16]. In turbulent flow over monochromatic waves with $ak < 0.1$ and no separation [20] a near surface critical layer causes the drag to increase. The simulations described here are highly idealized, but pose potentially interesting observational questions for a field of steep waves at high winds in the open ocean. When does flow separation occur and if so at what scale, what is the role of a critical layer for a spectrum of waves, and what is the role of wave unsteadiness in setting the surface drag.

Acknowledgements

This work was supported by the Office of Naval Research through the Physical Oceanography Program. PPS was supported by award numbers N00014-13-G-0223-0002, N00014-14-1-0626, N00014-17-1-2334, and the National Science Foundation through the National Center for Atmospheric Research (NCAR). MLB, RPM and WLP acknowledge support from award number N00014-12-10184. This research benefited greatly from computer resources provided by the NCAR Strategic Capability program managed by the NCAR Computational Information Systems Laboratory, http://n2t.net/ark:/85065/d7wd3xhc, and the Department of Defense High Performance Computing Modernization Program.

References

1. Alves, J.G.M., Banner, M.L., Young, I.R., 2003. Revisiting the Pierson-Moskowitz asymptotic limits for fully developed wind waves. J. Phys. Oceanogr. 33, 1301–1323.
2. Banner, M.L., 1990. The influence of wave breaking on the surface pressure distribution in wind-wave interaction. J. Fluid Mech. 211, 463–495.
3. Barthelemy, X., Banner, M.L., Peirson, W.L., Fedele, F., Allis, M., , Dias, F., 2018. On a unified breaking onset threshold for gravity waves in deep and intermediate depth water. J. Fluid Mech. in press.
4. Belcher, S.E., Hunt, J.C.R., 1998. Turbulent flow over hills and waves. Annu. Rev. Fluid Mech. 30, 507–538.
5. Buckley, M.P., Veron, F., 2016. Structure of the airflow above surface waves. J. Phys. Oceanogr. 46, 1377–1397.

6. Degani, A.T., Walker, J.D.A., Smith, F.T., 1998. Unsteady separation past moving surfaces. J. Fluid Mech. 375, 1–38.
7. Edson, J., Crawford, T., Crescenti, J., Farrar, T., French, J., Frew, N., Gerbi, G., Helmis, C., Hristov, T., Khelif, D., Jessup, A., Jonsson, H., Li, M., Mahrt, L., McGllis, W., Plueddmann, A., Shen, L., Skyllingstad, E., Stanton, T., Sullivan, P., Sun, J., Trowbridge, J., Vickers, D., Wang, S., Wang, Q., Weller, R., Wilkin, J., Yue, D., Zappa, C., 2007. The coupled boundary layers and air-sea transfer experiment in low winds (CBLAST-Low). Bull. Amer. Meteorol. Soc. 88, 342–356.
8. Gad-el-Hak, M., Bushnell, D.M., 1991. Separation control: Review. Journal of Fluids Engineering 113, 19–30.
9. Grare, L., Lenain, L., Melville, W., 2013. Wave-coherent airflow and critical layers over ocean waves. J. Phys. Oceanogr. 43, 2156–2172.
10. Hara, T., Sullivan, P.P., 2015. Wave boundary layer turbulence over surface waves in a strongly forced condition. J. Phys. Oceanogr. 45, 868–883.
11. Hristov, T., Miller, S.D., Friehe, C., 2003. Dynamical coupling of wind and ocean waves through wave-induced air flow. Nature 422, 55–58.
12. Miles, J.W., 1957. On the generation of surface waves by shear flow, Part I. J. Fluid Mech. 3, 185–204.
13. Miron, P., Vétel, J., 2015. Towards the detection of moving separation in unsteady flows. J. Fluid Mech. 779, 819–841.
14. Phillips, O.M., 1977. Dynamics of the Upper Ocean. Cambridge University Press.
15. Reul, N., Branger, H., Giovanangeli, J.P., 2007. Air flow structure over short-gravity breaking waves. Boundary-Layer Meteorol. 126, 477–505.
16. Sajjadi, S.G., Hunt, J.C.R., Drullion, F., 2014. Asymptotic multi-layer analysis of wind over unsteady monochromatic surface waves. J. of Engineering Mathematics 84, 73–85.
17. Sullivan, P.P., Banner, M.L., Morisson, R.P., Peirson, W.L., 2018. Turbulent flow over steep steady and unsteady waves under strong wind forcing. J. Phys. Oceanogr. 48, 3–27.
18. Sullivan, P.P., Edson, J.B., Hristov, T., McWilliams, J.C., 2008. Large eddy simulations and observations of atmospheric marine boundary layers above non-equilibrium surface waves. J. Atmos. Sci. 65, 1225–1245.
19. Sullivan, P.P., McWilliams, J.C., 2010. Dynamics of winds and currents coupled to surface waves. Annu. Rev. Fluid Mech. 42, 19–42.
20. Sullivan, P.P., McWilliams, J.C., Moeng, C.H., 2000. Simulation of turbulent flow over idealized water waves. J. Fluid Mech. 404, 47–85.
21. Sullivan, P.P., McWilliams, J.C., Patton, E.G., 2014. Large eddy simulation of marine boundary layers above a spectrum of moving waves. J. Atmos. Sci. 71, 4001–4027.
22. Veron, F., Saxena, G., Misra, S.K., 2007. Measurements of the viscous tangential stress in the airflow above wind waves. Geophys. Res. Lett. 34. L19603.

Available online at www.sciencedirect.com

ScienceDirect

Procedia IUTAM 26 (2018) 184–193

Procedia IUTAM

www.elsevier.com/locate/procedia

IUTAM Symposium Wind Waves, 4–8 September 2017, London, UK

Generation method of wind waves under long-fetch conditions over a broad range of wind speeds

Naohisa Takagaki[a] *, Satoru Komori[b, c], Koji Iwano[d], Naoya Suzuki[e], Hiroshige Kumamaru[a]

[a]*Department of Mechanical Engineering, University of Hyogo, Himeji 671-2280, Japan*
[b]*Research Center for Highly-Functional Nanoparticles, Doshisha University, Kyotanabe 610-0394, Japan*
[c]*Center for Earth Information Science and Technology (CEIST), Japan Agency for Marine-Earth Science and Technology (JAMSTEC), Yokohama, 236-0001, Japan*
[d]*Department of Mechanical Systems Engineering, Nagoya University, Nagoya 464-8603, Japan*
[e]*Department of Mechanical Engineering, Faculty of Science and Engineering, Kindai University, Osaka 577-8502, Japan*

Abstract

It is important to develop a wave generation method for extending the fetch in laboratory experiments, because current laboratory studies are limited to fetch shorter than 100 m. Two wave generation methods are proposed for generating wind waves under long-fetch conditions in a wind-wave tank using a programmable irregular-wave generator. The first method is the spectral-model-based wave-generation method (SBWGM), which is appropriate at normal wind speeds for extending the fetch. The SBWGM also can be used at extremely high wind speeds if we know the spectral shape. In SBWGM, a conventional model of the wind-wave spectrum is used for the movement of the programmable irregular-wave generator. The second method is the loop-type wave-generation method (LTWGM), which can be used at wide range of wind speeds and is especially appropriate to be used at extremely high wind speeds, where the spectral shape is unknown. In LTWGM, the waves whose characteristics are most similar to the wind waves measured at the end of the tank are reproduced at the entrance of the tank by the programmable irregular-wave generator to extend the fetch. Water-level fluctuations are measured at both normal and extremely high wind speeds using resistance-type wave gauges. The results show that SBWGM can produces wind waves with a fetch over 500 m, but only at normal wind speeds. However, LTWGM can produce wind waves with long fetches exceeding the length of the wind-wave tank across a broad range of wind speeds, but considerable time is required to produce wind waves at long-fetch conditions, i.e. fetch over 500 m. It is observed that the wind-wave spectrum with a long fetch reproduced by SBWGM is consistent with that of the modelled wind-wave spectrum, although the generated wind waves are different from those in the open ocean because of the finite width of the tank. In addition, the fetch laws with significant wave height and period are confirmed for wind waves under long-fetch conditions. This implies that

* Corresponding author. Tel./fax: +81- 79-267-4834.
E-mail address: takagaki@eng.u-hyogo.ac.jp

Peer-review under responsibility of the scientific committee of the IUTAM Symposium Wind Waves.
10.1016/j.piutam.2018.03.018

the ideal wind waves under long-fetch conditions can be reproduced using SBWGM with the programmable irregular-wave generator.

Peer-review under responsibility of the scientific committee of the IUTAM Symposium Wind Waves.

Keywords: wave generation method; fetch

1. Introduction

It is very important to predict the momentum, heat, and mass transfers across the air-sea interface, because the transfer mechanism across this interface has a significant influence on the accuracies of future climate-change predictions, the intensity of the tropical cyclones, and other meteorological phenomena. The momentum, heat, and mass transfers across the wind waves have thus been the focus of many laboratory-experimental and numerical investigations [e.g. 1, 2, 3, 4, 5, 6, 7, 8, 9, 10, 11, 12].

Previous laboratory measurements have estimated this momentum transfer with a wind-wave tank [e.g. 1], and they have shown that the drag coefficient (C_D) increases monotonically with the 10-m wind speed (U_{10}) over a broad range of wind speeds. Here C_D represents the magnitude of the momentum transfer across the sea surface, which is given by:

$$\tau = \rho u^{*2} = \rho C_D U_{10}^2 , \tag{1}$$

where τ is the sea-surface wind shear stress, ρ is the air density and u^* is the air friction velocity. Conversely, recent laboratory results [6, 7] have shown approximately constant C_D values at extremely high wind speeds. Takagaki et al. [7, 13, 14] discovered that the breaking of wind waves occurs at extremely high wind speeds, causing C_D saturation. In fact, Uda [15] and Black et al. [16] reported that the sea surface appears to be flat above Douglas sea scale 9 and Beaufort scale 15, respectively.

It is important to examine the scalar transfer submodels used in the atmosphere-ocean general circulation model to predict future climate change and abnormal weather with high precision. The submodels have been proposed by many laboratory experiments using a wind-wave tank [e.g. 11, 17, 18, 19]. However, because these studies were carried out under short-fetch conditions (< 100 m), the momentum, heat, and mass transfers have not yet been observed under long-fetch conditions in laboratory experiments. Therefore, we must obtain the laboratory data at conditions of considerably longer fetch to discuss the similarity between the laboratory and field measurements; however, it is difficult to construct such a long wind-wave tank, especially for strong wind speeds.

Therefore, we propose an original technique for extending the fetch in a normal wind-wave tank to discuss the air-sea momentum and scalar transfer over a broad range of wind speeds, including extremely high wind speeds. These laboratory experiments at such long-fetch conditions will be useful in modelling small-scale air-sea coupling.

2. Experiment

2.1. Equipment and measurement methods

A large wind-wave tank (LWWT) [e.g. 20, 21] and a high-speed wind-wave tank (HSWWT) [e.g. 7, 11, 19] (Figure 1) were used in the experiments. The LWWT consisted of a glass test section that was 20.0 m long, 0.6 m wide, and 1.3 m high. The HSWWT consisted of a glass test section that was 15.0 m long, 0.8 m wide, and 1.6 m high. Wind waves were generated in the water tank, which was filled with filtered tap water, at U_{10} = 6.6, and 10.7 m/s with 2.5 % variation for the LWWT, and at U_{10} = 19.3, 32, and 42 m/s with 2.5 % variation for the HSWWT. Mechanical waves were generated using a programmable piston-type irregular-wave generator, consisting of a wave generating board, a servomotor (Mitsubishi Electric HC-SFS-152B for the LWWT and HC-SFS-352 for the HSWWT), a function generator (NF circuit WF1973), a wave gauge, a data recorder, and a computer. The wave- generating board was

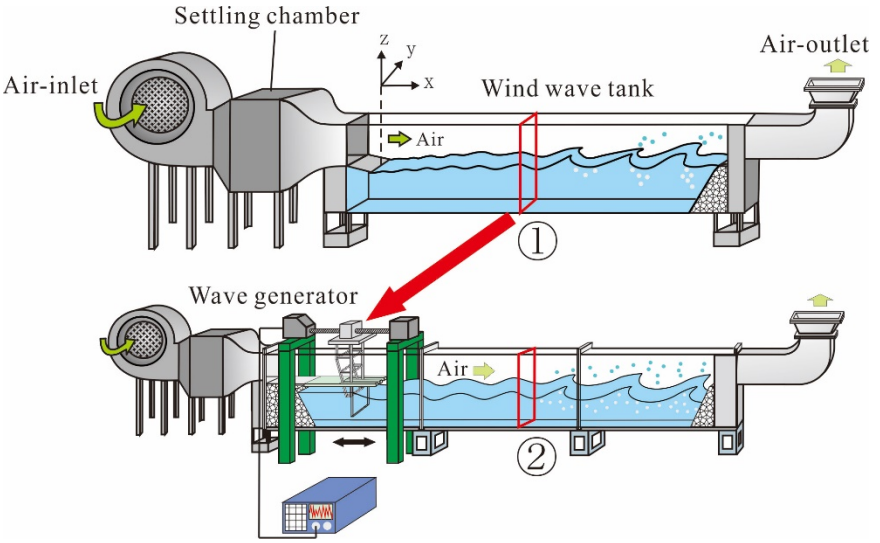

Fig. 1. Schematic diagram of high-speed wind-wave tank (HSWWT) and programmable irregular-wave generator for loop-type wave-generation method; (top) first wind waves generated by the fan; (bottom) second wind waves generated by the wave generator and fan along with first wind wave record.

an acrylic plate with a height, width, and thickness of 0.55 m, 0.598 m, and 0.015 m for the LWWT, and of 0.72 m, 0.78 m, and 0.02 m for the HSWWT, respectively. The center of the board stroke was set at x = -0.5 m under the entrance slope of both the LWWT and HSWWT. The maximum stroke was 0.2 m and 0.4 m for the LWWT and HSWWT, respectively.

A laser Doppler anemometer (Dantec Dynamics LDA) was used to measure the wind-velocity fluctuation. A high-power multi-line mode argon-ion (Ar^+) laser (Lexel model 95-7; λ = 488.0, 514.5 nm; 3 W power) was used. The Ar^+ laser beam was shot through the side glass-wall of the tank. Scattering particles of about 1 μm in diameter were generated by a fog generator (Dantec Dynamics F2010 Plus) and fed into airflow over the waves. The sampling frequency and sampling time were 500 – 5000 Hz and 240 s, respectively. The u^* in equation (1) was estimated using an eddy correlation method, such that $u^* = (-\langle u'v'\rangle)^{1/2}$ [e.g. 5, 22], where u' and v' are the streamwise and vertical air velocity fluctuations, respectively. Here, τ was estimated by extrapolating the measured values of the Reynolds stress $\langle u'v'\rangle$ to the mean surface at z = 0 m. Under neutral stratification, the wind-velocity profile over the rough boundary is expressed by the following logarithmic profile:

$$U(z)/u^* = \ln(z/z_0)/\kappa, \tag{2}$$

where $U(z)$ is the wind speed at elevation z, and κ (= 0.4) is the von Karman constant. From equations (1) and (2), C_D has a one-to-one correspondence with the roughness length (z_0) under neutral stratification:

$$\kappa C_D^{-1/2} = \ln(10/z_0), \tag{3}$$

Therefore, we evaluated z_0, C_D, and U_{10} using equations (1) – (3).

Water-level fluctuations were measured using resistance-type wave gauges (Kenek CHT4-HR60BNC). The resistance wire was placed in the water, and the electrical resistance at the instantaneous water level was recorded at 500 Hz for 600 s using a digital recorder (Sony EX-UT10). The energy of the wind waves (E) was estimated by integrating the spectrum of the water-level fluctuations over the frequency (f), where the peak frequency of the wind waves (f_m) was defined as the peak of the spectrum. To measure the wavelength (L_S) and the phase velocity (C_P) of the significant wind waves, another wave gauge was fixed downstream at Δx = 0.02 m (Runs 1-0, 2-0, and 3-0 to 3-

4), at Δx = 0.19 m (Runs 4-0 to 5-1), and at Δx = 0.2 m (Runs 1-M, 1-L, and 2-M), where Δx is the interval between the two wave gauges. The values of C_P were estimated using the cospectra method [e.g. 4].

The velocity and water level fluctuations measurements were conducted at a distance of x = 7.5 m from the edge (x = 0 m) of the entrance slope plate at the LWWT and at x = 5.5, 6.5, 8.5, or 11.5 m at the HSWWT (Figure 1). Wave absorbers were positioned at the inlet and outlet of the test section to prevent the reflection of surface waves.

2.2. Spectral-model-based wave-generation method (SBWGM)

Spectral models [e.g. 3, 23, 24, 25, 26] have been proposed for normal wind speeds. Therefore, a new method, referred to as the spectral-model-based wave-generation method (SBWGM), was employed to generate waves under long-fetch conditions in the LWWT by extending the actual fetch. First, the wind-wave spectrum at an arbitrary fetch was used as the input (Table 1) for the irregular-wave generator positioned at the inlet of the test section. Then, for a given initial fetch (500 m in this example), irregular wind waves were generated mechanically and forced with the fan, starting at an initial fetch $X_{initial}$ of 500 m and measured at fetch F = 507.5 m ($F = X_{initial} + X_{measure}$ = 500 + 7.5 = 507.5 m, where $X_{measure}$ is the measurement location of the waves for the wave analysis, see Table 1). In this study, the conditions with $F \leqslant$ 7.5 m and $F >$ 7.5 m are referred to as short- and long-fetch conditions, respectively, to distinguish pure wind-driven waves with a short fetch from the wind waves with a long fetch generated by SBWGM or loop-type wave-generation method (LTWGM).

Table 1. Measurement conditions. Wind waves at Runs 1-M, 1-L, and 2-M are generated by SBWGM. Wind waves at Runs 3-1 – 3-4, 4-1, 4-2, and 5-1 are generated by LTWGM. U_{10}: wind speed at a height of 10 m above the sea surface, N: number of loops in LTWGM, F: fetch (= $X_{initial}$ + $X_{measure}$), $X_{initial}$: extended length for spectrum method or LTWGM, $X_{measure}$: measurement location of waves for wave analysis this time, X_{loop}: measurement location of waves for LTWGM next time.

Run	U_{10}	N	F	$X_{initial}$	$X_{measure}$	X_{loop}
	[m/s]	[-]	[m]	[m]	[m]	[m]
1-0	6.6	-	7.5	-	7.5	-
1-M		-	507.5	500	7.5	-
1-L		-	2007.5	2000	7.5	-
2-0	10.7	-	7.5	-	7.5	-
2-M		-	507.5	500	7.5	-
3-0	19.3	0	6.5	-	6.5	11.5
3-1		1	17	11.5	5.5	8.5
3-2		2	25.5	11.5+8.5	5.5	8.5
3-3		3	34	11.5+8.5+8.5	5.5	8.5
3-4		4	42.5	11.5+8.5+8.5+8.5	5.5	-
4-0	32.0	0	6.5	-	6.5	411.5
4-1		1	17	11.5	5.5	8.5
4-2		2	25.5	11.5+8.5	5.5	-
5-0	42.0	0	6.5	-	6.5	11.5
5-1		1	17	11.5	5.5	-

2.3. Loop-type wave-generation method (LTWGM)

The above-mentioned spectral models proposed for normal wind speeds are not appropriate for the generation of wind waves at extremely high wind speeds, as the wind-wave properties are not well known. The LTWGM [27] is useful for generating waves under long-fetch conditions in the HSWWT. We only summarise the LTWGM manipulation here, since the manipulation is detailed in [27]. The LTWGM incrementally extends the actual fetch in a wind-wave tank. First, the wind waves are generated using a fan without the mechanical irregular-wave generator,

and the water-level fluctuation was measured at X_{loop} = 11.5 m (see upper image in Figure 1). The measured spectrum at $X_{initial}$ = 11.5 m is used as the input for the irregular-wave generator positioned at the inlet of the test section (lower image in Figure 1). Then, irregular wind waves were generated mechanically and forced with the fan, starting at $X_{initial}$ = 11.5 m and measured at F = 17 m ($F = X_{initial} + X_{measure}$ = 11.5 + 5.5 = 17 m, where $X_{measure}$ means the measurement location of waves for wave analysis, see Table 1). This iterative procedure is repeated to generate wind waves at different values of F. Wind waves were generated at F = 6.5, 17, 25.5, 34, and 42.5 m using LTWGM zero, one, two, three, and four times, respectively. However, wind waves at extremely high wind speeds were limited under F = 25.5 m because of the bottom-wall effects on wind waves. Note that the data from Runs 3-0 to 5-1 in Table 1 were reproduced using the measurements by [27].

2.4. Wave generation method

To generate wind waves using SBWGM, it is important that the power spectrum of the waves produced by the wave generator is the same as the input spectrum. The steps for employing SBWGM are similar to LTWGM [27], and are as follows.

The x-directional position, $P(t)$, of the wave-generating board is controlled using the servomotor and the function generator according to the following equation:

$$P(t) = \sum_i \frac{1}{2} L_i(f_i) \sin(2\pi f_i t + \theta_i), \tag{4}$$

where $L_i(f_i)$ is the stroke length at a neutral position (x = –0.5 m) and at an arbitrary frequency f_i, t is the elapsed time, and θ_i is the random phase. $L_i(f_i)$ is calculated using the single summation method [28]. Here, the energy of the waves $E_i(f_i)$, at an arbitrary frequency f_i is calculated by

$$E_i(f_i) = S_{\eta\eta}(f_i)\Delta f, \tag{5}$$

where $S_{\eta\eta}(f_i)$ is the power spectrum at an arbitrary frequency f_i and Δf is the frequency width for separating $S_{\eta\eta}(f_i)$ into frequency-direction bins, which is set at 0.001 Hz. Although f_i ideally ranges from zero to infinity, an actual wave generator has upper limits. Because the servomotor is not operational at frequencies above 3.2 Hz, the upper frequency limit of the wave generator is taken as 3.2 Hz. The relationship between the wave energy and the power spectrum is given by the following equations:

$$E_i(f_i) = S_{\eta\eta,model}(f_i)\Delta f \quad (0\ \text{Hz} < f_i < 3.2), \tag{6}$$

$$E_i(f_i) = 0 \quad (3.2\ \text{Hz} < f_i). \tag{7}$$

Here $S_{\eta\eta,model}$ is the power spectrum from the model proposed by [26]:

$$S_{\eta\eta,model}(f_i) = \alpha_D (2\pi)^{-4} g^2 f_m^{-1} f_i^{-4} \exp\left(-\left(\frac{f_i}{f_m}\right)^4\right) \gamma_D^{\Gamma}, \tag{8}$$

$$\Gamma = \exp\left(-\frac{(1-f_i/f_m)^2}{2\sigma_D}\right), \tag{9}$$

where α_D is the equilibrium range constant for the wind-wave spectrum, g is acceleration by gravity. Additionally, σ_D is the peak width parameter and γ_D is the peak enhancement factor. The relationship between the monochromatic wave energy $E_i(f_i)$, f_i, and $L_i(f_i)$ is calibrated through the preliminary experiment with monochromatic waves similar to that in [27], prior to generating the irregular waves. The position of the wave-generating board, $P(t)$, is calculated

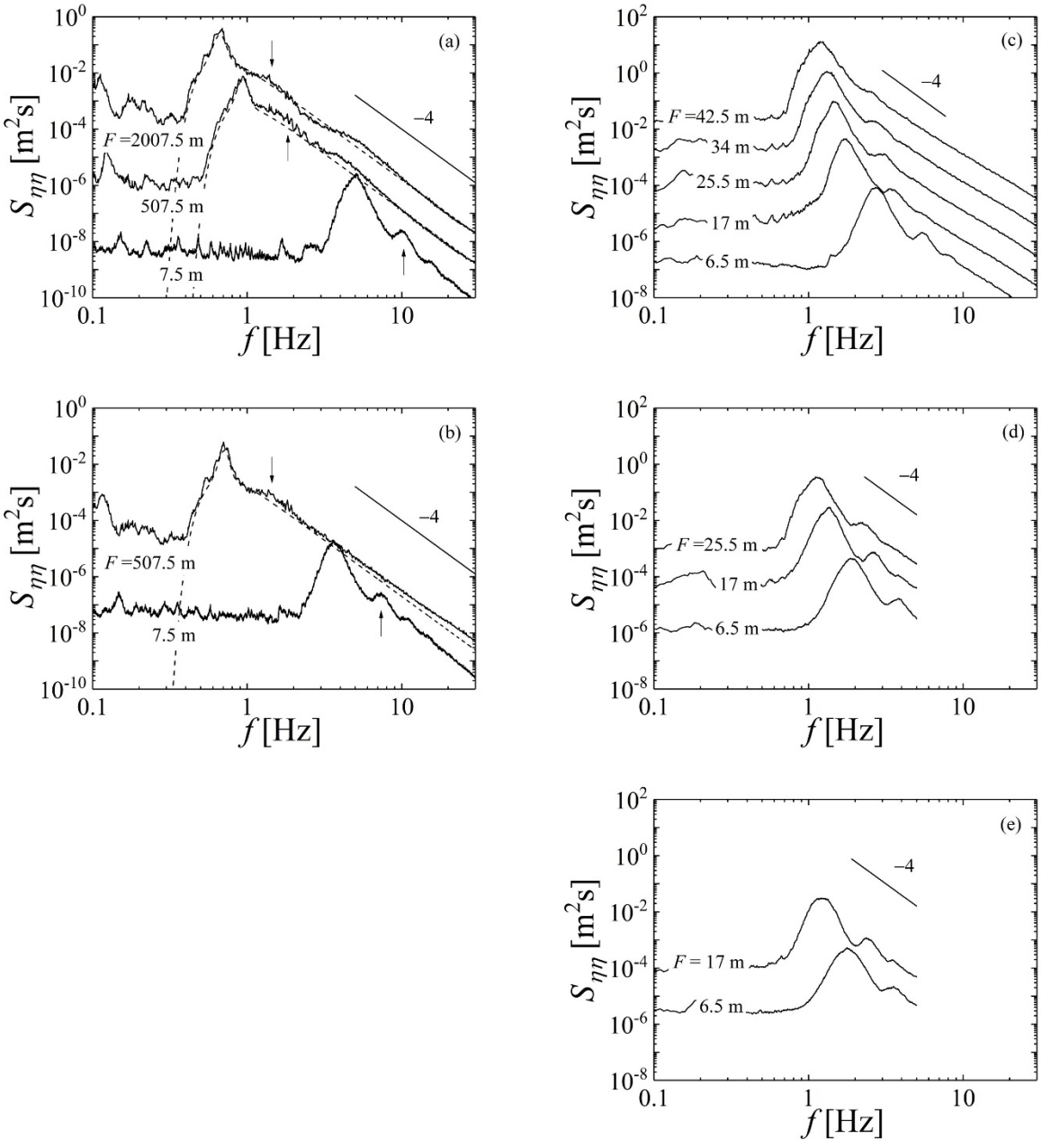

Fig. 2. Wind-wave Spectra $S_{\eta\eta}$ at (a – c) normal wind speeds (U_{10} = 6.6, 10.7, 19.3 m/s), and (d, e) extremely high wind speeds (U_{10} = 32.0, 42.0 m/s). Curves, from top to bottom, are for F = 2007.5, 507.5, and 7.5 m in Figure 2(a), F = 507.5, and 7.5 m in Figure 2(b), F = 42.5, 34, 25.5, 17, and 6.5 m in Figure 2(c), F = 25.5, 17, and 6.5 m in Figure 2(d), F = 17, and 6.5 m in Figure 2(e). Arrows in Figures 2(a, b) indicate secondary peaks. Spectra at high wind speeds (Figures 2d, 2e) are described for f = 5 Hz by removing impingement effects of droplets and bubbles on water-level measurements [e.g. 13]. Dashed curves represent a spectra calculated from a spectral model [26] in Figures 2(a – c). Spectra are offset for the clarity Figures 2(a – e). Solid lines represent a slope of –4 in Figures 2(a – e).

using the stroke length $L_i(f_i)$ at an arbitrary frequency from equation (4), and $L_i(f_i)$ is calculated from the wind-wave spectrum model. Therefore, by controlling $P(t)$, the wind waves at a fetch longer than the streamwise length of the LWWT can be generated by SBWGM.

3. Results and Discussion

To verify that the laboratory-generated wind waves using SBWGM are similar to those observed in the ocean, we have to investigate the wind-wave spectrum shape, fetch law, dispersion relation, and Toba's 3/2 power law [2], since these laws are observed for actual and pure wind-driven waves in both the ocean and the laboratory. Figure 2 shows the wind-wave spectra at U_{10} = 6.6, and 10.7 m/s for several fetch conditions. Note that the data in Figures 2(c – e) are reproduced using the measurements from [27]. It is observed that the wind-wave spectra (solid curves) generated by SBWGM correspond to those (dashed curves) proposed by [26]. This is attributed to the development of wind waves due to the increase in the fetch. While waves with frequencies higher than 3.5 Hz cannot be produced by the present wave generator, the slope at frequencies higher than f_m corresponds to a value of –4. Moreover, although the input spectral model [26] (see equations (8) and (9)) does not include a secondary peak at frequencies higher than f_m, the secondary peaks can be reproduced on the spectra by SBWGM. For example, the frequencies of the primary and secondary peaks are 1 and 2 Hz, respectively, at U_{10} = 6.6 m/s and F = 507.5 m. This implies that despite the generation of mechanical irregular waves by the wave generator, the wind shear itself produces a local equilibrium condition [3] between the wind shear and wind waves generated by SBWGM and the secondary peak.

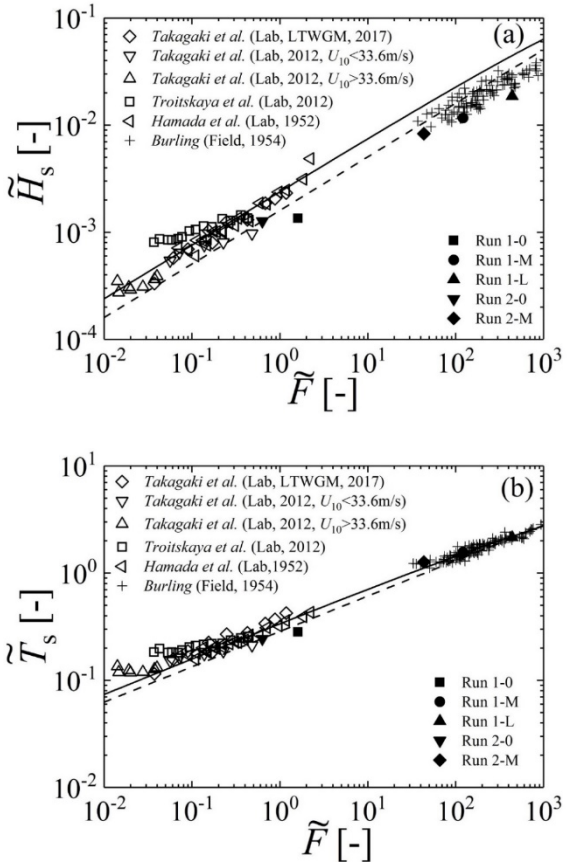

Fig. 3. Relationship between non-dimensional fetch $\widetilde{F}$ and (a) non-dimensional wave height $\widetilde{H_S}$, (b) non-dimensional wave period $\widetilde{T_S}$. Fetch, wave height, and wave period are normalized using wind speed U_{10} and gravity acceleration g. Solid curve: Wilson's formula IV [29]; Dashed curve: JONSWAP [25], both in (a, b). Laboratory values [10, 31] and field values [32] are added in the figure.

Therefore, it is concluded that SBWGM using the programmable irregular-wave generator can generate the ideal wind waves under long-fetch conditions. However, despite the fact that the input spectrum [26] decreases with a decrease in f for $f < f_m$, the SBWGM spectra level off due to the white noise. As mentioned in [27], the slope of LTWGM spectra at frequencies higher than f_m also correspond to a value of −4 (see Figures 2 (c – e)). Further details on the LTWGM spectra are in [27].

Figure 3 shows the relationships between the non-dimensional fetch $\widetilde{F}\ (= Fg/{U_{10}}^2)$ and both the non-dimensional wave height $\widetilde{H_S}(= H_S g/{U_{10}}^2)$ and non-dimensional wave period $\widetilde{T_S}(= T_S g/U_{10})$. Here the solid and dashed curves represent the fetch law from Wilson's formula IV [29] and JONSWAP [25], respectively. It is observed that the present plots, except Run 1-0, under both short- and long-fetch conditions, are concentrated around the previous plots and the solid and dashed curves, which implies that the SBWGM-generated wind waves follow the fetch law. Since the proposed fetch laws are proposed mainly based on field measurements, the plots at Run 1-0 (very short fetch) may scatter from the previous plots and empirical curves. The previous plots (Runs 3-0 to 3-4, symbol ∇) at $U_{10} < 33.6$ m/s are also concentrated around the solid and dashed curves, which implies that the LTWGM-generated wind waves also follow the fetch law, as mentioned in [27]. Figure 4 shows the dispersion relation and the relationship between the non-dimensional wave period T^* ($= T_S g/u^*$) and non-dimensional wave height H^* ($= H_S g/{u^*}^2$). Here, ω and k show the angular frequency and wavelength. In addition, the solid curves show the dispersion relation for a deep-sea wave [30] in Figure 4a and Toba's 3/2 power law [2] in Figure 4b, respectively. The figures show that the present plots under both short and long-fetch conditions (Runs 1-0 to 2-L) are concentrated around the solid curve, which

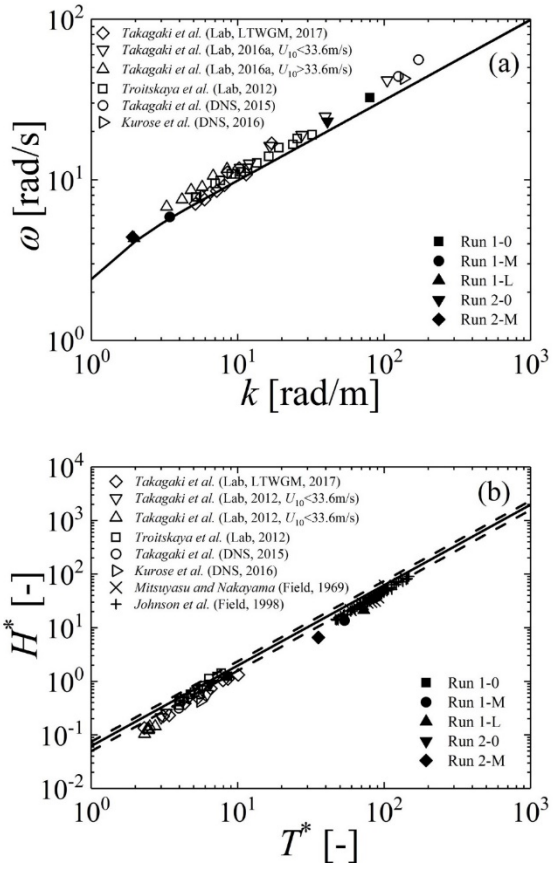

Fig. 4. (a) Dispersion relation, and (b) relationship between non-dimensional wave period T^* and non-dimensional wave height H^*. In (b), wave height and wave period are normalized using wind speed u^* and gravity acceleration g. Solid curve shows the dispersion relation and Toba's 3/2 power law [3] in (a, b), respectively. Dashed curves in (b) show the 20 % errors in Toba's 3/2 power law [3]. Laboratory values [10], predicted values [9, 12], and field values [33, 34] are added in the figure.

implies that the SBWGM-generated wind waves could be regarded as deep-sea waves following the Toba's 3/2 power law. The previous plots (Runs 3-0 to 3-4) are also concentrated around the solid curve, which implies that the LTWGM-generated wind waves follow the dispersion relation and Toba's 3/2 power law, as mentioned in [27].

Through the above verifications of the spectral shape, fetch law, dispersion relation, and Toba's 3/2 power law, it is confirmed that the ideal wind-driven waves under long-fetch conditions can be generated using SBWGM with the programmable irregular-wave generator. However, since SBWGM includes some of the same problems as LTWGM, and the wind waves generated by SBWGM do not correspond perfectly to those generated under the same field conditions. The differences between the present laboratory and field conditions are as follows: (1) The initial airflow entering the test section has a new turbulent boundary layer above the air-water interface under the present laboratory conditions; however, the boundary layer continues to develop under field conditions. (2) The present wave generator with SBWGM in the LWWT, with a width of 0.6 m, cannot produce the angular wave-wave spectrum, although the actual ocean waves spread to angular directions under field conditions. (3) Since there is the limitation due to the dispersion relation in the LWWT, with the depth of 0.7 m, we could not generate wind waves with the wavelengths longer than 1.4 m. These points should be improved before regarding the long-fetch laboratory conditions as true ocean conditions, but the present SBWGM is still helpful in laboratory experiments for modelling of small-scale air-sea coupling.

4. Conclusion

The abovementioned verifications of SBWGM in the LWWT, which is an original wind-wave generation technique, were demonstrated. Comparing SBWGM to LTWGM [27], the ideal wind waves at long-fetch conditions, such as 500 m or 2000 m, can be generated by SBWGM without the incremental steps required by LTWGM. Since SBWGM needs a conventional wind-wave spectrum, SBWGM cannot be applied to wind waves with an unknown wind-wave spectral shape at extremely high wind speeds. However, as incremental steps are required for LTWGM, it is difficult to generate the ideal wind waves at the long-fetch condition of 2000 m. If such wind waves are generated by LTWGM in a 10-m-long wind wave tank, ~ 200 incremental steps will be necessary. However, LTWGM does not need a conventional wind-wave spectrum, and can be applied to wind waves with an unknown wind-wave spectral shape and at extremely high wind speeds. In summary, SBWGM and LTWGM are suitable for wind-wave generation at normal and extremely-high wind speeds, respectively, although the generated wind waves are different from those in the open ocean because of the finite width of the tank. The present SBWGM, along with LTWGM, would be useful in laboratory experiments for modelling of small-scale air-sea coupling.

Acknowledgements

This work was supported by the Ministry of Education, Culture, Sports, Science and Technology (Grant-in-Aid Nos. 25249013 and 16K18015) and the Kawanishi Memorial ShinMaywa Education Foundation. We thank Prof. R. Kurose for useful discussions. We thank H. Muroya, M. Ishida, and S. Urakawa, for their assistance in conducting experiments at the LWWT, Kyoto University.

References

1. H. Kunishi, N. Imasato, On the growth of wind waves by high-speed wind flume (in Japanese), *Disaster Prevention Res. Inst. Annuals*, Kyoto Univ., Kyoto, 1966; **9**: pp. 667-676.
2. Y. Toba, Local balance in the air-sea boundary processes I. On the growth processes of wind waves, *J. Oceanogr. Soc. Japan*, 1972; **28**: 109–121.
3. Y. Toba, Local balance in the air-sea boundary processes III. On the spectrum of wind waves, *J. Oceanogr. Soc. Japan*, 1973; **29**: 209-220.
4. H. Mitsuyasu, Y. -Y. Kuo, A. Masuda, On the dispersion relation of random gravity waves. Part 2. An experiment, *J. Fluid Mech.*, 1979; **92**: 731-749, doi:10.1017/S0022112079000859
5. S. Komori, R. Nagaosa, Y. Murakami, Turbulence structure and mass transfer across a sheared air-water interface in wind-driven turbulence, *J. Fluid Mech.*, 1993; **249**: 161-183, doi:10.1017/S0022112093001120
6. M. A. Donelan, B. K. Haus, N. Reul, W. J. Plant, M. Stiassnie, H. C. Graber, O. B. Brown, E. S. Saltzman, On the limiting aerodynamic roughness of the ocean in very strong winds, *Geophys. Res. Lett.*, 2004; **31**: L18306, doi:10.1029/2004GL019460

7. N. Takagaki, S. Komori, N. Suzuki, K. Iwano, T. Kuramoto, S. Shimada, R. Kurose, K. Takahashi, Strong correlation between the drag coefficient and the shape of the wind sea spectrum over a broad range of wind speeds, *Geophys. Res. Lett.*, 2012; **39**: L23604, doi:10.1029/2012GL053988
8. N. Takagaki, R. Kurose, A. Kimura, S. Komori, Effect of Schmidt number on mass transfer across a sheared gas-liquid interface in a wind-driven turbulence, *Scientific Reports*, 2016; **6**: doi:10.1038/srep37059
9. N. Takagaki, R. Kurose, Y. Tsujimoto, S. Komori, K. Takahashi, Effects of turbulent eddies and Langmuir circulations on scalar transfer in a sheared wind-driven liquid flow, *Physics of Fluids*, 2015; **27**: 016603, doi:10.1063/1.4905845
10. Y. I. Troitskaya, D. A. Sergeev, A. A. Kandaurov, G. A. Baidakov, M. A. Vdovin, V. I. Kazakov, Laboratory and theoretical modeling of air-sea momentum transfer under severe wind conditions, *J. Geophys. Res.*, 2012; **117**: C00J21, doi:10.1029/2011JC007778
11. K. Iwano, N. Takagaki, R. Kurose, S. Komori, Mass transfer velocity across the breaking air-water interface at extremely high wind speeds, *Tellus B*, 2013; **65**: 21341, doi:10.3402/tellusb.v65i0.21341
12. R. Kurose, N. Takagaki, A. Kimura, S. Komori, Direct numerical simulation of turbulent heat transfer across a sheared wind-driven gas-liquid interface, *J. Fluid Mech.*, 2016; **804**: 646-687, doi:10.1017/jfm.2016.554
13. N. Takagaki, S. Komori, N. Suzuki, Estimation of friction velocity from the wind-wave spectrum at extremely high wind speeds, *IOP Conf. Series: Earth and Environmental Science*, 2016; **35**: 012009, doi:10.1088/1755-1315/35/1/012009
14. N. Takagaki, S. Komori, N. Suzuki, K. Iwano, R. Kurose, Mechanism of drag coefficient saturation at strong wind speeds, *Geophys. Res. Lett.*, 2016; **43**: 9829-9835, doi:10.1002/2016GL070666
15. M. Uda, *Marine Meteorology*, Tennensha, 1954; 297 page.
16. P. Black, R. W. Burpee, N. M. Dorst, W. L. Adams, Photo of the quarter – appearance of the sea surface in tropical cyclones, *Weather and Forecasting*, 1986; **1**: 102-107.
17. R. H. Wanninkhof, L. F. Bliven, Relationship between gas exchange, wind speed, and radar backscatter in a large wind-wave tank, *J. Geophys. Res.*, 1991; **96**: 2785-2796, doi:10.1029/90JC02368
18. S. Komori, R. Kurose, N. Takagaki, S. Ohtsubo, K. Iwano, K. Handa, S. Shimada, Sensible and latent heat transfer across the air-water interface in wind-driven turbulence, *GAS TRANSFER AT WATER SURFACES 2010* (Eds. S. Komori, W. McGillis, R. Kurose), Kyoto University Press, Kyoto, Japan, 2011; 78-89.
19. K. E. Krall, B. Jähne, First laboratory study of air–sea gas exchange at hurricane wind speeds, *Ocean Sci.*, 2014; **10**: 257-265, doi:10.5194/os-10-257-2014
20. K. Tanno, S. Ohtsubo, S. Komori, Effects of fetch on mass transfer across the air-water interface in wind-driven turbulence (in Japanese), *Transactions of the Japan Society of Mechanical Engineers, Series B*, 2007; **73**: 1510-1517, doi:10.1299/kikaib.73.1510
21. N. Takagaki, K. Iwano, E. Ilyasov, S. Komori, Y. Shirakawa, Development of an optical imaging technique for particle number density, *Journal of Fluid Science and Technology*, 2018; **13**: 17-00428, doi:10.1299/jfst.2018jfst0001
22. N. Takagaki, S. Komori, Effects of rainfall on mass transfer across the air-water interface, *J. Geophys. Res.*, 2007; **112**: C06006, doi:10.1029/2006JC003752
23. M. Phillips, The equilibrium range in the spectrum of wind-generated ocean waves, *J. Fluid Mech.*, 1958; **4**: 426-434, doi: 10.1017/S0022112058000550
24. W. J. Pierson, L. Moskowitz, A proposed spectral form for fully developed wind seas based on the similarity theory of S. A. Kitaigorodskii, *J. Geophys. Res.*, 1964; **69**: 5181-5190, doi:10.1029/JZ069i024p05181
25. K. Hasselmann, et al., Measurements of wind-wave growth and swell decay during the Joint North Sea Wave Project (JONSWAP), *Erganzugsh. Dtsch. Hydrogr. Z.*, 1973; **12**: 1-95.
26. M. A. Donelan, J. Hamilton, W. H. Hui, Directional spectra of wind generated waves, *Philos. Trans. R. Soc. London Ser. A*, 1985; **315**: 509–562, doi:10.1098/rsta.1985.0054
27. N. Takagaki, S. Komori, M. Ishida, K. Iwano, R. Kurose, N. Suzuki, Loop-type wave-generation method for generating wind waves under long-fetch conditions, *Journal of Atmospheric and Oceanic Technology*, 2017; **34**: 2129-2139, doi:10.1175/JTECH-D-17-0043.1
28. K. Hirayama, I. Miyazato, Generation method of directional random waves with arbitrary spectrum (in Japanese), *Report of the Port and Airport Researches*, 2009; **48**: 119-214.
29. B. W. Wilson, Numerical prediction of ocean waves in the north Atlantic for December, 1959, *Dt. Hydrogr. Z.*, 1965; **18**: 114-130.
30. H. Lamb, *Hydrodynamics*, 6th ed. Cambridge University Press, 1932.
31. T. Hamada, H. Mitsuyasu, N. Hase, An experimental study of wind effect upon water surface, *Rep. of Transportation Technical Research Institute*, 1953; **8**: 22 pp, doi:10.1049/cp.2014.1227
32. R. W. Burling, Surface waves on enclosed bodies of water, *Coastal Eng. Proc.*, 1954; **5**: 1-10, doi:10.9753/icce.v5.1.
33. H. Mitsuyasu, R. Nakayama, Measurements of waves and wind at Hakata Bay, *Rep. Res. Inst. Appl. Mech.*, 1969; **33**: 33-66.
34. H. K. Johnson, J. Hojstrup, H. J. Vested, S. E. Larsen, On the dependence of sea surface roughness on wind waves, *J. Phys. Oceanogr.*, 1998; **28**: 1702-1716, doi:10.1175/1520-0485(1998)028<1702:OTDOSS>2.0.CO;2

Available online at www.sciencedirect.com

ScienceDirect

Procedia IUTAM 26 (2018) 194–203

Procedia IUTAM

www.elsevier.com/locate/procedia

IUTAM Symposium Wind Waves, 4–8 September 2017, London, UK

Quasi-linear approximation for description of turbulent boundary layer and wind wave growth

Yu. Troitskaya[a,b,d]*, O.Druzhinin[a,b], D.Sergeev[a,b], A.Kandaurov[a,b], O.Ermakova[a,b], W. t. Tsai[c]

[a]*Institute of Applied Physics, Nizhny Novgorod, 603950, Russia,*
[b]*Nizhny Novgorod State University, Nizhny Novgorod, 603022, Russia*
[c]*National Taiwan University/Department of Engineering Science and Ocean Engineering, Taipei, 10617, Taiwan*
[d]*Obukhov Institute of Atmospheric Physics, Moscow, 143039, Russia*

Abstract

This study describes an approximate quasi-linear model for the description of the turbulent boundary layer over steep surface waves. The model assumes that wave-induced disturbances of the atmospheric turbulent boundary layer could be reasonably described in a linear approximation with the momentum flux from wind to waves retained as the only nonlinear effect in the model. For the case of periodic long-crested waves, the model has been verified with a set of the original laboratory and numerical experiments. The laboratory experimental study of the airflow over the steep waves was performed by means of the PIV technique. The numerical study was performed with direct numerical simulation (DNS) of the turbulent airflow over waved surface at Re=15,000 for quasi-homogeneous waves, wave trains and parasitic capillaries riding on the crest of a steep waves. Examples are given of the application of the quasi-linear approximation to describe the turbulent boundary layer over waves with the continuous spectrum under the assumption of random phases of harmonics. In the latter case the quasi-linear model provides the growth rate of surface waves in the inertial interval of the surface wave spectrum proportional to w7/3 in agreement with predictions in [1].

Peer-review under responsibility of the scientific committee of the IUTAM Symposium Wind Waves.

Keywords: wind; turbulence; atmospheric boundary layer; wind waves; DNS

* Corresponding author Yu. Troitskaya. Tel.: +7-831-436-8297; fax: +0-000-000-0000 .
E-mail address: yuliya@hydro.appl.sci-nnov.ru

2210-9838
Peer-review under responsibility of the scientific committee of the IUTAM Symposium Wind Waves.
10.1016/j.piutam.2018.03.019

1. Introduction

Interaction of the wind flow with surface waves is one of the central questions in the wave modelling, because it defines the wind input to waves. In spite of significant progress in the topic there is a number of questions, the most essential of which is strong dispersion in wind input obtained in different experiments, which is about 300–500% [1-3]. It is one of possible sources of errors in forecasts of wind waves.

Measuring wind input is a quite tricky experimental problem. The energy flux from wind to waves is determined by surface stresses (pressure and tangential stresses) at the water surface, which should be measured at curved liquid surface, including areas below the wave crests. These measurements can be performed by a wave-following contact technique [4-6]. Measurements of airflow below crests of the waves can be performed by seeding the flow with small particles visualized with a strobe source of light and application of special photograph technique [7]. Kawai's experiments demonstrated occurrence of the airflow separation from the crests of steep waves in a set of instant images. The state-of-art method applicable for investigation the structure of airflow over waves is the particle image velocimetry (PIV) [9]. In this method, the flow is seeded with small particles illuminated by laser beam, which makes them visible on digital images. Applications of the PIV in [10-14] clearly demonstrated a complex turbulent airflow with pronounced flow separation from the crests of waves and reattachment at the windward face of the wave on the instantaneous patterns of the vector velocity fields.

It should be noted that the separation of wind flow from the crest of the surface wave is a non-stationary turbulent process with a characteristic scale that is small compared with the period of the wave. It can be expected that the processes of turbulent exchange between the ocean and the atmosphere and wind induced generation of waves, whose timescales greatly exceed the period of the wave, are caused by the wind flow fields averaged over the turbulent pulsations. The velocity fields averaged over turbulent pulsations are smooth and un-separated. It was confirmed by averaging over the statistical ensembles of realizations of instantaneous velocity fields obtained with use of the time-resolved PIV in [13] and individual instantaneous vector velocity fields retrieved from the planar PIV in [14]. It encourage us to use the quasi-linear approximation for description of coupling of surface waves with turbulent atmospheric boundary layer, where wave-induced air-flow disturbances are described in linear approximation.

2. Formulation of the quasi--linear model of turbulent wind over waved water surface

There exists two classes of quasi-linear models, which can be distinguished by the model of wind wave growth. The first class (e.g., [15, 16]) is based on the quasi-laminar model [16, 17] model of wind wave growth. The second class (e.g., [19, 20]) assumes that the wind wave growth is governed by the effect of eddy viscosity.

Visualization of the air flow over steep wind waves [13] clearly demonstrates that turbulent vortices are much faster than waves. Then a model based on RANS (Reynolds-Averaged Navier-Stokes) equations can be used to describe the turbulent air flow over waves. The model reads:

$$\frac{\partial \langle u_i \rangle}{\partial t} + \langle u_j \rangle \frac{\partial \langle u_i \rangle}{\partial x_j} + \frac{1}{\rho_a} \frac{\partial \langle p \rangle}{\partial x_i} = \frac{\partial \sigma_{ij}}{\partial x_j} \tag{1}$$

where the turbulence stress tensor is:

$$\sigma_{ij} = \langle u_i' u_j' \rangle = \nu \left(\frac{\partial \langle u_i \rangle}{\partial x_j} + \frac{\partial \langle u_j \rangle}{\partial x_i} \right) \tag{2}$$

Here, <...> denotes the averaging operation over ensemble of turbulent fluctuations, ν is the turbulent eddy viscosity coefficient, which is a self-similar function of the distance, z, from the air-water interface:

$$\nu = \nu_a f\left(\frac{z u_*}{\nu_a}\right), \tag{3}$$

where ν_a is the air molecular viscosity, u_* is the friction velocity in the turbulent boundary layer. We used an empirical approximation for the function f obtained in [21].

$$\nu = \nu_a \left\{1 + \kappa \frac{u_* \eta \sqrt{\tau_{turb}/u_*^2}}{\nu_a}\left[1 - e^{-\frac{1}{L}\left(\frac{u_* \eta}{\nu_a}\right)^2 \left(\frac{\tau_{turb}}{u_*^2}\right)}\right]\right\} \tag{4}$$

In this expression, L is the scale of a viscous sub-layer, which depends on a flow regime. [21] suggested L=22.4 for the aerodynamically smooth surface that gives the roughness height of 0.11 ν_a / u_*. We consider the air-water interface in our approximate model as an aerodynamically smooth curved surface.

The boundary conditions at the air-water interface $z=\xi(x,y,t)$ are:

$$\frac{\partial \xi}{\partial t} + \langle u \rangle \frac{\partial \xi}{\partial x} + \langle v \rangle \frac{\partial \xi}{\partial y}\bigg|_{z=\xi(x,y,t)} = \langle w \rangle\big|_{z=\xi(x,y,t)} \tag{5}$$

$$\left\langle \vec{u}_\tau^{\,w} \right\rangle\big|_{z=\xi(x,y,t)} = \left\langle \vec{u}_\tau^{\,a} \right\rangle\big|_{z=\xi(x,y,t)}, \tag{6}$$

$\langle u \rangle$, $\langle v \rangle$, $\langle w \rangle$ are the averaged air velocity components aligned with the x-, y- and z- axes. To avoid strong geometrical nonlinearity we formulated RANS equations in the wave-following curvilinear coordinates.

The solution to the set of the Reynolds equations is searched as a sum of the mean flow and wave induced disturbances. Contrary to the turbulent vortices the wind interaction with waves is not parameterized, but described directly, within the approximate quasi-linear model, when the wave-induced disturbances of the air flow are considered within the linear approximation and the higher harmonics of perturbations are neglected. The only non-linear effect taken into account is the deformation of the mean flow velocity due to momentum flux to wave and the only nonlinear equation describes the momentum flux from wind to waves, which is completely determined by the three-dimensional surface wave spectrum (dependent on wave number, frequency and angle). The equations of the quasi-linear model used here are given in [22, 23]. The quasi-linear approach is applicable for small Reynolds numbers (see [24]). Although the Reynolds number Re_{eff} defined by the molecular viscosity is huge in turbulent flows, but the flow averaged over turbulent fluctuations described within the RANS equations is determined by the effective Reynolds number, which is defined by the eddy viscosity coefficient. Estimates in [13] show that $Re_{eff} \sim ka<1$, that confirms the quasi-linear approximation.

3. Verification of the quasi-linear model

Strong assumptions behind the quasi-linear approximation for disturbances induced by surface waves in the marine atmospheric boundary layer need to be verified on the base of laboratory physical and numerical experiments. In the physical experiment, turbulent airflow in a laboratory tank over mechanically generated periodic surface waves was studied with the use of the planar time-resolved PIV technique, based on high-speed video photography (see [13]). The data of these measurements were compared with the predictions of the quasi- linear model for the parameters of the waves (wavelength, celerity, steepness) and the air-flow (wind friction velocity and roughness height) retrieved from the experiment. The model reproduced not only the average velocity and stress profiles, but the parameters of the wave-induced velocity and pressure disturbances averaged over turbulent fluctuations. The latter can be retrieved directly from the RANS equations, since the time-resolved PIV gives the sequences of instant air flow velocity fields. In case of long-crested waves, the momentums of the air-flow velocity

fields are two-dimensional, and planar PIV is sufficient for retrieval average pressure field directly from the RANS – equations as follows:

$$\left(\frac{\langle p\rangle}{\rho_a}-\sigma_{33}\right)\Bigg|_{x_3-\xi(x_1,t)}^{H-\xi(x_1,t)}=-\int_{x_3-\xi(x_1,t)}^{H-\xi(x_1,t)}\left[\frac{\partial\langle v_3\rangle}{\partial t}+\frac{\partial}{\partial x_1}\left(\langle v_1\rangle\cdot\langle v_3\rangle-\sigma_{13}\right)\right]dx_3+$$
$$-\left[\langle v_3\rangle\left(\langle v_3\rangle-\left(\frac{\partial\xi(x_1,t)}{\partial t}+\langle v_1\rangle\frac{\partial\xi(x_1,t)}{\partial x_1}\right)\right)+\sigma_{13}\frac{\partial\xi(x_1,t)}{\partial x_1}\right]\Bigg|_{x_3-\xi(x_1,t)}^{H-\xi(x_1,t)} \tag{7}$$

Here H is the top boundary of the measuring domain.

3.1. Direct numerical simulation of turbulent boundary layer over waved water surface. Quasi-harmonic waves

The question why the simple quasi-linear approximation is applicable for description of the strongly nonlinear effect was studied within the direct numerical simulation (DNS) of the detailed structure and statistical characteristics of turbulent boundary layer over finite amplitude periodic surface wave [25]. These DNS modelled two-dimensional water waves with the wave slopes in the range ka=0-0.2 in the flow with the bulk Reynolds number Re = 15000. A number of wave age parameters in the range $c/u_* = 0 - 10$ where u_* is the friction velocity and c is the wave celerity were considered. The computational domain (periodic in the x- and y-directions) had the size $L_x = 6\lambda$, $L_y = 4\lambda$ and $L_z = \lambda$. The DNS code was solving fully three-dimensional Navier-Stokes equations in curvilinear coordinates in the frame of reference moving with the phase velocity of the wave. The flow was driven by the shear, which was created by the upper plane boundary moving horizontally in the x-direction with a prescribed bulk velocity.

Similarly to the physical experiment the instant realizations of the velocity field demonstrate flow separation at the crests of the waves, but the ensemble averaged velocity fields had typical structures similar to those existing in shear flows near critical levels, where the phase velocity of the disturbance coincides with the flow velocity [25]. Comparison with the calculations within the quasi-linear model showed, that the DNS runs supported the applicability of the quasi-linear model for description profiles of the mean wind velocity, the turbulent stress, amplitude and phase of the main harmonics of the wave-induced velocity components. This is confirmed by the close structures of the exact and approximate patterns of streamlines in the airflow above the waves with different steepness (Fig. 1).

The magnitude and phase of wave induced pressure fluctuations obtained within the quasi-linear model are also in a good agreement with the DNS data (see Fig. 2 (a), (b)). Fig. 2 (c) confirms, that the model reproduces the wind-wave interaction parameter as it was introduced by Miles (1957):

$$\beta=\frac{2}{(ka)^2\rho u_*^2}\frac{1}{\lambda}\int_0^{\lambda}\langle p\rangle\frac{d\xi}{dx}dx\,, \tag{8}$$

which determines the wind wave growth rate: $\mathrm{Im}\,\omega=\frac{1}{2}\frac{u_*^2}{c^2}\beta\frac{\rho_a}{\rho_w}\omega$. Notice the decrease of the wind-wave growth rate parameter β with the increase of the wave steepness (see Fig. 2 (c)).

The DNS results support applicability of the non-separating quasi-linear theory for description of average fields in the airflow over steep and even breaking waves, when the effect of separation is manifested in the instantaneous flow images and is explained by strong inhomogeneity of the separation zone in the transversal direction (along the wave front), shown in DNS. It appears that the vorticity is mostly concentrated in thread-like vortex structures, which have a horseshoe shape and resemble well-known λ-vortices extensively studied in the case of a "classical" boundary layer over a solid plane boundary [26]. The similar strongly inhomogeneous separation of the flow from the wave crests and the Kelvin cat-eyes patterns in the mean flow field were observed in DNS [27].

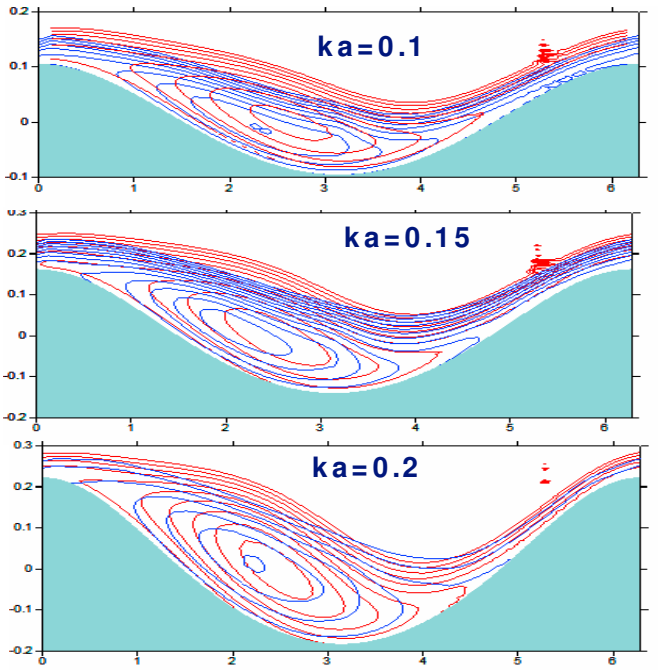

Fig.1. The streamline patters in the air flow over waves in the wave-following reference frame. The red lines - results of DNS, the blue lines – the quasi-linear model. Numbers at the curves are the wave steepness, $c/u_* \approx 1.6$.

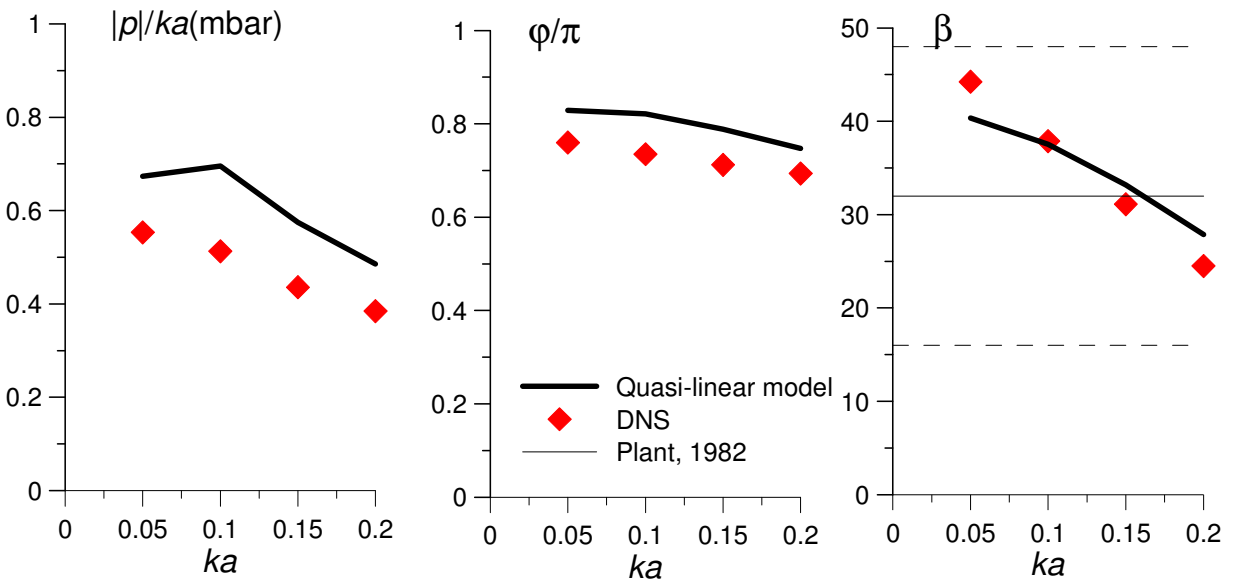

(a) (b) (c)

Fig.2. Comparing theory and DNS: magnitude (a) and phase shift (b) of the wave-induced pressure disturbances at the water surface, the Miles (1957) wind-wave interaction parameter β (c) via wave steepness. The bold line presents calculations within the quasi-linear model, symbols are the results of DNS.

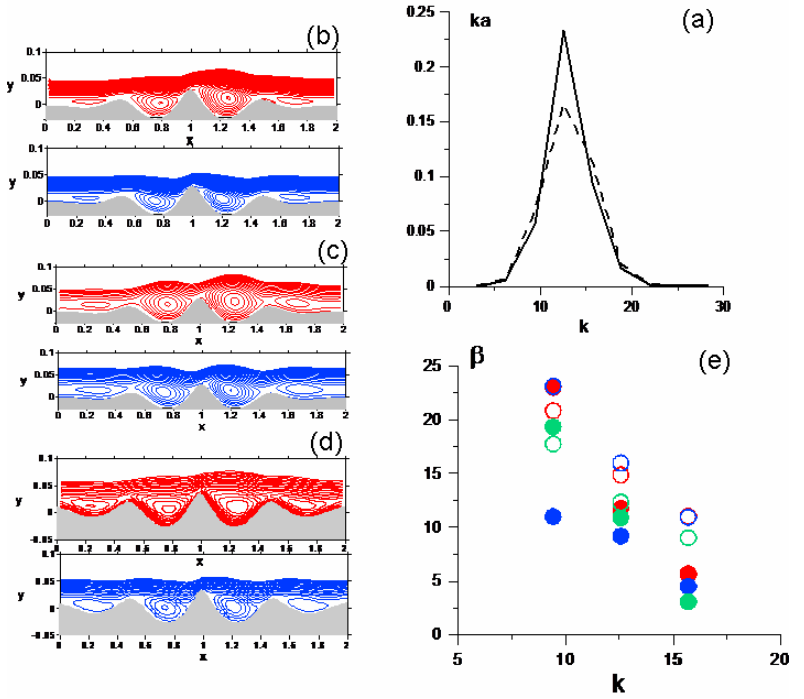

Fig.3. (a) The slope spectra of the wave-trains: solid line - *ka*=0.26, dashed line - *ka*=0.21.The stream line patterns of air flow of the air flow above the wave-train: (b) ka=0.21, c/u*=1.6, (c) ka=0.21, c/u*=3.2, (d) ka=0.26,c/u*=1.6. The red lines – DNS, the blue lines – the quasi-linear model. (e) The wind-wave interaction parameter for the individual harmonics of the wave-train: the red symbols - case (b), the blue symbols - case (c), the green symbols - case (d). The close symbols - DNS, the open symbols - the quasi-linear model.

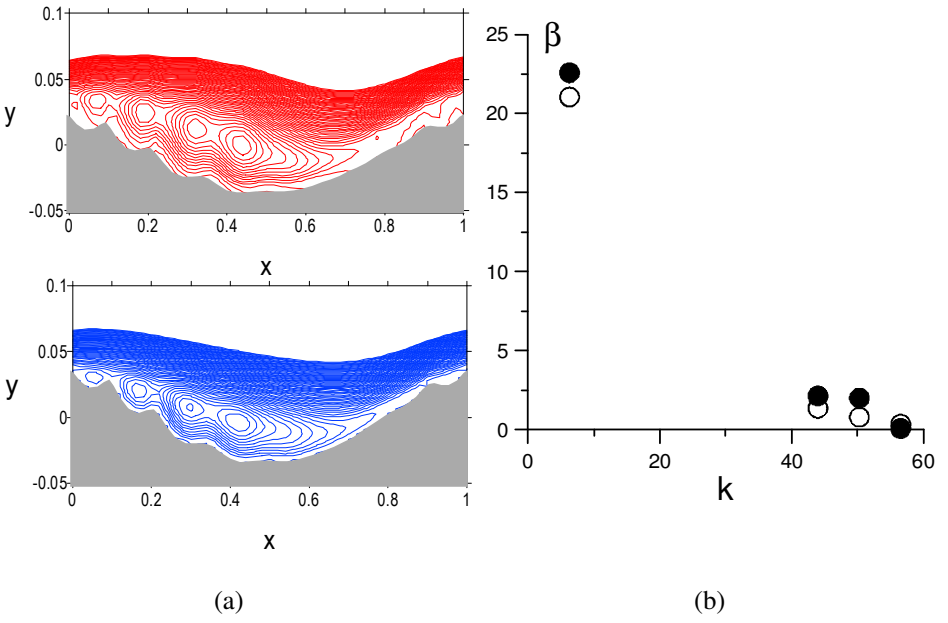

Fig.4. (a) The stream line patterns of air flow of the air flow above the steep surface wave with riding parasitic capillaries. The red lines – DNS, the blue lines – the quasi-linear model. (b) The wind-wave interaction parameter for the individual harmonics.

3.2.Wave trains and parasitic capillaries

It was found that quasi-linear approximation reproduces not only the air flow over the periodic quasi-harmonic wave, but also more complex above-the-surface shapes. We considered two cases of the wave forms typical for the waves in the ocean. First we performed DNS of the air turbulent boundary layer over two dimensional wavetrains. It was a purely model case, because we consider the simplest case of non-dispersive wave train with wide spectrum, where the spectral width is ¼ of the central frequency, and the integral slope is 0.21 and 0.26.

Comparison of the streamline patterns obtained within the DNS and quasi-linear models (Fig. 3, (b-d))shows, that even in case of this coherent wave-train the quasi-linear model gives close (not identical results) in comparison with DNS. We also calculated the wind-wave interaction parameter for the individual harmonics of the wave-train using Eq.(8) just as it is done in wave spectral models and compared it in Fig. 3 (e) with the prediction of the quasi-linear model. Obviously there is difference related to the coherent nonlinear effects which are neglected in the model. However, , the experimental error is below 50% for the central harmonic, which is usually below the measurement error in physical experiments.

Fig. 4 (a) compares the ensemble averaged stream-line patterns of the airflow over parasitic capillary waves riding on the crest of a steep wave. A two-dimensional surface wave with amplitude a, length λ, and phase velocity c, periodic in the x direction with slope $ka = 2\pi a/\lambda = 0.2$ is considered. Capillary ripples are modelled by the modulated high-frequency harmonic of the fundamental wave, which has the same phase velocity. The water surface is as follows:

$$\begin{aligned} x &= \xi - a_0 \sin k\xi - a_1\left(\sin k_1\xi + a_2\left[\sin\left(k_2\xi+\varphi\right)+\sin\left(k_3\xi-\varphi\right)\right]\right) \\ z &= a_0 \cos k\xi + a_1\left(\cos k_1\xi + a_2\left[\cos\left(k_2\xi+\varphi\right)+\cos\left(k_3\xi-\varphi\right)\right]\right) \end{aligned}, \tag{9}$$

where $k = 2\pi$ and a_0 are the wave number and amplitude of the fundamental wave, $k_1 = 8k$ and $a_1 = 0.05\,a_0$, are the wave number and amplitude of the ripples, $a_2 = 0.5$, $k_2 = 9k$, $k_3 = 7k$, $\varphi = -0.9$ are the parameters of the ripple modulation.

The stream-line patterns retrieved from DNS results and calculated within the quasi-linear model are not identical, but rather similar. Surprisingly the quasi-linear model reproduced the wind wave interaction parameter (see Fig. 4 (b)) even for capillaries. These results support the assumption, that the main nonlinear effect in wind-wave coupling is the deformation of the mean flow, well described by the quasi-linear model.

4. Applications of the quasi-linear approximation for processes in marine atmospheric boundary layer

In this section we discuss what the quasi-linear model can give for description of the aerodynamic resistance of the sea surface and growth rate of ocean wind waves. The wave field is parameterized by the growing sea spectrum in [28] with slightly modified Phillips' constant in accordance with [29]:

$$S\left(\vec{k}\right) = k^{-3}\left(B_l(k)+B_h(k)\right)\frac{2}{\pi}\cos^2\theta$$

$$B_l = \frac{0.006}{2}\Omega^{2/3}\begin{cases}\left(\dfrac{k}{k_p}\right)^{1/2}\exp\left\{-\dfrac{5}{4}\left(\dfrac{k}{k_p}\right)^2\left(1.7+6\log(\Omega)\right)^{\exp\left\{\frac{1}{2}\left(\frac{\sqrt{k}-\sqrt{k_p}}{0.08(1+4\Omega^{-3})\sqrt{k_p}}\right)^2\right\}}\right\} & k<k_0 \\ \left(\dfrac{k_0}{k_p}\right)^{1/2} & k>k_0\end{cases} \tag{10}$$

Here . $\Omega = \dfrac{U_{10}\omega_p}{g}$. is the wave age parameter, $\omega_p = \sqrt{gk_p}$, $k_0 = 9k_p$. $B_h(k)$ according to [30] is:

$$B_h = \frac{10^{-2}}{2}\left(1+3\ln\frac{u_*}{c}\right)\frac{u_*}{c}e^{-\frac{1}{4}\left(\frac{k}{k_m}-1\right)^2};k_m = \frac{2g}{\left(23cm/s\right)^2} \quad (11)$$

Comparison in Fig. 5 (a) shows that calculations within the quasi-linear model reproduce the surface drag coefficient within the experimental errors. The predicted wind wave growth rate is close to the data in [31, 32] (Fig. 6 (b)).

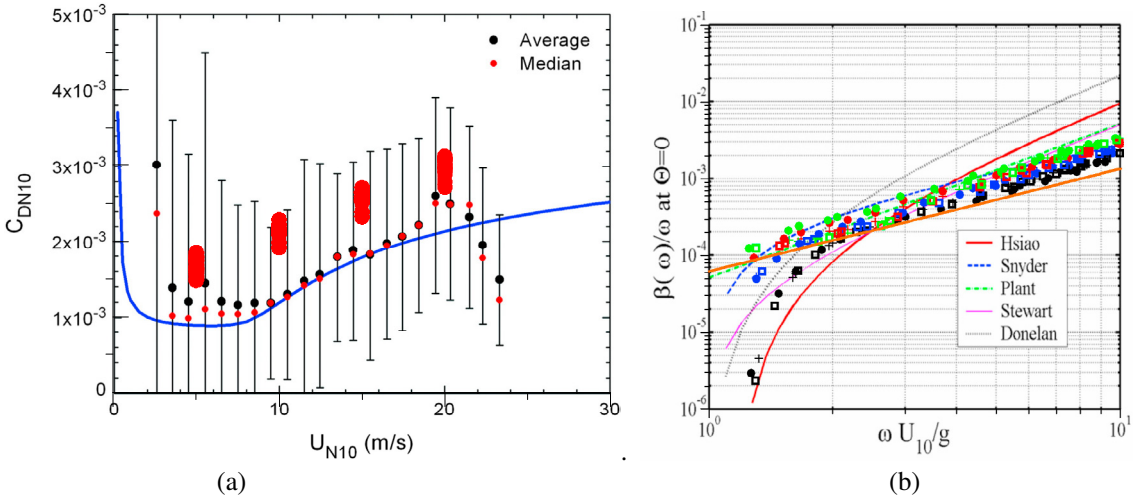

Fig.5. (a) Drag coefficient as a function of wind speed. Experimental data – from Andreas et al (2012). Red large symbols - calculations within the quasi-linear model. (b) Wind wave growth rate. Colored symbols - calculations within the quasi-linear model. Experimental data compilation adopted from Badulin, et al (2005).

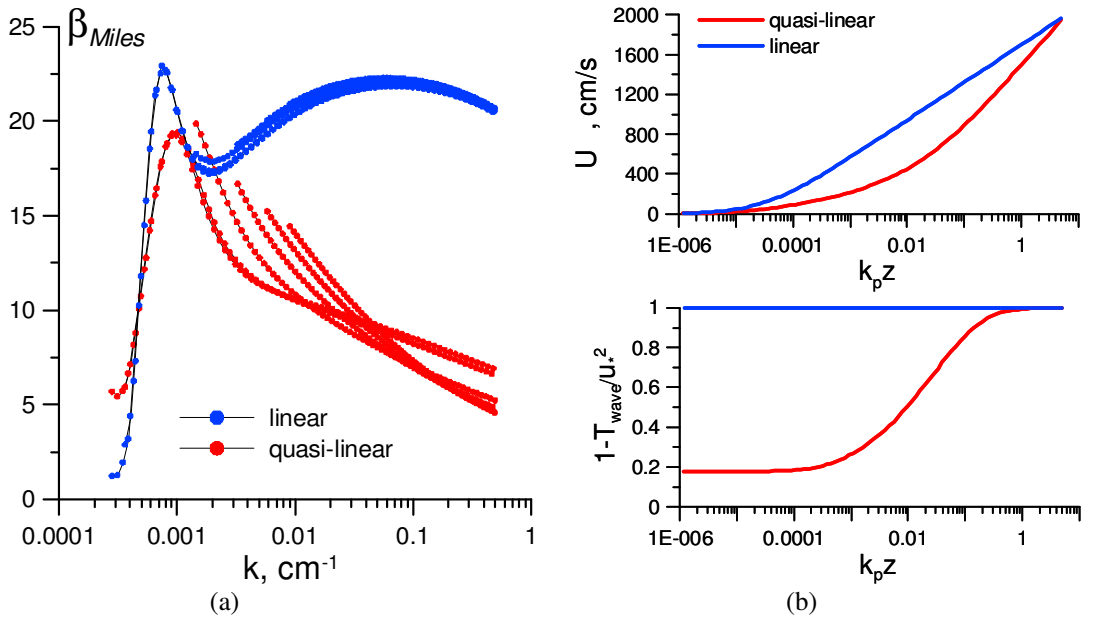

Fig.6. Growth rate of wind waves (a) and the wind velocity profile (top) and turbulent momentum flux (bottom) (b) calculated within the linear (blue lines) and quasi-linear (red) models. U_{10}=15 m/s.

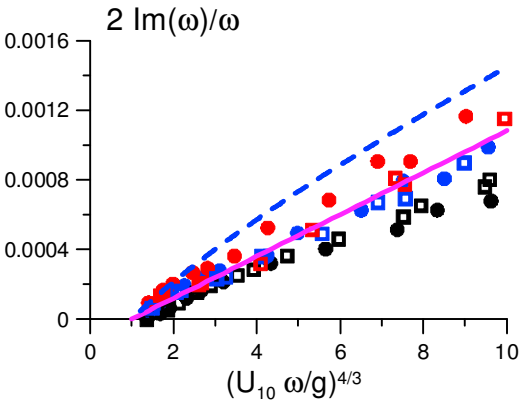

Fig.7. The growth rate of wind waves calculated within the quasi-linear model: black symbols U_{10}=5 m/s, blue symbols U_{10}=10 m/s, red symbols U_{10}=15 m/s. Different symbols corresponds to different models of the roughness height. The solid curve is fitting by Eq.(9), the dashed curve is the model by Hsiao, Shemdin (1983).

Note, that the wind-wave interaction parameter β calculated within the quasi-linear model is significantly reduced for short wave tail of the wind-wave spectra (compare the "linear" and "quasi-linear" β in Fig. 6 (a)). It can be explained by deformation of the wind velocity profile due to momentum flux from wind to waves (Fig. 6 (b)). As the result the shorter waves are interacting with the effectively decelerated air flow and their growth rate is reduced in comparison with the linear case.

Fig. 7 shows the relative growth rate as a function of dimensionless frequency $U_{10}\omega/g$ to degree 4/3, which can be well fitted by the linear function:

$$2\frac{\mathrm{Im}\,\omega}{\omega} = 0.00012\left(\left(\frac{U_{10}\omega}{g}\right)^{4/3} - 1\right) \tag{12}$$

Within the inertial interval of the surface wave spectra Eq.(9) provides the wind input term $S_{wind} \sim \omega^{7/3}\varepsilon(\omega)$ in the kinetic equation in agreement with [1].

5. Conclusions

In this paper we investigated applicability of a quasi-linear model for description turbulent boundary layer over steep surface waves. The model assumes that wave induced disturbances of the atmospheric turbulent boundary are described in linear approximation and the only nonlinear effect taken into account is momentum flux from wind to waves. The model was verified by special laboratory and numerical experiments. Experimental investigation of airflow over steep waves was performed by means of PIV technique. DNS of the airflow over waved surface was carried out for Re=15000. The best agreement is achieved for periodic waves, but for coherent wave trains and parasitic capillaries, the model also can reproduce the parameters of the wind turbulent flow over the waved water surface averaged over turbulent fluctuations and the wave growth rate. Basing on DNS an explanation of applicability of the quasi-linear model is suggested due to strong inhomogeneity of the separation zone in the transversal to wind direction. For the case of ocean waves with the continuous spectrum under the assumption of random phases of harmonics the quasi-linear model provides the growth rate of surface waves in the inertial interval of the surface wave spectrum proportional to $\omega^{7/3}$ in agreement with predictions in [1].

Acknowledgements

This work has been supported by the Russian Science Foundation (project 14-17-00667, 15-17-20009), Seventh Framework Programme (project PIRSES-GA-2013-612610) and Russian Foundation for Basic Research projects

(16-05-00839, 16-55-52022, 17-05-00703, 18-55-50005, 18-05-00265). Sergej Zilitinkevich additionally acknowledges support from the Academy of Finland project ABBA No. 280700, Alexander Kandaurov additionally acknowledges support by President grant for young scientists MC-2041.2017.5. The basic salary of the authors from IAP is financed by the government contract 0035-2014-0032. The experiments were performed at the Unique Scientific Facility "Complex of Large-Scale Geophysical Facilities" (http://www.ckp-rf.ru/usu/77738/).

References

1. V. Zakharov, D. Resio, A. Pushkarev, Balanced source terms for wave generation within the Hasselmann equation. *Nonlin. Processes Geophys.*, 2017, **24**: 581–597.
2. S. Badulin, A. V. Babanin, D. T. Resio, V. Zakharov, Weakly turbulent laws of wind-wave growth, *J. Fluid Mech*., 2007, **591:** 339–378.
3. A. Pushkarev, V. Zakharov, Limited fetch revisited: comparison of wind input terms, in surface wave modeling, *Ocean Model*., 2016, **103:** 18–37.
4. C. T. Hsu, E. Y. Hsu, On the structure of turbulent flow over a progressive water wave: theory and experiment in a transformed wave-following coordinate system. Part 2, *J. Fluid Mech*., 1983, **131**: 123–153.
5. C. T. Hsu, E. Y. Hsu, R. L. Street, On the structure of turbulent flow over a progressive water wave: theory and experiment in a transformed, wave-following co-ordinate system, *J. Fluid Mech.*, 1981, **105**: 87–117.
6. M. A. Donelan, A. V. Babanin, I. R. Young, M. L. Banner, McCormick C., Wave follower field measurements of the wind input spectral function. Part I: Measurements and calibrations, *J. Atmos. Oceanic Technol.*, 2005, **22(7)**: 799–813.
7. S. Kawai, Visualisation of air flow separation over wind wave crest under moderate wind, *Bound.-Layer Meteor.*, 2005, **21**: 93–104.
8. S. Kawai, Structure of air flow separation over wind wave crest, *Bound.-Layer Meteor.*, 1982, **23**: 503–521.
9. R. J. Adrian, Particle imaging techniques for experimental fluid mechanics, *Annu. Rev. Fluid Mech.*, 1991, **23**: 261–304.
10. N. Reul, H. Branger, J.-P. Giovanangeli, Air flow separation over unsteady breaking waves, *Phys. Fluids*, 1999, **11(7)**: 1959-1961.
11. N. Reul, H. Branger, J.-P. Giovanangeli, Air flow structure over short-gravity breaking water waves, *Bound.-Layer Meteor.*, 2008, **126**: 477–505.
12. F. Veron, G. Saxena, S. K. Misra, Measurements of the viscous tangential stress in the airflow above wind waves, *Geophys. Res. Lett.*, 2007, **34**: L19603.
13. Y. I. Troitskaya, D. A. Sergeev, O.S. Ermakova, G.N. Balandina, Statistical Parameters of the Air Turbulent Boundary Layer over Steep Water Waves Measured by the PIV Technique, *J. Phys. Oceanogr.*, 2011, **41**: 1421-1454.
14. M. P. Buckley, F. Veron, Structure of the airflow above surface waves, *J. Phys. Oceanogr.*, 2016, **46**: 1377–1397.
15. A. L. Fabrikant, Quasilinear theory of wind waves generation, *Izv. Atmos. Ocean. Phys.*, 1976, **12**: 858–862.
16. P. A. Janssen, Quasi-linear theory of wind wave generation applied to wave forecasting, *J. Phys. Oceanogr.*, 1991, **21**: 1631–1642.
17. J. W. Miles, On the generation of surface waves by shear flow. Part I, *J. Fluid Mech.,* 1957, **3**:185–204.
18. J. W. Miles, On the generation of surface waves by shear flows Part 3. Kelvin-Helmholtz instability, *J. Fluid Mech.*, 1959, **6(4)**: 583–598.
19. A. D. Jenkins, Quasi-linear eddy-viscosity model for the flux of energy and momentum to wind waves using conservation law equations in a curvilinear coordinate system, *J. Phys. Oceanogr.,* 1992, **22**: 843–858.
20. V. P. Reutov, Y. I. Troitskaya, On nonlinear effects due to water wave interaction with turbulent wind, *Izv. Russ. Acad. Sci., Atmos. Oceanic Phys.*, 1995, **31**: 825-834.
21. A. V. Smolyakov, Spectrum of the quadruple radiation of the plane turbulent boundary layer, *Acoust. Phys.,* 1973, **19(3)**: 420–425.
22. Y. I. Troitskaya, D. A. Sergeev, A. A. Kandaurov, G. A. Baidakov, M. A. Vdovin, and V. I. Kazakov, Laboratory and theoretical modeling of air-sea momentum transfer under severe wind conditions, *J. Geophys. Res.*, 2012, **117**: C00J21.
23. Y. I. Troitskaya, D. A. Sergeev, O.A. Druzhinin, A. A. Kandaurov, O.S. Ermakova, E.V. Ezhova, I. Esau, S. Zilitinkevich, Atmospheric boundary layer over steep surface waves, *Ocean Dyn.*, 2014, **64**: 1153–1161.
24. G. K. Batchelor, An introduction in fluid dynamics, *Cambridge University Press.,* 1967, 615.
25. O. A. Druzhinin, Y. I. Troitskaya, S. S. Zilitinkevich, Direct numerical simulation of a turbulent wind over a wavy water surface, *J. Geophys. Res., 2012,* **117**: C00J05.
26. P. Moin, J. Kim, The structure of the vorticity field in the turbulent channel flow. Part 1. Analysis of instantaneous fields and statistical correlations, *J. Fluid Mech.*, 1985, **155**: 441-464.
27. D. Yang, L. Shen, Direct-simulation-based study of turbulent flow over various waving boundaries, *J.Fluid Mech.*, 2010, **650**: 131-180
28. M. A. Donelan, W. J. Pierson, Radar Scattering and Equilibrium Ranges in Wind Generated Waves with Application to Scatterometry, *J. Geophys. Res.*, 1987, **92(5)**: 4971-5029.
29. D. T. Resio, C. E. Long, C. L. Vincent, Equilibrium-range constant in wind-generated wave spectra, *J. Geophys. Res.*, 109, 2004, **109**:C01018.
30. T. Elfouhaily, B. Chapron, K. Katsaros, D. Vandemark, A unified directional spectrum for long and short wind-driven waves, *J. Geophys. Res. Ocean.*, 1997, **102(7)**: 15781-15796.
31. S. V. Hsiao, O. H. Shemdin, Measurements of wind velocity and pressure with wave follower during Marsen, *J.Geophys.Res.*, 1983, **88**: 9841-9849.
32. R. L. Snyder, F. W. Dobson, J. A. Elliott, R. B. Long, Array measurement of atmospheric pressure fluctuations above surface gravity waves, *Journal of Fluid Mechanics,* 1981, **102**: 1-59.

Available online at www.sciencedirect.com

ScienceDirect

Procedia IUTAM 26 (2018) 204–213

Procedia IUTAM

www.elsevier.com/locate/procedia

IUTAM Symposium Wind Waves, 4–8 September 2017, London, UK

General Sea State and Drag Coefficient Observed near Shore in Taiwan Strait

Yuan-Shiang Tsai[a]*, Wang-Ting Chang[b], Chao-Ming Yu[b], Wen-Chang Yang[b]

[a]*National centre for Research On Earthquake Engineering, NARLabs, National centre for Research On Earthquake Engineering, NARLabs 200 Sec. 3, Sinhai Road, Taipei 10668, Taiwan*

[b]*Taiwan Ocean Research Institute, NARLabs, 96 Henan 2nd Road, 80143 Kaohsiung, Taiwan*

Abstract

The general characteristics of wind waves and drag coefficient are studied using the data from the buoy observation near shore in Taiwan Strait. An algorithm of the bulk aerodynamic method using 10-minute mean wind speed and the temperature difference between the air and sea surface was developed to calculate the equivalent wind speed at 10 m in height and the surface friction velocity. The observation shows that the sea states contains a wide range of wave ages driven by the synoptic wind systems, i.e. the strong northeast monsoon in winter and southwest monsoon in summer, mixed with the thermally diurnal variation across the sea-land boundaries. The large-scale winds generate a number of swells with long fetch and the mesoscale circulation perpendicular to the main streams causing wind and wave misalignments. The drag coefficients display considerable scattering around the linear growth formulation along with the increase of neutral wind speed. This is attributed to the dependence of surface roughness on wave ages. The present observation confirms that the drag coefficients are sensitive to the sea state described using the Charnock constant and hence the wave ages.

Peer-review under responsibility of the scientific committee of the IUTAM Symposium Wind Waves.

Keywords: Drag coefficient; surface roughness, diurnal cycle, buoy observation

1. Introduction

The interaction between the atmosphere and ocean is the physical process responsible for the transfer of momentum flux across the air-sea interface. From the microscale turbulent exchange to the macro scale ocean circulation and the global climate change, the surface wind stress τ is the most significant driving force to produce momentum transfer on the sea surface and lead to wave growth. For field experiments with measurement of mean quantities, the bulk aerodynamic scheme [1] is developed to parameterize the sea surface fluxes in which the wind stress is connected to the wind speed at 10 m in height via a drag coefficient with the relation:

2210-9838
Peer-review under responsibility of the scientific committee of the IUTAM Symposium Wind Waves.
10.1016/j.piutam.2018.03.020

$$\tau = \rho_a C_D U_{10}^2 \tag{1}$$

where ρ_a denotes the air density, U_{10} denotes the wind speed at the height of 10 m, and C_D denotes the drag coefficient. The surface wind speed profile in adiabatic condition is modelled in the logarithmic formulation:

$$\mathrm{u(z)} = \frac{u_*}{k}\ln\left(\frac{z}{z_o}\right) \tag{2}$$

where $u_*=(\tau/\rho_a)^{1/2}$ represents the friction velocity, k represents Karman constant, z represents the vertical height, and z_o represents the surface roughness length. In combination of equation (1) and (2) the drag coefficient is therefore expressed as follows:

$$C_{DN} = \left(\frac{u_*}{U_{10N}}\right)^2 = \left(\frac{k}{ln(z_{10}/z_o)}\right)^2 \tag{3}$$

where z_{10} represents 10 m in height and the subscription N represents under the atmospheric neutral stability. Comprehensive studies in terms of drag coefficient have been particularly carried out under the circumstance of neutral stratification. Earlier studies prior to 1975 suggested that the sea surface drag coefficient is constant [2]. Subsequent experiments over the past decades remarked that the drag coefficient increased with the increase of the neural wind speed [2, 3, 4, 5, 6]. A linear relation is formulated with:

$$C_{DN} = (a + bU_{10N}) \times 10^{-3} \tag{4}$$

where a and b are constant coefficient determined from the field or laboratory data. However, the increase of the drag coefficient is not valid in high wind speeds in excess of 40 m/s observed under the action of hurricanes [7].

Equation (3) indicates that the drag coefficient is also the surface roughness dependent. In the circumstance beyond the aerodynamic smooth surface, with the increase of wind speed, small scale wind waves grow and generate a rougher surface to effectively attract the momentum from the airflow. Charnock (1955) proposed that the surface roughness is proportional to the wind stress known as the Charnock relationship

$$z_o = C_h \frac{u_*^2}{g} \tag{5}$$

where C_h denoted the Charnock parameter, and g denoted gravitational acceleration. Charnock parameter was originally given to be a constant value. Using C_h=0.014, equations (2), (3), and (5) are solved under a specific wind speed to give the coefficients in drag coefficient equation (4) for a=0.75 and b=0.067 [3, 8].

However, the values of C_h vary in different observation results ranging from 0.011 to 0.018, which implies that for a given wind speed the surface roughness may be different. The reason is due to that in a practical field the development of wind waves and hence constitution of sea states relate to not only wind speed but other important factors, for example, the limitation of fetch and duration, wind and wave directional misalignment, and coastal shoaling. A sea state is characterised using the waves age C_p/u_* or C_p/U_{10} where C_p represents the phase velocity at the spectral peak of waves. Hence, the surface roughness is suggested to wave age dependent and the Charnock parameter is described using a power law formulation [11]:

$$z_o \frac{g}{u_*^2} = A\left(\frac{C_p}{u_*}\right)^{-B} \tag{6}$$

where A and B represents the constant coefficients. Guan and Xie [4] derived the linear growth of the drag coefficient along with the increase of the wind speed. Their analysis resulted the dependence of drag coefficient on Charnock parameter with a=0.78 and b=0.475$C_h^{1/2}$. The young wind waves with smaller Charnock constant causing larger wind shear than mature waves are explained from the FETCH experiment of Drennan et al. [12].

In the present study, wind and waves were observed using a buoy in Taiwan Strait offshore Changhua Taiwan. The place is well known for strong winds particularly in the winter season. The original objective of this program was to assess the site for establishment of an offshore wind farm. For the geographic position of the Strait, the wind

waves are primarily generated by the seasonal monsoons mixed with the secondary effect of thermal circulation across the sea-land boundaries. This phenomenon have not been fully examined to characterise the local sea states in terms of general sea states and the dependence of drag coefficient on wave ages. The results of the surface parameterizations are used for the engineering practice for wind turbine design. More importantly, the local drag coefficient parameters can improve the prediction accuracy of ocean and wave models, which are very useful for future wind farm operations with regard to wind and wave simulation. Currently the models only employ the drag coefficients interpreted from the 10 m mean wind speed.

2. Site description and buoy system

The wind and waves were observed using a wave following discus buoy with the size of 2.5 m in diameter developed by the Coastal Ocean Monitoring Centre. One year measurement was conducted during the period of August 2012 to July 2013 in Taiwan Strait, 14 km from the coast of Fangyuan Township (120°12′0″, 23°59′54″), Changhua County, in the middle west of Taiwan where the water depth was approximately 40 m. The site was 50 km north of the Tropic of Cancer. Strong solar heating induced diurnal circulation at the sea-land boundaries particularly in summer. Figure 1 shows the location of the experimental site and the buoy system. The Strait exposes to open water facing East China Sea in the northeast direction and South China Sea in the southwest direction, respectively. Hence, swells generated by large-scale trade winds propagating to the site were recorded.

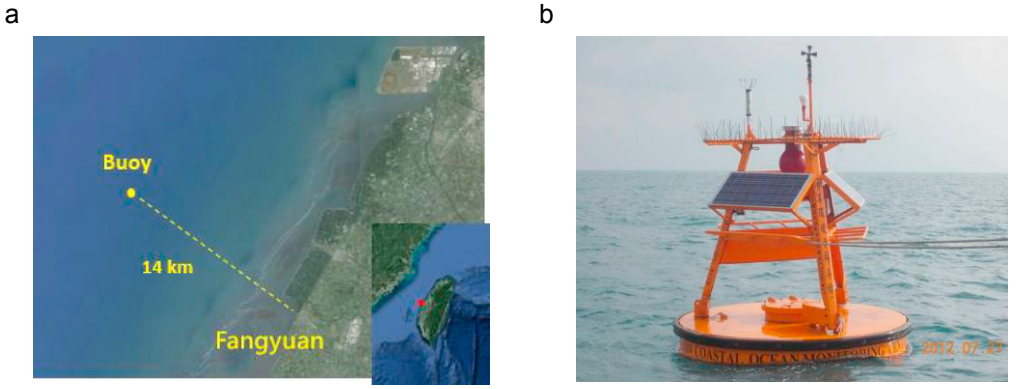

Fig. 1. The observation site and buoy deployed offshore of Fangyuan Township; (a) geographic position of the observation site near shore with a large scale map in right bottom; (b) the buoy system and instrumentations.

The instruments included the sensors to measure the wind speed, air and sea surface temperature, pressure and buoy motions. The wind speed and direction were observed using a two-dimensional ultrasonic anemometer, Gill-1390, and propeller anemometer, Young-05106 at the height of 2.9 m and 3.2 m, respectively. The buoy motions represented by linear accelerations and rotation angles in the three directions were measured using Watson SHR-A 1360-2A-30/105. The component of vertical accelerations was computed to obtain sea surface elevations. Besides, subsurface currents were observed using the ADCP, SonTek ADP0.5. Three solar panels with 80 W in total were employed for the power supply. The data logger simultaneously recorded the wind speed, air and sea temperature, pressure, and buoy motions for the first 10-minute in every hour with a sampling rate of 2 Hz. Mean values of the 10-minute data were transferred to office via wireless communication. Due to the weak sunlight in winter the system was automatically reduced the recording frequency to every four hours in December 2012. However, the sunlight was further weak in January 2013 to cause the power supply complete failure. Besides, the mooring anchored disconnected under the strong wave force in April 2013. The buoy recorded the passage of typhoon Soulik in 13 July 2013 with the wind speed in excess of 20 m/s. However, the typhoon event is excluded in the present study. 7673 10-minute datasets in 10 month observation are available in which the neutrally stratified condition over the sea are studied.

3. Data analysis

3.1. Buoy motion correction

The buoy title and rotation following the sea surface distort measurement results of the instantaneous wind velocity and wave heights. The apparent wind velocities are corrected using the method developed by Edson et al. [13] for which a coordinate transformation matrix was employed to correct the surface motions and obtain true wind velocities. The transform method was also applied for the measured vertical accelerations. The wave elevations are directly calculated from the integration of corrected accelerations. The integration induced a low frequency noise, which was removed using a high-pass filter Hp described as follows:

$$\eta(t) = Hp\left(\iint(\ddot{z}(t)dt)dt\right) \tag{7}$$

where η denoted the surface wave elevation and $\ddot{z}$ denoted the vertical acceleration after the motion correction. The significant wave height was calculated using the zero-up crossing method. The wave direction was assessed from the co-spectrum and quadrature spectrum direction, which was directly given by the buoy measurement system.

3.2. Atmospheric stability

To evaluate the atmospheric stability for the identity of neural wind, the 10-minute mean wind speed and temperature in air and sea were used to compute the bulk Richardson number Ri_b, introduced by Hsu [14] expressed as the following form:

$$Ri_b = \frac{gz_{10}(T_a - T_s)}{(T_a + 273)U_{10}^2} \tag{8}$$

where T_a represented the air temperature and T_s represented the sea temperature, respectively. The dimensionless stability parameter, z/L, where L denotes the Monin-Obukov length, is assessed from Richardson number giving by

$$\begin{cases} z/L = 7.6Ri_b, & T_a < T_s \\ z/L = 6.0Ri_b, & T_a > T_s \end{cases} \tag{9}$$

for unstable and stable condition. The neutral stratification is indicated in the range of $-0.1<z/L<0.1$ [9].

3.3. Surface roughness

For a sea state mixed with wind waves and swells, Taylor and Yelland [15] suggested that wave slopes were appropriate to describe sea surface roughness scaled by the significant wave height with the dimensionless relation:

$$\frac{z_o}{H_s} = 1200\left(\frac{H_s}{L_p}\right)^{4.5} \tag{10}$$

where H_s represented the significant wave height and L_p represented the peak wavelength. The peak wavelength is calculated from the dispersion relationship using wave peak period T_p at the peak frequency of the wave spectrum. Hence, the phase speed of the dominant waves at the spectral peak is $C_p=L_p/T_p$. Because the present observation shows a certain number of swells mixed with young wind waves equation (10) is used to estimate the sea roughness.

3.4. Calculation for U_{10} and u_*

The power law is employed to convert the wind speed at the measurement height at 2.9 m to the equivalent wind speed at 10 m in height described as follows:

$$\frac{U(z_{10})}{U(z_{2.9})} = \left(\frac{z_{10}}{z_{2.9}}\right)^{\alpha} \tag{11}$$

where $U(z_{2.9})$ denotes the reference wind speed at the measurement height 2.9 m and α denotes the power exponent. The surface friction velocity was evaluated using the velocity profile of Monin-Obukhov similarity theory (MOST)

$$u_* = k\mathrm{u(z)}\left(\ln\left(\frac{z}{z_o}\right) - \Psi_m\left(\frac{z}{L}\right)\right)^{-1} \tag{12}$$

where z_o was evaluated from equation (10) and Ψ_m denotes the stability function with the formulation given by [14]

$$\Psi_m(z/L) = \begin{cases} -5z/L, & z/L < 0 \\ 1.0496(-z/L)^{0.4591}, & z/L > 0 \end{cases} \tag{13}$$

Assuming that the vertical wind profile formulated using the power law is equivalent to the diabetic surface boundary layer described by MOST, at the height of 10 m the power exponent can be approximated by

$$\alpha \approx 0.1\phi_m \tag{14}$$

where $\phi_m(z/L)=kz/u_*\partial u/\partial z$ represents the dimensionless wind shear expressed by the following relation:

$$\phi_m(z/L) = \begin{cases} 1 + bz/L, & z/L < 0 \\ (1 - az/L)^P, & z/L > 0 \end{cases} \tag{15}$$

where a=15, b=4.7, and p=-1/4 in the flat and homogeneous terrain [16].

A C++ code was written to compute U_{10} and u_*. Over a general sea surface, Hsu et al. [14] recommended that the power exponent was 0.11, which was used to be an initial value. The power exponent and hence the friction velocity were iteratively solved after the convergence of the power exponent with $|\alpha_1-\alpha_o|<10^{-3}$ where α_1 was the solution of the next iteration of α_o.

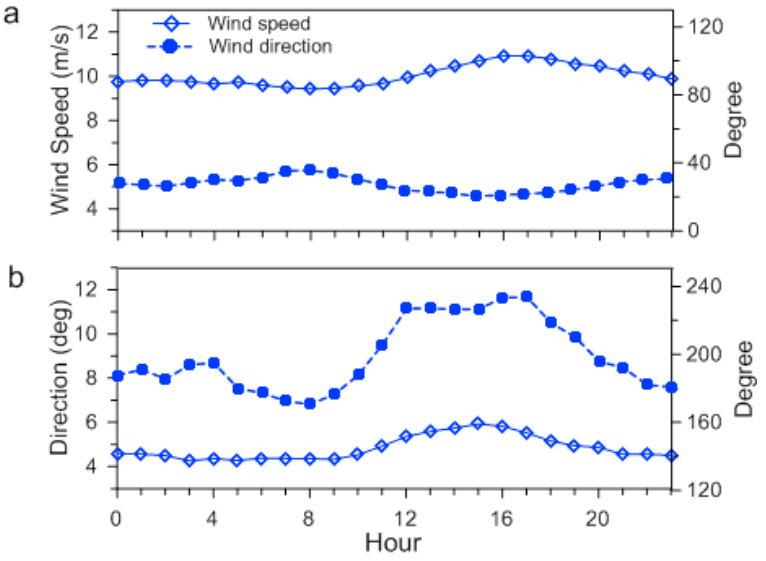

Fig. 2. Influence of thermal circulation on the synoptic winds causing the diurnally periodic motion for wind speed and direction, (a) northeast wind, (b) southwest wind.

4. Results and discussions

4.1. General features of wind and waves

The buoy observation shows that the wind in the Taiwan Strait is driven by two major synoptic frontal systems. The long period from late September to March of the next year is predominated by northeast monsoon which carries strong and cold wind with the maximum wind speed in excess of 20 m/s. In contrast, during the period from May to

August the warm air of southwest wind becomes dominant with the moderate wind speed not exceeding 10 m/s. As shown in figure 1(a) of the right bottom, the winds for these two prevailing directions travel long distance from open waters into the Strait. The generated swells are frequently observed at the observation site.

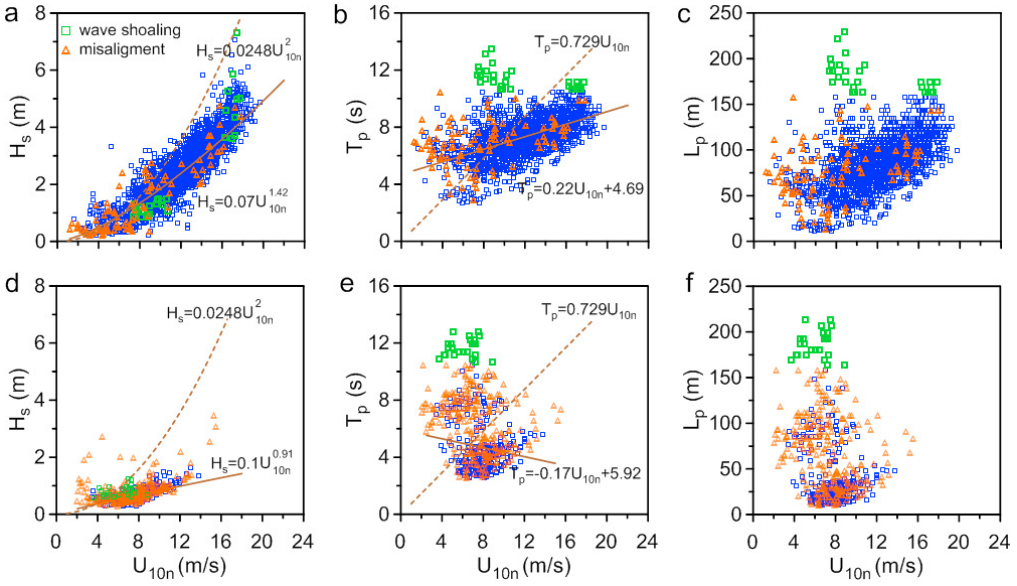

Fig. 3. Observation of wind wave data plotted against 10 m neutral wind speed, U_{10n} for northeast wind (upper row) and southwest wind (lower row), wave shoaling for $L_p/h>4$, misalignment of wind and wave for $|\Delta\theta|>30^o$, solid line: the present curve fitting; dash line, JONSWAP results [6]: (a) significant wave height; (b) wave period at the spectral peak of waves; (c) wavelength at the spectral peak of waves.

Apart from the synoptic weather systems, the thermally stratified mesoscale circulation across sea-land boundaries contributes the secondary effect on the wind patterns. The onshore wind in day and offshore wind in night is approximately perpendicular to the frontal wind. The mixed wind of the two scales is illustrated in figure 2. The daily ensemble average in the wind speed and direction clearly show the diurnal cycle. With the relatively strong wind from the northeast monsoon, the mean wind speed is approximately 10 m/s, however, varying with the amplitude of 1.5 m/s as displayed in figure 2(a). The thermally stratified flow increases the wind speed in day with the maximum wind speed appearing at 16:00 in the afternoon. The wind direction slightly varies within 15^o in one day. This steady wind direction indicates that the sea surface is acted on by the cold wind with a long fetch and duration. In contrast, with the relatively weak wind dominated from the southwest airflow, the mean amplitude increases to 1.7 m/s. The diurnal variation is significant observed for the wind direction with the directional change more than 60^o as shown in figure 2(b). The wind direction is altered by the sea breeze forming the west-southwest wind in day and land breeze forming the south-southeast wind in night. In this aspect of the directional change, the misalignment between wind and waves is substantial and the sea state is usually limited by a short fetch and duration. It is observed that in the absence of the synoptic winds, the mesoscale circulation becomes predominant in the coastal and near shore region. This slight wind speed is generally less than 6 m/s under the stratification condition leading to very young sea state.

Because the mesoscale diurnal cycle substantially influences the wind direction, particularly for the southwest wind, the general sea states are exhibited according to the two synoptic winds. The mean wind directions are limited to $0^o<\theta<45^o$ for northeast wind and $190^o<\theta<235^o$ for the southwest wind. In fact, these two ranges of direction are generally parallel to the coast. The waves travelling in these two directions could have been experienced a long distance movement from the East China Sea or South China Sea, respectively. Figure 3 demonstrates the development of the significant wave height, peak wave period, and peak wavelength depending on the neutral wind speed, U_{10n}. Considering the wave shoaling with $L_p/h>4$ where h denotes the water depth and the substantial misalignment between wind and wave defined with $|\Delta\theta|>30^o$ where $\Delta\theta$ denotes the directional difference between

the wind and waves, the data are distinguished in three groups. As shown in figure 3(a), the significant wave height increases with the increase of the wind speed. For the northeast wind with steady wind direction and stronger wind speed, the surface waves generated are considerably higher than those generated by southwest wind. However, using JONSWAP observation, Cater [16] derived that the relation between H_s and the wind speed is H_s=0.0248U_{10n}^2 which gave significantly larger H_s in the fully developed sea state when compared with the present observations with H_s=0.07$U_{10n}^{1.42}$ for the northeast wind and H_s=0.1$U_{10n}^{0.91}$ for the southwest wind.

The relationship between the peak wave period and neutral wind speed are depicted in figure 3(b). Regarding the surface waves generated by the northeast monsoons, the development of peak wave periods is considerably different from the JONSWAP fetch limit results with linear growth formulation T_p=0.729U_{10n} [16]. The present growth rate of the peak periods is lower, showing short wave periods with U_{10n}<10 m/s, however, longer wave periods in the strong wind speed with U_{10n}>10 m/s. It is likely that the winter sea state contains a certain number of swells which reduces the growth of peak wave periods in terms of the wind speed. For the wind from southwest, the data show distinct three groups with the peak wave periods approximately 2<T_p<6 s for pure wind waves, 6<T_p<10 s for swells, and T_p>10 s for the shoaling waves. The evolution of peak wavelengths calculated from the dispersion relationship using T_p along with the wind speed is given in figure 3(c). The patterns distributed are in analogous to T_p showing three different characterises of waves.

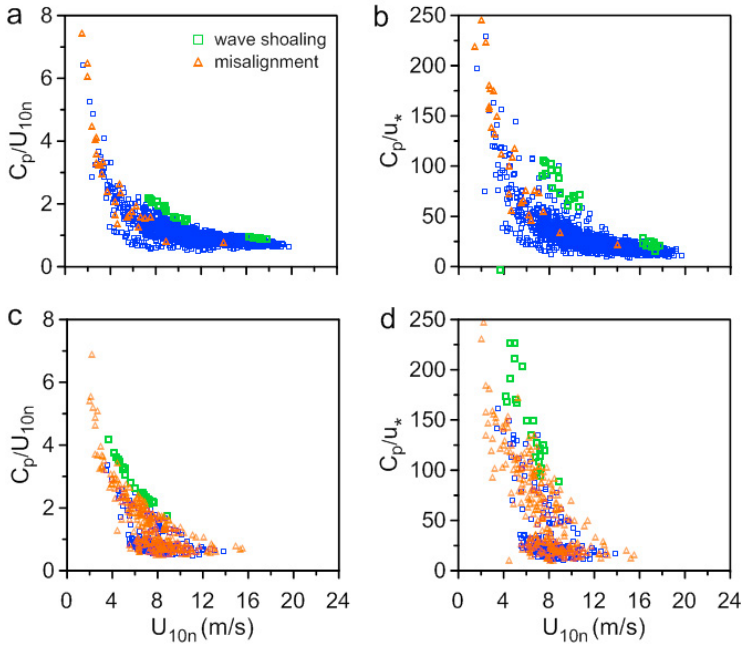

Fig.4. Relation between the wave age and the neutral wind speed at 10 m in height for northeast wind and southwest wind: (a) and (b) wave age represented by C_p/U_{10n} and C_p/u_* for northeast wind, (c) and (d) wave age represented by C_p/U_{10n} and C_p/u_* for southwest wind.

Figure 4 discusses sea state patterns generated by the two large-scale wind systems with northeast wind in figure 4(a) and 4(b) and southwest wind in figure 4(c) and 4(d). A criterion with C_p/U_{10n}=1.2 is used to characterize the wind sea and swell condition. When C_p/U_{10n}<1.2 the state are young and formed with short and steeper wind waves. In contrast, when C_p/U_{10n} >1.2, the sea waves is mature or fully-developed and dominated by long swells [12]. As displayed in figure 4, the wave age decreases with the increase of the wind speed. This implies that under the strong wind action the generated young waves can effectively attract energy from the wind until the waves become fully-developed. Under the northeast wind brought by the cold fronts with the period of several days, the sea states are formed with the mixed young and mature waves. The shoaling waves spreads in the upper bond of the distribution of wave ages. In addition, the wind and wave misalignment is observed in the weak wind speed with large wave ages observed in the termination of the cold front with the wind direction changed from northeast to south wind.

The wind sea, swell and shoaling phenomena are clearly appeared for the southwest wind in figure 4(c) and 4(d) with three individual groups represented by the upper shoaling waves, middle misalignment and mature waves, and lower young waves. The explanation is that the relatively weak wind from southwest in summer is considerably affected by the diurnally thermal stratified flow which is nearly perpendicular to the main stream direction. Hence, the composed wind direction is spatially varied when the wind moves along the near shore area. This results a large amount of wind and wave misalignments because the wave direction cannot immediately response to the change of the wind direction. The directional change also leads to a short duration of wind action and produces the young sea state as shown in figure 4(c) and 4(d) in the lowest groups. Nevertheless, the wind waves generated in a far distance away may still grow to mature waves as given in the middle groups in figure 4(c) and 4(d). Interestingly, the wave age patterns show a gap between the middle and lowest groups just with C_p/U_{10}=1.2 in figure 4(b) at the wave age criteria to classify young and mature waves. Observed from figure 4(d), the gap is located at C_p/u_*≈30-40. The value is close to the HEXOS results showing C_p/u_*≈37-36 with C_p/U_{10}=1.2 [17].

4.2. Roughness length and drag coefficient

In examination of the surface roughness depending on wave ages, the misalignment data shown in figure 4 are not considered because it is difficult to account the wind shear direction along with the wave direction. Also the shoaling waves are not included. The sea state subjects to the two synoptic winds collapse together in the roughness dimensionless form. Figure 5(a) shows the relationship between dimensionless roughness and wave age in comparison with the result of Drennan and Graber [12], who studied the sea surface roughness for developing wind waves with the wave age C_p/u_*<20 formulated with the relationship:

$$\frac{z_o}{\sigma} = C\left(\frac{C_p}{u_*}\right)^{-D} \tag{16}$$

where the coefficient C=13.4 and D=3.4 and σ represents the root mean square of the sea surface elevation. The present result gives C=146 and D=4 for the mixed sea state with a wide range of wave age 8<C_p/u_*<250, C=51 and D=3.66 for the developing sea state with C_p/u_*<30, and C=1380 and D=4.55 for the old sea state with C_p/u_*>30. The multiplicative factor is significant larger and the power exponent is smaller than that of Grennan and Graber [12]. This indicates that the roughness at the observation site is higher in the young waves, however, decaying more quickly to the state of lower roughness in the mature sea. The Charnock parameter depends on the wave age is displayed in figure 5(b). The best regression fitting line makes A=60 and B=2.67 in equation (6), for which the consequence is analogous to the case using the dimensionless parameter σ with a larger multiplier and smaller power exponent when comparing with previous studies with C ranging from 0.8 to 1.89 and D ranging from 1 to 1.7.

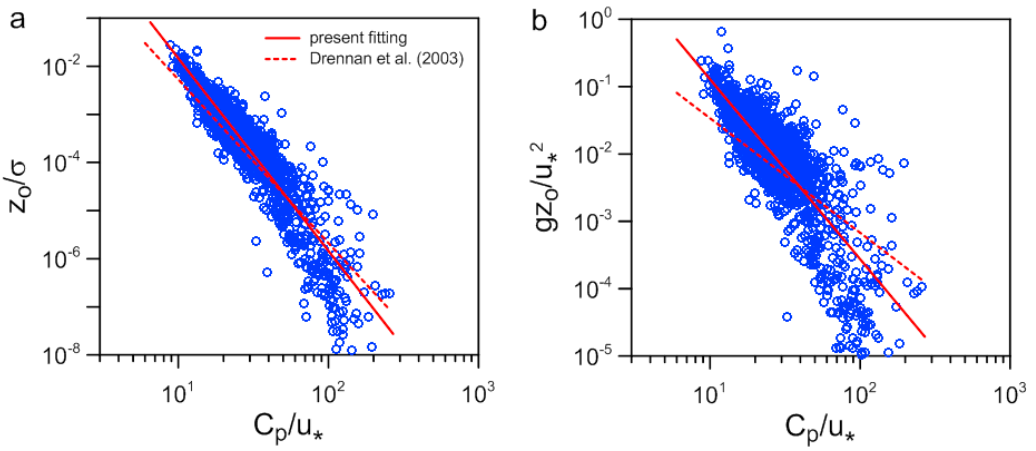

Fig.5. Dimensionless roughness length versus wave age in the mixed sea state without consideration of wave misalignment and shoaling: (a) non-dimensionalized using root mean square of sea surface elevation; (b) shown by Charnock constant.

The observation of the neural drag coefficient C_{DN} related to the wind speed at 10 in height is demonstrated in figure 6(a) in comparison with the previous results of drag coefficient curves. The linear regression fitted to the present data gives the following result:

$$C_{DN} = (0.13 + 0.124U_{10N}) \times 10^{-3} \tag{17}$$

with a=0.13 and b=0.124 which is close to the result of Drennan et al. [18] with a=0.15 and b=0.117. Yelland and Taylor [19] revealed that the drag coefficient increase with the decrease of the wind speed when U_{10N}<6 m/s. However, this phenomenon is unlikely to be observed in the present results.

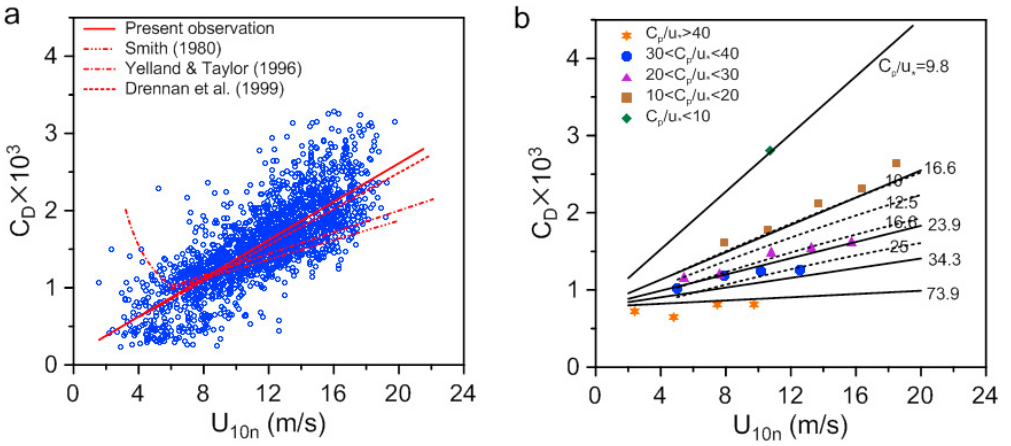

Fig.6. Drag coefficients in terms of the wind speed in the neutral stratification (a) total data points without wave misalignment and shoaling comparing with previous results (b) classified by the five groups of wave ages, solid line: the present curve fitting; dash line, FETCH results [12].

Substantial scattering of the data points is displayed in figure 6(a). This is likely due to the sea state containing a wide range of wave ages. It has been noted that wave ages determine the degree of wave development for which the momentum flux generated over a young wind sea larger than mature sea [12, 17]. The observed drag coefficients were re-examined by distinguishing the wave ages to five groups with C_p/u_*<10, 20>C_p/u_*>10, 30>C_p/u_*>20, 40>C_p/u_*>30, and C_p/u_*>40. In each group, C_{DN} was averaged for 2 m/s bins of the wind speed. Figure 6(b) shows the development of C_{DN} with respect to U_{10N} for each group of the wave age. Significant difference of the drag coefficients between the young and old sea state is observed. This is attributed to the developing wind waves with large steepness, that is, the wave slopes, which increase the transfer of the momentum flux between the air-sea interfaces [20]. Using the formulation of Guan and Xie [4] with a=0.78 and b=0.475$C_h^{1/2}$, the linear five growths subjected to mean wave ages are shown in figure 6(b) with the solid lines and the numeric values of mean wave ages at the right-hand side. The results confirm that the drag coefficient is wave age dependent. The FETCH wind sea data giving the drag coefficient curve in terms of wind speed and wave age [12] are plotted using the dash line in figure 6(b). For the old waves with C_p/u_*=25 the agreement with the present result is reasonably good. However, the discrepancy increases with the decrease of the wave age. For example, with very young wave age C_p/u_*=10, the difference to the FETCH results becomes significant. The growth process of very young waves requires further research.

5. Conclusion

The buoy observation shows the complex sea states generated by two seasonal monsoons with the prevail wind directions form the northeast and southwest in different seasons affected by the thermal circulation across the sea-land boundary. The diurnal cycle wind considerably rotates the direction of the relatively weak southeast airflow, contributing a large number of wind-wave misalignments. In addition, swells are usually observed at the

experimental site because the two large-scale winds with the directions from the open oceans. Hence, the sea state in Taiwan Strait contains a wide range of wave ages from very young waves to mature waves. The study shows that the dimensionless roughness lengths are wave age dependent for which the roughness is larger than previous experiments in the young developing waves. The roughness length rapidly decays with the increase of wave ages in the swell conditions. In spite of the mixed sea state, the mean drag coefficients show a slightly larger growth rate than previous studies with the increase of the mean wind speed in the neutral stratification. However, the scattering of individual dataset reveals that the drag coefficient is influenced by wave ages. The wind stress coefficient significantly increases in the young sea states when compared with those in the mature sea. A linear growth of the drag coefficient to the neutral wind speed depending on the Charnock parameter is in good agreement with the theoretical formulation.

Acknowledgements

The authors wish to express their acknowledgement to National Science Council for the project funding (NSC 99-3113-P-492-002). We are indebted to Coast Ocean Monitoring Centre, National Cheng Kung University for the deployment and maintenance of the buoy.

References

1. C. W. Fairall, J. B. Edson, S. E. Larsen, and P. G. Mesteyer, Inertial-dissipation of air–sea flux measurements: a prototype system using real-time spectral computations, *Journal of Atmospheric and Oceanic Technology*, 1990; **7**: 425-453.
2. S. D. Smith, Wind stress and heat flux over the ocean in gale force winds, *Journal of Physical Oceanography*, 1980; **8**, 709-726.
3. J. R. Garratt, Review of drag coefficients over oceans and continents, *Monthly Weather Review*, 1977; **105**, 915-929.
4. J. Wu, Wind-stress coefficients over sea surface near neutral conditions-A revisit, *Journal of Physical Oceanography*, 1980; **10**, 727-740.
5. W. G. Large and S. Pond, Open ocean momentum flux measurements in moderate to strong winds, *Journal of Physical Oceanography*, 1981; **11**, 324-336.
6. C. Guan, and L. Xie, On the Linear Parameterization of Drag Coefficient over Sea Surface, *Journal of Physical Oceanography*, 2004; **34**, 2847-2851.
7. M. D. Powell, P. J. Vickery, and T. A. Reinhold, Reduced drag coefficient for high wind speeds in tropical cyclones, *Nature,* 2003; **422**, 279-283.
8. V. K. Makin, V. N. Kudryavtsev, C. Mastenbroek, Drag of the sea surface, 1995; *Boundary-Layer Meteorology*, 1995, **73**, 159-182.
9. G. L. Geernaert, K. B. Katsaros, and K. Richter, Variation of the drag coefficient and its dependence on sea state, *Journal of Geophysical Research*, 1986; **91**, 7667-7679.
10. W. Lin, L. P. Sanford, and S. E. Suttles, Drag coefficient with fetch-limited wind waves, *Journal of Physical Oceanography*, 2002; **32**, 186-209.
11. S. D. Smith, R. J. Anderson, W. A. Oost, C. K. Maat, J. Decosmo, K. B. Katsaros, K. L. Davidson, K. Bumke, L. Hasse, and H. Chadwick, Sea surface wind stress and drag coefficients: the HEXOS results, *Boundary-Layer Meteorology*, 1992; 60, 109-142
12. W. M. Drennan and H. C. Graber, On the wave age dependence of wind stress over pure wind seas, 2003; *Journal of Geophysical Research*, **108**, FET 10-1-10-12.
13. J. B. Edson, A. A. Hinton, K. E. Prada, J. E. Hare, and C. W. Fairall, Direct covariance flux estimates from mobile platforms at sea, *Journal of Atmospheric and Oceanic Technology*, 1998; **15**, 547-561.
14. S. A. Hsu, Estimating overwater friction velocity and exponent of power-Law wind profile from gust factor during storms, *Journal of Waterway, Port, Coastal, and Ocean Engineering*, 2003; **129**, 174-177.
15. P. K. Taylor, and M. Y. Yelland, The dependence of sea surface roughness on the height and steepness of the waves, *Journal of Physical Oceanography*, 2001; **31**, 572-590.
16. D. T. J. Cater, Prediction of wave height and period for a constant wind velocity using JONSWAP formulae, *Ocean Engineering*, 1982; **9**, 17-33.
17. S. D. Smith, R. J. Anderson, W A. Oost, C. K. Nico Matt, J. DeCosmo, K. B. Katsaros, K. L. Davidson, K. Bumke, L. Hasse, and H. M. Chadwick, Sea surface wind stress and drag coefficients: The HEXOS results, *Boundary-layer meteorology*, 1992; **60**, 109-142.
18. W. M. Drennan, K. K. Kahma, K. K., and M. A. Donelan, On momentum flux and velocity spectra over waves, *Boundary layer Meteorology*, 1999; **92**, 489–515.
19. M. Yelland and P. K. Taylor, Wind stress measurements from the open ocean, *Journal of Physical Oceanography*, 1996; **25**, 541-558.
20. J. W. Miles, Generation of surface waves by wind, *Applied Mechanics Reviews*, 1997; **50**, R5-R9.

Available online at www.sciencedirect.com

ScienceDirect

Procedia IUTAM 26 (2018) 214–226

Procedia IUTAM

www.elsevier.com/locate/procedia

IUTAM Symposium Wind Waves, 4–8 September 2017, London, UK

Deterministic numerical modelling of three-dimensional rogue waves on large scale with presence of wind

Jinghua Wang[a], Shiqiang Yan[a,]*, Qingwei Ma[a]

[a]*City University of London, Northampton Square, London, EC1V 0HB, United Kingdom*

Abstract

Oceanic rogue waves are a subject of great interest and can cause devastating consequences. Rogue waves are abnormal in that they stand out from the waves that surround them. Rogue waves are often observed accompanied by high wind in reality, and some earlier studies have demonstrated that the energy input due to the wind can enhance the dynamics of the rogue waves, which further causes huge concern about the safety of the human's oceanic activities. Thus it is important, to better understand the mechanisms between the wind-wave interactions and to study the rogue waves with the presence of wind, especially on a three-dimensional large scale. In this study, numerical simulations are performed by using the Enhanced Spectral Boundary Integral (ESBI) method based on the fully nonlinear potential theory, in order to investigate the effects of wind on the rogue waves. The wind effects are introduced by imposing a wind-driven pressure on the free surface, which is empirically formulated based on intensive numerical investigation using multiple-phase Navier-Stokes solver. The results of the simulation confirm that the presented ESBI can produce satisfactory results on the formation of rogue waves under the action of wind. It provides a foresight of modelling rogue waves with presence of wind on a large scale in a phase-resolved fashion, which may motivate relevant studies in the future.

Peer-review under responsibility of the scientific committee of the IUTAM Symposium Wind Waves.

Keywords: Freak wave; Fully nonlinear potential theory; Focusing wave; Spreading sea.

* Corresponding author. Tel.: +44 (0)20 7040 3330.
E-mail address: Shiqiang.yan.1@city.ac.uk

2210-9838
Peer-review under responsibility of the scientific committee of the IUTAM Symposium Wind Waves.
10.1016/j.piutam.2018.03.021

1. Introduction

Rogue waves in the ocean are extreme waves with a maximum height larger than twice the significant wave height (*Hs*) and/or crest larger than 1.2*Hs* [1]. Studies on rogue waves have attracted extensive attentions from the community of engineers and applied scientists over the last few decades. They have been recognized as great threats to marine structures, whereas possible causes resulting their formation can be due to the spatial-temporal focusing, the instability of nonlinear Stokes waves, wave-topography or wave-current interactions, etc. Good reviews of rogue waves are given by Kharif, et al. [1] and Adcock & Taylor [2].

In addition, another factor that cannot be overlooked accounting for rogue wave occurrence is due to the presence of wind according to in-situ observation [3]. However, the question about how rogue waves are generated and/or influenced by wind cannot be completely understood at present. In general, there are two ways to study rogue waves: statistical and deterministic approaches (see discussion in second paragraph of Adcock et al. [31]). The former provides very useful information about the probability of rogue wave occurrence or the wave spectra, contributing to the wave forecasting and hindcasting. Nevertheless, the dynamic features of the waves are important as well and can only be obtained by the latter. To examine the mechanism of energy transferring from wind to waves, deterministic approaches are more straightforward and thus preferred. For example, investigations on wind effects on the rogue wave dynamics have been reported by Giovanangeli, et al. [4], Touboul, et al. [5], Kharif, et al. [6], Yan & Ma [7-9], etc., where it has been demonstrated that wind may dramatically affect the properties of two-dimensional rogue waves. More recently, studies about the effects of wind on rogue waves have been carried out in both laboratory [10-15] and numerical simulations [16-18], which provides significant insights for better understanding the mechanism between wind-wave interactions.

For numerically simulating the interaction between wind and waves, Yan and Ma [7] summarised four existing numerical strategies, in terms of how the wind flow is coupled with the waves. These include (1) a single-phase Navier-Stokes equation to model the air flow, whilst the waves are represented by a pre-described wavy surface [26-30]; (2) the fully nonlinear potential theory (FNPT) models the water waves, in which a wind-excited pressure term imposed on free surface [5-6]; (3) a two-phase Navier-Stokes model to model the air and water flow simultaneously [18]; and (4) a hybrid model combining Strategy 3 and 4 [7,16]. Strategy 1 primarily focuses on the air flow pattern on the pre-described wavy surface and provide useful information on vortex shedding and turbulence near the wavy surface. However, it cannot contribute to the question how the waves are influenced by the air flow. Theoretically, Strategy 3 and 4 can fully couple the air flow and wave motions and, thus, consider the effects of wind on wave field as well as the feedback from the waves to the wind field, the drawback is their low computational efficiency, which is prohibitive especially for large-scale three-dimensional simulations. This paper adopts Strategy 2 with focus on the evolution of waves rather than the variation of the wind field. The FNPT model with external forcing terms to represent the wind-driven pressure on the free surface is applied, following the work done by Touboul, et al. [5], Kharif, et al. [6] and Yan & Ma [9], who have successfully applied the strategy to investigate wind effects on 2D rogue waves generated by using temporal-spatial focus mechanism. However, according to Xiao, et al. [19], to study the weakly non-linear effects which may contribute to rogue waves, the spatial and temporal scale should be commensurate with those of quartet wave-wave interaction. This allows the effect of the Benjamin-Feir like instabilities (see section 4.3 in Janssen [32]), i.e., $L/L_0, T/T_0 \sim O(\varepsilon^{-2})$, where L_0 and T_0 are the peak wave length and peak period, respectively, ε is the wave steepness. Whereas for regional statistics of rogue waves in spreading seas, those scales should be applied to determine the domain size and duration of three dimensional simulations. Though two-dimensional rogue waves considering the wind effects in local area have been discussed in previous studies, investigation on the wind acting on three-dimensional rogue waves in large scale spreading seas is rare. Nevertheless, the nonlinear effects on transversal direction cannot be overlooked. For instance, the soliton envelope as one of the rogue wave prototype, is found to be transversally unstable, which requires consideration of the transverse wave direction [1]. Therefore, in this paper we focus on the wind effects on three-dimensional rogue waves.

As demonstrated by Touboul & Kharif et al [5-6] and Yan & Ma [9], the accuracy of this strategy relies on how the wind-pressure forcing term is formulated. Conventional theories explaining the wave growth subjected to wind, e.g. Miles' theory, usually gives the wind-drag or energy transfer from wind to waves. These can be adopted to model the spectral evaluation but may not be directly applied to the phase-resolved time-domain modelling. Two

existing techniques are used to introduce wind-pressure forcing term on the dynamic boundary condition in this paper. For completeness, they are summarised below.

i) Technique 1: Modified Jeffreys' sheltering theory

According to Kharif and Touboul, et al.[5-6], the air flow separation is responsible for large increments in the form drag, thus the Jeffreys' mechanism is more relevant than the Mile's theory to describe the air sea interaction process. They suggested a modified Jeffreys' sheltering mechanism, which assumes that the energy transform from wind to waves is due to the air flow separation occurring over very steep waves [5], the pressure can be expressed as

$$p_u = \frac{\rho_a}{\rho_w} s(U_w - c)^2 \eta_X \tag{1}$$

where $s = 0.5$ is the sheltering coefficient, ρ_a is the atmospheric density, U_w is the wind velocity, c is the wave phase velocity. The air flow separation often occurs when the local wave slope exceeds a critical value, η_{Xc}, according to the experimental observation. The above equation is only taken into effect when the local wave slope becomes larger than a critical value, i.e., $\eta_{Xmax} \geq \eta_{Xc}$; otherwise, $p = 0$. This means that wind forcing is applied locally in time and space.

ii) Technique 2: Empirical Formula based on CFD modelling

Yan & Ma [7] investigated the wind acting on two-dimensional rogue waves by using a hybrid model combing the FNPT with Navier-Stokes solver, and observed that the air flow separation occurred on the lee side of the rogue wave, as shown in Figure 1(bottom figure), which is consistent with that reported in laboratory [5], justifying the modified Jeffreys' theory, i.e. Eq. (1). However, it was found that the pressure distribution on the free surface described by using the modified Jeffreys' theory (Eq. 1) does not agree well with that numerical results obtained by using the hybrid model, as shown in Figure 1(top figure), especially on the lee side of the rogue wave. The analysis on the correlations between the free surface pressure and local wave profile & wind flow field suggested that the surface elevation, the local slope, air vortex shedding near the wave crest and wave breaking plays important roles. Based on the correlation analysis, Yan & Ma [8] proposed an improved formula by fitting the pressure on free surface in comparison with the CFD simulations, which is given by

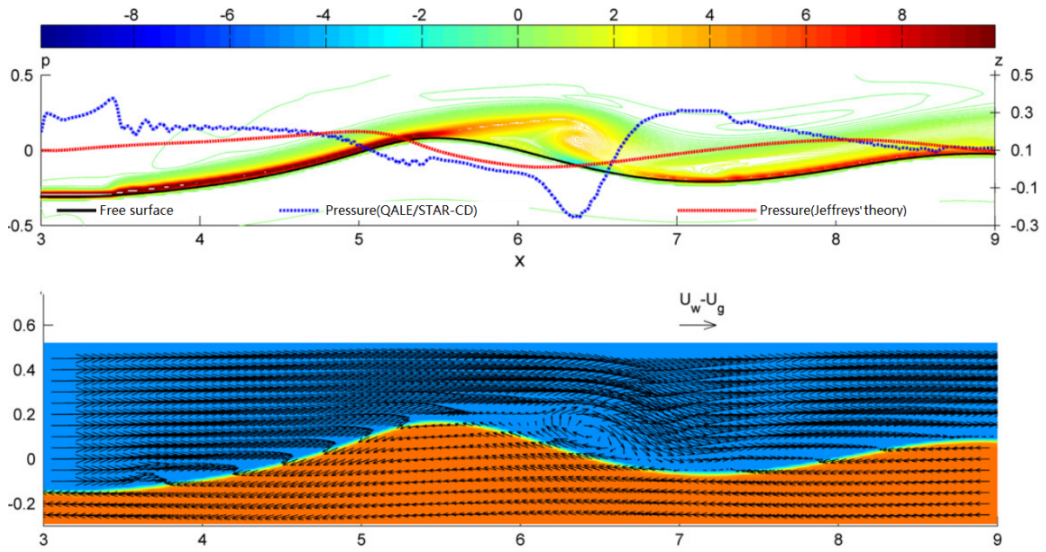

Figure 1. Air flow separation observed in numerical simulation (duplicated from Fig.10a in [7])

$$p_u = \frac{\rho_a}{\rho_w}\left(U_w - c_g - U_c\right)^2\left(C_a k_c \eta + C_b \frac{\partial \eta}{\partial X}\right) + p_{vor} \tag{2}$$

where $C_a = 0.1344u^3 - 0.9394u^2 + 1.9654u - 1.3881$, $C_b = -0.0170u^3 + 0.1369u^2 - 0.3786u + 0.5204$, $u = \left(U_w - c_g - U_c\right)/\sqrt{gd}$, $U_c = C_{cur}U_w$ is the speed of the wind driven current, C_{cur} is usually taken as 0.5%, while c_g is the wave group velocity and d is the water depth, p_{vor} is the additional pressure caused by vortex shedding and wave breaking, and disappears rapidly thus its effects is insignificant and can be neglected during the numerical simulation. According to Yan & Ma [8], Eq. (2) can be accurately used to predict the wind-driven pressure on the free surface for rogue waves in finite depth. It shall be noted that the development of Eq. (2) does not aims to explain the mechanism of wind wave generation/growth, but mainly focus on providing a more accurate wind-driven pressure to be coupled with FNPT model in order to take into account of the wind effects. By using this formulation, the simulations based on FNPT can produce an acceptable pressure distribution that is very close to that in the CFD simulations.

Unlike in our previous work in [8-9], where the Quasi Arbitrary Lagragian-Eulerian Finite Element Method (QALE-FEM) is used to solve the FNPT, in this paper, a more robust method, i.e. the Enhanced Spectral Boundary Integral (ESBI) method [20-24], is employed. Three-dimensional rogue waves in large scale spreading seas with presence of wind are numerical simulated. Both the modified Jeffreys' sheltering mechanism [6], Eq.(1), and the improved air pressure model [8], Eq. (2), are used to impose the wind-driven pressure. It should be noted that the authors are not trying to address the superiority of either the approaches for modelling the wind effect, instead, they will mainly look at the changes of the properties of the rogue waves due to the presence of wind. Note that this study is a preliminary investigation on wind-wave interaction system, thus is a very first step to investigate the wind-wave energy transfer mechanism. It provides the possibilities to extend the local-scale studies to large scales in a phase-resolved manner, and systematic investigations will be carried out in the future.

2. Numerical model and validation

2.1. Formulations of the ESBI

The fully nonlinear Enhanced Boundary Integral (ESBI) method is employed to simulate rogue waves under wind action. The method is well documented in [20-24], thus details are omitted here. However, the main formulations are briefed for completeness of the paper.

To model gravity surface waves on a irrotational and inviscid flow, the free surface boundary conditions can be written as

$$\frac{\partial \eta}{\partial T} - V = 0 \tag{3}$$

$$\frac{\partial \tilde{\phi}}{\partial T} + g\eta + p + \frac{1}{2}\left(\left|\nabla\tilde{\phi}\right|^2 - \frac{\left(V + \nabla\eta\cdot\nabla\tilde{\phi}\right)^2}{1+|\nabla\eta|^2}\right) = 0 \tag{4}$$

where η and $\tilde{\phi}$ are the free surface and velocity potential at free surface, respectively, ∇ the horizontal gradient operator, $V = \partial\phi/\partial n\sqrt{1+|\nabla\eta|^2}$, n is the unit vector normal to the surface pointing outwards, p is the pressure forcing term imposed on free surface to model wind effects, and g is the gravitational acceleration. The above equation can be reformulated as the skew-symmetric prognostic equation, i.e.,

$$\frac{\partial \boldsymbol{M}}{\partial T} + \Lambda\boldsymbol{M} + \boldsymbol{P} = \boldsymbol{N} \tag{5}$$

where

$$\boldsymbol{M}=\begin{pmatrix} KF\{\eta\} \\ \frac{K\Omega}{g}F\{\tilde{\phi}\} \end{pmatrix},\ \Lambda=\begin{bmatrix} 0 & -\Omega \\ \Omega & 0 \end{bmatrix},\ \boldsymbol{P}=\begin{pmatrix} 0 \\ \frac{K\Omega}{g}F\{p\} \end{pmatrix},$$
$$\boldsymbol{N}=\begin{pmatrix} K\left(F\{V\}-KF\{\tilde{\phi}\}\right) \\ \frac{K\Omega}{g}F\left\{\frac{1}{2}\left[\frac{\left(V+\nabla\eta\cdot\nabla\tilde{\phi}\right)^2}{1+|\nabla\eta|^2}-\left|\nabla\tilde{\phi}\right|^2\right]\right\} \end{pmatrix} \tag{6}$$

where $F\{*\}=\int * e^{-i\boldsymbol{K}\cdot\boldsymbol{X}}d\boldsymbol{X}$ is the Fourier transform and $F^{-1}\{*\}$ denote the inverse Fourier transform, $\boldsymbol{K}$ is the wave number in Fourier space and $K=|\boldsymbol{K}|$, $\Omega=\sqrt{gK}$. The solution to Eq.(5) can be given by

$$\boldsymbol{M}(T)=e^{-\Lambda(T-T_0)}\left[\boldsymbol{M}(T_0)+\int_{T_0}^{T}e^{\Lambda(T-T_0)}(\boldsymbol{N}-\boldsymbol{P})dT\right] \tag{7}$$

where

$$e^{\Lambda\Delta T}=\begin{bmatrix} \cos\Omega\Delta T & -\sin\Omega\Delta T \\ \sin\Omega\Delta T & \cos\Omega\Delta T \end{bmatrix} \tag{8}$$

Meanwhile, the evaluation of V can be achieved by using the boundary integral equations, and it can be split into four parts in terms of different degrees of nonlinearities, i.e., $V=V_1+V_2+V_3+V_4$, where

$$V_1=F^{-1}\left\{KF\{\tilde{\phi}\}\right\} \tag{9}$$

$$V_2=-F^{-1}\{KF\{\eta V_1\}\}-\nabla\cdot\left(\eta\nabla\tilde{\phi}\right) \tag{10}$$

$$V_3=F^{-1}\left\{\frac{K}{2\pi}F\left\{\int\tilde{\phi}'\left[1-\frac{1}{(1+D^2)^{3/2}}\right]\nabla'\cdot\left[(\eta'-\eta)\nabla'\frac{1}{R}\right]d\boldsymbol{X}'\right\}\right\} \tag{11}$$

$$V_4=F^{-1}\left\{\frac{K}{2\pi}F\left\{\int\frac{V'}{R}\left(1-\frac{1}{\sqrt{1+D^2}}\right)d\boldsymbol{X}'\right\}\right\} \tag{12}$$

and $R=|\boldsymbol{X}'-\boldsymbol{X}|$ is the horizontal distance between source point and evaluated point, and $D=(\eta'-\eta)/R$. Note that the dominant part of V_4 can be further written into third order convolutions, of which the calculation is fast owing to the Fast Fourier Transform (FFT). Otherwise, the estimation of the remaining integration part of V_4 and V_3 are relatively slow. Later, Wang & Ma [24] suggested three techniques to improve the efficiency of the model, where a new de-singularity method, a new de-aliasing approach and convolutions up to 7th order for evaluating V are introduced. For simplicity, details are omitted here but can be found in aforementioned papers.

To model the wind effects, pressure p can be given by either Eq.(1) or (2). However, Eq.(1) or (2) are designed for two-dimensional problems, where a uni-directional wave is subjected to a wind following the direction of the wave propagation. To extend that to directional waves, where the wind direction is the same as the main wave direction, the pressure can be estimated by using $p=p_u+p_{trs}$, where p_{trs} is the pressure due to the transversal variation of the surface and surface gradient. Nevertheless, due to that the drag effects on this direction is neglectable when the wind direction is the same with the main wave direction, it can be neglected during the simulation. By doing so, the ESBI method incorporating Eq. (1) is abbreviated as 'ESBI-T1', and Eq. (2) as 'ESBI-T2'. Note that the water depth is infinite, so that $u=0$, $C_a=-1.3881$, $C_b=0.5204$ in Eq. (2).

2.2. Validations

To demonstrate the accuracy of the ESBI-T1/2 for simulating rogue waves with presence of wind, two cases are considered here. In these cases, the rogue waves are generated by using different mechanisms, including the modulational instability and spatial-temporal focusing wave. The numerical results predicted by ESBI are compared with the experimental and/or numerical results available in the public domain.

2.2.1 Modulation instability

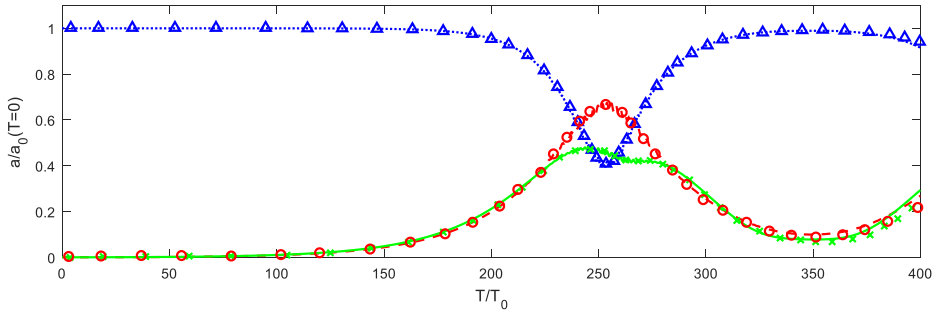

(a) Without wind presence

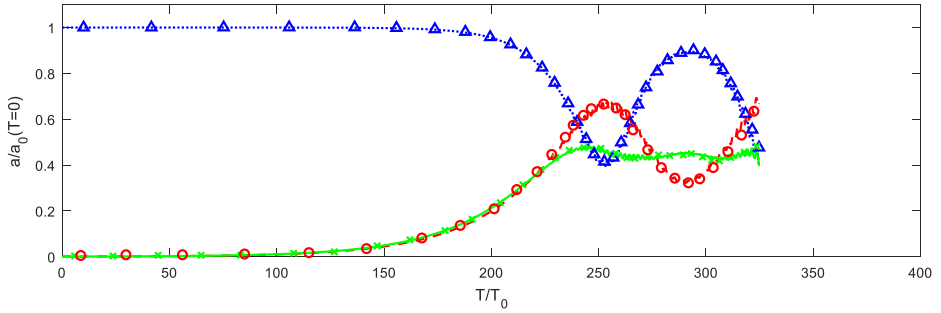

(b) With wind presence

Figure 2. Amplitude ratio against time. Blue: the carrier wave; Red: sub-harmonic mode; Green: the super-harmonic mode. Lines denote the ESBI-T1 and 'ΔXO' in Kharif, et al. [6].

The numerical model is firstly validated through comparing with the FNPT (HOS) results in Kharif, et al. [6], where a modulation instability case of five-wave perturbation to the uniform Stokes wave train is simulated. The steepness of the carrier waves equals to 0.11 and the side bands is 0.1% of that. The simulation is performed by using the ESBI-T1 and $\eta_{Xc} = 0.4$, i.e. the same wind-driven pressure model used by [6].

The ratio of the amplitude, i.e., the amplitude of individual mode over that of the carrier waves, against time without wind presence is shown in Figure 2(a) while with wind in Figure 2(b). Furthermore, the comparison of the free surface spatial distribution at the same time instant is shown in Figure 3. It can be found that the amplitude ratio and the free surface obtained by using the ESBI agree very well with that reported in Kharif, et al. [6]. This indicates that the ESBI can be accurately used to simulate the rogue waves due to modulation instability with wind presence.

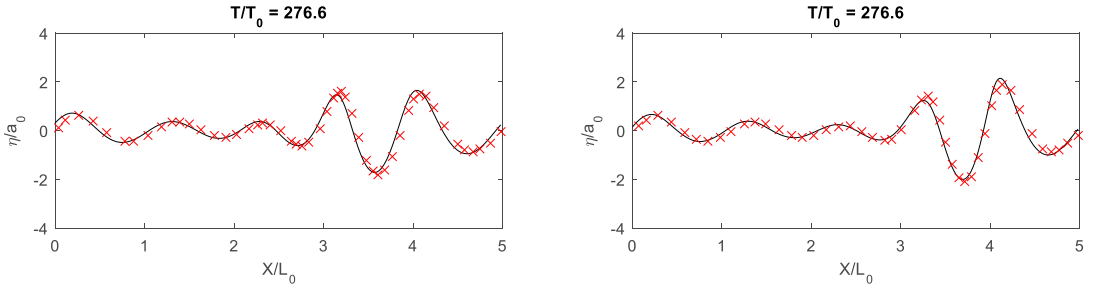

(a) Without wind presence (b) With wind presence

Figure 3. Free surface spatial distribution. 'Black line': ESBI-T1; 'Red X': Kharif, et al. [6].

2.2.1 Spatial-temporal focusing wave

The numerical model is then validated through comparing its predictions with the results obtained in the laboratory by Touboul, et al. [5], in which the focusing wave is generated using the spatial-temporal focusing mechanism and wind velocity is 6 m/s. Simulations by using both ESBI-T1 and ESBI-T2 are performed, where the $\eta_{Xc} = 0.5$. The variation of the amplification factor, $A(X) = H_{max}(X)/H_{ref}$, where H_{max} is the maximum wave height recorded at location X, and H_{ref} is the mean wave height at the probe 1m away from the wave maker, predicted using the ESBI are presented in Fig. 4, together with the experimental data[5]. It is found that without the wind, the ESBI successfully predicted the variation of $A(X)$ in space and the results agreed very well with experiment data. With the presence of wind, both ESBI-T1 and ESBI-T2 reasonably capture the changes of $A(X)$ behind the focusing point, although slight differences between the numerical and experimental results were observed. It implies that both ESBI-T1 and ESBI-T2 can give acceptable predictions of the amplification factor and thus can be used for modelling the focusing wave with wind presence.

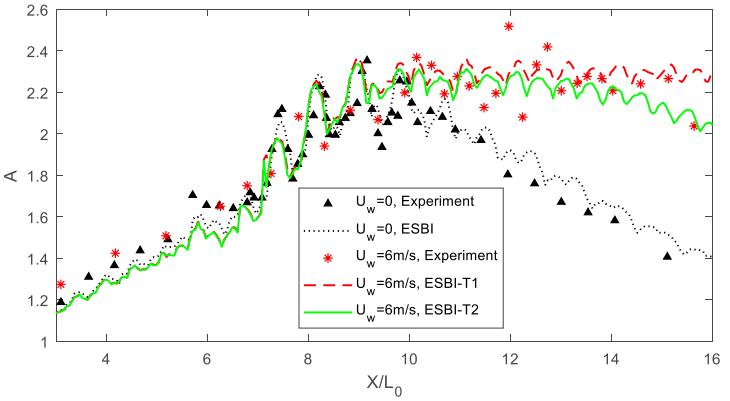

Figure 4. Comparison of the amplification factor

3. Results and discussion

The validation cases presented in the previous section conclude the results obtained by using the ESBI model are satisfactory, which implies that the ESBI model can deliver reliable results for the purpose of this study. In this section, it is employed to explore the wind effects on rogue waves in spreading seas. The computational domain covers 32×32 peak wave lengths and is resolved into 1024×1024 collocation points, which for example corresponding to a domain size of 23km^2 considering a typical wave length 150m in the North Sea. A convergent test indicates that the current resolution is sufficient to demonstrate the local effects of wind on the rogue waves

modelled by using the focusing wave technique in a short time window, after comparing with the results produced by using further refinement of the mesh (2048×2048) (the error of the maximum surface elevation is about 1.3%). The JONSWAP spectrum with $k_0 H_s = 0.3$ (k_0 the peak wave number) and peak enhancement factor $\gamma = 3$ are employed, where the spreading function $G(\theta) = 2/\pi \cos^2(\theta)$ is adopted.

A focusing wave is embedded in the random background waves, by using the method suggested by Wang, et al. [25], where the spectrum is split into three parts, i.e., a transient part, a background part and a correction part. The rogue wave is then embedded by the phase coherence of the transient part, while the spectral shape of the JONSWAP configuration is preserved. Here we only use 1% of the total spectral energy to generate the focusing waves. Since the sheltering mechanism is only effective within a limited time window, the duration of the simulation is made lasting for 20 peak periods, where the focusing occurs at the 10th peak period at the centre of the computational domain. To have a glance at the spatial scale of the simulation, an illustration of the free surface at the focusing time without presence of wind is shown in Figure 5.

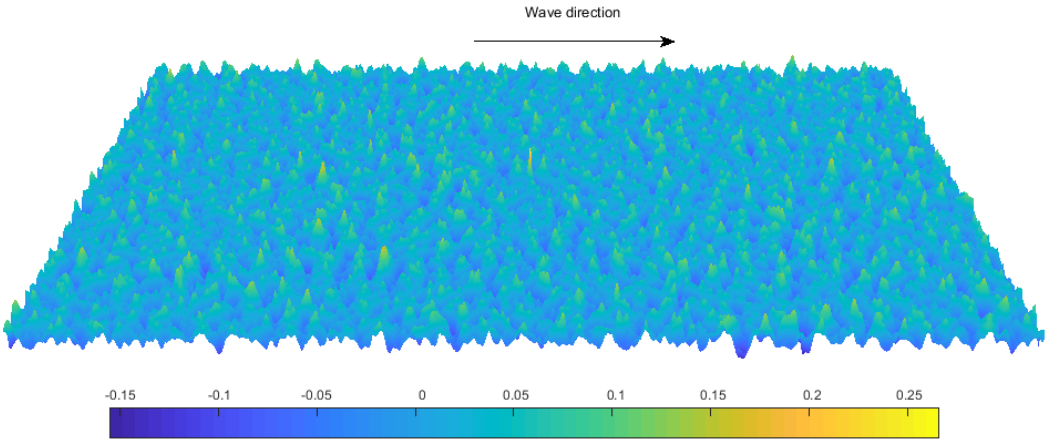

Figure 5. Illustration of the free surface spatial distribution

Three cases with different magnitude of wind speed are considered, i.e., $U_w/c_0 = 4$, 4.5 and 5, where c_0 is the wave phase speed corresponding to the peak component, and $\eta_{Xc} = 0.35$. The simulations without the presence of wind are also performed for comparison, while the cases with wind effects are simulated by using both the ESBI-T1 and ESBI-T2. Note that wave broke in the case $U_w/c_0 = 5$ by using the ESBI-T2 causing the simulation to terminate early.

Due to the nonlinearities, the real focusing point and time will be shifted from the specified ones. Therefore, a zoom in look at the free surface spatial distribution at the real focusing time are displayed in Figure 6. A detailed look along the longitudinal and cross sections are displayed in Figure 7.

The results by using both the ESBI-T1 and ESBI-T2 indicate that the maximum crest height of the rogue wave is enlarged due to the wind input as shown in Figure 7(a)(c)(e), as well as the width in cross direction as shown in Figure 7(b)(d)(f). This broadening of the crest is presumably due to the local nonlinear effects [33,34], which is triggered by the local enhancement of waves by the wind. To better examine the magnitude of enlargement, the crest ratio at focusing, i.e., the maximum surface elevation with wind over that without wind, in terms of the wind speed is presented in Figure 8(a), while the energy ratio, i.e., total energy at focusing time against that at initial time, is given in Figure 8(b). It can be found that the crest ratio gradually increases with the increase of the wind speed, as well as the energy ratio, which is understandable as stronger wind can lead to higher drag before breaking occurs and drag is saturated [13].

In addition, it is noted that the crest ratio and energy ratio predicted by using the ESBI-T1 is lower than that by using ESBI-T2. The reason is that, using the modified Jeffreys' theory [5] can lead to underestimation of the

maximum elevation compared with the CFD simulations where the wind effects are directly modelled, no matter how the critical surface gradient is selected from the range [0.3, 0.4] (see discussions in Yan & Ma [8]).

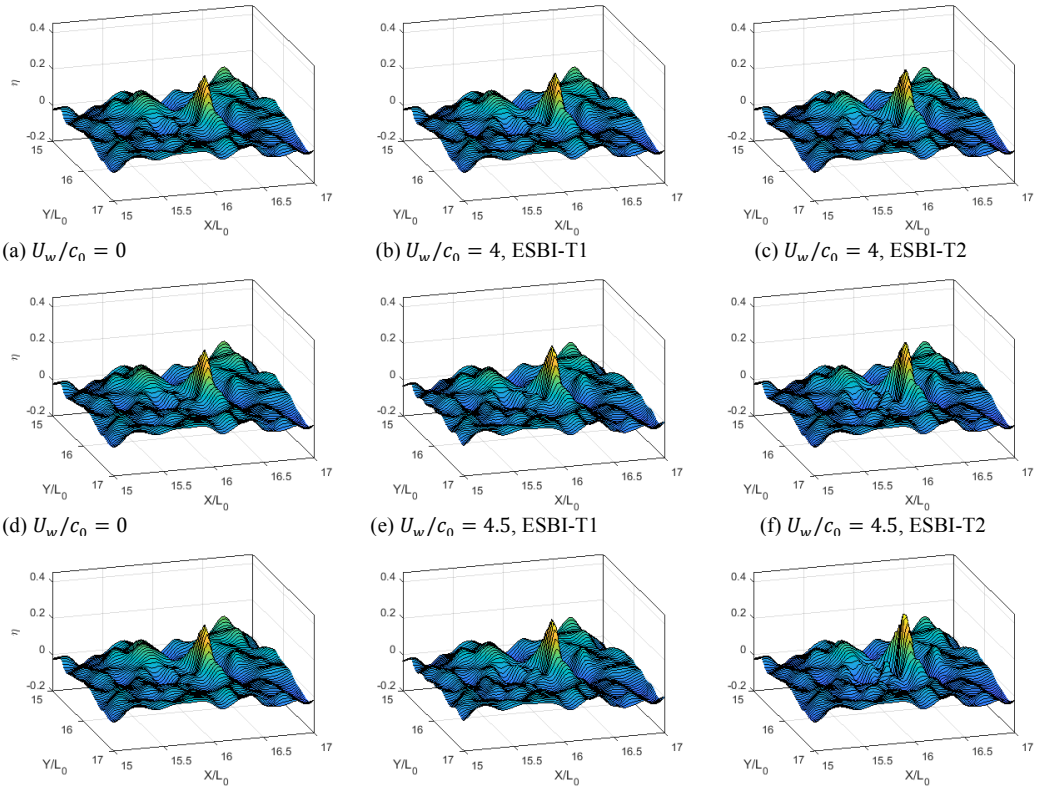

(a) $U_w/c_0 = 0$ (b) $U_w/c_0 = 4$, ESBI-T1 (c) $U_w/c_0 = 4$, ESBI-T2

(d) $U_w/c_0 = 0$ (e) $U_w/c_0 = 4.5$, ESBI-T1 (f) $U_w/c_0 = 4.5$, ESBI-T2

(g) $U_w/c_0 = 0$ (h) $U_w/c_0 = 5$, ESBI-T1 (i) $U_w/c_0 = 5$, ESBI-T2

Figure 6. Comparison of the free surface at focusing

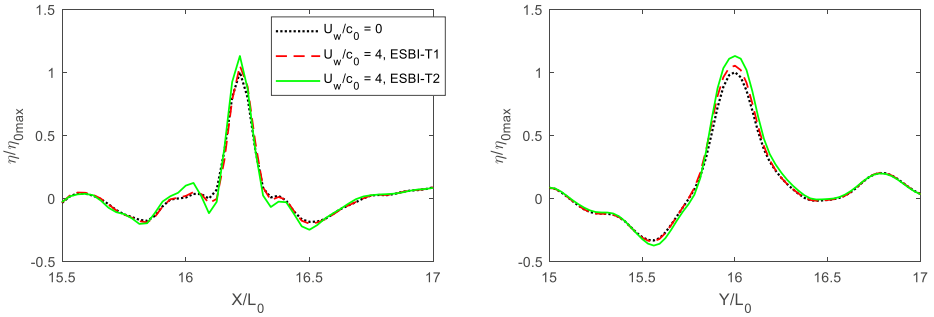

(a) $U_w/c_0 = 4$ longitudinal section (b) $U_w/c_0 = 4$ cross section

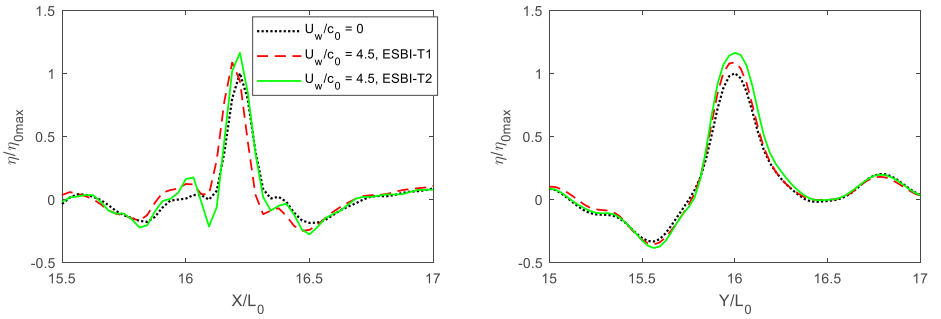

(c) $U_w/c_0 = 4.5$ longitudinal section (d) $U_w/c_0 = 4.5$ cross section

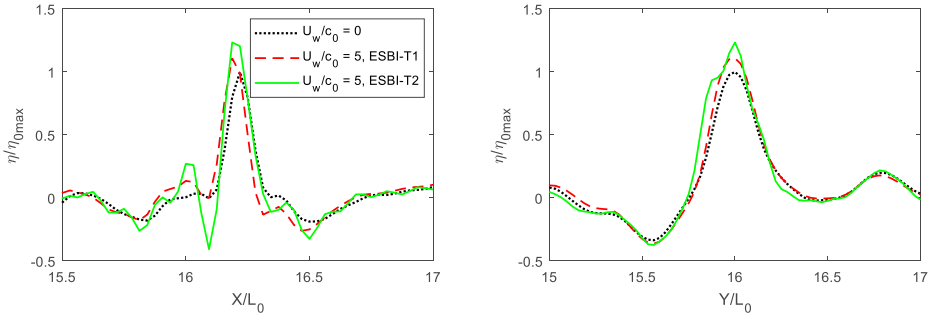

(e) $U_w/c_0 = 5$ longitudinal section (f) $U_w/c_0 = 5$ cross section

Figure 7. Comparison of the section surface profiles

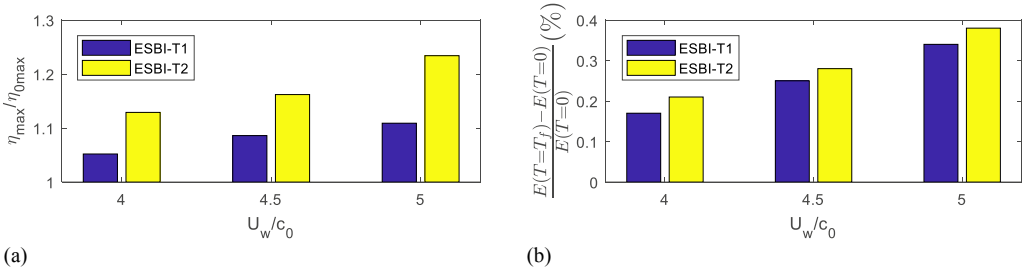

(a) (b)

Figure 8. Crest ratio (a) and energy ratio (b) at focusing against wind speed

Furthermore, another interesting comparison of the energy ratio evolving in time is shown in Figure 9, from which it can be observed that the total energy in the simulations by using the ESBI-T1 increases suddenly during the focusing stage, and remain constant after de-focusing, while in the ESBI-T2 simulations, the total energy gradually grows over time. This is because the pressure forcing term is not acting on the free surface unless the maximum gradient exceeds the specified value by using the ESBI-T1. However, there is no such assumption and the pressure keeps acting on the free surface during the wave propagation by using the ESBI-T2. In addition, the rate of the energy variation increases significantly when focusing wave occurred in the ESBI-T2 simulations, as can be observed by looking at the slope of the green solid line in Figure 9(b).

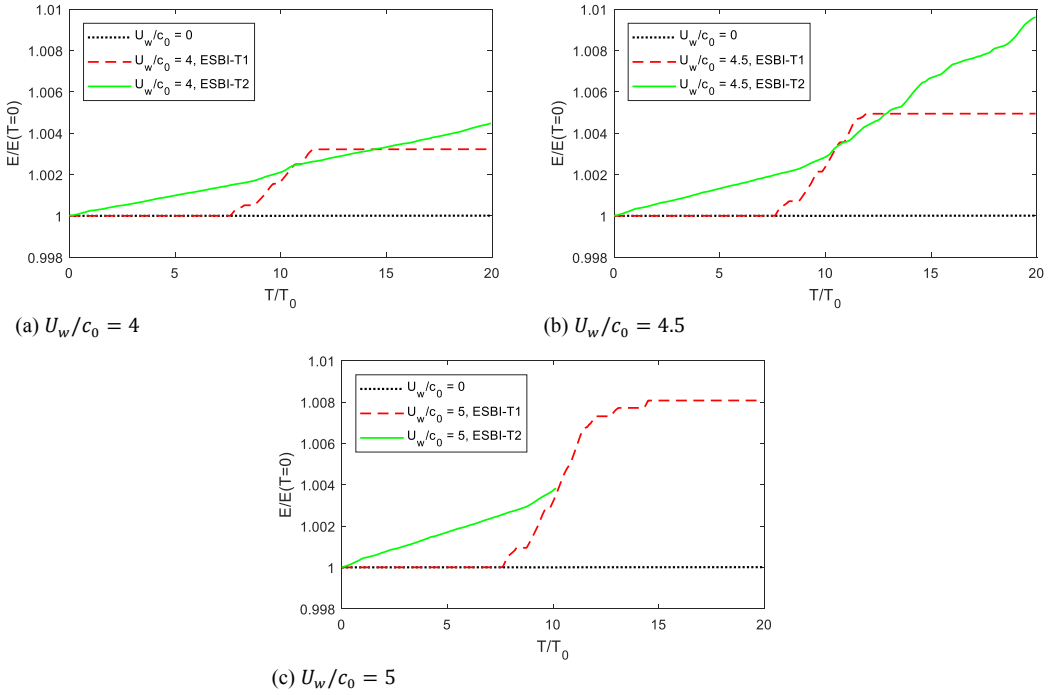

(a) $U_w/c_0 = 4$ (b) $U_w/c_0 = 4.5$

(c) $U_w/c_0 = 5$

Figure 9. Comparison of the energy ratio

Moreover, the real focusing time and location are extracted and examined. It is observed that the focusing time is shifted earlier by the wind in the simulation by using the ESBI-T1, and remain the same despite of the increase of the wind speed. On the contrary, the focusing time is postponed by the wind in the simulations by using the ESBI-T2, where higher wind speed causes further delay. Meanwhile, the focusing location are pushed to the upstream in both the simulations of the ESBI-T1 and ESBI-T2. However, further investigations need to be carried out in order to confirm this observation, as the initially specified focusing time and location can both affect the results as pointed out by Yan & Ma [9].

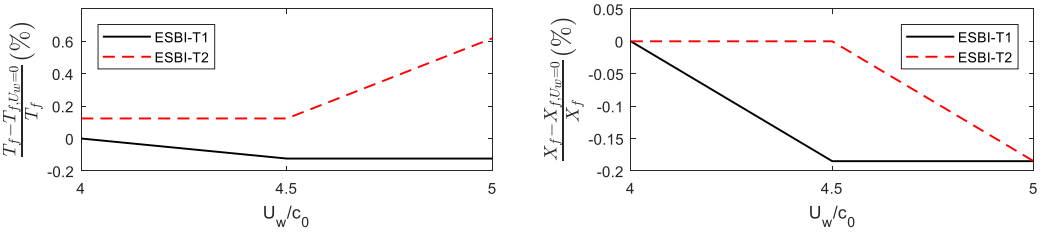

(a) (b)

Figure 10. Shift of focusing time (a) and location (b) against wind speed

4. Conclusions

In this paper, three-dimensional rogue waves on large scale (32×32 peak wave lengths which is equivalent to 23km^2 considering a typical wave length 150m in the North Sea) with the presence of wind are simulated in a phase-resolved manner by using the Enhanced Spectral Boundary Integral method based on the fully nonlinear potential theory. The wind effects are modelled by using the techniques suggested by Touboul, et al. [5] and Yan & Ma [8]. The results by using both the techniques indicate that higher wind speed produces rogue waves with larger crests

and more energy input. However, the results by using the technique by Touboul, et al. [5] shows a slightly lower maximum crest height and total energy compared with that by using the technique by Yan & Ma [8]. In addition, the focusing time and the location of the rogue waves are also shifted compared with that without the presence of wind. However, only waves with an underlying JONSWAP spectrum are considered, while the range of wind speed is very limited. The conclusion may change if these conditions are different. More tests on a wider range of input parameters will be carried out in the future.

Acknowledgements

The authors gratefully acknowledge the financial support of EPSRC, UK (EP/N006569/1, EP/N008863/1 and EP/M022382/1) and DST-UKIERI project (DST-UKIERI-2016-17-0029).

References

1. C. Kharif, E. Pelinovsky and A. Slunyaev, Rogue Waves in the Ocean, Berlin Heidelberg: Springer-Verlag, 2009.
2. T. A. A. Adcock and P. H. Taylor, The physics of anomalous ('rogue') ocean waves, *Reports on Progress in Physics,* 2014; **77**(10): 105901.
3. N. Mori, P. C. Liu and T. Yasuda, Analysis of freak wave measurements in the Sea of Japan, *Ocean Engineering,* 2002; **29** (11): 1399-1414.
4. J. P. Giovanangeli, C. Kharif and E. Pelinovski, Experimental study of the wind effect on focusing of transient wave groups, *arXiv preprint physics,* 2006; *0607010*.
5. J. Touboul, J. P. Giovanangeli, C. Kharif and E. Pelinovsky, Freak waves under the action of wind: experiments and simulations, *European Journal Mechanics B/Fluid,* 2006; **25**: 662-676.
6. C. Kharif, J. P. Giovanangeli, J. Touboul, L. Grare and E. Pelinovsky, Influence of wind on extreme wave events: experimental and numerical approaches, *J. Fluid Mech.,* 2008; **594**: 209-247.
7. S. Yan and Q. W. Ma, Numerical simulation of interaction between wind and 2D freak waves, *European Journal of Mechanics-B/Fluids,* 2010; **29** (1): 18-31.
8. S. Yan and Q. W. Ma, Improved model for air pressure due to wind on 2D freak waves in finite depth, *European Journal Mechanics B/Fluid,* 2011; **30**: 1-11.
9. S. Yan and Q. W. Ma, Numerical study on significance of wind action on 2-D freak waves with different parameters, *Journal of Marine Science and Technology,* 2012; **20**(1): 9-17.
10. K. Iwano, N. Takagaki, R. Kurose and S. Komori, Mass transfer velocity across the breaking air–water interface at extremely high wind speeds, *Tellus B: Chemical and Physical Meteorology,* 2013; **65** (1): 21341.
11. A. Chabchoub, N. Hoffmann, H. Branger, C. Kharif and N. Akhmediev, Experiments on wind-perturbed rogue wave hydrodynamics using the Peregrine breather model, *Physics of Fluids,* 2013; **25(**10): 101704.
12. N. Takagaki, S. Komori and N. Suzuki, Estimation of friction velocity from the wind-wave spectrum at extremely high wind speeds, *IOP Conference Series: Earth and Environmental Science ,* 2016; **35(**1): 012009.
13. N. Takagaki, S. Komori, N. Suzuki, K. Iwano and R. Kurose, Mechanism of drag coefficient saturation at strong wind speeds, *Geophysical Research Letters,* 2016; **43(**18): 9829-9835.
14. A. Toffoli, D. Proment, H. Salman, J. Monbaliu, F. Frascoli, M. Dafilis, E. Stramignoni, R. Forza, M. Manfrin and M. Onorato, Wind generated rogue waves in an annular wave flume, *Physical Review Letters,* 2017; **118(**14): 144503.
15. D. Eeltink, A. Lemoine, H. Branger, O. Kimmoun, C. Kharif, J. Carter, A. Chabchoub, M. Brunetti and J. Kasparian, Spectral up-and downshifting of Akhmediev breathers under wind forcing, *Physics of Fluid,* 2017; **29**(10): 107103.
16. X. Hao and L. Shen, Numerical investigation of energy transfer in coupled wind and wave system, In *APS Meeting Abstracts*, Portland, Oregon, 2016.
17. T. Li and L. Shen, Numerical study of wind-wave generation at the initial stage, *Bulletin of the American Physical Society,* Denver, Colorado, 2017.
18. Z. Yang, S. Tang, Y. H. Dong and L. Shen, Numerical study of wind over breaking waves and generation of spume droplets, *Bulletin of the American Physical Society*, Denver, Colorado, 2017.
19. W. Xiao, Y. Liu, G. Wu and D. K. P. Yue, Rogue wave occurrence and dynamics by direct simulations of nonlinear wave-field evolution, *J. Fluid Mech.,* 2013; **720**: 357-392.
20. D. Clamond and J. Grue, A fast method for fully nonlinear water-wave computations, *J. Fluid Mech.,* 2001; **447**: 337-355.
21. D. Fructus, D. Clamond, J. Grue and O. Kristiansen, An efficient model for three-dimensional surface wave simulations Part I: Free space problems, *Journal of Computational Physics,* 2005; **205**: 665-685.
22. D. Clamond, D. Fructus, J. Grue and O. Kristiansen, An efficient model for three-dimensional surface wave simulations. Part II: Generation and absorption, *Journal of Computational Physics,* 2005; **205**: 686-705.

23. J. Grue, Computation formulas by FFT of the nonlinear orbital velocity in three-dimensional surface wave fields, *J. Eng. Math.,* 2010; **67**:55-69.

24. J. Wang and Q. W. Ma, Numerical techniques on improving computational efficiency of Spectral Boundary Integral Method, *International Journal for Numerical Methods in Engineering,* 2015; **102**(10):1638-1669.

25. J. Wang, S. Yan and Q. W. Ma, An Improved Technique to Generate Rogue Waves in Random Sea, *Computer Modeling in Engineering & Sciences,* 2015; **106(**4): 263-289.

26. V. De Angelis, P. Lombardi, S. Banerjee, Direct numerical simulation of turbulent flow over a wavy wall, *Physics of Fluids*, 1997; **9**(8): 2429-2442.

27. P. P. Sullivan, J. C. McWilliams and C. Moeng, Simulation of turbulent flow over idealized water waves, *Journal of Fluid Mechanics*, 2000; **404**: 47-85.

28. P. P. Sullivan, Turbulent flow over water waves in the presence of stratification, *Physics of Fluids*, 2002; **14**(3): 1182-1195.

29. P. P. Sullivan, J. B. Edson, J. C. McWilliams and C. Moeng, Large-eddy simulations and observations of wave-driven boundary layers, In *Proc. 16th Symposium on Boundary Layers and Turbulence*, Portland, ME, 2004.

30. A. Nakayama and K. Sakio, Simulation of Flows over Wavy Rough Boundaries. *Annual Research Briefs, Center for Turbulence Research*, 2002; 313–324

31. T. A. A. Adcock, P. H. Taylor and S. Draper, Nonlinear dynamics of wave-groups in random seas: unexpected walls of water in the open ocean, Proc. R. Soc. A., 2015; **471(**2184): 20150660.

32. P. Janssen, The interaction of ocean waves and wind, Cambridge: Cambridge University Press, 2004.

33. R. H. Gibbs and P. H. Taylor, Formation of walls of water in fully nonlinear simulations, *Applied Ocean Research*, 2005; **27**(3): 142-157.

34. M. Latheef, C. Swan and J. Spinneken, A laboratory study of nonlinear changes in the directionality of extreme seas, *Proc. R. Soc. A.*, 2017; **473**(2199): 20160290.